Studying Turbulence Using Numerical Simulation Databases - VIII

Proceedings of the 2000 Summer Program
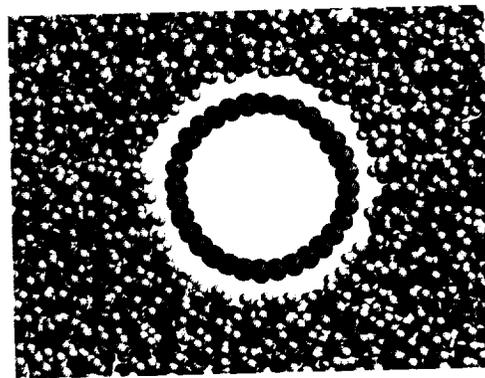
Center for Turbulence Research

November 2000

CONTENTS

iii

Preface

The eighth Summer Program of the Center for Turbulence Research took place in the four-week period, July 2 to July 27, 2000. This was the largest CTR Summer Program to date, involving forty participants from the U. S. and nine other countries. Twenty-five Stanford and NASA-Ames staff members facilitated and contributed to most of the Summer projects. Several new topical groups were formed, which reflects a broadening of CTR's interests from conventional studies of turbulence to the use of turbulence analysis tools in applications such as optimization, nanofluidics, biology, astrophysical and geophysical flows. CTR's main role continues to be in providing a forum for the study of turbulence and other multi-scale phenomena for engineering analysis. The impact of the summer program in facilitating intellectual exchange among leading researchers in turbulence and closely related flow physics fields is clearly reflected in the proceedings.

The development of the dynamic procedure at CTR has continued to generate renewed interest in LES over the past decade. During the Program, new averaging strategies, new equations and decompositions of the flow field using wavelets were evaluated and tested. In addition, efforts continued in modeling the near wall turbulence, which remains a pacing item, and in evaluating LES in predicting flow generated noise. The combustion group continued to attract researchers from around the world. Work on the development and assessment of combustion models was supplemented this year by a large efforts on evaluating the use of LES in industrial applications. The Reynolds Averaged Navier Stokes (RANS) modeling group continued its effort in developing models that capture the effects of rotation and stratification on turbulence. The ability of RANS models to predict transition was also evaluated. The program benefited from the infusion of novel new ideas from deterministic and stochastic optimization for flow control. These ideas were tested in optimizing microfluidic channels. A novel application of these optimization techniques was the use of evolutionary algorithms in developing strategies for the destruction of aircraft trailing vortices. The astrophysical group concentrated on proto-planetary disk modeling and simulation. New ideas and transformations of the governing equation promise new advances in this field in the near future. The geophysics group used DNS to study sediment transport on a wavy wall and the propagation of internal waves in the upper ocean thermocline. Finally, two new research topics were introduced to the CTR summer program, Nanofluidics and biology. The biology work on the life cycle of phytoplankton where turbulence plays a key role is a natural extension of CTR's expertise. The work on Nanofluidics which is based on molecular dynamics is an outgrowth of CTR's expertise in using advanced algorithms and large-scale simulations. Carbon nanotubes in water and flow in a nanometer-scale channel were simulated during the summer program.

As part of the Summer Program two review tutorials were given entitled: *Geophysical Turbulence and its Visible Consequences for the Giant Gaseous Planets - i.e., How Jupiter Earned its Stripes* (Phillip Marcus), and *Flamelet Modeling of Turbulent Reacting Flows* (Heinz Pitsch); and two seminars entitled *Molecular Dynamics Simulation* (Jonathan Freund), and *Immersed Boundary Technique for RANS/LES Simulations* (Gianluca Iaccarino) were presented. A number of colleagues from universities, government agencies, and industry attended the final presentations of the participants on July 27 and participated in the discussions.

There are twenty-nine papers in this volume grouped in six areas. Each group is pre-

2

ceded with an overview by its coordinator. Early reporting of eleven of the projects occurred at the Fiftieth Meeting of the Division of Fluid Dynamics of the American Physical Society in Washington, D.C., November 19-21, 2000.

This year's Summer Program was the last for Debra Spinks, the Center's long-term administrative associate, who has done an outstanding job of organizing the last seven programs and compiling the corresponding reports. She shall be missed, but carries with her our best wishes for success in her new position at Stanford.

Parviz Moin
William C. Reynolds
Nagi N. Mansour

The nanofluidics and biology group

The projects in this group draw on the considerable experience at CTR in using advanced algorithms and large-scale simulation used to analyze turbulence related phenomena. This group applied these capabilities to two new areas: nanofluidics and biological flows.

Nanofluidics plays an important role in biodetectors, tribology, and diffusion through porous media, and anywhere that non-continuum or discrete molecular effects play a significant role. Two projects studied nanofluidics. Walther, Jaffe, Halicioglu, and Koumoutsakos studied the interaction of water with carbon nanotubes, whose size and unique physical and electrical properties make them attractive building blocks for nanostructures. They have been proposed as ultra-fine tips for atomic force microscopes for probing complex molecules and for use in biosensors, both of which involve interactions with water. Yet their interaction with water is not well understood. Atomistic simulations were used to determine conditions for two nanotubes suspended in water to attract and to study their general hydro-phobic/-phyllic properties.

Similar atomistic simulation techniques were used by Freund to examine the details of electro-osmotic flow in a nanometer-scale channel. In electro-osmosis, an applied electric field pulls counter ions distributed above a charge surface to induce a net flow. This pumping mechanism is used in present-day micron-scale devices, often for biosensor application. However, the flow is driven by a near-wall nanometer-scale layer which is small enough to be studied atomistically. This project simulated the electro-osmotic flow of a aqueous solution of Cl^- in a 50Å wide channel. Differences were found between the present simulation results and standard theories that assume infinitesimal ions and constant dielectric properties.

In addition to studies of these physical systems, considerable progress was made in developing and implementing efficient algorithms for atomistic simulations. Walther, Jaffe, Halicioglu, and Koumoutsakos discuss a new formulation of the P^3M method for computing long-range electrostatic interactions. Freund and Darve implemented an efficient P^3M algorithm for a $1/r^6$ inter-atomic force potential which is being used in ongoing surface tension research. Some of the computer codes used in these studies have also been transferred to researchers in the Astrobiology Branch of NASA Ames for studying molecular biophysics. Collaboration with this group is ongoing.

Ghosal, Rogers, and Wray examined the role of turbulence in the life cycle of phytoplankton, which affect global ecology and sustain oceanic food chains. In the short term, phytoplankton impact people via the health of fisheries; in the long term, since their carbon uptake counters carbon-dioxide emissions from the burning fossil fuels, their response to increased carbon in the atmosphere and warmer seas will impact global climate. Because many phytoplankton are non-swimming and actually sink, turbulence is essential in transporting them and maintaining healthy populations in the sunlit upper layers of bodies of water. This project used population models in conjunction with simulation data to study the role of turbulence in their population dynamics.

Jonathan Freund

Molecular dynamics simulations of carbon nanotubes in water

By J. H. Walther†, R. Jaffe‡, T. Halicioglu‡ AND P. Koumoutsakos†¶

We study the hydrophobic/hydrophilic behavior of carbon nanotubes using molecular dynamics simulations. The energetics of the carbon-water interface are mainly dispersive but in the present study augmented with a carbon quadrupole term acting on the charge sites of the water. The simulations indicate that this contribution is negligible in terms of modifying the structural properties of water at the interface.

Simulations of two carbon nanotubes in water display a wetting and drying of the interstice between the nanotubes depending on their initial spacing. Thus, initial tube spacings of 7 and 8 Å resulted in a drying of the interface whereas spacing of > 9 Å remain wet during the course of the simulation.

Finally, we present a novel particle-particle-particle-mesh algorithm for long range potentials which allows for general (curvilinear) meshes and "black-box" fast solvers by adopting an influence matrix technique.

1. Introduction

The unique mechanical and electrical properties of carbon nanotubes (see Odom *et al.* (2000)) have prompted an interest for technical application in a number of fields including biosensors (Balavoine *et al.* (1999)), atomic force microscopy (Jarvis *et al.* (2000); Moloni *et al.* (1999); Li *et al.* (1999)), and fuel storage (Wang & Johnson (1999); Rzepka *et al.* (1998); Gordon & Saeger (1999); Lee & Lee (2000)). A key aspect of these applications is the interaction of the surrounding fluid with the carbon nanotube and, in particular, the hydrophobic/hydrophilic behavior of carbon nanotubes.

The graphite-water interface is known to be strongly hydrophobic (e.g. Müller *et al.* (1996)) and to exhibit a preferred orientation of the water dipole moment parallel to the interface (Ulberg & Gubbins (1995), Allen *et al.* (1999), and Shevade *et al.* (1999)). Most of the studies on graphite-water systems have involved planar interfaces or idealized geometries (Wallqvist & Berne (1995)). The presence of an electrostatic quadrupole moment interaction between graphite and water as proposed by Vernov & Steele (1992) and subsequently measured by Whitehouse & Buckingham (1993) has mostly been neglected in the previous studies. Marković *et al.* (1999, 2000) included the quadrupole interaction in their numerical study of water scattering from a graphite surface, but did not provide information of the importance of this term. Thus, to study the structural properties of water surrounding a carbon nanotube, we perform detailed molecular dynamics simulations of a 12.52 Å diameter carbon nanotube with chirality (16,0) in water (see Fig. 1) using Morse harmonic bond potentials and Lennard-Jones potentials to model the carbon nanotube and the flexible model for water by Teleman *et al.* (1987). We include

† Inst. of Computational Sciences, ETH Zürich, Switzerland
‡ NASA Ames Research Center, USA
¶ also at Center for Turbulence Research, NASA Ames/Stanford Univ.
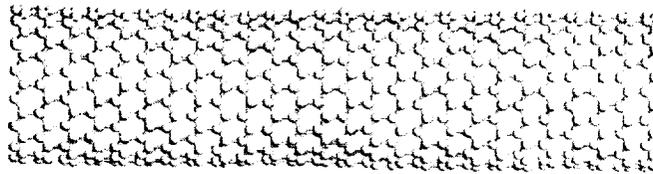
FIGURE 1. Sketch of the carbon nanotube.

and compare the effect of the electrostatic quadrupole as suggested in Vernov & Steele (1992).

Another important issue related to the carbon-water interface is the wetting and drying of the interstices in a bundle of carbon nanotubes. The drying can lead to hydrophobic aggregation of the tubes (Lum *et al.* (1999)), changing the mechanical and electrostatic properties of the system. Thus, in the second part of the study, we consider two carbon nanotubes in water initially aligned and with an initial spacing S_0 between the carbon nanotube walls.

2. Governing equations and solution procedure

The carbon nanotube-water system is modeled using classical molecular dynamics simulations in the micro canonical (NVE) ensemble. The governing Newton's equations are integrated in time using the leap frog scheme (Allen & Tildesley (1987)) subject to periodic boundary conditions.

The water is described by the flexible (TJE) water model of Teleman *et al.* (1987) featuring harmonic bonds between the oxygen and hydrogen sites, which also holds the partial charges.

The restrictions imposed on the time integrator by the eigen-frequency of water of the order of $3500\,\mathrm{cm}^{-1}$ (Dang & Pettitt (1987)) are not too severe since the highest eigen-frequency of the carbon nanotube is of the order of $1500\,\mathrm{cm}^{-1}$ (Saito *et al.* (1998)). Thus, a time step of $\delta t = 0.2\,\mathrm{fs}$ proved sufficient for stability and conservation of energy and has been used throughout.

2.1. *Potentials*

2.1.1. *Carbon nanotube*

The carbon nanotube is modeled by a Morse bond, a harmonic cosine angle, and a 2-fold torsion potential as

$$U(r_{ij}, \theta_{ijk}, \phi_{ijkl}) = K_{Cr}(\xi_{ij} - 1)^2 + \frac{1}{2}K_{C\theta}(\cos\theta_{ijk} - \cos\theta_C)^2 + \frac{1}{2}K_{C\phi}(1 - \cos 2\phi_{ijkl}),$$
(2.1)

where

$$\xi_{ij} = e^{-\gamma(r_{ij} - r_C)},$$
(2.2)

and θ_{ijk} and ϕ_{ijkl} represent all the possible bending and torsion angles, and r_{ij} represents all the distances between bonded atoms. K_C, $K_{C\theta}$, and $K_{C\phi}$ are the force constants of the bond, angle, and torsion potentials, respectively, and r_C, θ_C, and ϕ_C are the corresponding reference geometry parameters for graphene. The Morse and angle parameters given by Guo *et al.* (1991) and Tuzun *et al.* (1996) are listed in Table 1.

$$
\begin{array}{llll}
K_{Cr} & = & 478.9\,\mathrm{kJ\,mol^{-1}\AA^2} & r_C & = & 1.418\,\mathrm{\AA} \\
K_{C\theta} & = & 562.2\,\mathrm{kJ\,mol^{-1}} & \theta_C & = & 120.00^\circ \\
K_{C\phi} & = & 25.12\,\mathrm{kJ\,mol^{-1}} & \gamma & = & 2.1867\,\mathrm{\AA^{-1}} \\
\epsilon_{CC} & = & 0.4396\,\mathrm{kJ\,mol^{-1}} & \sigma_{CC} & = & 3.851\,\mathrm{\AA}
\end{array}
$$

TABLE 1. Parameters for the carbon interaction potentials (Tuzur *et al.* (1996) and Rappé *et al.* (1992)). K_{Cr}, r_C, and γ are the parameters for the Morse potential, $K_{C\theta}$ and θ_C are the angle parameters, and $K_{C\phi}$ is the torsion parameter. ϵ_{CC} and σ_{CC} are the Lennard-Jones parameters for the carbon-carbon interaction.

The Morse bond and angle terms maintain the C-C bond length and hexagonal ring structure of the carbon nanotube, and the torsion term is needed to provide a measure of the strain due to curvature of the reference graphene sheet. This curvature strain prevents collapse of the nanotobe and imparts stiffness with respect to bending deformations. To obtain a physically reasonable torsion parameter, quantum chemistry calculations were carried out for planar and curved tetracene ($C_{18}H_{12}$), which consists of 4 hexagonal rings fused together in a strip-like part of the circumference of a zigzag carbon nanotube. The calculations were carried out using the Gaussian98 software package (Frisch *et al.* (1998)). Tetracene is planar with a 9.778 Å separation between the C-C bonds on opposite ends of the molecule. If the tetracene molecule were extracted from a $(16,0)$ nanotube and held rigid such that end-to-end separation would be 8.795 Å. Quantum chemistry calculations were carried out using density functional theory (DFT) with the hybrid nonlocal B3LYP functional (Becke (1993)) as implemented in the Gaussian98 software package. For each amount of curvature, the molecular geometry was completely optimized except for the end-to-end distance constraint. The energy difference between the curved and planar tetracene molecules (ΔE_{curv}) was determined to be 71.11 kJ mol^{-1} using the standard 6-31G(d) contracted Gaussian atomic orbital basis set. The curvatures considered were appropriate for $(n,0)$ nanotubes with $n = 12, 24$. The torsion parameter $K_{C\phi}$ was determined from

$$
K_{C\phi} = 2\Delta E_{curv} \left(\sum_i^{84} 1 - \cos 2\phi_i \right)^{-1}, \tag{2.3}
$$

with the summation over the complete set of 84 torsion angles in the optimized curved tetracene molecule (4 for each C-C bond). For all cases studied, $K_{C\phi}$ was between 24.60 and 25.25 kJ mol^{-1}. The value of 25.12 kJ mol^{-1} was selected for the present study.

A Lennard-Jones term is furthermore added to account for the steric and van der Waals carbon-carbon interaction

$$
U(r_{ij}) = 4\epsilon_{CC} \left[\left(\frac{\sigma_{CC}}{r_{ij}} \right)^{12} - \left(\frac{\sigma_{CC}}{r_{ij}} \right)^6 \right]. \tag{2.4}
$$

where ϵ_{CC} and σ_{CC} are obtained from the UFF force field (Rappé *et al.* (1992)), see Table 1.

The bond potentials can be efficiently computed on scalar and vector architectures, in the latter case by rearranging the list of carbon bonds to secure vectorization. The non-bond Lennard-Jones potential is computed using a standard cell index table and spherical truncation.

$$
\begin{array}{llll}
K_{Wr} & = & 4637 \, \text{kJ} \, \text{mol}^{-1} \text{Å}^2 & r_W & = & 1.0 \, \text{Å} \\
K_{W\theta} & = & 383 \, \text{kJ} \, \text{mol}^{-1} \text{rad}^2 & \theta_W & = & 109.47^\circ \\
\epsilon_{OO} & = & 0.65017 \, \text{kJ} \, \text{mol}^{-1} & \sigma_{OO} & = & 3.166 \, \text{Å} \\
q_O & = & -0.82 \, \text{e} & q_H & = & 0.41 \, \text{e}
\end{array}
$$

TABLE 2. Parameters for the flexible (TJE) water model (Teleman *et al.* (1987)).

2.1.2. *Water model*

The flexible water model is described by harmonic bonds between the hydrogen-oxygen sites as

$$
U(r_{ij}, \theta_{ijk}) = \frac{1}{2} K_{Wr}(r_{ij} - r_W)^2 + \frac{1}{2} K_{W\theta}(\theta_{ijk} - \theta_W)^2, \tag{2.5}
$$

where K_{Wr} and $K_{W\theta}$ are the parameters of the potential and $r_W = 1.0$ Å the reference bond length and angle $\theta_W = 109.47^\circ$ in (Teleman *et al.* (1987)).

Non-bonded interactions between the water molecules involve a Lennard-Jones term between the oxygen atoms

$$
U(r_{ij}) = 4\epsilon_{OO} \left[\left(\frac{\sigma_{OO}}{r_{ij}} \right)^{12} - \left(\frac{\sigma_{OO}}{r_{ij}} \right)^6 \right], \tag{2.6}
$$

and a Coulomb potential

$$
U(r_{ij}) = \frac{1}{4\pi\epsilon_0} \frac{q_i q_j}{r_{ij}}, \tag{2.7}
$$

where ϵ_0 is the permittivity in vacuum, and q_i is the partial charge, $q_O = -0.82$ and $q_H = 0.41$, respectively (Teleman *et al.* (1987)). The Coulomb interaction is computed using a smooth truncation as

$$
U(r_{ij}) = \frac{1}{4\pi\epsilon_0} \left(\frac{q_i q_j}{r_{ij}} - E_s(r_{ij}) \right), \tag{2.8}
$$

where $E_s(r_{ij})$ is a smoothing function

$$
E_s(r_{ij}) = \frac{q_i q_j}{r_c} - (r_{ij} - r_c)\frac{q_i q_j}{r_c^2}, \tag{2.9}
$$

and r_c the radius of truncation (Levitt *et al.* (1997)). The truncation of the Coulomb potential has been shown to have little effect on the thermodynamic and structural properties of water for cutoffs larger than 6 Å (Andrea *et al.* (1984)), and in this study we employ a value of 9.50 Å ($3\sigma_{OO}$) The parameters of the potential are summarized in Table 2.

Alternatively, the Coulomb potential can be computed without truncation using the P^3M algorithm as described in Section 4.

2.1.3. *Carbon-water interaction*

The carbon-water interaction consists of a Lennard-Jones term between the carbon and oxygen sites

$$
U(r_{ij}) = 4\epsilon_{CO} \left[\left(\frac{\sigma_{CO}}{r_{ij}} \right)^{12} - \left(\frac{\sigma_{CO}}{r_{ij}} \right)^6 \right], \tag{2.10}
$$
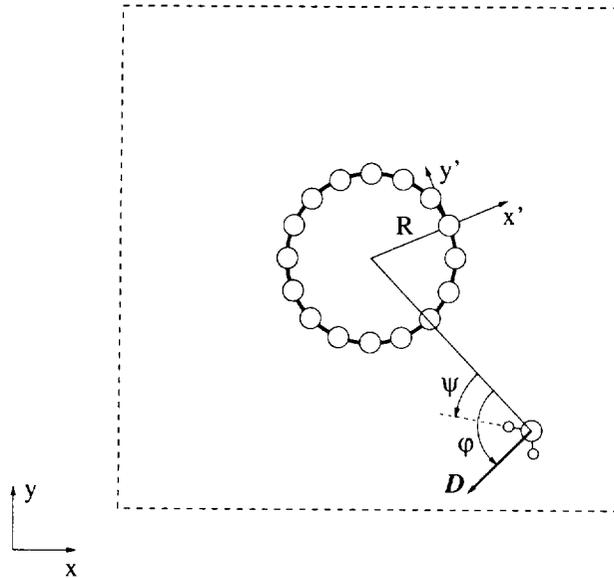
FIGURE 2. Sketch of the carbon nanotube-water system. R is the radius of the carbon nanotube, and D the water dipole moment. (x', y') is the local co-ordinate system used in the calculation of the quadrupole interactions. The orientation of the water molecules is given in terms of the angles φ and ψ. The dashed box indicates the position of the periodic boundary.

where parameters of the potential ϵ_{CO} and σ_{CO} are obtained from Vernov & Steele (1992), and a quadrupole interaction between the carbon atoms and the partial charges on the water hydrogen and oxygen atoms

$$U(r_\alpha, r_\beta) = \frac{1}{3}\frac{q}{4\pi\epsilon_0}\sum_{\alpha,\beta}\Theta_{\alpha,\beta}\frac{3r_\alpha r_\beta - r^2\delta_{\alpha\beta}}{r^5},\tag{2.11}$$

where α, β run over all Cartesian co-ordinates x, y, z, and r is the distance between the charge site and the quadrupole carbon site. $\delta_{\alpha\beta}$ is the delta function, and $\Theta_{\alpha,\beta}$ is the quadrupole moment tensor (Hansen & Bruch (1995)).

In the present study, we evaluate Eq. (2.11) in a local co-ordinate system (x', y', z') centered at the quadrupole site, see Fig. 2. If x' is the wall normal direction we have

$$\Theta_{xx} = -2\Theta_{yy} = -2\Theta_{zz},\tag{2.12}$$

with all other components equal to zero (see Hansen & Bruch (1995)). The quadrupole interaction is truncated at $r = r_c$, where r_c is the cutoff radius of the Lennard-Jones and Coulomb potentials. Note that the effect of the quadrupole moment is an attraction of positive charge (hydrogen) towards the nanotube wall and conversely a repulsion of negative charge (oxygen). The parameters for the carbon-water potentials are summarized in Table 3.

2.2. Simulation details

The water molecules are initially placed on a regular lattice, and the system is equilibrated to obtain the desired temperature and bulk density of the water. The equilibration is divided into two parts for the cases involving two carbon nanotubes. In the first part, the nanotubes are held at a fixed position ("frozen") in order to allow the water molecules

$$\epsilon_{CO} \;=\; 0.3126 \,\mathrm{kJ\,mol^{-1}} \quad \sigma_{CO} \;=\; 3.19\,\text{Å} \quad \Theta_{\alpha,\beta} \;=\; 3.03 \times 10^{-40}\,\mathrm{Cm^2}$$

TABLE 3. Parameters for the carbon-water interaction potentials, (see Vernov & Steele (1992) and Whitehouse & Buckingham (1993)).

to "settle" between the tubes. The carbon nanotubes are released in the second part of the equilibration which involves thermal equilibration and are free to move during the remainder of the simulation. The temperature control is performed by scaling the velocity of the atoms every 500 time steps (every 0.1 ps) and is switched off after the equilibration at 4 ps.

The volume of the computational box is adjusted to match the target density of water in the far-field. The regulation of the volume is performed by re-positioning the periodic boundary in the $x - y$ plane (see Fig. 2) while keeping the extent of the box in the z-direction fixed. This procedure prevents any deformation of the carbon nanotube during the volume adjustment.

3. Results

The molecular dynamics simulations involve single and a pair of carbon nanotubes in water at a temperature of 300 K and a bulk water density of $\rho_0 = 997\,\mathrm{kg\,m^{-3}}$. The carbon nanotube is a $(16,0)$ nanotube with a radius (R) in vacuum of 6.26 Å, and the length of the computational box (L) is $8.6R$ (53.8 Å).

The results are presented in terms of radial density and probability density profiles of the orientation of the water dipole moment $(P(\cos\varphi))$ and the orientation of the OH bonds $(P(\cos\psi))$ (see Fig. 2) where

$$P(\cos\varphi) = \frac{<\cos\varphi>_r + 1}{2}, \qquad P(\cos\psi) = \frac{<\cos\psi>_r + 1}{2}, \qquad (3.1)$$

and $< \ldots >_r$ denotes the average value at the position r. Notice that $\cos\varphi = +1$ indicates a direction along the outward surface normal, $\cos\varphi = 0$ a direction parallel to the normal, and $\cos\varphi = -1$ a direction in the negative surface normal. The profiles are sampled every 20 fs in 30 bins of constant volume extending from the surface of the nanotube.

Studies of bulk water and water with a free surface (slab) are provided as a reference. The average potential energies of the bulk are found in good agreement with previous studies using the same TJE water model by Teleman *et al.* (1987) (TJE), Wallqvist & Teleman (1991) (WT), and Mizan *et al.* (1994) (MSZ), see Table 4.

3.1. Single carbon nanotube

To study the influence of the quadrupole moment on the structural properties of water at the carbon-water interface, we have conducted simulations of one carbon nanotube in water. The nanotube consists of 832 carbon atoms and the water consists of 2088 water molecules. The system is equilibrated until the energetics settle around 4 ps, and the statistics are collected every 20 fs until $t = 40$ ps, a total of 1800 samples. The numerical parameters are summarized in Table 5.

The simulations of both one and two carbon nanotubes in water revealed damped oscillations of the potential energy of the carbon-carbon Lennard-Jones interaction with

		TJE	WT	MSZ	present work
Bond length	(Å)	1.016	1.017	1.016	1.017
Bond angle	(degree)	104.9	104.9	104.9	104.9
Dipole	(D)	2.43	2.44	2.43	2.44
U_{inter}	(kJ mol^{-1})	-45.3	-47.5	-47.3	-48.2
U_{intra}	(kJ mol^{-1})	5.1	6.3	6.3	6.2
U_{pot}	(kJ mol^{-1})	40.1	-40.7	-41.0	-41.9

TABLE 4. Comparison of present bulk properties with the results of Teleman *et al.* (1987) (TJE), Wallqvist & Teleman (1991) (WT), and Mizan *et al.* (1994) (MSZ).

Case	QP	N_W	N_C	t_m(ps)	type
1	no	2088	832	39	SCN
2	yes	2088	832	39	SCN
3	–	729	0	62	bulk
4	–	729	0		slab
5	–	–	832	39	vacuum

TABLE 5. Simulation cases for a single carbon nanotube (SCN), bulk and slab simulations, and a carbon nanotubes in vacuum. N_W is the number of water molecules, N_C is the number of carbon atoms, and t_m is the total simulation time.

a frequency in the range of $200 \, \text{cm}^{-1}$. A separate simulation of one carbon nanotube in vacuum was prepared to estimate the eigen-frequencies of the tube, in particular the breathing frequency A_g (the first radial mode) of the tube. Monitoring the potential energy of the carbon-carbon Lennard-Jones interaction revealed a frequency of $173 \, \text{cm}^{-1}$ in good agreement with the theoretical value of $180 \, \text{cm}^{-1}$ (Saito *et al.* (1998)). The correlation between the carbon-carbon Lennard-Jones energy and the motion of the tube was verified in a separate simulation in vacuum in which radial oscillations where specifically imposed (not shown).

The radial density profiles of hydrogen and oxygen are shown in FIg. 3a and 3b for the cases excluding and including the quadrupole moment. The maxima of the oxygen and hydrogen profiles nearly coincide near the interface, indicating that the plane of the water molecules is parallel to the interface. These profiles are markedly different from those of the liquid-vapor interface (see Fig. 4), exhibiting a characteristic layering and a presence of hydrogen atoms beyond the extent of the oxygen atoms (at $r/R < 1.4$).

The density profiles are, in general, in good agreement with the study of Wallqvist (1990) for polarizable water in contact with a smooth wall and with grand canonical Monte Carlo simulations of water adsorption in graphite pores by Ulberg & Gubbins (1995).

The orientation of the water molecules at the carbon-water interface is inferred from the orientation of the water dipole moment as shown in Fig. 5. The water molecules in the closest proximity of the nanotube ($r/R = 1.47 - 1.55$) display a small inclination of $\approx 4°$ towards the nanotube and turn to $74°$ (an inclination of $16°$ towards the bulk) at the point of minimum density ($r/R = 1.71 - 1.78$). The bulk properties are reached at
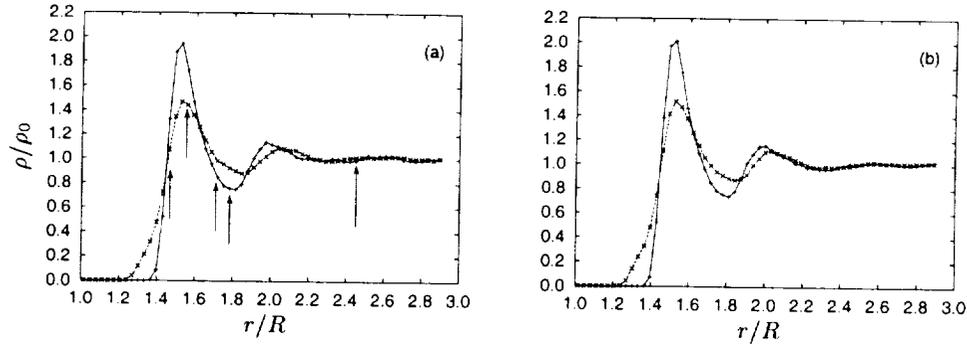
FIGURE 3. Water radial density profile. The arrows indicate the location of the bins used in the dipole orientation. (a) excluding the quadrupole moment; (b) including the quadrupole moment. -+-: oxygen density profile; -×-: hydrogen density profile.
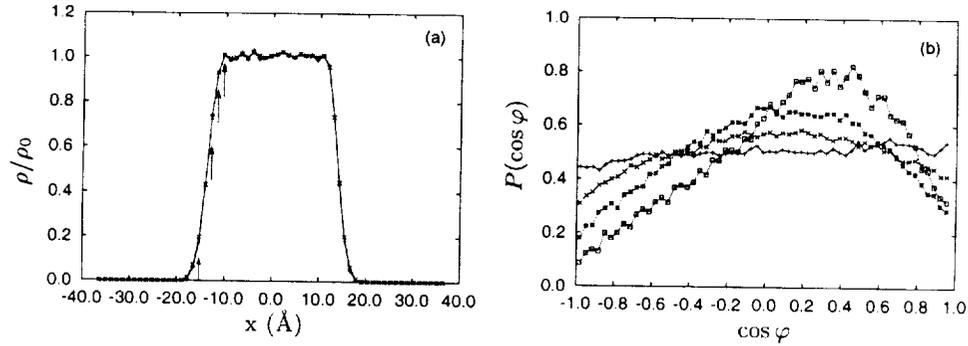
FIGURE 4. Density profile (a) and orientation of the water dipole moment (b) for a slab of water. The arrows in (a) indicate the the positions of the bin shown in (b): -+-: $x = -15.31$ Å; -×-: $x = -12.85$ Å; -*-: $x = -11.62$ Å; -□-: $x = -10.39$ Å.
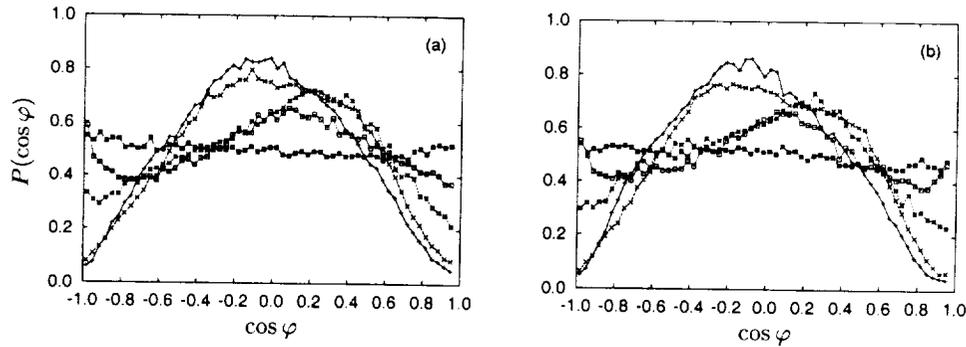
FIGURE 5. Dipole orientation at different distances from the carbon nanotube wall. (a) without the quadrupole moment; (b) with the quadrupole moment. -+-: $r/R = 1.47$; -×-: $r/R = 1.55$; -*-: $r/R = 1.71$; -□-: $r/R = 1.78$; -■- : $r/R = 2.45$.

$r/R \geq 2.4$. These results are in good agreement with the work of Wallqvist (1990) and with the study of (ST2) water between hydrophobic surfaces by Lee *et al.* (1984).

Finally, we consider the orientation of the OH bonds as shown in Fig. 6. At $r/R = 1.47$ the OH bonds are directed towards the nanotube with an angle of $\approx 4°$, indicating that
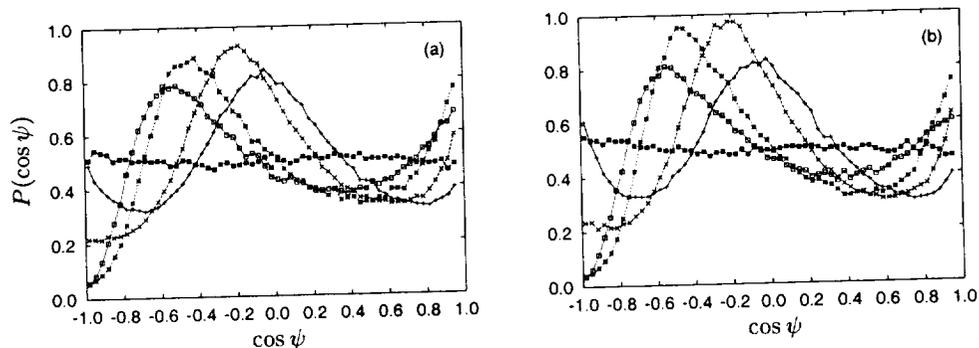
FIGURE 6. Orientation of the OH bonds at different distances from the carbon nanotube wall. (a) without the quadrupole moment; (b) with the quadrupole moment. -+- : $r/R = 1.47$; -×- : $r/R = 1.55$; -*- : $r/R = 1.71$; -□- : $r/R = 1.78$; -■- : $r/R = 2.45$.
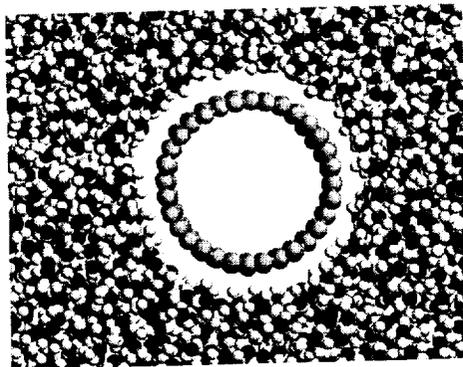
FIGURE 7. Snapshot of the atoms for the simulation of a single carbon nanotube in water. The interaction potentials include an electrostatic quadrupole moment (case 2).

the HOH plane is nearly parallel to the interface. A bimodal profile is observed for $r/R \leq 1.55$ with a high probability at 101°, 117°, and 123° for $r/R = 1,71$, 1.78, and 2.45, respectively. From these structural properties of water, we conclude that the effect of the quadrupole moment on the density and dipole moment profiles is clearly small, but it appears to increase the probability of the extrema of the OH orientation. However, since the contribution from the quadrupole moment to the total carbon-water energetics is of the order of 0.1 %, further studies are being conducted to confirm these findings. A snapshot from the simulation including the quadrupole moment (case 2) is shown in Fig. 7. One can see a large number of hydro atoms on the nanotube side of the interfacial layer

3.2. Twin carbon nanotubes

The second part of the study involves two carbon nanotube in water, with each tube consisting of 832 atoms and a total of 4536 water molecules present. Four simulations have been performed, including three different initial tube spacings ($S_0 = 7$, 8, and 9 Å), and a sensitivity study has been conducted to determine the influence of the equilibration procedure. The number of water molecules and their initial positions are identical for each simulation, and only the initial spacing of the nanotubes is varied. The simulations are performed in the canonical ensemble, heating the system every 500 time steps (every
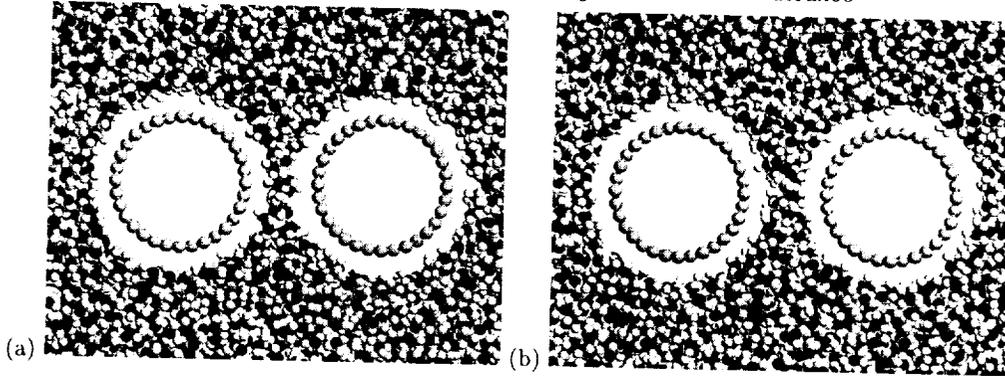
FIGURE 8. Snapshots of the water molecules after equilibration at 2 ps. (a): initial tube spacing of 7 Å (case 6); (b): initial tube spacing of 8 Å (case 7).

Case	$t_f/\delta t$	$t_h/\delta t$	S_0(Å)	N_W	N_C
6	10000	500	7.0	4536	1664
7	10000	500	8.0	4536	1664
8	10000	500	9.0	4536	1664
9	50000	500	7.0	4536	1664

TABLE 6. Simulation cases for a two carbon nanotubes. δt is the time step size, t_f the "freezing" time of the carbon nanotubes, $1/t_h$ the heating frequency, S_0 the initial distance between the nanotube walls, N_W the number of water molecules, and N_C the number of carbon atoms.

0.1 ps), but simulations in the micro canonical ensemble gave similar results (not shown). The equilibrated systems are shown in Fig. 8 for the two cases with an initial spacing of 7 Å and 8 Å, respectively. The numerical parameters are listed in Table 6.

The time history of the separation $S(t)$ between the carbon nanotubes is shown in Fig. 9 for the four cases. The simulation involving an initial tube spacing of 7 Å exhibits a decrease in spacing when the tubes are "released" after 10,000 time steps (2 ps). The spacing reaches a plateau of 5.8 Å at 4 ps but continues to decrease after 10 ps and reaches an equilibrium spacing of 3.49 ± 0.06 Å at 17 ps. This "drying" of the interface is in agreement with the studies on stacked plates by Wallqvist & Berne (1995), who showed that stable configurations of water in a hydrophobic environment requires the presence of two or more layers of water. Indeed, the level of the plateau coincides with the thickness of one layer of water $\approx 2\sigma_{OO} = 6.3$ Å. The position of the atoms during the drying is shown in Fig. 10.

An additional simulation was conducted to study the effect of the duration of the initial "freezing" of the nanotube. The equilibration was extended to 10 ps (case 9), but with a persistent drying of the interface cf. Fig. 9.

A similar time history is observed for the nanotube starting from an initial spacing of 8 Å. The plateau is reached after 7 ps, and the tube spacing decreases rapidly after 9–10 ps to reach the equilibrium distance after 12 ps.

Finally, the nanotubes placed with an initial spacing of 9 Å (case 8) remain wetted during the simulation cf. Fig. 9. This spacing is consistent with the thickness of two water layers of 9.2 − 10.2 Å depending on the staggering of the carbon-oxygen system.
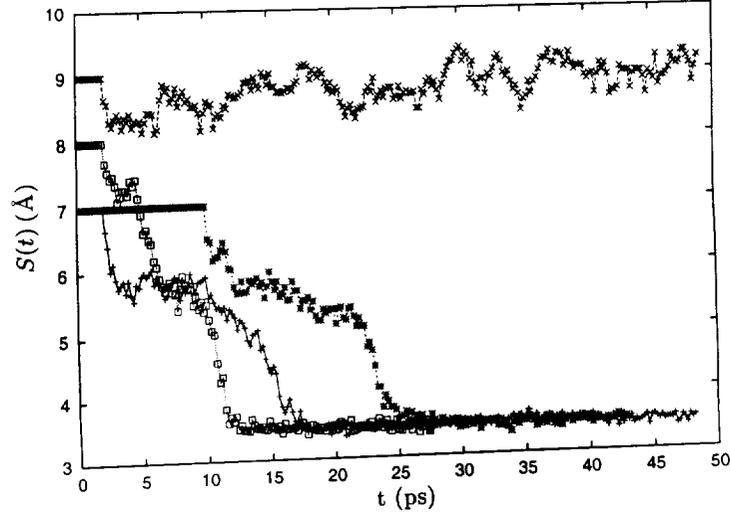
FIGURE 9. Time history of the spacing between two carbon nanotubes in water. —+—: Case 6;
—□—: Case 7; —x—: Case 8; —*—: Case 9.

4. P³M algorithm

The smooth truncation of long range potentials (eg. the Coulomb potential) is a viable approach for homogeneous systems ie. where the system is locally neutral $\sum_i q_i = 0$ (where q_i is the "generalized charge" or the strength of the particle). In molecular dynamics simulations neutral systems are often assumed, whereas such an assumption is invalid in astrophysics (where q_i corresponds to mass) and in fluid dynamics (where q_i corresponds to circulation or vorticity). For these problems and for simulations requiring higher accuracy than warranted by the smooth truncation, the Particle-Particle-Particle-Mesh algorithm (P³M) is an efficient alternative. The algorithm gains it efficiency by employing fast Fourier transforms on a regular mesh for the solution of the Poisson equation for the electrostatic potential (Φ)

$$\nabla^2 \Phi = -\frac{\rho}{\epsilon_0},$$ (4.1)

where ρ is the charge density and its accuracy by a local particle-particle correction to resolve any sub-grid scales not properly resolved by Eq. (4.1). Sub-grid scale are present if the projected charge density is a smooth approximation to the true charge density, which is normally the case in molecular dynamics simulation, but not the case in particle (vortex) methods. The original method by Hockney & Eastwood (1988) proceeds as follows:

- Project the particle charge onto the mesh to obtain the charge density (ρ).
- Solve Eq. (4.1) for the electrostatic potential (Φ).
- Compute the electrostatic field on the mesh as $E = -\nabla \phi$.
- Project the electrostatic field onto the particles and compute the resolved particle force as: $\tilde{f}_i = q_i E(x_i)$.
- Compute the sub-grid scale forces as a local particle-particle correction, $C(r_{ij})$.
- The total particle force is $f_p = \tilde{f}_p + C$, where C is the total sub-grid force.
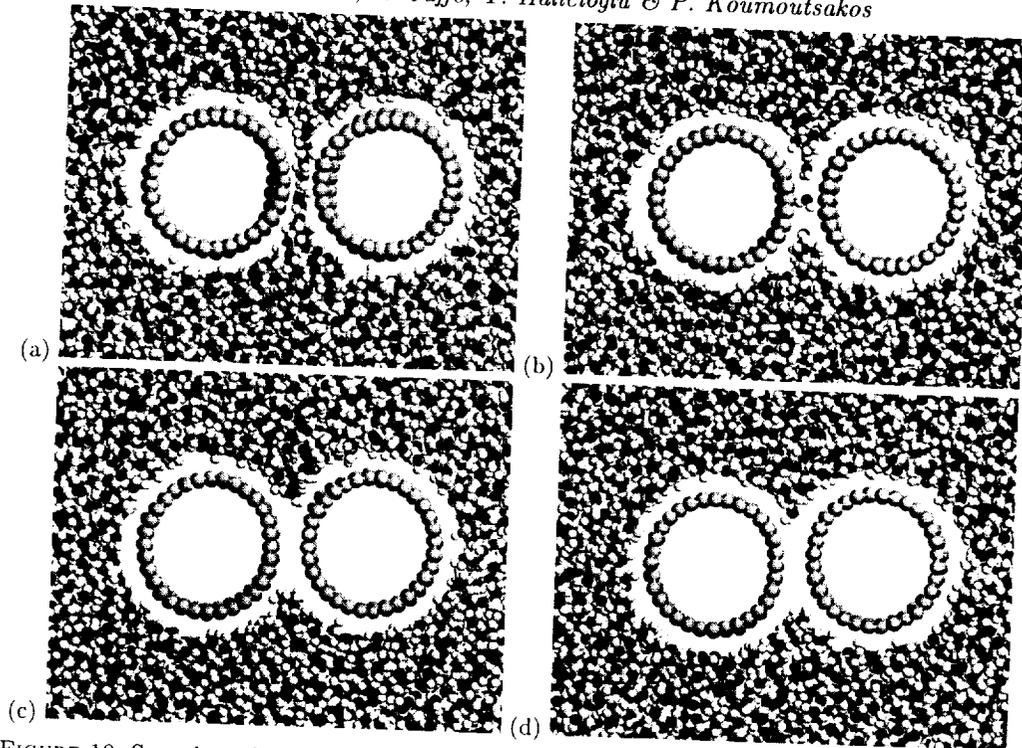
FIGURE 10. Snapshot of the water molecules during the drying process for case 7 at $t = 12$, 14, 16, and 18, ps (a-d), respectively.
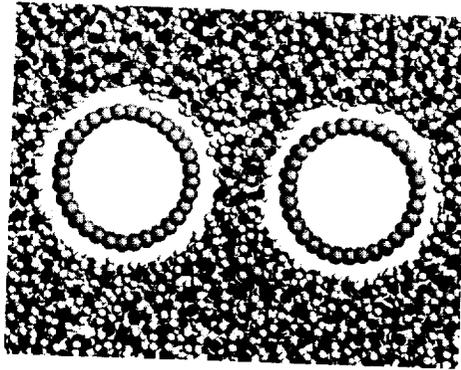
FIGURE 11. Snapshot of the water molecules during wetting (case 8) at $t = 18\,\mathrm{ps}$.

The success of the Hockney & Eastwood (1988) algorithm is based on an inversion of the Poisson equation

$$\Phi(x) = \int G(x - y) * \rho\,\mathrm{d}y, \qquad (4.2)$$

where G is the Green's function to ∇^2. The convolution (4.2) is computed in Fourier space employing an "optimized" Green's function ($\hat{\Phi} = \hat{G}_{opt} * \hat{\rho}$) to secure a prescribed and isotropic sub-grid scale ie. $C(x_i - x_j) = C(r_{ij})$, where $r_{ij} = |x_i - x_j|$.

An alternative P^3M algorithm proposed by Theuns (1994) estimates the resolved (anisotropic) electrostatic potential from the projected charge density by computing the
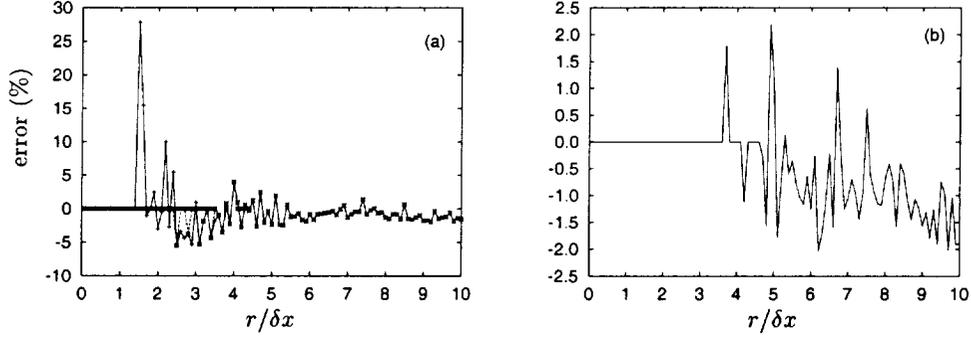
FIGURE 12. Comparison between the P^3M forces and the exact force for two particles in a periodic domain. The different curves in (a) demonstrate the effect of the cutoff radius (r_c) of the particle-particle correction. -+-: $r_c/h = 1$; -x-: $r_c/h = 2$; -□-: $r_c/h = 3$. (b) shows the error on a test particle displaced from a group of 10^4 particles centered in the computational domain.

convolution in real space as

$$\tilde{E}(x_j) \approx \frac{h^3}{4\pi\epsilon_0} \sum_i^M \rho_i \frac{x_i - x_j}{|x_i - x_j|^3}, \tag{4.3}$$

where h is the mesh spacing and M is the number of mesh points involved in the project step. The algorithm proceeds by subtracting this estimate for the resolved field for particles in close proximity, and the corresponding local particle-particle correction is the exact $1/r$ relation.

The present algorithm replaces the approximate convolution in real space (4.3) by an influence matrix technique as

$$\mathcal{E}_i^h = \mathcal{M}_{ij}^h \mathcal{R}_j^h, \tag{4.4}$$

where $\mathcal{M}_{ij}^h$ is the influence matrix describing the electrostatic field $\mathcal{E}_i^h$ at the i-th grid point as induced by the charge density $\mathcal{R}_j^h$ at the j-th grid point. The size of the vectors $\mathcal{E}_i^h$ and $\mathcal{R}_j^h$ is governed by the number of mesh points involved in the projection and the number of nearest grid points included in the particle-particle correction. The algorithm is described in more detail in (Walther & Koumoutsakos (2000)).

To demonstrate the accuracy of the present P^3M algorithm, we consider the electrostatic force between two charged particles in a periodic domain and study the errors for different particle spacings and for different cutoff distances (r_c) for the particle-particle correction. The difference between the P^3M force and the value compute by direct summation over a large number of images is shown in Fig. 12a. The present P^3M algorithm is exact for the particle within the cutoff and is dominated by the inherent errors on the mesh. In the present case, the errors are of the order of 30%, 10%, and 5%, for $r_c/h = 1$, 2 and 3, respectively.

A second test case involves 10^4 charged particles uniformly distributed at the center of the domain, and we consider the error of the force on a test particle at different distance from the group (see Fig. 12b). For this case, the maximum error is of the order of 2% for $r_c/h = 3$.

5. Summary and conclusions

We have presented molecular dynamics simulations of the hydrophobic/hydrophilic nature of carbon nanotubes in water. Using a detailed description of the carbon nanotube and classical potentials for the carbon-water interaction including an electrostatic quadrupole moment acting between the carbon atoms and the charge sites on the water, we find structural properties of water similar to those found for water at a idealized graphite surface. However, in the present case, the water is slightly inclined with an angle of $\approx 4°$ at the interface with a preferred orientation of the water dipole moment and OH bonds pointing towards the carbon nanotube. The quadrupole moment has a negligible contribution to the density and water dipole moment, but it appears to intensify the probability distribution of the orientation of the OH bonds. Further studies are being conducted to confirm these results.

Molecular dynamics simulations of two carbon nanotubes in water have revealed a continuous "wetting" or a "drying" of the interstice between the tubes depending on their initial spacing. For the present carbon nanotubes with a chirality of $(16, 0)$ (diameter of $12.52 Å$), tube spacings of 7 and $8 Å$ resulted in a drying of the interstice whereas an initial spacing of $9 Å$ resulted in a permanent wetting. These results are in agreement with earlier studies of stacked plates by Wallqvist & Berne (1995) which indicate that stable configurations of water in a hydrophobic environment require the presence of two or more water layers. We are currently in the process of analyzing these results to determine the driving mechanisms of the drying process.

REFERENCES

ALLEN, M. P. & TILDESLEY, D. J. 1987 *Computer Simulation of Liquids.* Clarendon Press Oxford.

ALLEN, T. W., KUYUCAK, S. & CHUNG, S.-H. 1999 The effect of hydrophobic and hydrophilic channel walls on the structure and diffusion of water and ions. *J. Chem. Phys.* **111** (17), 7985-7999.

ANDREA, T. A., SWOPE, W. C. & ANDERSEN, H. C. 1984 The role of long ranged forces in determining the structure and properties of liquid water. *J. Chem. Phys.* **79** (9), 4576-4584.

BALAVOINE, F., SCHULTZ, P., RICHARD, C., MALLOUH, V., EBBESEN, T. W. & MIOSKOWSKI, C. 1999 Helical crystallization of proteins on carbon nanotubes: A first step towards the development of new biosensors. *Angew. Chem.* **38** (13/14), 1912-1915.

BECKE, A. D. 1993 Density-functional thermochemistry. III. the role of exact exchange. *J. Chem. Phys.* **98**, 5648-5652.

DANG, L. X. & PETTITT, M. 1987 Simple intramolecular model potentials for water. *J. Phys. Chem.* **91**, 3349-3354.

FRISCH, M. J., *et al.* 1998 *Gaussian 98*, revision a.7. Tech. Rep. Gaussian, Inc., Pittsburgh PA.

GORDON, P. A. & SAEGER, R. B. 1999 Molecular modeling of adsorptive energy storage: Hydrogen storage in single-walled carbon nanotubes. *Ind. Eng. Chem. Res.* **38**, 4647-4655.

GUO, Y., KARASAWA, N. & GODDARD III, W. A. 1991 Prediction of fullerene packing in C_{60} and C_{70} crystals. *Nature.* **351**, 464-467.

HANSEN, F. Y. & BRUCH, L. W. 1995 Molecular-dynamics study of the dynamical excitations in commensurate monolayer films of nitrogen molecules on graphite: A test of the corrugation in the nitrogen-graphite potential. *Phys. Rev. B.* **51** (4), 2515-2536.

HOCKNEY, R. W. & EASTWOOD, J. W. 1988 *Computer Simulation Using Particles*, 2nd edn. IOP.

JARVIS, S. P., UCHIHASHI, T., ISHIDA, T. & TOKUMOTO, H. 2000 Local solvation shell measurement in water using a carbon nanotube probe. *J. Phys. Chem. B.* **104** (26), 6091-6094.

LEE, C. Y., McCAMMON, J. A. & ROSSKY, P. J. 1984 The structure of liquid water at an extended hydrophobic surface. *J. Chem. Phys.* **80** (9), 4448-4455.

LEE, S. M. & LEE, Y. H. 2000 Hydrogen storage in single-walled carbon nanotubes. *Appl. Phys. Lett.* **76** (20), 2877-2879.

LEVITT, M., HIRSHBERG, M., LAIDIG, K. E. & DAGGETT, V. 1997 Calibration and testing of a water model for simulation of the molecular dynamics of proteins and nucleic acids in solution. *J. Phys. Chem. B* **101**, 5051-5061.

LI, J., CASSELL, A. M. & DAI, H. 1999 Carbon nanotubes as AFM tips: Measuring DNA molecules at the liquid/solid interface. *Surface and Interface Analysis.* **28**, 8-11.

LUM, K., CHANDLER, D. & WEEKS, J. D. 1999 Hydrophobicity at small and large length scales. *J. Phys. Chem. B* **103**, 4570-4577.

MARKOVIĆ, N., ANDERSSON, P. U., NÅGÅRD, M. B. & PETTERSON, J. B. C. 1999 Scattering of water from graphite: simulations and experiments. *Chem. Phys.* **247**, 413-430.

MARKOVIĆ, N., ANDERSSON, P. U., NÅGÅRD, M. B. & PETTERSON, J. B. C. 2000 Erratum to "scattering of water from graphite: simulations and experiments" [Chem. Phys. **247** (1999) 413-430). *Chem. Phys.* **252**, 409-410.

MIZAN, T. I., SAVAGE, P. E. & ZIFF, R. M. 1994 Molecular dynamics of supercritical water using a flexible SPC model. *J. Phys. Chem.* **98**, 13067-13076.

MOLONI, K., BUSS, M. R. & ANDRES, R. P. 1999 Tapping mode scaling force microscopy in water using a carbon nanotube probe. *Ultramicroscopy.* **80**, 237-246.

MÜLLER, E. A., RULL, L. F., VEGA, L. F. & GUBBINS, K. E. 1996 Adsorption of water on activated carbons: A molecular simulation study. *J. Phys. Chem.* **100** (4), 1189-1196.

ODOM, T. W., HUANG, J.-L., KIM, P. & LIEBER, C. M. 2000 Structure and electronic properties of carbon nanotubes. *J. Phys. Chem. B.* **104**, 2794-2809.

RAPPÉ, A. K., CASEWIT, C. J., COLWELL, K. S., GODDARD III, W. A. & SKIFF, W. M. 1992 UFF, a full periodic table force field for molecular mechanics and molecular dynamics simulations. *J. Am. Chem. Soc.* **114**, 10024-10035.

RZEPKA, M., LAMP, P. & DE LA CASA-LILLO, M. A. 1998 Physisorption of hydrogen on microporous carbon and carbon nanotubes. *J. Phys. Chem. B.* **102**, 10894-10898.

SAITO, R., TAKEYA, T., KIMURA, T., DRESSELHAUS, G. & DRESSELHAUS, M. S. 1998 Raman intensity of single-wall carbon nanotubes. *Phys. Rev. B.* **57** (7), 4145-4153.

SHEVADE, A. V., JIANG, S. & GUBBINS, K. E. 1999 Adsorption of water-methanol mixtures in carbon and alumino-silicate poares: a molecuar simulation study. *Mol. Phys.* **97** (10), 1139-1148.

TELEMAN, O., JÖNSSON, B. & ENGSTRÖM, S. 1987 A molecular dynamics simulation of a water model with intramolecular degrees of freedom. *Mol. Phys.* **60** (1), 193-203.

THEUNS, T. 1994 Parallel P3M with exact calculation of short range forces. *Comp. Phys. Commun.* **78**, 238-246.

TUZUN, R. E., NOID, D. W., SUMPTER, B. G. & MERKLE, R. C. 1996 Dynamics of fluid flow inside carbon nanotubes. *Nanotech.* **7** (3), 241-248.

ULBERG, D. & GUBBINS, K. E. 1995 Water adsorption in microporous graphite carbons. *Mol. Phys.* **84** (6), 1139-1153.

VERNOV, A. & STEELE, W. A. 1992 The electrostatic field at a graphite surface and its effect on molecule-solid interactions. *Langmuir.* **8**, 155-159.

WALLQVIST, A. 1990 Polarizable water at a hydrophobic wall. *Chem. Phys. Lett.* **165** (5), 437-442.

WALLQVIST, A. & BERNE, B. J. 1995 Computer simulation of hydrophobic hydration forces on stacked plates at short range. *J. Phys. Chem.* **99**, 2893-2899.

WALLQVIST, A. & TELEMAN, O. 1991 Properties of flexible water models. *Mol. Phys.* **74** (3), 515-533.

WALTHER, J. H. & KOUMOUTSAKOS, P. 2000 An influence matrix P^3M algorithm with exact particle-particle correction. *In preparation* .

WANG, Q. & JOHNSON, J. K. 1999 Optimization of carbon nanotubes arrays for hydrogen adsorption. *J. Phys. Chem. B.* **103**, 4809-4813.

WHITEHOUSE, D. B. & BUCKINGHAM, A. D. 1993 Experimental determination of the atomic quadrupole moment of graphite. *J. Chem. Soc. Faraday Trans.* **89** (12), 1909-1913.

Atomistic simulation of electro-osmosis in a nanometer-scale channel

By J. B. Freund†

An atomistic simulation of an electro-osmostic flow in a 50Å wide channel is performed to examine models for such flows and study its physical details. The working fluid considered is a 1.1M mean concentration solution of Cl^- in water. For simplicity and computational efficiency, only negatively charged ions are in the solution. The water is modeled by the SPC/E potential, and the Cl^- are modeled as point charges plus an established Lennard-Jones potential. The channel walls are fixed lattices of positively charged Lennard-Jones atoms. An aperiodic implementation of the P^3M algorithm is used to compute electro-static interactions. The distribution of Cl^- adjacent to the charged walls differs somewhat from theoretical predictions that assume infinitesimal ions and constant electric permittivity, and this second assumption is called into question because it is found that the waters near the wall are preferentially oriented by the local electric field, which will alter their dielectric properties. When an electric field is applied parallel to the channel walls, a velocity profile develops that is consistent with a monolayer thick Stern layer fixed to the channel walls.

1. Introduction

Where an electrolyte fluid contacts a solid surface, it is common that the surface becomes charged with counter ions preferentially distributed above it in a thin layer (see Fig. 1). This layer of fluid that has a net charge is called the electric double layer, and the ion density within it is typically modeled by a Boltzmann distribution. To ease computational expense in the present study we only have counter ions in the fluid, so the ion number density is simply

$$n(y) = n_o e^{-e\psi(y)/k_B T}, \tag{1.1}$$

where T is the temperature of the fluid (assumed uniform), k_B is the Boltzmann constant, e is the elementary charge (positive), and ψ is the local electric potential which is a function of the wall coordinate y. If we choose the mid-channel potential $\psi(h/2) = 0$, then n_o is the ion concentration at mid-channel. The electric potential in (1.1) satisfies the Poisson-Boltzmann equation

$$\frac{d^2\psi}{dy^2} = -\frac{en(y)}{\varepsilon\varepsilon_o} = -\frac{en_o}{\varepsilon\varepsilon_o}e^{-e\psi(y)/k_B T}, \tag{1.2}$$

where ε_o is the permittivity of a vacuum and ε (assumed constant) parameterizes the dielectric behavior of the fluid. We have assumed monovalent ions. The solution of (1.2)

† Mechanical and Aerospace Engineering, University of California, Los Angeles
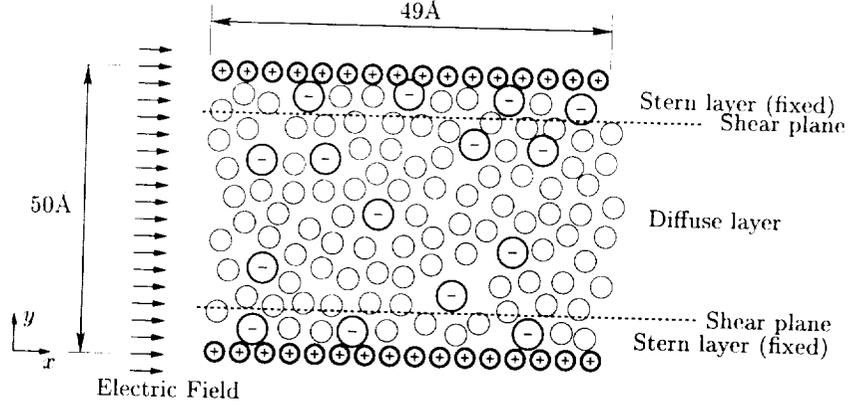
FIGURE 1. Schematic of the electric double layer in a nanometer-scale channel. For simplicity both this schematic and the present simulations only have counter ions in the solution. Two dimensions of the simulated channel are labeled. It also extends 49Å in the z-direction.

is (Israelachvili (1992))

$$\psi(y) = \frac{k_B T}{e} \log(\cos^2 Ky),$$ (1.3)

where

$$K^2 = \frac{e^2 n_o}{2\varepsilon\varepsilon_o k_B T}.$$ (1.4)

Overall electro-neutrality gives a boundary conditions on ψ in terms of the wall charge density Q_o,

$$Q_o = \varepsilon\varepsilon_o \frac{d\psi}{dy}\bigg|_{walls},$$ (1.5)

which can be used to determine n_o. Models have been developed to account for variable permittivity of the medium and variable viscosity (Dukhin & Derjaguin (1974)), but in this initial effort we focus on models that assume constant ε, smooth walls, and infinitesimal ions.

Typically, the ions nearest the wall are assumed to be bound to the surface in the so-called the Stern layer. Beyond the Stern layer is the diffuse layer which is potentially mobile. When there is flow, these two regions are usually assumed to be separated by a shear plane, but since the Stern layer may be only a few atoms thick, it is not clear that this continuum view strictly applies. The dynamics of this near-wall region are important for electro-osmosis, an electrokinetic process by which fluid is drawn through the channel by an applied electric field which exerts a body force on the fluid wherever it has net charge. This process is used to pump fluid in microfluidic devices (e.g. Herr et al. (2000)) and move fluid through porous material and clays (e.g. Coelho et al. (1996)). Electro-osmosis is also used in conjunction with theories similar to the one presented above to deduce the ζ-potential, the constant electric potential at the supposed shear plane, so the correctness of these models is also important for making these measurements.

Unfortunately, the small scales involved make it difficult to test electro-osmosis models in detail. For this reason we have developed the capability of simulating the process atomistically. This approach is, of course, limited to channels and pores that are signifi-

Interaction	A (J Å^{12})	C (J Å^6)	ϵ (J)	σ (Å)	r_o (Å)
O-O	4.37×10^{-15}	4.35×10^{-18}	1.08×10^{-21}	3.17	3.55
Cl-O	6.75×10^{-14}	1.03×10^{-17}	3.93×10^{-22}	4.33	4.86
Cl-Cl	1.81×10^{-13}	2.43×10^{-17}	8.16×10^{-22}	4.42	4.96
W-O	5.00×10^{-15}	5.44×10^{-18}	1.48×10^{-21}	3.12	3.50
W-Cl	7.72×10^{-14}	1.29×10^{-17}	5.38×10^{-22}	4.26	4.78

TABLE 1. All parameters for the Lennard-Jones potential. For convenience, two equivalent forms are given: $U(r) = A/r^{12} - C/r^6$ and $U(r) = 4\epsilon(\sigma^{12}/r^{12} - \sigma^6/r^6)$. The final column list r_o, the separation distance corresponding to zero force. All Lennard-Jones potentials were cut off and shifted (Frenkel & Smit (1996)) at the standard $r_c = 2.5\sigma$.

cantly smaller than in present-day manufactured devices, but in many cases the double layers are of nanometer scale and can, therefore, be studied directly by atomistic simulation. This report discusses initial results of this effort. We focus on ion-laden water flow in between idealized surfaces made up of atoms all having the same charge. The interatomic potentials are modeled with established empirical models which are discussed in §2. This section also discusses the numerical methods, the flow parameters, and the simulation procedure. Section 3 presents results for simulated double layers and makes some comparisons with theoretical predictions. A brief summary is provided in §4.

2. Atomistic simulations

2.1. *Physical model*

The waters were modeled using the fixed bond length SPC/E model of Berendsen *et al.* (1987) , which represents hydrogens and oxygens as point charges ($q_H = +0.4258e$ and $q_O = -0.8476$). The oxygens also interact with other atoms by a Lennard-Jones potential. Tests in a nanometer-scale Couette flow showed that the SPC/E model predicted the viscosity of water at $T = 300$K to within 10 percent of the accepted value. The Cl$^-$ were modeled using the parameters of Chandrasekhar *et al.* (1984), and the walls are modeled by fixed square arrays of Lennard-Jones atoms. Parameters for all Lennard-Jones interactions are given in table 1.

2.2. *Numerical method*

A standard velocity Verlet algorithm (Frenkel & Smit (1996)) was used to integrate Newton's equation of motion with a numerical time step of 1fs. Lennard-Jones interactions were computed point-to-point using a cutoff of 2.5σ; Coulomb interactions were computed using an aperiodic implementation (Pollock & Glosli (1996)) of the a P^{3}M algorithm (Hockney & Eastood (1988)). The mesh for the Poisson solver in the P^{3}M method had $48 \times 128 \times 48$ points in x, y, and z, respectively, with the same uniform mesh spacing in all three coordinate directions. The 128 mesh points in the y-direction extended over twice the height of the channel and were used to remove the periodicity (Pollock & Glosli (1996)). In our implementation, the point-to-point and mesh portions

of the potential were split using the standard Ewald decomposition,

$$\mathbf{F}_i = \frac{1}{2} \sum_{i \neq j} \frac{q_i q_j}{4\pi\varepsilon_o} \left(-\frac{2\alpha e^{-\alpha^2 |\mathbf{x}_{ij}|^2}}{\sqrt{\pi} |\mathbf{x}_{ij}|} - \frac{\text{erfc}(\alpha|\mathbf{x}_{ij}|)}{|\mathbf{x}_{ij}|^2} \right) \frac{\mathbf{x}_{ij}}{|\mathbf{x}_{ij}|}$$
$$- \frac{1}{2} \sum_{\mathbf{k} \neq 0} \sum_{j=1}^{N} \frac{q_i q_j}{L^3 \kappa^2 \varepsilon_o} e^{-\frac{\kappa^2}{4\alpha^2}} i\kappa e^{i\kappa \cdot \mathbf{x}_{ij}}, \tag{2.1}$$

where q_i is the charge and $\mathbf{x}_i$ is the position of the ith atom, and κ is a wavenumber vector. The first term in (2.1) was computed using a cutoff of 2.75σ, and the second term was computed on the mesh using fast Fourier transforms. The α parameter, which regulates the relative contributions from the two sums, was set based on numerical experimentation to be $\alpha = 0.262\text{Å}^{-1}$. A matrix constraint method was used to fix the bond lengths of the waters as specified by the SPC/E model.

2.3. *Flow parameters*

The channel dimensions are shown in Fig. 1. The $L_x = L_z = 49\text{Å}$ dimensions given in the figure are the periodicity lengths of the domain in x and z. The given channel height, $L_y = 50\text{Å}$, is measured between the centers of the wall atoms. The wall charge density was $Q_o = 0.24\text{C/m}^2$, which is equivalent to $0.184e$ per wall atom. This high but physically realizable wall charge was selected in this initial study because it gives a relatively large number of counter ions in the fluid and thus provides a good statistical sample within a reasonable computational time. Still, there were only 72 chloride atoms dissolved in the 3,600 waters in the channel. Each wall was constructed from 196 atoms. These charges and numbers are such that the overall system was neutral.

The applied electric field acted on the Cl^- in the x-direction with $F_E = 1.12 \times 10^{-11}\text{N}$. For reference, this is the same force that would be exerted by a point charge 45.3Å away. The energy of this analogous point-charge/point-charge interaction is $12.25k_B T$.

2.4. *Simulation procedure*

To equilibrate the ion distributions, an initial simulation was run with only 2816 atoms, one quarter the eventual number. It was initialized with an approximately uniform distribution of Cl^- and was run for 1 million time steps to obtain a statistically stationary distribution. At this point the domain was doubled in both the x- and z-directions by adding periodic images. When this was done, all atomic positions were perturbed with uniformly distributed random displacements with peak 10^{-3}Å. Because the system is Lyaponov unstable, this small randomization rapidly broke the symmetries. Eight different randomized atomic positions were used as initial conditions for eight separate ensembles that were run simultaneously on different computers to accumulate statistics. For each ensemble, 50,000 time steps were computed to re-equilibrate and allow the different ensembles to develop away from their similar initial conditions. This was followed by 250,000 time steps to gather statistics.

A Berendsen thermostat was used to counter viscous heating and a small temperature drift associated with the P^3M scheme which is accurate but not exactly energy conserving. Velocities were rescaled as

$$\tilde{\mathbf{v}}_i = \chi \mathbf{v}_i \tag{2.2}$$
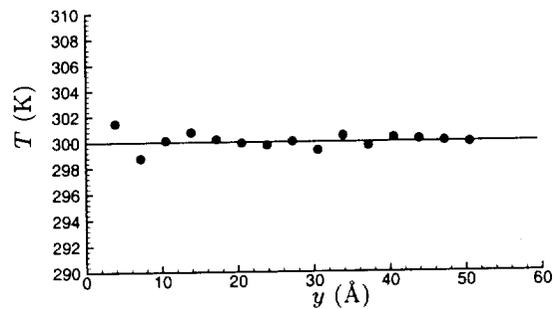
FIGURE 2. Mean temperature. On this and all plots, $y = 0$ corresponds to the centers of the atoms that constitute the low wall.

where

$$\chi = \left[1 - \frac{\Delta t}{\tau}\left(\frac{T_{\text{tar}}}{T} - 1\right)\right]^{\frac{1}{2}}, \tag{2.3}$$

and T is the temperature, Δt is the numerical time step (1fs), T_{tar} is the target temperature (300K), and τ is a parameter to regulate the strength of the rescaling. Solutions were shown to be insensitive to the value of τ. The mean scaling factor was nearly unity: $\bar{\chi} = 1 + 4 \times 10^{-7}$. Its greater-than-one value indicates that the numerical energy drift was negative for this flow. Since the instantaneous χ was rarely out of the range $0.9995 < \chi < 1.0005$, it did not alter the dynamics significantly. A difficulty arises in applying thermostats when there is a mean flow because the mean flow must be known *a priori* for its kinetic energy to be distinguishable from thermal kinetic energy. The problem is that the mean is not available until the simulation has run long enough to compute it. Nevertheless, it was found in the present case that results were insensitive to the parabolic flow profile used to estimate the relative contributions, which is no surprise since the mean flow has a peak of approximately 5m/s† and thus constitutes only a tiny fraction of the total kinetic energy of the particles. Ideally, one should remove heat via the walls as in a real channel as done for simple Lennard-Jones fluids by Travis & Gubbins (2000) to avoid any unphysical artifacts associated with the thermostat, but this approach does not provide a rigid control of the temperature in the channel. We also note that (2.2) should technically be applied separately at different distances from the wall because shear and thereby viscous heating is not uniform across the channel. However, application of a single thermostat for the whole channel in the present case resulted in the desired uniform temperature of 300K across the channel as seen in Fig. 2. Pressure was regulated to be one atmosphere by making minor adjustments to the volume of the channel domain.

† In atomistic simulations the time step must be short enough to track the velocities of atoms, which for ordinary temperatures and atomic masses are $\sim 10^3$m/s. Unfortunately, these high atomic velocities make it difficult to converge mean flow statistics when mean flows are typically many times (often several orders of magnitude) smaller than the thermal velocities. Thus seemingly unphysical flow velocities are often used to overcome the signal-to-noise problem. Couette flow tests showed that the SPC/E viscosity was independent of shear rate to considerably higher shear rates than in the present simulations.
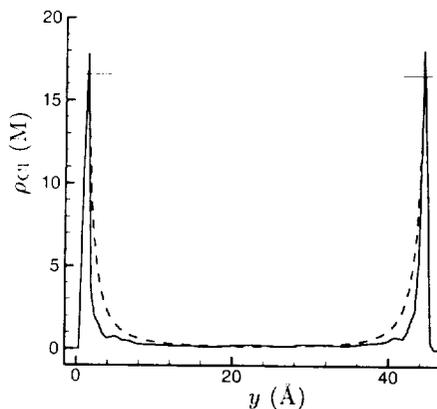
FIGURE 3. Chloride number density: ——— simulation; ‒ ‒ ‒ ‒ (1.1) with ψ from (1.3). The ········ line is $\rho_{Cl} = 0$. The horizontal line segments demark the peak reached by the ‒ ‒ ‒ ‒ curve.
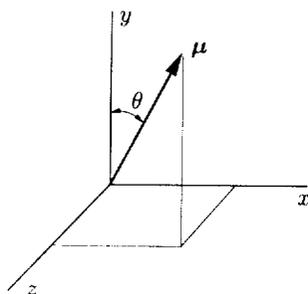
FIGURE 4. Schematic defining θ as the angle that the dipole vector μ makes with the y-axis.

3. Results

The Cl^- density as a function of distance from the wall is plotted in Fig. 3. As expected, the profile is sharply peaked near the walls and falls to a low value by the middle of the channel. The small bumps near the peak at both walls are believed to result from molecular stacking. They are roughly one water molecule width away from the peak.

The computed profiles differ from the theoretical prediction of (1.1) with $\psi(y)$ from (1.3). The computed profiles have higher peaks at the walls and fall away faster into the channel. A possible explanation for this discrepancy is the finite size of the ions which is neglected in the theory. For example, it is unclear where to apply (1.5) since the precise location of the wall is not well defined. For the theoretical curve in Fig. 3, (1.5) was applied so that the concentration peaks would coincide with those from the simulation, but this is not the closest approach made by the Cl^- in the simulations. Another possible explanation is that the dispersion energy ($U \sim 1/r^6$) is not taken into account in (1.1), but since the Lennard-Jones energy well is deeper (larger ϵ) for the oxygen-wall interaction than for the chloride-wall interaction (see table 1), we expect this to decrease the Cl^- concentration at the wall rather than increase it.

Another possible explanation for the disagreement seen in Fig. 3 is that the dielectric properties of the solvent are altered in the near neighborhood of the charged surfaces. Since the wall is charged, we expect there to be a preferred orientation of the water
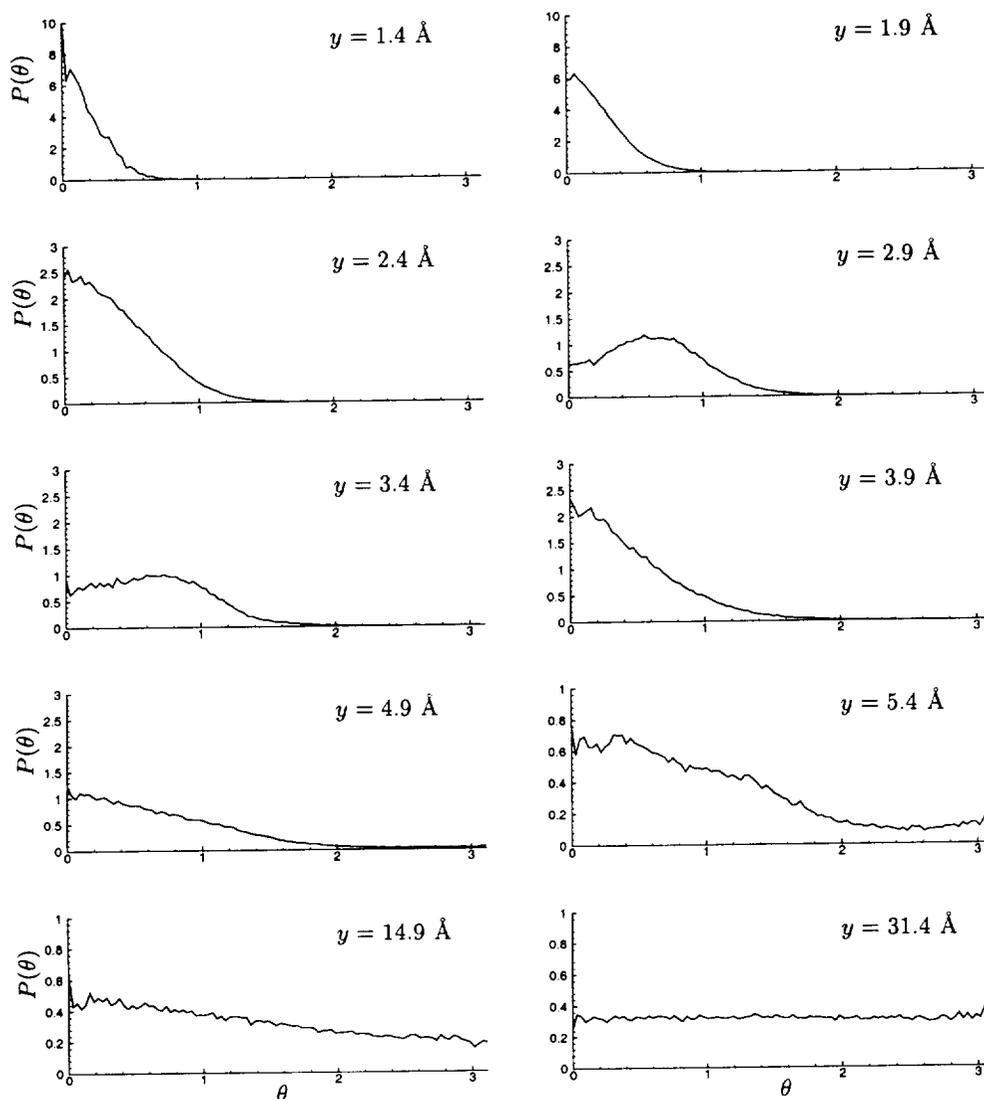
FIGURE 5. Probability density function of water molecule orientations. The angle θ is defined in figure 4. The y-locations correspond to the center of the oxygen atom.

molecules adjacent to it, which will in turn alter their dielectric properties since these waters can not respond to an electric field as they do in bulk. There is experimental evidence for reduced permittivity near a charged surface (Hunter (1981)). With the dipole angle θ defined as in Fig. 4, Fig. 5 shows the probability density (p.d.f.) function of the angular orientation of the waters at different distances from the wall. The p.d.f.'s are weighted so that a random orientation gives a uniform distribution. We see in Fig. 5 that closest to the wall, the dipole vectors are all within 45° of being perpendicular to the wall. Interestingly, the waters at around $y = 3$Å have $\theta \approx 45°$ as their most probable angular orientation, but by $y = 3.9$Å the most probable orientation is again perpendicular to the wall. At larger distance the distribution becomes much more uniform and is nearly flat
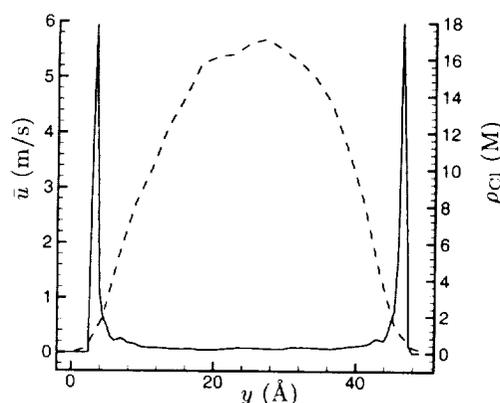
FIGURE 6. The mean flow velocity across the channel ---- . The mean chloride density is shown on the right axis ——— .

by $y = 15\text{Å}$. A preferential orientation would tend to decrease ε and thus increase the apparent strength of the electric field near the wall consistent with Fig. 3.

The computed velocity profile is shown in Fig. 6. We see that it is approximately parabolic in the middle of the channel, but it does not continue as a parabola all the way to the wall. Instead there is considerably more resistance close to the wall. Immediately adjacent the wall the atoms appear fixed in a Stern layer. The details of this are the subject of continuing investigations.

4. Summary

This paper has presented simulations of electro-osmotic flow of an aqueous solution in a 50Å wide channel. It was shown that the ion distribution is in general agreement with a theory that assumes constant permittivity and infinitesimal ions, and it was suggested that non-uniform permittivity due to the preferential orientation of the water molecules in the near-wall region might explain the observed disagreement with this theory. The velocity was found to be approximately parabolic in the middle of the channel, but it flattened out near the walls in the Stern layer. These simulations represent a first step in a continuing effort to identify and model mechanisms in electrically driven nanometer-scale flows.

REFERENCES

BERENDSEN, H. J. C., GRIGERA, J. R. & STRAATSMA, T. P. 1987 The missing term in effective pair potentials. *J. Phys. Chem.* **91**, 6269.

CHANDRASEKHAR, J., SPELLMEYER, D. & JORGENSEN, W. 1984 Energy component analysis for dilute aqueous solutions of Li+, Na+, F-, and Cl- ions. *J. Am. Chem. Soc.* **106**, 903.

COELHO, D., SHAPIRO, M., THOVERT, J.-F. & ADLER, P. 1996 Electro-osmotic phenomena in porous media. *J. Coll. Interf. Sci.* **181**(1), 169-190.

DUKHIN, S. S. & DERJAGUIN, B. V. 1974 *Surface and Colloid Sciences*, volume 7,

chapter Equilibrium double layer and electrokinetic phenomena. John Wiley & Sons, New York.

FRENKEL, D. & SMIT, B. 1996 *Understanding Molecular Simulation.* Academic Press.

HERR, A. E., MOLHO, J. I., SANTIAGO, J. G., MUNGAL, M. G. & KENNY, T. W. 2000 Electroosmotic capillary flow with nonuniform zeta potential. *Anal. Chem.*, **72**, 1053-1057.

HOCKNEY, R. W. & EASTOOD, J. W. 1988 *Computer simulation using particles.* Institute of Physics Publishing.

HUNTER, R. J. 1981 *Zeta potential in colloid science.* Academic Press, London.

ISRAELACHVILI, J. 1992 *Intermolecular and Surface Forces.* Academic Press.

POLLOCK, E. & GLOSLI, J. 1996 Comments on PPPM, FMM, and the Ewald method for large periodic Coulombic systems. *Comp. Phys. Comm.* **95**, 93-110.

TRAVIS, K. P. & GUBBINS, K. E. 2000 Poiseuille flow of Lennard-Jones fluids in narrow slit pores. *J. Chem. Phys.* **112**(4), 1984-1994.

The turbulent life of phytoplankton

By S. Ghosal†, M. Rogers‡ AND A. Wray‡

Phytoplankton is a generic name for photosynthesizing microscopic organisms that inhabit the upper sunlit layer (euphotic zone) of almost all oceans and bodies of freshwater. They are agents for "primary production," the incorporation of carbon from the environment into living organisms, a process that sustains the aquatic food web. It is estimated that phytoplankton contribute about half of the global primary production, the other half being due to terrestrial plants. By sustaining the aquatic food web and controlling the biogeochemical cycles through primary production, phytoplankton exert a dominant influence on life on earth. Turbulence influences this process in three very important ways. First, essential mineral nutrients are transported from the deeper layers to the euphotic zone through turbulence. Second, turbulence helps to suspend phytoplankton in the euphotic zone since in still water, the phytoplankton, especially the larger species, tend to settle out of the sunlit layers. Third, turbulence transports phytoplankton from the surface to the dark sterile waters, and this is an important mechanism of loss. Thus, stable phytoplankton populations are maintained through a delicate dynamic balance between the processes of turbulence, reproduction, and sinking. The first quantitative model for this was introduced by Riley, Stommel and Bumpus in 1949. This is an attempt to extend their efforts through a combination of analysis and computer simulation in order to better understand the principal qualitative aspects of the physical/biological coupling of this natural system.

1. Introduction

The word "plankton" comes to us (Thurman (1997)) from a Greek word ($\pi\lambda\alpha\nu\kappa\tau o\zeta$) meaning "wanderers" or "drifters" first coined by the German scientist Victor Heusen (1887). They refer to the large class of microscopic organisms (2–200 μm) that are carried around by the currents in any natural body of water. Biologists have various ways of organizing the many species of plankton into classes and subclasses¶. At the lowest level, they are divided into two classes "phytoplankton" and "zooplankton". The members of the former class photosynthesize with the help of chlorophyll and thereby contribute to primary production, the latter do not photosynthesize, but sustain themselves by "grazing" on the phytoplankton.

The distribution of phytoplankton is not uniform, but varies over large as well as small length and time scales‖. The phytoplankton density, like weather patterns, shows chaotic dynamics and is influenced by a wide range of conditions. Though a fully predictive

† Mechanical Engineering, Northwestern University
‡ NASA Ames Research Center, Moffett Field, CA
¶ Excellent illustrated compilations of plankton species exist on the internet, see e.g. http://www.calacademy.org/research/diatoms/diatoms.html.
‖ NASA's SeaWiFS project continuously provides global maps, similar to "weather maps", of the worldwide phytoplankton distribution through satellite imaging, see http://seawifs.gsfc.nasa.gov/SEAWIFS.html.

model does not seem attainable in the near future, a fundamental understanding of the basic physical processes underlying this variability is of great importance.

Because photosynthesis removes carbon dioxide from the atmosphere and releases oxygen, the global primary production due to phytoplankton is an important variable in climate models. There are also more subtle but extremely important effects on global biogeochemistry. For example, it has been suggested (Charlson *et al.* (1987)) that dimethylsulphide released by phytoplankton algae is a major source of cloud condensation nuclei. Cloud albedo is believed to be a critical factor in climate models since it controls global absorption of solar irradiance. The health of the marine system is closely linked to phytoplankton productivity, the richest fisheries tend to be concentrated in areas where upwellings bring mineral nutrients to the surface and support large phytoplankton populations. In addition to providing organic material to feed the higher animals, phytoplankton sustain aquatic life by enriching the water with oxygen, a byproduct of photosynthesis. Sudden explosions of the phytoplankton population (known as a "bloom") can have disastrous effects, especially in coastal regions. Certain species produce deadly toxins and, when present in large concentrations, they poison fish and animals higher up in the food chain. Filter feeders such as shell fish tend to concentrate these toxins in their bodies and may poison animals that feed on them (including humans). Even species that do not create toxins can kill fish populations over a wide area. The large concentrations of plankton produced during a bloom can physically clog the gills of fish, and when the plankton die after rapidly using up the mineral nutrients, their decomposing bodies deplete the water of oxygen suffocating fish that get trapped in the bloom. The large concentrations of plankton can sometimes physically color the water giving rise to the term "red tide", though HAB ("Harmful Algal Blooms") is preferred in the scientific literature†.

The large scale dynamics of plankton concentration is controlled jointly through the effects of advection by large scale flow patterns, turbulent diffusion, gravitational settling, reproduction, and loss through grazing by zooplankton, various filter feeders, and other marine animals.

Since phytoplankton convert carbon dioxide to organic material with the aid of sunlight, the reproduction rate depends directly on the rate of photosynthesis, which in turn is controlled by the light intensity. The rate of photosynthesis increases almost linearly with light intensity (Reynolds (1984)) until it saturates. A further increase in intensity results in a slight decrease in the photosynthetic rate, an effect known as "photo-inhibition". Phytoplankton, therefore, can survive and multiply only in the upper layers of oceans and lakes known as the "euphotic zone". The depth of the euphotic zone varies widely depending on water clarity, latitude, and season. For the open ocean it is often in the range of 50 to 100 meters.

After the "light climate", the most important factor in phytoplankton productivity seems to be the concentration of inorganic salts, primarily nitrates and phosphates. These salts accumulate in the deep layers of the ocean due to runoffs from land over geological time and due to the constant "rain" of dead planktonic matter from the upper productive layers. The productivity of phytoplankton is strongly constrained by the need for light, which is only available in the upper layers, and the need for mineral nutrients, available only in the deeper layers. Terrestrial plants are in a similar predicament and have evolved roots, trunks, and branches to solve their transport problem. Phytoplankton, on the other hand, rely on vertical upwelling and turbulent transport to dredge up nutrients

† Woods Hole Oceanographic Institution maintains a very informative web site on HAB s, see http://www.redtide.whoi.edu/hab.

from the deeper waters. In the ocean, a significant correlation exists between regions of high primary productivity and regions of upwelling. The carbon dioxide needed in photosynthesis is utilized from dissolved carbonates and bi-carbonates, which are plentiful and are rarely a limiting factor in primary production.

Various other factors directly or indirectly affect plankton productivity. Water temperature and salinity have a selective effect on plankton production as individual species are adapted to survive in certain optimal temperature and salinity ranges. More importantly, temperature and salinity control the stability of water columns and, therefore, the degree of turbulent mixing. Turbulent mixing in turns controls the transport of minerals and suspension of the phytoplankton in the euphotic zone; both of these physical effects are of great importance in the population dynamics of plankton.

Grazing by zooplankton is an important mechanism of loss. The phytoplankton-zooplankton coupling gives rise to a predator/prey system with well known dynamical behavior such as limit cycles and chaos (Edwards & Brindley (1999), Truscott & Brindley (1994)). Larger animals, primarily the "filter feeders" ranging from rotifers and larvae of various kinds to whales, also crop the phytoplankton stock. In shallow bays and estuaries (the San Francisco bay, for example), "benthic grazers" such as oysters that live at the bottom form a copious sink of phytoplankton (Lucas *et al.* (1999a), Lucas *et al.* (1999b), Lucas *et al.* (1998)).

2. The role of turbulence

Phytoplankton are typically about 2 to 5 percent denser than the water in which they live. In the absence of special adaptations, they would sink out of the euphotic zone. Some species have developed gas vacuoles that make them buoyant. The physical basis for the adoption of various strategies by microscopic aquatic organisms has been discussed by Alexander (1990). The two most common classes of phytoplankton are the diatoms and the dinoflagellates. The dinoflagellates are weak swimmers and swim by means of flagella, thereby counteracting the effect of gravity. The diatoms do not actively swim, but they do have a variety of adaptations to reduce the sinking speed. This, together with the fact that natural bodies of water are often turbulent, allow stable populations to exist even though each individual organism does ultimately sink out of the euphotic zone.

Suppose that each phytoplankton sinks from the surface to the bottom of the euphotic zone in a time t_s in still water, and, in a time exactly equal to t_r from birth, each organism multiplies to form new individuals. Clearly, if $t_r > t_s$, no individual can reproduce and the population cannot be sustained. If, on the other hand, the waters are turbulent, each organism may be carried either upward or downward by eddies. The mean lifetime is not changed as a result, however; there is now a wide distribution of lifetimes around the mean t_s. Thus, even if $t_r > t_s$, a significant fraction of the population gets an opportunity to reproduce, and if the resultant increase is sufficient to offset the losses, a stable population may exist. On the other hand, if $t_r < t_s$, stable populations can exist in both still waters as well as turbulent waters. However, whereas in still waters every individual would have had an opportunity to reproduce, in the turbulent case the fraction of the population with lifetime exceeding t_s would sink before reproducing. Turbulence can therefore be either a help or a hindrance in the life of phytoplankton. This depends primarily on the size of the phytoplankton species being considered. Since smaller organisms tend to both reproduce faster and sink slower, turbulence in general tends to be essential for the survival of larger species but an impediment for the smaller ones. Some very rough estimates may be made taking 50 meters as the depth of the euphotic zone. The smallest plankton have

sizes in the range of a few microns and sink at speeds (Reynolds (1984), Eppley *et al.* (1967)) of the order of 0.1 meters per day. Therefore, for these species, $t_s \sim 500$ days. The reproduction time (Reynolds (1984), Fenchel (1974)) $t_r \sim 5$ days. These species are therefore not dependent on the mechanism of turbulent suspension, and turbulence has a negative impact: it carries viable organisms to the dark aphotic zone. The largest of the phytoplankton ($\sim 200\mu m$) sink much faster at speeds ~ 20 meters per day. For these organisms, $\tau_s \sim 2.5$ days whereas $t_r \sim 5$ days. These species depend on turbulence to survive. For the same reason, turbulence is a hindrance to the dinoflagellates that are active swimmers or the negatively buoyant phytoplankton species that naturally rise to the surface due to buoyancy aids. The relative population of diatoms and dinoflagellates in the open ocean is known to be a sensitive function of the intensity of turbulence (Margalef (1978), Gibson (2000)). During periods of high winds, diatoms are found to dominate while in periods of calm, the dinoflagellates predominate. "Red Tides" which are caused by dinoflagellates are usually preceded by days of calm conditions.

In addition to its role in suspending phytoplankton, turbulence has a second important effect on plankton population dynamics. The mineral nutrients, primarily nitrates and phosphates, needed by phytoplankton are often transported from the deep aphotic layers to the euphotic zone by turbulence. In the oceans, these mineral nutrients are often depleted in the surface layers. Their concentration typically rises with depth and reaches saturation in layers that can be as much as 500 to 1000 meters below the surface (Riley *et al.* (1949)). The character of the environment in which phytoplankton live may be broadly classified as *eutrophic* or *oligotrophic*, depending on whether mineral nutrients for phytoplankton growth are plentiful or are a limiting factor in plankton population dynamics. Examples of eutrophic environments are lakes and shallow waters in tropical and temperate zones. Deep alpine lakes and deep oceans are examples of typically oligotrophic environments. Generally, clear blue waters are indicative of an oligotrophic environment whereas greenish or brownish waters are typical of an eutrophic environment. The "eutrophication" of inland waters due to runoff of phosphate and nitrate rich effluents due to human activity is an issue of great concern in contemporary ecology. In this paper we will only consider a eutrophic environment so that the maximum plankton population is light limited and depletion of mineral nutrients plays no role.

Turbulence in natural bodies of waters is to be expected since in nature turbulent flow is the rule rather than the exception. In large lakes and the open ocean, turbulence is most often driven by the breaking of surface waves. Another mechanism is the breaking of internal waves at density interfaces. Thermal and salinity gradients due to heating by the sun and/or the ebb and flow of tides can lead to convective instability that breaks into turbulence. Stable stratification can also develop during warmer months, stabilizing the surface layers against wind driven turbulence. All these geophysical processes naturally have a profound impact on the population distribution of phytoplankton. The intensity of turbulence in natural waters varies between wide limits; dissipation rates, ϵ from 2.8×10^{-7} to $47\,\mathrm{cm^2 s^{-3}}$, have been reported in the ocean (Peters & Marrase (2000)).

3. A simplified description

Population dynamics of phytoplankton may be described through the following simplified partial differential equation:

$$\frac{\partial \phi}{\partial t} + \mathbf{u} \cdot \nabla \phi = S\phi - v_p \frac{\partial \phi}{\partial z} + k_T \nabla^2 \phi. \tag{3.1}$$

This is a balance equation for the plankton density ϕ and may be readily derived by considering an elementary volume of liquid (much larger than the mean separation of phytoplankton though small on the scale of variation of mean fields) being advected by the mean flow $\mathbf{u}$. The random motion due to turbulence is described through the eddy diffusivity coefficient k_T. The water surface is considered at $z = 0$ and the z axis is directed downwards. The second term on the right-hand side is a result of writing the advective term as a sum of displacements due to the average fluid flow and that due to gravitational sinking of the phytoplankton with a speed v_p relative to still water. If birth and death processes are random and independent, the net source is proportional to the concentration ϕ. A reasonable model for the net growth rate is

$$S = P(I) - L \tag{3.2}$$

where $P(I)$ is the production, which in an eutrophic environment may be parametrized by the local value of the light intensity I, and L is a constant loss rate due to natural deaths and grazing by higher animals. A constant L is clearly a simplifying approximation; coupling to the zooplankton population density is neglected in this analysis. For $P(I)$ we will use the Jassby-Platt model (Jassby & Platt (1976))

$$P(I) = \frac{r + L}{2} \left[1 + \tanh \left\{ \alpha \left(\frac{I}{I_c} - 1 \right) \right\} \right] \tag{3.3}$$

where r, α, and I_c are parameters characterizing the photosynthetic response of the given phytoplankton species. The light intensity decays exponentially from its value at the surface I_0 so that the intensity at depth z is given by

$$I(z) = I_0 \exp(-\mu z). \tag{3.4}$$

The extinction coefficient μ is represented as the sum of a background extinction μ_0, characterizing the transparency of the water in the absence of the phytoplankton cells, and a term due to the "shading" of the phytoplankton at a given layer by those that lie above it,

$$\mu = \mu_0 + \mu_1 \int_0^z \phi \, dz. \tag{3.5}$$

The coefficient in the expression for $P(I)$ in (3.3) has been written as $(r + L)/2$ for later convenience; it is merely a constant independent of I. We will assume that α is large so that when $I = 0$, $P(I) \approx 0$, and when $I > I_c$, $P(I)$ reaches the saturation level $r + L$, so that the net growth rate is r. The photosynthetic response of many phytoplankton species have been documented. They typically increase linearly with the light intensity for low light and then rapidly saturate. A further increase in the light intensity results in a slight depression of the photosynthesis rate, an effect known as "photoinhibition". Although Eq. (3.3) ignores photoinhibition, it is a reasonably good representation of this response curve.

In this paper we will assume that the layer of water that is turbulent is infinitely thick; that is, the "turbocline" is much below the euphotic zone. Such a model certainly does not apply in all situations. The depth of the turbocline depends on the convective stability of the water column and may very well be comparable to or much shallower than the euphotic zone depth. Such a situation may give rise to very different kinds of effects than those considered in this paper. In particular, the "Sverdrup Critical Depth Model" (SCDM) may apply in determining whether phytoplankton blooms can occur (Sverdrup (1953)).

The boundary conditions for ϕ are those of no flux at the surface and vanishing plankton density deep below the euphotic zone:

$$\left[k_T \frac{d\phi}{dz} - v_p \phi \right]_{z=0} = 0 \tag{3.6}$$

$$\phi(z \to \infty) = 0. \tag{3.7}$$

It should be noted that the formulation of the problem as presented here is nonlinear, and the amplitude as well as the shape of the profile are fully determined.

4. Layer models

It is instructive to consider the limit $\alpha \to \infty$ in the above formulation. We look for steady one-dimensional solutions $\phi = \phi(z)$. In this case, the source term S is a step function

$$S = \begin{cases} r & \text{if } z < H; \\ -L & \text{if } z \geq H \end{cases} \tag{4.1}$$

where '$z = H$' is the location of the boundary of the euphotic zone. Since $I = I_c$ determines this boundary, from (3.4) and (3.5) it follows that

$$H = \frac{H_0}{1 + \sigma \int_0^H \phi \, dz} \tag{4.2}$$

where

$$H_0 \equiv \frac{1}{\mu_0} \log \left(\frac{I_0}{I_c} \right) \tag{4.3}$$

and

$$\sigma \equiv \frac{\mu_1}{\mu_0}. \tag{4.4}$$

The steady plankton density then obeys a linear one-dimensional differential equation

$$k_T \frac{d^2\phi}{dz^2} - v_p \frac{d\phi}{dz} + S(z)\phi = 0 \tag{4.5}$$

with a piecewise constant coefficient $S(z)$ given by (4.1). The boundary conditions are (3.6) and (3.7).

We do not present the details of the algebra leading up to the solution, but sketch the general procedure and present the final analytical result. In the aphotic zone ($z > H$), Eq. (4.5) allows an exponentially growing and an exponentially decaying solution; only the latter is consistent with (3.7). In the euphotic zone ($z < H$), there are two linearly independent solutions of the form $\sim \exp(mz)$ so that the general solution is a superposition of the two with unknown coefficients A and B. The boundary condition (3.6) and the requirement that both ϕ and $d\phi/dz$ be continuous across the interface $z = H$ results in three homogeneous equations for determining the three constants A, B, and the coefficient of the exponentially decaying solution in the aphotic zone, D. Nontrivial solutions can exist if and only if the discriminant of this system of three equations is zero. This is a condition for determining H and, therefore, the amplitude of the mode since the amplitude is related to H through Eq. (4.2). Physically meaningful solutions can exist if and only if the eigenvalue H is real, positive, and $H \leq H_0$. From inspection of the solvability condition, the requirement that these conditions are valid can be deduced, and this determines a critical curve in a two-dimensional parameter space defining the region in which steady one-dimensional solutions can exist.
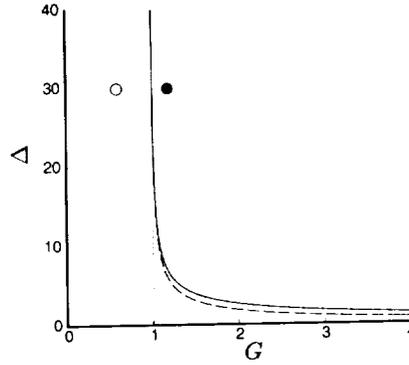
FIGURE 1. The critical curve for existence of stable populations, ——— : zero boundary condition, – – – – : no flux boundary condition. Symbols correspond to parameters for DNS.

The physical parameters characterizing the system are the net growth rate in the euphotic zone, r, the loss rate in the aphotic zone, L, the sinking speed in still water, v_p, the coefficient of turbulent diffusivity, k_T, and the clear water euphotic zone height, H_0. The analytical solution is most conveniently expressed in terms of the following two parameters, λ and Λ, with dimensions of length that determine the scale of spatial variability of the population distribution in the euphotic and aphotic zones respectively:

$$\lambda = \frac{2k_T}{v_p} \tag{4.6}$$

$$\Lambda^{-1} = \frac{v_p}{2k_T}\left[\sqrt{1 + \frac{4Lk_T}{v_p^2}} - 1\right]. \tag{4.7}$$

The two dimensionless parameters determining the critical curve are the dimensionless growth rate

$$G = \frac{2r\lambda}{v_p} = \frac{4rk_T}{v_p^2} \tag{4.8}$$

and the dimensionless height of the euphotic zone for clear water, Δ,

$$\Delta = \frac{H_0}{\lambda} = \frac{v_p H_0}{2k_T}. \tag{4.9}$$

The condition for existence of physically meaningful steady one-dimensional solutions can then be written in the following simple form

$$G > 1 \tag{4.10}$$

and

$$\Delta \geq \frac{\frac{\pi}{2} - \theta_*}{\sqrt{G - 1}} \tag{4.11}$$

where

$$\theta_* \equiv \tan^{-1}\left(\frac{G - \rho}{\rho\sqrt{G - 1}}\right) \tag{4.12}$$
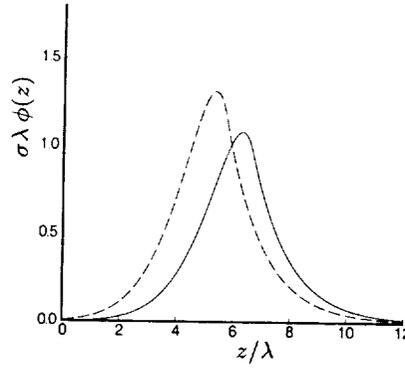
FIGURE 2. Phytoplankton profiles determined by theory, ——— : zero boundary condition, - - - - : no flux boundary condition.

and

$$\rho \equiv 2 + \frac{\lambda}{\Lambda}. \tag{4.13}$$

Figure 1 shows the critical curve in the space of parameters $G - \Delta$. Steady solutions are only possible if conditions are such that the pair of values (G, Δ) characterizing the system lies above the critical curve.

The distribution of phytoplankton with depth is given by

$$\phi(z) = \begin{cases} A_{ep} \exp\left(\frac{z}{\lambda}\right) \left[\sqrt{G-1}\cos\left(\frac{z}{\lambda}\sqrt{G-1}\right) + \sin\left(\frac{z}{\lambda}\sqrt{G-1}\right)\right] & \text{if } z \le H; \\ A_{ap} \exp\left(-\frac{z}{\Lambda}\right) & \text{if } z > H. \end{cases} \tag{4.14}$$

where

$$A_{ep} = \Phi \frac{(G^2 - 2\rho G + \rho^2 G)^{1/2}}{(\lambda\rho + \Lambda G)\sqrt{G-1}\exp\left(\frac{\pi/2-\theta_*}{\sqrt{G-1}}\right)} \tag{4.15}$$

$$A_{ap} = \Phi \frac{G}{\lambda\rho + G\Lambda} \exp\left[\frac{\lambda}{\Lambda}\frac{\pi/2-\theta_*}{\sqrt{G-1}}\right] \tag{4.16}$$

and

$$\Phi = \int_0^\infty \phi(z)\, dz \tag{4.17}$$

is the integrated phytoplankton density. The height of the euphotic zone, H, and the integrated phytoplankton density are given by

$$\frac{H}{\lambda} = \frac{\frac{\pi}{2} - \theta_*}{\sqrt{G-1}} \tag{4.18}$$

and

$$\sigma\left(1 + \frac{G\Lambda}{\rho\lambda}\right)\Phi = \frac{\lambda\Delta}{H} - 1. \tag{4.19}$$

The formulation and the analytical solution presented above is a generalization of an analysis by Riley, Stommel & Bumpus (Riley *et al.* (1949)). It differs from this previous work in that the "self-shading" effect introduced through Eq. (4.2) was not considered in the earlier paper. Riley *et al.* considered the depth of the euphotic zone H as fixed.

They then interpreted the eigenvalue equation to mean that a certain relation must exist between the parameters v_p, k_T, r, L, and the depth of the euphotic zone H ($= H_0$) for solutions to exist. Such a condition, however, seems rather artificial as these parameters assume values independently and only in rare circumstances can they be expected to fall on the curve determined by the eigenvalue equation. The present formulation provides a natural interpretation for the eigenvalue condition. It determines the amplitude of the mode or, equivalently, the integrated phytoplankton density Φ. Riley *et al.* also concluded that for steady non negative solutions, one must have $G > 1$ and the depth of the euphotic zone should *not exceed* a certain critical value. In our formulation, the requirements for physically acceptable solutions are that $G > 1$ and the dimensionless clear water euphotic zone depth $\Delta = H_0/\lambda$ should *exceed* a certain critical value given by (4.11). Unlike the previous analysis which was linear, in our formulation both the amplitude as well as the shape of the depth distribution of phytoplankton are determined because of the nonlinearity introduced in the problem through the self-shading effect.

5. Direct numerical simulation

The analysis presented here is based on a number of simplifying assumptions, not all of which can be expected to hold in natural environments. Measurements of phytoplankton density are available from various sources; however, not all of the parameters needed in the theory may have been measured in a given investigation. Further, interpretation of such data is often complicated by poorly characterized or unknown factors in the physical environment. It would seem reasonable, therefore, to first test the principal results of the analysis by comparing with a "numerical experiment" that is free of all the uncertainties inherent in data from the natural environment. In order to reduce uncertainties arising from the departure from isotropy near the free surface, the simulation is performed for a fast sinking species so that the phytoplankton concentration peaks well below the free surface.

A direct numerical simulation (DNS) is performed in a computational box of aspect ratio $1 : 1 : 4$, the depth D being the longest dimension. The velocity field $\mathbf{u}$ is determined by the incompressible Navier-Stokes equations while the phytoplankton density ϕ obeys the evolution equation

$$\frac{\partial \phi}{\partial t} + \mathbf{u} \cdot \nabla \phi = S\phi - v_p \frac{\partial \phi}{\partial z} + k_0 \nabla^2 \phi \qquad (5.1)$$

where k_0 is a small "molecular diffusion" coefficient that is introduced to stabilize the calculation by smoothing out any excessively sharp gradients in the scalar iso-surface.

We assume periodic boundary conditions for the velocity $\mathbf{u}$ and pressure p in all three directions. For the scalar ϕ, we assume periodic boundary conditions for the lateral boundaries and zero boundary conditions at the top and bottom surfaces of the box

$$\phi(x, y, 0, t) = 0 \qquad (5.2)$$

$$\phi(x, y, D, t) = 0. \qquad (5.3)$$

The assumption of periodic boundary conditions at the top and bottom surfaces for the velocity and pressure is chosen for the purpose of this investigation primarily for reasons of simplicity of implementation. It allows us to treat the turbulence as isotropic, consistent with the assumptions in the analytical work. Deviations from isotropy near the free surface are to be expected in a realistic situation, but it is reasonable to undertake a careful investigation of the isotropic case first. The isotropic assumption is rendered

somewhat more plausible if the "upper" boundary is interpreted as an imaginary surface located not at the true free surface, but somewhat below it. Similarly, the "lower" boundary is considered to be an arbitrarily chosen plane well below the euphotic zone where the phytoplankton concentration is essentially zero. The outward flux, F of phytoplankton at the surface $z = 0$ is given by

$$F = -\overline{w\phi} - v_p\overline{\phi} + k_0\overline{\frac{\partial\phi}{\partial z}} \qquad (5.4)$$

where the overbar signifies horizontal average. If the layer of water between $z = 0$ and the physical surface is sufficiently thin, phytoplankton production in this layer may be neglected so that a balance prevails between the turbulent transport across $z = 0$ and the flux due to sinking. The appropriate boundary condition for modeling this situation would be

$$F_{z=0} = 0. \qquad (5.5)$$

The difficulty of implementing the boundary condition (5.5) is that it provides a constraint on the mean field but not on the fluctuations. Further assumptions about the nonzero Fourier modes of the scalar field need to be introduced for a numerical solution. The only exception to this is the situation where the sinking speed of phytoplankton, v_p, is sufficiently large so that the phytoplankton distribution peaks well below the surface and the surface concentration of phytoplankton is negligible. Here the parameters are chosen to correspond to this situation. In this case, (5.5) may be replaced by (5.2) as a reasonable approximate boundary condition. Further, under these conditions any uncertainties due to possible deviations from isotropy of the turbulent field near the free surface would presumably have a negligible effect on the phytoplankton concentration profile. Since $G \propto 1/v_p^2$ and $\Delta \propto v_p$, $G \to 0$ and $\Delta \to \infty$ as $v_p \to \infty$. In order to remain within the zone of steady solutions in phase space, parameters for the numerical simulation must be chosen so that the point (G, Δ) is in the upper left-hand corner of the parameter space shown in Fig. 1, very close to but above the critical curve.

In order to perform the numerical simulation, an existing pseudospectral code designed for simulating forced isotropic turbulence in the presence of a passive scalar was modified in the following manner to implement the Jassby-Plat model discussed in Section 3. The representation of the scalar field ϕ was changed from Fourier to physical in the z-direction only. The z-derivative operator was changed from spectral to second-order central difference at interior points, reverting to second-order one-sided finite difference at the grid points closest to the boundaries. A scalar field for the light intensity was added and updated at every time step in accordance with the requirements of (3.4) and (3.5). The basic algorithm, which is discussed at length elsewhere (Rogallo (1977)), uses a second-order Runge-Kutta method to execute the time step and uses the phase shift algorithm to dealias. Dealiasing in the z direction was turned off for the scalar field. A grid size of 64 × 64 × 256 was chosen as this seemed to provide a reasonably robust representation of the turbulent field with a well-resolved vertical profile for the mean phytoplankton concentration at a tolerable computational cost. The simulations took about 7.7 seconds per time step on a 650 MHz PC with an Athlon Processor, and the longest run involved 36,000 steps.

For the numerical experiment, the following parameters were chosen in the Jassby-Plat model (in code units†): $r = 0.1$, $L = 0.18$, $I_0/I_c = 12$, $\mu_0 = 0.05$, $\mu_1 = 0.01$, $v_p = 0.28$,

---

† That is, these numbers are directly used in the equations with horizontal domain size being 2π. However, all results are presented as dimensionless quantities.
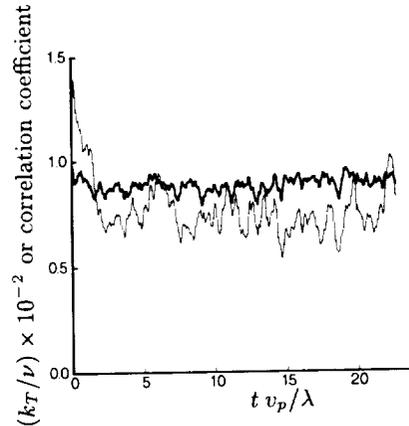
FIGURE 3. The best value of eddy-diffusivity determined by fitting a regression line (————)
and correlation coefficient indicating goodness of fit (————) as a function of time.

and, in order that the Jassby-Platt model approximates closely the "Layer Model" a large value was chosen for the parameter α, $\alpha = 10$. The point in the $G - \Delta$ parameter space corresponding to this simulation is indicated in Fig. 1 by the filled circle. The turbulent velocity field was initialized in the usual manner (Rogallo (1977)). The Taylor microscale Reynolds number of the turbulence is $\Re_\lambda \approx 29$, and the Schmidt number is chosen to be $Sc = 0.7$.

The solid line in Fig. 2 is the prediction of the theoretical model presented in Section 4 with a value of the eddy diffusivity that corresponds to that found in the DNS. The theoretical model assumes zero flux at the upper surface while the DNS uses zero concentration. With the parameters chosen, the difference between the solutions using the no flux and the zero boundary conditions is expected to be small. To quantify the degree of dependence of the profile on boundary conditions, we worked out the analytical results corresponding to the $\phi = 0$ rather than the zero flux boundary condition at the upper surface. This solution is very similar to that presented in Section 4. The formulae are omitted for brevity, but the profile corresponding to it is plotted in Fig. 2 as a dashed line. Clearly the two curves are qualitatively similar, but quantitatively the difference is not negligible. The critical curve in parameter space corresponding to the zero boundary condition solution is also depicted in Fig. 1 as a dashed curve. The boundary condition is seen to have a minor impact on the critical curve.

In order to determine the correct value of the diffusivity to use in place of k_T in the analytical results, we perform a linear regression of the form $Y = k_T X$ to the data, where $X = (\partial \bar{\phi}/\partial z)$ and $Y = -\overline{w\phi}$. The slope of the regression line then gives k_T. Figure 3 shows the time history of the regression line slope, k_T, together with the correlation coefficient characterizing the goodness of the fit. The average value of k_T was determined by time averaging the data after the initial transient, i. e. for $tv_p/\lambda > 5$. This value is augmented slightly by the small "molecular" diffusivity k_0 for use in computing the analytical profiles.

In order to test the stability of the solution numerically and also to test that the profile indeed does evolve towards a steady state, we started the simulation from an initial condition well below the theoretical prediction. The initial phytoplankton profile was arbitrarily chosen as a "sine to the fourth" distribution with an amplitude of about 10 percent of that expected from the theory. In Fig. 4 the lines show concentration profiles
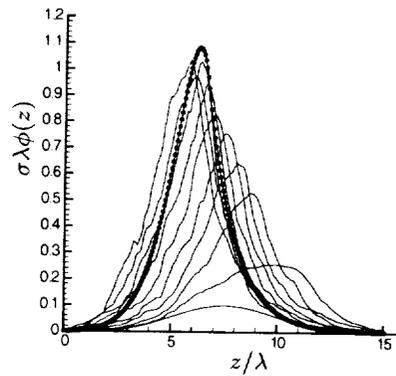
FIGURE 4. The time evolution of the horizontally averaged plankton concentration as a function of depth, the symbols represent the theoretically predicted profile.
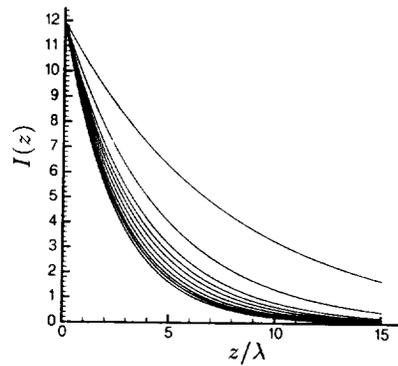
FIGURE 5. The time evolution of the light intensity as a function of depth; the highest curve is the initial profile.

evolving from this initial condition and approaching the theoretical profile depicted by the symbols. The "self-shading" effect is obvious in Fig. 5, which contains the evolution of the light intensity. As the phytoplankton concentration increases, the light reaching any given layer decreases, resulting in a decreased rate of production.

As a final test, we performed another simulation using the theoretical profile with the zero concentration boundary condition at the surface. However, we reduced the growth rate to $r = 0.05$, corresponding to the point depicted by the open circle in the parameter space in Fig. 1. Since this is below the critical curve, it is expected the the phytoplankton profile would decay away. This is indeed what is observed. Figure 6 shows the decay of the depth integrated phytoplankton concentration density Φ as a function of time.

These are preliminary results. It is not yet clear that the distributions have reached a statistically stationary state. The results of more detailed investigations will be presented at a future date.
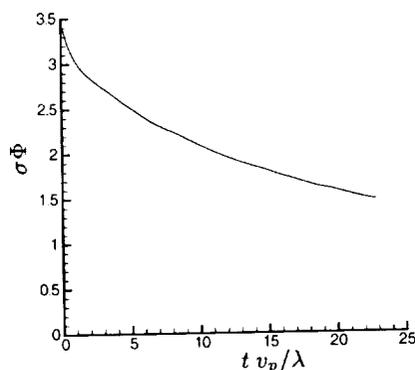
FIGURE 6. The time evolution of the depth integrated plankton concentration showing the decay of a healthy population when the operating point (G, Δ) lies below the critical curve.

6. Conclusion & future plans

Biology and geophysical phenomena are intricately interconnected and are merely two essential components of a vast and complex machinery that operates on the planetary scale. This complexity starts to become comprehensible only if we view it through the lens of a highly simplified model that captures only the essential and then add in the details as successive refinements when comparison with data warrants it. The present paper represents merely a first step in this incremental process.

A general conclusion that may be drawn from the comparison of the numerical simulations and the theory is that an eddy diffusivity model for turbulent transport appears to be adequate for the purpose of predicting the mean concentration of organisms. Also, the simulations seem to indicate that the solution corresponding to the analytical profile is globally stable in the appropriate region of parameter space. Below the critical curve, the zero solution seems to be globally stable. This conclusion, however, is tentative as it is based on a very limited number of simulations.

The most serious shortcoming of the present model is that it applies only in eutrophic environments. A natural extension of the model would be the introduction of the dynamics of nutrients into the model. A certain formal similarity of the mathematics of plankton dynamics with that of combustion is obvious (both are reaction-diffusion systems). Carrying this analogy further, the distinction between eutrophic and oligotrophic environments is not unlike the distinction between "premixed" and "diffusion flames" (the latter being dominated by the depletion of reactants, similar to depletion of nutrients in the case of plankton dynamics).

The second critical constraint is the implicit assumption that the entire water column is uniformly turbulent. In many lakes the onset of warmer conditions during spring causes the water column to become stably stratified so that the wind driven turbulence cannot penetrate to very deep layers. The change in the relative position of the turbocline with respect to the boundary of the euphotic zone due to stratification effects brought about by thermal and salinity gradients is a very important component of phytoplankton dynamics. In particular, the classical Sverdrup Critical Depth Model (SCDM), which is supported by a wide range of geophysical data, correlates phytoplankton blooms with the turbocline becoming shallower than a certain critical depth. Generalization of the current model would be necessary to include these very important effects.

The current model assumes the plankton distribution to be statistically homogeneous in the horizontal directions. This simplified model fails to throw any light on the rich and varied horizontal structure seen in satellite images of the plankton distribution in natural waters. Phytoplankton patches are transported by horizontal currents, but they can also be expected to show intrinsic dynamics. For example, if a small patch of phytoplankton are introduced in waters for which the point (G, Δ) in parameter space is favorable to phytoplankton growth, what are the dynamics of the process by which the steady state distribution in the above model gets established? The solution is likely to be analogous to the problem of the propagation of an ignition front leading to the formation of a flame sheet. The details of such processes for the phytoplankton system are poorly understood and would be interesting areas for future investigations.

Acknowledgments

REFERENCES

ALEXANDER, R. M. 1990 Size, speed and buoyancy adaptations in aquatic animals. *Amer. Zool.* **30**, 189.

ALEXANDER, R. M. 1992 *Exploring Biomechanics: Animals in motion.* Scientific American Library.

CHARLSON, R.J., LOVELOCK, J. E., ANDREAE, M. O. & WARREN, S. G. 1987 Oceanic phytoplankton, atmospheric sulphur, aloud albedo and climate. *Nature.* **326**, 655.

EDWARDS, A. M. & BRINDLEY, J. 1999 Zooplankton mortality and the dynamical behavior of plankton population models. *Bull. Math. Biol.* **61**, 303.

EPPLEY, R. W., HOLMES, R. W. & STRICKLAND, J. D. W. 1967 Sinking rates of marine phytoplankton measured with a fluorometer. *J. Exp. Mar. Biol. Ecol.* **1**, 191.

FENCHEL, T. 1974 Intrinsic rate of natural increase: the relationship with body size. *Oecologia.* **14**, 317.

GIBSON, C. H. 2000 Laboratory and ocean studies of phytoplankton response to fossil turbulence. *Dynamics of atmospheres and oceans.* **31**, 295.

JASSBY, A. D. & PLATT, T. 1976 Mathematical formulation of the relationship between photosynthesis and light for phytoplankton. *Limnol. Oceanogr.* **21**, 540.

JIMENEZ, J. 1997 Oceanic turbulence at millimeter scales. *Scientia Marina.* **61**, Suppl. 1, 47. ["Lectures on plankton & turbulence", ed. Marrase, C., Saiz, E. & Redondo, J. M."]

KOSEFF, J. R., HOLEN, J. K., MONISMITH, S. G. & CLOERN, J. E. 1993 Coupled effects of vertical mixing and benthic grazing on phytoplankton populations in shallow, turbid estuaries. *J. Marine Res.* **51**, 843.

LUCAS, L. V., CLOERN, J. E., KOSEFF, J. R., MONISMITH, S. G. & THOMPSON, J. K. 1998 Does the Sverdrup critical depth model explain bloom dynamics in estuaries? *J. Marine Res.* **56**, 375.

LUCAS, L. V., KOSEFF, J. R., CLOERN, J. E., MONISMITH, S. G. & THOMPSON, J. K. 1999 Processes governing phytoplankton blooms in estuaries. I: The local production-loss balance. *Marine Ecology Progress Series.* **187**, 1.

LUCAS, L. V., KOSEFF, MONISMITH, S. G., CLOERN, J. E. & THOMPSON, J. K. 1999

Processes governing phytoplankton blooms in estuaries. II: The role of horizontal transport. *Marine Ecology Progress Series.* **187**, 17.

MARGALEF, R. 1978 Life-forms of phytoplankton as survival alternatives in an unstable environment. *Oceanological Acta.* **1**, 493.

PETERS, F. & MARRASE, C. 2000 Effects of turbulence on plankton: an overview of experimental evidence and some theoretical considerations. *Marine Ecology Progress Series* (in press).

REYNOLDS, C. S. 1984 *The ecology of freshwater phytoplankton.* Cambridge University Press.

RILEY, G. A., STOMMEL, H. & BUMPUS, D. F. 1949 Quantitative ecology of the plankton of the western north atlantic. *Bull. Bingham Oceangr. Coll.* **XII**(3), 1.

ROGALLO, R. 1977 An ILLIAC program for the numerical simulation of homogeneous incompressible turbulence. *NASA Tech. Mem.* **NASA TM-73203**.

SVERDRUP, H. U., JOHNSON, M. W. & FLEMING, R. H. 1946 *The Oceans Their Physics, Chemistry, and General Biology.* Prentice Hall.

SVERDRUP, H. U. 1953 On conditions for the vernal blooming of phytoplankton. *J. Conseil Exp. Mer.* **18**, 287.

THURMAN, H. V. 1997 *Introductory Oceanography, 8th edition* Prentice Hall.

TRUSCOTT, J. E. & BRINDLEY, J. 1994 Ocean plankton populations as excitable media. *Bull. Math. Biol.* **56**(5), 981.

The optimization group

The optimization group of the CTR summer program focused on the development and implementation of novel deterministic and stochastic optimization techniques to the design of micro-fluidic channels and to the destruction of trailing aircraft vortices. The CTR summer program was instrumental in facilitating, for the first time, the close interaction of scientists working in the areas of deterministic and stochastic optimization, allowing a critical assessment of both techniques and opening new areas for collaborative, interdisciplinary research.

The optimization of microfluidic channels used in bioanalytical applications served as a common testbed for the application of novel optimization techniques. Mohammadi, Molho and Santiago implemented a dynamic minimization technique developed by Mohammadi and Pironneau (2000) and conducted an extensive study of the optimization of the geometry of these channels in a CAD-free framework. Their results revealed an array of novel efficient designs for serpentine channels with 90 and 180 degree turns. Moreover, the study of this group demonstrated how advanced optimization techniques developed for the needs of aerodynamic applications can transcend and impact domains such as those of microfluidics.

In parallel, Sbalzarini, Müller and Koumoutsakos developed and implemented evolution strategies with step size adaptation and in parallel computer architectures for a class of microfluidic channels with 90-degree turns. They obtained a series for designs encompassing the optimal results obtained by the deterministic schemes, albeit at higher computational cost. An additional purpose of this group study was the development of novel evolutionary multi-objective optimization strategies. These studies resulted in an array of designs compensating between manufacturing costs and minimal dispersion.

The portability for evolutionary algorithms allowed for another study by Cottet, Koumoutsakos and Sbalzarini on the destruction of trailing aircraft vortices. Using fast, viscous vortex methods and a set of vortices modeling the wake of airplanes at landing configurations, evolution algorithms recovered in an automated optimization cycle the results found by linear stability theory (Crouch, 1997). Moreover, novel vortical arrangements were revealed that allow for larger distortion of the tip vortices.

In summary, this CTR summer program laid the foundation for a critical assessment of various optimization techniques while demonstrating the interdisciplinary character of the developed optimization tools. A preliminary conclusion of this study is that deterministic optimization techniques are the method of choice for well defined problems where gradient information is readily available. However, this information may come at the expense of linearizations and constrained parameterizations of the problem. Evolutionary algorithms circumvent these difficulties at the expense of higher computational cost. An additional difficulty with evolutionary techniques is the absence of rigorous results regarding their convergence. On the other hand evolutionary algorithms are robust, embarrassingly parallel and highly portable algorithms that may make them the method of choice in certain engineering problems. We hope that the works of this CTR Summer Program would serve in initiating further interactions between researchers in deterministic and stochastic optimization as applied to a wide range of interdisciplinary engineering problems.

Petros Koumoutsakos

Design of minimal dispersion fluidic channels in a CAD-free framework

By B. Mohammadi† J. I. Molho‡ AND J. G. Santiago‡

We show the application of our shape optimization approach to the design of electroosmotic micro-fluidic channels realizing minimal geometrical dispersion on 90- and 180-degree turns.

1. Introduction

Microfluidic channel systems used in bio-analytical applications are fabricated using technologies derived from microelectronics industry including lithography, wet etching, and bonding of substrates. One important class of these channel system uses capillary zone electrophoresis to separate and detect chemical species. This technique separates chemical species suspended in a liquid buffer based on their electrophoretic mobility. The electric field in these systems is applied along the axis of the channel using electrodes immersed at reservoirs at the end of the micro-channels. The ability to discriminate between sample species of nearly equal mobility is enhanced by increasing the channel length (Culbeston, Jacobson & Ramsey (1998), Molho *et al.* (2000)). In order to achieve channel lengths of order 1 m and yet confine the micro-channel system to a compact configuration with dimensions less than about 10 cm, curved channel geometries are required. Unfortunately, curved channel geometries introduce skew, which creates a dispersion of the electrophoretic sample bands in the flow. This curved-channel dispersion has been identified as an important factor in the decrease of separation efficiency of electrophoretic micro-channel systems. The goal of the current work is to analyze and then minimize the skew that is introduced by turns in electrokinetic microchannels. Unfortunately, we notice that reducing the skew often introduces a new type of residual dispersion associated with band advection away from the channel boundaries. To avoid this effect it is necessary for the channel walls to be as smooth as possible with minimal curvature variation. However, optimizations based only on skew minimization do not yield smooth walls. We therefore add a constraint on the wall smoothness to our optimization.

The optimization formulation for such devices has to include therefore the following points:

- minimize the skew due to turns,
- minimize the residual dispersion associated with band advection,
- avoid too much variations in walls curvature,
- maximize the length of the channel,
- minimize the occupied surface.

Our aim in this paper is to show how to use our optimization platform, first designed

† University of Montpellier and INRIA, France
‡ Mechanical Engineering Dept., Stanford University, Stanford, CA, USA

for aeronautical applications (Mohammadi (1997a),Mohammmadi & Pironneau (2000)), for the design of minimal dispersion electrokinetic channels.

An important ingredient in the platform is the Computer-Aided-Design-free parameterization of the micro-fluidic channel geometry which has shown its ability to produce various new shapes not necessarily reachable in the original CAD parameterization. In this parameterization, the control space is quite rich compared to a CAD parameterization (Mohammmadi & Pironneau (2000)). We will see also that this parameterization allows for modeling of dimensional uncertainties introduced by the manufacturing step.

Another important ingredient is to use dynamic minimization algorithms. We showed how to put well known minimization algorithms in the form of dynamic systems, having a decreasing energy like in Hamilton-Jacobi systems, suitable to reach stationary point for the solution of coupled problems. Indeed, in this approach, the minimization algorithm is seen as an extra state equation (for the parameterization) and the whole system is marched in a pseudo-time to a stationary point. Global minimization can also be introduced by coupling several dynamic systems from different parameterization states (Mohammmadi & Pironneau (2000)).

Finally, we would like to point out the use of incomplete sensitivities in the design process. The aim is to perform analysis and design at the same time. The main idea is to use two different state equations for the evaluation of the state variables and for the evaluation of sensitivities. The first is usually complex and probably available in a commercial package; the second one simpler, but of which we have complete control and knowledge. The two different state equations are used because we would like the simulation and design problems to have about the same complexity. We widely used this technique in shape design in aerodynamical applications (Mohammmadi & Pironneau (2000)) where the gradient of aerodynamical coefficients were approximated keeping only geometrical contributions (Mohammadi (1997a),Mohammmadi & Pironneau (2000)). This is especially important where the number of control parameters is large and would otherwise require the use of an adjoint solver. This simplification is also important when the size of the direct simulation problem is near the limit of what can be treated in a reasonable amount of time by existing computer facilities.

We show the application of this technique by minimizing the dispersion of chemical species moving electrokinetically through 90 and 180 degree turns. These turns are important as they can be used to make serpentine channels that provide long separation lengths within a compact area. Typical cross-section sizes for these channels are 100 μm in width and 10 μm in depth.

2. Governing equations

This problem is multi-model in the sense that several PDE are involved in the definition of the state variables and the cost function. We will see that different levels of approximation can be introduced for these state equations.

2.1. *Electric field*

We desire to simulate the motion of species in an electric field $E(t, x)$. In general, E can be either stationary or unsteady, but in this work, we consider only steady electric fields.

$E = \nabla v$ is defined solving a Poisson equation for the potential v:

$$-\Delta v = 0, \quad \text{in} \quad \Omega \tag{2.1}$$

$$v(\Gamma_{in}) = v_1, \quad v(\Gamma_{out}) = v_2, \quad \frac{\partial v}{\partial n} = 0 \quad \text{on other boundaries.}$$

2.2. Flow motion

For typical electrokinetic microchannel applications, the observed flow motion has a velocity of about $10^{-4} m/s - 10^{-3} m/s$, channel thickness of 100 μm, and kinematic viscosity about $10^{-5} m^2 s^{-1}$. This leads to Reynolds numbers ranging from 0.001 to 0.01. Due to spontaneous charge separation that occurs at the channel walls, there is formation of an electric double layer (Probstein). The typical size of this layer is a few nano meters. The stiffness of this electric double layer makes it difficult to compute using classical numerical approaches applied to the Stokes model with a Lorentz force term. However, it is known that at the edge of the double layer the flow is parallel and directly proportional to the electric field. The first model describing the flow motion can therefore be the Stokes system with a slip velocity at the channel walls.

$$\frac{\partial U}{\partial t} - \mu \Delta U + \nabla p = 0, \quad \text{in the channel} \tag{2.2}$$

$$U = \mu_{ek} E \quad \text{on the inner and outer walls,}$$

$$-\mu \frac{\partial U}{\partial n} + p.n = 0 \quad \text{on in and outflow boundaries,}$$

where μ_{ek} is the electrokinetic mobility of the flow, μ the dynamic viscosity, and n the unit external normal to the boundaries.

2.3. Reduced models for the flow

In the absence of a pressure gradient, the previous model reduces to two elliptic equations for the velocity components and states that the velocity vector is locally parallel to the walls and proportional to the local electric field $U = \mu_{ek} E \tilde{U}$ with $\tilde{U}$ obtained solving for $\tilde{U} = (\tilde{u}_1, \tilde{u}_2)$:

$$-\Delta \tilde{u}_1 = 0, \quad -\Delta \tilde{u}_2 = 0, \quad \text{in} \quad \Omega, \tag{2.3}$$

$$\tilde{U} = (\tilde{u}_1, \tilde{u}_2) = \tau = (\tau_1, \tau_2), \quad \text{on channel walls,} \quad \frac{\partial \tilde{U}}{\partial n} = 0 \quad \text{on other boundaries,}$$

where τ is the local unit tangent to channel walls. Noticing that the electric field itself is parallel to walls, this means that the velocity is everywhere parallel and proportional to the electric field:

$$U = \mu_{ek} E. \tag{2.4}$$

We use this latter model in our optimization problem. In addition, this model is interesting for incomplete sensitivity evaluation (see below), where different models are used for the state and gradient computations. In other words, even when using more complex models, we should consider this model as the state equation to be used for sensitivity evaluation.

2.4. Advection of species

The motion of a species a at infinite Peclet number by the velocity field U computed above is described by:

$$a_t(x, t) + U(x) \nabla a = 0, \quad \text{in} \quad \Omega, \tag{2.5}$$

$$a(\Gamma_{inlet}) = \text{given.}$$
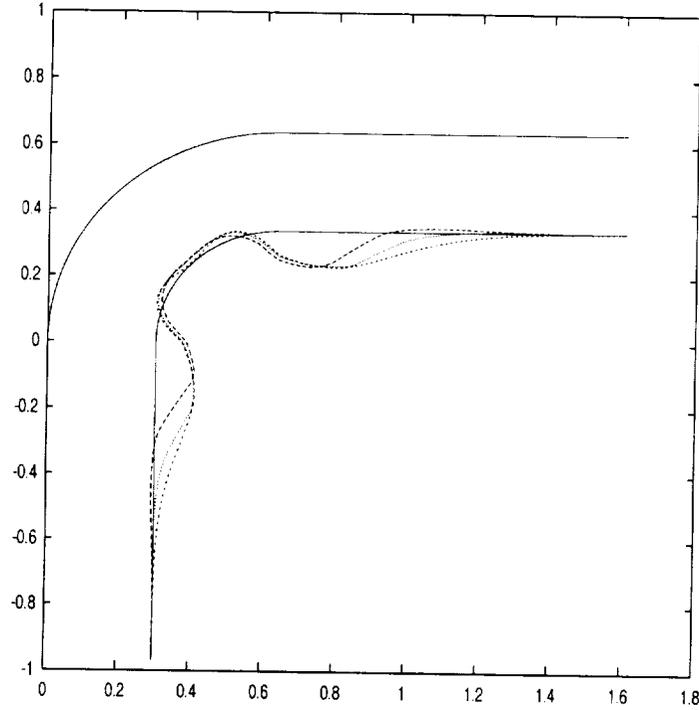
FIGURE 1. Shapes obtained under the same optimization conditions for three admissible spaces with different minimum required regularity for the shape. I: initial (————), II: less regular (— — —), III: medium regularity (— — — —), IV: most regular (········).

As we consider the velocity field defined by the stationary electric field, this step is therefore only a post-processing step and is devoted to the quantification of the skew.

3. Design problem formulation

We consider the following constrained minimization problem:

$$\min_{x(t) \in X} J(x, q(x), u(q, x)),\qquad (3.1)$$

$$E(x, q(x), u(q, x)) = 0,$$

$$g_1(x) \leq 0, g_2(q(x)) \leq 0, \quad g_3(q, u(q, x)) \leq 0,$$

where $x \in X \subset R^{n_c}$ describe our CAD-Free parameterization (Mohammadi (1997a)). $q(x)$ describes all geometrical entities (normals, surfaces,...). $u \in R^N$ denotes the state variables (here the potential, electric field, fluid velocity, and the advected species) and $E \in R^N$ the state equations described above. g_1 defines the constraints expressed directly on the parameterization and is taken into account in the definition of the admissible space X, g_2 defines constraints on geometrical quantities (for instance concerning the regularity of the shape) and g_3 state constraints on u (for instance concerning the regularity of the velocity field).

3.1. *Robustness*

In many microfabricated fluidic channel systems (Molho *et al.* (2000)), it is difficult to exactly realize proposed shapes due to small but significant errors introduced in the manufacturing step. One way to account for these variations is to introduce a random perturbation operator in the optimization algorithm in the sense that the proposed shape is equivalent to any shapes in a given range (e.g. 5% in normal variation). The minimization problem (3.1) can therefore be reformulated as:

$$\min_{x(t) \in X} \max_{y \in Y(X)} J(y, q(y), u(q, y)), \tag{3.2}$$

with the state equation and constraints as above. Here the admissible space $Y(X)$ for the worst case analysis approach is defined by:

$$Y(X) = \{y \in [\frac{1}{\alpha}x, \alpha x], \forall x \in X\} \subset R^{n_c},$$

which, for instance, for $\alpha = 1.05$ defines a 5% variation range around the proposed shape. If $\alpha = 1$, there is no randomness and the two optimization problems (3.1-3.2) are similar.

Another way to proceed is to perform the optimization in an admissible space with slightly less regularity required than what would be realizable by the manufacturing. Hence, the obtained shapes includes a possible imperfection. We propose the following approach:

- Define the admissible space X for the manufacturing,
- Extend X to X' including less regular shapes,
- Perform the optimization (3.1) in X',
- Project the optimized shape into X,
- Validate the regularized shape for the skew.

This approach is easy to account for in our CAD-Free parameterization presented below. We show in (Fig. 1) a possible loss of regularity for the shape; three designs have been performed under the same conditions but with slightly different minimum required regularity for the admissible spaces.

4. CAD-Free shape and mesh deformation tools

The shape deformation is done in a CAD-Free framework (Mohammmadi & Pironneau (2000)) in the sense that the only entity known during optimization is the mesh. This parameterization has several characteristics:

1. All of the nodes on the inner wall of the channel are control points. More precisely, we use the local normal to the inner channel wall and specify the deformations in the direction of this normal $n(x)$. Hence, for a curve $\gamma(x)$, a deformation of amount $f(x)$, defined for each node, leading to the deformed curve $\tilde{\gamma}(x)$, can be expressed in the normal direction to γ by:

$$\tilde{\gamma}(x) = \gamma(x) + f(x)n(\gamma(x)).$$

2. To avoid oscillations, a 'local' smoothing operator is defined over the shape.

The smoothing operator is required because the gradient has less regularity than the parameterization. Indeed, suppose that the cost function is a quadratic function of the parameterization: $J(x) = (Ax - b)^2$ with $x \in H^1(\Gamma)$, $A \in H^{-1}(\Gamma)$ and $b \in L^2(\Gamma)$. The gradient $J'_x = (2(Ax-b)A) \in V$ with $H^{-1}(\Gamma) \subset V \subset L^2(\Gamma)$. Hence, any parameterization variation using J'_x as descent direction will have less regularity than x: $\delta x = -\rho J'_x =$

$-\rho(2(Ax - b)A) \in V$, where $H^{-1}(\Omega) \subset V \subset L^2(\Omega)$. We need therefore to project into $H^1(\Omega)$ using the localized solution of a second order elliptic system in regions where the deformation is not smooth enough.

$$(I - \varepsilon\Delta)\delta\tilde{x} = \delta x, \tag{4.1}$$

$$\delta\tilde{x} = \delta x = 0 \quad \text{where constrained,}$$

where $\delta\tilde{x}$ is the smoothed shape variation for the shape nodes and δx is the variation given by the optimization tool. By 'local' we mean that if the predicted shape is locally smooth, it remains unchanged during this step and ε is set to zero for these regions if,

$$\frac{\delta_{ij}(\delta x)}{(\delta x)_T} < TOL, \tag{4.2}$$

where $\delta_{ij}(\delta x)$ is the difference between the variations of the two nodes of each boundary edge and $(\delta x)_T$ the mean variation on this edge and TOL a regularity tolerance factor.

To include a loss of regularity as discussed above, it is sufficient to ask for more tolerance in the step above.

Once the shape deformation is defined, it is propagated over the computational domain using an elasticity based procedure as described in (Mohammmadi & Pironneau (2000)). These shape and mesh deformation tools have been used in optimization problems in two- and three-dimensional configurations for incompressible and compressible flows (Mohammmadi & Pironneau (2000)).

5. Cost function and constraints

We want to minimize the skew, which can be quantified in different ways. For example, we can ask for iso-values of the advected species to be always normal to the flow field. In this case, we can consider:

$$J(x) = \int_0^T \int_\Omega (\nabla a(x,t) \times U(x))^2 dx dt, \tag{5.1}$$

where T is the maximum migration time. These integrals are not suitable for cheap sensitivity evaluation as they involve information over the whole domain. In addition, this cost function is too restrictive as we are actually interested only in minimizing the final skew. The cost function reduces to:

$$J(x) = \int_\Omega (\nabla a(x,T) \times U(x))^2 dx, \tag{5.2}$$

which again reduces away from the turn, and therefore where U is constant, to:

$$J(x) = \int_\Omega (\frac{\partial a(x,T)}{\partial n})^2 dx, \tag{5.3}$$

where n is the normal direction to the local walls.

Another way to reduce the skew, which avoids the previous restriction, is to ask for all particles traveling on characteristics to have the same migration time. Hence, the cost function is given by:

$$J(x) = (\int_\chi \frac{ds}{U} - \int_{\chi'} \frac{ds}{U})^2, \tag{5.4}$$
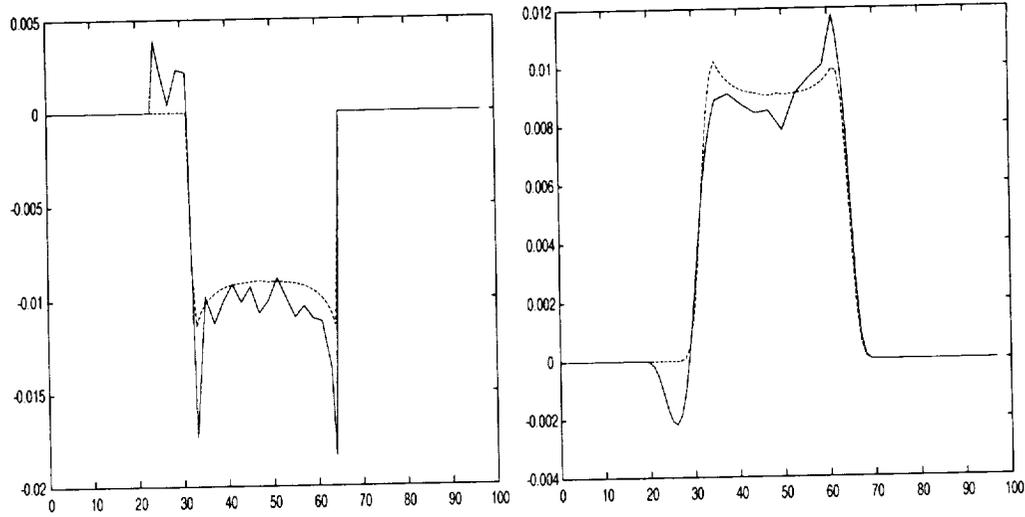
FIGURE 2. Sensitivity evaluation around the initial 90-degree turn for control points along the inner channel wall. Comparison between the exact (———) and incomplete (– – – –) gradient evaluations (left). The deformations obtained using these gradients (right).

for any couple of characteristics χ and χ' linking the outlet to the inlet. Here again, the cost function is over the whole space, but we can consider only a few characteristics. The two main characteristics are those defined by the internal and external walls of the channel:

$$J(x) = (\int_{\Gamma_i} \frac{ds}{U.\tau} - \int_{\Gamma_o} \frac{ds}{U.\tau})^2. \tag{5.5}$$

where Γ_i is the inner wall and Γ_o the outer wall in a turn. This last formulation is interesting as it only involves boundaries which we know to be suitable for the application of our incomplete sensitivity. Another interesting feature of formulations (5.4 and 5.5) over (5.1) is that they do not require the knowledge of the distribution of the advected species.

As we said, we notice that the residual band advection dispersion away from the channel walls increases with the variation of the shape curvature. We therefore add the following constraint to the cost function (5.5) above:

$$J(x) \leftarrow J(x) + (\int_{\Gamma_i} \|\frac{\partial n}{\partial s}\| - \int_{\Gamma_i^0} \|\frac{\partial n}{\partial s}\|)^2 + (\int_{\Gamma_o} \|\frac{\partial n}{\partial s}\| - \int_{\Gamma_o^0} \|\frac{\partial n}{\partial s}\|)^2, \tag{5.6}$$

where 0 denotes initial inner and outer walls. Thus, when we allow both walls to move, we obtain about the same amount of skew but a higher residual dispersion inside the channel. The second constraint vanishes in cases where the outer wall is kept unchanged.

Two other types of geometrical constraints concern the amplitude of the deformations and the regularity of the deformed shape. In the first constraint, shape variations are allowed between two limiting curves. Regularity requirements are enforced using the smoothing operator of the CAD-Free parameterization described above.

6. Sensitivity and incomplete sensitivities

Consider the general simulation loop, involved in (3.1), leading from shape parameterization to the cost function:

$$J(x) : x \to q(x) \to U(q(x)) \to J(x, q(x), U(q(x))).$$

The Jacobian of J is given by:

$$\frac{dJ}{dx} = \frac{\partial J}{\partial x} + \frac{\partial J}{\partial q}\frac{\partial q}{\partial x} + \frac{\partial J}{\partial U}\frac{\partial U}{\partial q}\frac{\partial q}{\partial x}.$$

In most applications, the cost function is, or can be reformulated to have, the following characteristics:

• The cost function J and the parameterization x are defined on the shape (or some part of it),

• J is of the form

$$J(x) = \int_{\text{shape or part of the shape}} f(x, q)g(u)d\gamma,$$

which means that it involves a product of geometrical and state based functions.

We have shown that for such cost functions, the sensitivity with respect to the state can be neglected in regions where the curvature of the shape is not too large (Mohammadi (1997a)-Mohammadi (1999)).

The concept of incomplete sensitivities was first introduced for aerodynamical applications involving hyperbolic and parabolic PDEs (Mohammmadi & Pironneau (2000)). In that work, we showed that where the cost function, constraints, and controls are defined over the shape (through boundary integrals for instance), a good estimation of gradients are obtained by keeping only geometrical sensitivities. This means that only the shape deformation tool has to be differentiated and not the whole simulation loop. In particular, neither the mesh deformation nor the state equation solver have to be linearized (Mohammadi (1997b)). Hence, we consider the following approximation for the gradient:

$$\frac{dJ}{dx} \sim \frac{\partial J}{\partial x} + \frac{\partial J}{\partial q}\frac{\partial q}{\partial x}.$$

We can illustrate this idea by the following simple example. Consider as cost function $J = a^n u_x(a)$ and for the state equation the following diffusion equation:

$$-u_{xx} = 1, \quad \text{on }]\epsilon, 1[, \quad u(\epsilon) = 0, \quad u(1) = 0,$$

which has as solution $u(x) = -x^2/2 + (\epsilon + 1)/2 - \epsilon/2$. We are in the domain of application of the incomplete sensitivities (Mohammmmadi & Pironneau (2000)):

• the cost function is product of state and geometrical quantities (larger is n, better is the approximation),

• it is defined at the boundary,

• the curvature of the boundary is small (here no curvature at all).

The gradient of J with respect to ϵ is given by:

$$J_\epsilon(\epsilon) = \epsilon^{n-1}(nu_x(\epsilon) + \epsilon u_{x\epsilon}(\epsilon)) = \frac{\epsilon^{n-1}}{2}(-n(\epsilon + 1) - \epsilon).$$

The second term between parenthesis is the state linearization contribution which is neglected in incomplete sensitivities. We can see that the sign of the gradient is always correct and the approximation is better for large n.

As we stated above, the cost function (5.5) is suitable for the application of incomplete sensitivities. We can increase direct geometrical contributions because the velocity is parallel to the walls. The cost function we consider for derivation is therefore:

$$J(x) = (\int_{\Gamma_i} \frac{ds}{\vec{\tau}\mu_{ek}|E|} - \int_{\Gamma_o} \frac{ds}{\vec{\tau}\mu_{ek}|E|})^2., \qquad (6.1)$$

where $\vec{\tau}$ is the local unit tangent vector to the wall.

To evaluate the accuracy of these gradients, we compare the results obtained with this approximation of the gradients with those coming from finite differences. This incomplete sensitivity evaluation shows the importance of redefining cost functions as boundary integrals when possible (as shown above) and of locating the cost function and control definition locations as close to each other as possible. This is in particular important for three-dimensional configurations and it also permits optimization of an entire microfluidic network and not only a small section of the network. In fact, optimization becomes possible for any geometry for which simulation is affordable as the cost of simulation and design becomes equivalent. Indeed, sensitivity analysis is now equivalent to the linearization of the following approximate simulation loop:

$$\tilde{J}(x) : x \to q(x)|_\Gamma \to J(x, q(x), U(q(x))),$$

which means that we only account for the modification in the geometrical part defined over the inner channel wall.

6.1. *Multi-level gradient construction*

The above discussion of incomplete sensitivities demonstrates that an accurate state evaluation and an approximate gradient is preferable over an accurate gradient based on an inaccurate state obtained from a coarse mesh.

Consider a bilinear cost function involving state u and geometrical q contribution and defined over the same region as the control x.

$$|\frac{d}{dx}(u.q) - u(\text{fine})\frac{dq}{dx}| < |\frac{d}{dx}(u.q) - \frac{du}{dx}(\text{coarse}).q + u(\text{coarse})\frac{dq}{dx}|.$$

The left-hand side is the difference between exact and incomplete gradient computed on a fine mesh.

This error is often present and is due to the fact that the cost of iterative minimization and gradient evaluations limits the user to coarser meshes than what would have been used for a pure simulation.

One method for avoiding this difficulty is to use different levels of refinement for the state and the gradient. This is the idea behind multi-level shape optimization where the gradient is only computed on the coarse level of a multi-grid construction and where the state comes from the finer level (Beux & Dervieux (1997)):

$$\frac{d}{dx}(u.q)(\text{fine level}) = I(\frac{du}{dx}(\text{coarse level})).q(\text{fine}) + u(\text{fine level})\frac{dq}{dx}(\text{fine}).$$

The first term of the left-hand side is the interpolation of the gradient computed on the coarse grid over the fine level.
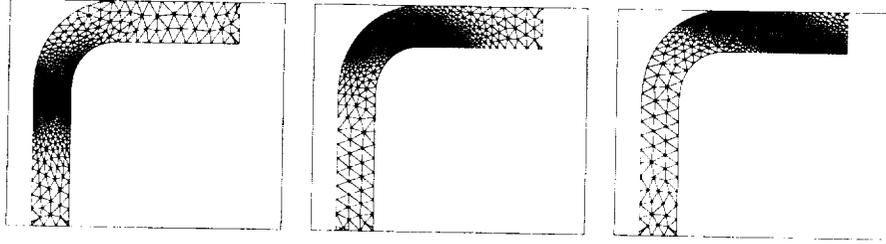
FIGURE 3. Adaptive simulation to accurately capture the skew.

7. Pseudo-unsteady closure equation for x

Consider the following time dependent equation for the shape parameterization x. Here, the time is fictitious and is similar to the descent parameter.

$$\dot{x} + \epsilon \; \ddot{x} = -F(\Pi, \mathcal{M}^{-1}, \nabla_x J).$$

F is a function of the exact or incomplete gradient; it accounts for the projection over the admissible space and the smoothing operator $(\Pi, \mathcal{M})$. This system represents most minimization algorithms. If $\epsilon = 0$, we recover the steepest descent approach. If $\epsilon > 0$, this is the heavy ball method (Attouch & Cominetti (1996)) The aim in this approach is to access different minima of the problem and not only the nearest local minimum. Conjugate gradient and quasi-Newton methods can also be cast in this form (Mohammadi & Pironneau (2000)).

To advance in time (7), we use a central difference scheme (denoted by δx^p, the shape deformation at step p):

$$\left(\frac{\epsilon}{\lambda^2} + \frac{1}{\lambda}\right)\delta x^{p+1} = \frac{\epsilon}{\lambda^2}\delta x^p - F(\nabla_{x^p} J^p). \tag{7.1}$$

After defining the shape parameterization, x^0, the dynamical algorithm we use is as follows:

Optimization iterations

1. compute the gradient: $\frac{dJ^p}{dx}$ or $\frac{d\tilde{J}^p}{dx}$,
   if $(\|\frac{d\tilde{J}^p}{dx}\| < TOL$ or $J^p < TOL)$ stop.
2. define the new admissible shape deformation using (7.1): δx^p,
3. smooth the deformations using (4.1),
4. deform the mesh.
5. compute the new state: u^{p+1}.
6. compute the new cost: J^{p+1}.
7. $p \leftarrow p + 1$ and goto 1.

End of optimization loop.

8. Numerical results

In addition to the characteristics presented above, we use a Delaunay mesh adaptation technique by local metric control that is widely used in various simulations involving the solution of PDE's (Frey & George (1999), Hecht & Mohammadi (2000)). The impact of this coupling has been shown on the advection of a passive scalar by the electric field (Fig. 3). It is clear that to have the same quality without mesh adaptation implies the
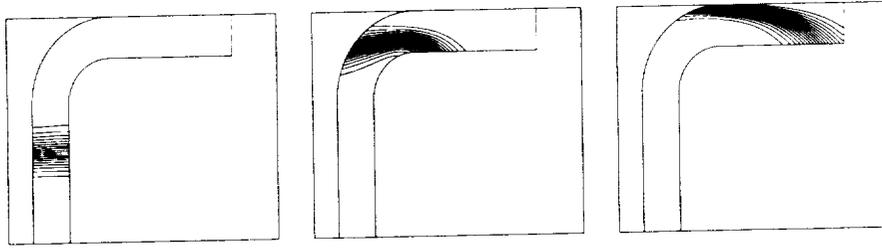
FIGURE 4. Initial shape for the 90-degree turn: effect of the turn on the advected species.
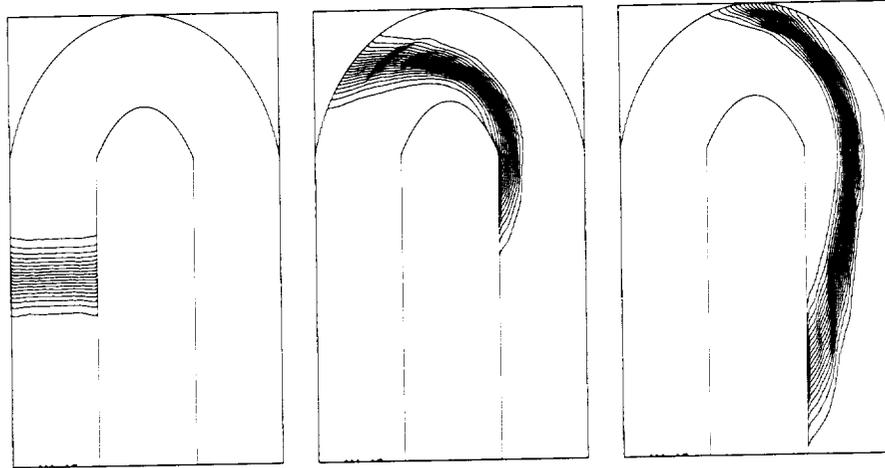
FIGURE 5. Initial shape for the 180-degree turn: effect of the turn on the advected species.
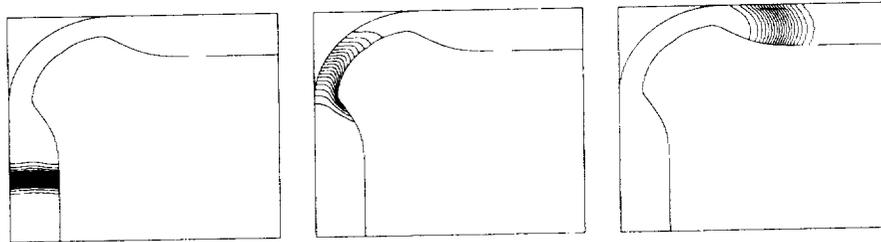
FIGURE 6. First class of optimized shapes for the 90-degree turn. The magnitude of the skew has been reduced by one order.

use of a regular fine mesh everywhere, which is out of reach for general applications. The remeshing is also important and absolutely necessary as the large deformations introduced for the shape makes the mesh too distorted to be effective for finite element simulations.

We show the skews produced by 90- and 180-degree turns in Figs. (4-5). We then applied our optimization approach to these configurations. No symmetry assumption has been made. The first class of optimized shapes for the 90- and 180-degree turns (Figs. 6-7) correspond well with what was found by an intuitive design (Molho *et al.* (2000)). This is important as it permits some confidence on the global design approach. The second classes of optimized shapes for the 90- and 180-degree turns (Figs. 8-9) have been obtained by
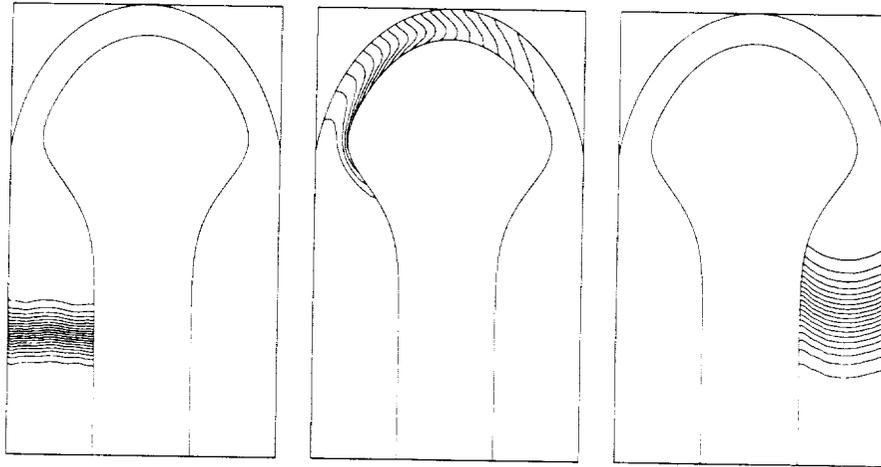
FIGURE 7. First class of optimized shapes for the 180-degree turn. The magnitude of the skew has been reduced by more than one order.
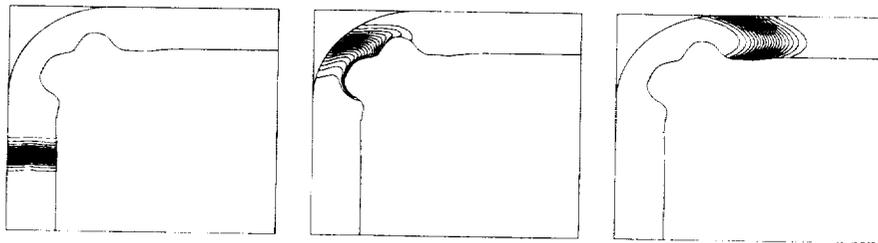
FIGURE 8. Second class of optimized shapes for the 90-degree turn. The magnitude of the skew is about the same than for the first class above with 15% less reduction in cross-section, but there is more dispersion in the advection band as the wall curvature variation is higher.
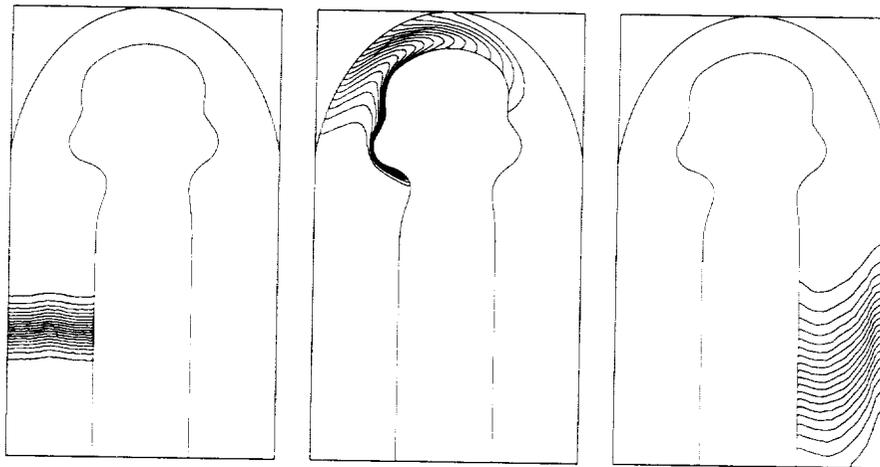
FIGURE 9. Second class of optimized shapes for the 180-degree turn. Here again, larger curvature variation introduces more dispersion in the advection band away from walls.
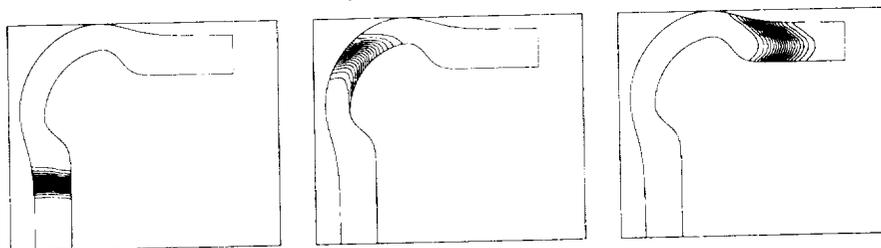
FIGURE 10. Third class of optimized shapes for the 90-degree turn with both the inner and outer walls modified. The skew is about the same than for the first class of the 90-degree optimized turn but with a much larger cross-section, but also more band dispersion away from walls.
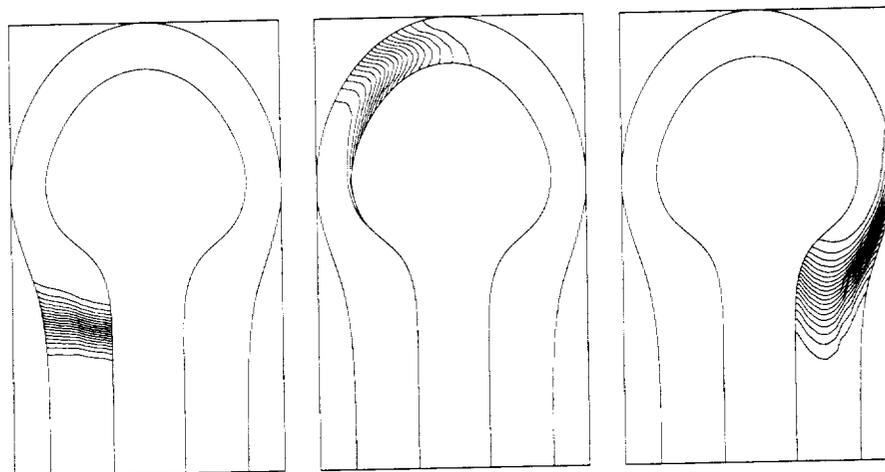
FIGURE 11. Third class of optimized shapes for the 180-degree turn with both the inner and outer walls moving. The skew has been quite reduced and the cross-section conserved (compared to the first class of shape), but there is much more band dispersion away from walls.

constraining the reduction in cross-sectional area and by requiring less regularity for the shapes. However, the increase in irregularity leads to more band dispersion away from the channel walls. The optimizations described above were performed without altering the shape of the outer wall. To avoid too much restriction in the channel cross-section, a third class of shape can be obtained by allowing both the inner and outer walls to deform (Figs. 10-11). However, this turn is less interesting as two such turns would interfere when used to create a serpentine channel pattern.

9. Concluding remarks

We have shown how to combine incomplete sensitivity analysis and the pseudo-unsteady optimization approach to design reduced dispersion electrokinetic microchannel devices. This analysis implies a redefinition of the cost function used for sensitivity evaluation based on approximate formula through boundary integrals. In addition, it has been shown that, to reduce the dispersion associated with band advection away from the channel walls, these walls need to be smooth with minimal curvature variation along the walls. Using the ingredients presented in this paper, minimal dispersion 90- and 180-

degree turns have been obtained which enable, by their combination, the construction of long microfluidic channels within a compact area.

Acknowledgments

REFERENCES

CULBESTON, C. T., JACOBSON, S. C. & RAMSEY, J. M. 1998 Dispersion Sources for Compact Geometries on Microchips. *Analytical Chemistry.* **70**, 3781-3789.

MOLHO, J. I., HERR, A. E., MOSIER, B. P., SANTIAGO, J. G., KENNY, T. W., BRENNEN, R. A. & GORDON, G. B. 2000 Designing Corner Compensation for Electrophoresis in Compact Geometries. *Proc. Micro Total Analysis Systems 2000.*

MOHAMMADI, B. 1997 Practical Applications to Fluid Flows of Automatic Differentiation for Design Problems. *VKI lecture series, 1997-05.*

MOHAMMADI, B. 1997 A New Optimal Shape Design Procedure for Inviscid and Viscous Turbulent Flows. *Int. J. for Num. Meth. in Fluid.* **25**, 183-203.

MOHAMMADI, B. & PIRONNEAU, O. 2000 *Applied Shape Design for Fluids*, Oxford Univ. Press.

MOHAMMADI, B. 1999 Flow Control and Shape Optimization in Aeroelastic Configurations. *AIAA 99-0182.*

PROBSTEIN, R. F. 1995 *Physicochemical Hydrodynamics*, Wiley.

BEUX, F. & DERVIEUX, A. 1997 A Hierarchical approach for shape optimisation. *Inria report 1868.*

ATTOUCH, H., COMINETTI, R. 1996 A Dynamical Approach to Convex Minimization Coupling Approximation with the Steepest Descent Method. J. Diff. Eq. **128**(2), 519-540.

FREY, P. & GEORGE, P. L. 1999 *Maillages*, Hermes.

HECHT, F. & MOHAMMADI, B. 2000 Mesh Adaptation for Time Dependent Simulation and Optimization, *Revue Européenne des Elements Finis*, submitted.

Multiobjective optimization using evolutionary algorithms

By Ivo F. Sbalzarini†, Sibylle Müller† AND Petros Koumoutsakos†‡

Multiobjective evolutionary algorithms for shape optimization of electrokinetic micro channels have been developed and implemented. An extension to the Strength Pareto Approach that enables targeting has been developed. The results of the automated optimization cycle show shapes previously obtained by physical understanding as well as novel shapes of even higher efficiency.

1. Introduction

Evolutionary algorithms (EAs) such as evolution strategies and genetic algorithms have become the method of choice for optimization problems that are too complex to be solved using deterministic techniques such as linear programming or gradient (Jacobian) methods. The large number of applications (Beasley (1997)) and the continuously growing interest in this field are due to several advantages of EAs compared to gradient based methods for complex problems. EAs require little knowledge about the problem being solved, and they are easy to implement, robust, and inherently parallel. To solve a certain optimization problem, it is enough to require that one is able to evaluate the objective (cost) function for a given set of input parameters. Because of their universality, ease of implementation, and fitness for parallel computing, EAs often take less time to find the optimal solution than gradient methods. However, most real-world problems involve simultaneous optimization of several often mutually concurrent objectives. Multiobjective EAs are able to find optimal trade-offs in order to get a set of solutions that are optimal in an overall sense. In multiobjective optimization, gradient based methods are often impossible to apply. Multiobjective EAs, however, can always be applied, and they inherit all of the favorable properties from their single objective relatives.

Section 2 of this paper introduces main concepts of single objective EAs. Section 3 extends these ideas to multiobjective cases and introduces the principles of dominance and Pareto optimality. Section 4 describes the Strength Pareto Approach used in this work, and in section 5 we extend it with a targeting capability. In section 6 the results of both single and multiobjective optimization of a microchannel flow are shown and discussed.

2. Single objective evolutionary algorithms

The basic idea for single objective EAs is to imitate the natural process of biological evolution. The problem to be solved is therefore described using a certain number of

† Inst. of Computational Sciences, ETH Zürich, Switzerland, {ivo,sibylle,petros}@inf.ethz.ch
‡ also at Center for Turbulence Research, NASA Ames/Stanford Univ.

parameters (design variables). One then creates a group of $\lambda (> 0)$ different parameter vectors and considers it as a *population of individuals*. The quantity λ is called the *population size*. The quality of a certain vector of parameters (i.e. an *individual* in the population) is expressed in terms of a scalar valued *fitness function* (objective function). Depending on whether one wants to minimize or maximize the objective function, individuals (i.e. parameter vectors) with lower or greater fitness are considered better, respectively. The algorithm then proceeds to choose the $\mu, (\mu < \lambda)$ best individuals out of the population to become the parents of the next generation (natural *selection*, survival of the fittest). Therefore, μ denotes the *number of parents*. The smaller μ is chosen compared to λ, the higher the *selection pressure* will be. Out of the μ individuals chosen to be parents for the next generation, one then creates a new population of λ offspring $\mathbf{x}_i^{g+1}$ by applying *mutation* on the parents $\mathbf{x}_j^g$ as follows:

$$\mathbf{x}_i^{g+1} = \mathbf{x}_j^g + \mathcal{N}(0, \Sigma) \quad, i = 1, \ldots, \lambda \quad, j \in \{1, \ldots, \mu\} \tag{2.1}$$

where $\mathcal{N}(0, \Sigma)$ denotes a vector of jointly distributed Gaussian random numbers with zero mean and covariance matrix Σ. The standard deviations (i.e. the square roots of the diagonal elements σ_i^2 of Σ) of the additive random numbers determine "how far away from its parent a child will be" and are called *step sizes* of the mutation. Now, the first iteration is completed and the algorithm loops back to the evaluation of the fitness function for the new individuals. Several different techniques for adaptation and control of the step size have been developed (see e.g. Bäck (1997a), Bäck (1997b), Bäck (1993), Hansen & Ostermeier (1996), or Hansen & Ostermeier (1997)). In the following subsections, some of the single objective Evolution Strategies used in this work are outlined.

2.1. The (1+1)-ES

One of the simplest and yet powerful evolution strategies is the "one plus one evolution strategy", denoted by (1+1)-ES. In this strategy, both the number of parents and the population size (i.e. number of offspring) are set to one: $\mu = \lambda = 1$. Mutation is accomplished by adding a vector of usually uncorrelated Gaussian random numbers, i.e. $\Sigma = diag(\sigma_i^2)$ is a diagonal matrix. Step size adaptation can be performed according to Rechenberg's 1/5-rule: if less than 20% of the generations are successful (i.e. offspring better than parent), then decrease the step size for the next generation; if more than 20% are successful, then increase the step size in order to accelerate convergence. This adaptation is done every $N \cdot L_R$ generations where N is the number of parameters (i.e. dimension of search space) and L_R is a constant, usually equal to one. Selection is done out of the set union of parent and offspring, i.e. the better one of the two is chosen to become the parent of the next generation.

2.2. The (μ, λ)-ES

A slightly more advanced method is to take one or more parents and even more offspring, i.e. $\mu \geq 1$ and $\lambda > \mu$. Mutation is accomplished in a similar way as with the (1+1)-ES. Besides the 1/5 rule, another method for step size adaptation becomes available which is called *self-adaptive mutation* (Bäck (1997a)). In this method, the mutation steps are adapted every generation. They are either increased, decreased, or kept the same, each with a probability of 1/3. On the average, 1/3 of the offspring will now be closer to their parents than before, 1/3 keeps progressing at the same speed, and 1/3 explores further areas. Depending on how far away from the optimum we currently are, one of these three groups will do better than the others and, therefore, more individuals out of it will be

selected to the next generation, where their step sizes are inherited. The algorithm adapts the step size by itself, i.e. by means of mutation and selection.

2.3. The $(\mu/\mu_I, \lambda)$-CMA-ES

The covariance matrix adaptation (CMA) is a sophisticated method for online adaptation of step sizes in (μ, λ)-ES with intermediate recombination (i.e. averaging of parents). It was first described by Hansen & Ostermeier (1996) and further improved and evaluated by Hansen & Ostermeier (1997). For a complete description of the algorithm, the reader is referred to the latter publication. The basic idea is to adapt step sizes and covariances in such a way that the longest axis of the hyperellipsoid of mutation distribution always aligns in the direction of greatest estimated progress. This is done by accumulating information about former mutation steps and their success (*evolution path*) and searching it for correlations. Besides this very sophisticated method for step size adaptation, a CMA-ES also includes mutation (with Σ now being a full matrix) and selection.

3. Multiobjective evolutionary algorithms

As soon as there are many (possibly conflicting) objectives to be optimized simultaneously, there is no longer a single optimal solution but rather a whole set of possible solutions of equivalent quality. Consider, for example, the design of an automobile. Possible objectives could be: minimize cost, maximize speed, minimize fuel consumption and maximize luxury. These goals are clearly conflicting and, therefore, there is no single optimum to be found. Multiobjective EAs can yield a whole set of potential solutions - which are all optimal in some sense - and give the engineers the option to assess the trade-offs between different designs. One then could, for example, choose to create three different cars according to different marketing needs: a slow low-cost model which consumes least fuel, an intermediate solution, and a luxury sports car where speed is clearly the prime objective. Evolutionary algorithms are well suited to multiobjective optimization problems as they are fundamentally based on biological processes which are inherently multiobjective.

After the first pioneering work on multiobjective evolutionary optimization in the eighties (Schaffner (1984), Schaffner (1985)), several different algorithms have been proposed and successfully applied to various problems. For comprehensive overviews and discussions, the reader is referred to Fonseca & Fleming (1995), Horn (1997), Van Veldhuizen & Lamont (1998) and Coello (1999).

3.1. Dominance and Pareto-optimality

In contrast to fully ordered scalar search spaces, multidimensional search spaces are only partially ordered, i.e. two different solutions are related to each other in two possible ways: either one dominates the other or none of them is dominated.

DEFINITION 1: *Consider without loss of generality the following multiobjective optimization problem with m decision variables x (parameters) and n objectives y:*

$$\text{Maximize} \quad \mathbf{y} = \mathbf{f}(\mathbf{x}) = (f_1(x_1, \ldots, x_m), \ldots, f_n(x_1, \ldots, x_m))$$
$$\text{where} \quad \mathbf{x} = (x_1, \ldots, x_m) \in X$$
$$\mathbf{y} = (y_1, \ldots, y_n) \in Y$$

(3.1)

and where **x** *is called* decision (parameter) vector, X parameter space, **y** objective vector *and* Y objective space. *A decision vector* **a** $\in X$ *is said to* dominate *a decision vector* **b** $\in X$ *(also written as* **a** $\succ$ **b**) *if and only if:*

$$\begin{aligned} \forall i \in \{1, \ldots, n\} : \quad & f_i(\mathbf{a}) \geq f_i(\mathbf{b}) \\ \wedge \quad \exists j \in \{1, \ldots, n\} : \quad & f_j(\mathbf{a}) > f_j(\mathbf{b}) \end{aligned} \tag{3.2}$$

Additionally, we say **a** *covers* **b** (**a** $\succeq$ **b**) *if and only if* **a** $\succ$ **b** *or* **f(a)** = **f(b)**.

Based on this convention, we can define nondominated, *Pareto-optimal* solutions as follows:

DEFINITION 2: *Let* **a** $\in X$ *be an arbitrary decision (parameter) vector.*

(*a*) *The decision vector* **a** *is said to be* nondominated *regarding a set* $X' \subseteq X$ *if and only if there is no vector in* X' *which dominates* **a**; *formally:*

$$\nexists \mathbf{a}' \in X' : \mathbf{a}' \succ \mathbf{a} \tag{3.3}$$

(*b*) *The decision (parameter) vector* **a** *is called* Pareto-optimal *if and only if* **a** *is nondominated regarding the whole parameter space* X.

If the set X' is not explicitly specified, the whole parameter space X is implied.

Pareto-optimal parameter vectors cannot be improved in any objective without causing a degradation in at least one of the other objectives. They represent in that sense *globally optimal* solutions. Note that a Pareto-optimal set does not necessarily contain all Pareto-optimal solutions in X. The set of objective vectors **f(a')**, **a'** $\in X'$, corresponding to a set of Pareto-optimal parameter vectors **a'** $\in X'$ is called *"Pareto-optimal front"* or *"Pareto-front"*.

3.2. *Difficulties in multiobjectve optimization*

In extending the ideas of single objective EAs to multiobjective cases, two major problems must be addressed:

1. How to accomplish fitness assignment and selection in order to guide the search towards the Pareto-optimal set.

2. How to maintain a diverse population in order to prevent premature convergence and achieve a well distributed, wide spread trade-off front.

Note that the objective function itself no longer qualifies as fitness function since it is vector valued and fitness has to be a scalar value. Different approaches to relate the fitness function to the objective function can be classified with regard to the first issue. For further information, the reader is referred to Horn (1997). The second problem is usually solved by introducing elitism and intermediate recombination. *Elitism* is a way to ensure that good individuals do not get lost (by mutation or set reduction), simply by storing them away in a external set, which only participates in selection. *Intermediate recombination*, on the other hand, averages the parameter vectors of two parents in order to generate one offspring according to:

$$\begin{aligned} \mathbf{x}'_j &= \alpha \mathbf{x}^g_{j1} + (1 - \alpha)\mathbf{x}^g_{j2} \quad , j, j_1, j_2 \in \{1, \ldots, \mu\} \\ \mathbf{x}^{g+1}_i &= \mathbf{x}'_j + \mathcal{N}(0, \Sigma) \qquad , i = 1, \ldots, \lambda \qquad\qquad , j \in \{1, \ldots, \mu\} \end{aligned} \tag{3.4}$$

Arithmetic recombination is a special case of intermediate recombination where $\alpha = 0.5$.

4. The Strength Pareto Approach

For this work, the *Strength Pareto Approach* for multiobjective optimization has been used. Comparative studies have shown for a large number of test cases that, among all major multiobjective EAs, the *Strength Pareto Evolutionary Algorithm (SPEA)* is clearly superior (Zitzler & Thiele (1999), Zitzler & Thiele (2000)). It is based on the above-mentioned principles of Pareto-optimality and dominance. The algorithm as proposed by Zitzler & Thiele (1999) was implemented in a restartable, fully parallel code as follows:

Step 1: Generate random initial population P and create the empty external set of nondominated individuals P'.

Step 2: Evaluate objective function for each individual in P in parallel.

Step 3: Copy nondominated members of P to P'.

Step 4: Remove solutions within P' which are covered by any other member of P'.

Step 5: If the number of externally stored nondominated solutions exceeds a given maximum N', prune P' by means of clustering.

Step 6: Calculate the fitness of each individual in P as well as in P'.

Step 7: Select individuals from $P + P'$ (multiset union), until the mating pool is filled.

Step 8: Adapt step sizes of the members of the mating pool.

Step 9: Apply recombination and mutation to members of the mating pool in order to create a new population P.

Step 10: If maximum number of generations is reached, then stop, else go to Step 2.

4.1. *Fitness assignment*

In Step 6, all individuals in P and P' are assigned a scalar fitness value. This is accomplished in the following two-stage process. First, all members of the nondominated set P' are ranked. Afterwards, the individuals in the population P are assigned their fitness value.

Step 1: Each solution $i \in P'$ is assigned a real value $s_i \in [0,1)$, called *strength*. s_i is proportional to the number of population members $j \in P$ for which $i \succeq j$. Let n denote the number of individuals in P that are covered by i and assume N to be the size of P. Then s_i is defined as: $s_i = \frac{n}{N+1}$. The fitness f_i of i is equal to its strength: $f_i = s_i \in [0,1)$.

Step 2: The fitness of an individual $j \in P$ is calculated by summing the strengths of all external nondominated solutions $i \in P'$ that cover j. Add one to this sum to guarantee that members of P' always have better fitness than members of P (note that the fitness is to be minimized):

$$f_i = 1 + \sum_{i, i \succeq j} s_i \quad , f_i \in [1, N) \tag{4.1}$$

4.2. *Selection and step size adaptation*

Step 7 requires an algorithm for the selection of individuals into the mating pool and Step 8 includes some method for dynamical adaptation of step sizes (i.e. mutation variances). For this paper, selection was done using the following binary tournament procedure:

Step 1: Randomly (uniformly distributed random numbers) select two individuals out of the population P.

Step 2: Copy the one with the better (i.e. lower for SPEA) fitness value to the mating pool.

Step 3: If the mating pool is full, then stop, else go to Step 1.

Adaptation of the step sizes was done using the self-adaptive mutation method (c.f. section 2.3). Each element of P and P' is assigned an individual step size for every parameter, i.e. $\Sigma = diag(\sigma_i^2)$ is a diagonal matrix for each individual. The step sizes of all members of the mating pool are then either increased by 50%, cut to half, or kept the same, each at a probability of $1/3$.

4.3. Reduction by clustering

In Step 5, the number of externally stored nondominated solutions is limited to some number N'. This is necessary because otherwise P' would grow to infinity since there always is an infinite number of points along the Pareto-front. Moreover, one wants to be able to control the number of proposed possible solutions because, from a decision maker's point of view, a few points along the front are often enough. A third reason for introducing clustering is the distribution of solutions along the Pareto-front. In order to explore as much of the front as possible, the nondominated members of P' should be equally distributed along the Pareto-front. Without clustering, the fitness assignment method would probably be biased towards a certain region of the search space, leading to an unbalanced distribution of the solutions. For this work, the *average linkage method*, a clustering algorithm which has proven to perform well on Pareto optimization, has been chosen. The reader is referred to Morse (1980) or Zitzler & Thiele (1999) for details.

5. Strength Pareto approach with targeting

Compared to other methods such as, for example, the energy minimization evolutionary algorithm (EMEA) (c.f. Jonathan, Zebulum, Pacheco & Vellasco (2000)), the SPEA has two major advantages: it finds the whole Pareto-front and not just a single point on it, and it converges faster. The latter is a universal advantage whereas the former is not. There are applications where a target value can be specified. One then wants to find the point on the Pareto-front which is closest to the user-specified target (in objective space). This eliminates the need to analyze all the points found by SPEA in order to make a decision. EMEA offers such a possibility, but it converges slower than SPEA and, what's more, it is fundamentally unable to find more than one point per run. Hence we wish to extend SPEA with some targeting facility that can be switched on and off depending on whether one is looking for a single solution or the whole front, respectively. We added this capability to SPEA by the following changes to the algorithm:

1. Between Step 6 and Step 7 the fitnesses of all individuals in P and P' are scaled by the distance D of the individual from the target (in objective space) to some power q:

$$f_i = f_i \cdot D_i^q$$

This ensures that enough nondominated members close to the target will be found so that the one with minimal distance will appear at higher probability. The parameter q determines the sharpness of the concentration around the target.

2. Another external storage P_{best} is added which always contains the individual out of P' which is closest to the target. Therefore, between steps 4 and 5, the algorithm

Parameter	Value
Dimension of parameter space (m)	5
Size of population (λ)	50
Size of mating pool (μ)	30
Size of nondominated set (N')	70
Number of generations	250
Target value for (f_1, f_2)	(0.5, 0.7)
Concentration parameter q	4

TABLE 1. Settings for targeting SPEA

calculates the distances of all members of P' to the target and picks the one with minimal distance into P_{best}. At all times, P_{best} only contains one solution.

3. At the end of the algorithm, not only the Pareto-front is output but also the solution stored in P_{best}. Note: due to clustering and removal in P', the solution in P_{best} is not necessarily contained in P'. It is, therefore, an optimal solution which otherwise would not have appeared in the output.

The algorithm has been implemented and tested for convex and nonconvex testfunctions. Figures 1 to 4 show some results for the nonconvex testfunction $\mathcal{T}_2$ as proposed in Zitzler & Thiele (2000):

$$
\begin{aligned}
\text{Minimize} \quad & \mathcal{T}_2(\mathbf{x}) = (f_1(x_1), f_2(\mathbf{x})) \\
\text{subject to} \quad & f_2(\mathbf{x}) = g(x_2, \dots, x_m) h(f_1(x_1), g(x_2, \dots, x_m))
\end{aligned}
$$

$$
\begin{aligned}
\text{where} \quad & \mathbf{x} = (x_1, \dots, x_m) \\
& f_1(x_1) = x_1 \\
& g(x_2, \dots, x_m) = 1 + 9 \cdot \sum_{i=2}^{m} x_i / (m - 1) \\
& h(f_1, g) = 1 - (f_1/g)^2
\end{aligned}
\tag{5.1}
$$

where m is the dimension of the parameter space and $x_i \in [0, 1]$. The exact Pareto-optimal front is given by $g(\mathbf{x}) = 1$. The parameters of the algorithm were set as summarized in table 1.

The chosen target value is slightly off-front. Therefore, the targeting error will never be zero. Figure 1 shows the final population after 250 generations without targeting. The diamonds indicate members of the external nondominated set (Pareto-optimal front) whereas members of the regular population are denoted by crosses. In Fig. 2 the same run has been repeated with targeting. Figure 3 shows the targeting error as a function of the generation number. The dashed line indicates the theoretical minimum of the distance. After about 80 to 100 generations, the point on the front which is closest to the target has been found with good accuracy. Figure 4 shows the path of P_{best} towards the target. The jumps are due to the fact that the individual stored in P_{best} gets replaced as soon as another individual is closer to the target.

The best objective value that was achieved was: $\mathbf{f}(P_{best}) = (0.5265, 0.7247)$, its Euclidean distance from the target is $3.6287 \cdot 10^{-2}$, which is equal to the theoretical minimal distance within the given computational accuracy.
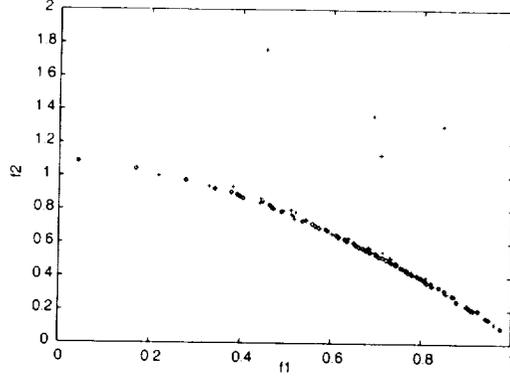
FIGURE 1. Final population without targeting.
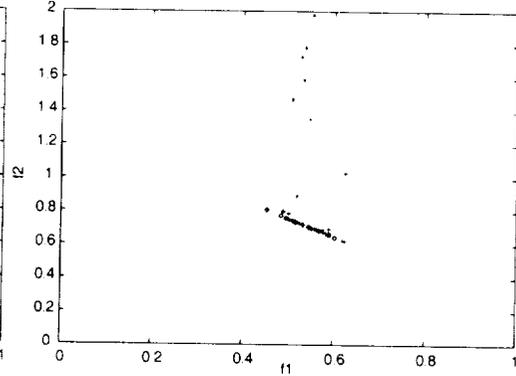
FIGURE 2. Final population with targeting.
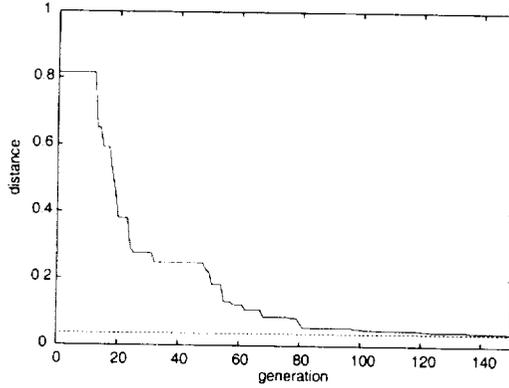
FIGURE 3. Distance between P_{best} and target.
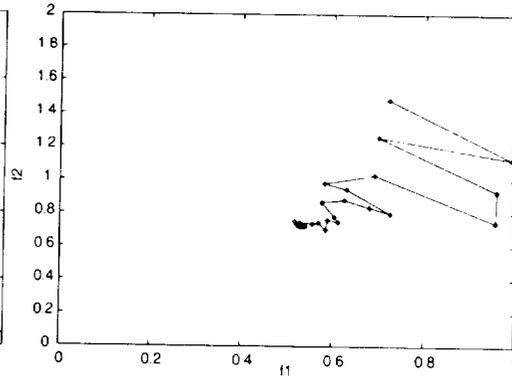
FIGURE 4. Path of P_{best} towards the target.

6. Microchannel flow optimization

Both single and multiobjective EAs have been applied to a fluidic microchannel design problem. Bio-analytical applications require long thin channels for DNA sequencing by means of electrophoresis. In order to pack a channel of several meters in length onto a small square plate, curved geometries are required. However, curved channels introduce dispersion and, therefore, limit the separation efficiency of the system. The question is now how to shape the contour of the channel in order to minimize dispersion. A detailed description of the problem as well as an optimization solution using gradient methods can be found in Mohammadi, Molho & Santiago (2000).

6.1. Single objective optimization

The goal of this optimization run was to minimize the final skewness of the flow inside the channel, i.e. it was required that the iso-values of the advected species a be normal to the flow field U by time T, when they exit the channel. The objective function defined by Mohammadi, Molho & Santiago (2000) is, therefore:

$$J = \int_\Omega \left(\nabla a(x, T) \times U(x) \right)^2 \, dx \qquad (6.1)$$
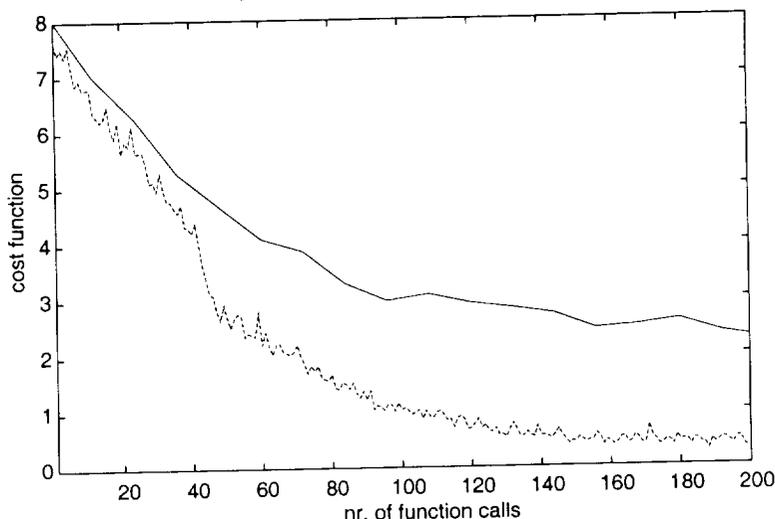
FIGURE 5. Convergence of (3,12)-CMA-ES [——] and (1+1)-ES [- - - -] vs. number of evaluations of the objective function.

with Ω being the cross section of the channel exit. The shape of the 90-degree turn is described by 11 parameters. Therefore, the parameter search space is of dimension 11. The objective space is scalar since it is a single objective problem.

The calculation of the flow field and evaluation of the objective function was done by an external flow solver provided by Mohammadi, Molho & Santiago (2000). Both a (1+1)-ES and a (3,12)-CMA-ES were applied to the problem and their convergence was compared. The results were statistically averaged from 5 runs with different initial conditions, i.e. starting points.

Since the CMA-ES has a population size of 12, it performs 12 function evaluations per generation. Figure 5 shows the convergence normalized to the same number of function calls. Figure 6 and 7 show the corresponding solutions after 20 and 180 generations of the best 1+1 run out of the ensemble (the lines are iso-potential lines of the electric field). After 20 generations the contour of the channel gets a clearly visible dent in it. After 80 evaluations of the objective function, the algorithm has found a double-bump shape to be even better, and after 180 calls to the solver, the optimum has been reached. The value of the objective function has dropped to about 10^{-6} for the best run out of the ensemble. This means that dispersion is almost zero and the channel will have very good separation properties.

6.2. Multiobjective optimization

We then introduced the total deformation of the channel contour as a second objective to be minimized simultaneously in order to minimize manufacturing costs. The second objective was thus given by:

$$K = \sum_{i=1}^{11} p_i^2 \qquad (6.2)$$

where p_i are the shape parameters of the channel as introduced by Mohammadi, Molho & Santiago (2000). The first objective remained unchanged. The algorithm used for this
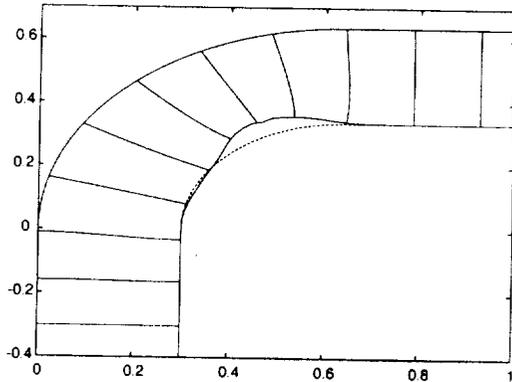
FIGURE 6. Solution at generation 20.
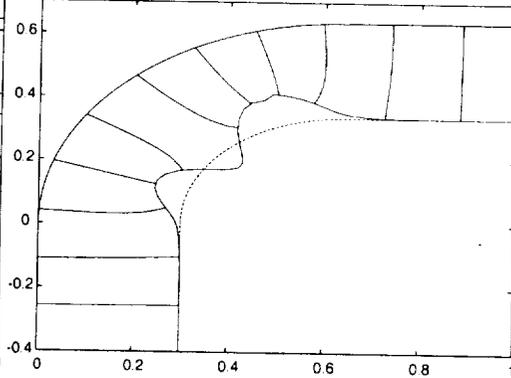
FIGURE 7. Solution at generation 180.
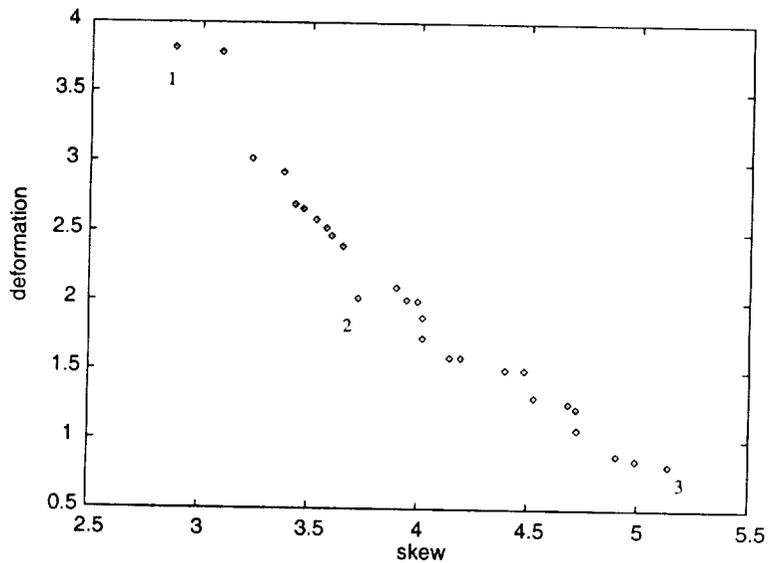
FIGURE 8. Pareto-front of nondominated solutions after 80 generations.

optimization was a SPEA with a population size of 20, a maximum size of the external nondominated set of 30, and a mating pool of size 10.

Figure 8 shows the Pareto-optimal trade-off front after 80 generations of the algorithm, and Figs. 9 and 10 show the corresponding solutions, i.e. optimized shapes of the channel. One is now free to choose whether to go for minimal skewness at the expense of a higher deformation (c.f. Fig. 9), choose some intermediate result, or minimize deformation in order to minimize manufacturing costs and still get the lowest skewness possible with the given amount of deformation (c.f. Fig. 10).

The results obtained with evolutionary optimization are comparable to the results of the gradient based method. However, far less mathematics and complex formulas were involved here, which leads to greater flexibility and shorter "time-to-solution".
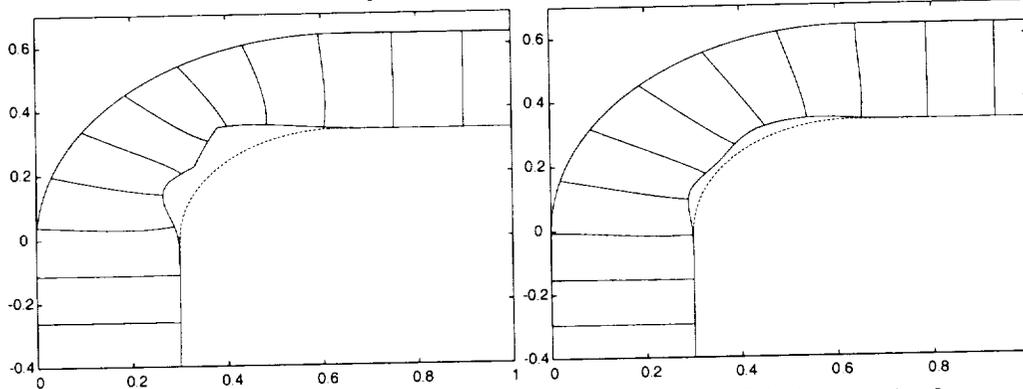
FIGURE 9. Solution at point 1.

FIGURE 10. Solution at point 3.

7. Conclusions and future work

Single and multiobjective evolutionary algorithms have been implemented and assessed. The SPEA has successfully been extended to support targeting in objective space. It has been shown that these algorithms are easy to apply to fluid dynamical problems and that their solutions are comparable to those found by gradient based methods. In cases where gradient methods cannot be applied or where they would involve too complex mathematical calculations, evolution strategies are a good alternative to solve an optimization problem or reduce the time needed to do so as part of hybrid processes.

Future and present work addresses the acceleration of convergence of these algorithms and their implementation in hybrid processes.

REFERENCES

BÄCK, T. 1993 Optimal mutation rates in genetic search. In Forrest, S., editor, *Proceedings of the 5th International Conference on Genetic Algorithms, Urbana-Champaign, IL, July 1993*. Morgan Kaufmann, San Mateo, CA. 2-8.

BÄCK, T. 1997a Self-adaptation. In Bäck, T., Fogel, D. B. & Michalewicz, Z., editors, *Handbook of Evolutionary Computation.* **97/1**, C7.1, IOP Publishing Ltd. and Oxford University Press.

BÄCK, T. 1997b Mutation parameters. In Bäck, T., Fogel, D. B. & Michalewicz, Z., editors, *Handbook of Evolutionary Computation.* **97/1**, E1.2, IOP Publishing Ltd. and Oxford University Press.

BEASLEY, D. 1997 Possible applications of evolutionary computation. In Bäck, T., Fogel, D. B. & Michalewicz, Z., editors, *Handbook of Evolutionary Computation.* **97/1**, A1.2, IOP Publishing Ltd. and Oxford University Press.

COELLO, C. A. C. 1999 A comprehensive survey of evolutionary-based multiobjective optimization. *Knowledge and Information Systems.* **1(3)**, 269-308.

FONSECA, C. M. & FLEMING, P. J. 1995 Am overview of evolutionary algorithms in multiobjective optimization. *Evolutionary Computation.* **3(1)**, 1-16.

HANSEN, N. & OSTERMEIER, A. 1996 Adapting Arbitrary Normal Mutation Distributions in Evolution Strategies: The Covariance Matrix Adaptation. *Proceedings of the 1996 IEEE International Conference on Evolutionary Computation (ICEC '96)*, 312-317.

HANSEN, N. & OSTERMEIER, A. 1997 Convergence Properties of Evolution Strate-

gies with the Derandomized Covariance Matrix Adaptation: The $(\mu/\mu_I, \lambda)$-CMA-ES. *Proceedings of the 5th European Conference on Intelligent Techniques and Soft Computing (EUFIT '97)*, 650-654.

HORN J. 1997 Multicriteria decision making. In Bäck, T., Fogel, D. B. and Michalewicz, Z., editors, *Handbook of Evolutionary Computation.* **97/1**, F1.9, IOP Publishing Ltd. and Oxford University Press.

JONATHAN, M., ZEBULUM, R. S., PACHECO, M. A. C., & VELLASCO, M. B. R. 2000 Multiobjective Optimization Techniques: A Study Of The Energy Minimization Method And Its Application To The Synthesis Of Ota Amplifiers. *Proceedings of the second NASA/DoD Workshop on Evolvable Hardware*, July 13-15, 2000, Palo Alto, CA, 133-140.

MOHAMMADI, B., MOLHO, J. I. & SANTIAGO J. A. 2000 Design of Minimal Dispersion Fluidic Channels in a CAD-Free Framework. *Summer Program Proceedings*. Center for Turbulence Research, NASA Ames/Stanford Univ. This volume.

MORSE, J. N. 1980 Reducing the size of the nondominated set: Pruning by clustering. *Computers and Operations Research.* **7**(1-2), 55-66.

SCHAFFNER, J. D. 1984 Multiple Objective Optimization with Vector Evaluated Genetic Algorithms. *Unpublished Ph.D. thesis*, Vanderbilt University, Nashville, Tennessee.

SCHAFFNER, J. D. 1985 Multiple objective optimization with vector evaluated genetic Algorithms. *Proceedings of an International Conference on Genetic Algorithms and Their Applications*, sponsored by Texas Instruments and the U.S. Navy Center for Applied Research in Artificial Intelligence (NCARAI), 93-100.

VAN VELDHUIZEN, D. A. & LAMONT, G. B. 1998 Multiobjective evolutionary algorithm research: A history and analysis. Technical Report *TR-98-03*, Department of Electrical and Computer Engineering, Graduate School of Engineering, Air Force Institute of Technology, Wright-Patterson AFB, Ohio.

ZITZLER, E. & THIELE, L. Nov. 1999 Multiobjective Evolutionary Algorithms: A Comparative Case Study and the Strength Pareto Approach. *IEEE Transactions on Evolutionary Computation.* **3**(4), 257-271.

ZITZLER, E. & THIELE L. 2000 Comparison of Multiobjective Evolutionary Algorithms: Empirical Results. *Evolutionary Computation.* **8**(2), 173-195.

Optimization of trailing vortex destruction by evolution strategies

By G.-H. Cottet†, I. Sbalzarini‡, S. Müller‡ AND P. Koumoutsakos‡

We apply evolution strategies to optimize the instability growth of several pairs of vortices which model the wake of airplanes in landing configuration. For the case of two pairs, the evolution strategy finds a set of optimal parameters strikingly similar to those found in the linear stability analysis of Crouch (1997). The case of four pairs is also considered and leads to a larger distortion of the tip vortex.

1. Introduction

Trailing vortices are naturally shed by airplanes. They result in a strong down-wash which extends for several miles behind the plane and poses a hazard to following aircraft, in particular, at take-off and landing. Several previous studies propose to alleviate the hazard by introducing perturbations to trigger instabilities, and ultimately, break up the vortices (Bilanin & Widnall 1973, Crow & Bate 1997).

Most of these studies have focused on exciting the Crow instability, which operates on a single pair of counter-rotating vortices and has a wavelength much larger than the vortex core size. Unfortunately, however, for realistic perturbation amplitudes (those which would not cause large unsteady forces on the plane) excitation of the Crow instability would lead to vortex destruction at large distances behind the plane that exceed current FAA separation rules for aircraft in IFR conditions.

Recent studies (Crouch 1997, Rennich & Lele 1998) have considered instabilities unique to several pairs of vortices which model aircraft wakes in landing configuration (Spalart 1998, see Fig. 1). Some of these vortices quickly merge, but others persist for long times. At a distance of several spans behind a typical airplane, three persistent vortex pairs can generally be observed, originating at the tips of the wings, the outboard flaps, and the fuselage (respectively numbered 50, 52, and 55 in Fig. 1). Crouch (1997) has studied the linear stability of two pairs of corotating vortices (tip and outboard flap, 50 and 52 in Fig. 1). He identified several instability modes depending on the angle, wavelength, and amplitudes of the perturbations that are imparted to each pair. The modes are summarized in Fig. 2. Roughly speaking, a long wave instability (top sketch in Fig. 2), similar to the Crow instability, takes place when the two pairs are excited in a symmetric fashion. An instability with a wavelength shorter than for the Crow instability (but still much longer than the core size) can also result (bottom sketch). The most efficient instability (middle sketch) arises when the eigenmodes are non-orthogonal leading to transient growth rates exceeding the maximum eigenvalue. This instability mechanism produces long waves which, when the outboard vortices are initially unperturbed, grow at a rate several times larger than the Crow instability for a single vortex pair.

† LMC-IMAG, University Joseph Fourier, Grenoble, France
‡ Institute of Computational Sciences, ETH Zürich, Switzerland
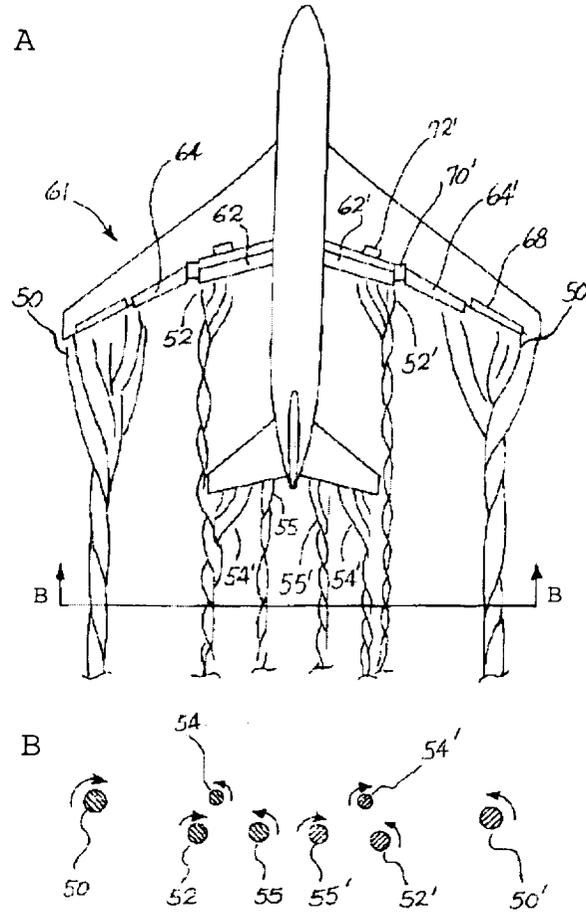
FIGURE 1. Sketch of vortex system shed by an airplane (Courtesy of J. Crouch, 2000). B is a cross section of A as shown.

Based on the analysis of Crouch (1997), Crouch & Spalart (2000) propose a strategy for breaking up the vortices that relies on appropriate cycling of control surfaces. Their experiments and numerical simulations indicate that this strategy could reduce separation rules.

Alternatively, Rennich & Lele (1998) have studied the system of vortex pairs with opposite signs, corresponding to inboard and outboard flaps. Vortex filament and direct numerical simulations (DNS) indicate in this case also large amplification rates for certain values of vortex separation times, which could also loosen the current mandatory separations.

Despite the fact that the points of view adopted in these works differ in several respects, in particular in the way the instability growth is measured, they have in common the ability to provide us with a better understanding of the mechanisms by which the cooperative instabilities of several pairs can result in enhanced growth rates. Moreover, the configurations studied in these works are investigated with a view to implementing them in actual wing designs.
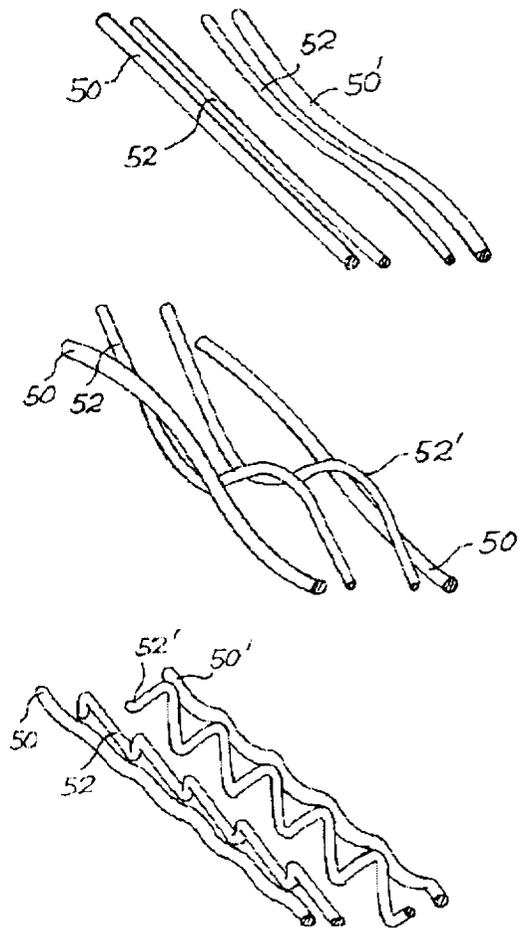
FIGURE 2. Three types of instabilities according to Crouch (1997). From top to bottom: long wave, transient growth, and short wave instabilities.

One of the findings reported in Crouch (1997) and Rennich & Lele (1998) is the extreme sensitivity of the overall dynamics with respect to the initial state of the vortex pairs. In Crouch (1997), the most effective transient growth was achieved when the outboard pair was not initially perturbed, while in Rennich & Lele (1998), early reconnection was obtained for a particular value of the inboard vortices separation.

This motivated our attempt to perform a more systematic parameter search and identify the wake system which would produce the largest instability growth. In other words, our goal was to revisit the above studies from the point of view of optimization.

The tools used in the present work are evolution strategies and viscous vortex methods.

On the one hand, evolution strategies have proven to be a flexible tool for optimization of unsteady flow dynamics when traditional gradient-based methods would be very difficult to implement. One the other hand, vortex methods are well adapted to wake
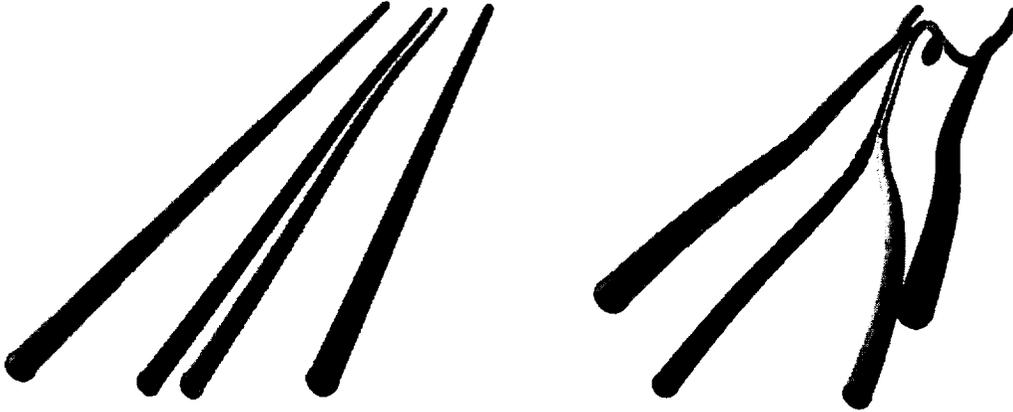
FIGURE 3. Initial stage (left) and reconnection for a configuration of two vortex pairs of opposite sign, according to Rennich & Lele (1998). Courtesy of S. Lele.

simulation as they require the discretization of only the region of vorticity. Note that the work of Rennich & Lele (1998) is in part based on vortex filament method. Viscous vortex methods offer the advantage of enabling calculations all the way to reconnection (Cottet *et al.* 2000).

An outline of the paper is as follows: Section 2 recalls the basic features of evolution strategies and vortex methods; Section 3 presents our findings, and Section 4 is devoted to a discussion of results and future plans.

2. Approach

2.1. *Evolution strategies*

We want to minimize $f(X), X \in R^N$. Basic one-member evolution strategies (ES) consist in performing successive mutations on the vector X followed by the evaluation of f. The new vector is then selected or rejected depending on whether it improves (in which case the mutation is said to be successful) or does not improve the value of f. The mutation consists of a random walk of the vector X, the size of which depends on the success rate of the mutation. The algorithm can be represented as the following iteration:

$$X_{t+1} = \begin{cases} X_t + \sigma_t Z_t & \text{if } f(X_t + \sigma_t Z_t) \leq f(X_t), \\ X_t & \text{otherwise.} \end{cases}$$

In the above formula, Z_t denotes a random Gaussian vector with zero mean and unit standard deviation. In order to speed the convergence, the radius σ_t is updated according to the success rate of the previous iterations. A high success rate means that one is far away from the minimum and induces an increase in σ_t. In this work we have implemented the so-called 1/5 rule: the variance is increased if the success ratio during the last iterations is greater than 1/5. In order to achieve faster convergence, mutation can be done in an anisotropic fashion on the various components of the parameter vector. This leads to the so-called covariance matrix adaptation technique. We attempted this technique in the last stage of the iterations.

2.2. *Viscous vortex methods*

Vortex methods operate on the vorticity formulation of the incompressible Navier-Stokes equations (Cottet & Koumoutsakos 2000). The method we are using is a time-splitting algorithm with alternating advection and diffusion. Advection is achieved by tracking particles along flow trajectories. Particles carry circulation, which is updated to account for stretching. Diffusion is dealt with by vorticity redistribution among nearby particles. To enable fast velocity evaluations, circulations are interpolated on a fixed grid (vortex-in-cell scheme). The Poisson equation is then solved by a Fourier type method, and velocities are obtained by finite-differences on the grid and then interpolated back on particles. Finally, to maintain a smooth particle distribution, which is essential for accuracy, particles are frequently re-meshed on a regular lattice. Systematic comparisons with spectral methods have been done to validate this method as a tool for DNS (Cottet *et al.* 2000).

3. Results

Our study focused on the case of two pairs of co-rotating vortices studied by Crouch (1997). The parameters which the evolution strategy optimized were:

- the initial perturbation amplitude of the tip (ϵ_1) and outboard (ϵ_2) vortices
- the angles of the perturbation planes α_1 and α_2
- the wavelength of the perturbations, λ
- the separation between the two vortices, δ
- the circulation ratio between the outboard and tip vortices, Γ

Quantities were non-dimensionalized by the distance b_0 between the tip vortices and the total circulation. To work with parameters in the same order of magnitude as Crouch (1997), the total perturbation amplitude was constrained to be below 10% of b_0:

$$\sqrt{\epsilon_1^2 + \epsilon_2^2} \leq 0.1.$$

The following additional constraints were imposed to remain within achievable design configurations:

$$0.25 \leq \delta \leq 0.4; \quad 0.5 \leq \lambda \leq 10; \quad 0. \leq \Gamma \leq 0.5.$$

Note that the constraints on λ allow for a wide range of wavelengths, varying from short wavelengths of the order of a few core sizes to long wavelengths of the type found in the Crow instability.

Our goal was to optimize the instability on the tip vortex. To measure its deformation, we computed the average angle, inside the core of the tip vortex, of the vorticity vector relative to the axis of the unperturbed vortex. More precisely, the objective function was given by the formula

$$f = \int dz \int_{A(z)} \frac{\omega_x^2 + \omega_y^2}{\omega_z^2} dA(z),$$

where

$$A(z) = \{(x,y), |\omega(x,y,z)| \geq 1/2|\omega|_{max}\}.$$

Figure 5 shows the convergence history of the evolution algorithm. After iteration 150 the ES algorithm was run with the covariance matrix adaptation technique, which only slightly improved the value of the objective function. It is not clear that at this stage a global optimum has been reached.
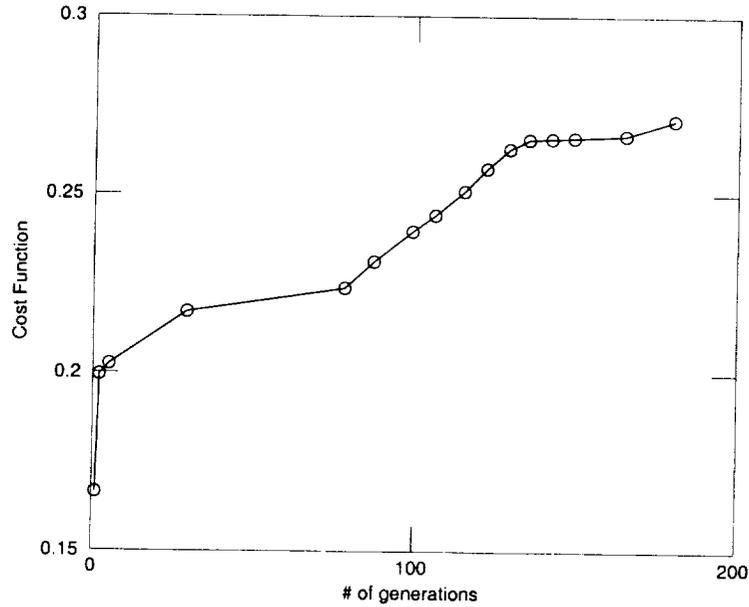
FIGURE 4. Convergence history for the evolution strategy.

	α_1	α_2	ϵ_1	ϵ_2	δ	Γ	λ
Optimal parameters	0.47	0.73	0.098	0.008	0.26	0.31	0.72
Parameters in Crouch (1997)	$\pi/4$	$\pi/4$	0.1	0.	0.3	0.4	0.7

TABLE 1. Comparison of the parameters found by the evolution strategy and those studied in Crouch (1997).

The parameter values finally obtained by the ES are listed on Table 6 together with the parameters reported in Crouch (1997) as leading to efficient transient growth. Some striking similarities can be noticed between these two sets of parameters. In particular, the ES has selected perturbations that are mostly located on the tip vortex, confirming the observation in Crouch (1997) of efficient transient growth when the outboard flap vortex was unperturbed. The wavelengths of the perturbations are also very close to the ones given in Crouch (1997).

Finally Fig. 5 shows the evolution of the objective function for various parameter vectors: the two sets of parameters shown in Table 1, parameters similar to the ones found by the ES but with perturbations of same magnitude for the two pairs and a third set of parameters obtained by optimizing on 4 pairs instead of 2 pairs. Theses simulations confirm that, in the early stages of the dynamics, the evolution strategies have picked up the most efficient parameters for two pairs. One can also notice that adding more degrees of freedom to the optimization can pay off and lead to increased efficiency. However, an inspection of the vorticity angle at later times show that the differences between the configurations involving pairs of co-rotating pairs tend to disappear. A similar observation was made in Rennich (1997) by considering a different measure of the perturbation (namely the maximum displacement).
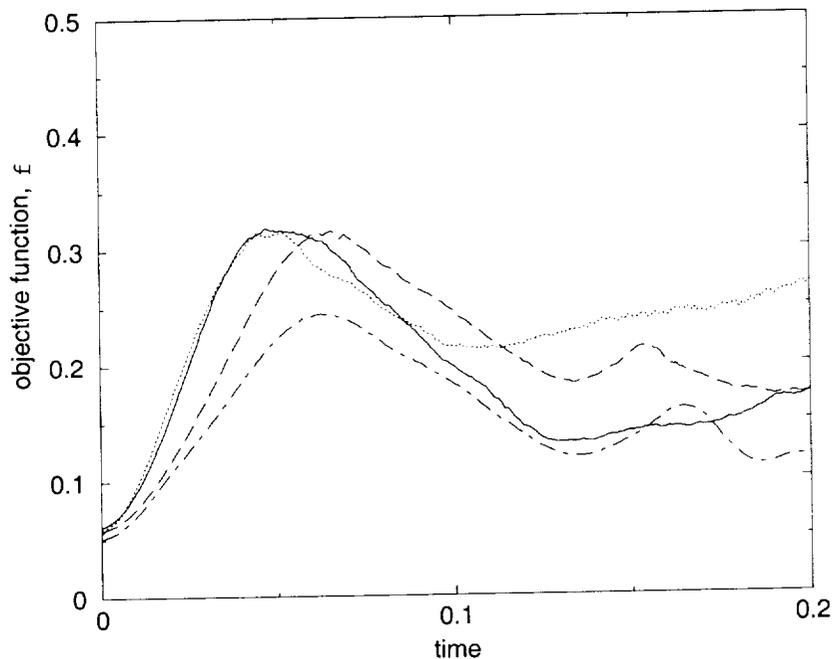
FIGURE 5. Evolution of the objective function. ———— : optimal parameters for 2 pairs; – – – – : parameters of Crouch (1997); ········ : optimal parameters for 4 pairs; —·— : case of 2 pairs with equal initial perturbations.

4. Conclusion

Our goal was to investigate whether optimization techniques could be helpful in determining parameters enhancing vortex break-up in trailing vortices. These preliminary results show that evolution strategies are a valuable tool to explore realistic configurations in a systematic way. Their flexibility makes it easy to modify the number of parameters as desired without having to reformulate the optimization problem. Note, however, that considering configurations involving more than two pairs cannot be done without keeping in mind that these configurations have to be in accordance with current design constraints.

To keep the computational cost at a reasonable level, our study has focused on the preliminary stages of the dynamics. However, because of the relative rotations of the pairs, it is not clear that the trends observed initially persist for long times. In other words, parameters leading to the greatest growth rates may not be those which lead to fastest reconnection.

It thus appears necessary to elucidate the relevant time-scale on which optimization should be performed.

Acknowledgments

REFERENCES

BILANIN, A. J. & WIDNALL, S. E. 1973 Aircraft wake dissipation by sinusoidal instability and vortex breakdown. *AIAA Paper 73-107.*

COTTET, G.-H., MICHAUX, B., OSSIA, S. & VANDERLINDEN, G. 2000 A comparison of spectral and vortex methods in three-dimensional incompressible flows, *submitted.*

COTTET, G.-H.& KOUMOUTSAKOS, P. 2000 *Vortex methods.* Cambridge University Press.

CROUCH, J. D. 1997 Instability and transient growth for two trailing-vortex pairs. *J. Fluid Mech.* **350**, 311-330.

CROUCH, J. D. & SPALART, P. R. 2000 Active system for early destruction of trailing vortices. *US Patent 6082679* issued July 4, 2000.

CROW, S. C. & BATE, E. R. 1976 Lifespan of trailing vortices in a turbulent atmosphere. *J. Aircraft.* **13**, 476-482.

RENNICH, S. C. 1997 Accelerated destruction of aircraft wake vortices. *Ph.D. thesis,* Stanford.

RENNICH, S. C. & LELE S. K. 1998 A method for accelerating the destruction of aircraft wake vortices. *AIAA Paper* 98-0667.

SPALART, P. R. 1998 Airplane trailing vortices. *Ann. Rev. Fluid Mech.* **30**, 107-138.

The astrophysical and geophysical flows group

Astrophysical and geophysical fluid flows are usually dominated by large lengths and velocities, so the flows are often turbulent. The 2000 Summer Program focused on the late stages of star formation, planet formation, sediment transport, and turbulence in the upper ocean. Modeling and computing the turbulence within a protostar's thin accretion disk, in which the primary flow is near-Keplerian, are made complicated by the strong rotation and shear, the compressibility, and a small overall aspect ratio. The group's work in star formation was motivated by an unsolved problem in mass and momentum transport: to form a star, gas must move radially inward from the outer edge of the disk and accrete onto the central object, but it also must maintain a nearly-Keplerian azimuthal velocity as it moves. Therefore, the inward mass transport requires that the moving parcels of gas give up some of their angular momentum (and energy) to the ambient gas. The disk must, therefore, create a secondary flow to transport this angular momentum radially outward. There is no known way to do this. The traditional astrophysical literature suggests that turbulence within the disk is responsible for this angular momentum transport, despite the fact that the required transport is in the *same* direction as the mean angular momentum gradient of the disk (which is contrary to our usual expectation: turbulence usually transports quantities into regions where their densities are relatively low). The group's goal was to determine how a secondary flow, turbulent or otherwise, might carry out this transport and still allow mass to accrete onto the central star fast enough to agree with observations.

Our group's motivation for our work in planet formation was inspired by the recent discoveries of planets outside our solar system. Their large sizes and proximity to their suns violate accepted scenarios of planet formation and bring into question much of what has been previously written. Our group focused on the question of how turbulence and coherent vortices within the protoplanetary disk could promote or inhibit the accumulation of dust grains into planetesimals (objects of sufficient mass that their own self-gravity allows them to accrete mass in the turbulent disk environment).

The motivation for the work in sediment transport was the understanding of how pollutants such as heavy metals and pesticides, which bind to sediment particles, spread through harbors and rivers. The work in turbulence in the upper ocean was inspired by recent observations that vertically propagating, internal wave packets in the upper thermocline of the ocean may be important for sustaining turbulent mixing.

The research group of Barranco, Marcus & Umurhan was faced with the difficulties of unknown equations of energy and state in the disk (which in some parts is optically thin and in others thick) and unknown boundary conditions (since the gas is in-falling at the outer edge and joins at the inner edge onto the star through a boundary layer in which magnetic fields are likely to be important). The group concentrated on formulating a well-posed problem that was numerically tractable. They found that through judicious use of asymptotic expansions, the boundary conditions and equations of state and energy could be easily parameterized. Their analyses were based on the premise that turbulence alone was not likely to solve the transport problems and that coherent vortices were needed. This premise was bolstered by Orlandi's numerical calculations of cross-stream mass transport in a shearing channel, which showed that coherent and numerically-resolvable flow structures can account for this type of mass/momentum transport. Since previous calculations as well as calculations by others indicated that subsonic vortices

with order-unity Rossby numbers (ratios of the inertial to the Coriolis forces) would be the most long-lived, the asymptotics were developed in this parameter regime. Formal asymptotics were carried out, and three sets of self-consistent equations were found. It was shown that all three sets had the same boundary condition requirements as the anelastic Euler equation. It was shown analytically that a barotropic protoplanetary disk obeying any one of these asymptotic equations could not solve the transport problem. A small amount of baroclinicity was required. The analysis showed that the vortices were efficient transporters of mass and angular momentum and that only two or three vortices at each radial location were sufficient for observed star formation rates. The asymptotics were formulated for calculations in a thin, annular section of the protoplanetary disk, so the equations could be mapped into a Cartesian domain. Although the equations were periodic in the mapped azimuthal coordinate, they were not in the radial coordinate. By applying a Rogallo transform to the equations, Shariff was able to make them periodic in the radial direction as well and modify an existing code to solve the asymptotic equations.

Barranco & Marcus considered the role of vortices in the process of aggregating dust grains into large planetesimals. They found that grains moving initially in non-circular and/or non-planar orbits with respect to the disk quickly moved into planar, near circular orbits due to the drag of the gas within the disk when the flow was laminar. They showed numerically that dust grains were attracted to vortices within the disk and could create large (and strongly self-gravitating) density perturbations. This seems paradoxical since it would be expected that the centrifugal force of a vortex would eject grains. However, Barranco derived a simple physical argument why this is not so and went on to numerically compute the attracting regions of the dust in or near the vortex. As a function of the grain-stopping time, the attracting region changes from a single point within the vortex to a ring within the vortex and then to a large ring around the vortex (and in the plain of the disk).

Boersma numerically examined sediment transport by carrying out direct numerical calculations of three-dimensional flow in a channel. The wavy bottom boundary was designed to simulate both a rippled river or ocean bottom and previous wind tunnel experiments. Like the experiments, the calculations of the fluid motion and the particle paths showed that Langmuir-like vortices were created that were aligned in the longitudinal direction. The particles tended to concentrate downstream of the wave tops.

Carnevale & Orlandi used two-dimensional numerical simulations to examine internal waves in the upper ocean thermocline. In their numerical experiments, wave packets propagated vertically in a manner that was consistent with the observed vertical scales in the ocean. Strong packets generated turbulence that formed a continuous 'scar' of small-scale perturbations in their wakes that were much longer than the size of the packets themselves. The results are important due to their implications for turbulent mixing in the upper ocean.

Philip S. Marcus

Scalings and asymptotics of coherent vortices in protoplanetary disks

By J. Barranco†, P. Marcus‡ AND O. M. Umurhan

Gas that is transported radially inward from the outer edge of an accretion disk and onto a forming central star must be in a nearly Keplerian orbit at all radii. To do this, it must give up part of its angular momentum and energy to the ambient gas, which in turn advects angular momentum outward via a secondary flow. Here, we set up the numerical calculation for computing this flow by obtaining simplified sets of 3D, asymptotic equations that are well-posed and can be computed by the same techniques that are used for the 3D, anelastic Euler equation. The asymptotics allow an easy parameterization of the unknown equations of energy and state and boundary conditions. It is shown analytically that the required mass and angular momentum transport cannot occur if the protoplanetary disk is barotropic. However, a small baroclinicity allows it. Scale analysis shows that if 20% of the protoplanetary disk is filled with vortices, then the required transport can occur with a large enough radially inward mass flux to satisfy the astronomical observations.

1. Introduction

The traditional picture of protoplanetary accretion disks is that they are quiescent, without coherent features (Balbus & Hawley 1996). Some researchers have argued that they are laminar (unless they are well-coupled to magnetic fields so that the Balbus-Hawley instability can be invoked), despite the fact that their Reynolds numbers are greater than 10^{14}. In contrast, we believe that the disks are likely to be filled with structures, and the goal of this paper is to lay out a framework to compute them numerically. Our motivation is that we believe that long-lived vortices are the key to solving the angular-momentum transport problem in accretion disks and also to understanding the formation of planetesimals (Barranco & Marcus, this volume). Recently, calculations of two-dimensional vortices embedded within accretion disks have been published (Adams & Watkins 1995, Bracco *et al.* 1998, Godon & Livio 1999, 2000), but they were computed with the quasi-geostrophic, shallow-water, or two-dimensional Euler equation, and we argue below that none of these are valid for protoplanetary disks.

The hydrodynamics of a protoplanetary accretion disk are governed by the Euler equation (ignoring viscosity), the continuity equation, an energy equation, and an equation of state, along with appropriate boundary and initial conditions. The equations are difficult to solve numerically because: (1) There are two very large terms present in the equations – centrifugal force and radial gravity. They nearly cancel and their small remainder governs the physics of the coherent features. (2) There are wide ranges of length and time scales which demand high resolution and small time steps in numerical computations.

† University of California at Berkeley, Department of Astronomy
‡ University of California at Berkeley, Department of Mechanical Engineering

(3) The energy equation is not known (depending upon location, the gas could be optically thick or thin). (4) The boundary and initial conditions are not well known because the disk is the end-product of a collapsing, spinning gas cloud, and how that forms the disk and continues to feed energy and matter in and out of it are not known. Without knowledge of the energy equation and equation of state, it would seem hopeless to try to compute solutions; however, we shall show that with a judicious choice of asymptotic scalings, our ignorance of this information can be readily parameterized and progress can be made.

2. Physical constraints and mathematical assumptions

Radio and infrared observations indicate that protoplanetary disks are cool. In fact, they are sufficiently cold that the gas within them is not strongly ionized and cannot couple to magnetic fields. Thus we have ignored the effects of magnetic fields. Because the characteristic speed of sound c_s^2 is nearly proportional to the gas temperature for most relevant equations of state, the coolness of the disk at most locations (say, at distances from the protostar greater than 1 A.U.),

$$c_s/V_k \equiv \delta \ll 1 \tag{2.1}$$

where $V_k \equiv \sqrt{GM/r}$ is the Keplerian velocity, M is the mass of the central protostar, G is the gravitational constant, and (r, ϕ, z) are the cylindrical coordinates. We ignore the self-gravity of the mass in the disk and treat the protostar as if it were a point mass. Before considering a solution to the equations of motion that includes coherent features, we first examine a base flow solution (denoted by an overbar) that is steady in time and axisymmetric and in which the radial and vertical components of the velocity are zero $\bar{V}_z = \bar{V}_r = 0$. In this case the radial and z components of the Euler equation reduce to

$$\bar{V}_\phi^2/r = GMr/R^3 + (1/\bar{\rho})\partial\bar{P}/\partial r \tag{2.2}$$

and

$$0 = GMz/R^3 + (1/\bar{\rho})\partial\bar{P}/\partial z \tag{2.3}$$

where P and ρ are the pressure and density, and R is the spherical radial coordinate. Because $c_s^2 \sim \bar{P}/\bar{\rho}$, Eq. (2.3) implies that the disk is thin,

$$H/r \sim c_s/V_k = \delta \ll 1 \tag{2.4}$$

where H is both the disk thickness and the vertical scale-height of $\bar{P}$. Eqs. (2.2) and (2.3) along with the ϕ-component of the Euler equation can be written as

$$(\bar{V}_\phi^2/r)\hat{r} = \nabla\Phi + (\nabla\bar{P})/\bar{\rho} \tag{2.5}$$

where the gravitational potential is $\Phi \equiv -GM/R$. The curl of Eq. (2.5) shows that regardless of the of the form of the energy equation or equation of state, if the flow were barotropic, $\bar{V}_\phi$ is a function of r only. Eq. (2.2) (along with the assumption that the radial scale of $\bar{P}$ is not smaller than r) shows that $\bar{V}_\phi = V_k(r)\left(1 + \mathcal{O}\left(\delta^2\right)\right)$. Therefore we can write

$$\bar{V}_\phi(r, z) = V_k(r)\left(1 + \delta^2 f(r) + \delta^2 g(r, z)\right) \tag{2.6}$$

where f and g are order unity and where $g \equiv 0$ for a barotrope. Thus, although the disk can be time-dependent and contain coherent and long-lived hydrodynamic features such as vortices, the overall flow (denoted by the overbars) is nearly Keplerian.

It would appear that to make progress we either need to know the energy equation and equation of state or the functional forms of f and g; however, in the following we show that since the disk is symmetric about the mid-plane, we only need to know one dimensionless, scalar property of $\bar{V}_\phi$: $\beta \equiv -H^2(\partial^2\bar{V}_\phi/\partial z^2)/(2V_k(r_0)\gamma)$ where $\gamma \equiv L_r/r_0$, L_r is the characteristic radial length scale, *i.e.*, $r - r_0$ of any coherent feature, and where the derivative is computed at mid-plane ($z = 0$) and at the radial location r_0 defined below. Eq. (2.6) requires that $\beta\gamma \leq \delta^2$.

3. Equations, scalings and asymptotic reductions in the rotating frame

In a reference frame rotating with angular velocity $\Omega \equiv \bar{V}_\phi(r = r_0, z = 0)/r_0 = \sqrt{GM/r_0^3}\left(1 + \mathcal{O}\left(\delta^2\right)\right)$, the Euler and continuity equations can be written

$$\frac{Dv_r}{Dt} = \frac{v_\phi^2 - \bar{v}_\phi^2}{r} + 2\Omega(v_\phi - \bar{v}_\phi) - \frac{1}{\rho}\frac{\partial P}{\partial r} + \frac{1}{\bar{\rho}}\frac{\partial\bar{P}}{\partial r} \tag{3.1}$$

$$\frac{Dv_\phi}{Dt} = -\frac{1}{r\rho}\frac{\partial P}{\partial\phi} - \frac{v_r v_\phi}{r} - 2\Omega v_r \tag{3.2}$$

$$\frac{Dv_z}{Dt} = -\frac{1}{\rho}\frac{\partial P}{\partial z} + \frac{1}{\bar{\rho}}\frac{\partial\bar{P}}{\partial z} \tag{3.3}$$

$$\frac{D\rho}{Dt} = -\rho\nabla\cdot\mathbf{v}, \tag{3.4}$$

where the velocity in the rotating frame is written in lower case and where $\bar{V}_\phi$ in the rotating frame is

$$\bar{v}_\phi(r, z) = -\left(3\Omega(r - r_0)/2\right)\left(1 + \mathcal{O}\left(\gamma, \delta^2\right)\right) - \beta c_s\gamma(z/H)^2/\delta \tag{3.5}$$

in which we have dropped the z-derivatives in v_ϕ higher than second.

Our requirement in this paper that $\gamma \ll 1$ is important is the result of the following set of physical arguments. Keplerian disks are special environments. Numerical calculations by others as well as our own experiences in hypersonic flows suggest that hypersonic and supersonic waves are transients that radiate away and leave behind subsonic vortices. Although this might not always be true, we believe that our best chance of finding coherent structures is subsonic vortices. Also, from our experience in computing long-lived 2D (Marcus 1993) and 3D (Marcus 1984, Marcus & Tuckerman 1987) coherent vortices embedded in shearing flows, we have always found that the vortices are ripped apart by the shear unless their characteristic velocities are at least as large as the differential velocity of the ambient, shearing flow. These two arguments along with Eqs. (2.4) and (3.5) and the definition of γ give the scaling

$$1 \gg \langle v\rangle/c_s \sim \Omega L_r/c_s = \Omega r_0\gamma/c_s = \gamma/\delta = L_r/H \tag{3.6}$$

where $\langle v\rangle$ is the characteristic value of v_ϕ. Eq. (3.6) implies $\gamma \ll \delta$ and $H \gg L_r$. It also implies that the Rossby number $Ro \equiv \langle v\rangle/2\Omega L_r$ is order unity. This is unlike the physical conditions of the vortices embedded in the shearing, azimuthal flows on Jupiter, where the rapid rotation of the planet, compared with the shear, makes the Coriolis force dominate the inertial force. Here, they are the same order. The relation $H \gg L_r$ implies that even though the protoplanetary disks are thin, they are not "shallow" in the context of the shallow-water equations or quasi-geostrophic equations (which are derived using the assumptions that $H \ll L_r$ and $H^2 \ll L_r^2 Ro$, respectively). Thus subsonic, coherent

vortices in a protoplanetary disk are not shallow, and attempting to use the shallow-water equations or quasi-geostrophic equations to compute them is inconsistent.

Defining $P \equiv \bar{P} + \tilde{P}$, $\rho \equiv \bar{\rho} + \tilde{\rho}$, and $\epsilon^2 \sim \tilde{P}/\bar{P} \sim \tilde{\rho}/\bar{\rho}$, we can write the Euler and continuity equations in Cartesian form with $v_r \rightarrow v_y$, $v_\phi \rightarrow -v_x$, $(r - r_0) \rightarrow y$, and $r_0\phi \rightarrow -x$. Keeping leading order terms to $\mathcal{O}\left(\delta^2, \epsilon^2, \gamma\right)$:

$$\frac{\partial u_x}{\partial t} = -\nabla \cdot \left(\mathbf{u}u_x/\bar{\rho}(r_0, z)\right) + 2\Omega u_y - \frac{\partial \tilde{P}}{\partial x} \tag{3.7}$$

$$\frac{\partial u_y}{\partial t} = -\nabla \cdot \left(\mathbf{u}u_y/\bar{\rho}(r_0, z)\right) - 2\Omega(u_x - \bar{u}_x) - \frac{\partial \tilde{P}}{\partial y} \tag{3.8}$$

$$\frac{\partial u_z}{\partial t} = -\nabla \cdot \left(\mathbf{u}u_z/\bar{\rho}(r_0, z)\right) - \frac{\partial \tilde{P}}{\partial z} - \tilde{\rho}z\Omega^2 \tag{3.9}$$

$$\nabla \cdot \mathbf{u} = 0 \tag{3.10}$$

Here the momentum $\mathbf{u} \equiv \bar{\rho}(r_0, z)\mathbf{v}$, $\bar{u}_x \equiv \bar{\rho}(r_0, z)\bar{v}_x$, and in deriving Eq. (3.10) we assume that the time-scale is of the same order as the advective time (in the rotating frame) or slower, (*cf.*, Eq. (3.11) below). Note that acoustic and other fast waves are neglected in this approximation.

We plan to solve Eqs. (3.7)-(3.10) numerically using the standard methods for the Euler equation with an anelastic equation of state, but to see what the solutions might look like and to make analytic progress, we now examine three different asymptotic regimes. To do so, we choose units for the thermodynamic quantities, momenta, x, y, and z, such that the non-dimensionalized quantities are order unity. Only the leading order terms to $\mathcal{O}\left(\delta^2, \epsilon^2, \gamma\right)$ are retained. Although the units of x, z, and u_z will differ for the different asymptotic scalings, all three share the following (where square brackets mean "units of"):

$$[\bar{\rho}] = \bar{\rho}(r_0, 0) \qquad [\bar{P}] = [\bar{\rho}]c_s^2 \qquad [L_y] \equiv L_r = \epsilon H$$

$$[u_x] = \epsilon[\bar{\rho}]H\Omega \qquad [u_y] = \epsilon^2[\bar{\rho}]H^2\Omega/[L_x] \qquad [t] = [L_x]/\epsilon H\Omega$$

$$[\tilde{\rho}] = \epsilon^2[\bar{\rho}] \qquad [\tilde{P}] = \epsilon^2[\bar{P}], \tag{3.11}$$

where c_s is evaluated at the mid-plane of the disk at $r = r_0$. The scaling for u_x follows from requiring that the Rossby number be order unity. The length scale L_y results from this and our desire to have the Mach number $[v_x]/c_s \equiv \epsilon$. The scale of u_y is chosen by demanding that the Coriolis terms are of the same order as the pressure terms. As a consequence of this last scaling, the x- and y-components of the advective derivative also have the same order. The scaling for $\bar{P}$ follows from the definition of c_s. The scaling for the pressure deviations $\tilde{P}$ arises from the requirement that the pressure and Coriolis terms are of the same order in the y-component of the momentum equation. The scaling for $\tilde{\rho}$ comes from the requirement that the fractional changes in pressure and density are the same order. The choice of time scale comes from requiring that it is the advective time-scale. We shall see that it replaces the dynamics continuity equation with the kinematic condition that the mass flux is divergence-free. This removes a temporal degree of freedom, and so sound and supersonic waves are removed from the system of equations.

The scaling for $[L_x]$ displayed in Eq. (3.11) as well as $[L_y]$ and $[u_z]$ have been left unspecified at this point because there is some freedom in how we choose them. This freedom will lead to different physical and dynamical regimes which we will show below.

Equation (2.4), the scaling $[L_y]$, and the definition of γ show that ϵ, γ, and δ are not independent but instead satisfy

$$\epsilon \equiv \gamma/\delta \ll 1. \tag{3.12}$$

The non-dimensionalized equations can now be written in terms of the (not yet specified) constants $[L_z]$, $[L_x]$, and $[u_z]$,

$$\frac{\partial u_x}{\partial t} = -\nabla_\perp \cdot \left(\frac{\mathbf{u}_\perp u_x}{\bar{\rho}(r_0, z)} \right) - \frac{\partial \left(u_z u_x / \bar{\rho}(r_0, z) \right)}{\partial z} \left\{ \frac{[u_z]}{[u_x]} \frac{[L_x]}{[L_z]} \right\} + 2u_y - \frac{\partial \tilde{P}}{\partial x} \tag{3.13}$$

$$\frac{\partial u_y}{\partial t} = -\nabla_\perp \cdot \left(\frac{\mathbf{u}_\perp u_y}{\bar{\rho}(r_0, z)} \right) - \frac{\partial \left(u_z u_y / \bar{\rho}(r_0, z) \right)}{\partial z} \left\{ \frac{[u_z]}{[u_x]} \frac{[L_x]}{[L_z]} \right\}$$

$$-2(u_x - \bar{u}_x) \left\{ \frac{[L_x]^2}{[L_y]^2} \right\} - \frac{\partial \tilde{P}}{\partial y} \left\{ \frac{[L_x]^2}{[L_y]^2} \right\} \tag{3.14}$$

$$\frac{\partial u_z}{\partial t} = -\nabla_\perp \cdot \left(\frac{\mathbf{u}_\perp u_z}{\bar{\rho}(r_0, z)} \right) - \frac{\partial \left(u_z^2 / \bar{\rho}(r_0, z) \right)}{\partial z} \left\{ \frac{[u_z]}{[u_x]} \frac{[L_x]}{[L_z]} \right\}$$

$$-\frac{\partial \tilde{P}}{\partial z} \left\{ \frac{[u_x]}{[u_z]} \frac{[L_x]}{[L_z]} \right\} - \tilde{\rho}z \left\{ \frac{[u_x]}{[u_z]} \frac{[L_x]}{H} \frac{[L_z]}{H} \right\} \tag{3.15}$$

where the $\perp$ subscript means the x and y components. The non-dimensional steady state azimuthal velocity is

$$\bar{u}_x = \left(\frac{3}{2}y + \beta z^2 [L_z]^2 / H^2 \right) \bar{\rho}(r_0, z) \tag{3.16}$$

It should be kept in mind that unlike the momenta and thermodynamic quantities, the non-dimensional z can be much greater than unity: the dimensional z is order H; the non-dimensional z is order $H/[L_z]$ which can be big (see §3.2).

Without an energy equation, it is impossible to obtain an expression for $\bar{\rho}$ which is needed in the buoyancy terms of the equations above, so we exploit a standard method used in geophysical fluid dynamics. The $\bar{\rho}$ is sensitive to the equations of state and energy (and boundary conditions) because it represents a long-time balance within the disk of energy sources and sinks (*e.g.*, we cannot compute the $\bar{\rho}$ in the earth's atmosphere without taking into account the effects of ground heating, cloud cover, cooling, *etc.*). However, the density disturbances $\bar{\rho}$ within the disk are created by advection of fluid parcels. If the advective time is fast compared with the thermal time (which is unknown and due to complicated physics), then $\bar{\rho}$ is nearly equal to that of an adiabatic displacement, and if the time scales have the opposite ordering, then $\bar{\rho}$ is approximated as an isothermal displacement. In the case where the two time scales are equal (which would be unusual since they are determined by very different dynamics), an energy equation is needed. Most previous computations of protoplanetary disks use an adiabatic approximation for $\bar{\rho}$ and assume an ideal gas equation of state, and that will also be our starting assumption (to be modified later if it is required).

We have found three different relationships for $[L_x]$, $[L_z]$, and $[u_z]$ that are physically meaningful and yield mathematically consistent asymptotic equations. We believe them to be exhaustive and present them below.

3.1. *Columnar dynamics*

One set of asymptotic equations is obtained from Eqs. (3.13)- (3.15) by setting $[L_x] = [L_y] = \epsilon H$, $[L_z] = H$, and $[u_z] = \epsilon[u_x]$. Retaining terms to $\mathcal{O}\left(\delta^2, \epsilon^2, \gamma\right)$, we obtain

$$\frac{\partial u_x}{\partial t} = -\nabla_\perp \cdot \left(\frac{\mathbf{u}_\perp u_x}{\bar\rho(r_0, z)}\right) + 2u_y - \frac{\partial \tilde P}{\partial x} \tag{3.17}$$

$$\frac{\partial u_y}{\partial t} = -\nabla_\perp \cdot \left(\frac{\mathbf{u}_\perp u_y}{\bar\rho(r_0, z)}\right) - 2\left(u_x - \bar\rho(r_0, z)(3y/2 + \beta z^2)\right) - \frac{\partial \tilde P}{\partial y} \tag{3.18}$$

$$\frac{\partial u_z}{\partial t} = -\nabla_\perp \cdot \left(\frac{\mathbf{u}_\perp u_z}{\bar\rho(r_0, z)}\right) - \frac{\partial \tilde P}{\partial z} - \tilde\rho z \tag{3.19}$$

$$\nabla_\perp \cdot \mathbf{v}_\perp = 0 \tag{3.20}$$

These equations in which the 2-dimensional component of the velocity is divergence-free describe coherent features whose lengths and velocities are similar in the plane of the disk but are columnar in the sense that $[L_z] \gg [L_x] = [L_y]$. In these equations there is no contribution from the z component of the advective derivative. The fluid is decoupled from itself in the z direction. If the vertical layers in a coherent feature begin to decouple from one another, then the the vertical gradients become large, the vertical scale-height of the flow becomes much smaller than H, and the underlying scaling breaks down. The dynamics would then become governed by the more general Eqs. (3.13)-(3.15) which would tend to recouple the layers. The decoupling of the flow in z makes it easy to compute steady solutions to Eqs. (3.17)- (3.20), so these equations are particularly useful to find steady solutions, but not to explore dynamics or test stability.

3.2. *Round vortices*

The second asymptotic limit comes from setting $[L_z] = [L_x] = [L_y] = \epsilon H$, and $[u_z] = [u_x] = [u_y]$,

$$\frac{\partial u_x}{\partial t} = -\nabla \cdot \left(\frac{\mathbf{u} u_x}{\bar\rho(r_0, z)}\right) + 2u_y - \frac{\partial \tilde P}{\partial x} \tag{3.21}$$

$$\frac{\partial u_y}{\partial t} = -\nabla \cdot \left(\frac{\mathbf{u} u_y}{\bar\rho(r_0, z)}\right) - 2\left((u_x - \bar\rho(r_0, z)(3y/2 + \epsilon^2\beta z^2)\right) - \frac{\partial \tilde P}{\partial y} \tag{3.22}$$

$$\frac{\partial u_z}{\partial t} = -\nabla \cdot \left(\frac{\mathbf{u}_\perp u_z}{\bar\rho(r_0, z)}\right) - \frac{\partial \tilde P}{\partial z} - \epsilon^2\tilde\rho z \tag{3.23}$$

$$0 = \nabla \cdot \mathbf{u} \tag{3.24}$$

Note, to be consistent, we have kept the $\mathcal{O}\left(\epsilon^2\right)$ terms in the baroclinic β term in Eq. (3.22) and in the buoyancy term in in Eq. (3.23). As we stated after Eq. (3.16), $z \sim H/L_z = \epsilon^{-1}$. Thus the β term is actually order unity and the buoyancy term in Eq. (3.23) is $\mathcal{O}(\epsilon)$ and must be retained. Qualitatively speaking, this scaling is valid for nearly spherically shaped vortices.

3.3. *Elongated dynamics*

In this final set, $[L_x] = [L_z] = H$ and $[u_x] = [u_z]$, resulting in,

$$\frac{\partial u_x}{\partial t} = -\nabla \cdot \left(\frac{\mathbf{u} u_x}{\bar\rho(r_0, z)}\right) + 2u_y - \frac{\partial \tilde P}{\partial x} \tag{3.25}$$

$$0 = -2\left(u_x - \bar{\rho}(r_0, z)(3y/2 + \beta z^2)\right) - \frac{\partial \tilde{P}}{\partial y} \tag{3.26}$$

$$\frac{\partial u_z}{\partial t} = -\nabla \cdot \left(\frac{\mathbf{u} u_z}{\bar{\rho}(r_0, z)}\right) - \frac{\partial \tilde{P}}{\partial z} - \tilde{\rho} z \tag{3.27}$$

$$\nabla \cdot \mathbf{u} = 0. \tag{3.28}$$

Vortices with this scaling are stretched in the azimuthal direction. Furthermore, the dynamics in the radial (y) direction is geostrophic, making the effective Rossby number in that direction zero. It can be shown that these equations, even though there is no time derivative in Eq. (3.26), have the same boundary condition requirements as the anelastic Euler equations.

4. Linear theory

In this section we examine the linear stability of the unperturbed disk using the asymptotic equations (3.25)-(3.28) derived for the elongated dynamics in §3.3. Stability (or instability) computed with these equations does not guarantee stability (or instability) when computed with the full equations, but any eigenmode computed with Eqs. (3.25)-(3.28) whose length and time scales are consistent with the those of the assumptions in §3.3 is valid. The dual purposes of this section are first to illustrate some possible dynamics of the unperturbed disk and second to show that subtle changes in boundary conditions can lead to big differences. For one choice of boundary conditions we show that the disk modes exhibit algebraic singularities at some critical time t_{sing}. However, at early times prior to t_{sing} the solutions are consistent with the assumptions used to derive the asymptotic equations. Nonetheless, the prediction of a violent instability suggests that when the full equations are used, the disk is either unstable or there are initial conditions that lead to transient modes that grow before they decay. Even if the disk is linearly stable when computed with the full equations, if the transients reach large amplitudes they could trigger a finite-amplitude instability. This suggests that we look for these transients in the numerical simulations. For the other set of boundary conditions, stability properties change. This suggests that numerical simulations will need to be computed with a variety of physically reasonable boundary conditions to understand fully the physics of the disk.

We linearize Eqs. (3.25)-(3.28) about the unperturbed disk with momentum flux $\bar{u}_x$. We choose the simplest energy equation and equation of state: the fluid has constant density. This makes $\tilde{\rho} \equiv 0$, $\nabla \cdot \mathbf{v} = 0$, and $\beta \equiv 0$. Writing perturbed quantities with a "prime" and using $\mathbf{v}$ rather than $\mathbf{u}$ as the independent variable, we obtain

$$\left(\frac{\partial}{\partial t} + \bar{v}_x \frac{\partial}{\partial x}\right) v_x' = -\frac{\partial \tilde{P}'}{\partial x} + \tfrac{1}{2} v_y' \tag{4.1}$$

$$0 = -\frac{\partial \tilde{P}'}{\partial y} - 2v_x' \tag{4.2}$$

$$\left(\frac{\partial}{\partial t} + \bar{v}_x \frac{\partial}{\partial x}\right) v_z' = -\frac{\partial \tilde{P}'}{\partial z} \tag{4.3}$$

$$0 = \nabla \cdot \mathbf{v}' \tag{4.4}$$

We now consider two types of boundary conditions.

4.1. Channel geometry

Here we use the boundary conditions similar to those in an inviscid channel flow:

$$\text{(i)} \; v'_z = 0 \; \text{ at } z = \pm\zeta \quad \text{and} \quad \text{(ii)} \; v'_y = 0 \; \text{ at } y = \pm 1, \tag{4.5}$$

with periodic boundary conditions in x. Making each perturbation quantity have x and t dependence of $e^{i(\omega t + k_x x)}$, we combine Eqs. (4.1)-(4.4) into a single equation for $\tilde{P}'$,

$$-(\omega + \tfrac{3}{2}k_x y)^2 \frac{\partial^2 \tilde{P}'}{\partial y^2} + \frac{\partial^2 \tilde{P}'}{\partial z^2} = 0, \tag{4.6}$$

where the velocity can be expressed in terms of $\tilde{P}'$:

$$v'_x = \frac{1}{2}\frac{\partial \tilde{P}}{\partial y} \quad , \quad v'_y = -i\,(\omega + \tfrac{3}{2}k_x y)\frac{\partial \tilde{P}'}{\partial y} + 2ik_x \tilde{P}'. \tag{4.7}$$

Equation (4.6) is separable, so we write

$$\tilde{P}' \equiv \Psi_{m\ell}(y) Z_m(z). \tag{4.8}$$

In enforcing the boundary condition at $z = \pm\zeta$, we find that

$$Z_m(z) = \cos\big((2m+1)\pi z/2\zeta\big), \tag{4.9}$$

where m is an integer. The velocities in the x and y directions and the pressure are proportional to cosines in z, and v'_z is proportional to a sine. The equation for $\Psi_{m\ell}$ is now an equi-density equation with power-law solution:

$$\Psi_{m\ell} = \left(\frac{\omega_{m\ell} + \tfrac{3}{2}k_x y}{\omega_{m\ell} - \tfrac{3}{2}k_x}\right)^{\tfrac{1}{2}+i\tfrac{1}{2}\Delta} + \left(\frac{5+3i\Delta}{5-3i\Delta}\right)\left(\frac{\omega_{m\ell} + \tfrac{3}{2}k_x y}{\omega_{m\ell} - \tfrac{3}{2}k_x}\right)^{\tfrac{1}{2}-i\tfrac{1}{2}\Delta}, \tag{4.10}$$

where

$$\Delta \equiv \left(\frac{4\pi^2(2m+1)^2}{9\zeta^2 k_x^2} - 1\right)^{\tfrac{1}{2}}, \tag{4.11}$$

and where the frequencies ω are labeled with two subscripts, $\omega_{m\ell}$, and satisfy the dispersion relation

$$\omega_{m\ell} = \tfrac{3}{2}k_x \coth\left(\tfrac{\ell\pi}{\Delta}\right), \quad \text{for } 2\pi|2m+1| - 3\zeta|k_x| > 0 \tag{4.12}$$

$$\omega_{m\ell} = i\tfrac{3}{2}k_x \cot\left(\tfrac{\ell\pi}{|\Delta|}\right), \quad \text{for } 2\pi|2m+1| - 3\zeta|k_x| < 0, \tag{4.13}$$

and where ℓ is a non-zero integer. The eigenmodes are unstable when $\omega_{m\ell}$ has a positive real part or when $2\pi|2m+1| - 3\zeta|k_x| < 0$ and $0 < \mathrm{mod}_\pi(\ell\pi/|\Delta|) < \pi/2$ hold simultaneously.

4.2. Sliding box coordinates

In this section we show that the "sliding box" boundary conditions give algebraic rather than exponential behavior. We introduce the "sliding box" coordinates that were previously used in studies (Marcus & Press 1977, Rogallo 1981 and Korycansky 1992) of plane Couette and other shearing flows:

$$\hat{x} \equiv x + \frac{3}{2}yt \qquad \hat{t} \equiv t \qquad \hat{y} \equiv y \qquad \hat{z} \equiv z \tag{4.14}$$

Eqs. (4.1)-(4.4) are autonomous in the new spatial coordinates but no longer so in time. Making all of the perturbed variables proportional to $e^{i(k_y \hat{y} + k_z \hat{z})}$, the linearized Eqs. (4.1) - (4.4) in the new coordinates are:

$$\frac{\partial v'_x}{\partial \hat{t}} = -ik_x \tilde{P}' + \tfrac{1}{2} v'_y \tag{4.15}$$

$$0 = -2v'_x - i(k_y - \tfrac{3}{2} k_x \hat{t}) \tilde{P}' \tag{4.16}$$

$$\frac{\partial v'_x}{\partial \hat{t}} = -\frac{\partial}{\partial \hat{z}} \tilde{P}' \tag{4.17}$$

$$0 = ik_x v'_x + i(k_y - \tfrac{3}{2} k_x \hat{t}) v'_y + \frac{\partial}{\partial \hat{z}} v'_z. \tag{4.18}$$

Requiring, as before, that there be no vertical flow at $\hat{z} = \pm \zeta$ requires that $\tilde{P}'$ be proportional to $Z_m(\hat{z})$ where Z_m and m are defined as they were in Eq. (4.9). Writing $\tilde{P}' \equiv \mathcal{P}(t) Z_m(\hat{z}) e^{i(k_y \hat{y} + k_z \hat{z})}$, Eqs. (4.15)-(4.18) can be combined into a single ordinary differential equation in time for $\mathcal{P}$,

$$\tfrac{9}{4} k_x^2 \frac{d}{dT} \left(2T + T^2 \frac{d}{dT} \right) \mathcal{P} + \frac{\pi^2 (2m+1)^2}{\zeta^2} \mathcal{P} = 0, \tag{4.19}$$

where we have used the temporal coordinate

$$T \equiv = \tfrac{3}{2} k_x \hat{t} - k_y. \tag{4.20}$$

Equation (4.19) has a regular singular point at $T = 0$ which shows that the solution $\mathcal{P}$ will be algebraically unstable. $\mathcal{P}$ is given by,

$$\mathcal{P} = a \left(\tfrac{3}{2} k_x \hat{t} - k_y \right)^{\chi_+} + b \left(\tfrac{3}{2} k_x \hat{t} - k_y \right)^{\chi_-} \qquad \chi_\pm = -\frac{3 \pm \nu}{2}, \ \nu = \left(1 - \frac{4(2m+1)^2 \pi^2}{9 \zeta^2 k_x^2} \right)^{\frac{1}{2}}, \tag{4.21}$$

where a and b are integration constants and depend on the initial condition.

All perturbations in which $k_y k_x > 0$ have an algebraic singularity at $t_{\text{sing}} \equiv 2k_y / 3k_x$ and grow in time. Modes with $k_y k_x < 0$ decay algebraically. This suggests that the unperturbed disk computed with the full equations of motion is either algebraically unstable or has transients that grow before they decay. This behavior is different from that computed with the channel boundary conditions in §4.1.

5. Discussion and conclusions

Although we have not yet numerically solved our asymptotic equations, we can draw several conclusions about their solution. First, it is almost certain that they allow coherent anti-cyclones (vortices opposite in sign to Ω). Two- and three-dimensional numerical calculations of vortices embedded in shearing flows show that if the shear and the vorticity are of the same order, they must also be the same sign; otherwise, the vortices are stretched by the ambient flow and destroyed (Marcus 1993). Moreover vortices embedded in like-signed shearing flows with Rossby numbers less than or order unity (ours are designed to be order unity by our choice of the asymptotic scalings) are very stable; small ones tend to merge together and become large; when turbulence rips a vortex apart, the fragments often merge and restore the vortex. Since the shear in a Keplerian disk is anti-cyclonic, anti-cyclones would likely be stable in protoplanetary disks. Two-dimensional simulations of near-Keplerian disks (Adams & Watkins 1995, Bracco *et al.*

1998, Godon & Livio 1999, 2000) confirm this, and we expect the stability to remain valid in 3-dimensional disks.

Moreover, because our solutions have Rossby numbers of order unity, they will be in partial geostrophic balance (*i.e.* the Coriolis force will partially balance the pressure gradient). Geostrophic balance makes anti-cyclones have relatively high pressures in their interiors or positive $\tilde{P}$ and cyclones have relatively low pressures or negative $\tilde{P}$. For isothermal or adiabatic perturbations (the types considered here), positive $\tilde{P}$ goes along with positive $\tilde{\rho}$ (see §3), which means that anti-cyclones in a protoplanetary disk correspond to mass over-densities.

Our overall picture of mass and angular momentum transport in a protoplanetary disk is that the perturbations of the in-falling mass at the outer edge of the disk create anti-cyclones, or lumps of mass over-densities that are long-lived. In future work we shall test this hypothesis numerically. However, the question still remains as to whether the lumps migrate radially inward. We can state with certainty that if the disk is barotropic they do not. This can easily be seen from Eqs. (3.7)-(3.10) (or any of our three sets of asymptotic equations.) In all cases, if $\beta = 0$, the equations are invariant under the symmetry $x \to -x$, $y \to -y$. Due to this symmetry, there is nothing to distinguish the radially inward direction from the radial outward direction (other than the geometrical curvature of the disk which is small compared to other small quantities and is ignored in a first-order asymptotic expansion). This means that if a mass lump or anti-cyclone were placed in the flow, it could not migrate radially. When the flow is baroclinic and $\beta \neq 0$, this symmetry is broken, and the vortex is free to drift radially.

An important question to answer before tackling the equations numerically is whether the secondary flow due to the vortices is large enough to transport the requisite angular momentum radially outward. The inward mass flux that forms the star (due to the inward drift of anti-cyclonic lumps in our picture and due to unspecified "turbulence" or laminar inward flow in other scenarios) also carries angular momentum inward. The secondary flow due to the vortices must compensate for this angular momentum flux which is $r^2 \Omega_k \dot{M}$ where $\dot{M}$ is the radially inward mass flux and equal to the rate at which the protostar gains mass, and Ω_k is the Keplerian angular velocity. The outward flux of momentum due to secondary flows (including vortices) is approximately $2\pi r^2 H[u_y][u_x]/[\rho] C f = f C \epsilon^2 2\pi r^2 H^3[\rho]\Omega_k^2$, where we have used the round scaling in section 3.2 to estimate the characteristic radial and azimuthal velocities of the secondary flow $[u_y]$ and $[u_x]$, C is the correlation between the radial and azimuthal components of the velocity, and f is the fraction of the disk filled with the secondary flow (vortices). Setting these two fluxes equal and using (at r equal to one A.U. - the distance from the earth to the sun) $[\rho] = 1.4 \times 10^{-9}$g/cm^3, $r = 1.5 \times 10^{13}$cm, $H = 4.5 \times 10^{11}$cm, $\Omega_k = 2\pi$ year^{-1}, and $\dot{M} = 10^{-8}$ solar masses per year (with one solar mass equal to 2.0×10^{33}g), we obtain $f C \epsilon^2 = 4 \times 10^{-3}$. We do not know the value of C *a priori*; it must be computed. However, numerical simulations of the vortices in Couette-Taylor flow in which the vortices are the main transporters of the radial angular momentum flux have $C \sim 0.1$. We set $\epsilon^2 = 0.2$. (Our *physical* assumption that robust vortices are subsonic restricts $\epsilon^2 < 1$; our *mathematical* requirement to obtain the asymptotics of the round-vortex equations requires that $\epsilon^2 \ll 1$ so that ϵ^2 could be an expansion parameter. Setting $\epsilon^2 = 0.2$ may be too conservative, and in the future it may be necessary to obtain an asymptotic expansion for the disk equations in δ and γ that does not require $\epsilon^2 \ll 1$.) With these values we obtain $f = 1/5$, meaning that if one fifth of the disk were filled with vortices, then angular momentum balance could be maintained with the observed mass accretion rates. We caution the

reader that the estimates for the observed ρ and H could be incorrect by factors of 2 or more, and so could our scaling estimates for the values of $[u_y]$ and $[u_x]$. However, it is encouraging that the estimates of f are not several orders of magnitude greater than unity.

Of course, the way to interpret these results from a physical point of view is that computations (or the physics of an actual protoplanetary disk) provide the values of f, C, H, u_x, u_y, and ρ, which in turn determine the observed value of $\dot{M}$. With this in mind, our goals in computing solutions to Eqs. (3.13)-(3.15) are: (1) Start with an initial anti-cyclone embedded in a nearly-Keplerian, three-dimensional disk and determine if it is stable and long-lived. Since we shall not know *a priori* its equilibrium shape, watch it relax to its equilibrium and determine the physics of how it relaxes. (2) Determine the anti-cyclone's sensitivity to the boundary conditions of the disk. (3) Determine how a large anti-cyclone can be created when it is not initially present in the flow. Can it be created by repeated mergers of much smaller (initial) anti-cyclones or from an initial set of disturbances in $\tilde{\rho}$? Determine whether an anti-cyclone can be created in an initially undisturbed flow (*i.e.* the base disk flow written with the overbars). Is the flow linearly unstable? If the flow is stable, can an anti-cyclone be created in the base disk flow if the mass in-flow through the outer boundary condition is made time-dependent and variable in ϕ (thereby creating mass "lumps" at the outer boundary)? (4) Determine the rate at which the anti-cyclones drift radially inward as a function of baroclinicity and determine whether it is sufficient to reproduce the observed mass accretion rates.

REFERENCES

ADAMS, F. C. & WATKINS, R. 1995 Vortices in circumstellar disks. *Ap. J.* **451**, 314-327.

BRACCO, A., PROVENZALE, A., SPIEGEL, E. A. & YECKO, P. 1998 Spotted Disks, In *Proceedings of the Conference on Quasars and Accretion Disks*. (M. Abromowicz, Ed.), Cambridge University Press, Cambridge.

BALBUS, S. A. & HAWLEY, J. F. 1998 Instability, turbulence, and enhanced transport in accretion disks. *Rev. Mod. Phys.* **70**, 1-53.

BALBUS, S. A. & HAWLEY, J. F. & STONE, J. M. 1996 Nonlinear stability, hydrodynamic turbulence, and transport in disks. *Ap. J.* **467**, 76-86.

BENDER, C. M. & ORSZAG, S. A. 1999 Advanced Mathematical Methods for Scientists and Engineers: Asymptotic Methods and Perturbation Theory. Springer Verlag.

GODON, P. & LIVIO, M. 1999 Vortices in protoplanetary disks, *Ap. J.* **523**, 350-356.

GODON, P. & LIVIO, M. 2000 The formation and role of vortices in protoplanetary disks. *Ap. J.* **537**, 396-404.

KNOBLOCH, E. & SPRUIT, H. C. 1986 Baroclinic waves in a vertically stratified thin disk. *Astron. Astrophys.* **166**, 359-367.

MARCUS, P. S. 1984 Simulation of Taylor-Couette flow. II. Numerical results for wavy-vortex flow with one traveling wave. *J. Fluid Mech.* **146**, 65-113.

MARCUS, P. S. 1993 Jupiter's Great Red Spot and other vortices. *ARAA.* **31**, 523-573.

MARCUS, P. S. & PRESS, W. H. 1977 On Green's Functions for Small Disturbances of Plane Couette Flow. *J. Fluid Mech.* **79**, 525-534.

MARCUS, P. S. & TUCKERMAN, L. S. 1987 Simulation of flow between concentric rotating spheres - Part II - Transitions. *J. Fluid Mech.* **185**, 31-66.

ROGALLO, R. S. 1981 Numerical experiments in homogeneous turbulence. *NASA Tech. Mem.* **81315**, 1-91.

Vortices in protoplanetary disks and the formation of planetesimals

By J. A. Barranco† AND P. S. Marcus‡

The least understood step in the formation of planets is the creation of kilometer-size planetesimals from centimeter-size dust grains. It has been suggested that vortices within the protoplanetary disk may concentrate dust particles at their centers, which may enhance the dust density enough to trigger a gravitational instability to clumping. Our companion paper in this volume discusses the fluid dynamics of 3D vortices in a protoplanetary disk. Here, we present preliminary calculations of the motion of dust grains within such 3D vortices. We confirm that grains are focused toward the centers of vortices, and offer a simple physical picture as to why heavy particles are not centrifuged out.

1. Introduction: The planetesimal formation problem

A protostar forms when a dense region of the interstellar medium collapses due to its self-gravity (the Jeans instability). Due to conservation of angular momentum, matter cannot fall directly onto the central protostar, but spirals in, forming a protoplanetary accretion disk. It is within such dusty protoplanetary disks that protoplanets form. See Shu, Adams, & Lizano (1987) for a general review of star formation, and Lissauer (1993) for a general review of planet formation.

1.1. *Binary agglomeration versus gravitational instability*

In the earliest stages of planetesimal formation, micron-sized dust grains collide and combine to form larger particles – a process called binary agglomeration. However, it is unclear whether this mechanism can efficiently work once particles reach centimeter to meter sizes, since impact cratering and disruption become important. The mechanical and chemical processes involved in grain agglomeration are poorly understood for particles in this size regime. It would seem that two colliding "rocks" are just as likely, if not more likely, to break one another apart as opposed to combining to form a larger one (Weidenschilling 1984, Weidenschilling & Cuzzi 1993). Such slow growth for decimeter particles via binary agglomeration leads to a problem with the timescale associated with the formation of the giant planets. Rocky cores of several Earth masses must be formed in order to gravitationally capture sufficient gas to create the extensive atmospheres of the giant planets. However, this must be done in less than a million years, before the disk gas is dispersed via accretion, photoevaporation, stellar winds, or close stellar encounters (Hollenbach, Yorke, & Johnstone 1999).

An alternative theory is that if the protoplanetary disk is quiescent (that is, not turbulent), the dust grains can settle into a thin sub-layer that might be dense enough to be

† Department of Astronomy, University of California, Berkeley
‡ Department of Mechanical Engineering, University of California, Berkeley

gravitationally unstable to clumping (Safronov 1960, Goldreich & Ward 1973). Whether the disk is turbulent or not is still an unresolved and greatly contested issue. Even if the dust could settle into a thin sub-layer at the midplane, Weidenschilling (1980) has argued that a Kelvin-Helmholtz instability would develop between the dust-dominated layer at the midplane (which orbits at the Keplerian velocity) and the gas-dominated regions above and below the midplane (which orbit at sub-Keplerian velocities due to partial support by the internal pressure gradient). This instability might generate turbulence that would "kick-up" the dust and inhibit the gravitational clumping (Champney, Dobrovolskis, & Cuzzi 1995, Cuzzi, Champney & Dobrovolskis 1993).

1.2. *Vortices in a protoplanetary disk*

Within the past five years, theorists have turned their attention to vortices within protoplanetary disks, and the role they might play in angular momentum transport, as well as the "seeding" of planet formation. Lovelace, *et al.* (1999) have found a linear instability for nonaxisymmetric Rossby waves in thin, nonmagnetized, Keplerian disks. They noted that in the nonlinear limit, such Rossby waves might break and coalesce to form vortices. Bracco, *et al.* (1998), using the incompressible "shallow-water" equations, have shown that long-lived, coherent, anticyclonic vortices form in a Keplerian disk that was initially seeded with a random perturbation field. They noted that smaller vortices merged to form larger vortices, reflecting the inverse cascade of energy from small to large scales that is characteristic of 2D turbulent flows. Godon & Livio (1999a, 1999b, 2000) have also studied the stability and lifetime of vortices in protoplanetary disks, and have shown that anticyclonic vortices can survive in the flow for hundreds of orbits. Barge & Sommeria (1995) and Tanga, *et al.* (1996) have proposed that vortices in a protoplanetary disk can capture dust grains and concentrate them in their centers. This would locally enhance the grain surface density which may trigger gravitational instability and form planetesimals.

The focusing of dust grains into protoplanetary disk vortices may seem quite surprising to those more familiar with laboratory flows in which heavy particles are typically centrifuged out of vortices on a short timescale. The key difference here is gravity. What follows is our physical picture for how vortices focus dust grains into their centers. The base flow in a cool, thin disk (with very weak radial pressure support) is Keplerian: $V_k = \sqrt{GM/r}$, and $\Omega_k = \sqrt{GM/r^3}$, where V_k is the linear (azimuthal) velocity, Ω_k is the angular velocity, r is the cylindrical radius from the center of the disk (where the protostar is) and M is the mass of the central protostar (Frank, King, & Raine, 1995). Physically, the Keplerian velocity is just the usual orbital velocity of any object in a circular orbit about a central gravitational source. The Keplerian shear is anticyclonic and of the same order of magnitude as the Keplerian angular velocity itself: $\sigma_k \equiv r d\Omega_k/dr = -\frac{3}{2}\Omega_k$. Marcus's extensive work with the Great Red Spot and other jovian vortices has shown that in order for a vortex in a shear to be long-lived, the vorticity of the vortex must be of the same sign as, and of at least the same order of magnitude as, the background shear (Marcus 1988, 1989, 1990, 1993, Marcus & Lee, 1994). Consider one such anticyclonic vortex in the disk orbiting the central protostar at a cylindrical radius r_0 from the center of the disk (see Fig. 1 & 2). The flow around the vortex on the side $r > r_0$ opposes the overall rotation of the disk, making the total angular velocity of the gas sub-Keplerian. For $r < r_0$, the anticyclonic vortex enhances the overall rotation of the disk, making the angular velocity super-Keplerian. (We have ignored the fact that the average gas flow in the disk is probably slightly sub-Keplerian due to partial support by an internal pressure gradient – our argument will be basically unchanged.)
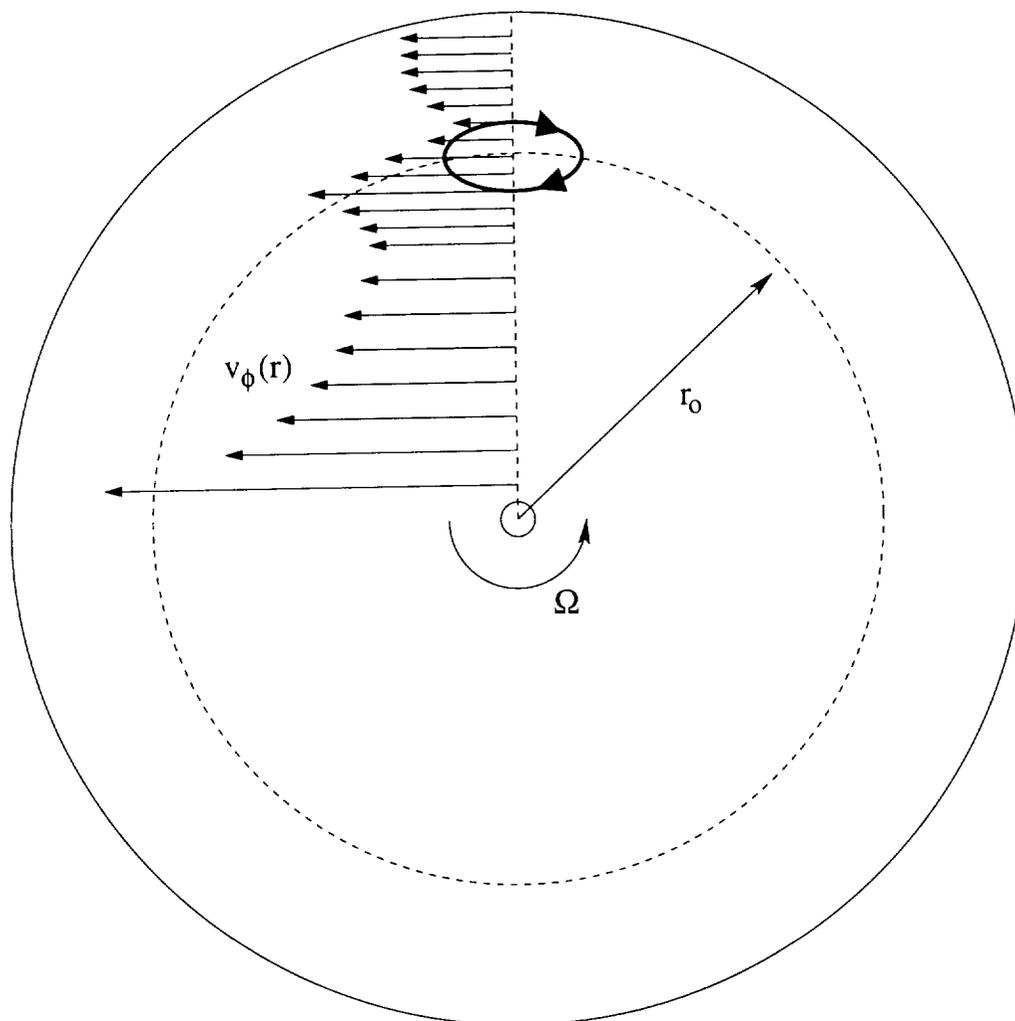
FIGURE 1. Keplerian disk with anticyclone. Anticyclone is located at cylindrical radius r_0 from the center of the disk, where the protostar is located. Arrows indicate the total azimuthal velocity in the inertial frame (mean velocity of the Keplerian disk plus that due to the anticyclone). The mean azimuthal velocity (without vortices) is Keplerian: $V_k = \sqrt{GM/r}$, where M is the mass of the central protostar. Note that the anticyclone increases the azimuthal velocity within the disk for $r < r_0$ and decreases the azimuthal velocity for $r > r_0$.

Let us now consider the motion of dust grains in the disk. If there were no forces acting on the grains other than gravity from the central protostar, the grains would naturally follow circular, Keplerian orbits. However, drag between the grains and the gas can alter such orbits in non-intuitive ways. First, let's consider a grain in a Keplerian orbit with $r > r_0$. When it approaches the vortex (or more precisely, as the vortex approaches the dust grain since the grain is on an outer, slower orbit), the ambient flow will be sub-Keplerian. Since the dust grain is going faster than the gas, any drag by the gas will cause an azimuthal deceleration of the grain. This decrease of the grain's angular momentum does not cause its azimuthal velocity to decrease, but instead, the grain moves inward
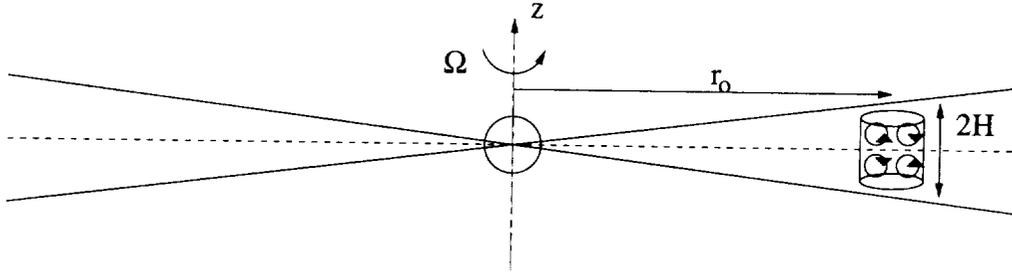
FIGURE 2. Side view of Keplerian disk with anticyclone. The disk is believed to be "flared", with scale height H increasing with radius. The anticyclone fills the disk in the vertical direction.

toward the protostar, which is also the direction towards the vortex center. On the other hand, when a grain orbiting at a radius less than r_0 encounters the anticyclone, the ambient fluid flow is super-Keplerian and drag accelerates the grain azimuthally, pushing it radially outwards and towards the radius of the vortex center. Thus, any type of fluid drag causes grains to be deflected towards the location of the anticyclone. For similar, but slightly more complex reasons, dust grains are also attracted (under some conditions) azimuthally towards the vortex center.

Drag is not the only way that vortices can trap dust grains. We know that the Great Red Spot on Jupiter sustains itself against dissipation by capturing small vortices and "consuming" their vorticity. We propose to study this possibility for vortices in a proto-planetary disk. We suspect that a long-lived vortex will be in a dynamic balance between growth via mergers with smaller vortices and dissipation via Rossby wave radiation. We hypothesize that as a large vortex consumes smaller vortices, Rossby waves will carry away excess angular momentum, keeping the area of the large vortex nearly constant, but that these waves will not drive out dust grains. In other words, the large vortex consumes the dust, but not the area, of the smaller vortices, and hence the grain density would increase.

2. Equations of motion

2.1. $Ro \approx 1$, 3d vortices

The reader is directed to our companion paper in this volume (Barranco, Marcus, & Umurhan, 2000) that discusses the details of finding vortex solutions within a protoplan-etary accretion disk. Here, we would just like to highlight some key assumptions and scalings that make our work significantly different from that of others who are studying vortices in the context of planetesimal formation.

As previously discussed, the Keplerian shear in the disk is anticyclonic and of the same order of magnitude as the Keplerian angular velocity itself: $\sigma_k \equiv rd\Omega_k/dr = -\frac{3}{2}\Omega_k$. Since the vorticity associated with an anticyclone must be of the same order as the background shear if the vortex is to be long-lived, then the relative vorticity associated with the vortex is of the same order as the "planetary vorticity" of the disk itself: $[\omega] \sim \sigma_k \sim \Omega_k$. (Here, we use square brackets to indicate order of magnitude of the bracketed quantity.) This immediately implies that the Rossby number for vortices in a Keplerian shear is of order unity: $Ro = [\omega]/2\Omega_k \sim 1$.

Another key assumption is that long-lived vortices should be subsonic; otherwise shocks would develop that would quickly dissipate the vortex motion. The characteristic velocity
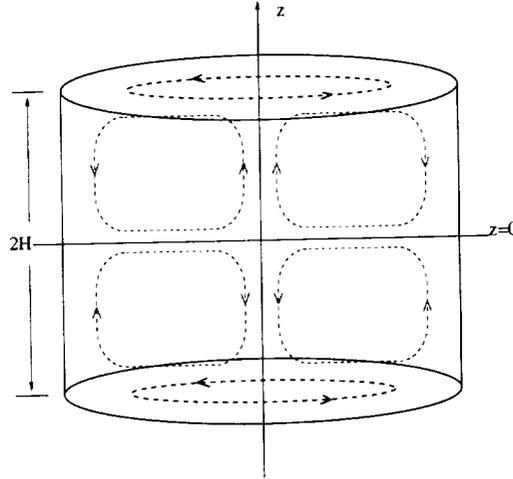
FIGURE 3. Schematic representation of flow within a 3D vortex in a protoplanetary disk. Note that the vertical velocity vanishes in the midplane of the disk.

of the vortex motion is: $[v] \sim (dV_k/dr)L_r \sim (L_r/r)V_k$, where L_r is the characteristic radial extent of a vortex. It can easily be shown that hydrostatic balance in the vertical direction implies $c_s/V_k \sim H/r$, where c_s is the sound speed, and H is the scale height of the disk (Frank, King, & Raine 1985). Hence, $[v] \sim (L_r/H)c_s$, or $L_r/H \sim [v]/c_s$. Thus, in order to have subsonic vortices, their horizontal extent must be less than the thickness of the disk, and the vortices are 3-D, not 2-D.

The three dimensionality, as well as the fact the vortex flow is of order unity Rossby number, has been neglected by all previous researchers (Adams & Watkins 1995, Bracco, *et al.* 1998, Sheehan, *et al.* 1999, Godon & Livio 1999a, 1999b, 2000). The quasi-geostrophic and "shallow-water" sets of equations are not appropriate for the study of vortices in a protoplanetary disk, and one must develop a new set from a rigorous asymptotic analysis. Again, the reader is referred to our companion paper for more details. In this article, we are concerned with the motion of dust particles in and around 3D vortices. Figure 3 shows a schematic of the type of 3D vortices we believe exist in protoplanetary disks. For this preliminary study, we have assumed that the horizontal component of the gas velocity is due to an elliptical patch of constant vorticity embedded within a Keplerian shear flow (Moore & Saffman, 1971). The vertical component of the gas velocity is an approximate analytical fit for the vertical velocity of 3-D vortices in numerical simulations of Taylor-Couette flow.

2.2. *Lagrangian tracking of particles*

Now we consider the motion of individual grains of dust in and around a vortex in a protoplanetary disk. Consider a vortex whose center is located at a cylindrical radius r_0 from the protostar. Henceforth, we work in a rotating frame so that the center of the vortex is stationary. The angular velocity of the rotating frame, with respect to the inertial frame of "fixed stars", is $\Omega_0 = \sqrt{GM/r_0^3}$. We will also "Cartesianize" the domain of interest: let x be the (negative) azimuthal direction $(-\phi \to x)$, y be the radial direction $(r = r_0 + y$, so that $y = 0$ at center of vortex), and z be the height above the midplane. The forces acting on a grain are gravity from the central protostar, Coriolis and centrifugal forces, and frictional drag due to the relative velocity between the gas

and dust particles. The equations of motion for the grains are:

$$\ddot{x} = 2\Omega_0 \dot{y} - \frac{1}{t_s}(\dot{x} - V_x^{gas}), \tag{2.1}$$

$$\ddot{y} = -\frac{GM}{(r_0 + y)^2} + \Omega_0^2(r_0 + y) - 2\Omega_0\dot{x} - \frac{1}{t_s}(\dot{y} - V_y^{gas}), \tag{2.2}$$

$$\ddot{z} = -\frac{GMz}{(r_0 + y)^3} - \frac{1}{t_s}(\dot{z} - V_y^{gas}), \tag{2.3}$$

where $V_{x,y,z}^{gas}$ is the velocity of the gas in the rotating frame, and t_s is the stopping time, i.e., is the e-folding time for the particle to come to rest.

The exact form for the stopping time depends on the size and shape of the dust grains as well as on the physical conditions within the protoplanetary nebula. The Reynolds number for the flow around a grain is of order unity: $Re = [v]d/\nu \sim 1$, where we have taken the characteristic velocity in a vortex to be bounded by the sound speed $[v] \sim c_s \sim$ 1 km/s, the diameter of a grain is of order $d \sim 10$ cm, and the kinematic viscosity for the gas is of order $\nu \sim 10^6$ cm^2/s. In fact, this is an overestimate for the the Reynolds number since the velocity we used in computing the Reynolds number should actually be the *differential* velocity between the grain and the gas, which is typically much less than the velocity of the gas itself. Thus, for this preliminary study, we assume that the flow around grains is approximated by Stokes flow:

$$t_s = \frac{1}{36}\frac{\rho_{grain}}{\rho_{gas}}\frac{d_{grain}^2}{\nu} \sim 10^4 \text{s} \sim 0.001 \times T_{orb}, \tag{2.4}$$

where ρ_{grain} is the density of an individual dust grain, of order a few g/cm^3, $\rho_{gas} \sim$ 10^{-9} g/cm^3 is the density of gas in the disk, d_{grain} is the diameter of the dust grains, of order a few decimeters, and T_{orb} is the orbital period of the vortex around the protostar, of order a year at 1 AU (one astronomical unit, equal to the distance between the Earth and the Sun, 1.5×10^{13} cm). It turns out that the mean free path of the gas molecules within the nebula is of the same order as the size of the grains, so the Stokes flow assumption may not be an entirely valid one. In this regime, the interaction between the grains and the gas particles is a problem of kinetic theory, not fluid or continuum mechanics. However, we don't expect that the qualitative behavior of the motion of the dust grains will depend strongly on the exact nature of the drag. This will be explored in more detail in future work.

3. Preliminary results

3.1. *The settling of particles in the midplane*

Figure 4 shows the 3D evolution of an ensemble of randomly placed grains in and around a 3D vortex in a protoplanetary disk. For clarity, the vortex flow itself is not shown. The vortex center is located at a distance 1 AU away from the protostar. Regarding the scale, one unit on the axes corresponds to approximately 0.25 AU. Note how quickly grains settle into the midplane of the disk. The timescale for the settling is a few stopping times. This was expected as we have not yet included any turbulence within the disk. Although the vortex does have a vertical component of velocity, it is zero within the midplane. Most particles have settled in the midplane long before they encounter the vortex, and thus are not excited by the vertical velocity of the vortex. We expect these results to be fundamentally altered when we explicitly include the effects of turbulence.
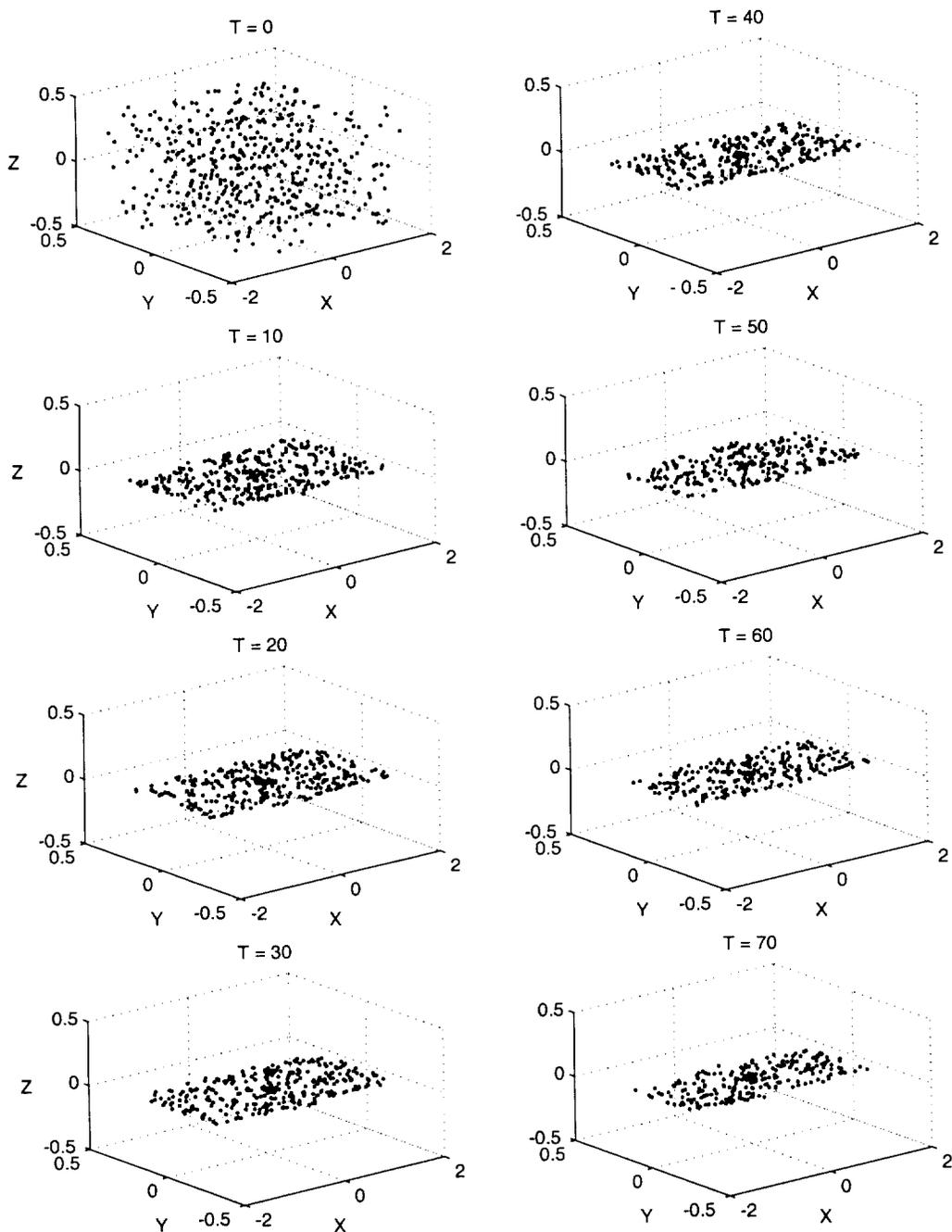
FIGURE 4. 3D plots of the evolution of an ensemble of grains in and around a vortex in a protoplanetary disk. For clarity, the vortex flow is not shown. The center of the vortex is located 1 AU from the protostar. One unit on the axes corresponds to approximately 0.25 AU. The x-direction is the azimuthal direction, the y-direction is the radial direction, and the z-direction is the height above the midplane. Timestep between each snapshot is 10 orbital periods.
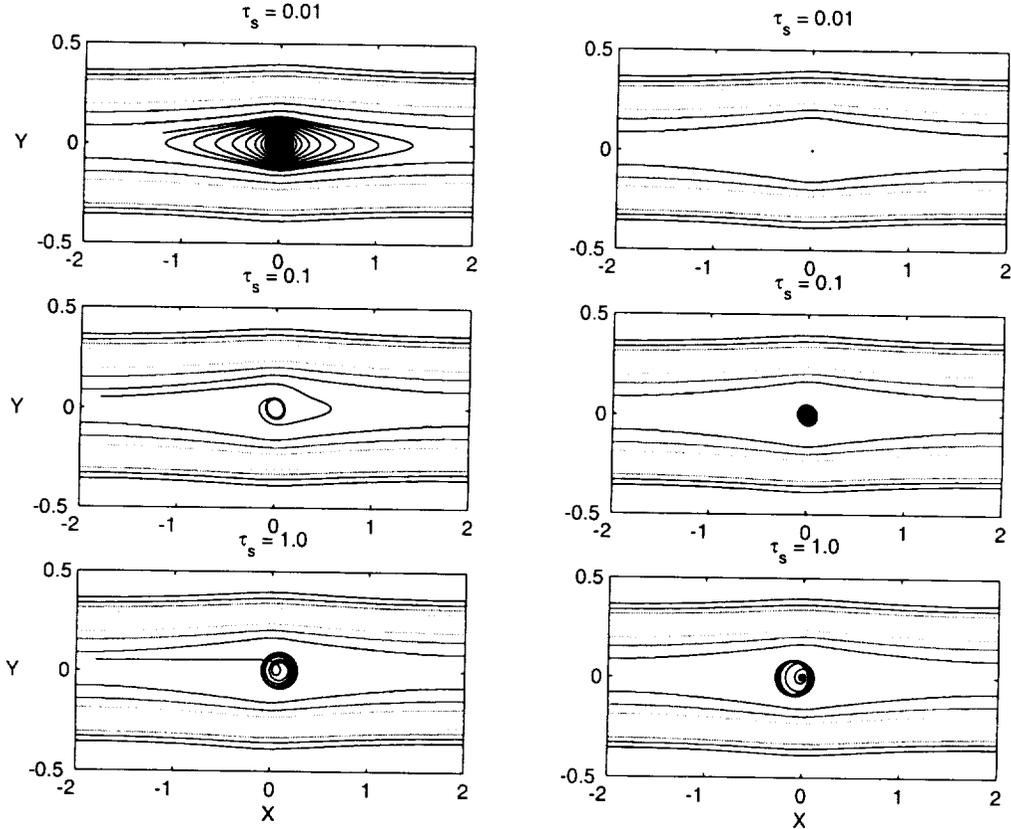
FIGURE 5. Trajectories (projected into the midplane) of individual grains. The gray lines of various shades indicate the streamlines of the gas flow around the vortex. The vortex itself is not shown for clarity. Solid black lines are the trajectories of individual grains. $\tau_s \equiv t_s/T_{orb}$ is the stopping time normalized by the orbital period. From the top down, $\tau_s = 0.01, 0.1, 1.0$. First column shows trajectories of grains that were started outside the vortex on Keplerian orbits. Second column shows trajectories of grains started at the center of the vortex.

Turbulence will "kick up" the grains, preventing them from settling into a thin layer about the midplane. Particles that encounter the vortex out of the midplane will be excited by the vortex's vertical velocity, further stirring up the particle motion.

3.2. *The spiraling of particles to the centers of vortices*

Figure 5 shows the trajectories (projected into the midplane) of individual grains. The vortex location and scale are the same as that described in the previous section. Here, we vary the stopping time, now normalized by the orbital period (1 year at 1 AU for a solar mass protostar): $\tau_s \equiv t_s/T_{orb}$. A shorter stopping time corresponds to smaller particles, which quickly react to the gas flow. We expect that the trajectories of these smaller particles will closely follow the streamlines of the gas. Longer stopping times correspond to larger particles, which, because of their inertia, take longer to adjust to the gas flow.

In the first column of figures in Fig. 5, the grains start outside the vortex on Keplerian orbits around the protostar. Note that the lighter particle immediately reacts to the presence of the vortex, closely following the closed streamlines, yet slowly spiraling into
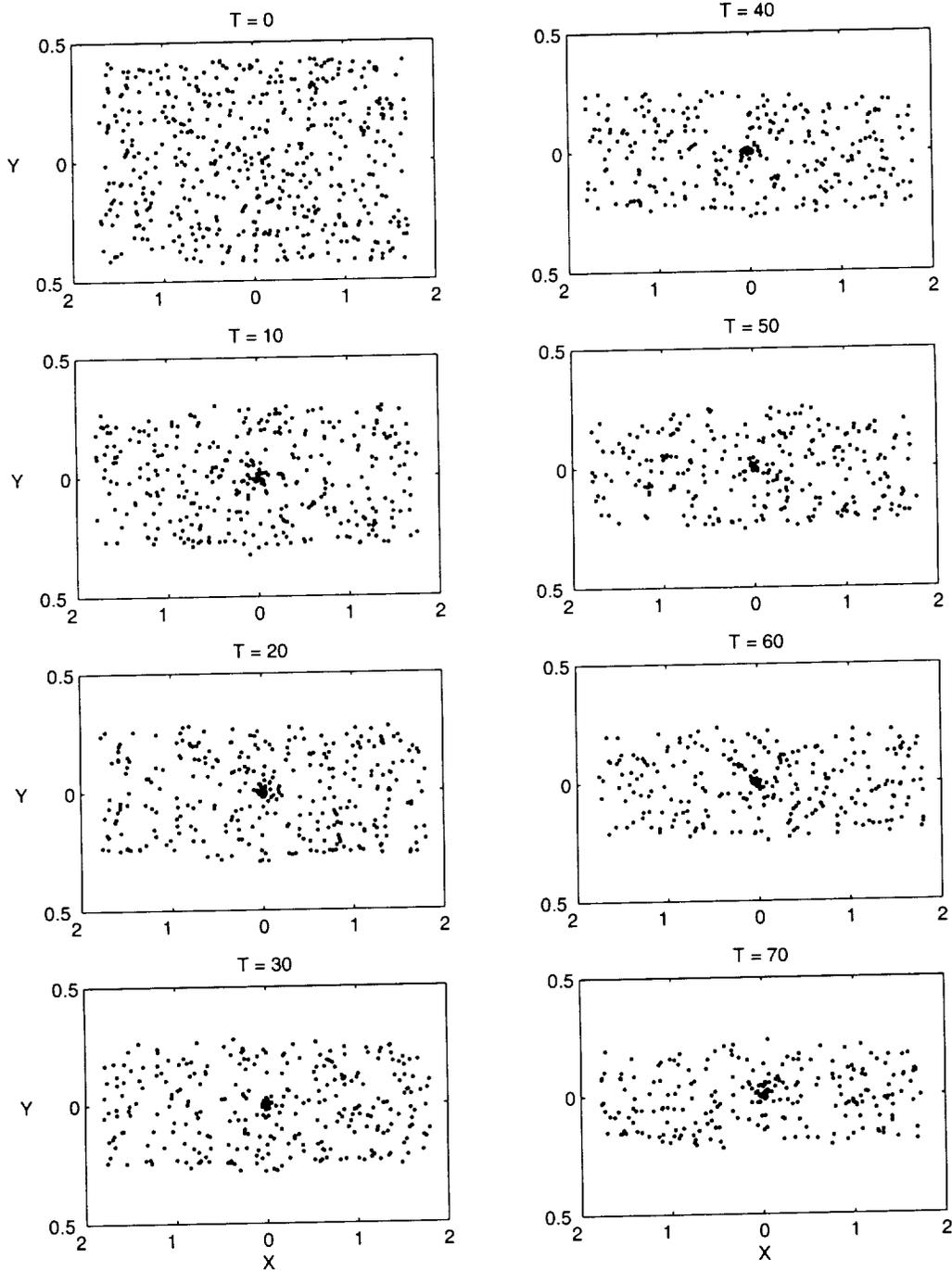
FIGURE 6. Same as Fig. 4, but projected into the midplane of the disk. For clarity, the vortex flow is not shown. The center of the vortex is located 1 AU from the protostar. One unit on the axes corresponds to approximately 0.25 AU. The x-direction is the azimuthal direction, the y-direction is the radial direction, and the z-direction is the height above the midplane. Timestep between each snapshot is 10 orbital periods.
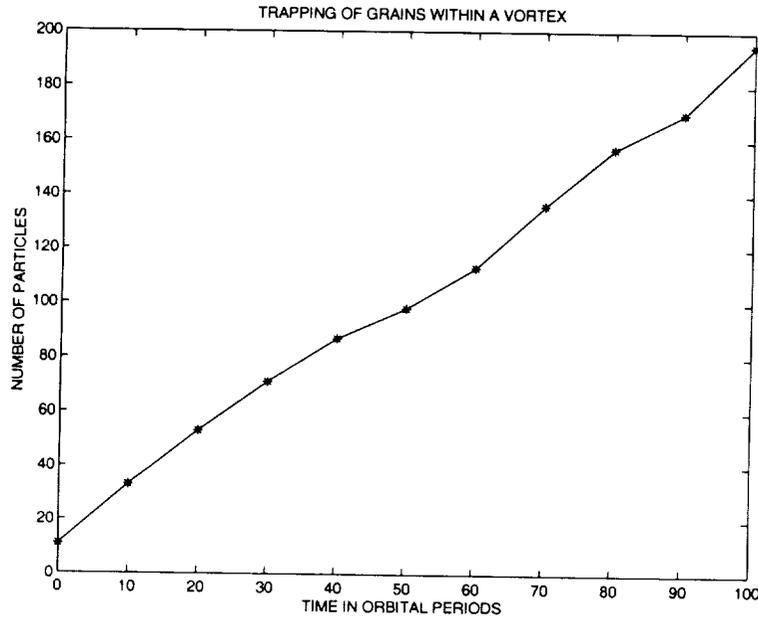
FIGURE 7. Number of particles trapped within vortex as a function of time. The vortex boundary is defined by the boundary of the patch of constant vorticity.

the center. The heavier particles follow their Keplerian orbits, not reacting to the vortex until they get very close.

Also notice that whereas the lightest particle eventually spirals in very deep into the center of the vortex, the heavier particles settle down onto orbits around the center of the vortex. The longer the stopping time, the larger the radius of the final orbit. We wanted to test this further by starting the grains an infinitesimal distance away from the center of the vortex (see the second column of Fig 5). The lightest particle remains at the center of the vortex; this is a stable point. The heavier particles are seen to spiral out, eventually settling into orbits around the vortex center. In fact, the final orbit for these particles is the same whether they start outside or inside the vortex. In the future, we would like to further explore the exact nature of these "attractors".

Figure 6 shows the 2D projection into midplane of the same data shown in Fig. 4. One can start to see the concentration of grains within the vortex. Figure 7 is a much clearer illustration of this phenomenon. The number of grains within the vortex boundary (i.e. the boundary of the elliptical patch of constant vorticity) is plotted as a function of time (expressed in orbital periods). We observe that the density of grains inside the vortex increases by a factor of roughly 20 in 100 orbital periods, consistent with the previous results of Barge & Sommeria (1995) and Tanga, *et al.* (1996).

4. Future work

There are many unresolved issues regarding planetesimal formation in vortices, specifically with regard to turbulence in the protoplanetary disk. Until now, most have focused only on whether 2D *laminar* vortices can capture dust in a 2D *laminar* disk. Even if a vortex can capture dust grains, it has not yet been demonstrated that this triggers gravitational instability, given that disk turbulence prevents the dust grains from settling. All

previous research on disk vortices has been 2D, and therefore unable to even consider the vertical settling of dust grains within a vortex. Our research will focus on 3D vortices, and we will be well-positioned to tackle these issues. Specifically, we want to examine whether vortices laminarize the flow in their interiors (the way laboratory vortices do), shielding the captured dust from the turbulence and allowing the grains to settle into a dense enough layer that becomes gravitationally unstable. We also want to examine the effect of the vertical velocity within the vortex on the accumulation of grains.

REFERENCES

ADAMS, F. C. & WATKINS, R. 1995 Vortices in circumstellar disks. *ApJ.* **451**, 314-327.

BARGE, P. & SOMMERIA, J. 1995 Did planet formation begin inside persistent gaseous vortices? *A&A.* **295**, L1-4.

BRACCO, A., PROVENZALE, A., SPIEGEL, E. A. & YECKO, P. 1998 Spotted disks. In *Proceedings of the Conference on Quasars and Accretion Disks* (M. Abramowicz, Ed.), Cambridge University Press, Cambridge.

CHAMPNEY, J. M., DOBROVOLSKIS, A. R. & CUZZI, J. N. 1995 A numerical turbulence model for multiphase flows in the protoplanetary nebula. *Phys. Fluids.* **7**, 1703-1711.

CUZZI, J. N., DOBROVOLSKIS, A. R. & CHAMPNEY, J. M. 1993 Particle-gas dynamics in the midplane of a protoplanetary nebula. *Icarus.* **106**, 102-134.

FRANK, J., KING, A. & RAINE, D. 1985 *Accretion Power in Astrophysics.* Cambridge University Press, Cambridge.

GODON, P. & LIVIO, M. 1999 On the nonlinear hydrodynamic stability of thin Keplerian disks. *ApJ.* **521**, 319-327.

GODON, P. & LIVIO, M. 1999 Vortices in protoplanetary disks. *ApJ.* **523**, 350-356.

GODON, P. & LIVIO, M. 2000 The formation and role of vortices in protoplanetary disks. *ApJ*, **537**, 396-404.

GOLDREICH, P. & WARD, W. R. 1973 The formation of planetesimals. *ApJ.* **183**, 1051-1061.

HOLLENBACH, D., YORKE, H. W. & JOHNSTONE, D. 2000 Disk dispersal around young stars. In *Protostars and Planets IV*, in press.

LISSAUER, J. J. 1993 Planet formation. *ARAA.* **31**, 129-174.

LOVELACE, R. V. E., LI, H., COLGATE, S. A. & NELSON, A. F. 1999 Rossby wave instability of Keplerian accretion disks. *ApJ.* **513**, 805-810.

MARCUS, P. S. 1988 Numerical simulations of the Great Red Spot of Jupiter. *Nature.* **331**, 693-696.

MARCUS, P. S. 1989 Vortex dynamics. *Physics Today.* S40-41.

MARCUS, P. S. 1990 Vortex dynamics in a shearing zonal flow. *J. Fluid Mech.* **215**, 393-430.

MARCUS, P. S. 1993 Jupiter's Great Red Spot and other vortices. *ARAA.* **31**, 523-573.

MARCUS, P. S. & LEE, C. 1994 Jupiter's Great Red Spot and zonal winds as a self-consistent one-layer quasi-geostrophic flow. *Chaos.* 4, 269-288.

MOORE, D. W. & SAFFMAN, P. G. 1971 Structure of a line vortex in an imposed strain. In *Aircraft Wake Turbulence and its Detection.* (J. Olsen, A. Goldberg, & N. Rogers, Eds.), Plenum, New York.

SAFRANOV, V. S. 1960 *Ann. Astrophys.* **23**, 901-904.

SHEEHAN, D. P., DAVIS, S. S., CUZZI, J. N. & ESTBERG, G. N. 1999 Rossby wave propagation and generation in the protoplanetary nebula. *Icarus.* **142**, 238-248.

SHU, F. H., ADAMS, F. C. & LIZANO, S. 1987 Star formation in molecular clouds: Observation and theory. *ARAA.* **25**, 23-81.

TANGA, P., BABIANO, A., DUBRULLE, B. & PROVENZALE, A. 1996 Forming planetesimals in vortices. *Icarus.* **121**, 158-170.

WEIDENSCHILLING, S. J. 1980 Dust to planetesimals: Settling and coagulation in the solar nebula. *Icarus.* **44**, 172-189.

WEIDENSCHILLING, S. J. 1984 Evolution of grains in a turbulent solar nebula. *Icarus.* **60**, 555-567.

WEIDENSCHILLING, S. J. & CUZZI, J. N. 1993 Formation of planetesimals in the solar nebula. In *Protostars and Planets III* (E. H. Levy and J.I. Lunine, Eds.), University of Arizona Press, Tucson.

Particle distributions in the flow over a wavy wall

By Bendiks Jan Boersma†

In this paper we will present the results of direct numerical simulation (DNS) of the flow over a small amplitude wavy wall. The evolution in space and time of particles are released in this flow will be examined. It will be shown that small waves on the channel bottom can generate large longitudinal vortices similar to Langmuir vortices that are observed in flows with waves at the free-surface. The simulation results show that the concentration of the particles is maximal on the downstream side of the wave crest.

1. Introduction

Water flow over a rippled bottom is an important flow geometry in civil engineering applications. Knowledge of flow statistics and sediment transport in such a geometry is useful for the maintenance of coastal structures, harbors, and rivers. Moreover, pollutants such as heavy metals and pesticides tend to chemically bind to the sediment particles. Ripples on river beds have in general a complicated three-dimensional shape. In this paper we will study a slightly simplified problem, namely the sediment transport over a smooth two-dimensional nearly sinusoidal bottom with a small amplitude.

In the recent literature, various experimental and theoretical/numerical results are reported for such a geometry (see for instance De Angelis *et al.* (1997), Cherukat *et al.* (1998), and Gong *et al.* (1996)). De Angelis *et al.* (1997) and Cherukat *et al.* (1998) report results obtained from DNS. The amplitude of the wave in these simulations is relatively large. which results in a separated flow downstream of the wave crest. Gong *et al.* (1996) report wind tunnel experiments for the flow over a wavy surface with a relative small amplitude. They shown that in a flow over a wavy wall without flow separation, large longitudinal vortices similar to Langmuir vortices (Leibovich (1983)) are generated. This observation is supported by a theoretical analysis performed by Philips *et al.* (1996).

In this study we will use DNS to simulate the flow over a low amplitude wavy wall. The amplitude of the waves on the channel bottom in the DNS is comparable to those used in the wind tunnel experiments of Gong *et al.* (1996). The Reynolds number based on channel height and bulk velocity is $3,500$. The wave length of the waves on the channel bottom is equal to the channel height, and the amplitude of the waves is 5% of the wavelength (or channel height). The flow solver used for the DNS is very similar to the one used by Van Haarlem *et al.* (1998). To study sediment transport, small spherical particles are placed in the flow and their motion is tracked in space and time.

In §2, we will give the governing equations and we will briefly discuss the solution techniques. In §3, we shortly discuss the equation for the sediment particles. Finally, in §4 we will present results both for the flow and sediment particles. In §5 we will give some conclusions.

† Delft University of Technology, Laboratory for Aero- and Hydrodynamics, The Netherlands
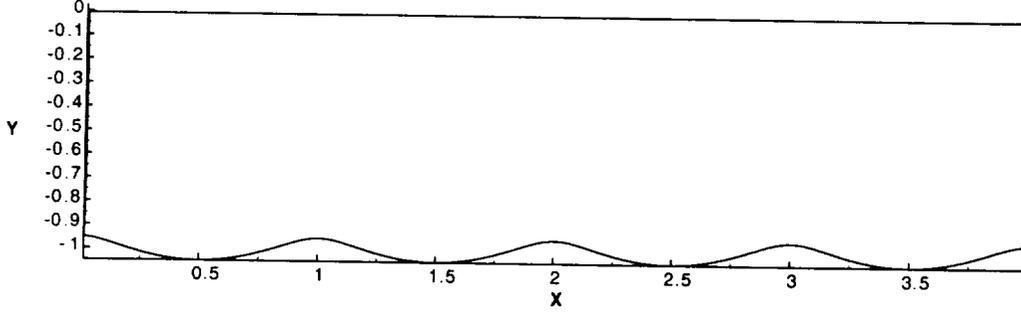
FIGURE 1. The computational domain.

2. Governing equations

In this section we will give the governing equations for the flow over a wavy wall and briefly discuss the solution technique which has been used to solve these equations.

The physical domain is shown in Fig. 1. The wave on the bottom is nearly sinusoidal. This is for computational reasons only. A fully sinusoidal bottom in combination with a flat surface can not be calculated using an orthogonal grid. From a computational point of view, an orthogonal grid is preferable over an non-orthogonal grid. With help of the following two-dimensional orthogonal coordinate transformation, the physical domain is mapped onto a rectangular computational domain.

$$x = -x' + A\sinh(-kz')\sin(kx'), \tag{2.1}$$

$$y = y', \tag{2.2}$$

$$z = -z' - A\cosh(-kz')\cos(kx'), \tag{2.3}$$

where x, y, and z denote the coordinates in the physical domain (Fig. 1) and x', y', and z' denote the coordinates in the rectangular (computational) domain, with A the amplitude and k the wave number. With help of vector algebra (see for instance Morse and Feshback (1953)), the Navier-Stokes equations in the transformed computational domain can be written as (we have dropped the primes for convenience):

$$\frac{\partial u}{\partial t} + \frac{1}{h^2}\left(\frac{\partial huu}{\partial x} + \frac{\partial h^2 uv}{\partial y} + \frac{\partial huw}{\partial z}\right) + \frac{w}{h^2}\left(u\frac{\partial h}{\partial z} - w\frac{\partial h}{\partial x}\right) =$$
$$-\frac{1}{\rho h}\frac{\partial P}{\partial x} + \frac{1}{h^2}\left(\frac{\partial h\tau_{xx}}{\partial x} + \frac{\partial h^2\tau_{xy}}{\partial y} + \frac{\partial h\tau_{xz}}{\partial z}\right) + \frac{\tau_{xz}}{h^2}\frac{\partial h}{\partial z} - \frac{\tau_{zz}}{h^2}\frac{\partial h}{\partial x} + F_x, \quad (2.4)$$

$$\frac{\partial v}{\partial t} + \frac{1}{h^2}\left(\frac{\partial huv}{\partial x} + \frac{\partial h^2 vv}{\partial y} + \frac{\partial hvw}{\partial z}\right) =$$
$$-\frac{1}{\rho}\frac{\partial P}{\partial y} + \frac{1}{h^2}\left(\frac{\partial h\tau_{xy}}{\partial x} + \frac{\partial h^2\tau_{yy}}{\partial y} + \frac{\partial h\tau_{yz}}{\partial z}\right) + F_y, \quad\quad (2.5)$$

$$\frac{\partial w}{\partial t} + \frac{1}{h^2}\left(\frac{\partial huw}{\partial x} + \frac{\partial h^2 vw}{\partial y} + \frac{\partial hw^2}{\partial z}\right) + \frac{u}{h^2}\left(w\frac{\partial h}{\partial x} - u\frac{\partial h}{\partial z}\right) =$$
$$-\frac{1}{\rho h}\frac{\partial P}{\partial z} + \frac{1}{h^2}\left(\frac{\partial h\tau_{xz}}{\partial x} + \frac{\partial h^2\tau_{yz}}{\partial y} + \frac{\partial h\tau_{zz}}{\partial z}\right) + \frac{\tau_{xz}}{h^2}\frac{\partial h}{\partial x} - \frac{\tau_{xx}}{h^2}\frac{\partial h}{\partial z} + F_z, \quad (2.6)$$

with the geometric scale factor

$$h = \sqrt{1 - 2Ak\sinh(kz)\cos(kx) - A^2k^2\cos^2(kx) + A^2k^2\cosh^2(kz)},$$

and u, v, w the velocity components in the x, y, and z direction respectively, with p the pressure and τ_{ij} the Newtonian stress term. The components of τ_{ij} are given as follows:

$$\tau_{xx} = 2\nu\left[\frac{\partial}{\partial x}\left(\frac{u}{h}\right) + \frac{u}{h^2}\frac{\partial h}{\partial x} + \frac{w}{h^2}\frac{\partial h}{\partial z}\right],$$

$$\tau_{xy} = \nu\left[\frac{\partial u}{\partial y} + \frac{1}{h}\frac{\partial v}{\partial x}\right],$$

$$\tau_{xz} = \nu\left[\frac{\partial}{\partial z}\left(\frac{u}{h}\right) + \frac{\partial}{\partial x}\left(\frac{w}{h}\right)\right],$$

$$\tau_{yy} = 2\nu\left[\frac{\partial v}{\partial y}\right],$$

$$\tau_{yz} = \nu\left[\frac{1}{h}\frac{\partial v}{\partial z} + \frac{\partial w}{\partial y}\right],$$

$$\tau_{zz} = 2\nu\left[\frac{\partial}{\partial z}\left(\frac{w}{h}\right)\frac{u}{h^2}\frac{\partial h}{\partial x} + \frac{w}{h^2}\frac{\partial h}{\partial z}\right]. \tag{2.7}$$

In which ν is the kinematic viscosity of the fluid. The equations given above are non-dimensionalized with the mean friction velocity U_* at the channel bottom and the channel height H. In the streamwise and spanwise direction, periodic boundary conditions are used. At the channel bottom no-slip boundary conditions are used, and at the surface free-slip conditions are used. The normal component of the velocity is also set to zero at the free surface. The flow in the channel is driven by a constant pressure gradient $(2\rho U_*^2/H)$ in the x-direction. The spatial derivatives in Eqs. (2.4)-(2.7) are integrated with help of a fully central second-order finite-volume method on a staggered grid. The time integration of Eq. (2.4)-(2.6) has been carried out with a second-order Adams-Bashforth method. The pressure-correction method is used to satisfy the incompressibility constraint.

3. Particle equation

The motion of a small spherical particle, under the assumption that the lift force, Basset history force, added mass force, and pressure gradient force are small (see Maxey and Riley (1983)), can be described by the following equation (Maxey and Riley (1983))

$$\frac{4}{3}\pi\rho_p a^3\frac{d\mathbf{u}_p}{dt} = 6\pi\mu(\mathbf{u}_f - \mathbf{u}_p) + \frac{4}{3}\pi(\rho_p - \rho_f)a^3 g,$$

$$\frac{d\mathbf{x}_p}{dt} = \mathbf{u}_p, \tag{3.1}$$

where $\mathbf{u}_p$ is the particle velocity, $\mathbf{x}_p$ the particle position, a the particle radius, $\mathbf{u}_f$ the fluid velocity, ρ_p the particle density, ρ_f the fluid density, and g the gravity. The first term on the right-hand side of Eq. (3.1) denotes the Stokes drag and the second term the gravity on the particle. Equation (3.1) can be rewritten as

$$\frac{d\mathbf{u}_p}{dt} = \frac{1}{\tau}(\mathbf{u}_f - \mathbf{u}_p) + \frac{\rho_p - \rho_f}{\rho_p}g,$$

$$\frac{d\mathbf{x}_p}{dt} = \mathbf{u}_p, \tag{3.2}$$

B. J. Boersma
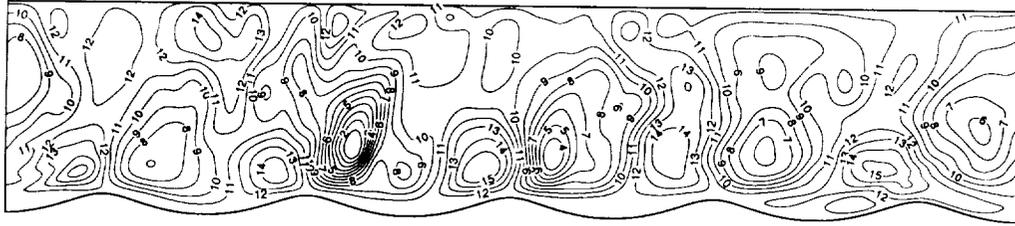
FIGURE 2. The wall normal velocity in the wavy channel. (The flow is going from left to right.) W ranges from -2.50 (Level 1) to 0.81 (Level 15).
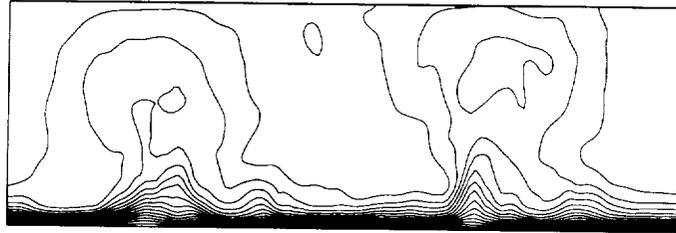
FIGURE 3. The streamwise velocity u in the cross flow plane.

where τ is the particle relaxation (or response) time given by

$$\tau = \frac{2\rho_f a^2}{9\rho_p \nu}. \tag{3.3}$$

Typical radii of sand grains are 10^{-5} to 10^{-3} meters, and typical densities are $3000 kg/m^3$, which results in $\tau \approx 10^{-2}$ and $(\rho_p - \rho_f)/\rho_p \approx 0.7$. The time integration of Eq. (3.2) is performed with the same method and time step as the Navier-Stokes equations. The particle velocities at the particle positions $\mathbf{x}_p$ are obtained with help of a quadratic interpolation using 27 neighboring velocity points. Periodic boundary conditions for the particles are used the stream- and spanwise directions. When a particle reaches the bottom of the channel, the sign of the vertical velocity is changed, i.e. the particle bounces back. When a particle reaches the surface of the channel, its vertical velocity component is set to zero and the gravity force will pull it back into the flow.

4. Results

In this section we will present some results obtained from the DNS. All simulations have been performed on a computational grid with 256 points in the streamwise direction, 128 points in the spanwise direction, and 96 points in the wall normal direction (all uniformly spaced). The Reynolds number based on U_* was equal to 250. The grid size in the wall normal direction is this $250/96 \approx 2.5Y^+$. The domain size in the streamwise and spanwise direction was $5H$ and $3H$ respectively, which corresponds to a grid spacing of $5Y^+$ in the streamwise direction and $6Y^+$ in the spanwise direction. This grid should be fine enough
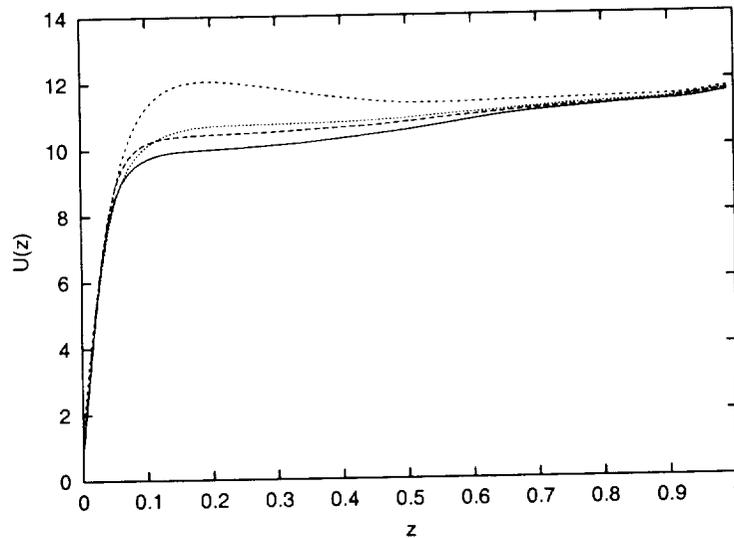
FIGURE 4. The mean velocity profile as a function of the wall normal direction, at various positions along the wave. Wave trough: ———— and — — — ; Wave crest: ---- and ········· .
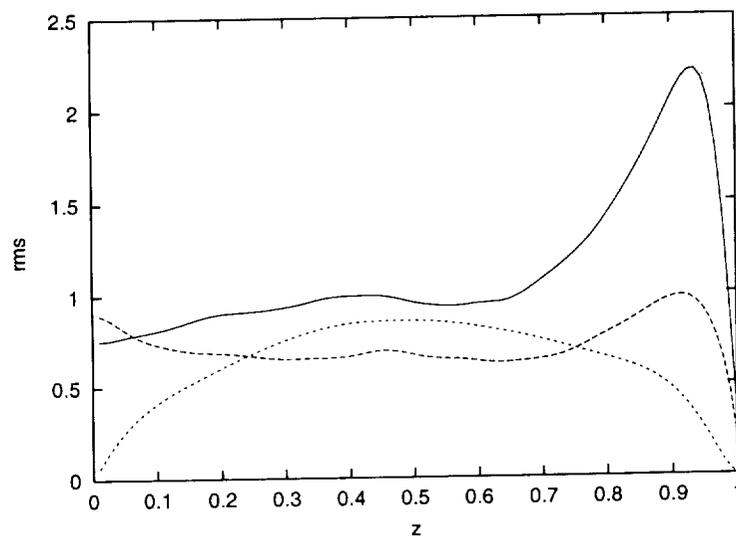
FIGURE 5. The streamwise (————), spanwise (----), and wall normal (·········) rms profiles averaged over the streamwise and spanwise direction.

to capture all important scales of motion. The statistics we will present in this section are calculated over 20 independent samples, each separated by $0.1H/U_*$ in time.

Figure 2 shows an instantaneous plot of the vertical velocity in the wavy channel. Just upstream of the wave crest we observe a rather large positive (upward) velocity. Behind the wave crest the velocity is negative.

In Figure 3, we show an isosurface plot of the averaged axial velocity in the cross flow plane. The two large structures visible in this figure are due to a Langmuir type circulation, Leibovich (1983), which is induced by the waves on the channel bottom. Numerical experiments with smaller and larger spanwise domains also show this phenomena. A de-
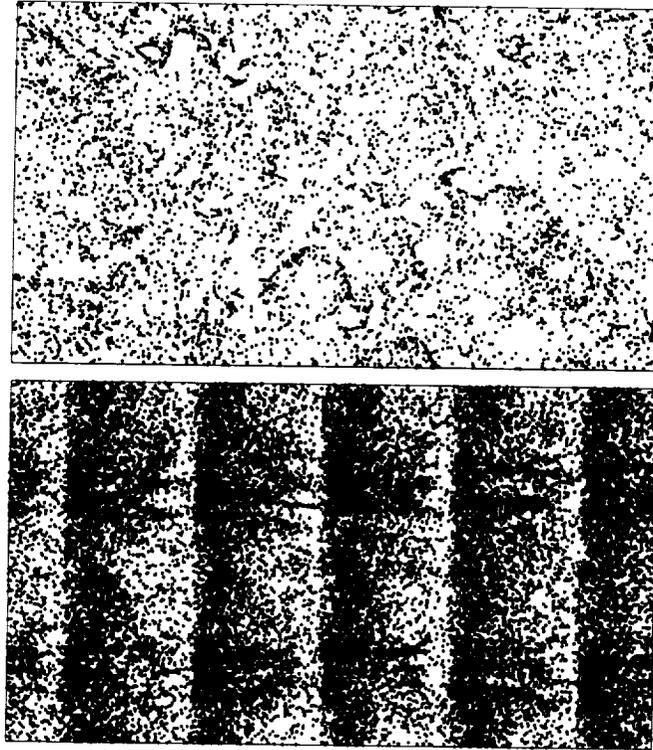
FIGURE 6. An instantaneous particle distribution in the top and bottom plane of the wavy channel (bin width = $H/40$).
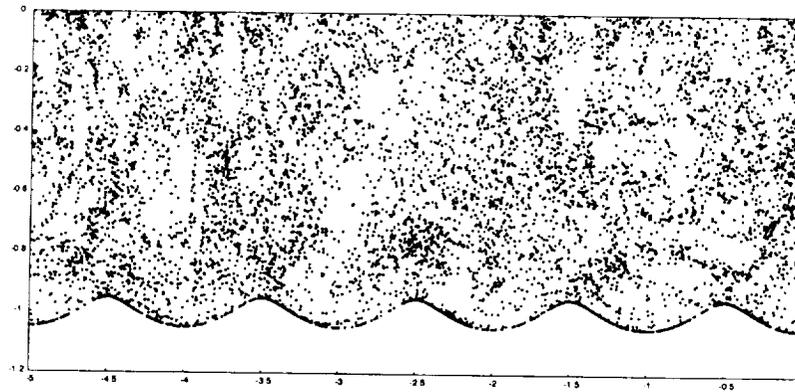
FIGURE 7. The particle distribution in an $x - z$ plane.

tailed theoretical explanation of the physical mechanism behind this phenomena can be found in Philips *et al.* (1996) and experimental verification in Gong *et al.* (1996).

The axial velocity profile is shown in Fig. 4 at various positions along the wavy channel. Our simulation does not show flow separation (or back flow) as has been reported by other researchers, Cherukat *et al.* (1998) and De Angelis *et al.* (1997), for channels with slightly larger wave amplitudes. The analysis of Philips *et al.* (1996) shows that it is unlikely to observe Langmuir type circulation if flow separation occurs. This is probably
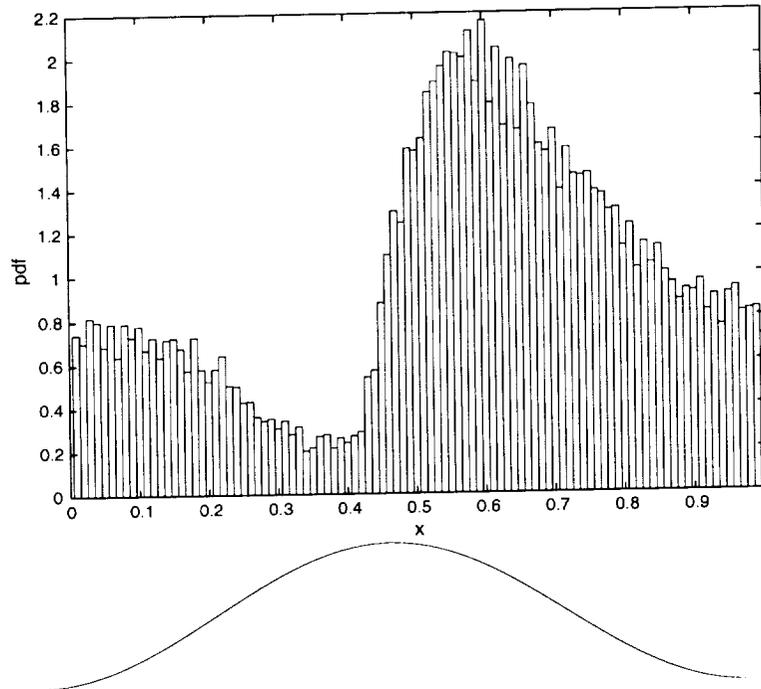
FIGURE 8. The particle concentration along the wave (the flow is going from left to right).

the reason why this phenomena is not observed by Cherukat *et al.* (1998) and De Angelis *et al.* (1997).

To finish the presentation of the flow statistics, we show in Fig. 5 the axial, spanwise, and wall normal root mean squire profiles averaged over the streamwise and spanwise direction in the wavy channel. These rms-profiles compare reasonable well with the profiles reported by Van Haarlem *et al.* (1998) and Pan & Banerjee (1995) for flat channels. The values of the rms maxima in the wavy channel are slightly lower than in the standard channel.

4.1. *Particle statistics*

Once the flow has reached a statistical steady state, half a million particles are randomly distributed over the channel. The motion of these particles is governed by Eq. (3.2). The simulations are continued for $3H/U_*$ to reach a statistical steady state for the particles. Statistics are then gathered over another additional $2H/U_*$. For the statistical analysis, the channel is in all three directions divided into 80 equally spaced bins over which particle concentrations are computed.

An instantaneous particle distribution is shown at the top $(-H/80 < z < 0)$ and at the bottom of the channel $(-1 < z < 79H/80)$ in Fig. 6. The two long streaky structures at the channel bottom are probably caused by the longitudinal vortices generated by the wavy bottom (see also Fig. 3).

Figure 7 (top) shows the instantaneous particle distribution in a $x - z$ plane. Most particles are laying on the bottom of the channel or are very close to it; this is, of course, due to the gravity force. Just above the wave crest, we also observe slightly higher particle concentrations that are probably caused by strong shear stress fluctuations at the channel wall upstream of the wave crest which will shoot particles back into the flow.
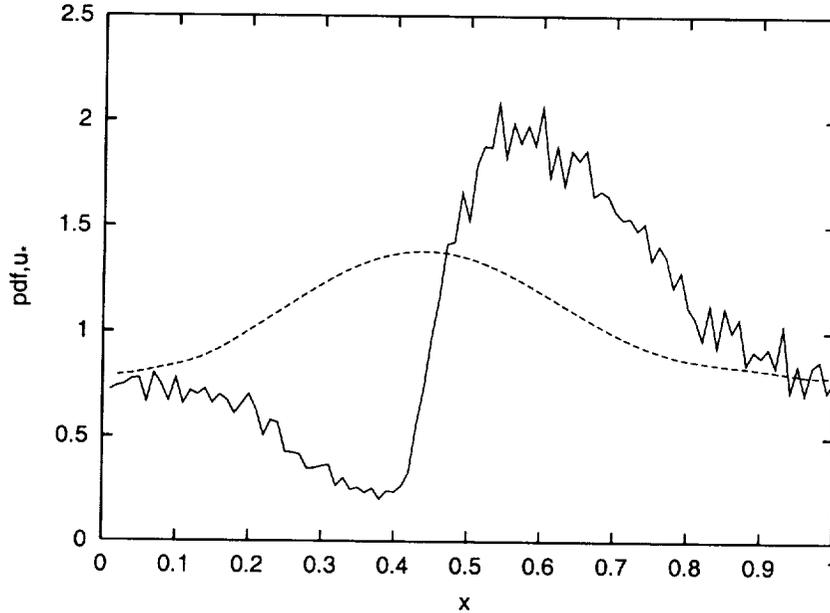
FIGURE 9. The particle concentration (———) and the local wall shear stress (— — — —) along the wave wall.

The mean concentration along the wave is shown in Fig. 6. The particle concentration has its maximum just behind the wave crest and has its minimum just before the wave crest. The sediment concentration is often modeled (see Blondeaux (1990)) with a relation of the form,

$$C_p = \alpha u_*^\beta \qquad (4.1)$$

where C_p is the sediment concentration and α and β are empirical constants. In Fig. 9, we show a plot of u_* and the particle concentration (see also Fig. 5) as a function of the axial coordinate. Clearly the particle concentration is minimal at the location where u_* is maximal. The profile of the wall shear stress is nearly symmetric, and if it is raised to some power β, it will not describe the particle concentration shown in Fig. 8. An additional gravity term in Eq. (4.1) will probably help, but it will not predict the high particle concentration just downstream of the wave crest.

5. Conclusion

In this paper we have presented results of a DNS of the flow over a wavy wall with suspended particles. It has been shown that the waves at the channel bottom can generate large longitudinal vortices similar to Langmuir vortices observed in flows with waves on the surface, Leibovich (1983). It is not likely that these longitudinal vortices are a computational artifact because these vortices are also observed experimentally by Gong et al. (1996). Furthermore, it has been shown that the sediment particle concentration has its maximum just downstream of the wave top (on the downstream side). The frequently used relation that the sediment concentration is related to the shear stress does not seem to hold.

REFERENCES

MAXEY, M. R. & RILEY J. J. 1983 Equation of motion for a small rigid sphere in nonuniform flow. *Phys. Fluids.* **26**, 883.

GONG, W., TAYLOR, P. A. & DÖRNBRACK, A. 1996 Turbulent boundary-layer flow over fixed aerodynamically rough two-dimensional sinusoidal waves. *J. Fluid Mech.* **364**, 1-31.

DE ANGELIS, V., LOMBARDI, P., & BANERJEE, S. 1997 Direct numerical simulation of turbulent flow over a wavy wall. *Phys. Fluids.* **9**, 2429-2442.

PHILIPS, W. R. C., WU, Z. & LUMLEY, J. L. 1996 On the formation of longitudinal vortices in a turbulent boundary layer over wavy terrain. *J. Fluid Mech.***326**, 285-321.

CHERUKAT, P., NA, Y., HANRATTY, T. J. & MCLAUGHLIN, J. B. 1998 Direct numerical simulation of a fully developed turbulent flow over a wavy wall. *Theoret. Comput. Fluid Dyn.* **11**, 109-134.

VAN HAARLEM, B. A., BOERSMA, B. J. & NIEUWSTADT, F. T. M. 1998 Direct numerical simulation of particle deposition onto a free-slip and no-slip surface. *Phys.Fluids.* **10**, 2608.

PAN, Y. & BANERJEE, S. 1995 A numerical study of free-surface turbulence in channel flow. *Phys. Fluids.* **7**, 1649.

MORSE, P. M. & FESHBACH, H. 1953 Methods of Theoretical Physics. McGraw-Hill, New York.

PHILIPS, W. R. C., WU, Z. & LUMLEY, J. L. 1996 On the formation of longitudinal vortices in a turbulent boundary layer over wavy terrain. *J. Fluid Mech.* **326**, 285-321.

LEIBOVICH, S. 1983 The form and dynamics of Langmuir circulations. *Ann. Rev. Fluid Mech.* **15**, 391-427.

BLONDEAUX, P. 1990 Sand ripples under sea waves part 1. Ripple formation. *J. Fluid Mech.* **218**, 1-17.

Propagation of internal wave packets in the thermocline

By G. F. Carnevale† AND P. Orlandi‡

Internal wave packets propagating vertically in the oceanic thermocline are investigated with numerical simulations. For a typical set of environmental and packet parameters, it is shown that linear dispersion will have a significant effect on the spreading and decay in amplitude of these packets. Sufficiently strong packets are shown to generate turbulence that forms a continuous 'scar' of small-scale perturbations in their wake.

1. Introduction

Internal wave groups or packets play an important role in the dynamics of the oceanic thermocline, the upper few hundred meters of the ocean where the temperature changes from high surface values to the much lower values below. Recent observations (Alford and Pinkel, 2000) show vertically propagating wave packets at depths from 150 to 350 m. These packets have vertical extent of about 50 m with internal vertical wavelengths of about 12 m and are associated with overturning events with vertical scales of about 2 m. Because overturns can lead to small-scale turbulence and mixing, they form a subject of intense investigation. Recent theoretical analysis by Thorpe (1999) provides a criterion for determining whether the small-scale turbulence generated by a packet will be left behind in just small patches or in continuous 'scars' much longer than the size of the packet. Stimulated by these developments, we have embarked on a numerical investigation of internal wave packets. Numerical simulations in this area may be of great benefit because the available oceanic data is primarily one-dimensional, and the full three-dimensional structure obtainable through simulation may aid in deciphering observational data.

Assuming a constant background Brunt-Vaisala frequency, N, and ignoring the effects of the earth's rotation, the intrinsic frequency for internal waves is

$$\sigma = N\frac{k_h}{k}, \tag{1.1}$$

where k is the magnitude of the wavevector and k_h is the magnitude of the horizontal component of the wavevector. The observed frequency for one of the wavepackets in the Alford and Pinkel (2000) data is 4 cph. This is higher than the ambient $N \approx 3$ cph. Since $\sigma_{max} = N$, it is assumed that the observed frequency for this packet is the sum of the intrinsic frequency plus a Doppler shift. To predict this shift, it is necessary to know the wavelength of the packet, the magnitude of the ambient current, and the ambient current's direction relative to the packet propagation direction. Alford and Pinkel (2000)

† Scripps Institution of Oceanography, University of California San Diego, 9500 Gilman Dr., La Jolla, CA 92093
‡ Università di Roma "La Sapienza" Dipartimento di Meccanica e Aeronautica, via Eudossiana 18 00184 Roma, Italy

suggest that the intrinsic frequency for their packet with observed frequency of 4 cph is near 0.14 cph, which leads one to a wavelength of 180 m. This suggests that the horizontal wavelengths in both directions are much larger than the vertical wavelength. For our numerical modeling this represents a difficulty. We are reluctant to introduce anisotropic grids for fear of the distortions that might result, especially when applying simple sub-grid scale models. Thus, in this preliminary work we decided to consider only the case in which horizontal and vertical wavelengths were equal. The corresponding intrinsic frequency would then be about 2 cph which would still be, consistent with the observed packet, just requiring less of a Doppler shift to match the observed frequency.

As for the amplitude of the observed packets, this can be given in terms of the peak magnitude of the observed strain rate $\partial w/\partial z$. The maximum value of vertical strain rate in the Alford and Pinkel (2000) observations is approximately N, and in the case of the particular packet discussed above, it seems that the maximum is about $0.38N$.

In what follows, we will examine the evolution of a particular wave packet with both two- and three-dimensional simulations. In an attempt to reproduce the kind of behavior evident in the observations, we began with two-dimensional simulations in a domain of 200 m in both width and depth. We used a packet with non-dimensional wavenumbers of 12 in both directions corresponding to vertical and horizontal wavelengths of (200 m)/12 $\approx$ 17m. Our 2D simulations had an effective resolution corresponding to a cutoff wavelength of $\approx$ 0.8 m. Using these parameters allowed us to perform a large number of simulations in a reasonable period of time and to capture the basic phenomena of interest down to scales slightly smaller than the overturning scale. To follow this phenomenon in DNS with all relevant scales well resolved would require resolution from 200 m down to a few cm, which is impractical even in two dimensions. Thus, in the two-dimensional simulations, we had recourse to hyperviscosity (with the Laplacian taken to the eighth power). At this point we have only performed the three-dimensional simulations with resolution down to wavelengths of $\approx$ 3 m and with Laplacian viscosity and diffusivity, and this misses much of the smaller scales of interest. Nevertheless, even these under-resolved three-dimensional simulations capture some features of interest.

The two-dimensional simulations illustrated here are from a spectral code dealiased with the 3/2 rule (Orszag, 1971). Although there are 768 wavevectors used in each direction, after application of the 3/2 rule this leaves only 512 active modes in each direction. The three-dimensional results shown are from a finite difference code with a staggered grid of 128 points in each direction.

2. Linear propagation

The linearized version of the Boussinesq evolution equations can be used to obtain a model of the internal wave packet. The vorticity and density of a plane internal wave can be written dimensionally as

$$(\omega_x, \omega_y, \omega_z, \rho') = A\mathbf{e_k} \exp i(\mathbf{k} \cdot \mathbf{r} - \sigma t), \tag{2.1}$$

where A is an arbitrary amplitude and $\mathbf{e}$ is the eigenvector

$$\mathbf{e_k} = (gkk_y/Nh_h, -gkk_x/Nh_h, 0, \rho_0). \tag{2.2}$$

Taking a linear superposition of such waves distributed continuously in wavevector space and centered on a particular wavevector, say $\mathbf{k_0}$, would produce an internal wave packet.

For example,

$$(\omega, \rho') = \mathcal{R}e \int G(\mathbf{k} - \mathbf{k}_0) \mathbf{e_k} e^{i(\mathbf{k} \cdot \mathbf{r} - \sigma t)} d^3 k, \tag{2.3}$$

with

$$G(\mathbf{p}) \equiv A \exp\left(-\frac{a^2}{2}p_x^2 - \frac{b^2}{2}p_y^2 - \frac{c^2}{2}p_z^2\right), \tag{2.4}$$

where a, b, and c are length scales, represents a propagating ellipsoidal packet. A slight generalization using simple coordinate rotations will also permit an arbitrary choice for the orientation of the ellipsoidal envelope relative to the crests internal to the packet. Within the envelope, the vorticity and density fields will have a phase velocity in the direction of $\mathbf{k}_0$ and group velocity

$$\mathbf{c}_g = \nabla_{\mathbf{k}} \sigma_{\mathbf{k}}, \tag{2.5}$$

which is perpendicular to the phase velocity.

By varying the dimensions a, b, and c, we can change the shape of the packet as needed. A likely candidate for the packets whose effects are observed in Alford and Pinkel's (2000) data would suggest that at least one of these lengthscales is very large. For the present calculations we take a to be infinite. Then we chose b and c and the orientation of the system to be such that the envelope is an ellipse with major axis aligned along the direction of propagation. Other choices may also be of interest, but that will be explored in future work. With the ellipse as chosen, the phase velocity is directed along the short axis and the group velocity along the long axis. In a numerical simulation, the packet can only be approximated, with the integral replaced by a discrete sum of wavevectors. By using (2.3) and (2.4) with $t = 0$, we are able to construct the initial condition for a packet that is both reasonably confined in space and well resolved internally.

The first issue that we need to address is the dispersive spreading of the wave packet. Simple arguments suggest that the physical extent of the wave packet will grow as $\Delta c_g t$ in the direction of the group velocity, where Δc_g represents the spread in group velocities calculated for the individual wavevectors that contribute significantly to the wave packet. We can make some crude dimensional estimates for the rate of dispersion by setting $c_g \sim N/k_0$ and $\Delta c_g \sim (N/k_0^2)\Delta k_0$, where Δk_0 measures the spread of wavenumbers in the packet. If we call Δx_0, the initial length of the wavepacket, then the time t_d in which the packet will double in size can be found with an estimate for the uncertainties for the positions of the various components of the packet given by Jackson (1962):

$$\Delta x = \sqrt{(\Delta x_0)^2 + (\Delta c_g t)^2}. \tag{2.6}$$

The doubling time is given by $t_d \sim \sqrt{3}\Delta x_0 / \Delta c_g$, and the distance that the packet can travel before doubling is

$$x/\Delta x_0 = \sqrt{3}k_0/\Delta k_0. \tag{2.7}$$

In Fig. 1, we show the evolution of the density perturbation field during the propagation of our packet following purely linear dynamics. In each panel, only the contour level corresponding to $0.5|\rho'/\rho_0|$ is drawn. Positive and negative values have not been indicated, but clearly the sign of ρ' will alternate from one wave crest to the next. We see that the packet propagates along the diagonal. This is in agreement with the fact that the wavevector is $\mathbf{k} = (12, 12)$ and that the group velocity is perpendicular to this. It is less obvious from the few panels that we can include here that the phase of the waves within the packet advances in the direction of $\mathbf{k}$. The average speed of the packet
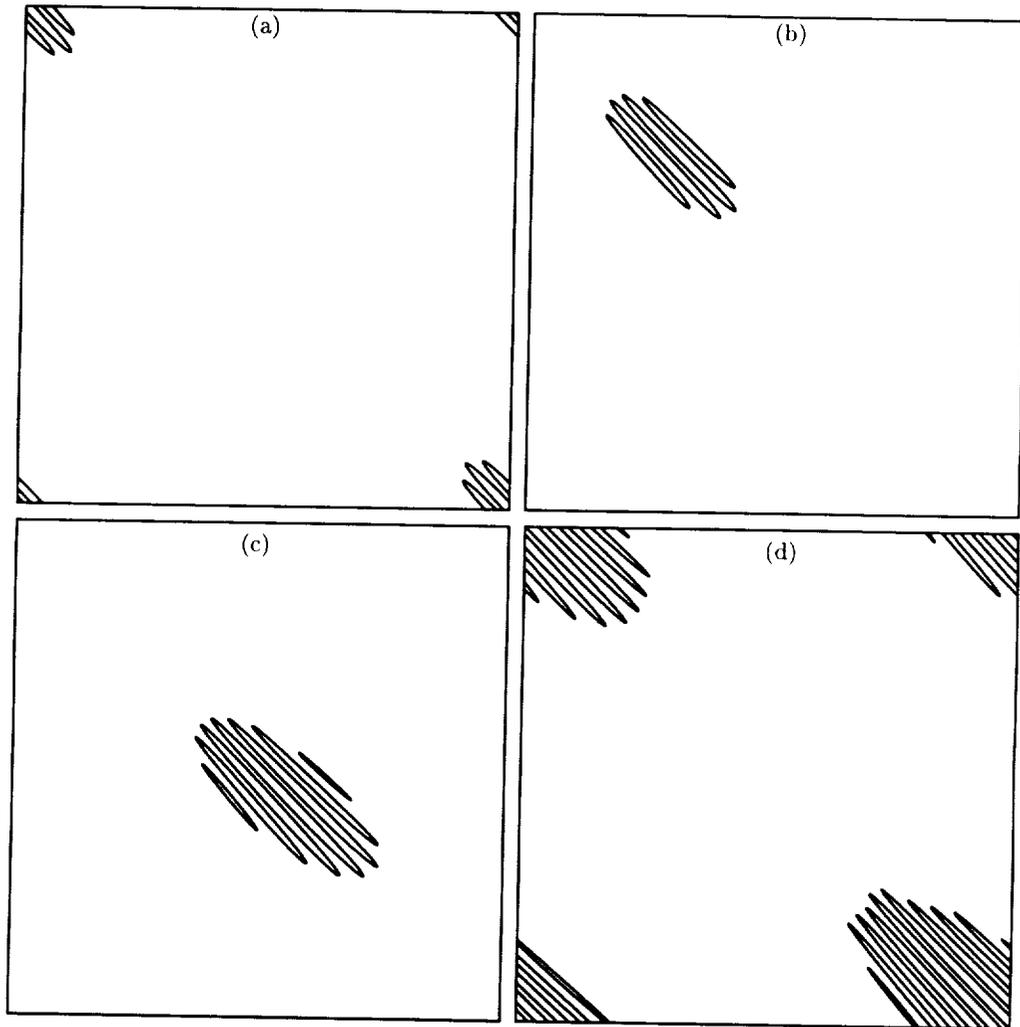
FIGURE 1. Contours of the magnitude of the perturbation density $|\rho'/\rho_0|$ from a simulation of the linear propagation of a wavepacket. The domain size is 200 m on each side. The vertical axis is depth. The only contour level drawn is that at 0.5 of the maximum field value. The time sequence of the panels is a) t=0, b) t=60, c) t=120, and d) 210 in units of $N^{-1} \approx 3$ min.

in propagating from one corner of the domain to the opposite corner is correctly given by $|c_g|$. Furthermore, we see that the width and length of the packet grow to a little more than double their original values in the time it takes to cross from one corner of the domain to the other, and this is correctly predicted by the formula (2.7). During the period of evolution illustrated, the peak amplitude of the packet decays to 25% of its initial value.

Although the amplitude of the packet can be changed arbitrarily in this purely linear simulation, we may simply assign an amplitude to see the effect of such a packet on the full density field. This is done in Fig. 2. The amplitude used represents fluctuations in

(a)   (b)

(c)   (d)
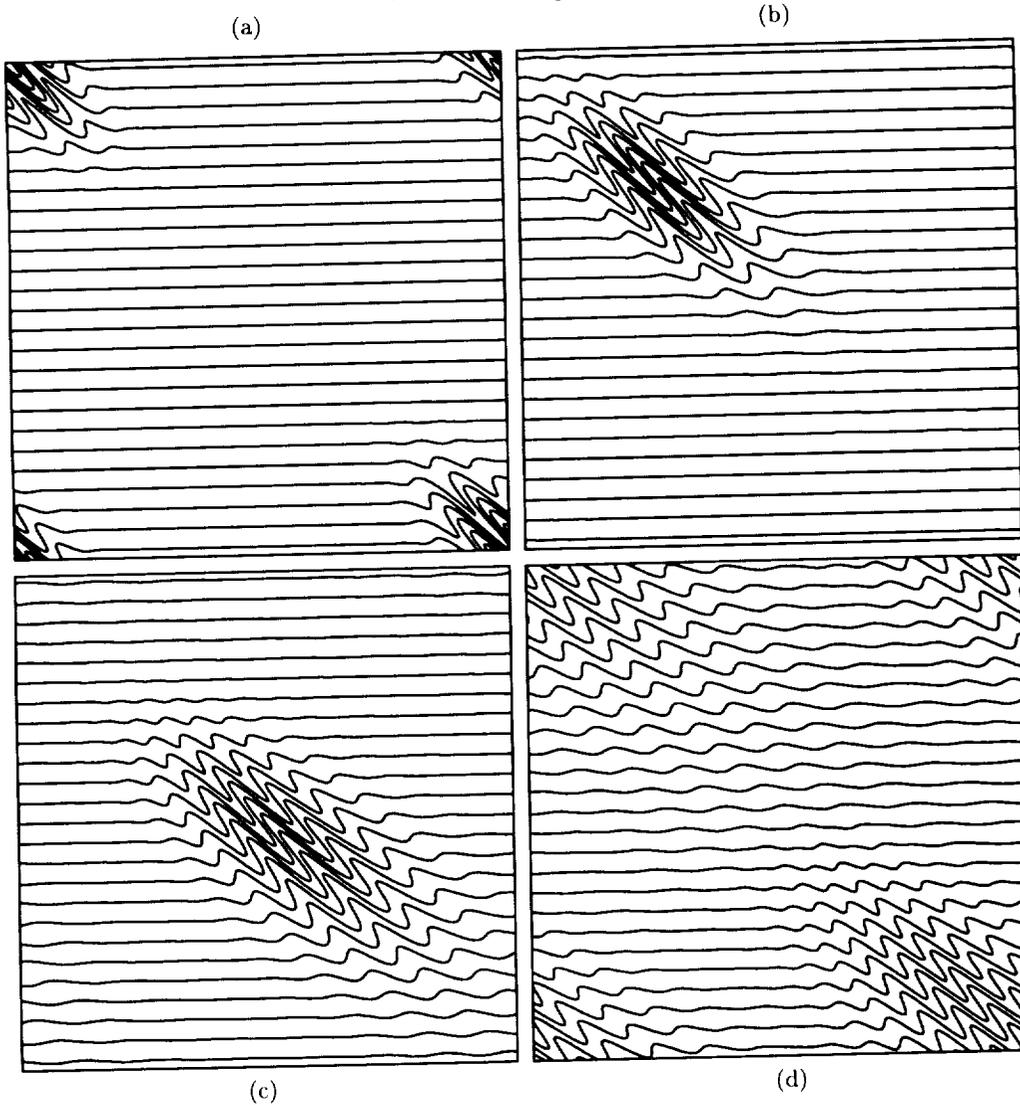
FIGURE 2. Contours of ρ/ρ_0 from a simulation of the linear propagation of a wavepacket. The domain size is 200 m on each side. The vertical axis is depth. The time sequence of the panels is the same as in Fig. 1. The contour increment is such that the vertical separation between unperturbed isopycnals is 8 m.

$\partial w/\partial z$ about five times the maximum actually observed in the Alford & Pinkel (2000) data. Nevertheless, we have used this packet with exaggerated amplitude to more clearly illustrate the nature of the linear propagation. In such a strong packet, there are regions of strong overturning, which, if the packet is not propagating too rapidly, would develop convective instability under the full nonlinear dynamics.

3. Nonlinear propagation

Having determined that our packet propagates correctly under linear dynamics, we then investigated its evolution with the complete Boussinesq equations. The amplitude
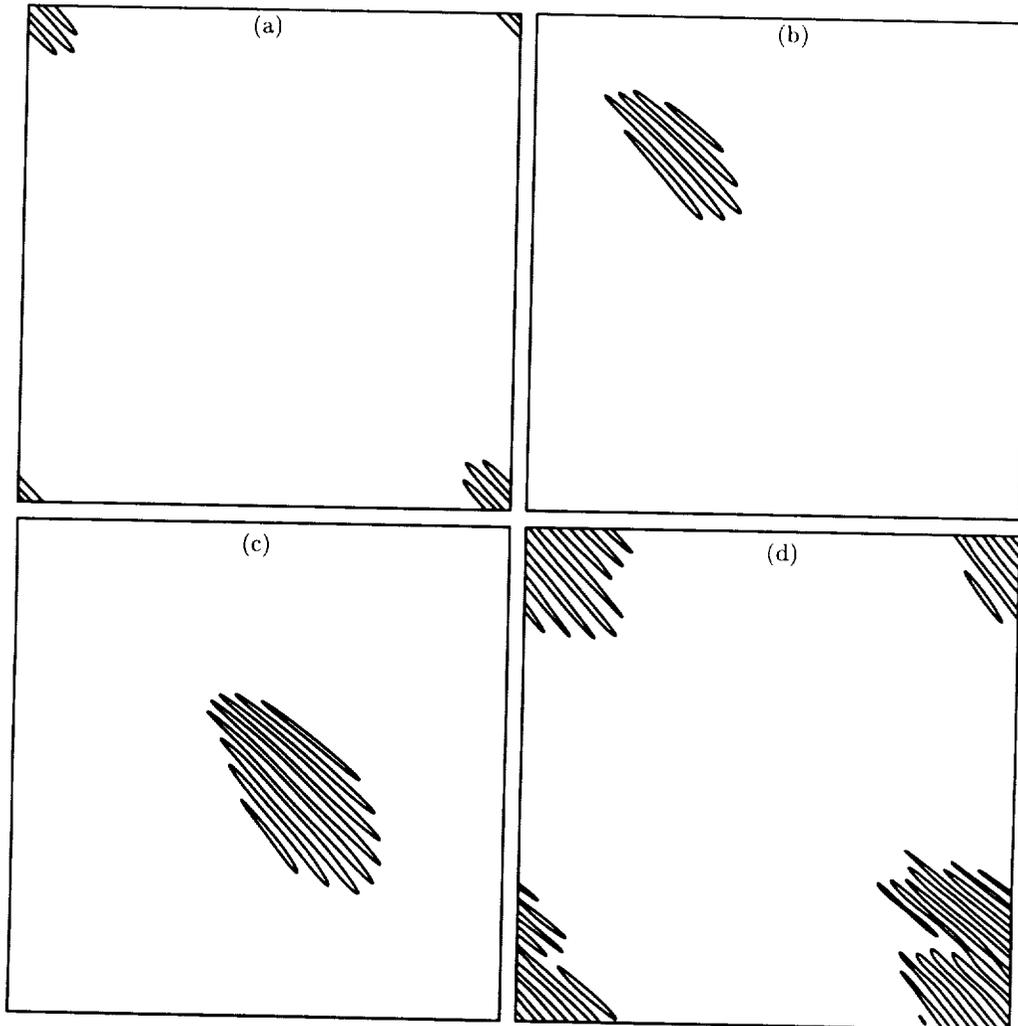
FIGURE 3. Contours of the magnitude of the perturbation density $|\rho'/\rho_0|$ from a simulation of the nonlinear propagation of a wavepacket with max $\partial w/\partial z \approx 0.38N$. The domain size is 200 m on each side. The vertical axis is depth. The only contour level drawn is that at 0.5 of the maximum field value. The time sequence of the panels is the same as in Fig. 1.

of the observed packet discussed in the introduction is such that the maximum value of the strain rate $\partial w/\partial z$ is about $0.38N$. With the packet amplitude set to match this value as its maximum $\partial w/\partial z$, we performed the simulation illustrated by contour plots of ρ'/ρ in Fig. 3. This figure should be compared to the corresponding figure for linear evolution, Fig. 1. The times represented are the same in each figure. By the time of panel (b), a clear asymmetry in the form of the packet has developed in the nonlinear case and there is some clear distortion of the packet in the final panel. Nevertheless, the overall evolution of this nonlinear packet is not very different from the linear case. This packet is so weak that the initial condition is not overturning anywhere and the Richardson

(a)   (b)
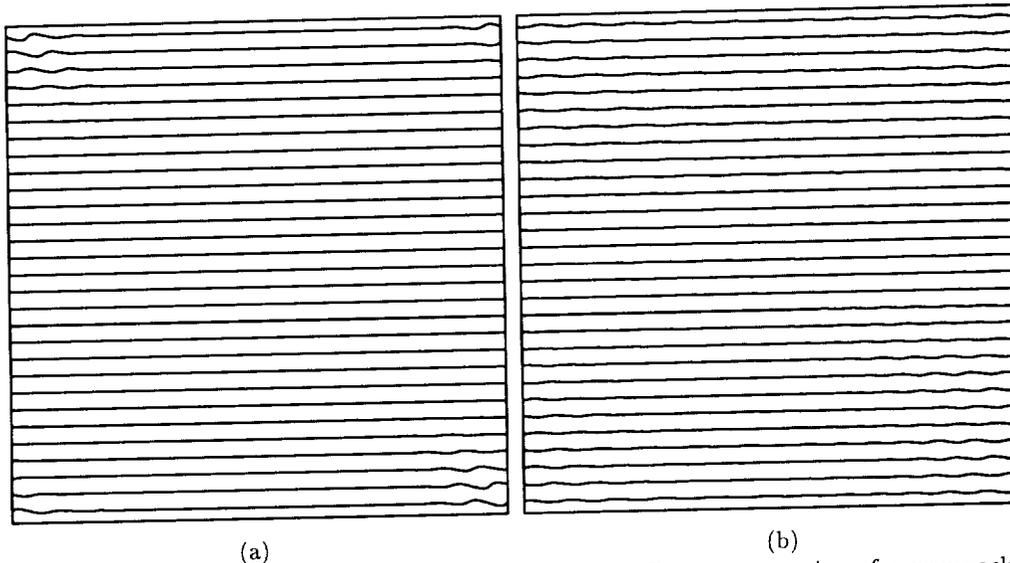
FIGURE 4. Contours of ρ/ρ_0 from a simulation of the nonlinear propagation of a wavepacket with initially max $\partial w/\partial z \approx 0.38N$. The domain size is 200 m on each side. The vertical axis is depth. The two times illustrated correspond to the first and last times of Fig. 1. The contour increment is such that the vertical separation between unperturbed isopycnals is 8 m.

number is above 1 everywhere. Thus, the classical criteria for convective instability and shear instability are not satisfied in this packet. This continues to be the case throughout the simulation in spite of small-scale generation by nonlinear wave-wave interactions. An idea of how weak this packet is can be obtained graphically from the plots of the density contours as illustrated in Fig. 4.

The next case that we will treat is one for which the amplitude of the packet is just above the threshold for overturning. The amplitude of this packet in terms of its maximum strain rate is $\partial w/\partial z = 0.76N$. In Fig. 5, we display the contour plots for the perturbation density at the same times as in the previous figures. We see that there is some early production of small scales that are evident in the wake of the packet. By time 120 N^{-1}, the packet itself has become badly distorted, and by time 210 N^{-1}, it has degenerated into small-scale structures, although these still retain to some extent an organization and alignment related to the original structure of the packet. To better illustrate the decay of this packet, we display contour plots of the full density field from $t = 47N^{-1}$ to $t = 90N^{-1}$ in Fig. 6. Each frame is an enlarged image centered on the wave packet, showing only a portion of the domain (a square of size 200/3 m on a side). In panel (a) we see an early stage in which the wave is overturning at points, but there has not yet been any strong production of energy in scales smaller than 2 m (note that the spacing between the unperturbed isopycnals is 2 m). There are four relatively strong crests evident in panel (a). These crests are advancing from bottom-left to top-right in these figures. The weakest crest (bottom-left) is just entering the packet in panel (a). In the linear evolution as each crest passes through the packet from bottom-left to top-right, its amplitude first increases and then decreases. As envisioned by Thorpe (1999), if in amplifying the crest surpasses some threshold for turbulence production, it will leave
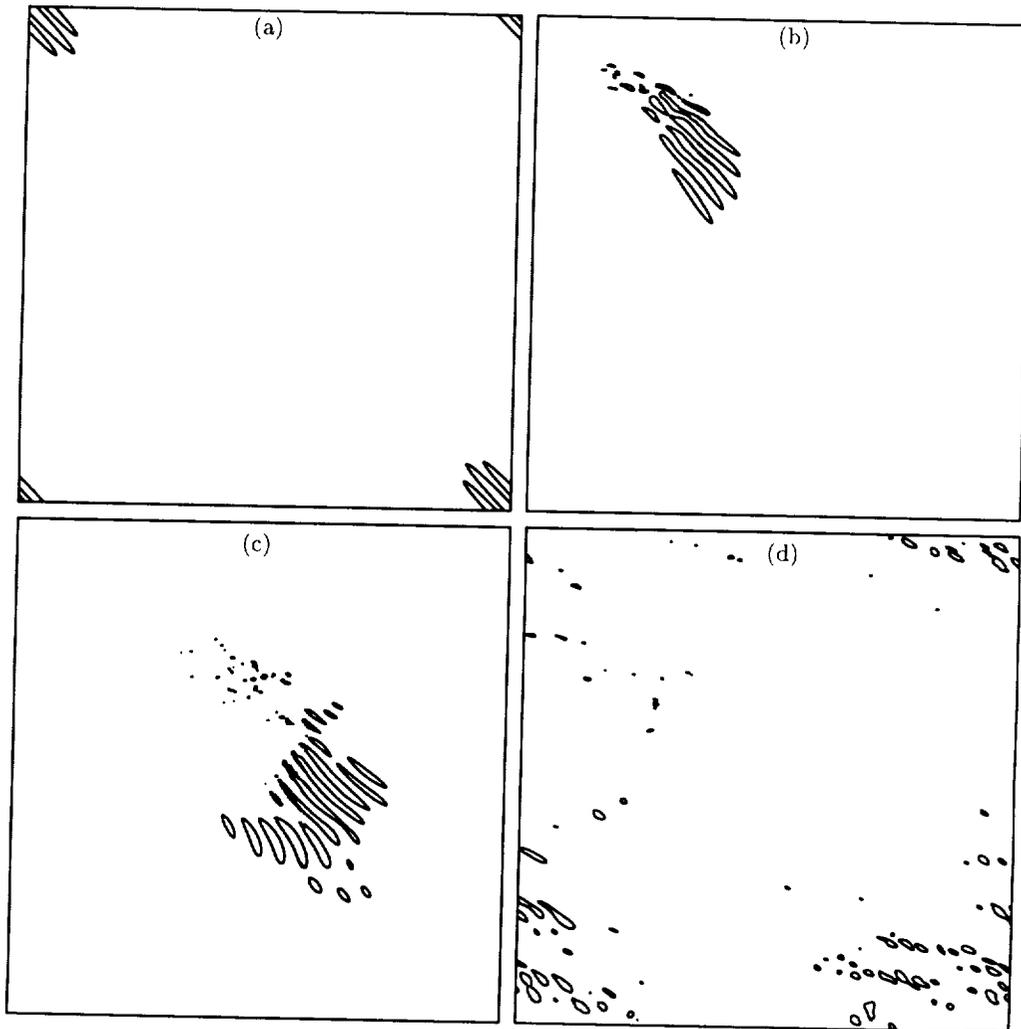
FIGURE 5. Contours of the magnitude of the perturbation density $|\rho'/\rho_0|$ from a simulation of the nonlinear propagation of a wavepacket with max $\partial w/\partial z \approx 0.76N$. The domain size is 200 m on each side. The vertical axis is depth. The only contour level drawn is that at 0.5 of the maximum field value. The time sequence of the panels is the same as in Fig. 1.

a 'scar' of small-scale perturbations that perhaps may link up with the scars produced by the previous and following crests as they pass through the packet. Thorpe (1999), gives a criterion for whether such overlapping will take place based on the makeup of the packet and the duration of the small-scale perturbations. The period of the sequence of panels shown here is long enough for the weak crest on the lower-left side of the packet in panel (a) to move completely through the packet, finally becoming the weak crest on the upper-right side. In fact, as envisioned by Thorpe (1999), this crest does overturn and produces small-scale perturbations that do form a somewhat continuous scar when combined with the remnants of the breaking of the previous and trailing crests. One
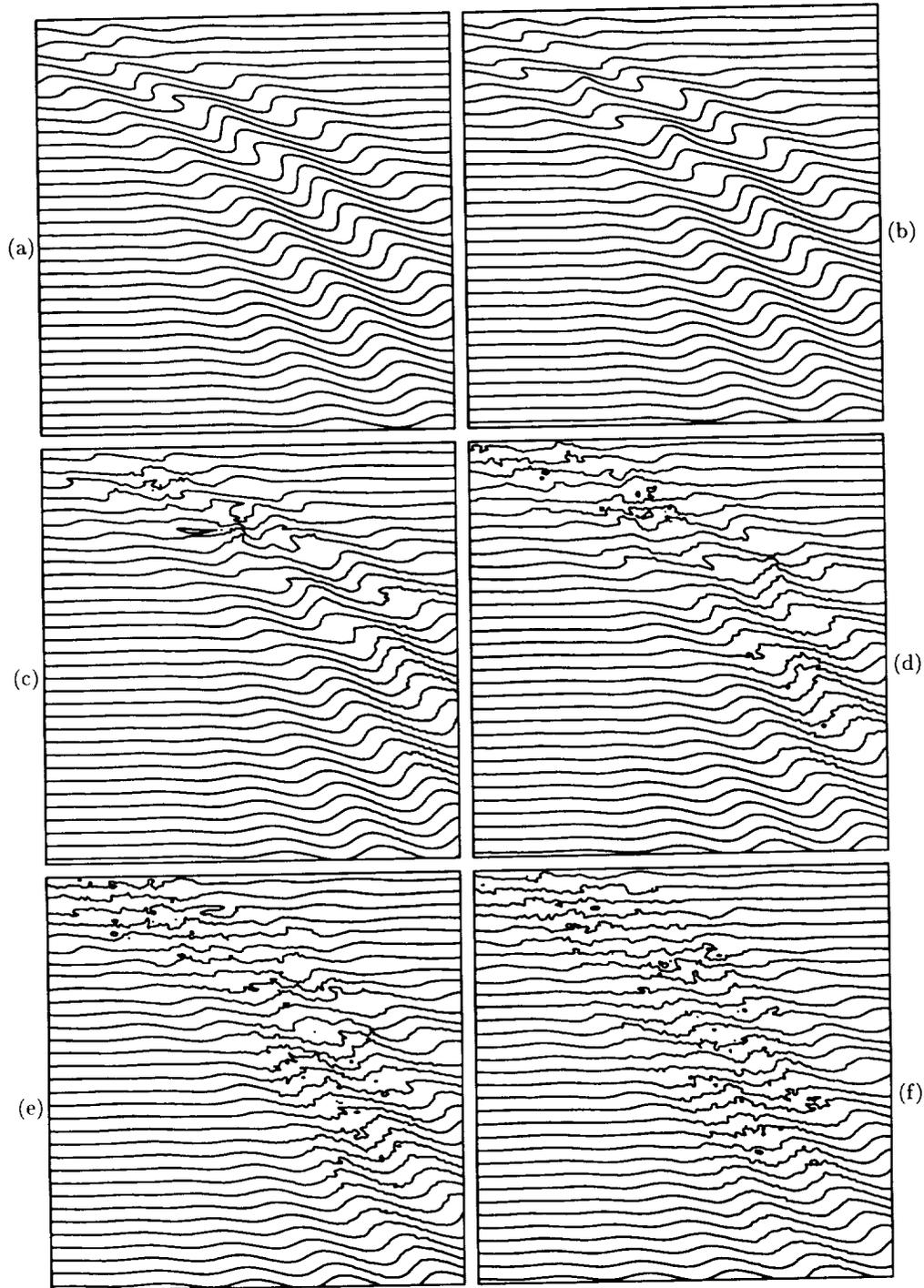
FIGURE 6. Contours of ρ/ρ_0 from a simulation of the nonlinear propagation of a wavepacket with initially max $\partial w/\partial z \approx 0.76N$. Only a portion of the computational frame is shown, and this corresponds to a square 200/3 m on each side. The contour increment is such that the vertical separation between unperturbed isopycnals is 2 m. The times corresponding to the panels are (a) 47, (b) 54, (c) 66, (d) 73, (e) 83, and (f) 90, all in units of N^{-1}.
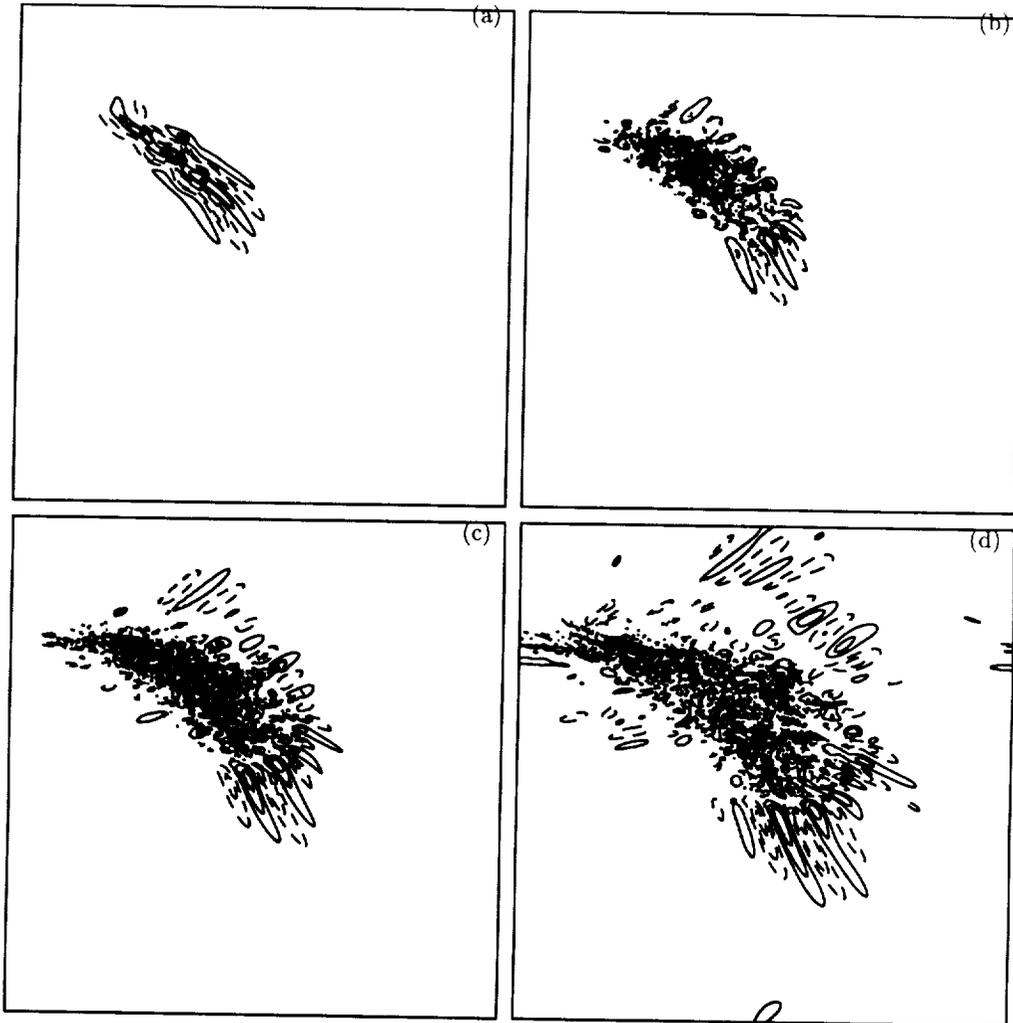
FIGURE 7. Contours of the magnitude of the perturbation density $|\rho'/\rho_0|$ from a simulation of the nonlinear propagation of a wavepacket with max $\partial w/\partial z \approx 1.3N$. The domain size is 200 m on each side. The vertical axis is depth. The only contour level drawn is that at 0.5 of the maximum field value. The time sequence of the panels is a) t=19, b) t=34, c) t=43, and d) 58 in units of N^{-1}.

should note, however, that during the period when a particular crest is actually breaking, the overturning and small-scale production is not uniform along the length of the crest but rather appears in spots along the crest (see panels (c) and (d)). Also the breaking and subsequent scar formation does not continue indefinitely. The strength of the packet is both dispersed and dissipated, so that by $t = 210N^{-1}$ the process of scar formation has ceased.

We next examine the case of a packet that initially is strongly overturning. This packet does not survive long, but the manner in which it breaks up is of interest. We use

(a) (b)
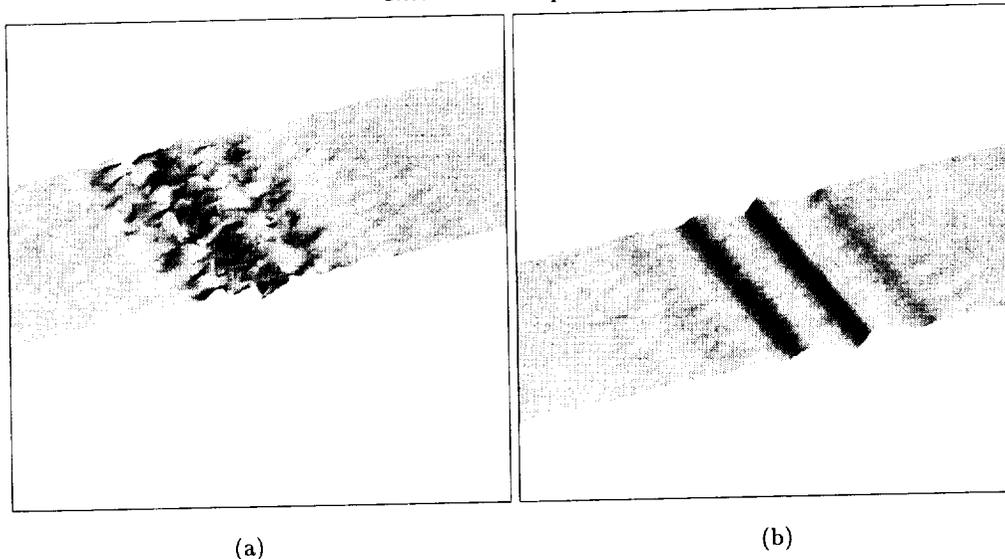
FIGURE 8. Density isosurfaces from a three-dimensional simulations of the evolution of a wavepacket. The view is from above and to the front of the computational domain. The iso-surface in (a) cuts through the trailing part of the packet, while that in (b) cuts through the leading part.

an amplitude such that max $\partial w/\partial z = 1.3N$. In Fig. 7, we show the contour plots of the perturbation density from this case. For this simulation, we have shifted the initial position of the packet away from the corner so that the relevant evolution can be more clearly observed. In addition to the production of much small-scale energy during the disintegration of the packet, there is also a significant amount of radiation obvious in these graphs. As the packet begins to break up, most of the radiation appears to be at right angles to the original packet propagation direction. This would indicate that the source of this secondary radiation is primarily oscillating at the same frequency as the central wavevector of the packet. This follows because the angle of propagation is linked to the frequency of the source; waves propagating at $\pm 45°$ from the horizontal must all have the same frequency. As the breakup continues, however, the range of radiation angles increases, indicating that the source is no longer dominated by a single frequency. This could be the result of either strong nonlinear effects or the fact that a transient source necessarily comprises many frequencies which would stimulate radiation at various angles even in linear theory.

Finally, we turn to the question of three-dimensional simulations. We performed a series of simulations with a computational domain representing a cube of the ocean 200 m on a side. The computational grid had 128 points in each direction. We used only Laplacian diffusion for both momentum and density. To initiate three-dimensional motions, we added small-scale background noise to the initial wavepacket. To make a comparison with the two-dimensional results, we averaged the density field along the x direction and prepared plots of ρ and ρ'. The basic behavior from the three-dimensional simulations for large-scale aspects of the flow was very similar to the two-dimensional results. The resolution for the three-dimensional simulations, however, was not adequate to reproduce all the details of the overturning events seen in the two-dimensional flow. In the two-dimensional cases, with a high number of wavenumbers and a hyperviscosity

dissipation, we were resolving wavelengths down to 0.8 m. For the 3D flow the best we could do with the resolution used and the Laplacian dissipation was perhaps 3 m. In Fig. 8, we display the results from one such run with the initial amplitude set so that max $\partial w/\partial z = N$. Here we show isosurface plots of the full density of the flow. In 8a we see an isodensity surface that cuts through the tail region of the packet, which has already produced a substantial amount of small-scale energy. Due to the poor resolution, however, we cannot discern any realistic looking overturning events. In 8b we see a density isosurface that cuts through the leading end of the packet at the same instant of time as that in 8a. These two isosurfaces confirm the picture that we had already seen from the two-dimensional simulations (cf. Fig. 6).

4. Conclusions

Our two-dimensional simulations with hyperviscosity were sufficiently well resolved and had a sufficiently large computational domain to capture the basic phenomena of interest. Thus we were able to see a packet with approximately the correct vertical structure propagate through a substantial portion of a thermocline as observed in the Alford and Pinkel (2000) data. We were able to see overturning events on the scale of about 2 m, which is entirely consistent with Alford and Pinkel's observational census of overturns that places their median vertical scale at about this value. Unfortunately, these simulations could not also simultaneously capture the large horizontal scales of the rapidly advected packet suggested by Alford and Pinkel (2000) as a model for one of the packets in their observations. Our three-dimensional simulation was able to capture only the large-scale aspects of the packet propagation. We hope in the future to improve on this by using a smaller computational domain, increasing the resolution of the model and incorporating an eddy viscosity.

Acknowledgments

REFERENCES

ALFORD, M. H. & PINKEL, R. 2000 Observations of overturning in the thermocline: the context of ocean mixing. *J. Phys. Ocean.* **30**, 805-832.

JACKSON J.D. 1962 *Classical Electrodynamics.* Wiley.

ORSZAG, S.A. 1971 On the elimination of aliasing in finite-difference schemes by filtering high-wavenumber components. *J. Atmos. Sci.* **28**, 1074.

THORPE, S.A. 1999 On internal wave groups. *J. Phys. Ocean.* **29**, 1085-1095.

The combustion group

During the CTR 2000 Summer Program, seven projects related to combustion and sprays covered a large variety of topics ranging from the fundamental understanding of spray development and combustion processes to the modeling of real applications. As in previous summer programs, large-eddy simulation (LES) of chemically reacting flows was a main subject. In contrast to previous years, in 2000 the main focus was not only on the development and assessment of combustion models, but also on the evaluation of the merits and feasibility of LES for industrial applications. This trend towards the simulation of practical applications is reflected in the following facts: Three of the seven projects have industrial participation; two of the projects are related to the modeling of spray development, a key issue for modeling real combustion devices, which typically burn liquid fuels; and three projects are related to partially premixed combustion, which is the main combustion mode in many modern gas turbines and piston engines.

An example of the latter is the work by Jiménez, Haworth, Poinsot, Cuenot and Blint. This group extended a project initiated in the 1998 CTR Summer Program where the first direct simulations of premixed flames propagating into a stratified mixture were conducted with full treatment of complex chemistry. In 2000, globally lean mixtures were studied and NO_x formation added. In a parallel project, Haworth studied a new model which combines the capabilities of flamelet and pdf methods. This model has the capacity of handling stratified combustion and pollutant formation.

Legier, Poinsot, and Veynante performed an LES of combustion instabilities in a diffusion burner built at Ecole Centrale Paris for SNECMA. The main issue was to test whether LES could predict the different stabilization processes of this flame.

In an attempt to develop an efficient and robust premixed combustion model for LES of engineering applications, Flohr and Pitsch developed an LES formulation of a turbulent flame speed closure model which was originally proposed for RANS modeling. The model was implemented in a commercial flow solver with LES capability and applied to a generic premixed burner with focus on the combustor response to forced inflow modulations. An important part of this work is the evaluation of the LES capability of the flow solver by comparing DNS results for a turbulent pipe with those obtained using an existing, extensively validated CTR DNS code.

Although reactive flow problems in chemical engineering typically reveal a chemistry considerably different from hydrocarbon chemistry of fossil fuels observed in engine combustion, similar combustion models might be applicable in both cases. During this program, the methyl chloride chlorination process was investigated by Harvey and Pitsch. In order to evaluate the level of modeling complexity required in typical industrial applications, flamelet models were implemented in a RANS and an LES code, and predictions for a model reactor using both codes were compared to simulations neglecting chemical closure. Some important findings are that the temperature is substantially overpredicted if chemical closure is neglected. The LES also exhibited considerably lower scalar dissipation rates and higher maximum temperatures compared to the RANS calculations.

An issue of particular importance to numerical simulations of combustion in technical devices is the modeling of spray dynamics and vaporization. In most gas-turbine combustors and in modern diesel engines, liquid fuels are injected at subcritical temperatures into a supercritical environment. Common spray models fail to predict the transitional behavior which is important in this regime. Oefelein and Aggarwal addressed this problem

by developing a unified high-pressure evaporation model which includes the description of transcritical and supercritical processes. The second spray related project by Smith, Cha, Pitsch, and Oefelein performed DNS of evaporating and reacting sprays in isotropic turbulence. Using the analysis of the resulting statistics for the mixture fraction and the scalar dissipation rate, they provided a novel formulation of mixture fraction based combustion models, such as conditional moment closure or unsteady flamelet models, which can be applied to spray combustion.

<div align="right">Heinz Pitsch and Thierry Poinsot</div>

Numerical simulations of combustion in a lean stratified propane-air mixture

By C. Jiménez†, D. Haworth‡, T. Poinsot†¶, B. Cuenot† AND R. Blint‖

Direct numerical simulation (DNS) of combustion in globally lean non-homogeneous propane-air mixtures has been performed for several initial distributions of non-homogeneities. Results have shown a strong influence of the scale and asymmetry of this distribution on both the combustion efficiency and thermal NO production, in accordance with experimental results. The simulations also have made possible a quantitative assessment of flamelet modeling for the primary flame, which yielded remarkably good results.

1. Introduction

In direct-injection engines, liquid fuel is injected directly into the combustion chamber to generate a highly stratified fuel/air mixture at ignition time. This has the potential to significantly improve the engine performance, especially at low-speed light-load operation (Takagi, 1998), and is the subject of intense research for both spark-ignition gasoline (Zhao *et al.*, 1999) and compression-ignition Diesel (Krieger *et al.*, 1997) engines.

This flame propagating into a non-homogeneous mixture is a first example of partially premixed combustion, in which the reactants are not completely mixed nor completely separated before combustion and for which modeling can not be based on the traditional premixed/non-premixed combustion scenarios. A second example can be found in aircraft engines, in which fuel and secondary air are injected at various locations, resulting in a nonuniform equivalence ratio at the flame front (Légier *et al.*, 2000).

Research in the field of partially premixed combustion has shown contradictory results concerning the propagating speed and efficiency of a flame in non-homogeneous premixed conditions as compared to the equivalent (in the sense of containing the same amount of fuel and air) uniformly premixed case. The experimental results of Zhou et al., 1998 suggest an enhanced heat release related to the presence of non-homogeneous pockets of rich/lean mixture for a wide range of variation of the parameters of the experiment. On the other hand, theoretical (Peters, 2000) and numerical (Hélie & Trouvé, 1998) results predict exactly the opposite behavior.

One of the motivations of the present project was to try to resolve such contradictions. Results of previous work (Poinsot *et al.*, 1996, Haworth *et al.*, 2000a, Haworth *et al.*, 2000b) had suggested that both the distribution of inhomogeneities in the equivalence ratio space and its spatial length scales would play a major role in increasing/decreasing global heat release, which can in part explain the discrepancies above.

A second objective was to contribute to the modeling of partially premixed combustion.

† CERFACS
‡ Pennsylvania State University
¶ IMFT
‖ GM

Previous studies have shown that in partially premixed systems, combustion occurs in two stages:

- A primary flame is first established that consumes all primary fuel and produces most of the heat release. It is expected that it can be described using a progress variable and laminar flamelet concepts.

- A secondary reaction zone appears behind when fuel fragments from the rich zones, oxidizer from the lean zones, and combustion products mix. There is still controversy on whether it can be seen as a diffusion flame and described by diffusion flamelets or should be described as distributed combustion.

Moreover, the issue of pollutant formation had to be addressed, as higher peak temperatures can increase the pollutant emission level of a stratified lean-charge engine as compared to a homogeneous lean-charge engine (Takagi, 1998). Formation of pollutants such as NO in premixed systems is most commonly computed by adopting equilibrium and steady-state hypotheses that permit postprocessing of production rate as a function of local N_2 and O_2 concentration and temperature (Glassman, 1987). An assessment of the validity of this approach in the present partially premixed case was needed, and for that reason a full thermal NO mechanism was included in this study.

The approach adopted is to perform DNS of a premixed flame propagating into non-homogeneous propane-air mixtures at conditions that approximate the gasoline direct injection (GDI) engine operating conditions in part-load, low-speed operation (Haworth *et al.*, 2000a). A detailed reaction mechanism based in 30 species and 76 reactions (including thermal NO chemistry), multicomponent molecular transport of species, and full resolution of both the turbulent and the chemical scales permits reliable simulations from which information relative to characterization and modeling of these systems can be extracted.

2. Numerical simulation

DNS of a compressible multi-component gas mixture evolving under turbulent velocity conditions is used to perform this study. The conservation equations for mass, momentum, chemical species mass fractions, and energy are solved using the NTMIX-CHEMKIN code (Baum *et al.*, 1994). High-order space and time integration of the equations is performed by sixth-order compact finite-differences (Lele, 1992) and a third-order Runge-Kutta temporal scheme. The elementary reaction production terms and multicomponent molecular transport coefficients are computed using the CHEMKIN and TRANSPORT packages (Kee *et al.*, 1980, Kee *et al.*, 1983).

DNS is extremely expensive. On one hand, a large number of species mass fractions is needed if one wants to represent realistically the chemistry and transport; on the other hand, very fine spatial and temporal grids are needed if the turbulence and chemistry are to be resolved without modeling in order to capture the smallest scales. This results in a severe limitation of the size of the systems that can be simulated if computations are to be performed at affordable costs. The flame width given by the present chemistry is of the order of 0.15 mm, which imposes a minimum size for the computing domain, but much larger sizes are needed to attain realistic turbulent length scales. A three-dimensional simulation of a cubic domain only a few millimeters on each side with the present chemistry would demand CPU times of the order of years. A two-dimensional simulation of the present chemistry in a planar domain a few millimeters on each side requires CPU times on the order of 2-3 days on a NEC SX-5 computer. Of course some turbulent features

are lost in the two-dimensional approximation, and the present computations would be badly suited to the quantitative characterization of the effects of turbulence on mixing and reaction (not only because of the two-dimensionality but also because of the low Reynolds number). But it is a reasonable choice in the present study where turbulence (2D turbulence) is only used as a means of deforming the flame front and no quantitative correlations between turbulence and the flame are sought.

3. Description of the configuration

The selection of the configuration for the present work was guided by previous results (Haworth *et al.*, 2000a) which had shown no great influence of non-homogeneities on the overall heat release, in contradiction with experiments. Analysis of the phenomena that can affect the overall heat release suggests that four main effects are in competition in non-homogeneous premixed systems:

• First, differences in local reaction rate due to local variations in the equivalence ratio produce a deformation of the flame as segments of flame initially propagating at a uniform speed begin to propagate at different speeds. This effect will in all cases produce an *increase in the flame surface* (or length in 2D) as compared to that of a flame propagating into homogeneous reactants. The magnitude of the increase should depend on the spatial distribution and range of inhomogeneities as well as on laminar flame propagation properties.

• Second, differences in local reaction rate give rise to local variations in heat release per unit flame area. This can contribute to *either an increase or a decrease* in global heat release as compared to the homogeneous case, depending mainly on the distribution of non-homogeneities in equivalence ratio space and flame propagation properties.

• Third, turbulent straining effects usually *decrease locally the reaction rate* as the flame surface tends to be aligned with tangential strain, whose effect is to reduce locally the reaction rates. This may affect the homogeneous and the non-homogeneous flames differently as the flame-front shape in the former is totally determined by turbulence, while non-homogeneities can change the flame shape as described above.

• Lastly, locally higher/lower temperatures occur in a non-homogeneous flame as compared to a homogeneous one. Diffusion, conduction, and turbulent mixing would then tend to decrease or increase the mean temperature at the flame front, resulting in *lower/ higher reaction rates* as compared to the values based on the local stoichiometry and strain rate. For example, a locally higher temperature than that of the unburned reactants could result in burning at local equivalence ratios beyond the flammability limits.

In Haworth *et al.*, 2000a, results for a *stoichiometric initially laminar flame* propagating into a non-homogeneous turbulent mixture were compared to those of a homogeneous mixture having the same amount of fuel/air, that is, *conserved mean stoichiometry*. Locally fuel-lean or fuel-rich regions correspond in this case to lower reaction rates (laminar flame speed peaks at a slightly fuel-rich equivalence ratio; Fig. 1). The resulting reduction in mean heat release per unit flame length approximately compensated for the flame surface increase, yielding essentially the same overall heat release for non-homogeneous and homogeneous flames. Maximum differences were approximately of 10%. Later work (Haworth *et al.*, 2000b) showed that variations in the spatial scales of inhomogeneities have a strong effect due to the change of scale of the flame-front deformations. For example, very small rich/lean pockets are not able to produce an appreciable deformation in the flame front, and thus the net effect is a reduction in heat release.
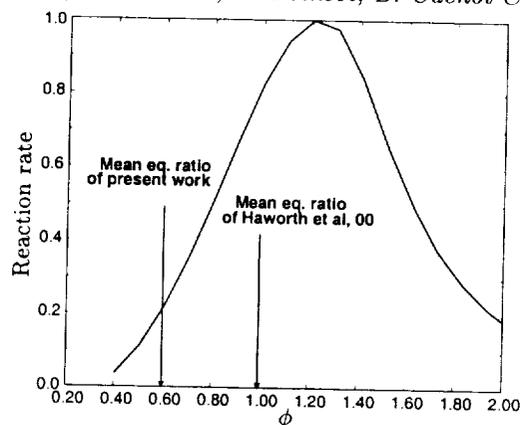
FIGURE 1. Normalized reaction rate of a premixed propane-air laminar flame as a function of equivalence ratio ϕ.

Case	ϕ_{min}	ϕ_{max}	$\langle\phi\rangle$	$\langle\phi'^2\rangle$	λ_ϕ
A Hom.	.6	.6	.6	0	0
B1 Non-hom.	.06	1.14	.6	.15	1
C1 Non-hom.	.03	2.06	.6	.45	1
C2 Non-hom.	.03	2.06	.6	.45	4

TABLE 1. Description of equivalence ratio distributions in the simulations.

L_x, L_y	n_x, n_y	τ_{T0}/τ_f	u'_{T0}/s_l^0	l_{T0}/δ_l^0	Re_{T0}
3 mm	451	.136	11.6	1.58	105

TABLE 2. Description of parameters of simulations.

A different configuration was selected for the present study. Here an *initially laminar lean flame* was established and propagated into a non-homogeneous turbulent mixture having the *same global lean stoichiometry*. This corresponds more closely to conditions in a stratified-charge direct injection engine at part-load, low-speed operation. In a globally lean mixture, where the distribution of local reaction rates is symmetric about the mean the mean reaction rate per unit flame length would be similar in homogeneous and non-homogeneous cases (see Fig. 1). This combined with an increase in flame length would result in the global heat release being higher in the non-homogeneous case. Here different distributions about the mean were explored to establish the effects in efficiency of combustion and NO formation. In a first simulation (B1 in table 1), mixture inhomogeneities were symmetrically distributed around the mean and thus limited to $\Delta\phi = \pm.6$. Results showed a small gain in heat release as compared to homogeneous combustion (see Fig. 2), as only a small portion of the mixture was close to stoichiometric or rich. A second configuration (C1) was designed in which inhomogeneities were introduced in an asymmetrical way with a thinner but higher peak towards the rich side. This is expected to correspond more closely to conditions in an engine, where fuel is injected as a liquid. Case C1 presented a clear gain in efficiency (see Fig. 2) mainly due to a higher mean heat release per unit flame length, as total flame length was essentially the same as for the previous configuration (Fig. 2).
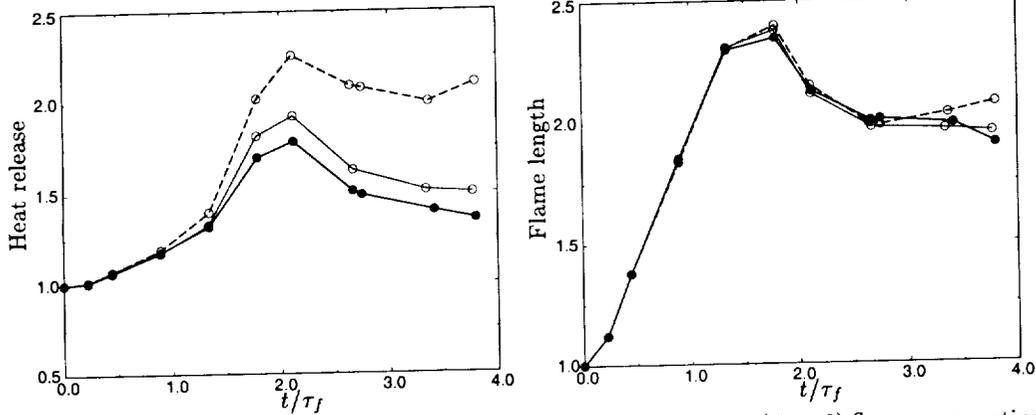
FIGURE 2. Global heat release (left) and flame length (right) of a lean ($\phi = .6$) flame propagating into a homogeneous lean mixture (-•-), a non-homogeneous mixture symmetrically distributed around $\phi = .6$ (-o-), and a non-homogeneous mixture biased to the rich side (- -o - -). Values are normalized by those corresponding to a planar laminar flame with $\phi = .6$.

The simulations were initialized with reactants on one side of the computing domain and products on the other side, separated by a lean ($\phi = .6$) planar laminar premixed flame. Two-dimensional turbulence was imposed as an initial condition using an energy spectrum parametrized by the initial rms turbulent velocity u'_{T0} and the initial turbulence integral length scale l_{T0} or characteristic time τ_{T0} (Haworth & Poinsot, 1992). Other parameters are the initial turbulent Reynolds number Re_{T0}, the initial laminar flame propagation speed s_l^0, the initial laminar flame thickness δ_l^0, and the flame time τ_f, defined in Haworth et al., 2000a as: $\tau_f = 2\delta_l^0/(s_l^0(1 + \rho_u/\rho_b))$. The values of these parameters for the present simulations are reported in table 2. The different simulations performed differ only in the length scales λ_ϕ and ranges of equivalence ratio imposed as initial conditions (table 1).

The chemical mechanism adopted was a 28-species 73-reaction propane mechanism proposed in Haworth et al., 2000a to which two additional species (N and NO) and three reactions were added for thermal NO (extended Zeldovich mechanism). Chemistry parameters for the NO mechanism were taken from Hanson and Salimian, 1984.

4. Primary flame characterization

The computed fuel mass fraction and heat release fields corresponding to times $t/\tau_f = 2$ and $t/\tau_f = 4$ obtained in three simulations (A, C1, and C2) are shown in Fig. 3. Also shown are the stoichiometric contour line of the mixture fraction field z_{C+H} and contours of the progress variable c, defined as (Haworth et al., 2000a):

$$z_{C+H} = \sum_{n=1}^{Nspecies} (Y_C^n + Y_H^n), \qquad c = 1 - Y_{C3H8}/z_{C+H}.$$

Case A corresponds to a homogeneous reactant mixture with equivalence ratio $\phi = .6$, case C1 to a non-homogeneous reactant mixture in which the initial length scale of inhomogeneities is $\lambda_\phi = 1$, and case C2 to a non-homogeneous mixture with $\lambda_\phi = 4$. The same initial turbulence was imposed in the three cases. At time $t/\tau_f = 2$ the flame front displays the same shape in all three cases, while differences are apparent by time $t/\tau_f = 4$. Locally different propagation speeds due to inhomogeneities have deformed the
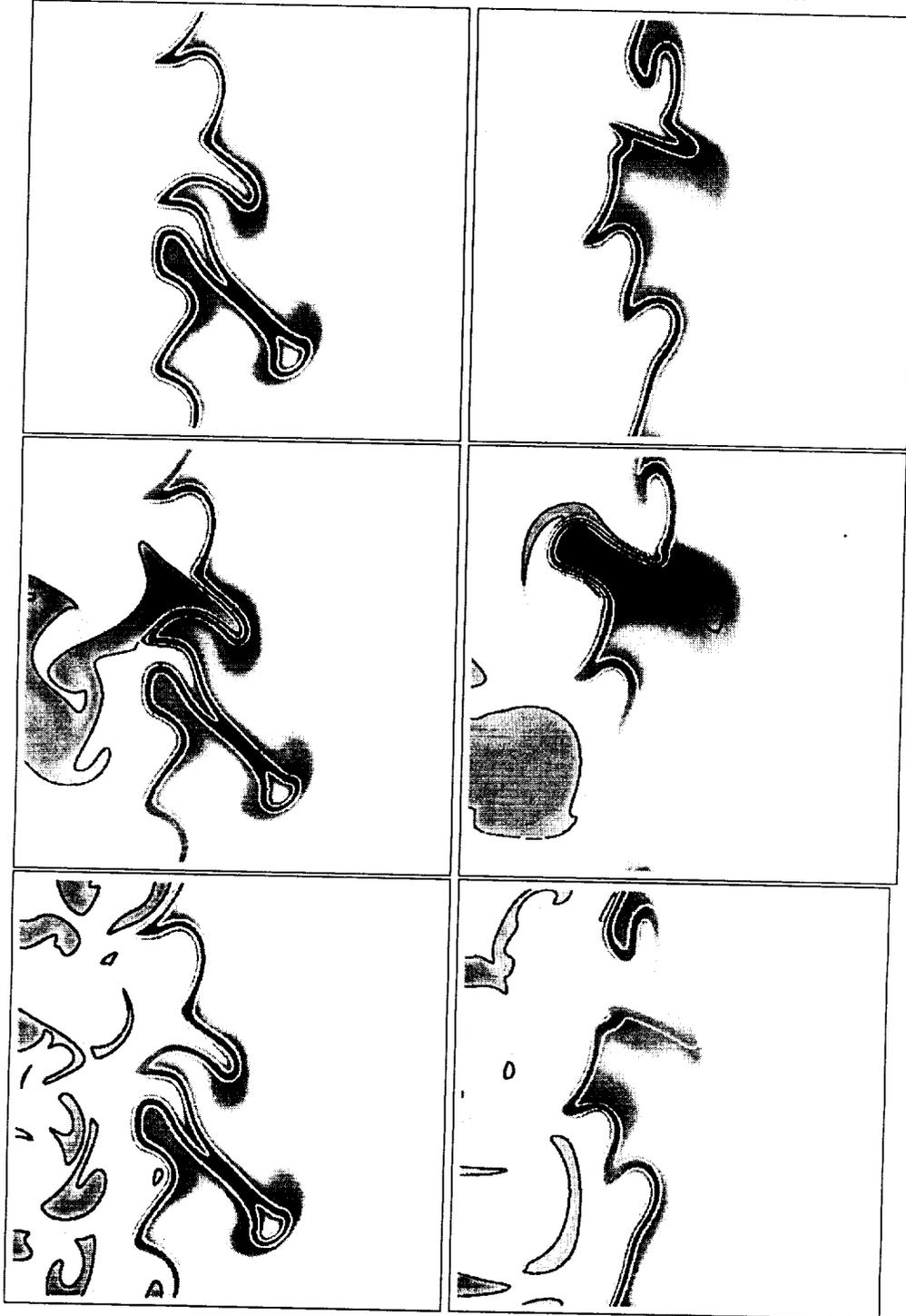
FIGURE 3. Heat release (marked by white lines representing progress variable isocontours) and fuel mass fraction (marked by black line representing the stoichiometric isocontour) fields. Results correspond to times $t/\tau_f = 2$ (left) and $t/\tau_f = 4$ (right) and to r A (top), C1 (middle), and C2 (bottom) simulations. Scale goes from white at zero values to light grey for fuel mass fraction and to black for heat release.
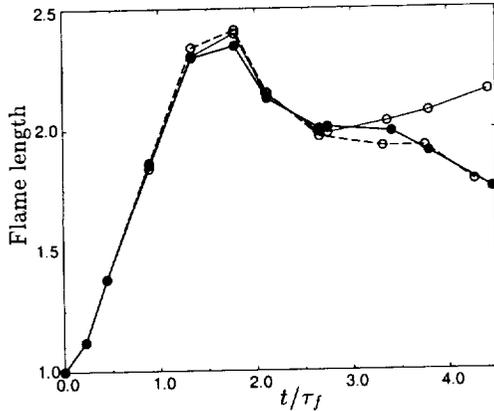
FIGURE 4. Time evolution of flame length in A (-●-), C1 (-○-) and C2 (- -○- -).
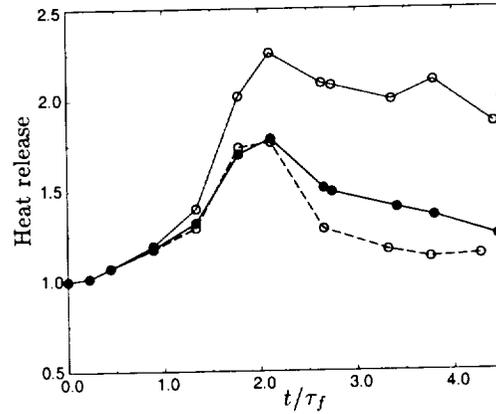
FIGURE 5. Time evolution of global heat release in A (-●-) C1, (-○-) and C2 (- -○- -).

flame front in C1 at the later time, resulting in a longer flame compared to flame A. The flame front is only slightly deformed in simulation C2 as a result of the smaller size of the rich/lean pockets.

Time evolution of the flame length, computed as the length of a progress variable iso-contour ($c = 0.9$), is plotted in Fig. 4. Time is normalized in this figure by the flame time τ_f, and flame length is normalized by the length of the initial laminar planar lean ($\phi = .6$) flame. All three flames present a similar initial increase in length up to time $t/\tau_f = 1.25$, where they all reach twice their initial length. This similar evolution suggests that turbulent wrinkling dominates at this stage. Later, small differences in length appear, with the non-homogeneous flames growing faster than the homogeneous one. These are the first signs of the effect of non-homogeneities and are too small to be visible in Fig. 3. Flame length then decreases in all three cases, probably as the pocket visible in Fig. 3 at time 2 is consumed. At late times flame C1 clearly separates from the other two, presenting a net increase in flame length corresponding to a rapidly propagating close-to-stoichiometric/rich flame segment that can be identified in Fig. 3 in the upper third of C1. Flames A and C2 continue to have similar lengths as expected from the lack of deformation of flame C2.

Figure 5 displays the evolution of global heat release for the same simulations. Heat release is computed by integrating the local heat release over the computational domain and normalizing by the heat release of the initial planar laminar lean ($\phi = .6$) flame. Its rate of increase is smaller than that of flame length; by time 1.25 it has reached only 1.25 times its initial value in all cases. Differences in global heat release increase become significant after this time, with flame C1 increasing much more rapidly than the other two. Since flame length is identical for all three flames up to times > 3, this different behavior must be due to locally greater heat release per unit flame length in C1.

Mean heat release per unit flame length is plotted in Fig. 6. At early times the same decreasing tendency is seen for all three flames, which must be associated with turbulent straining effects. The effects of higher local equivalence ratio in the C1 case begin to dominate after some time. This delay is due to the initial conditions: there is a separation between the initial flame front and the region where non-homogeneities are introduced to avoid numerical problems. The flame must propagate across this separation to reach the rich/lean pockets. In case C2 the mean heat release follows the same trend as in the homogeneous case. While cases C2 and C1 initially have the same mean and fluctuation
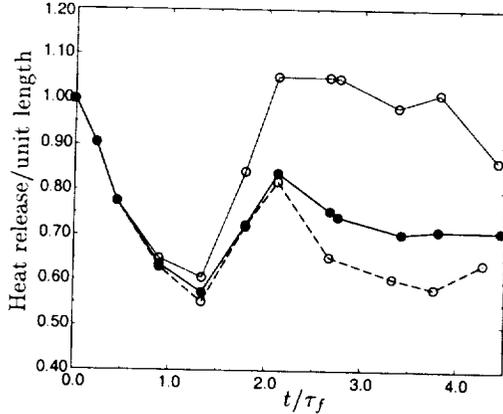
FIGURE 6. Time evolution of mean heat release per unit flame length in A (-•-), C1 (-o-) and C2 (- -o- -).
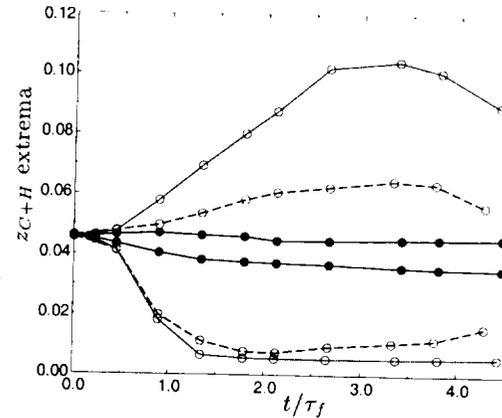
FIGURE 7. Time evolution of the maxima and minima of z_{C+H} on the $c = .9$ isocontour in A (-•-), C1 (-o-) and C2 (- -o- -).

in the equivalence ratio distribution, the smaller length scales of case C2 make turbulent mixing more effective in bringing the mixture towards homogeneity; by the time the flame front reaches the non-homogeneous region, the equivalence ratio fluctuations have been damped.

A somewhat surprising effect is observed at the latest times, where the mean heat release for simulation C2 is even smaller than that of the homogeneous case. This can be explained by local extinction effects in extreme lean zones (see Fig. 3), which are much more important in C2 than in C1. Although the global initial distribution of rich/lean zones is the same for flames C1 and C2 and they eventually evolve towards the same final distribution, the evolution of the distribution on the flame front is quite different. In Fig. 7 the time evolutions of the maximum and minimum values of z_{C+H} at the flame front (given by the $c = 0.9$ isocontour) are plotted for the three simulations. The distribution is clearly shifted to lean values for all three cases, but in C1 it is shifted later to rich values. The effect of shifting towards leaner values is to reduce the mean heat release per unit length, and this could be the explanation for the more important decrease in mean heat release seen in case C2.

This shifting effect was already observed in Poinsot *et al.*, 1996. There it was attributed to a longer residence time, thus a larger probability of occurrence of lean pockets as compared to rich ones due to smaller flame speeds. In the present simulation, this effect is larger for the C2 case as it is probably enhanced by the asymmetrical small-scale initial distribution of inhomogeneities there with richer pockets smaller than lean pockets, thus mixing more rapidly. In case C1, where scales of inhomogeneity are larger, mixing effects are less important and the shift towards leaner values can intermittently be compensated by rich pockets arriving at the flame front (Fig. 7).

5. Post flame characterization

The secondary reaction zone is usually defined by means of the progress variable c as the zone in which primary fuel has totally disappeared ($c > .9999$ or even $c = 1$). As in previous studies, it was found that only a very small portion of the global heat release occurs in this post-primary flame zone. The most important secondary reaction zone in the present simulations, corresponding to case C1, can be seen in Fig. 3 behind the richer

flame segment and close to the stoichiometric line, and represents a very small percentage of the total heat release. In simple chemistry, the fact that the flame is located near the stoichiometric line would directly suggest a diffusion flame, but in complex chemistry this is much more difficult to establish. The secondary flame reactants are not the original reactants, but are species derived from them. The stoichiometric line represents the line at which the C+H and O concentration are in the same proportions as if there were 5 moles of O_2 and 1 of C_3H_8, so that in the global reaction $C_3H_8 + 5O_2 = 3CO_2 + 4H_2O$ they would be totally consumed to produce 3 moles of CO_2 and 4 of H_2O.

But there is no propane in the secondary reaction zone, and the reactions that do occur there do not have the same stoichiometry as the global reaction. Reaction close to global stoichiometry occurs between products of the rich zone (that is, products derived from propane cracking) and products of the lean zone (mainly O and O_2), but does not imply that they are mixed or unmixed.

In Fig. 8 we have tried to illustrate the post flame structure by plotting the mass fractions and production rates of some representative species. All figures correspond to simulation C1 and time $t/\tau_f = 4$, and production rates are plotted so that negative rates are always white and positive rates black. The grey background represents zero net production rate, and the scale has been chosen to allow a better visualization of the secondary flame (it is not linear). The scale for mass fraction is linear with white representing minimum values and black maximum values. The stoichiometric line shows the separation between rich zones in which excess H_2 and CO are found and lean zones in which excess O_2 is found. In examining secondary reaction production rates, it can be seen that O_2 is consumed at the stoichiometric line, suggesting a diffusion flame structure. But for other species reaction is occurring also in other zones: H_2 is consumed right on the stoichiometric line but is then produced in the region delimited by this line, that is, in the rich zone; CO is also consumed in the rich zone. Then H_2 is probably reacting with O_2 in a non-premixed mode, but there are other reactions in which H_2 and CO are involved (as well as other species not shown), occurring in a premixed mode. No clear description in terms of a classical diffusion flame can be depicted for this secondary reaction; in fact, many reactions of different stoichiometries are occurring in the post flame region, and probably some occur in a premixed mode and others in a non-premixed mode.

6. NO formation

NO formation occurs at higher temperatures than those of the primary flame and thus mainly in the post-flame region. Production of NO is enhanced in the non-homogeneous lean cases, as compared to the homogeneous lean case, as higher temperatures and concentrations of O atoms are reached. Figure 9 displays the time evolution of the total mass of NO for simulations A (homogeneous), C1 (non-homogeneous large-scale), and C2 (non-homogeneous small-scale). NO mass is higher in both non-homogeneous cases compared to the homogeneous one, but significant differences exist as well between the two non-homogeneous simulations. While NO mass in case C1 reaches a value 40% higher than in the homogeneous case, in case C2 it is only 5% higher. Higher heat release rates are giving much higher local temperature values in the C1 case compared to C2, which together with higher O concentrations explains this enhanced production effect.
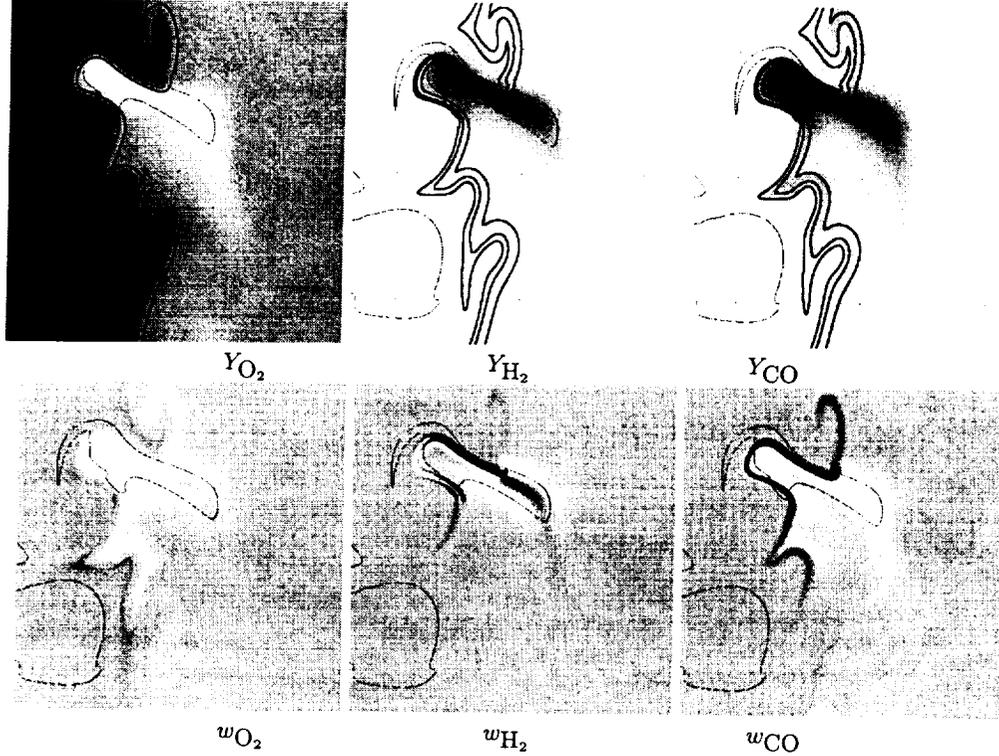
FIGURE 8. Mass fractions (top) and production rates (bottom) of O_2 (left), H_2 (middle) and CO (right) corresponding to C1 at $t/\tau_f = 4$. For reaction rates white represents negative values and black positive values, background grey corresponds to zero net production, and the scale is adapted to emphasize secondary reactions. For mass fractions white represents minimum and black maximum values, and the scale is linear.

7. A test for the flamelet assumption

A simple new test concerning the modeling of the primary flame has been performed in this work by directly comparing the heat release obtained in the DNS with that predicted by a flamelet model. It is usually accepted that a variable equivalence ratio premixed flamelet assumption is well suited for partially premixed combustion, but quantitative testing of this assumption was not feasible with previous DNS results as no significant differences between heat release in non-homogeneous and homogeneous flames were found.

A simplified formulation of this modeling assumption has been adopted here: The turbulent flame is assumed to be locally equivalent to an unstrained premixed laminar flamelet with the same z_{C+H}. By using a library for the heat release associated with a premixed laminar flamelet as a function of mixture fraction $h(z_{C+H})$, modeled heat release was computed as the integral of $h(z_{C+H})$ along a progress variable isocontour $c = c^*$:

$$H = \int_{c=c*} h(z_{C+H}) d\Sigma_{c=c*}.$$

Results of this computation are compared in Fig. 10 to the results of DNS for the homogeneous (A) and the non-homogeneous (C1) cases. The model appears to predict the global heat release remarkably well. Differences at initial times probably are due to the dismissal of strain-rate effects. In Fig. 6 it has been shown that at early times
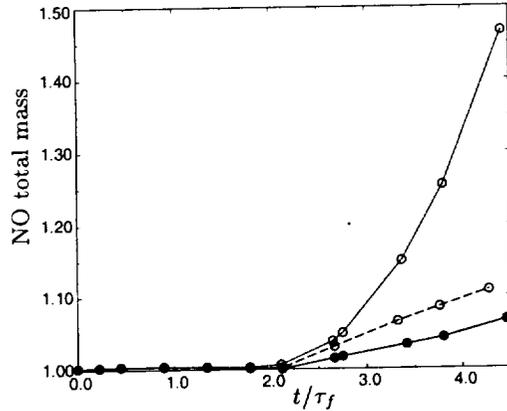
FIGURE 9. Time evolution of NO global mass in A (-●-), C1 (-o-) and C2 (- -o- -) simulations.
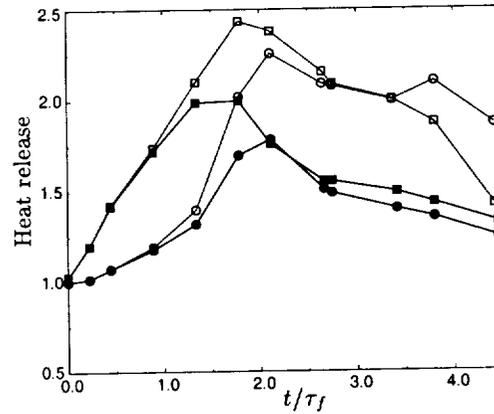
FIGURE 10. Computed and modeled global heat release for cases A (● computed, ■ modeled value) and C1 (o computed and ▢ modeled value).

effects of turbulent strain rate are very important in reducing the mean heat release per unit flame area. Using an unstrained flamelet to compute heat release gives a too-high estimation for the local heat release and results in a high global heat release. Later, the model appears to correctly predict the heat release in both cases, but at the latest times there is an appreciable departure in the non-homogeneous case, with the model predicting a heat release about 60% smaller than that given by simulations.

This could be an effect of temperature mixing: at late times in the non-homogeneous case, temperature may have diffused from locally stoichiometric high-temperature zones to locally leaner or richer zones. The higher temperature may make some flame segments burn fast compared to the equivalent laminar flame. On examination of the picture corresponding to late times in the C1 simulation in Fig. 3, one finds that the high heat release zone corresponding to the stoichiometric reactants is, in fact, extended far beyond the stoichiometric line to reach leaner and richer flame zones. This is an effect that a flamelet model based only on the local equivalence ratio will not be able to predict.

8. Conclusions

Simulations of combustion in a stratified premixed propane-air mixture have been performed under global lean conditions, approaching those of a gasoline direct injection (GDI) engine. Detailed transport, thermodynamics, and chemistry, including thermal NO production, were included, which suggests high reliability of results. However, the low Reynolds number and the two-dimensionality of the turbulence demand some precaution in generalizing directly to practical combustion systems. Substantial differences in the amount of heat release between homogeneous and non-homogeneous reactants have been obtained. This has permitted a detailed study of the different phenomena affecting combustion efficiency in partially premixed systems. In particular, a strong influence of the spatial distribution of the nonhomogeneities on heat release and NO formation was found. Moreover, a quantitative assessment of flamelet models for the primary flame has been made, yielding excellent agreement. A qualitative study of the secondary reaction zone has shown the difficulties that a flamelet interpretation would present.

REFERENCES

BAUM, M., POINSOT, T., HAWORTH, D., & DARABIHA, N. 1994 Direct numerical simulation of $H_2/O_2/N_2$ flames with complex chemistry in two-dimensional turbulent flows. *J. Fluid Mech.* **281**, 1-32.

GLASSMAN, I. 1987 *Combustion.* Academic Press.

HANSON, R. K. & SALIMIAN, S. 1984 *Combustion Chemistry.* Springer-Verlag.

HAWORTH, D., BLINT, R., CUENOT, B., & POINSOT, T. 2000 Numerical simulation of turbulent propane-air combustion with non-homogeneous reactants. *Comb. Flame.* **121**, 395-417.

HAWORTH, D., CUENOT, B., POINSOT, T. & BLINT, R. 2000 Direct numerical simulation of turbulent propane-air combustion with non-homogeneous reactants. In *Eighth International Conference on Numerical Combustion, Amelia Island, FL.*

HAWORTH, D., & POINSOT, T. 1992 Numerical simulations of Lewis number effects in turbulent premixed flames. *J. Fluid Mech.* **244**, 405-436.

HÉLIE, J. & TROUVÉ, A. 1998 Turbulent flame propagation in partially premixed combustion. *27th Symposium (Int.) on Combustion.*

KEE, R. J., MILLER, J. A. & JEFFERSON, T. H. 1980 Chemkin: a general-purpose, problem-independent, transportable FORTRAN chemical-kinetics package. *SANDIA Tech. Report: SAND 83-8003.*

KEE, R. J., WARNATZ, J. & MILLER, J. A. 1983 A FORTRAN computer code package for the evaluation of gas-phase viscosities, conductivities and diffusion coefficients. *SANDIA Tech. Report: SAND 83-8209.*

KRIEGER, R. B., SIEBERT, R. M., PINSON, J. A., GALLOPOULOS, N. E., HILDEN, D. L., MONROE, D. R., RASK, R. B., SOLOMON, A. S. P, & ZIMA, P. 1997 Diesel engines: one option to power future personal transportation vehicles. *SAE paper no. 972683.*

LÉGIER, J. P., POINSOT, T., VEYNANTE, D., & NICOUD, F. 2000 Dynamically thickened flame LES model for premixed and non-premixed combustion. *Proc. Summer Program,* Center for Turbulence Research, NASA Ames/Stanford Univ., this volume.

LELE, S. K. 1992 Compact finite difference schemes with spectral-like resolution. *Journal of Computational Physics.* **103**, 16-42.

PETERS, N. 2000 *Turbulent Combustion.* Cambridge Univ. Press.

POINSOT, T., VEYNANTE, D., TROUVÉ, A., & RUETSCH, G. 1996 Turbulent flame propagation in partially premixed flames. *Proc. Summer Program,* Center for Turbulence Research, NASA Ames/Stanford Univ. 111-136.

TAKAGI, Y. 1998 A new era in spark-ignition engines featuring high-pressure direct injection. *27th Symposium (Int.) on Combustion.*

ZHAO, F. Q., LAI, M. C., & HARRINGTON, D. L. 1999 Automotive spark-ignited direct-injection gasoline engines. *Prog. Energy Combust. Sci.* **25**, 437-562.

ZHOU, J., NISHIDA, K., YOSHIKAZI, T. & HIROYASU, H. 1998 Flame propagation characteristics in a heterogeneous concentration distribution of a fuel-air mixture. *SAE paper no. 982563.*

A probability density function/flamelet method for partially premixed turbulent combustion

By D. C. Haworth†

A methodology is formulated to accommodate detailed chemical kinetics, realistic turbulence/chemistry interaction, and partially premixed reactants in three-dimensional time-dependent device-scale computations. Specifically, probability density function (PDF) methods are combined with premixed laminar flamelet models to simulate combustion in stratified-charge spark-ignition reciprocating-piston IC engines. A hybrid Lagrangian/Eulerian solution strategy is implemented in an unstructured deforming-mesh engineering CFD code. Modeling issues are discussed in the context of a canonical problem: one-dimensional constant-volume premixed turbulent flame propagation. Three-dimensional time-dependent demonstration calculations are presented for a simple pancake-chamber engine.

1. Introduction

In most practical combustion devices, the conversion of chemical energy to sensible energy takes place in a turbulent flow environment. A variety of turbulent combustion models have been implemented in computational fluid dynamics (CFD) codes to facilitate device-scale analysis and design. In general, a different modeling approach has been required to deal with each combustion regime (e.g., premixed versus nonpremixed). Next-generation low-emission/low-fuel-consumption combustion systems are characterized by multiple combustion regimes, i.e., "mixed-mode" or "partially premixed" turbulent combustion. Examples include lean premixed combustion systems for reducing NO_X emissions from gas-turbine combustors and gasoline direct-injection spark-ignition engines for reducing the fuel consumption of personal transportation vehicles (Zhao, Lai & Harrington 1999).

Next-generation turbulent combustion models for device-scale CFD also must include detailed chemical kinetics and must be suitable for three-dimensional time-dependent calculations (e.g., large-eddy simulation - LES) in complex geometric configurations. More chemistry is required to deal with kinetically controlled phenomena (e.g., low-temperature autoignition) to predict trace pollutant species (e.g., NO_x, unburned hydrocarbons, particulate matter) and to address fuel-composition issues (e.g., alternative fuels and fuel additives). Increasingly, the phenomena of interest are inherently three-dimensional and time-dependent. For example, it is unlikely that statistically stationary computations will suffice to address combustion instabilities in gas-turbine combustors. And the ensemble-averaged formulation that has been dominant in piston-engine modeling (e.g., Khalighi *et al.* 1995) cannot capture cycle-to-cycle flow and combustion variability.

Thus an outstanding modeling/methodology issue in turbulent combustion can be

† The Pennsylvania State University

stated as: how can increasingly complex chemical kinetics, realistic turbulence/chemistry interaction, and multiple combustion regimes be accommodated in three-dimensional time-dependent device-scale CFD? It is the purpose of this report to formulate, implement, and provide an initial demonstration of an approach that addresses this question.

The model is a hybrid of two of the most promising approaches for turbulent reacting flows: probability density function (PDF) methods and laminar flamelet models. PDF methods have the important advantage that the mean chemical source term appears in closed form; molecular transport ("mixing") remains to be modeled (Pope 1985). While advantages of PDF methods have been amply demonstrated in laboratory configurations, device-scale application has been slowed by the unconventional Lagrangian particle-based algorithms that are used to solve PDF transport equations numerically. Flamelet models, on the other hand, maintain strong coupling between chemical reaction and molecular transport (Peters 2000). However, the coupling is correct only under specific (essentially boundary-layer-like) conditions, which are not always valid in practical combustion devices. In cases where flamelet combustion does occur (e.g., homogeneous flame propagation in a stoichiometric premixed spark-ignition engine), flamelet models have proven highly successful. It is relatively straightforward to implement flamelet models in standard Eulerian grid-based CFD codes.

Following earlier work on PDF methods for complex geometric configurations, a hybrid Lagrangian/Eulerian strategy is adopted. Several implementation issues including mean estimation, particle tracking through unstructured deforming meshes, and particle number density control have been addressed by Subramaniam & Haworth (2000). There a composition PDF method and Reynolds-averaged (RANS) formulation were used to model turbulent mixing with large density variation in an engine-like configuration. Other key issues in Lagrangian/Eulerian PDF methods have been addressed by Muradoglu *et al.* (1999).

The present report expands on Subramaniam & Haworth (2000) in several respects. First, heat release is included. Second, a hybrid PDF/flamelet method is formulated to take advantage of the strengths of each these two modeling approaches. Third, both velocity-composition PDF and composition PDF methods are explored. Fourth, physical and numerical issues are discussed in the context of a canonical problem (turbulent premixed flame propagation in a one-dimensional constant-volume chamber). And finally, preliminary three-dimensional time-dependent RANS computations are presented for a simple piston-engine configuration.

2. Formulation

The approach is developed in the context of a stratified-charge gasoline-direct-injection spark-ignition piston engine. A three-stage combustion process is postulated (Fig. 1). By design, a healthy propagating premixed flame is established initially via spark discharge at a location where the composition is close to stoichiometric. Soon (within a few millimeters, depending on engine operating conditions), the flame encounters fuel-rich and fuel-lean mixtures. Behind the flame in locally fuel-rich zones are combustion products and fuel fragments (mainly the stable intermediates CO and H_2, to be precise); behind the flame in locally fuel-lean zones are combustion products and oxygen. Eventually the post-flame fuel fragments and oxygen combine to complete the heat-release process. Stage I aerothermochemical processes (in front of the primary flame) include turbulent mixing and low-temperature chemistry (e.g., autoignition, under suitable operating con-
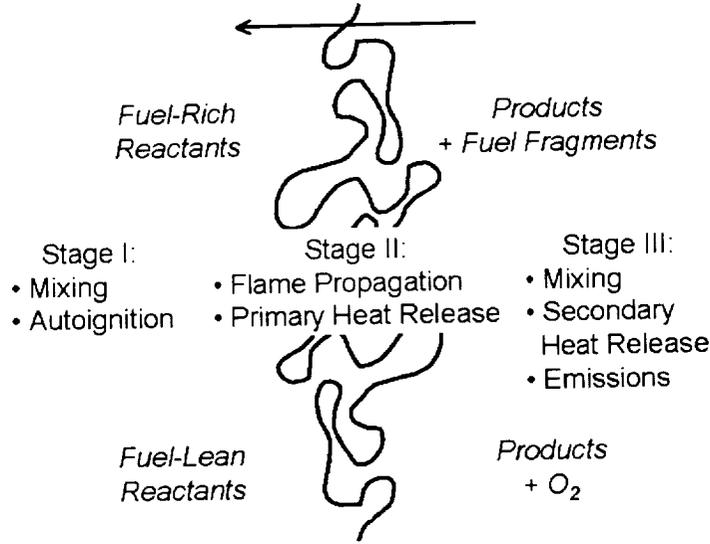
FIGURE 1. A three-stage combustion process for partially premixed reactants.

ditions). Stage II comprises flame propagation and the primary heat release. And Stage III (behind the primary flame) includes turbulent mixing, secondary heat release, and the finite-rate chemistry that characterizes key pollutant-formation processes such as CO burnout, NO_x formation, and soot formation/oxidation.

Finite-rate chemistry and turbulence/chemistry interaction in Stages I and III are naturally described using a PDF formulation, while the flame propagation of Stage II is amenable to laminar flamelet modeling. The essence of the approach is to combine these two models in a consistent manner that deals naturally with all three regimes.

2.1. Governing equations

Reynolds-averaged equations are used in density-weighted (Favre-averaged) form. Thus the PDF's considered formally are mass-density functions (Pope 1985). A multicomponent reacting ideal-gas mixture comprising N_S chemical species is considered. At low Mach number, the mixture mass density ρ and chemical production rates $\underline{S}$ are functions of species mass fractions $\underline{Y}$, enthalpy h, and a reference pressure p_0 that is, at most, a function of time: $\rho = \rho(\underline{Y}, h, p_0(t))$, $\underline{S} = \underline{S}(\underline{Y}, h, p_0(t))$. Key Eulerian equations express conservation of mixture mass, momentum, enthalpy, and species mass. A conventional two-equation $\tilde{k} - \tilde{\epsilon}$ turbulence model with wall functions is invoked (e.g., Khalighi *et al.* 1995). The mean momentum and enthalpy equations have the form:

$$\frac{\partial[\langle\rho\rangle\tilde{u}_i]}{\partial t} + \frac{\partial[\langle\rho\rangle\tilde{u}_j\tilde{u}_i]}{\partial x_j} = -\frac{\partial\langle p\rangle}{\partial x_i} + \frac{\partial(\langle\tau_{ji}\rangle + \tau_{T,ji})}{\partial x_j} , \qquad (2.1)$$

$$\frac{\partial[\langle\rho\rangle\tilde{h}]}{\partial t} + \frac{\partial[\langle\rho\rangle\tilde{u}_j\tilde{h}]}{\partial x_j} = \frac{\partial\langle p\rangle}{\partial t} + \tilde{u}_j\frac{\partial\langle p\rangle}{\partial x_j} + \mu(\frac{\partial\tilde{u}_i}{\partial x_j} + \frac{\partial\tilde{u}_j}{\partial x_i})\frac{\partial\tilde{u}_i}{\partial x_j} + \langle\rho\rangle\tilde{\epsilon}$$

$$- \frac{2}{3}\mu\frac{\partial\tilde{u}_i}{\partial x_i}\frac{\partial\tilde{u}_j}{\partial x_j} + \frac{\partial}{\partial x_j}\Big[(\frac{\lambda}{C_p} + \frac{\mu_T}{\sigma_{T,h}})\frac{\partial\tilde{h}}{\partial x_j}\Big] . \qquad (2.2)$$

Here $\underline{u}$ denotes velocity, p pressure, and h enthalpy: $h \equiv \sum_{\alpha=1}^{N_S} Y_\alpha \left(\Delta h_{f,\alpha}^0 + \int_{T^0}^T C_{p,\alpha}(T')dT' \right)$, $\Delta h_{f,\alpha}^0$ being the species-α formation enthalpy at reference temperature T^0. The viscous stress is $\tau_{ji} = \mu(\partial u_j/\partial x_i + \partial u_i/\partial x_j) - \frac{2}{3}\mu\partial u_l/\partial x_l \delta_{ji}$. A tilde $\sim$ denotes a Favre-averaged mean quantity, while angled brackets $\langle \rangle$ are used for the conventional mean; a double-prime denotes a fluctuation about the Favre mean. Mixture molecular transport coefficients are the viscosity μ and thermal conductivity λ; C_p is the mixture specific heat (at constant pressure). The effective turbulent stress is $\tau_{T,ji} = -\langle\rho\rangle\widetilde{u_j''u_i''} = \mu_T(\partial\tilde{u}_j/\partial x_i + \partial\tilde{u}_i/\partial x_j) - \frac{2}{3}\mu_T\partial\tilde{u}_l/\partial x_l\delta_{ji} - \frac{2}{3}\langle\rho\rangle\tilde{k}\delta_{ji}$ where $\mu_T = C_\mu\langle\rho\rangle\tilde{k}^2/\tilde{\epsilon}$ is the effective turbulence viscosity and C_μ is a standard $\tilde{k} - \tilde{\epsilon}$ model constant. The turbulent Prandtl number is $\sigma_{T,h}$.

A modeled PDF transport equation governs the mixture's thermochemical state. This equation is solved using a Lagrangian method for a large number N_P of notional particles. In the case of a composition PDF, the position and composition of the ith particle ($i = 1, \ldots, N_P$) evolve by,

$$\underline{x}^{(i)}(t + \Delta t) = \underline{x}^{(i)}(t) + \tilde{\underline{u}}(\underline{x}^{(i)}(t),t)\Delta t + \Delta\underline{x}_{turb}^{(i)} \ ,$$
$$\underline{\Phi}^{(i)}(t + \Delta t) = \underline{\Phi}^{(i)}(t) + \underline{S}^{(i)}(\underline{\Phi}^{(i)}(t),p_0(t))\Delta t + \Delta\underline{\Phi}_{mix}^{(i)} \ . \tag{2.3}$$

Here $\underline{\Phi}^{(i)}(t)$ denotes the vector of composition variables required to specify the thermochemical state of the mixture (e.g., mass fractions and enthalpy), $\Delta\underline{x}_{turb}^{(i)}$ is the increment in particle position due to turbulent diffusion in time interval Δt, and $\Delta\underline{\Phi}_{mix}^{(i)}$ is the increment in particle composition due to molecular mixing.

The above equations are supplemented by a thermal equation of state $\rho = \rho(\underline{Y}, T, p_0(t))$, a caloric equation of state $T = T(\underline{Y}, h, p_0(t))$, fluid property specification (molecular transport coefficients and specific heats), and a chemical reaction mechanism $\underline{S} = \underline{S}(\underline{Y}, h, p_0(t))$. Additional equations are introduced in Section 2.3.

2.2. *Solution algorithm*

The CFD code solves the Reynolds- (Favre-) averaged compressible equations for a multicomponent reacting ideal-gas mixture using a finite-volume method on an unstructured deforming mesh of (primarily) hexahedral volume elements. Collocated cell-centered variables are used with a segregated time-implicit pressure-based algorithm similar to SIMPLE or PISO. The discretization is first-order in time and up to second-order in space. Further information can be found in Subramaniam & Haworth (2000).

2.3. *Physical models*

A hierarchy of models is considered. This staged development is intended to elucidate key aspects of the approach.

2.3.1. *Model 1*

Model 1 comprises infinitely fast chemistry, constant specific heats and molecular transport coefficients, and a composition PDF for a single scalar reaction progress variable c that ranges from zero in unburned reactants to unity in burned products (perfectly premixed reactants). Heat release is specified via a parameter which corresponds to the normalized temperature rise across an adiabatic flame: $\beta \equiv -\Delta h_f^0/(C_p T_{ref})$. Temperature and density then are simple functions of c: $T = h/C_p + c\beta T_{ref}$; $\rho = p/RT$ ($R = C_p - C_v$).

Turbulent diffusion is modeled as a diffusion process in physical space,

$$\Delta x_{turb}^{(i)} = [\nabla \Gamma_{T,c}/\langle \rho \rangle]_{\underline{x}^{(i)}(t)} \Delta t + [2\Delta t \Gamma_{T,c}/\langle \rho \rangle]^{1/2}_{\underline{x}^{(i)}(t)} \underline{\eta} \quad . \tag{2.4}$$

Here $\Gamma_{T,c} = C_\mu \langle \rho \rangle \sigma_{T,c}^{-1} \widetilde{k}^2/\widetilde{\epsilon}$ is a turbulent diffusivity and $\underline{\eta}$ is a vector of independent identically distributed standardized (zero mean, unit variance) Gaussian random variables.

In a laminar flamelet, chemical reaction and molecular transport are, in principle, treated exactly: $\Delta c^{(i)} = [S + \rho^{-1}\partial(\Gamma \partial c/\partial x_j)/\partial x_j]_{c^{(i)}(t)}\Delta t$. That is, both are known from the given laminar flame profile. At high Damköhler number, however, direct implementation is impractical. The length and time scales associated with the flamelet are much smaller than those associated with the PDF evolution; the latter correspond to the turbulence integral scales. Instead, following Anand & Pope (1987) the fast-chemistry limit is treated as:

$$c^{(i)}(t + \Delta t) = c^{(i)}(t) + \Delta c^{(i)}_{reaction} + \Delta c^{(i)}_{mix} \quad . \tag{2.5}$$

Here $\Delta c^{(i)}_{reaction}$ takes $c^{(i)}$ to unity as soon as $c^{(i)}$ exceeds c_{thresh} (a small positive number, of the order of the reciprocal of the Damköhler number); and $\Delta c^{(i)}_{mix}$ denotes a conventional turbulence mixing model. Here a stochastic pair-exchange model is used (Pope 1985).

Thus for Model 1, Eqs. (2.1) and (2.2) plus modeled equations for $\widetilde{k}$ and $\widetilde{\epsilon}$ are solved by a finite-volume method, and the PDF of the reaction progress variable c is computed using a stochastic particle method (Eqs. 2.3-2.5). Mean velocity and turbulence scales are passed from the finite-volume side to the particle side; and the mean density $\langle \rho \rangle$ (computed using the mean-estimation algorithm described in Subramaniam & Haworth 2000) is passed from the particle side to the finite-volume side.

2.3.2. *Model 2*

Model 2 retains the thermochemistry of Model 1 and replaces the composition PDF with a velocity-composition PDF. In this case, a finite-volume $\widetilde{k}$ equation is not needed; the turbulent stress in Eq. (2.1) and the turbulence kinetic energy $\widetilde{k}$ are computed as,

$$\tau_{T,ji} = -\langle \rho \rangle \widetilde{u''_j u''_i} \quad , \quad \widetilde{k} = (\widetilde{u''_1 u''_1} + \widetilde{u''_2 u''_2} + \widetilde{u''_3 u''_3})/2 \quad , \tag{2.6}$$

where $\widetilde{u''_j u''_i}$ is computed from particle velocities. A standard $\widetilde{\epsilon}$ equation provides the necessary turbulence scales.

The PDF transport equation is modeled and solved by considering the positions, compositions (progress variable c), and velocities of N_P notional particles. Particle progress variable is governed by Eq. (2.5) while particle positions and velocities evolve according to,

$$\underline{x}^{(i)}(t + \Delta t) = \underline{x}^{(i)}(t) + \underline{u}^{(i)}(t)\Delta t \quad ,$$
$$\underline{u}^{(i)}(t + \Delta t) = \underline{u}^{(i)}(t) - \rho^{(i)\,-1}\nabla \langle p \rangle \Delta t + \Delta \underline{u}^{(i)}_{turb} \quad . \tag{2.7}$$

The particle turbulent velocity increment $\Delta \underline{u}^{(i)}_{turb}$ is modeled using a simplified Langevin equation (Haworth & Pope 1987),

$$\Delta \underline{u}^{(i)}_{turb} = -(\frac{1}{2} + \frac{3}{4}C_0)(\underline{u}^{(i)} - \widetilde{\underline{u}})\Delta t\,\widetilde{\epsilon}/\widetilde{k} + [C_0\widetilde{\epsilon}\Delta t]^{1/2}_{\underline{x}^{(i)}(t)}\underline{\eta} \quad , \tag{2.8}$$

with the model constant $C_0 = 2.1$.

Model 2 is intentionally similar to the model developed by Anand & Pope (1987) for steady one-dimensional constant-enthalpy freely propagating turbulent premixed flames. An important difference is in the solution strategy. There a Lagrangian method limited to the problem considered (steady, one-dimensional, constant-enthalpy, unconfined flame propagation) was used; here a general-purpose three-dimensional time-dependent hybrid algorithm is adopted.

In this case Eqs. (2.1), (2.2), and a dissipation equation are solved on the finite-volume side, while Eqs. (2.5), (2.7), and (2.8) are solved on the particle side. Mean momentum effectively is computed twice: this redundancy is resolved by forcing particle mean velocities to remain consistent with the finite-volume mean. Quantities passed from the finite-volume side are the mean velocity and dissipation rate; the mean density and Reynolds stresses (Eq. 2.6) are passed from the particle side to the finite-volume side.

2.3.3. *Model 3*

In Model 3, flame propagation and primary heat release (Stage II, Fig. 1) are governed by a modeled Eulerian mean-progress-variable equation:

$$\frac{\partial[\langle\rho\rangle\tilde{c}]}{\partial t} + \frac{\partial[\langle\rho\rangle\tilde{u}_j\tilde{c}]}{\partial x_j} = \frac{\partial}{\partial x_j}\left[\left(\Gamma + \frac{\Gamma_T}{\sigma_{T,c}}\right)\frac{\partial\tilde{c}}{\partial x_j}\right] + \langle\rho\rangle\tilde{S}_c \quad . \tag{2.9}$$

The chemical source term corresponds to a premixed laminar flamelet model, e.g., El Tahry (1990):

$$\langle\rho\rangle\tilde{S}_c = \rho_u\tilde{\gamma}/\tau_l \quad , \tag{2.10}$$

where ρ_u is the local unburned gas density, τ_l is a laminar-flame characteristic time, and $\tilde{\gamma}$ is the probability of being in an active reaction front. In general, a modeled transport equation is solved for $\tilde{\gamma}$ (El Tahry 1990); here $\tilde{\gamma}$ is specified algebraically and is proportional to $\tilde{c}(1 - \tilde{c})$. Local unburned-gas properties are needed to determine ρ_u and τ_l; it is important to recognize that these are not available from $\tilde{c}$ and $\tilde{\gamma}$ alone in a moment formulation. In the present formulation, $\rho_u = \langle\rho|c = 0\rangle$, the local mean density conditioned on being in the unburned gas.

Equations of state and fluid properties remain the same as for Models 1 and 2. The chemistry is generalized to allow for arbitrary finite-rate chemistry ahead of (Stage I) and behind (Stage III) the primary flame. A composition PDF for the reaction progress variable c and an arbitrary set of species mass fractions is considered; the latter are passive with respect to the thermochemistry. The value of the particle progress variable is either zero (pre-flame) or one (post-flame); the rate of conversion from $c = 0$ to $c = 1$ is governed by the finite-volume-computed mean (Eq. 2.9). A conventional turbulent mixing model is used (the same pair-exchange model as for Models 1 and 2), but with conditioning on the value of the particle progress variable: pre-flame and post-flame particles cannot mix with one another. The chemical source term also is conditioned on the value of c to allow for different Stage I versus Stage III chemistry:

$$\underline{Y}^{(i)}(t + \Delta t) = \underline{Y}^{(i)}(t) + \underline{S}^{(i)}\left(\underline{Y}^{(i)}(t), c^{(i)}(t), p_0(t)\right)\Delta t + \Delta\underline{Y}_{mix}\big|_{c^{(i)}}^{(i)} \quad . \tag{2.11}$$

Principal finite-volume equations are Eqs. (2.1), (2.2), and (2.9), (2.10) plus equations for $\tilde{k}$ and $\tilde{\epsilon}$. Particle positions and compositions evolve by Eqs. (2.3)-(2.5) and (2.11). Mean velocity, mean progress variable, $\tilde{k}$ and $\tilde{\epsilon}$ are passed from the finite-volume side to particles; $\langle\rho\rangle$, $\underline{Y}$, and the unburned-gas properties required for the flamelet model are passed back.

2.3.4. *Model 4*

Model 4 extends Model 3 to multicomponent reacting ideal-gas mixtures and a library-based premixed laminar flamelet model. This is the form that is intended for use in engineering applications (piston engines, in particular). No Model 4 results are presented in this initial report. A skeletal description is provided to indicate salient model features and issues.

The flamelet model adopted is that developed in El Tahry (1990) and Khalighi *et al.* (1995); this includes a modeled equation for $\tilde{\gamma}$ in addition to Eq. (2.9) for $\tilde{c}$. A library of one-dimensional steady unstrained premixed laminar flames with detailed hydrocarbon-air chemistry is parameterized in terms of pressure, unburned-gas temperature, equivalence ratio (or mixture fraction), and dilution (Blint & Tsai 1998). A particle enthalpy equation is carried to account for enthalpy (or temperature) fluctuations. Because a mean enthalpy equation is carried on the finite-volume side, consistency between the two representations must be maintained (Muradoglu *et al.* 1999). Particle species mass fractions are no longer passive with respect to thermochemistry. A binary particle progress variable is carried as in Model 3. And as in Model 3, the particle progress variable is used to compute local unburned-gas properties and to switch between Stage I and Stage III chemistry. "Jump conditions" from the flamelet library are used to increment particle compositions as $c^{(i)}$ switches from zero to one. For example, flame-front-generated NO (thermal and prompt) from the flamelet library provides the appropriate initial condition for post-flame thermal NO kinetics corresponding to local thermochemical conditions.

3. Results

3.1. *1D premixed flame propagation in a constant-volume chamber*

This configuration has been selected for its relevance to the piston engine and as a natural extension of the freely propagating turbulent premixed flames that have been studied extensively in the literature. The initial flow is quiescent in the mean. Initial turbulence parameters are the turbulence kinetic energy k_0 and turbulence length scale l_0. The initial rms turbulence velocity, turbulence time scale, and dissipation rate then are given by $u_0' = (2k_0/3)^{1/2}$, $\tau_0 = l_0/u_0'$, and $\epsilon_0 = k_0/\tau_0 = (2/3)^{1/2}k_0^{3/2}/l_0$. The turbulence can be forced so that $\tilde{k}$ does not decay in the unburned gas, and the turbulence time scale τ can be constrained to remain equal to τ_0 at all times, effectively replacing the dissipation equation. These definitions and constraints facilitate comparison with Anand & Pope (1987). The computational domain has planes of symmetry at $x = 0$ and $x = L$. The flame is ignited at $x = L$ and propagates towards $x = 0$. As the flame propagates, chamber pressure increases; the Mach number is low so that spatial gradients in pressure remain small.

Computations have been performed for a range of aerothermochemical conditions (p_0, T_0, β, k_0, l_0; forcing versus no forcing of turbulence; constant $\tau = \tau_0$ versus standard $\tilde{\epsilon}$ equation), for different physical models (Model 1, Model 2, Model 3), and for variations in numerical parameters (number of finite-volume cells N_C; number of computational particles N_P). The results presented here correspond to an initial chamber pressure and temperature of $p_0 = 100$ kPa and $T_0 = 300$ K, respectively. The working fluid is an ideal gas having a molecular weight of 24.945 kg/kmol ($\rho_0 = 1$ kg/m^3 at p_0, T_0). The computational domain has a length of $L = 40l_0$. Turbulence is forced and $\tau = \tau_0 = $ constant. A velocity-composition PDF is used (Model 2) with $N_C = 200$, $N_P/N_C \approx 100-200$. For comparison, in a stoichiometric homogeneous-charge automotive
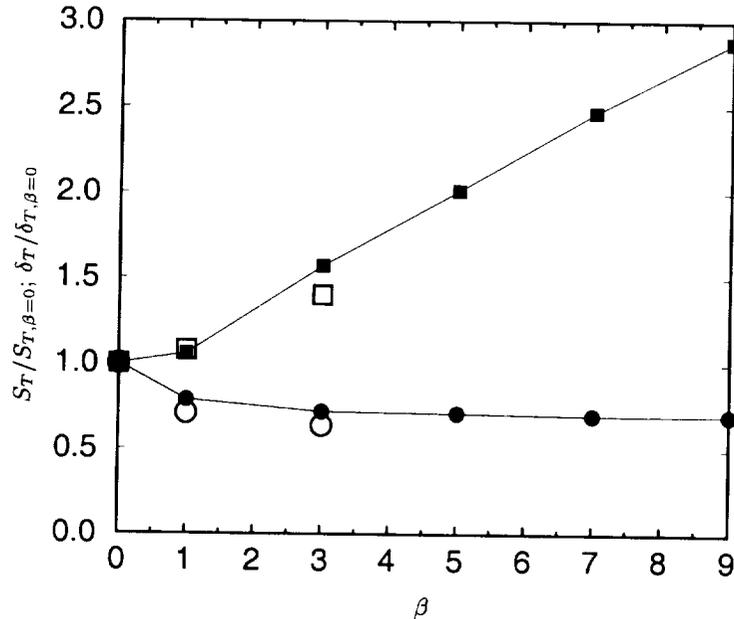
FIGURE 2. Variation of normalized turbulent burning velocity and flame thickness with heat-release for one-dimensional premixed turbulent flame propagation. Open symbols are Model 2 results: ○ $S_T/S_{T,\beta=0}$; □ $\delta_T/\delta_{T,\beta=0}$. Filled symbols are Anand & Pope (1987) results: ● $S_T/S_{T,\beta=0}$; ■ $\delta_T/\delta_{T,\beta=0}$.

spark-ignition piston engine at the time of ignition: the clearance height corresponds to 4-8 turbulence integral scales and the bore diameter to 40-80; the pressure and temperature are approximately 15-20 atm and 700-900 K; the heat release parameter is between $\beta = 5$ and $\beta = 6$ with $T_{ref} = 300$ K; and the ratio of unburned- to burned-gas density is between three and four.

With forced turbulence, flame thickness and propagation speed remain approximately constant away from the end planes ($L/4 < x < 3L/4$, say). For $\beta = 0$, the present results are essentially the same as the $R = 1$ results of Anand & Pope (1987). (The density ratio R used there corresponds to the initial unburned- to burned-gas density ratio for the confined flame with $T_{ref} = T_0$; the density ratio decreases in time for the confined flame.) The quasi-steady mass burning rate (or turbulent flame speed S_T) and turbulent flame thickness δ_T, each normalized by their $\beta = 0$ value, are plotted as functions of β in Fig. 2. Here δ_T is the width of the $\tilde{c} \cdot (1 - \tilde{c})$ profile. Anand & Pope (1987) results are shown for comparison, using $R = R_0 = \beta + 1$. Global trends are consistent with the freely propagating flame results. The mass burn rate initially drops with increasing β and asymptotes to a value that is about 70% of the $\beta = 0$ value. Flame thickness increases with increasing β; the increase is slow initially and becomes approximately linear with β for $\beta > 1$.

The internal structure of the flame at an instant when it has propagated across approximately one-half of the chamber is shown in Fig. 3 ($\beta = 3$). The mean velocity is zero at $x = 0$ and $x = L$; there is expansion ($\partial \tilde{u}/\partial x > 0$) through the flame while the gases ahead of and behind the flame are compressed ($\partial \tilde{u}/\partial x < 0$). A consequence of this
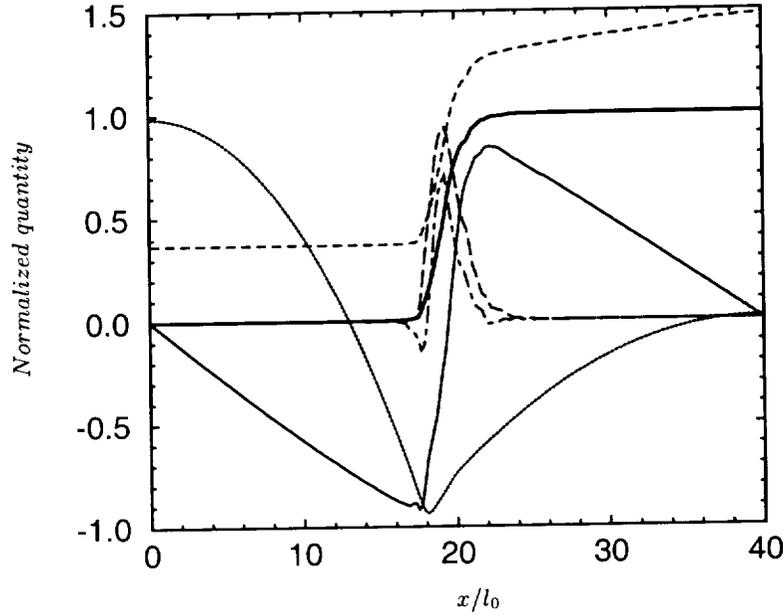
FIGURE 3. Turbulent flame structure at time $t/\tau_0 = 4.62$ for one-dimensional premixed flame propagation in a constant-volume chamber (Model 2, $\beta = 3$): —— $\tilde{c}$; —— $\tilde{u}/u_0'$; ·········· $p'/(100\rho_{u,0}k_0)$; - - - - $T/1000$ K; — — — — $\widetilde{c''^2}$; — · — · $\widetilde{u''c''}/u_0'$.

compression is the positive temperature gradient ($\partial T/\partial x > 0$) behind the flame, which results from compressional heating terms in the enthalpy equation (Eq. 2.2).

An important difference between the confined flame and a freely propagating flame is the mean pressure gradient $\partial \langle p \rangle/\partial x$. In Fig. 3, $p'(x) = \langle p(x) \rangle - L^{-1} \int_0^L \langle p(x) \rangle dx$ is the difference between the local mean pressure and the volume-mean chamber pressure. In a steady freely propagating flame, the mean momentum equation reduces to an expression relating the gradient in $\langle p \rangle$ to gradients in $\widetilde{u''^2}$ and $\tilde{c}$ (Eq. 17 of Anand & Pope 1987); this simplification cannot be made for the unsteady confined flame. The pressure gradient can have a significant influence on flame structure. In particular, $\partial \langle p \rangle/\partial x < 0$ results in preferential $+x$ acceleration of lower-density products ($c = 1$) compared to higher-density reactants ($c = 0$). For sufficiently high density ratio and $|\partial \langle p \rangle/\partial x|$, there is countergradient diffusion in the mean: $\widetilde{u''c''}$ becomes positive, corresponding to a turbulent flux up the gradient in $\tilde{c}$. Countergradient diffusion is evident through much of the flame thickness at the instant plotted in Fig. 3. However, $\widetilde{u''c''}$ varies considerably in response to changes in the pressure profile as the flame advances.

3.2. A simple reciprocating-piston engine

As an initial demonstration for a three-dimensional time-dependent configuration, Model 3 (a composition PDF) is applied to a simple piston engine. Fluid property specification is the same as for the one-dimensional flame-propagation example, and $\beta = 6$ at $T_{ref} = 300$ K. A coarse mesh of 7,695 volume elements represents a pancake (flat head and piston) combustion chamber having 0.5 L displacement volume (86 mm bore × 86 mm stroke) and a geometric compression ratio of 10:1. Nominal particle number density is
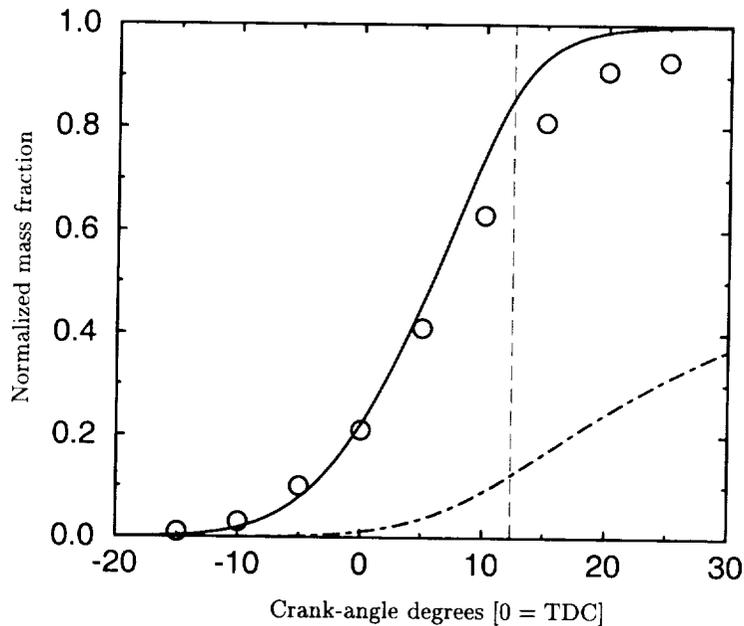
FIGURE 4. Mass-burned fraction and global species 3 mass fraction versus crank angle degrees of rotation for a simple pancake-chamber engine, Model 3: —— computed mass-burned fraction; — — — computed $10^4 \cdot Y_{3,global}$; o measured mass-burned-fraction curve (typical); — — — computed location of peak pressure.

25 per cell. Computations are initialized at piston bottom-dead-center; initial pressure and temperature are 100 kPa and 300 K, respectively. The initial mean velocity field has a swirl ratio of 2.0 (angular momentum about the cylinder axis, divided by the fluid moment of inertia about that axis and normalized by the crankshaft rotational speed) and a tumble ratio of 1.0 (similarly normalized angular momentum about an axis normal to the cylinder axis). The initial turbulence kinetic energy is two times the mean piston speed, and the initial turbulence integral length scale is 10 mm. Engine speed is 1200 r/min with ignition at 25 crank-angle degrees before piston top-dead-center. All walls (head, liner, and piston) are isothermal at 600 K.

Three species are carried in addition to the reaction progress variable c. Species 1 and 2 correspond to two trace contaminants that initially are segregated in the axial (z) direction: ($Y_1 = 1$, $Y_2 = 0$ for $z < (z_{piston} + z_{head})/2$; $Y_1 = 0$, $Y_2 = 1$ for $z \geq (z_{piston}+z_{head})/2$). The third species is the product of chemical reaction between species 1 and 2. An irreversible finite-rate Arrhenius reaction of the form $S_3 = AY_1Y_2\exp\{-T/T_a\}$ ($S_1 = S_2 = -S_3/2$) is used with $A = 1$ s^{-1} and $T_a = 10,000$ K. This reaction occurs only after species 1 and 2 have mixed to the molecular level; moreover, because of the high activation temperature, the reaction rate becomes significant only after the primary flame has passed. Species 3 represents a generic trace pollutant.

Computed mass-burned fraction through the combustion event is plotted in Fig. 4. Burn duration corresponds to 50-60 crank-angle degrees of rotation, and the computed location of peak pressure is 12.5° after top-dead-center: there are reasonable values. A typical measured mass-burned fraction curve for an open-chamber engine under similar

operating conditions is shown for reference. Experimental curves typically asymptote to less than 100% total mass burned because of blowby past piston rings and other effects not present in the model. This figure shows that the global rate of heat release (governed by Eulerian flamelet equations, with local unburned-gas properties taken from the particles) is captured reasonably well. The final curve on Fig. 4 shows the computed global mass fraction of pollutant species 3.

4. Concluding remarks

Hybrid PDF/premixed laminar flamelet models and a hybrid Lagrangian/ Eulerian solution methodology have been formulated, implemented, and demonstrated. These provide a framework for incorporating detailed chemical kinetics, realistic turbulence/chemistry interaction, and mixed-mode combustion (Fig. 1) in three-dimensional time-dependent CFD for device-scale applications. The philosophy has been to use the model that most naturally represents the physics at each stage of the combustion process. The principal issue is integration of the different models in a consistent and natural way. While the development has been carried out with spark-ignition piston engines in mind, model formulation and numerical methodology, and to a lesser extent the specific physical models adopted, are intended to be broadly applicable to other mixed-mode combustion systems. Moreover, the approach is readily extended to subgrid-scale combustion modeling for LES using a filtered-density-function method (e.g., Colucci *et al.* 1998); the key difference is in the specification of appropriate turbulence scales.

Subsequent reports will expand on the preliminary findings reported here. This will include: a deeper discussion of confined propagating turbulent premixed flames and differences with respect to freely propagating flames; presentation of parametric numerical studies; and further results for stratified combustion in piston engines.

Acknowledgments

REFERENCES

ANAND, M. S. & POPE, S. B. 1987 Calculations of premixed turbulent flames by PDF methods. *Combust. Flame.* **67**, 127-142.

BLINT, R. J. & TSAI, P.-H. 1998 C_3H_8-air-N_2 laminar flames calculated for stratified IC engine conditions. *Twenty-Seventh Symposium (International) on Combustion*, The Combustion Institute, Pittsburgh, PA. Poster W1E18.

COLUCCI, P. J., JABERI, F. A., GIVI, P., & POPE, S. B. 1998 Filtered density function for large eddy simulation of turbulent reacting flows. *Phys. Fluids.* **10**, 499-515.

EL TAHRY, S. H. 1990 A turbulent combustion model for homogeneous charge engines. *Combust. Flame.* **79**, 122-140.

HAWORTH, D. C. & POPE, S. B. 1987 A pdf modeling study of self-similar turbulent free shear flows. *Phys. Fluids.* **30**, 1026-1044.

KHALIGHI, B., EL TAHRY, S. H., HAWORTH, D. C., & HUEBLER, M. S. 1995 Computation and measurement of flow and combustion in a four-valve engine with intake variations. *SAE Paper No. 950287.*

MURADOGLU, M., JENNY, P., POPE, S. B., & CAUGHEY, D. A. 1999 A consistent hybrid finite volume/particle method for the pdf equations of turbulent reactive flows. *J. Comput. Phys.* **154**, 342-371.

PETERS, N. 2000 *Turbulent Combustion.* Cambridge University Press.

POPE, S. B. 1985 Pdf methods for turbulent reactive flows. *Prog. Energy Combust. Sci.* **11**, 119-192.

SUBRAMANIAM, S. & HAWORTH, D. C. 2000 A pdf method for turbulent mixing and combustion on three-dimensional unstructured deforming meshes. *Int'l. J. Engine Res.* to appear.

ZHAO, F., LAI M.-C., & HARRINGTON, D. L. 1999 Automotive spark-ignited direct-injection gasoline engines. *Prog. Energy Combust. Sci.* **25**, 437-562.

Dynamically thickened flame LES model for premixed and non-premixed turbulent combustion

By J. P. Legier†, T. Poinsot†‡ AND D. Veynante¶

A new LES subgrid scale turbulent combustion model, adapted to combustion regimes which are neither perfectly premixed nor non-premixed, is tested in a simplified configuration. This model does not require any *a priori* assumption on the flame structure and is able to compute flows where both premixed and non-premixed flamelets coexist. Three combustion regimes identified in an experiment conducted at Ecole Centrale Paris, anchored, lifted and blown-off flames, are successfully recovered in numerical simulations.

1. Motivations and objectives

Turbulent flames in most gas turbines are neither perfectly premixed nor perfectly non-premixed and require the development of large eddy simulation (LES) model adapted to this situation. Unfortunately, very few studies have tried to address these problems because they gather the complexities of pure mixing (without combustion) of ignition, of partially or perfectly premixed combustion, and of non-premixed combustion. All of these regimes may be encountered simultaneously in a gas turbine, and a proper model should be able to handle all of them. This is especially true for recent technologies like LPP (lean premixed prevaporized) combustors which are designed to mainly operate in a lean premixed mode but are prone to flame flashback (i.e. a flame propagation upstream of its designed location), a regime dominated by diffusion flames. Being able to predict flashback requires models which are not yet available.

Many LES studies have been published for mixing (Pierce & Moin (1998)), for premixed flames (Bourlioux Moser & Klein (1996), Veynante & Poinsot (1997), Im, Lund & Ferziger (1997), Piana, Ducros & Veynante (1997), Boger *et al.* (1998), Colin *et al.* (2000a)), or for diffusion flames (Desjardins & Frankel (1999), Moin, Pierce & Pitsch (2000)). But all of these models are derived taking explicitly into account the flame topology, premixed or not, thereby limiting the predictive character of simulations when the exact regime of combustion is not *a priori* known.

In the present work, a new model called DTF (Dynamic Thickened Flame) is proposed to compute mixing, diffusion, and premixed flames simultaneously. This objective is achieved modifying the thickened flame model derived for premixed flames. Instead of using a constant thickening factor (Colin *et al.* (2000a)), a local thickening factor F is active only in the vicinity of the flame front ($F > 1$) and relaxes to $F = 1$ (no effect) far away from the flame. A potential advantage of the model is that outside of the flame zones, thickening is suppressed and mixing can be predicted correctly. This point

† CERFACS, Av Coriolis, Toulouse Cedex, France
‡ Institut de Mécanique des Fluides de Toulouse, Institut National Polytechnique de Toulouse and CNRS, 31400 Toulouse CEDEX, France
¶ Ecole Centrale de Paris and CNRS, 92295 Chatenay Malabry CEDEX, France

is important in gas turbines where pure mixing (without chemical reaction), premixed, and non-premixed zones may coexist.

The DTF model (Section 2), is tested in a two-dimensional geometry corresponding to an experimental burner developed at Ecole Centrale Paris and described in Section 3. Simple one-dimensional tests are presented in Section 4. Section 5 presents LES runs and discusses numerical results.

All computations are performed with AVBP, the LES code developed by CERFACS. The numerical scheme is third order both in space and time (Colin & Rudgyard (2000b)).

2. Principle of the Dynamically Thickened Flame (DTF) model

In this work, a simple one-step scheme is used to describe propane/air chemistry:

$$C_3H_8 + 5(O_2 + 3.76N_2) \rightarrow 3CO_2 + 4H_2O + 18.8N_2 \tag{2.1}$$
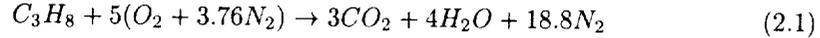
The fuel consumption rate is given by:

$$\dot{\omega}_F = A\nu_F W_F \left(\frac{\rho Y_F}{W_F}\right)^{\nu_F} \left(\frac{\rho Y_O}{W_O}\right)^{\nu_O} \exp\left(-\frac{T_a}{T}\right) \tag{2.2}$$

where T_a is the activation temperature, W_F and W_O are respectively the atomic weights of propane ($W_F = 44$) and oxygen ($W_O = 32$). The prexponential constant A is fitted to provide correct flame speeds for lean premixed flames when compared to full chemistry results. Chemical parameters are:

$$A = 1.65.10^{11} \text{ cgs} \quad ; \quad T_a = 15080\,\text{K} \quad ; \quad \nu_F = 0.5 \quad ; \quad \nu_O = 1 \tag{2.3}$$

The fuel mass fraction Y_F balance equation is:

$$\frac{\partial \rho Y_F}{\partial t} + \nabla \cdot (\rho \mathbf{u}) = \nabla \cdot (\rho \mathcal{D} \nabla Y_F) - \dot{\omega}_F \tag{2.4}$$

where usual notations are retained.

The thickened flame model is an extension of the initial model proposed by Butler & O' Rourke (1977) for premixed flames. These authors showed that multiplying species and heat diffusion coefficients by a factor F (i.e. $\mathcal{D}$ becomes $\mathcal{D}F$) and decreasing the exponential constant by the same factor F (A is replaced by A/F) in Eq. (2.4) provides a flame propagating at the same laminar flame speed s_l^0 than the non-thickened flame but its thickness is increased by a factor F and becomes $\delta_L^1 = F\delta_L^0$. Adjusting F to sufficiently large values (typically between 10 and 100 in most gas turbines) allows the flame to be resolved on an LES grid.

This initial model can be easily extended to dynamic thickening, depending on time and spatial location, by recognizing that a premixed flame where the thickening factor F changes spatially still propagates at the laminar flame speed s_l^0 (Cuenot, 2000, private communication). The mathematical proof of this finding is formally similar to the derivation of the Howarth-Dorodnitzyn transformation introduced to analyze variable density flows under boundary layer approximations as constant density flows (Williams (1985)). The thickening factor F may then be modulated from large values inside the reaction zone (where the reaction rate, inducing large gradients, has to be numerically resolved) to unity away from the flame front (to avoid a modification of mixing description by changing molecular diffusion coefficients), keeping the right propagation speed of a laminar premixed flame. The sensor used to determine whether the flame should be
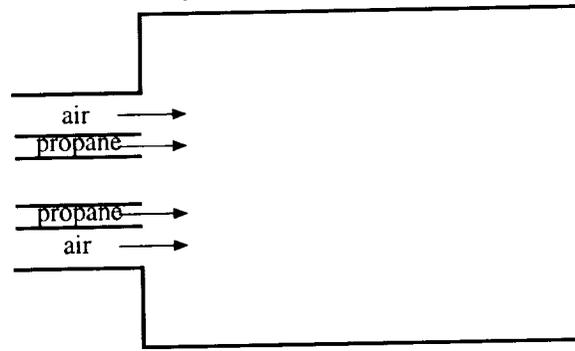
FIGURE 1. Dump-stabilized burner configuration. Experiment developed at EM2C lab., Ecole Centrale Paris, France.

thickened or not is based on a "Arrhenius-like" expression:

$$\Omega = Y_F^{\nu_F} Y_O^{\nu_O} \exp\left(-\Gamma\frac{T_a}{T}\right) \tag{2.5}$$

This sensor detects the presence of the reaction zone but is active in a broader zone than the reaction rate because of the Γ parameter which artificially decreases the activation temperature ($\Gamma < 1$). The sensor Ω controls the value of the thickening coefficient F through:

$$F = 1 + (F_{max} - 1)\tanh\left(\beta\frac{\Omega}{\Omega_{max}}\right) \tag{2.6}$$

where Ω_{max} is the maximum of Ω (which can be determined analytically for a stoichiometric premixed flame) and β is a parameter controlling the thickness of the transition layer between thickened and non-thickened zones.

As shown by Angelberger *et al.* (1998), the thickening procedure allows propagation of the flame on a coarse grid but reduces the flame response to the smallest turbulent motions. To overcome this difficulty, Angelberger *et al.* (1998) and Colin *et al.* (2000a) have derived an efficiency function E to account for the unresolved flame wrinkling. This function E depends on the thickening factor F, the length scale Δ_e/δ_L^0, and the velocity u'_{Δ_e}/s_L^0 ratios (Δ_e is the combustion LES filter size and u'_{Δ_e} the subgrid scale rms velocity) and is used, as a first step, without modification in the present work. In the practical implementation of the thickened flame model, the molecular diffusion coefficient $\mathcal{D}$ is replaced by $EF\mathcal{D}$ and the pre-exponential constant A of the Arrhenius law (Eq. 2.2) by EA/F.

3. Experimental configuration and stability maps

Fig. 1 presents the experimental configuration developed at the EM2C laboratory (Ecole Centrale Paris, France) and used here to test the DTF model. Two propane streams are injected through small slots (5 mm height) into an air coflow. Two backward facing steps (25 mm height each) promote the flame stabilization. The combustion chamber, downstream of the fuel injector lips, is 300 mm long, 100 mm height, and 80 mm depth. The experiment is designed to produce two-dimensional flows to simplify optical diagnostics (CH and C_2 radical emission, laser induced fluorescence on OH radical,...) and model developments and validations. The maximum burner power is 300 kW.
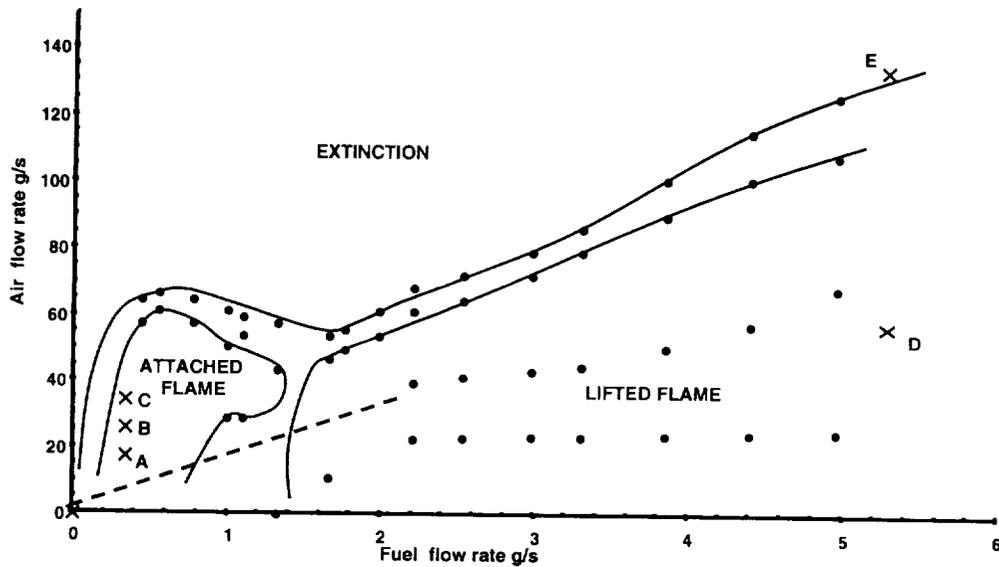
FIGURE 2. Combustion regimes observed in the EM2C burner displayed in Fig. 1 and plotted as a function of the fuel and air mass flow rates. The global stoichiometric line, where fuel and air are injected in stoichiometric proportions, is also indicated.

The burner exhibits various operating regimes, summarized in terms of air and fuel mass flow rates in Fig. 2:

• *Rim stabilized (anchored) flames*: for low fuel and air flow rates powers and, accordingly, low burner powers, flames are stabilized a few millimeters downstream of the fuel injectors (Fig. 3a). This regime corresponds to "anchored" flames.

• *lifted flames*. For higher reactant flow rates (higher powers) and rich overall equivalence ratio (excess of fuel compared to the among of air injected), the flames lift from the injectors and are stabilized a few cm downstream of the injectors in the vicinity of recirculation zones induced by the backward facing steps (Fig. 3b). This regime is referred here as "lifted" (flames are far from the injectors lips) but is very different from the so-called lifted flames encountered in jet diffusion flames without recirculation zones. Here, combustion is stabilized by the hot gases recirculating behind the steps near the injectors.

• *Extinction*. For high reactant flow rates but too lean overall equivalence ratio, the flame gets quenched.

• The transition from one regime to another is accompanied by oscillations (instabilities).

This simplified burner exhibits many characteristics observed in modern gas turbine burners: the existence of multiple flame regimes (anchored or lifted) and of sudden extinctions. This combustor appears, therefore, to be a good test configuration for models.

(a)

(b)
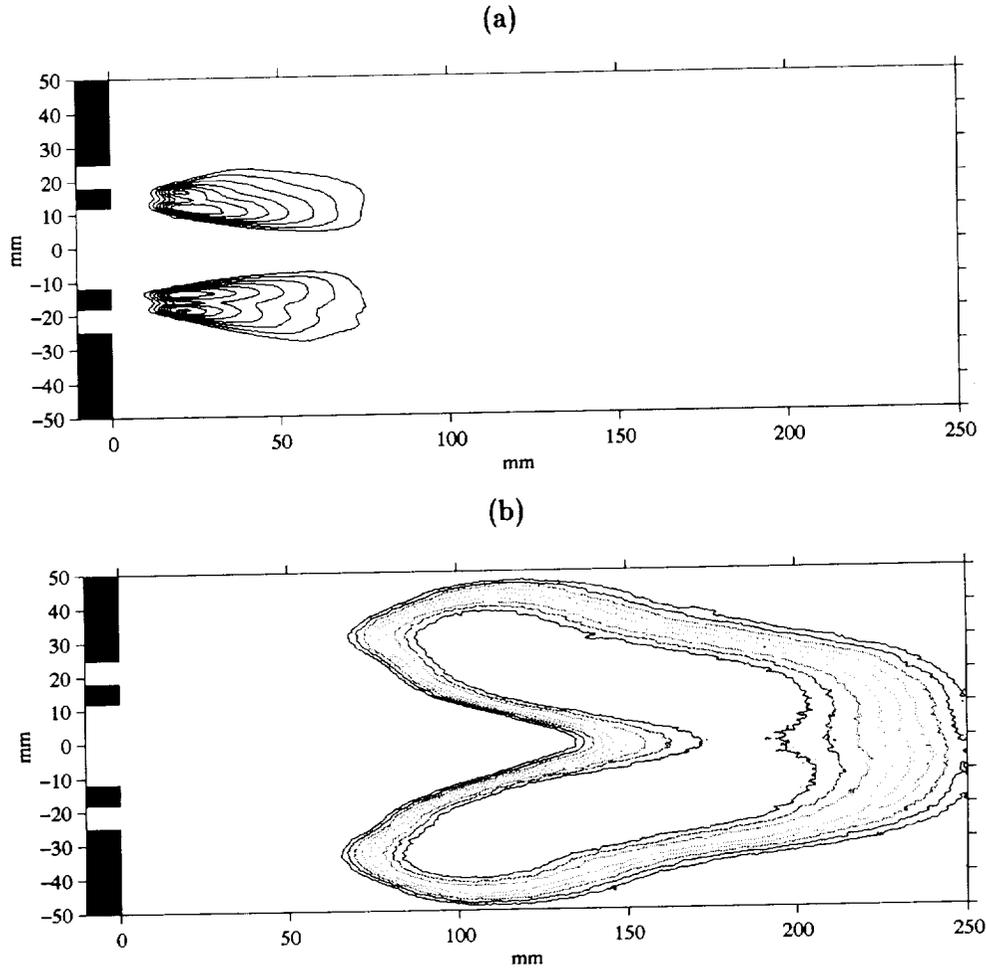
FIGURE 3. Combustion regimes observed in the EM2C burner and visualized using mean CH radical spontaneous emission, corresponding to the mean reaction rate. (a): "anchored flame" regime. The flame is stabilized in the vicinity on the fuel injectors but is not anchored on the lips. (b) "lifted flame" regime where the flame is stabilized by recirculation zones induced by the two backward facing steps. Experiments performed by B. Varoquié, EM2C Lab., Ecole Centrale Paris.

4. One-dimensional laminar premixed flame computations

As a first validation example, one-dimensional laminar premixed flames temperature profiles are compared in Fig. 4 for a non-thickened flame ($F = 1$), a thickened flame with constant thickening factor ($F = 20$ everywhere), and a dynamically thickened flame with $F_{max} = 20$.

For the chosen conditions ($P = 1$ atm, equivalence ratio $\phi = 0.6$, and fresh gases temperature $T_u = 300$ K), all flames propagate at the same speed $s_L^0 = 14$ cm/s. The thickened flames are obviously much broader and can be resolved with coarser grid meshes: the thermal thickness of the unthickened flame is 0.65 mm and becomes 13 mm for the two thickened flames. The dynamically thickened flame is slightly thinner than the initial
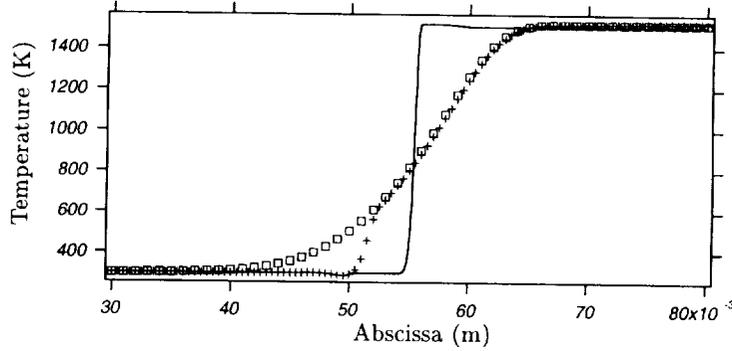
FIGURE 4. Temperature profiles for a non-thickened lean premixed propane/air flame (solid line), a thickened flame with F=20 (squares) and a dynamically thickened flame with $F_{max} = 20$ (crosses). Atmospheric pressure ($P = 1$ atm), fresh gases temperature $T_u = 300$ K, equivalence ratio $\phi = 0.6$.

Case	Fuel flow rate (g/s)	Air flow rate (g/s)	Global equivalence ratio ϕ	Air speed (m/s)	Fuel speed (m/s)	Reynolds number
Anchored (C)	0.33	35	0.15	13	0.6	23000
Lifted (D)	5	58	1.34	23	11	35000
Blow-off (E)	5	145	0.54	55	11	88000

TABLE 1. Operating flow conditions for LES tests. The Reynolds number is evaluated in the outlet section of the burner. The air and fuel speeds correspond to the maximum velocities measured in the air and fuel inlets. The global equivalence ratio ϕ compares the overall amount of fuel and air injected in the burner but is not the local equivalence ratio involved in laminar diffusion flames. Points C, D, and E are also displayed in Fig. 2.

thickened flame in the preheating zone because the sensor Ω is based on a reaction rate type formulation, but differences remain small.

5. LES results

LES were conducted for three regimes, referred to as B, D, and E (see Fig. 2). The first case, (C), corresponds to an anchored flame; in the second one, (D), the flame is lifted whereas a flame blow-off is expected in regime (E). Unresolved fluxes are modeled using a filtered Smagorinsky model (Nicoud & Ducros (1997)), and combustion is described using the DTF model (section 2). Two meshes were used: a coarse grid (62644 nodes) and a fine one (262000 nodes). For these first tests, two-dimensional simulations are performed and only the upper half of the burner is computed (the flow field is assumed to be symmetrical along the burner axis). All model parameters were kept constant for all simulations. Operating flow conditions are summarized in Table 1.
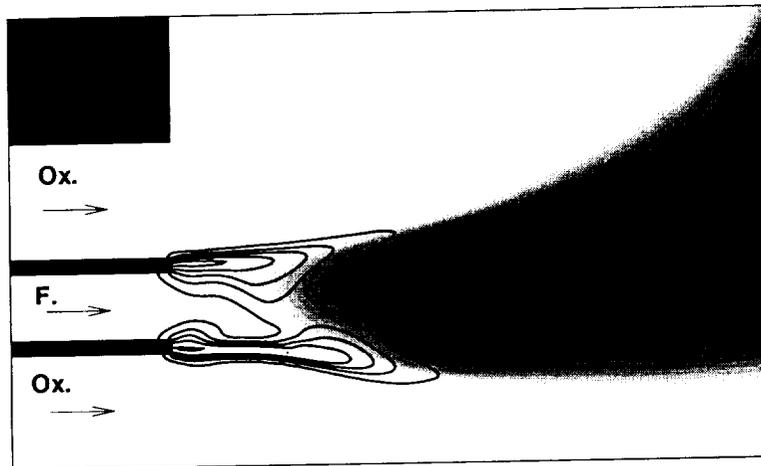
FIGURE 5. Anchored flame (case C): mixing index $Y_F Y_O$ (lines) and temperature (gray-scale) fields. Zoom in the vicinity of the upper fuel injector.

5.1. *Anchored flame (Case C)*

For low reactant flow rates and low powers, flames are stabilized in the vicinity of the fuel injector, but they do not touch the injector. A small lift-off height is observed experimentally (Fig. 3a) as well as in the LES results. Fig. 5 presents a view of the flow close to the fuel injector for case C: the mixing index $Y_F Y_O$ (lines) and the temperature (gray scale) fields are displayed.

The flame is stabilized by a couple of "triple flames": one for the upper air jet and some part of the fuel stream, and another one for the central air jet and the rest of the fuel stream. Even though the attachment region flaps slightly, the structure of the zone close to the injectors appears rather steady. Downstream, pockets of burnt gases oscillate in the duct, but the anchoring mechanism seems unaffected by these flow perturbations. The recirculation zone does not contain hot gases and is not involved in the stabilization process.

5.2. *Lifted flame (Case D)*

For larger reactants flow rates and higher burner powers, the flame cannot remain attached to the injector lips and is stabilized by the recirculation zones. A typical snapshot of the flowfield in case D is presented in Fig. 6: the fuel mass fraction Y_F (gray scale) is superimposed on the reaction rate field and the two stoichiometric lines (bold lines). The first striking feature of this computation is that, even though fuel and oxidizer are injected separately into the burner, only a few flame zones exhibit a diffusion-like structure and lie around the stoichiometric iso-surface; in fact, strong mixing occurs before any combustion starts. When combustion begins, a strong premixed flame is observed. This premixed flame burns rich mixtures and leaves fuel in its product. This fuel can burn with air downstream or in the recirculation zone.

This description is confirmed by cuts performed at two locations (A and B). For location A on Fig. 6, a cut (Fig. 7a) reveals a typical diffusion flame structure where oxidizer and fuel are found on separate sides of the flame front. However, the fuel found at point A is mixed with burnt products so that the diffusion flame structure observed for this point is very different from the usual fuel (cold)/oxidizer configuration used in flamelet models. First, the maximum fuel mass fraction is about $Y_F \approx 0.05$, far from the maxi-
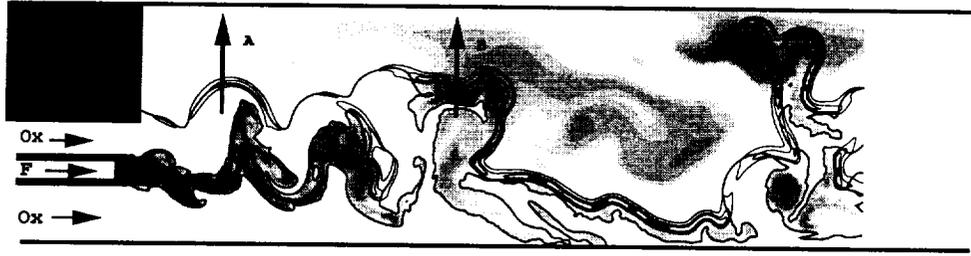
FIGURE 6. Lifted flame (case D): fuel mass fraction Y_F (gray scale) and reaction rate (contour lines) fields are superimposed on the stoichiometric iso-surface (bold lines). Arrows A and B denote locations of cuts displayed in Fig. 7.

(a)   **(b)**
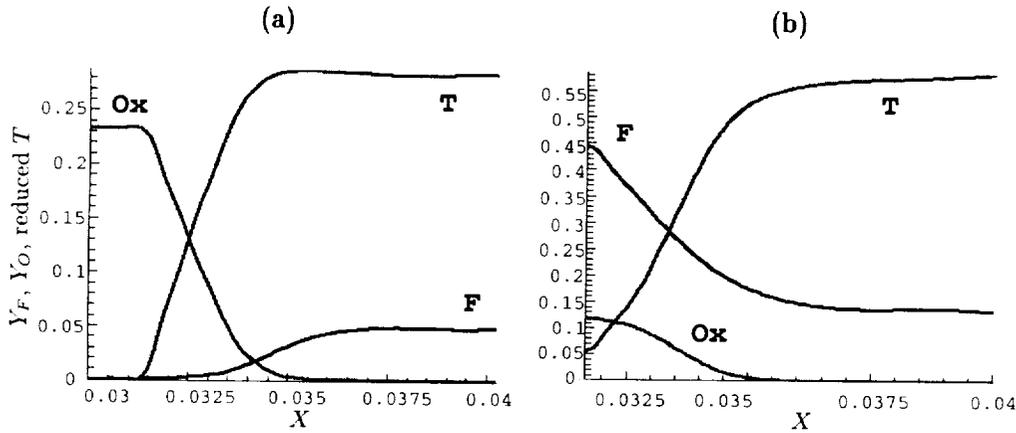
FIGURE 7. Lifted flame (case D): fuel, oxidizer and temperature profiles across the flame front in locations A (left) and B (right) displayed in Fig. 6.

mum value $Y_F = 1$ found in a pure propane/air diffusion flame (the fuel is diluted within burnt gases). The fuel temperature also corresponds to the burnt gases temperature of the previous rich premixed flames. The diffusion flame in location B burns cold oxidizer with a hot mixture of fuel and combustion products. At location B (Fig. 7b), a rich premixed flame is observed: fuel and oxidizer enter the flame front from the same side at a very high equivalence ratio. This premixed flame separates cold fuel/air rich mixture and burnt combustion products.

This occurrence of a rich premixed flame in the flame stabilization process is, *a priori*, surprising but may be easily explained. The mixture fraction z is defined as (Williams (1985)):

$$z = \frac{1}{\Phi + 1}\left(\Phi\frac{Y_F}{Y_F^0} - \frac{Y_O}{Y_O^0} + 1\right) \tag{5.1}$$

where Y_F^0 and Y_O^0 are respectively the fuel and the oxidizer mass fractions in the pure fuel and air streams. $\Phi = sY_F^0/Y_O^0$ is the local equivalence ratio and s the stoichiometric mass coefficient, which corresponds to the mass of oxidizer required to burn a unit mass of fuel. For a propane/air diffusion flame: $Y_F^0 = 1$; $Y_O^0 = 0.23$; $s = 3.64$ and $\Phi = 15.8$. The
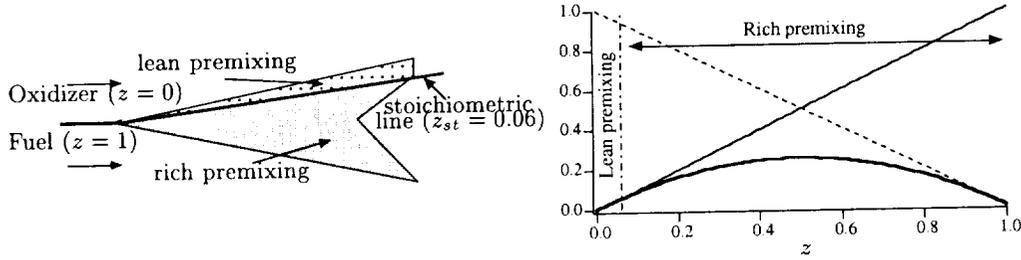
FIGURE 8. Analysis of the rich premixing formation by molecular diffusion when the stoichiometric mixture fraction $z_{st} \approx 0.06$. Left: mixing layer. Right: the fuel (Y_F/Y_F^0; ———), oxidizer (Y_O/Y_O^0; ----) and the mixing index ($Y_F Y_O/Y_F^0 Y_O^0$; ———) are plotted as a function of the mixture fraction z. The stoichiometric mixture fraction $z_{st} \approx 0.06$ is also indicated (— - —).

mixture fraction z is a passive scalar, unaffected by combustion processes and verifying $z = 0$ in the air stream and $z = 1$ in pure propane streams.

Molecular mixing between air ($z = 0$) and propane ($z = 1$) streams occurs around the intermediate z-level $z = 0.5$, but reactants are in stoichiometric proportions when the mixture fraction takes the value $z_{st} = 1/(\Phi + 1) \approx 0.06$ (for usual hydrocarbons, the stoichiometric value z_{st} is strongly shifted towards the oxidizer stream). Mixtures are lean when $0 < z \leq z_{st} \approx 0.06$ but rich for $z_{st} \approx 0.06 \leq z < 1$. Accordingly, most of the premixed reactants correspond to rich mixtures. This point is illustrated in Fig. 8. Of course, this analysis holds only at a local level when mixing is controlled by molecular diffusion between pure oxidizer and fuel streams. If all of the reactants injected into the combustor chamber perfectly mix before burning, the mixture equivalent ratio would be the global equivalence ratio ϕ.

The LES data can also be averaged in order to be compared to measurements. Fig. 9 shows mean fuel mass fraction, temperature, and reaction rate fields: the reaction rate field confirms that the flame is lifted and stabilized in the vicinity of the recirculation zone. This zone contains hot gases and acts as a heat tank providing the energy required to stabilize the flame. The fuel mass fraction field shows that the leakage of fuel towards the recirculation zone due to the previous burning of rich mixtures appears even on the mean flow.

5.3. Blow-off (Case E)

Starting from operating conditions of point D where a lifted flame was observed (Fig. 2), a computation is performed increasing the air flow rate to reach the regime E (see Table 1 and Fig. 2). Very rapidly, after a time of about 20 ms, the fresh air entering the combustion chamber dilutes the mixture involved in rich premixed flames (Fig. 10) and starts filling and cooling the recirculation zone. As soon as this zone is too cold, the whole stabilization process is compromised and the flame quenches as seen in the last snapshots of Fig. 10 where the hot gases are convected towards the burner exhaust while the combustor is filled with premixed cold reactants. This test confirms that blow-off can be predicted with the DTF model (usual simple flamelet models cannot predict blow-off because the flame is generally assumed to burn in a steady state regime). Moreover, this blow-off is found for flow rate values corresponding to experimental observations. Of course, more tests are required to determine the exact quenching limits and to validate the DTF model, but this finding is very promising.

FIGURE 9. From top to bottom, averaged fuel mass fraction, temperature, and reaction rate fields for case D (lifted flame).
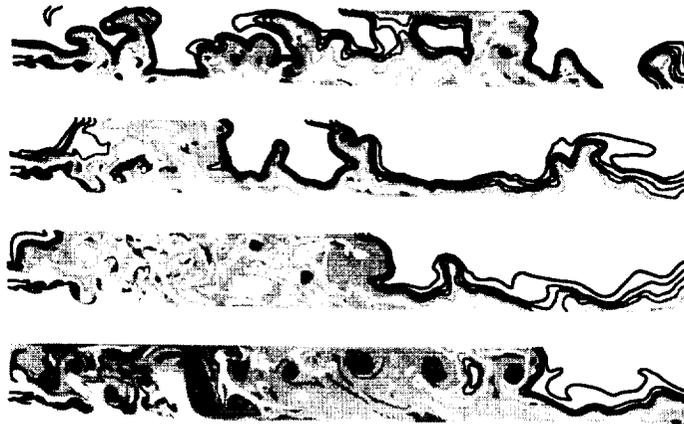
FIGURE 10. Blow-off description. Starting from operating conditions of point D (established lifted flame), the air flow rate is increased to reach the point E conditions (see Fig. 2). Mixing index $Y_F Y_O$ (gray scale) and temperature (contour lines) fields are displayed for four successive instants from top to bottom. The burner is progressively filled with cold premixing and the flame blows off.

6. Conclusions

A dynamic thickened flame (DTF) model is developed for large eddy simulations of turbulent reacting flows and is tested against experimental data. This model extends the thickened flame model (TF) developed by Angelberger et al. (1998) and Colin et al. (2000a) from the pioneering work of Butler & O' Rourke (1977). In the DTF model, the thickening factor F is larger than unity only in reaction zones, and diffusion processes

without chemical reactions are not affected. Accordingly, the DTF model is expected to be suited to situations where non-premixed, partially premixed, and perfectly premixed flames are encountered such as lean premixed prevaporized (LPP) combustors developing for gas turbines.

The DTF model implemented is the AVBP code of CERFACS, and numerical results are compared to experimental data obtained in a turbulent propane/air non-premixed burner at Ecole Centrale Paris (France). This burner exhibits various regimes ("anchored", "lifted", and "extinction") recovered in numerical simulations. In the so-called "lifted" flame regime, the numerical simulations show that combustion mainly occurs in rich premixed flames stabilized by the recirculation zone acting as a hot gases tank. This finding is *a priori* surprising but is in agreement with a simple physical analysis: when propane and air are mixed by molecular diffusion without combustion, most of the pre-mixing corresponds to rich mixtures (fuel in excess) because the stoichiometric iso-surface is strongly shifted towards pure oxidizer for usual stoichiometric flames ($z_{st} \approx 0.06$ when mixing develops around $z \approx 0.5$). Some diffusion flames are also observed but do not correspond to usual flamelets because cold oxidizer burns with a hot mixture of fuel and combustion products. Accordingly, usual flamelet models are not adapted to correctly predict such of lifted flame regimes.

Numerical results are very promising, but further validations against precise instantaneous and averaged experimental data, not yet available, are required.

REFERENCES

ANGELBERGER, C., VEYNANTE, D., EGOLFOPOULOS, F. & POINSOT, T. 1998 Large eddy simulation of combustion instabilities in turbulent premixed flames. *Proceedings of the Summer Program*, Center for Turbulence Research, NASA-Ames/Stanford Univ. 61-82.

BOGER, M., VEYNANTE, D., BOUGHANEM, H. & TROUVE, A. 1998 Direct Numerical Simulation analysis of flame surface density concept for Large Eddy Simulation of turbulent premixed combustion. *27th Symp. (Int.) on Combustion*, The Combustion Institute, Pittsburgh, 917-927.

BOURLIOUX, A., MOSER V. & KLEIN R. 1996 Large eddy simulations of turbulent premixed flames using a capturing/tracking hybrid approach. *Sixth Int. Conf. on Numerical Combustion*, New-Orleans, Louisiana.

BUTLER T.D. & O' ROURKE P.J. 1977 A numerical method for two-dimensional unsteady reacting flows. *16th Symp. (Int.) on Combustion*, The Combustion Institute, Pittsburgh, 1503-1515.

COLIN, O. , DUCROS, F., VEYNANTE, D. & POINSOT, T. 2000 A thickened flame model for large eddy simulations of turbulent premixed combustion. *Phys. Fluids.* **12**, 7, 1843 - 1863.

COLIN, O. & RUDGYARD, M. 2000 Development of high-order Taylor-Galerkin schemes for LES. *J. comp. Phys.* **162**, 338 - 371.

DESJARDINS, P.E. & FRANKEL, S.H. 1999 Two dimensional Large Eddy Simulation of soot formation in the near field of a strongly radiating nonpremixed acetylene-air jet flame. *Comb. Flame.* **119**(1), 121-133.

NICOUD, F. & DUCROS, F. 1997 Subgrid-scale stress modeling based on the square of the velocity gradient tensor. *Flow, Turbulence and Combustion.* **62**(3), 183 - 200.

IM, H. G., LUND, T. S. & FERZIGER, J. H. 1997 Large eddy simulation of turbulent front propagation with dynamic subgrid models. *Phys. Fluids.* **9**(12), 3826 - 3833.

MOIN, P., PIERCE, C. & PITSCH, H. 2000 Large eddy simulation of turbulent nonpremixed combustion. *Advances in Turbulence VIII*, C. Dopazo ed., CIMNE, Barcelona, Spain.

PIANA, J., DUCROS, F. & VEYNANTE, D. 1997 Large eddy simulations of turbulent premixed flames based on the G-equation and a flame front wrinkling description. *Eleventh Symposium on Turbulent Shear Flows*, Grenoble, France.

PIERCE, C. D. & MOIN, P. 1998 A dynamic model for subgrid-scale variance and dissipation rate of a conserved scalar. *Phys. Fluids*, **10**(12), 3041 - 3044.

VEYNANTE, D. & POINSOT, T. 1997 Large Eddy Simulation of combustion instabilities in turbulent premixed burners. *Annual Research Briefs*, Center for Turbulence Research, NASA Ames/Stanford Univ. 253-274.

WILLIAMS, F. A. 1985 Combustion theory, Benjamin Cummings.

A turbulent flame speed closure model for LES of industrial burner flows

By P. Flohr† AND H. Pitsch

A combustion model based on a turbulent flame speed closure (TFC) model is proposed for large-eddy simulations (LES) of lean premixed combustion in industrial gas turbine burners. This model has been originally proposed in a RANS context; the extension to LES is found to be fairly straight-forward, i.e. the turbulent quantities that determine the turbulent flame speed are obtained at the level of the grid cut-off. The model has been applied to a simple premixed jet flame in a backward-facing step combustor to investigate the combustor response to forced excitations.

1. Introduction

The demand for ever decreasing emissions levels of modern gas turbines has led to the development of lean-premixed combustor technology. Here, low emissions can be achieved by perfecting the premixing of the fuel-air mixture and by operating at low flame temperatures, i.e. fuel-lean conditions. The desire to operate gas turbines in low emission mode over the full engine operating range often brings the combustion process dangerously close to lean extinction. As a consequence, the combustion at part-load levels is often accompanied by thermo-acoustic instabilities which may deteriorate the combustion process or even reduce the combustor life. Therefore, there is a strong need for predicting stability limits of industrial combustors.

LES is often seen as a suitable tool for accurately predicting both flame stability and fuel-air mixing (Angelberger *et al.* 1998). Because the largest turbulence scales are explicitly computed in LES and only the smallest, low-energy modes are modeled (where the assumption of local isotropy is expected to hold better than for the largest scales), the prediction of mean flow and mixing is often found to be superior to classical steady RANS models which frequently fail in the highly turbulent, strongly swirling flows that are typically employed in gas turbine burners (Kim *et al.* 1999). On top of that, it intrinsically captures the unsteadiness of extinction and instability processes.

While LES has reached some degree of maturity for non-reacting flows, its application to reacting flows is still being developed, and various modeling approaches have been proposed in the context of premixed combustion, see Veynante & Poinsot (1997), Peters (2000) and references therein. Most of the proposed models have previously been used, or could very similarly be applied, in steady RANS calculations. This is not surprising because the characteristic length- and time-scales where combustion takes place are typically well below the resolved grid scales, and the combustion process has to be modeled entirely at the subgrid level.

In this work we explore the Turbulent Flame speed Closure (TFC) model, which has

† ALSTOM Power Ltd., Segelhof 1, CH-5405 Baden-Daettwil, Switzerland

previously been successfully applied in a RANS context to gas turbine combustion (Zimont *et al.* 1997, Polifke *et al.* 2000). The model is based on solving the one transport equation in addition to the non-reactive case for the reaction progress variable c. Closure is achieved via a source term involving a turbulent flame speed S_T. The turbulent flame speed is obtained from theoretical analysis based on the assumption that combustion is in the "thickened flamelet" regime, which is typical of premixed combustion at gas turbine conditions. The robustness and efficiency of the model (Polifke *et al.* 2000) render it suitable for engineering applications.

The final goal of this work is to perform LES of unstable combustion processes in industrial burner flows. Here, we apply the model to a generic premix burner that has already been extensively studied, both experimentally and numerically (Poinsot *et al.* 1987; Angelberger *et al.* 1998). This configuration showed strong self-excited instabilities at certain operating conditions and provides an example for the investigation of the mechanisms by which the unsteady flow and heat release fields are coupled; the case is also suitable for determining whether the subgrid closure suggested above is suitable to capture such effects.

In addition to the need for an appropriate combustion subgrid closure, the application of a LES tool to industrial configurations must meet two important criteria: first, the tool has to be able to handle complex geometries and secondly, it must be efficient and robust if it is to be used in a design process. It is, therefore, desirable to incorporate LES models in the frame of standard, unstructured, industrial flow solvers. However, it is not yet clear whether such tools which necessarily have to balance robustness against numerical accuracy and solver speed against model flexibility are suitable for engineering-level LES. Therefore, part of this summer research program included performing a basic test of turbulent pipe flow to assess the LES capabilities of an industrial flow solver.

2. Model formulation

2.1. *The filtered c-equation*

The chemical reaction is described using a progress variable c, which is defined as a normalized mass fraction of products such that $c = 0$ in the unburnt mixture and $c = 1$ in the products. Using the Favre-averaged filtering on the transport equation of the progress variable one obtains

$$\frac{\partial \bar{\rho}\tilde{c}}{\partial t} + \nabla \cdot (\bar{\rho}\tilde{\mathbf{u}}\tilde{c}) = \nabla \cdot (\bar{\rho}\kappa\nabla\tilde{c}) + \nabla\mathbf{q} + \overline{\dot{w}_c} \tag{2.1}$$

where $\tilde{c}$ denotes the Favre-averaged progress variable, such that $\bar{\rho}\tilde{c} = \overline{\rho c}$. κ is the molecular diffusivity, $\mathbf{q}$ incorporates the subgrid fluxes, and $\overline{\dot{w}_c}$ is the reactive source term.

Closure for the subgrid flux

$$\mathbf{q} = \tilde{c}\tilde{\mathbf{u}} - \widetilde{c\mathbf{u}} \tag{2.2}$$

is obtained by making the usual gradient-diffusion assumption

$$\mathbf{q} = \kappa_t \nabla\tilde{c} \tag{2.3}$$

where the eddy diffusivity κ_t is obtained from the turbulent viscosity ν_t by making the assumption of the existence of a turbulent Schmidt number,

$$\kappa_t = \nu_t/\mathrm{Sc}_t. \tag{2.4}$$

In this work, we assume the turbulent Schmidt number to be constant, $\mathrm{Sc}_t = 0.7$, and

we obtain the turbulent viscosity from the standard Smagorinski model

$$\nu_t = (C_s \Delta)^2 \sqrt{2\overline{S}_{ij}\overline{S}_{ij}}, \tag{2.5}$$

where $C_s = 0.1$ is a model constant, Δ is the filter cut-off scale, and $\overline{S}_{ij}$ is the large-scale strain rate tensor.

The chemical reaction term in (2.1) is modeled by

$$\overline{\dot{w}_c} = \overline{\rho}_u S_t^\Delta |\nabla \tilde{c}|, \tag{2.6}$$

where $\overline{\rho}_u$ is the density of the unburnt mixture and S_t^Δ is a turbulent flame speed that depends on the physico-chemical characteristics of the combustible mixture and the local turbulence at the subgrid level. Using (2.3) and (2.6) in (2.1) and neglecting molecular diffusion effects, we obtain

$$\frac{\partial \overline{\rho}\tilde{c}}{\partial t} + \nabla \cdot (\overline{\rho}\tilde{u}\tilde{c}) = \nabla \left(\overline{\rho}\frac{\nu_t}{\mathrm{Sc}_t}\nabla \tilde{c} \right) + \overline{\rho}_u S_t^\Delta |\nabla \tilde{c}|. \tag{2.7}$$

Equation (2.7) describes a combustion front that is characterized by a turbulent flame speed which quickly adapts to a local equilibrium value and a flame brush thickness which grows according to turbulent dispersion by the subgrid scales.

It is noted that the assumption of gradient-diffusion transport is not in contradiction with the existence of counter-gradient diffusion, and counter-gradient transport is, in fact, implicitly modeled in the chemical source term (2.6) as shown by Zimont *et al.* (2000).

For very large times, the increase in thickness of the flame brush is compensated by the local flamelet propagation, and the first term on the right-hand side of (2.7) should be incorporated in the reactive source term. However, it can be shown that the time scale required to achieve this equilibrium is much larger than the integral turbulent time scale τ_t (Zimont *et al.* 2000). In industrial combustors the residence time is usually comparable to the turbulent time τ_t, and (2.7) is therefore the appropriate model equation.

2.2. *Zimont's model of the turbulent flame speed*

For a complete closure in (2.7) one has to provide a model for the turbulent flame speed S_t. The models are usually of the form

$$\frac{S_t}{S_l} = 1 + f(\mathrm{Re}, \mathrm{Da}, \mathrm{Pr}), \tag{2.8}$$

where S_l is the laminar flame velocity and f is a functional of the hydrodynamical and physico-chemical parameters, expressed via the Reynolds, Damköhler, and Prandtl numbers,

$$\mathrm{Re} = \frac{u_t l_t}{\nu}, \quad \mathrm{Da} = \frac{\tau_t}{\tau_c}, \quad \mathrm{Pr} = \frac{\nu}{\chi}. \tag{2.9}$$

u_t, l_t and $\tau_t = l_t/u_t$ are the integral turbulent scales, $\tau_c = \chi/S_l^2$ is the chemical time scale, and χ is the thermal conductivity.

Zimont (1979) proposed a model for S_t which is valid in the "thickened flamelet" regime. This regime is characterized by very large Reynolds numbers and moderately large Damköhler numbers such that

$$\mathrm{Re} \gg 1, \quad 1 < \mathrm{Da} < \mathrm{Re}^{1/2}. \tag{2.10}$$

The second inequality indicates that the Damköhler number is large, but not large enough

for the combustion to occur in the laminar flamelet regime. In other words, the laminar flame thickness is much smaller than the integral length l_t but significantly larger than the Kolmogorov scale η. Zimont's (1979) analysis for this regime led to the following expression for the turbulent flame speed

$$\frac{S_t}{S_l} \simeq (\mathrm{RePr})^{1/2} \mathrm{Da}^{-1/4} \tag{2.11}$$

Without repeating his analysis, which is based only on dimensional arguments and the existence of a turbulent cascade according to Kolmogorov (1941), we state here his two main modeling assumptions:

(a) The smallest eddies which are smaller than the laminar flame front thickness penetrate the front to increase the internal diffusion process and thus the thickness of the flame; this process is repeated until equilibrium is reached between convective and diffusive effects, leading to a thickened flame front of thickness δ^*.

(b) Turbulent eddies which are larger than the effective flame front thickness δ^* wrinkle the front to increase the effective front surface; the increase in flame speed is proportional to the area increase due to the turbulence.

The application of this model to LES is straightforward. The turbulent large scales u_t and l_t only enter Zimont's analysis via the energy dissipation rate $\epsilon \sim u_t^3/l_t$, which holds for any length scale l and associated velocity scale u_l in the Kolmogorov cascade, $\epsilon \sim u_l^3/l$, where $l_t \geq l \geq \eta$. This implies that we can replace the turbulent large-scale fluctuations by the fluctuations at the cut-off scale (u_Δ, Δ), provided that the large-eddy filter scale Δ is larger than the flame thickness δ^*. We obtain for the turbulent flame speed S_t^Δ defined at the cutoff level,

$$\frac{S_t^\Delta}{S_l} = 1 + A\,(\mathrm{Re}_\Delta \mathrm{Pr})^{1/2}\,\mathrm{Da}_\Delta^{-1/4}, \tag{2.12}$$

where

$$\mathrm{Re}_\Delta = \frac{u_\Delta \Delta}{\nu}, \quad \mathrm{Da}_\Delta = \frac{\Delta}{u_\Delta \tau_c}. \tag{2.13}$$

The original formulation of Zimont (1979) has been modified to recover the laminar flame speed in regions of low turbulence activity. Equation (2.12) also includes a proportionality constant A of order unity. $A = 0.52$ was found by Zimont & Lipatnikov (1995), where turbulent flame speeds were computed from integral turbulent scales. Assuming that the subgrid closure results in the appropriate level of energy dissipation, the same model constant has been used in the present study.

The filter scale Δ is obtained from the box filter over grid cells

$$\Delta = 2(\Delta_x \Delta_y \Delta_z)^{1/3}, \tag{2.14}$$

and the subgrid scale velocity u_Δ is estimated from the Smagorinski subgrid viscosity as

$$u_\Delta = \frac{\nu_t}{C_s \Delta} = C_s \Delta \sqrt{2\overline{S}_{ij}\overline{S}_{ij}}. \tag{2.15}$$

It is to be noted that the model formulation is now grid dependent, and it should be verified that the flame thickness does not exceed the grid scales, i.e. $\mathrm{Da}_\Delta > 1$. Indeed, Zimont et al. (1997) estimate $\mathrm{Da} = 3$ for a gas turbine burner which would invalidate the subgrid closure if $\Delta \ll l_t$.

2.3. The effect of flame stretch

Equation (2.12) leads to larger flame speeds for increasing turbulence intensity; however, at very high levels of turbulence intensity, it is observed experimentally that the turbulent burning rate is limited or may even decrease (Zimont & Lipatnikov 1995). This "bending effect" has been incorporated in (2.12) by introducing a stretch parameter G as a correction factor for the turbulent burning velocity (Zimont & Lipatnikov 1995), which we adopt here at the velocity subgrid level. G is the probability of unquenched flamelets and is defined as

$$G = \frac{1}{2}\mathrm{erfc}\left\{-\left(\frac{1}{2\sigma}\right)^{1/2}\left[\ln\left(\frac{\epsilon_{cr}}{\epsilon} + \frac{\sigma}{2}\right)\right]\right\}. \tag{2.16}$$

$\sigma \simeq \ln(\Delta/\eta)$ is the standard deviation of the log-normal distribution of the dissipation rate $\epsilon = u_\Delta^3/\Delta$, and $\epsilon_{cr} = 15\nu g_{cr}^2$. g_{cr} is a critical flamelet quench rate that is obtained either from laminar flame computations or can be estimated from $g_{cr} \sim S_l^2/\chi$.

In writing (2.16) for the turbulent flame speed at the grid cut-off level, we assume that the significant contribution for the dissipation spectrum is contained entirely in the subgrid scales. For very low dissipation rates $\epsilon \ll \epsilon_{cr}$, no flame quenching occurs ($G = 1$). For very high dissipation rates $\epsilon \gg \epsilon_{cr}$, all flames are quenched locally by the turbulence ($G = 0$). It should be noted that the modeling of flame quench in this way is only qualitatively correct. In particular, estimates of the appropriate stretch rate g_{cr} are connected with relatively large uncertainties; for more details see Polifke *et al.* (2000). Also, (2.16) does not take into account unsteady effects which are known to be very important for extinction and (re-)ignition.

The uncertainty of this model parameter is perhaps mostly related to the fact that G depends on the entire turbulence spectrum. Specifically, G decreases for smaller Kolmogorov scales at constant ϵ, ϵ_{cr}. In fact, no clear experimental evidence exists for flame extinction by small-scale turbulence, let alone its dependence on Reynolds number. Indeed, the simulations by Meneveau & Poinsot (1991) suggest that the smallest eddies have no effect on the flame front mainly because their lifetime is too short. Further research is necessary to clarify whether (2.16) is appropriate in a LES context or whether the flame stretch should be associated only with the largest turbulent motions which are explicitly computed.

In this work, the application of the stretch parameter at the subgrid level was found to be crucial in the case of a flame that is stabilized in the vicinity of a backward-facing step (see Section 4), and a similar finding has been reported by Weller *et al.* (1998). Flamelet straining reduces the effective reaction rate close to the expansion, which has a large impact on the local heat release in the flame-front roll-up.

3. Numerical implementation

Equation (2.7) has been implemented in a standard industrial flow solver (Fluent 5). This solver provides a basic LES capability of cold flow simulations with the standard Smagorinski subgrid closure with near-wall damping and approximate log-law wall boundaries. The unstructured finite-volume solver uses second-order central differencing for convective momentum fluxes and second-order upwinding for scalar fluxes (such as for the reaction progress variable c). The SIMPLE pressure-correction scheme is used for time-advancement; discretization of pressure in the correction step is second-order accurate.

test case	grid ($N_x \times N_r \times N_\phi$)	resolution (r^+)
DNS_IFS	$38 \times 32 \times 64$	0.6
DNS_REF	$38 \times 32 \times 64$	0.6
DNS_FINE	$64 \times 32 \times 128$	0.3

TABLE 1. Setup for pipe flow at $\mathrm{Re}_\tau = \frac{u_\tau R}{\nu} = 180$, $R = 1$, $L = 10$.

(a)   (b)
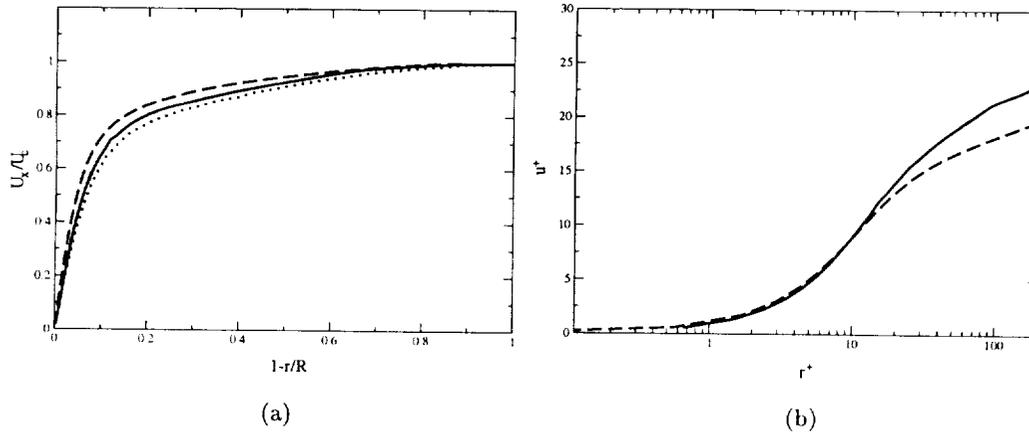
FIGURE 1. Mean flow profiles. (a) velocity scaled with center line velocity U_c; (b) velocity scaled with friction velocity $u_\tau = \sqrt{\tau_w/\rho}$. Symbols: DNS_{IFS} (———); DNS_{REF} (– – – –); DNS_{FIN} (········).

This setup is generally acceptable for performing engineering-level LES. However, because no validation data exists for the LES implementation, it was felt that a basic solver validation should be carried out as part of this study. The capabilities of the flow solver to resolve the turbulent fluctuations were assessed at the most basic level: Is the solver capable of maintaining statistically steady turbulence in a periodic wall-bounded flow, or does the inherent numerical diffusion damp out all fluctuations? If turbulence can be maintained, how do statistics compare with those obtained from the thoroughly validated flow solver that has been developed at CTR?

To exclude any effects of the subgrid closure and the approximate wall model, a DNS of streamwise periodic pipe flow was chosen as a test case. The parameters of the setup and flow are given in table 1. The computation with Fluent (DNS_IFS) is compared with two results that were obtained with CTR's DNS code; DNS_REF is a reference computation on the same grid, and DNS_FINE is a reference computation at higher resolution. The reference flow solver is also second-order accurate.

The results for the mean flow profiles are presented in Fig. 1. While the rescaling with the center line velocity (Fig. 1a) suggests that the accuracy of DNS_IFS is in between the reference computations at different resolutions, the rescaling with the friction velocity in Fig. 1b reveals that the velocity levels in the log-law region are overestimated by at least 10%. This is an indication for stronger damping in the near-wall region for Fluent
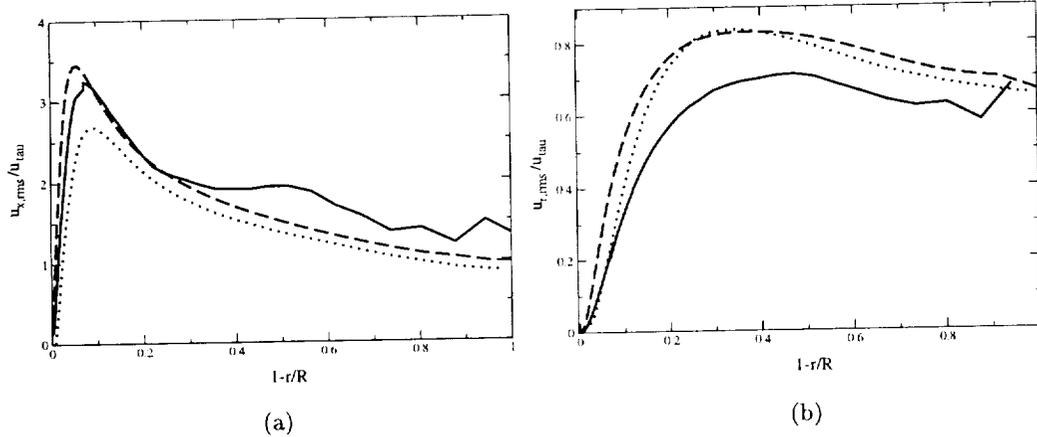
FIGURE 2. Velocity fluctuations of the resolved scales, normalized with the friction velocity. (a) - streamwise fluctuations; (b) - radial fluctuations. See Fig. 1 for symbols.
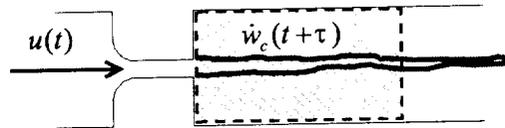
FIGURE 3. Sketch of the simple jet flame from the experiment by Poinsot *et al.* (1987).

which is likely to be due to higher levels of numerical diffusion. This is confirmed by the second-order statistics which are presented in Fig. 2. While streamwise fluctuations display a reasonable agreement with the reference computations, Fig. 2b reveals that wall-normal fluctuations are significantly underpredicted. It is also interesting to note that computing times for Fluent are about 100 times slower than for the optimized DNS flow solver (corresponding to several days on a 4-processor workstation for a full simulation). However, in light of the fact that the time-advancement scheme is not optimized for a simulation where the timestep is limited by the smallest turbulent time scale and usually not by numerical stability, and given that an unstructured general purpose code is compared here with a structured, vectorized solver, this overhead is, in fact, acceptable.

4. Application to a model combustor

The TFC subgrid closure model has been applied to a generic premixed propane-air jet flame that is stabilized in the expansion behind the injection slot; the configuration, shown in Fig. 3, is based on an experiment by Poinsot *et al.* (1987). The experiment consisted of five parallel, essentially two-dimensional slots, of which one is indicated in the sketch. The experiments showed various modes of instability with strong self-excited oscillations. The mode at 530Hz was found to be one of the most unstable.

The self-excitation of combustion instabilities is linked to the phase relationship between the acoustic pressure field and unsteady heat release via Rayleigh's criterion. The criterion implies that acoustic instabilities are amplified if pressure and heat release fluctuations are in phase. The phase relationship is thus important when quantifying the stability properties of a burner, and it is used here to qualify the usefulness of the LES flame speed closure for the simulation of unsteady combustion.

numerical setup			model parameters					
no. cells	Δ_{min}	u_{in}	Δt	S_l	T_u	T_{ad}	χ	g_{cr}
31500	0.1mm	6.4 m/s	$5 \cdot 10^{-6}$	0.36 m/s	300 K	2190 K	$2.2 \cdot 10^{-5}$	6000 1/s

TABLE 2. Setup for slot burner of a premixed, stoichiometric propane-air flame at atmospheric conditions.

4.1. Setup and model parameters

The numerical simulation is based on a single slot with symmetry conditions at the top and bottom boundaries as indicated in Fig. 3. We adopt here the model setup by Angelberger *et al.* (1998), who numerically investigated this combustor with a flame model based on artificial flame front thickening. The computations were performed in two dimensions since flow visualizations in the experiment have indicated that large-scale structures produced by the unsteady combustion were essentially two-dimensional, and the computations by Angelberger *et al.* (1998) have indicated that this assumption is reasonable.

Parameters of the setup and the combustion model parameters are summarized in table 2. The model parameters for the TFC model are based on the detailed chemistry calculations presented in Angelberger *et al.* (1998), while the critical strain parameter g_{cr} is based on the rescaling procedure proposed in Polifke *et al.* (2000) to estimate critical flame stretch in a fresh-to-burnt, opposed jet configuration. The local Damköhler number has been estimated for this configuration as $Da_\Delta > 2$, and the assumption of combustion in the thickened flamelet regime with flame thickness below the subgrid level is expected to hold.

The numerical setup does not contain the feedback between heat release and acoustic fields because it is based on the incompressible (but variable density) flow equations. Therefore, the self-excited instability from the experiment is simulated via the artificial situation where the incoming mass flow rate is varied (assuming that the acoustic perturbations do not travel upstream to the fuel injector such that the fuel-air equivalence ratio could be altered). The amplitude of the mass flow variations was set to ±25% of the mean flow rate, which is comparable to the experimentally observed fluctuation levels, and the single-frequency, sinusoidal forcing was fixed at 530Hz, corresponding to the strongest instability mode in the experiment.

4.2. Results

The forced simulations were started after an initial transient in which the statistically steady flame was established, starting from steady-state computations. In Fig. 4 we plot snapshots of the unstable flame during one cycle of oscillation; as in the experiment, the formation of mushroom like vortices is observed in the simulation. However, the vortices form significantly further downstream than in the experiment as indicated in Fig. 4*(c)* where we compare directly with a snapshot of the experiment obtained at the same phase angle within the 530Hz cycle. A possible explanation for this effect is that the definition of u_Δ does not take into account dilatation effects, and thus the turbulent flame speed is likely to be overestimated in regions of relatively weak turbulence intensity where a
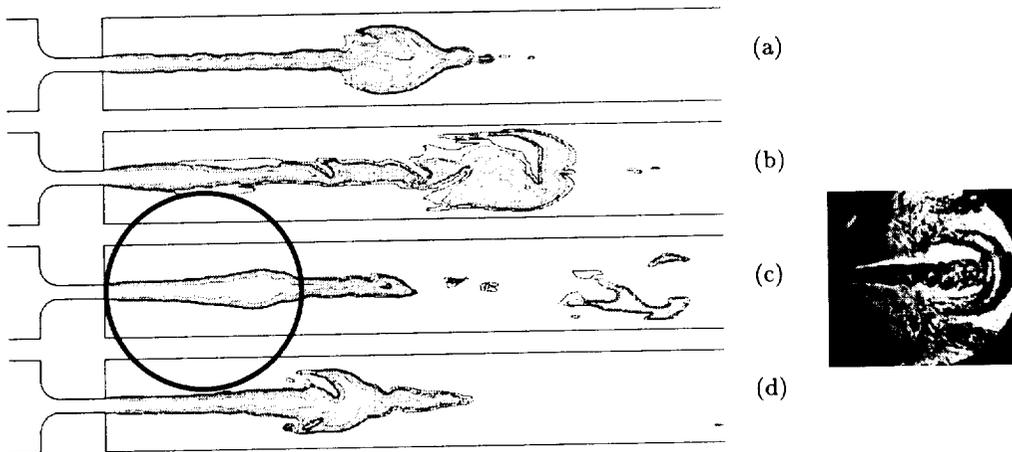
FIGURE 4. Instantaneous snapshots of the reaction progress variable during one forcing cycle at 530 Hz. The time between each picture corresponds to a quarter period. Also included in the figure is a snapshot taken from Poinsot *et al.* (1987), obtained at the same phase angle.
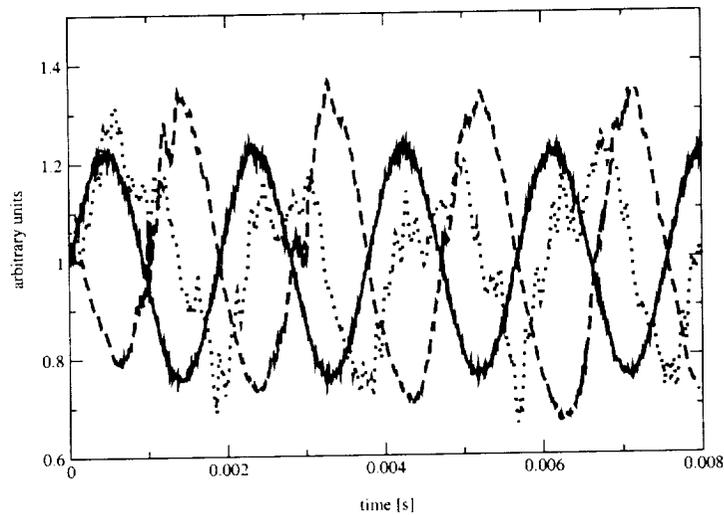
FIGURE 5. Time history of reaction rates with and without flame stretch. Symbols: ——— , inflow rate; – – – – , reaction rate; ········· , reaction rate, no stretch.

roll-up would otherwise be observed. More sophisticated approaches to model u_Δ are suggested in Colin *et al.* (2000).

Box-averaging the heat release rate over a region that resembles the observation window from the experiment (see Fig. 3) allows one to measure the phase-lag τ between reaction rate $\overline{\dot{w}_c}(t + \tau)$ and forced inflow rate $\overline{u}(t)$; both numerical and experimental results are plotted in Fig. 5. Initially, numerical simulations were carried out with the correction factor $G = 1$ everywhere because the effects of flame quenching were considered negligible in a case where turbulence levels are generally moderate. However, without the stretch
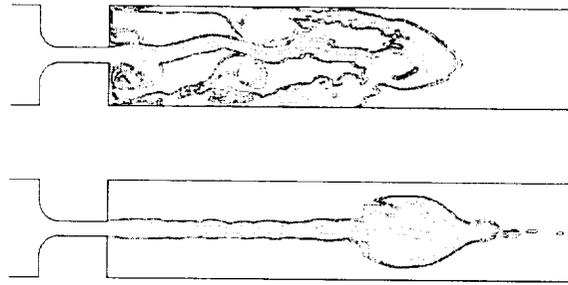
FIGURE 6. Snapshots of the ECB burner. Effect of flame stretch.

factor the heat release rate peaks immediately after the area expansion, and this peak remains attached throughout the forcing cycle, leading – contrary to the experiment where a phase angle of π has been measured – to an almost in-phase relation between heat release and inflow rate as also indicated in Fig. 5. This behavior is unphysical because the large strain in the vicinity of the step leads to reduced reaction rates and thus a detachment of the flame. Applying the stretch factor (2.16) to this configuration significantly altered the situation; the flame was detached and the phase-angle π from the experiment was recovered as shown in Fig. 5. A possible weakness of the model is the presence of the reaction rate reduction parameter in the entire flow field. One consequence of this is that the instantaneous flame structures are strongly affected by the extinction strain rate. In Fig. 6 we show two snap-shots at the same phase angle within the forcing cycle. While the lower figure is obtained with a stretch parameter $g_{cr} = 6000$, the upper figure corresponds to $g_{cr} = 2000$ (corresponding to the extinction strain for the opposed jet configuration of fresh mixtures). Obviously, local variations in reaction rates are observed; more importantly, however, the general flame shape, i.e. the formation of the vortices and their phase-angle, is found to be very insensitive to the absolute value of this model parameter, which is not known with great accuracy.

5. Conclusions

A model for premixed turbulent combustion based on a turbulent flame speed closure (TFC) has been proposed in the context of large-eddy simulations. The model is an extension of the original formulation in a RANS context. Possible limitations of the model due to its definition at the cutoff level and the uncertainties in modeling subgrid flame quenching have been broadly discussed.

The model has been applied to a simple premixed jet flame in a backward-facing step combustor. The results have indicated that a large-eddy simulation based on the TFC model is able to predict the forced combustor response. The agreement with a self-excited instability mode at the same frequency as observed in the experiment is good in terms of its phase angle between the incoming flow rate and the box-window integrated heat release rate.

The simulations in this study were based on a general-purpose industrial flow solver which includes basic LES capabilities but which has not yet been validated in detail. A simple validation study of a resolved low Reynolds number pipe flow revealed that the solver is capable of reproducing first and second-order statistics with reasonable

accuracy. While further validation work is necessary for both the flow solver and the TFC-LES combustion model, the tool developed here appears to be appropriate to study a full-scale gas turbine combustor in the near future.

Acknowledgments

REFERENCES

ANGELBERGER, C., VEYNANTE, D., EGOLFOPOULOS, F., & POINSOT, T. 1998 Large eddy simulations of combustion instabilities in premixed flames. In *Proceedings of the Summer Program* (Center for Turbulence Research, NASA Ames/Stanford Univ.) 61-82.

COLIN, O., DUCROS, F., VEYNANTE, D., & POINSOT, T. 2000 A thickened flame model for large eddy simulations of turbulent premixed combustion. *Phys. Fluids.* **12**, 7.

KIM, W.-W., MENON, S., & MONGIA, H. C. 1998 Large-eddy simulation of a gas turbine combustor flow. *Comb. Sci. and Tech.* **143**, 25-62.

MENEVEAU, C., & POINSOT, T. 1991 Stretching and quenching of flamelets in premixed turbulent combustion. *Combustion and Flame.* **86**, 311-332.

PETERS, N. 2000 *Turbulent combustion*, Cambridge University Press.

POINSOT, T., TROUVE, A., VEYNANTE, D., CANDEL, S., & ESPOSITO, E. 1987 Vortex driven acoustically coupled combustion instabilities. *J. Fluid Mech.* **177**, 265-292.

POLIFKE, W., FLOHR, P., & BRANDT, M. 2000 Modeling of inhomogeneously premixed combustion with an extended TFC model. In *Proceedings of ASME TURBO EXPO 2000* 2000-GT-0135.

VEYNANTE, D., & POINSOT, T. 1997 Reynolds-averaged and large eddy simulation modeling for turbulent combustion. In *New tools in turbulence modeling*, O. Metais & J. Ferziger Eds., Les Editions de Physique.

WELLER, H. G., TABOR, G., GOSMAN, A. D., & FUREBY, C. 1998 Application of a flame-wrinkling LES combustion model to a turbulent mixing layer. In *27th Int. Symp. on Combustion*, The Combustion Institute, 899-907.

ZIMONT, V. L. 1979 The theory of turbulent combustion at high Reynolds numbers. *Combust. Expl. and Shock Waves.* **15**, 305-311.

ZIMONT, V. L., BIAGIOLI, F., & SYED, K. J. 2000 Modelling turbulent premixed combustion in the intermediate steady propagation regime. *Int. J. Comp. Fluid Dyn.* **1**(1-3).

ZIMONT, V. L., & LIPATNIKOV, A. N. 1995 A numerical model of premixed turbulent combustion of gases. *Chem. Phys. Reports.* **14**(7), 993-1025.

ZIMONT, V. L., POLIFKE, W., BETTELINI, M., & WEISENSTEIN, W. 1997 An efficient computational model for premixed turbulent combustion at high Reynolds numbers based on a turbulent flame speed closure. *J. Eng. for Gas Turb. and Power, Transactions of the ASME.* **120**, 526-532.

Modeling turbulent reacting methane thermochlorination flows

By A. D. Harvey† AND H. Pitsch

Motivations for and complications involved in modeling turbulent reacting chlorination flows are discussed. A confined turbulent nonpremixed reacting methyl chloride chlorination flow is investigated numerically using large eddy simulation and a Reynolds (Favre-)averaged Navier-Stokes approach with fully coupled chemistry and a detailed multi-step kinetic mechanism. A laminar diffusion flamelet turbulent combustion model is coupled with both the LES and the RANS codes to close the chemical source terms. A RANS solution neglecting chemical source term closure is also obtained. The different calculations are compared, and differences in the solutions are discussed. Computations including the flamelet turbulent combustion model predict a lower peak reaction temperature and a more gradual temperature increase than predictions neglecting closure.

1. Motivations and objectives

Methylene dichloride (M_2), chloroform (M_3), and carbon tetrachloride (M_4) are three basic products of methane chlorination and are produced by high temperature gas phase chlorination of methane or methyl chloride, (M_1). Their primary uses are as industrial solvents, making refrigerants, and the manufacturing of silicon. Methane chlorination reactions proceed by a multi-step series of exothermic reactions which are stabilized in a confined jet configuration where reactants are typically introduced at temperatures well below the minimum activation temperature. Thus, sustained autothermal operation of the device is strongly dependent on the re-circulation of heat furnished by the confined jet design.

As cold incoming gases are heated by re-circulated products, chlorine atom concentration increases exponentially. Eventually a sufficient chlorine radical concentration is attained for the propagation reactions to proceed (producing heat). A portion of the heat is recirculated back into the incoming feed and the remainder is convected out the exit. As the flow in a confined jet reactor whose inlet temperature is sufficiently low is made to increase, in premixed situations the flame speed decreases and the proportion of heat re-circulated will eventually be insufficient to heat the resulting higher volume of incoming fluid to levels capable of sustaining the reaction.

In large scale industrial chlorination devices operated near extinction, complex behaviors have been observed which include low frequency pressure and temperature oscillations and thermoacoustic excitations. This ultimately leads to extinction of the reaction, excessive undesirable by-product formation, or the convection of highly reactive chlorine in downstream equipment ill-suited for this type of exposure. Obviously these outcomes are undesirable, and an important long term goal is to develop an improved understanding of the unstable behaviors which preempts extinction and/or shutdown of

† The Dow Chemical Company, Plaquemine, Louisiana, bharvey@dow.com
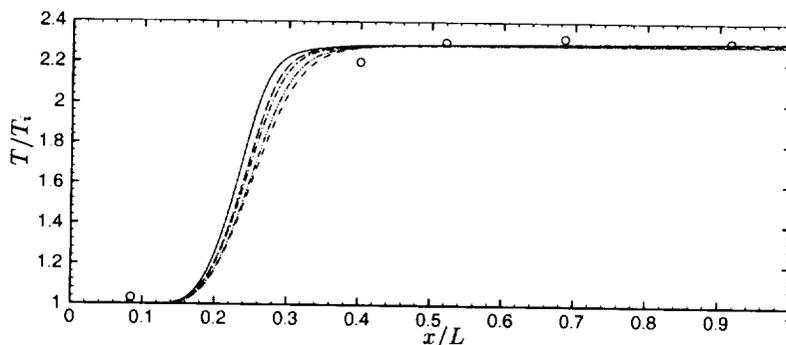
FIGURE 1. Comparison of computed (RANS/no closure) centerline temperature profiles in a commercial scale premixed chloromethanes reactor: o - plant data with inflow velocity, $u = 2U_r$; ——— $u = U_r$; ————— $u = 1.5U_r$; —·— $u = 2U_r$; —··— $u = 2.8U_r$; ———— $u = 4U_r$.

a chloromethanes reactor. In the present study we use a laminar flamelet combustion model, detailed kinetics, and current LES and RANS solution methodologies to study a model nonpremixed methane chlorination device. We discuss combustion modeling issues which will be addressed in ongoing and future studies to ultimately model more realistic chlorination flows. The objectives of this summer research project are:

(a) Incorporate a laminar flamelet combustion closure model and detailed, multi-step kinetics into both a chemically reacting RANS code and an LES code.

(b) Use the resulting codes to compute the turbulent reacting flow in a nonpremixed methane thermochlorination device.

(c) Compare computational results, including the effects of turbulence closure with results obtained with the reacting RANS neglecting closure, and determine the importance of closure modeling for chloromethane chemistry.

1.1. Past work

There have been a few documented attempts to model thermal chlorination of methane. West *et al.* (1999) used a 5-step irreversible mechanism in a simple perfectly stirred reactor model that produced dynamical behavior similar to that observed in real reactors operated near the extinction point. Acharya *et al.* (1991) used a second moment closure method in which they assumed fluctuations in temperature and density were small and considered only the correlations $\overline{y''_{M_1} y''_{Cl_2}}$ and $\overline{y''_{M_2} y''_{Cl_2}}$ to model a methane chlorination flow. They conclude that without more detailed kinetics and source term closure, CFD does a poor job of predicting finite-rate chemistry effects, minor species formation, and local reaction extinction. Often, undesirable side reactions, leading to complete decomposition of the products, compete with the main desired chemistry. To study reactor designs and operating conditions which improve selectivity to desirable products, it is important to develop solution strategies capable of handling detailed kinetics. In this study we use a relatively detailed mechanism consisting of 38 species and 152 reactions (Shah & Fox, 1999).

Industrial scale chlorination devices are often more than a meter in diameter and > 10 meters in length with Reynolds numbers exceeding 10^6 at design operation. Three-dimensional velocity fluctuations occur on length scales ranging in sizes equal to this integral scale to a factor of $Re^{0.75}$ smaller and on a correspondingly broad range of time scales (dynamic range of $Re^{0.5}$). Relevant chemical time and length scales can be even
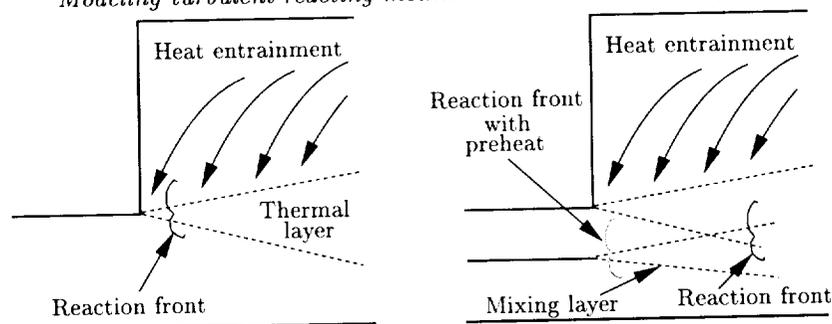
FIGURE 2. Premixed (left) and nonpremixed (right) illustrating the structure of the mixing and reaction front location from preheated and non-preheated feed streams.

broader. Fully resolved LES of such a commercial scale device still remains a considerable computational challenge, and past computational efforts have been restricted to averaged techniques.

Figure 1 compares computed mean temperature profiles for a typical premixed commercial scale reactor with experimental data. Mean temperature measurements were obtained using fixed thermocouples housed in thick thermowells. Due to both the unavailability of optical access and the corrosive environment inside the reactor, measurements on shorter time-scales are difficult to obtain. Axisymmetric calculations were performed at 5 different flow rates, which differ by a factor of 4 using a RANS code including chemical reactions (to be described later) with 15 species and 21 reactions. The chemical source terms in the species equations were evaluated with Favre-averaged values of mass fraction and temperature, neglecting chemical source term closure. The reference velocity is $U_r = 9$ m/s. The data (at the median flow rate) compare reasonably well with the predictions. However, the somewhat limited data suggests a more gradual temperature rise across the reaction zone than the calculations predict. Shah & Fox (1999) did computational studies using a more detailed mechanism and full PDF calculations in an adiabatic, well-stirred device. By varying the mixing time, they show that the increase in temperature is more gradual when the mixing time is longer.

The calculations of Fig. 1 also fail to predict observed sensitivities to variations in flow rates. It is not possible to double (or half) the flow in this particular device without causing undesirable effects such as unsteady pressure oscillations or extinction of the reaction. Computational studies similar to that of Fig. 1, neglecting source term closure and involving variation of other operating parameters such as inlet feed concentration, also fail to predict observed sensitivities in the actual operation of the device.

In the present study we compute the turbulent reacting flow in a chlorination device using detailed kinetics both with and without chemical source term closure, compare differences in solutions, and evaluate the importance of closure.

1.2. Chlorination modeling difficulties

Feed streams can typically consist of chlorine, methane, M_1, and M_2 and can be introduced either premixed or nonpremixed through a coaxial configuration with molecular chlorine in one feed entrance and premixed organics in the other. In the present study we investigate the preheated, nonpremixed case; in the future we will look at and report on others. Here we provide a brief description of several inlet configurations to indicate differences in features and reveal relevant modeling issues.

For the premixed case, reaction is initiated and sustained by the confined jet re-

circulation as the cold incoming feed stream is heated (Fig. 2). As flow rates are increased above the flame speed, the reaction front moves farther downstream. The introduction of cold nonpremixed feed can result in a number of complex flame structures. If one of the feed streams is sufficiently heated (typically Cl_2), combustion and flame structure follows that of typical nonpremixed flames. The flame is situated very close to the inlet location, and stable operation is only weakly dependent on the autothermal, confined jet design. However, for cold, nonpremixed applications, flame position and structure are highly dependent on the mixing and heat entrainment processes and can be significantly different depending on which inlet the chlorine is introduced (Raman *et al.*, 2000).

Turbulent reacting flow in chlorination devices can be further complicated by the introduction of liquid chlorine at the inlet (in addition to gas) as a means of increasing chlorine inlet concentration. Thus future combustion modeling of these particular chlorination devices require accounting for the effects of spray vaporization.

In this initial study we use a nonpremixed flamelet combustion model to study a preheated, nonpremixed M_1/M_2 chlorination device. We will couple the combustion model with both LES and Favre-averaged solutions for the flow, turbulence, and scalar mixing. Model characteristics, solution details, and comparisons of computed results are presented next.

2. Solution methodologies

The Favre-averaged Navier-Stokes, LES and Laminar Flamelet codes are briefly described below, referring to available references when possible to conserve space. We use conventional notation, a tilde denoting Favre averaging and an overbar for time-averaged quantities. The ith species partial pressure, density, mass fraction, molecular weight, and enthalpy is p_i, ρ_i, Y_i, W_i, and h_i, and the thermodynamic pressure, mixture density, velocity components, and temperature are given by p, ρ, u, v, w, and T, respectively. Vector quantities are in bold type, and the Favre mean mixture fraction and variance are denoted $\widetilde{Z}$ and $\widetilde{Z''^2}$. Turbulent and laminar diffusivities are denoted by D_t and D_l with constant Schmidt numbers assumed.

2.1. *Reynolds-averaged Navier-Stokes*

A structured, finite-volume, multi-block pressure based low Mach number preconditioned Favre-averaged Navier-Stokes code for a mixture of chemically reacting gases is used. All species are assumed to obey an equation of state: $p_i = \rho_i RT/W_i$. The 3-D equations for n-species partial pressures, momentum, and energy are solved simultaneously in a standard generalized frame of reference. The appropriate vector equation is of the form:

$$\Lambda \partial_\tau \hat{\mathbf{Q}} + \partial_\xi (\hat{\mathbf{E}} - \hat{\mathbf{E}}_v) + \partial_\eta (\hat{\mathbf{F}} - \hat{\mathbf{F}}_v) + \partial_\zeta (\hat{\mathbf{G}} - \hat{\mathbf{G}}_v) = \hat{\mathbf{H}} \qquad (2.1)$$

Where $\hat{\mathbf{Q}}$ is the vector of primitive variables, $\tilde{p}_i$, $\tilde{u}$, $\tilde{v}$, $\tilde{w}$, and $\tilde{T}$. The preconditioning matrix Λ is of a form similar to Choi & Merkle (1993). The hats are used to represent inviscid and viscous flux vectors $\hat{\mathbf{E}}$, $\hat{\mathbf{E}}_v$, etc. in the generalized coordinate system and are related to the flux vectors in the Cartesian frame by an expression of the form

$$\hat{\mathbf{E}} = \frac{1}{J}(\kappa_x \widetilde{\mathbf{E}} + \kappa_y \widetilde{\mathbf{F}} + \kappa_z \widetilde{\mathbf{G}}) \qquad (2.2)$$

The mean convective fluxes are differenced using the low-diffusion flux-splitting scheme of Edwards (1997). Flux vectors are linearized and resulting implicit Jacobians, $\partial \hat{G}/\partial \hat{Q}$,

are constructed using derivatives of the fluxes with respect to each of the primitive variables. The exact form of the fluxes and Jacobians can be found in Harvey & Edwards (1998). $\hat{H}$ contains the chemical production rates per unit volume of each species, $\dot{m}_i$, which, for calculations neglecting closure, we assume to be equivalent to $\dot{m}_i(\bar{\rho}_i, \widetilde{T})$. Closure of this term is introduced later. The thermodynamic pressure is computed as the sum of partial pressures of each species. Mass fractions are computed from partial pressures, and the enthalpy of each species is computed from

$$h_i = h_{f_i}^\circ + \int_{T_r}^{T} C_{p_i} \, \mathrm{d}T \tag{2.3}$$

where $h_{f_i}^\circ$ is the species enthalpy of formation at $T = T_r$ and the species specific heat, C_{p_i}, is obtained using 4th order polynomials in temperature. The mixture-specific heat is obtained by mass fraction weighting.

An arbitrary number of Arrhenius type reactions can be considered. For the present work, the mechanism found in Shah & Fox (1999) is used.

A zonal two-layer k-ϵ model is solved de-coupled from the flow. The eddy viscosity is computed as $C_\mu k^2/\epsilon$. The following transport equations are solved for mean mixture fraction, $\widetilde{Z}$, and variance, $\widetilde{Z''^2}$

$$\bar{\rho}\frac{\partial \widetilde{Z}}{\partial t} + \bar{\rho}\widetilde{\mathbf{u}} \cdot \nabla \widetilde{Z} = \nabla \cdot (D_t \nabla \widetilde{Z}) \tag{2.4}$$

$$\bar{\rho}\frac{\partial \widetilde{Z''^2}}{\partial t} + \bar{\rho}\widetilde{\mathbf{u}} \cdot \nabla \widetilde{Z''^2} = \nabla \cdot (D_t \nabla \widetilde{Z''^2}) + 2\bar{\rho}D_t(\nabla \widetilde{Z})^2 - \bar{\rho}\widetilde{\chi} \tag{2.5}$$

where a gradient transport assumption for turbulent fluxes is used and the mean scalar dissipation rate, $\widetilde{\chi}$, appearing as a sink term in the equation for the mixture fraction variance is calculated as:

$$\widetilde{\chi} = 2\frac{\epsilon}{k}\widetilde{Z''^2} \tag{2.6}$$

The multi-block code employs a multi-level grid refining strategy using three grid levels and is similar to a multigrid V-cycle. Each zone in the grid is solved sequentially using an ILU solver. Additional details can be found in Harvey & Edwards (1998).

2.2. Large eddy simulation

The 3-D cylindrical code of Pierce & Moin (1998b) is used for the LES calculations. An equation similar to that above for the RANS is solved for the mixture fraction. As in Pitsch & Steiner (2000), the sub-grid scalar mixture fraction variance is expressed as $\widetilde{Z''^2} = C_Z\Delta^2|\nabla \widetilde{Z}|^2$ with the coefficient, C_Z, determined using the dynamic procedure of Pierce & Moin (1998a). Further details of the LES solution techniques and modeling scalar mixing and dissipation rate can be found in these references.

2.3. Flamelet combustion modeling

Laminar diffusion flamelet modeling (Peters, 1984; Peters, 2000) has been successfully applied to nonpremixed methane combustion flames in both RANS (Pitsch *et al.*, 1998) and LES (Pitsch & Steiner 2000) frameworks. Following these references the unsteady flamelet equations for the species mass fraction, Y_i, and the temperature are written as

$$\rho\frac{\partial Y_i}{\partial \tau} - \rho\frac{\chi}{2}\frac{\partial^2 Y_i}{\partial Z^2} - \dot{m}_i = 0 \tag{2.7}$$

$$\rho\frac{\partial T}{\partial \tau} - \rho\frac{\chi}{2}\left(\frac{\partial^2 T}{\partial Z^2} + \frac{1}{C_p}\frac{\partial C_p}{\partial Z}\frac{\partial T}{\partial Z}\right) + \frac{1}{C_p}\sum_{k=1}^{N} h_k\dot{m}_k = 0 \tag{2.8}$$

where $\dot{m}_i$ is the chemical production rate per unit volume of species i and the scalar dissipation rate is $\chi = 2D_Z\nabla Z \cdot \nabla Z$ with the diffusion coefficient of the mixture fraction denoted as D_Z. In the so called Lagrangian flamelet model (LFM), flamelets are introduced at the nozzle inlet and are allowed to convect downstream through the flow. An expression which relates the axial position of the flamelet to Lagrangian flamelet time, $d\tau = \langle\widetilde{u}_{\widetilde{Z}}|\widetilde{Z}_{st}\rangle dx$, is defined by

$$\tau = \int_0^x \frac{dx'}{\langle\widetilde{u}_{\widetilde{Z}}|\widetilde{Z}_{st}\rangle(x',t)} \tag{2.9}$$

where $\langle\widetilde{u}_{\widetilde{Z}}|\widetilde{Z}_{st}\rangle$ is the resolved velocity component along the mixture fraction contour surface corresponding to the stoichiometric value, $\widetilde{Z}_{st}$. For steady flamelet modeling, the first term on the rhs of (2.7) and (2.8) is zero. Additional derivations and discussions on laminar flamelet equation modeling can be found in Pitsch & Steiner (2000) and Peters (2000).

Solution of Eqs. (2.7)-(2.9) yield the laminar flamelet structure of all scalar quantities $\phi = Y_i$, T. Using an assumed β-function pdf, $\widetilde{P}(Z, \mathbf{x}, t)$, whose shape is determined by the local mean and variance of the mixture fraction, Favre-averaged (RANS) or resolved values (LES) scalar quantities are obtained using

$$\widetilde{\phi}_i = \int_{Z=0}^1 \phi_i(Z, \mathbf{x}, t)\widetilde{P}(Z, \mathbf{x}, t)dZ \tag{2.10}$$

for all scalars quantities $\phi_i = Y_i$ and T. Note that for RANS calculations, $\widetilde{P}$ denotes the pdf for long time sampling, while for LES, $\widetilde{P}$ is the instantaneous pdf within the filter volume.

The form of the laminar flamelet model described above is not strictly suited to account for regions of strong flow re-circulation and radial diffusion due to the lack of a full description of spatial convection in the flamelet equations. However, for the preheated application to be presented in the next section, the effects of re-circulation is minimized. Application of an extended laminar flamelet concept which incorporates multi-dimensional effects is the subject of a future study.

2.4. RANS/flamelet model coupling

Implementation of the steady laminar flamelet (SLF) model entails solving Eqs. (2.7)-(2.10) for all scalar quantities at all possible values of the mean mixture fraction, $0 \leq \widetilde{Z} \leq 1$, variance, $0 \leq \widetilde{Z''^2} \leq 0.25$, and scalar dissipation rate, $0 \leq \widetilde{\chi} \leq \widetilde{\chi}_q$, where $\widetilde{\chi}_q$ is the quenching scalar dissipation rate. A table is then constructed containing $\widetilde{\phi}_i = \widetilde{\phi}_i(\widetilde{Z}, \widetilde{Z''^2}, \widetilde{\chi})$ for the scalars variables $\widetilde{\phi} = \bar{\rho}$, $\widetilde{T}$ and the mixture molecular weight $\widetilde{W}_m$ (required in the RANS implicit Jacobian terms). The flow is solved with the reacting RANS code using a single species equation with a variable molecular weight. At each
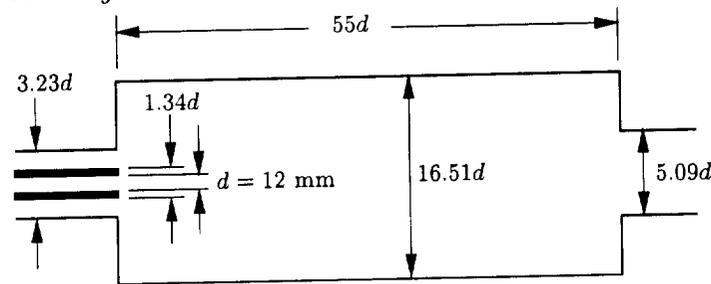
FIGURE 3. Model chloromethanes reactor geometry.

iteration the scalar dissipation rate is obtained from current values of k and ϵ, and $\widetilde{Z}$ and $\widetilde{Z''^2}$ are obtained from Eqs. (2.4) and (2.5), and then reference to the flamelet table is made to obtain new values of the scalar quantities $\bar{\rho}$, $\widetilde{T}$, and $\widetilde{W}_m$. The temperature equation in the RANS code is deactivated, and energy conservation is left to the flamelet code (Eq. 2.8).

In steady flamelet modeling the flamelet time does not appear in the equations, and it is assumed that the scalars, $\tilde{\phi}$, everywhere in the domain have the same functional dependence $\tilde{\phi}_i = \tilde{\phi}_i(\widetilde{Z}, \widetilde{Z''^2}, \widetilde{\chi})$. Once the solution has converged, the mass fractions of each species can be found from a similar flamelet table containing $\widetilde{Y}_i = \widetilde{Y}_i(\widetilde{Z}, \widetilde{Z''^2}, \widetilde{\chi})$.

In the Lagrangian flamelet model (LFM), a different flamelet solution is obtained at each axial plane in the computational grid. Computations incorporating unsteady flamelets involve first obtaining a converged steady flamelet solution to the flow as described above. The velocity of the stoichiometric surface, $\langle \tilde{u}_{\widetilde{Z}} | \widetilde{Z}_{st} \rangle (x)$, and conditional mean scalar dissipation rate at each plane $\langle \widetilde{\chi} | \widetilde{Z}_{st} \rangle (x)$ are computed in the RANS code. Equations (2.7)-(2.10) are solved for all scalar quantities in all $\widetilde{Z}$ and $\widetilde{Z''^2}$-space, and an unsteady flame table is constructed containing $\tilde{\phi}_i = \tilde{\phi}_i(\widetilde{Z}, \widetilde{Z''^2}, x)$ for $\tilde{\phi} = \bar{\rho}$, $\widetilde{T}$, and $\widetilde{W}_m$. This table is used by the RANS until the mixture field adjusts, at which time a new LFM table is constructed. This whole process is repeated until convergence.

The main implementation difference between SLF and LFM is that $\widetilde{\chi}$ in the SLF table is replaced by the axial coordinate in the LFM table. Each axial coordinate is treated as a separate flamelet with Lagrangian flamelet time given by Eq. (2.9) and with a unique conditionally averaged scalar dissipation rate.

2.5. LES/flamelet model coupling

Coupling of the LES calculations and the flamelet model proceeds in much the same manner as the coupling for the RANS. The major difference is in the way the conditional averages, scalar dissipation rate, and mixture fraction variance are computed. Further details can be found in Pitsch & Steiner (2000).

3. Results and discussion

A model nonpremixed chlorination flow is constructed by considering a confined coaxial jet configuration with inner pipe diameter, d (see Fig. 3). The use of subscripts p and a will denote quantities in the inner pipe and annulus, respectively. Chlorine preheated to $T_p = 800K$ is introduced through the inner jet and premixed M_1 ($Y_{M_1} = 0.47$) and M_2 ($Y_{M_2} = 0.53$) at $T_a = 323K$ is introduced through the annulus. The velocity ratio is
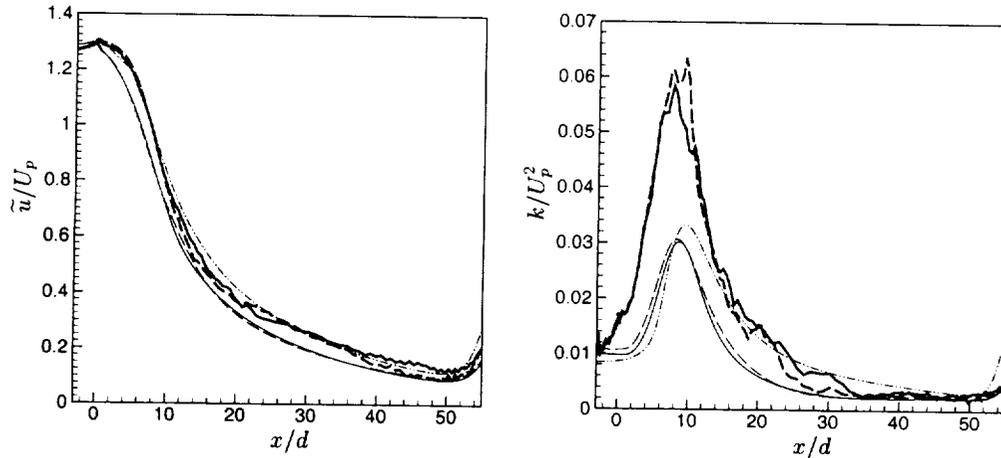
FIGURE 4. Centerline mean axial velocity (left) and kinetic energy profiles (right);
——— LES/LFM; – – – – LES/SLF; ——— RANS/LFM; – – – – RANS/SLF; —··— RANS/NC.
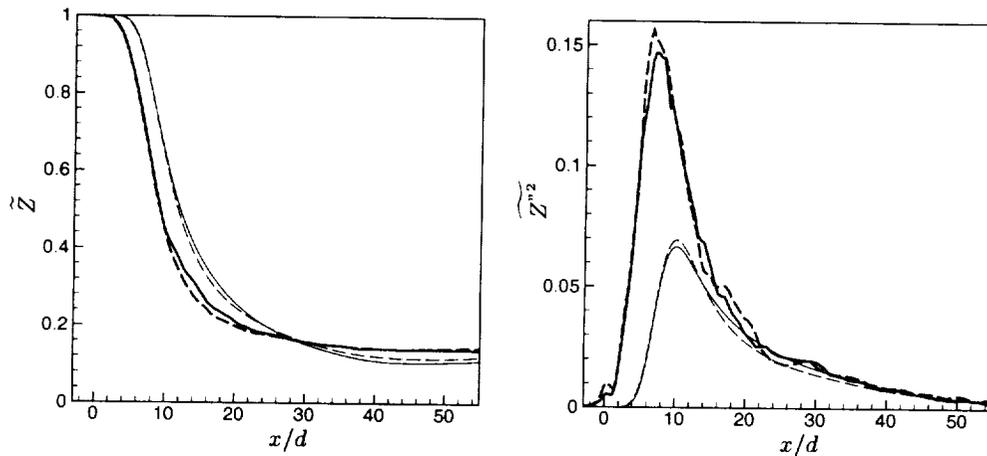
FIGURE 5. Centerline mean mixture fraction (left) and mixture fraction variance (right);
——— LES/LFM; – – – – LES/SLF; ——— RANS/LFM; – – – – RANS/SLF.

$U_p/U_a = 5$, the total Cl_2 mass fraction is 24%, and the bulk inner pipe velocity, U_p, is 7.905 m/s ($Re_p = 11910$). In all the RANS and LES calculations, fully developed turbulent profiles were computed using an appropriately long coaxial pipe. LES calculations were performed on a $130 \times 50 \times 24$ grid. For the present RANS work, 2-D axisymmetric calculations were carried out on a 6-zone grid with a total combined resolution of 225×129.

Computed centerline mean velocity and turbulent kinetic energy profiles are shown in Fig. 4 for all calculations. Predictions of velocity decay rates are similar for both RANS and LES. Mean velocity for the RANS calculations with flamelet combustion modeling drop off faster near the inlet, primarily due to the delay in the rise of kinetic energy near the entrance compared to the LES computations. LES predictions of kinetic energy showed a spike at the centerline which could possibly be an artifact of the boundary
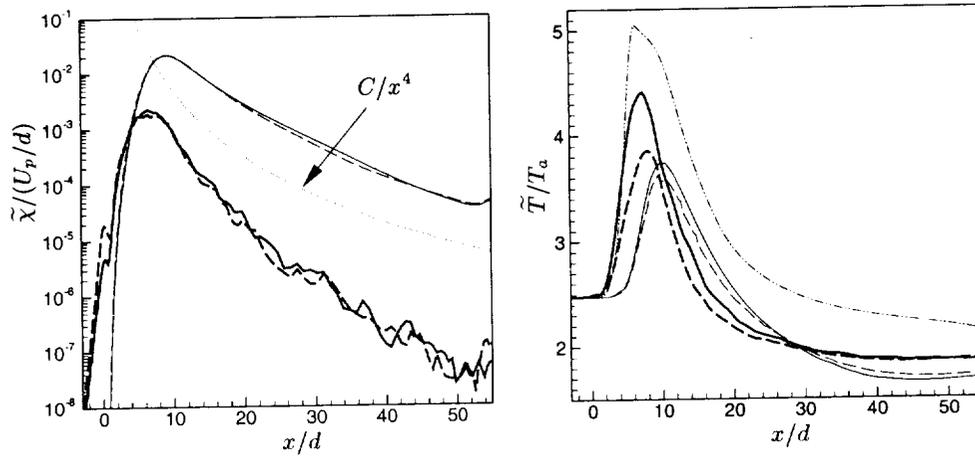
FIGURE 6. Centerline mean scalar dissipation rate (left) and mean temperature (right);
———— LES/LFM; - - - - LES/SLF; ———— RANS/LFM; - - - - RANS/SLF; —··— RANS/NC.

treatment and is currently being investigated further. The RANS computation neglecting closure closely follows the LES predictions of centerline velocity. This is because the temperature (shown later) is higher near the entrance than all other calculations, further resulting in an increased velocity compared to the other RANS calculations and offsetting the effect due to the lower kinetic energy levels seen in the LES.

Mean mixture fraction and mixture fraction variance are shown in Fig 5. Decay rates of $\widetilde{Z}$ are similar for the LES and RANS calculations. Unlike the velocity, which falls off quicker near the entrance for the RANS, the LES predicts a more rapid drop in $\widetilde{Z}$ at the nonpremixed nozzle exit. Differences between predicted centerline decay rates and overall levels of $\widetilde{Z}$ and $\widetilde{Z''^2}$ using the steady and unsteady flamelet model (SLF vs. LFM) are small.

Computed scalar dissipation rate along the centerline is shown in Fig. 6. RANS predictions are much higher than the LES calculations. Both techniques, however, predict similar decay rates that compare reasonably well with an C/x^4 scaling for an arbitrary constant C (dotted line).

Centerline temperature profiles are shown on the right of Fig. 6. Peak temperatures are highest and the temperature increase is steepest for the calculations neglecting closure. The significantly higher temperature predicted by the RANS calculation neglecting closure can be partially attributed to the fact that this is the only calculation performed in this study that takes into full account the effects of the flow re-circulation in the energy equation. The Lagrangian flamelet model (LFM) predicts higher peak temperatures and a faster temperature increase in the reaction zone than the steady flamelet model (SLF) results. The differences in the flow and mixing results are negligible.

Figure 7 shows differences in the computed mean velocity fields for the LES calculations (upper) and RANS (lower) coupled with the unsteady flamelet model. Results compare well; the largest discrepancies appear to be closest to the centerline.
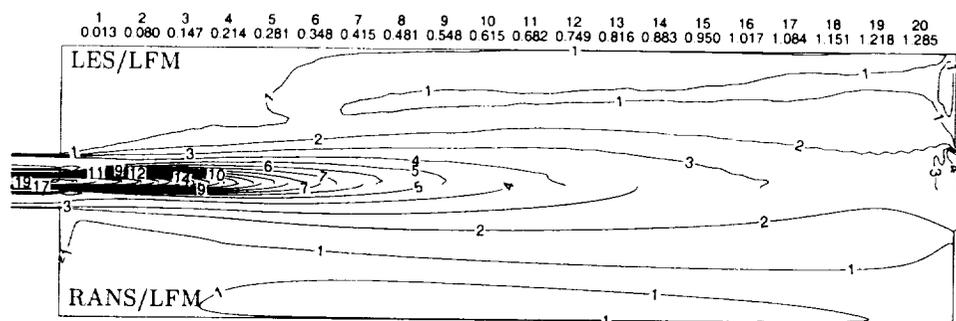
FIGURE 7. Comparison of mean velocity, $\tilde{u}/U_p$; LES/LFM (upper); RANS/LFM (lower).

4. Conclusions

Issues associated with modeling gas phase reacting methane thermochlorination flows in the petrochemical industry have been discussed. Commercial scale devices can be very large, and accurate model development and application must ultimately take into account both nonpremixed and premixed combustion physics with spray evaporation. RANS modeling neglecting turbulence closure fails to predict finite-rate chemistry effects, intermediate species formation, and localized reaction extinction.

A laminar diffusion flamelet combustion model was successfully coupled with a RANS code and a CTR-developed LES code. The turbulent reacting flow in a preheated, non-premixed methyl chloride thermochlorination device was computed. The largest differences between the RANS and LES computational results are in the predictions of the turbulent kinetic energy and scalar mixing. LES predictions of turbulent kinetic energy are significantly higher than the RANS calculations. Naturally one suspects the LES methodology to fare better in this regard. The differences in the centerline kinetic energy between the RANS and LES results are being examined further.

All calculations using the laminar flamelet closure predict lower peak temperatures in the reaction zone than the fully coupled reacting RANS calculation-neglecting closure. Use of the flamelet combustion model results in a more gradual increase in temperature in the reaction zone and possibly indicates that inclusion of source term closure results in a slower reaction rate compared to computations-neglecting closure. It could also be possible that the steeper gradient in the calculations-neglecting closure results because a higher maximum temperature must be reached at a comparable flame location.

Related ongoing work in support of this effort includes further investigations into nonpremixed turbulent chlorination flows. This work includes using an extended flamelet model which accounts for multi-directional diffusion effects between neighboring flamelets as well as the solution of a G-equation coupled with a flamelet model for premixed chlorination applications. These computational techniques should bring us closer to the longer term goal of developing methods for predicting complex combustion phenomena such as lifted flames, localized extinction, and re-ignition in thermochlorination devices.

for providing a stimulating research environment in which this work took place. In particular, Professor Parviz Moin for providing the opportunity to participate and Dr. Chong Cha and Professor Dan Haworth for many educational discussions on turbulent combustion modeling.

REFERENCES

ACHARYA, S., JANG, D. S., WEST, D. H. & HEBERT, L. A. 1991 A moment closure method for modeling a multistep chlorination reaction. *AIChE Paper 33a*, AIChE Spring National Meeting, Houston TX.

CHOI, Y. & MERKLE, C., L. 1993 The application of preconditioning in viscous flows. *J. Comp. Phys.* **105**, 207-223.

EDWARDS, J. R. 1997 A low-diffusion flux-splitting scheme for Navier-Stokes calculations. *Computers & Fluids.* **26**, 645-659.

HARVEY, A. D. & EDWARDS, J. R. 1998 Preconditioned Navier-Stokes for laminar methane-air nonpremixed combustion. (Unpublished), presented at American/Japanese Flame Research Committee International Symposium, Maui Hawaii.

PETERS, N. 1984 Laminar diffusion flamelet models in nonpremixed turbulent combustion. *Prog. Energy Combust. Sci.* **10**, 319-339.

PETERS, N. 2000 Turbulent Combustion, Cambridge University Press.

PIERCE, C. D., & MOIN, P. 1998a A dynamic model for subgrid-scale variance and dissipation rate of a conserved scalar. *Phys. Fluids.* **10**, 3041-44.

PIERCE, C. D., & MOIN, P. 1998b Large eddy simulation of a confined coaxial jet with swirl and heat release. AIAA Paper 98-1892.

PITSCH, H., CHEN, M. & PETERS, N. 1998 Unsteady flamelet modeling of turbulent hydrogen/air diffusion flames. *Twenty-seventh Symposium (Int.) on Combustion*, The Combustion Institute, 1057-1064.

PITSCH, H. & STEINER, H. 2000 Large-eddy simulation of a turbulent piloted methane/air diffusion flame (Sandia flame D). *Phys. Fluids.* **12**, to appear.

RAMAN, V., FOX, R. O., & HARVEY, A. D. 2000 Full PDF simulation of a coaxial thermochlorination reactor. *Paper JL.005,* 53rd APS Annual Meeting of DFD, Washington, DC.

SHAH, J. J. & FOX, R. O. 1999 CFD simulation of chemical reactors: application of in situ adaptive tabulation to methane thermochlorination chemistry. *Ind. Eng. Chem. Res.* **38**, 4200-12.

WEST, D. H., HEBERT, L. A. & PIVIDAL, K. A. 1999 Detection of quenching and instability in industrial chlorination reactors. *AIChE Paper 4b,* AIChE Fall National Meeting, Miami FL.

Toward a unified high-pressure drop model for spray simulations

By J. C. Oefelein and S. K. Aggarwal†

This research focuses on the development of a unified drop vaporization model for use in simulations of high-pressure spray combustion processes. Emphasis is placed on the analysis of supercritical and transcritical processes. These processes occur when a liquid drop that is initially at a subcritical temperature is injected into a high-pressure gaseous environment that exceeds the thermodynamic critical pressure of the interfacial mixture. For this situation the gas-liquid interface undergoes what is commonly referred to as a transcritical heating process. This process is dominated by thermodynamic nonidealities and transport anomalies. Classical models derived using the quasi-steady approximation fail in this limit because of the fundamental assumption that drop vaporization rates are dominated by quasi-steady convective processes. In the transcritical limit, drop vaporization rates are dominated by unsteady diffusion processes. These rate-limiting modes represent two extremes. Here we investigate these extremes by presenting the results from a series of direct numerical simulations. Emphasis is placed on the existence of two rate-limiting parameters and on obtaining a unified approach for modeling the transitional behavior of vaporizing drops over a range of pressures from atmospheric to supercritical.

1. Introduction

Transcritical drop vaporization occurs when the surface of a drop, initially at a subcritical temperature, reaches the critical mixing state (where both phases of the interfacial mixture exist in equilibrium simultaneously) sometime during its lifetime. As a drop evolves in a supercritical ambient, its temperature starts increasing due to heat transfer from the ambient, and vaporization is initiated. Since the drop surface has the highest liquid temperature, it attains the critical mixing state sometime during the drop lifetime. As the the surface approaches the critical mixing state, both surface tension and enthalpy of vaporization go to zero, solubility effects become important, and interfacial boundary conditions change significantly. The subsequent drop regression process is qualitatively different from that in the subcritical state.

A major difficulty in modeling transcritical vaporization stems from the fact that it is governed by processes which are fundamentally different from those which occur at subcritical or "low-pressure" conditions. As a consequence, the classical, quasi-steady, low-pressure models (see for example Godsave (1953), Spalding (1953), Faeth (1977), Law (1982), Faeth (1983), Sirignano (1983), Aggarwal, Tong & Sirignano (1984), Faeth (1987)) can not be used to describe this transcritical behavior. The fundamental difficulty with the classical models in the transcritical limit can be best illustrated by examining the

† University of Illinois at Chicago

quasi-steady equation for vaporization:

$$\tau_{l,LP} = \frac{d_p^2}{12} \frac{Pr_s}{\nu_s} \frac{1}{\ln(1 + B_{T,LP})} \tag{1.1}$$

where the thermal transfer number $B_{T,LP}$ is given by

$$B_{T,LP} = \frac{C_p(T_\infty - T_s)}{\Delta h_{v_p}} \tag{1.2}$$

Here d_p^2 represents the drop diameter, Pr_s the Prandtl number defined at the drop surface, and ν_s the kinematic viscosity at the drop surface. The terms C_p and Δh_{v_p} in Eq. (1.2) represent the constant pressure specific heat and enthalpy of vaporization, respectively. The term T_∞ represents the ambient temperature, and T_s the drop surface temperature. As the drop surface approaches the critical mixing state, C_p approaches infinity and Δh_{v_p} approaches zero, making the transfer number go to infinity. This condition implies that the vaporization rate becomes infinitely fast when in reality there is still a finite-rate effect.

Other fundamental differences between classical low-pressure and high-pressure vaporization phenomena include thermodynamic nonidealities and transport anomalies in the vicinity of gas-liquid interfaces. Interfacial mixture properties exhibit liquid-like densities and gas-like diffusivities. Solubility effects, which are typically negligible at low pressures, become essential considerations at high pressures. Treatment of interfacial thermodynamics becomes significantly more complex and liquid mass transport in the drop interior becomes important. The collective effect of these differences significantly enhances transient effects and drop deformation processes, and the quasi-steady approximation becomes invalid. A quantitative investigation of the quasi-steady assumption for high-pressure conditions has been reported recently by Zhu, Reitz & Aggarwal (2001).

Several recent studies (Shuen, Yang & Hsiao (1992), Jia & Gogos (1993), Givler & Abrahm (1996), Zhu & Aggarwal (2000), Yang (2000)) have focused on transcritical and supercritical vaporization phenomena and have considered many of the high-pressure effects outlined above. Comprehensive reviews of these investigations are provided by Givler & Abrahm (1996) and Yang (2000). Generally, a transient, spherically-symmetric model has been formulated to simulate gas- and liquid-phase processes associated with a drop evaporating in an ambient whose pressure and temperature exceed the critical values of the liquid. High-pressure effects such as gas-phase nonidealities, liquid-phase solubility of gases, and liquid-vapor equilibrium have been represented using appropriate cubic equations of state, or modified Benedict-Webb-Rubin equations of state, along with consistent sets of mixing rules for multicomponent mixtures.

The current investigation focuses on drops that are initially in a subcritical state and are introduced into a gaseous supercritical environment. For this set of conditions, drop surface mixture properties undergo transient heating and mass exchange processes that initially exhibit the classical low-pressure trends given by Eq. (1.1), then, after a period of time, transition to highly transient diffusion dominated processes. This transition occurs when the drop surface attains the critical mixing state. At this point, Eq. (1.1) fails and transcritical vaporization processes dominate at finite-rates.

The objective of this research is to characterize both modes of vaporization and the time-history effect associated with the transition process between these modes. We consider n-hexane–nitrogen systems over the range of pressures, temperatures, and thermodynamic regimes given in Fig. 1. The approach is based on previous work done by Zhu,
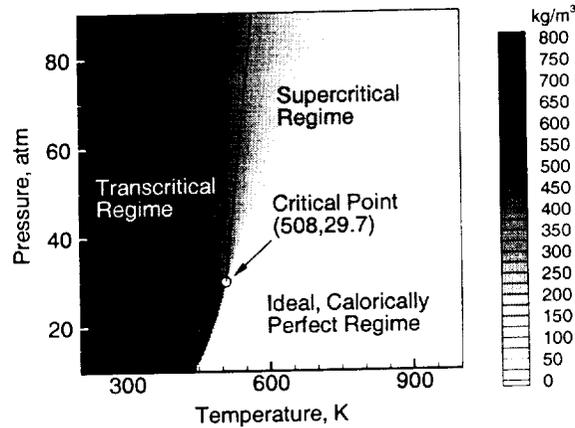
FIGURE 1. Contours of density as a function of pressure and temperature for n-hexane. The critical temperature and pressure is 508 K and 29.7 atm, respectively.

Reitz & Aggarwal (2001), Zhu & Aggarwal (2000), Yang (2000) and Oefelein (1997). We focus on two distinct issues. The first is on the development of a general correlation which is analogous to Eq. (1.1) and can be used to characterize vaporization rates above over a range of ambient conditions from atmospheric to supercritical. The second is on the development of a model which characterizes the associated transitional time-history effects. The goal is to develop a model that is sufficiently simple so that it can be feasibly applied in large-scale spray simulations in a manner analogous to the widely used low-pressure models.

2. Theoretical-numerical framework

The analysis was conducted by performing a series of direct numerical simulations (DNS) using two established theoretical-numerical frameworks, one developed by Oefelein (1997), the other by Zhu & Aggarwal (2000). Both frameworks solve the fully-coupled conservation equations of mass, momentum, total energy, and species for both the gas and liquid phases and take full account of gas-liquid interface dynamics.

The framework developed by Oefelein (1997) uses an extended corresponding states principle similar to that developed by Rowlinson & Watson (1969) to model thermophysical mixture properties over the relevant range of pressures and temperatures. A 32-term Benedict-Webb-Rubin (BWR) equation of state similar to that developed by Jacobsen & Stewart (1973) is used to predict PVT behavior for real gas, liquid, or gas-liquid mixtures. Enthalpy, Gibbs energy, and the constant pressure specific heat are obtained as a function of temperature and pressure using thermodynamic departure functions. Viscosity and thermal conductivity are obtained in a similar manner using the methodologies developed by Ely and Hanley Ely & Hanley (1981a), Ely & Hanley (1981b), Ely & Hanley (1981c). The effective mass diffusion coefficients are calculated using two models. Gas phase quantities, as dictated by phase equilibrium theory, are evaluated using the mixing rules given by Bird, Stewart & Lightfoot (1960) coupled with Chapman-Enskog theory, the Lennard-Jones intermolecular potential function Wilke & Lee (1955), and a high-pressure correction proposed by Takahashi (1974). Liquid phase quantities are evaluated
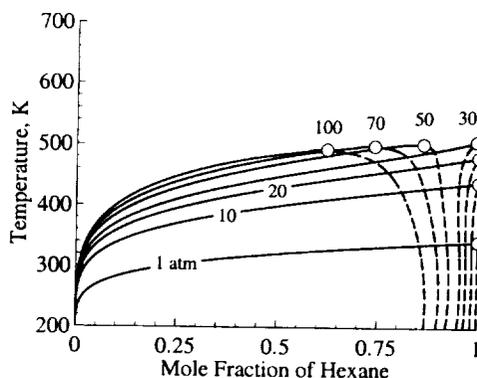
FIGURE 2. Vapor-liquid phase equilibrium composition for an n-hexane–nitrogen system at different pressures. Symbols: – – – – , liquid; ——— , vapor; o , critical mixing state.

using the mixing rules proposed by Perkins and Geankoplis Reid, Prausnitz & Poling (1987) and Hayduk & Minhas (1982).

The framework developed by Zhu & Aggarwal (2000) uses a similar property evaluation scheme but with a Peng-Robinson (PR) equation of state to represent nonideal behavior. This framework uses an arbitrary Lagrangian-Eulerian (ALE) numerical method which allows a dynamically adaptive mesh to be used to analyze interfacial time-history effects as a function of various initial conditions. For this situation transport across the discontinuity is balanced by the continuity of mass and energy fluxes and the condition of phase equilibrium. The accuracy of this scheme and that described above has been demonstrated in the works cited. Figure 1, for example, was obtained using the 32-term BWR equation of state with the corresponding states principle. This methodology has been shown to model the PVT behavior of liquid, vapor, and gaseous hydrocarbon mixtures to factors well within 2% of measured values. It is particularly accurate in the difficult region near the critical point. The PR equation of state exhibits similar accuracy but is slightly less accurate in its ability to map liquid-gas saturation properties.

3. Results and discussion

The modeled system is an isolated liquid-hexane drop surrounded by nitrogen gas in a spherically-symmetric domain. Calculations were performed by imposing two fundamentally different initial conditions at the drop surface. One set of results were obtained using the framework developed by Oefelein (1997) with the drop surface conditions initialized to the critical mixing state. A second set of results were obtained using the framework developed by Zhu & Aggarwal (2000) with the drop surface conditions initialized using jump conditions balanced by continuity of mass and energy fluxes and the condition of phase equilibrium. These initial conditions represent the limiting extremes. The former yields vaporization rates which are dominated by transient transcritical diffusion processes. The latter yields vaporization rates which are first dominated by quasi-steady subcritical processes, then, after a period of time, become dominated by transient transcritical diffusion processes.

Modeling drop vaporization processes hinges on an accurate representation of the gas-liquid interface. At subcritical conditions, the interface is characterized by jump conditions due to the presence of surface tension. When the critical mixing state is reached,
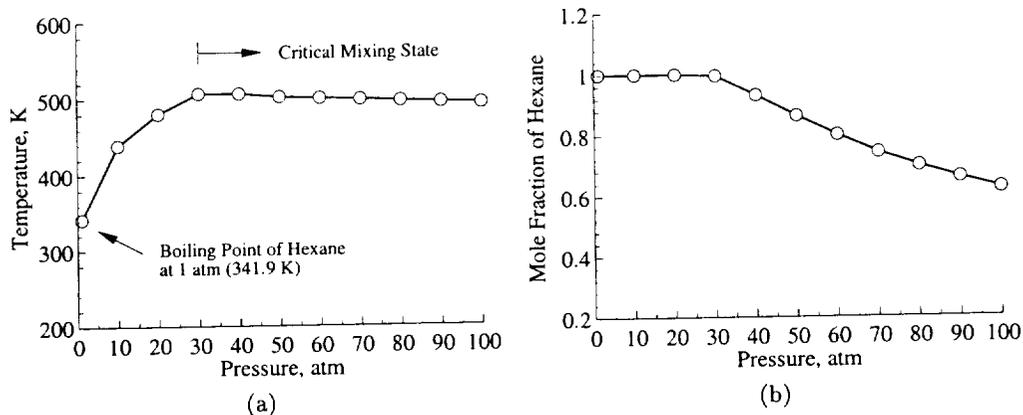
FIGURE 3. Equilibrium mixture temperature (a) and composition (b) as a function of pressure showing the boiling line and critical mixing line.
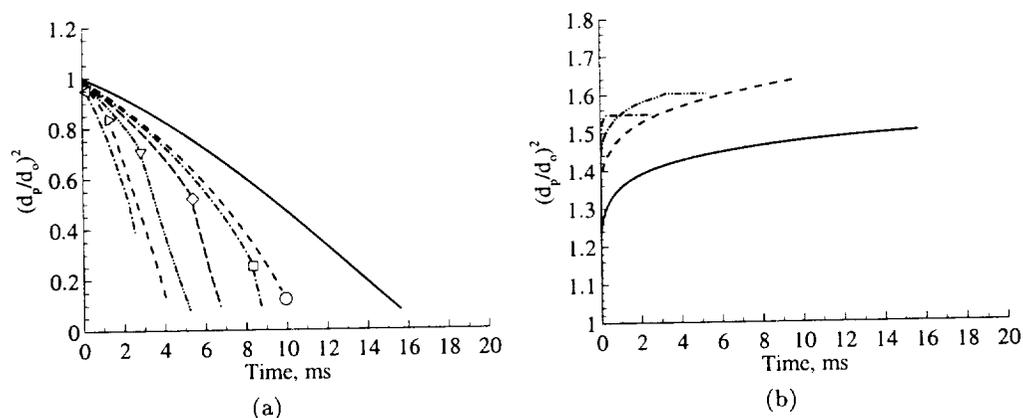
FIGURE 4. Temporal variation of the dimensionless drop surface (a) and surface temperature (b) for an n-hexane–nitrogen system. The initial temperature is 300 K, ambient temperature is 1500 K, and initial drop diameter is 100 μm. Attainment of the critical mixing state is represented with symbols. (a): ———— , 30; o , 90, □ ; 100, ◇ , 120; ∇, 150; ▷, 180; ◁, 220. (b): ———— , 30; – – – – , 90; —··— , 150; —·— , 220.

however, the drop surface becomes indistinguishable from the gas phase and subsequent drop regression is characterized by the motion of the critical surface. This surface is characterized by assuming that the interfacial mixture is in a state of thermodynamic equilibrium. Figure 2 shows the calculated equilibrium composition for an n-hexane–nitrogen system over the relevant range of pressures. The dashed lines represent the liquid phase, the solid lines represent the vapor phase, and the symbols represent the critical mixing state, which is the only point on the curve where both vapor and liquid can exist in equilibrium simultaneously. The locus of points represent the critical mixing state. These points are plotted in Fig. 3. The curve to the left of the critical pressure gives n-hexane boiling temperatures as a function of pressure. The curve to the right gives the critical mixing state as a function of pressure. In this limit, all other thermophysical surface properties can be calculated as a function of these primitives.

Figure 4 shows the dual modes of vaporization that can occur when drop surface conditions are initialized using jump conditions. Here the temporal variation of the di-
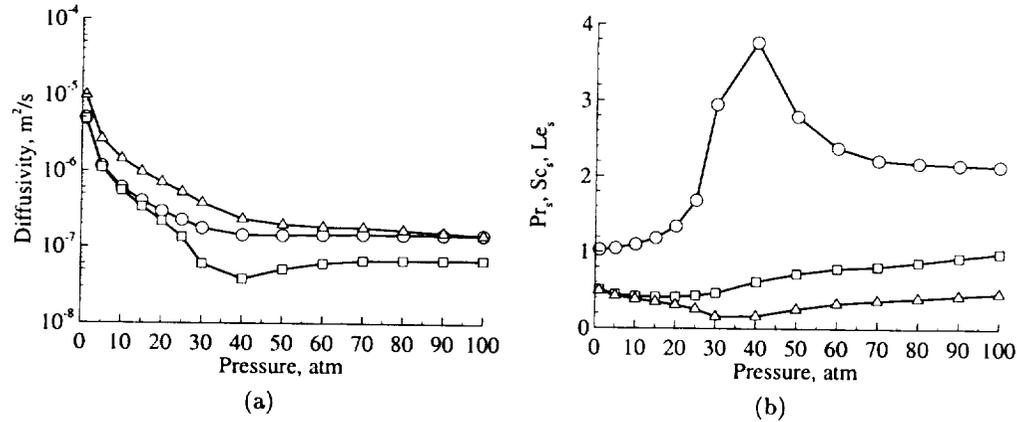
FIGURE 5. Mean variation in kinematic viscosity ν_s thermal diffusivity α_s and mass diffusivity $\mathcal{D}_{ij}$ (a) and the corresponding Prandtl, Schmidt, and Lewis numbers (b) as a function of pressure for an n-hexane–nitrogen system with initial liquid and ambient temperatures of 300 and 1500 K, respectively. Symbols: (a) $\circ$, ν_s; $\square$, α_s; $\triangle$, $\mathcal{D}_{ij}$. (b) $\circ$, Pr_s; $\square$, Sc_s; $\triangle$, Le_s.

mensionless surface area and surface temperature is given for a range of pressures which includes both the quasi-steady subcritical and the transient transcritical vaporization regimes. These histories have been validated with measurements reported by Nomura, Ujiie, Rath, Sato & Kono (1996). The attainment of the critical mixing state is indicated by respective symbols. Prior to reaching this state, drop vaporization rates are dominated by quasi-steady convective processes that are characterized quite accurately by Eq. (1.1). Upon reaching the critical mixing state, however, a distinct change in the vaporization rate occurs and Eq. (1.1) is no longer valid. The time associated with this transition can be significant.

3.1. Correlation for transcritical vaporization

Subcritical vaporization rates are well characterized by Eq. (1.1). This classic equation implies that drops vaporize according to a d_p^2 law and that the rate of vaporization for a fixed diameter is inversely proportional to the product of the thermal diffusivity at the surface and the term $\ln(1 + B_{T,LP})$, where $B_{T,LP}$ is the thermal transfer number given by Eq. (1.2). $B_{T,LP}$ is directly proportional to the product of the constant pressure specific heat and the temperature difference between the drop surface and ambient gas, and inversely proportional to the enthalpy of vaporization. Figures 5 and 6 show how the diffusion coefficients, enthalpy of vaporization, and surface tension vary as a function of pressure for a representative n-hexane–nitrogen system.

Difficulties arise with Eq. (1.1) in the limit as the drop surface approaches the critical mixing state. In this limit drop surface properties (as characterized by the pressure, temperature, and composition given in Fig. 3) become invariant with time and the drop surface regression rate is determined by the rate at which the critical surface moves inward. The diffusion coefficients remain well behaved, but the enthalpy of vaporization (which dominates relative to the rise in C_p) becomes zero. This drives Eq. (1.2) toward infinity, and, as a consequence, Eq. (1.1) incorrectly predicts the occurrence of an infinitely fast vaporization rate. In reality finite-rate effects are still prevalent.

Yang (2000) has identified two rate limiting parameters which can be used to quantify finite-rate vaporization processes in the transcritical limit. The first is a correction due to the spatial variation in thermal diffusivity which occurs between the ambient gas and
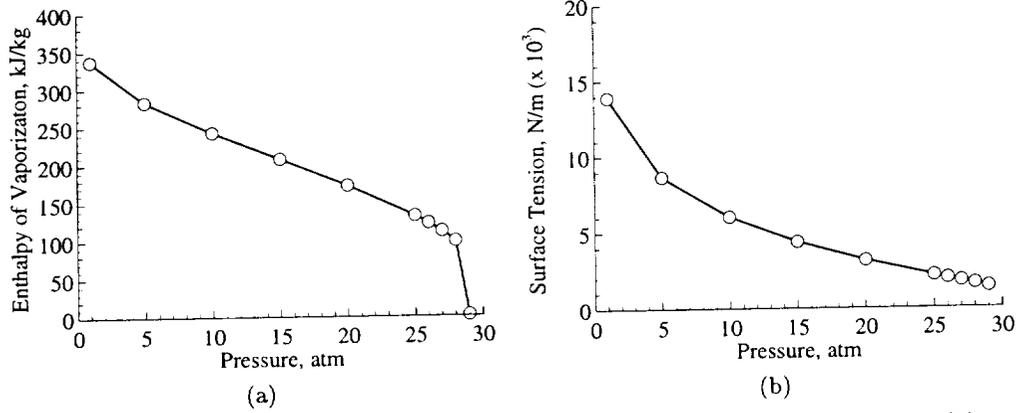
FIGURE 6. Mean variation in enthalpy of vaporization Δh_{v_p} (a) and surface tension σ_s (b) as a function of pressure for an n-hexane–nitrogen system with initial liquid and ambient temperatures of 300 and 1500 K, respectively.

drop. The second is a transfer number based on the critical mixing temperature:

$$B_{T,HP} = \frac{T_\infty - T_{cm}}{T_{cm} - T_p} \tag{3.1}$$

where T_∞ represents the ambient temperature, T_{cm} the critical mixing temperature, and T_p the temperature of the drop. The utility of these parameters has been validated for liquid-oxygen–hydrogen systems. The correction associated with the thermal diffusivity characterizes the limiting behavior of transient diffusion processes at the critical surface. Equation (3.1) characterizes the limiting behavior of energy exchange processes across the drop surface.

To obtain a general correlation, an expression analogous to Eq. (1.1) was sought that exhibited the correct limiting behavior over the interval $0 \le B_T < \infty$. This expression was obtained by solving the transient heat conduction equation for a solid sphere initially at a uniform temperature T_o in a quiescent ambient gas initially at a uniform temperature T_∞. After solving for the reduced temperature $(T_\infty - T)/(T_\infty - T_o)$ as a function of time and space, the resultant expression is integrated over the dimensionless time interval $0 \le \tau^* \le \tau_l^*$ to obtain an expression for the dimensionless drop life time:

$$\tau_l^* = \frac{\tau_l}{d_o^2/\alpha_o} \tag{3.2}$$

This solution is obtained in a manner consistent with the behavior of the critical interface by assuming that the surface temperature is constant. For this set of conditions, the reduced drop lifetime is only a function of the reduced interface temperature. This expression is given as:

$$(T_\infty - T_{cm})/(T_\infty - T_o) = B_{T,HP}/(1 + B_{T,HP}) \tag{3.3}$$

and, as shown above in Eq. (3.3), is directly related to the high-pressure transfer number defined by Eq. (3.1). The final solution is given by:

$$\frac{B_{T,HP}}{1 + B_{T,HP}} = \mathrm{erf}\left(\frac{1}{\sqrt{4\tau_l^*}}\right) - \frac{1}{\sqrt{\pi\tau_l^*}} \exp\left(\frac{1}{\sqrt{4\tau_l^*}}\right) \tag{3.4}$$

TABLE 1. Curve fit coefficients corresponding to Eqs. (3.5) (and (3.6)) for the interval $0 \leq B_T < \infty$.

	Set 1	Set 2	Set 3	Set 4
a_0	1.00×10^0	8.44×10^{-1}	5.37×10^{-1}	2.77×10^{-1}
a_1	1.94×10^0	3.36×10^{-1}	3.07×10^{-2}	1.76×10^{-3}
a_2	1.12×10^1	1.78×10^{-1}	1.82×10^{-3}	1.08×10^{-5}
a_3	5.22×10^1	6.88×10^{-2}	7.37×10^{-5}	4.43×10^{-8}
a_4	1.63×10^2	1.81×10^{-2}	1.99×10^{-6}	1.20×10^{-10}
a_5	3.35×10^2	3.21×10^{-3}	3.58×10^{-8}	2.18×10^{-13}
a_6	4.44×10^2	3.76×10^{-4}	4.23×10^{-10}	2.58×10^{-16}
a_7	3.64×10^2	2.78×10^{-5}	3.14×10^{-12}	1.93×10^{-19}
a_8	1.68×10^2	1.17×10^{-6}	1.33×10^{-14}	8.18×10^{-23}
a_9	3.35×10^1	2.15×10^{-8}	2.46×10^{-17}	1.51×10^{-26}

Set 1: $0 \leq 1/\ln(1 + B_T) < 1$ $1.718 \times 10^0 \leq B_T < \infty$
Set 2: $1 \leq 1/\ln(1 + B_T) < 10$ $1.052 \times 10^{-2} \leq B_T < 1.718 \times 10^0$
Set 3: $10 \leq 1/\ln(1 + B_T) < 100$ $1.005 \times 10^{-2} \leq B_T < 1.052 \times 10^{-1}$
Set 4: $100 \leq 1/\ln(1 + B_T) < 1000$ $0 \leq B_T < 1.005 \times 10^{-2}$

This equation establishes an analytic relation between the transfer number and the dimensionless drop lifetime.

The roots of Eq. (3.4) must be obtained numerically. After performing this operation and analyzing various trends, a functional dependence of the form:

$$\ln(1 + B_T)\, \tau_l^\star = \sum_{n=0}^{9}(-1)^n \frac{a_n}{[\ln(1 + B_T)]^n} \tag{3.5}$$

was obtained. The coefficients corresponding to this equation are given in Table 1. This equation approaches 0 in the limit as $B_T \to 0$, and 1 in the limit as $B_T \to \infty$. It is also interesting to note that for $a_0 = 1$ and $a_n = 0$ (n = 1-9), this equation reduces to the same form as Eq. (1.1). These well bounded characteristics suggest a correlation of the form:

$$\tau_{l,HP} = \frac{d_p^2}{12}\,\frac{Pr_s}{\nu_s}\,\frac{1}{\ln(1 + B_{T,HP})}\, f\left(\frac{\alpha_s}{\alpha_p}\right)\,\sum_{n=0}^{9}(-1)^n \frac{a_n}{[\ln(1 + B_T)]^n} \tag{3.6}$$

where here the time constant in Eq. (3.2) was replaced with the ratio d_p^2/α_s (with α_s represented above using the definition of the Prandtl number) and a correction factor of the form $f(\alpha_s/\alpha_p)$ was applied to account for the spatial variation in the thermal diffusivity. This variation is not accounted for in the analytic approximation.

To validate Eq. (3.6) a set of 43 simulations were performed. The matrix of cases considers pressures of 40, 50, 60, 70, 80, 90, and 100 atm with initial ambient temperatures of 600, 900, 1200, 1500, 1800 and 2100 K. In all cases the initial drop temperature was 300 K. Dimensional analysis shows that the initial drop diameter is the only length scale and that the drop lifetime is proportional to the diameter-squared. Thus only drops with an initial diameter of 100 μm are considered in the present analysis. The resultant drop lifetimes are plotted in Fig. 7a. To analyze the effectiveness of Eq. (3.6), the drop lifetimes plotted in Fig. 7a were compared to respective predictions using a fitted value
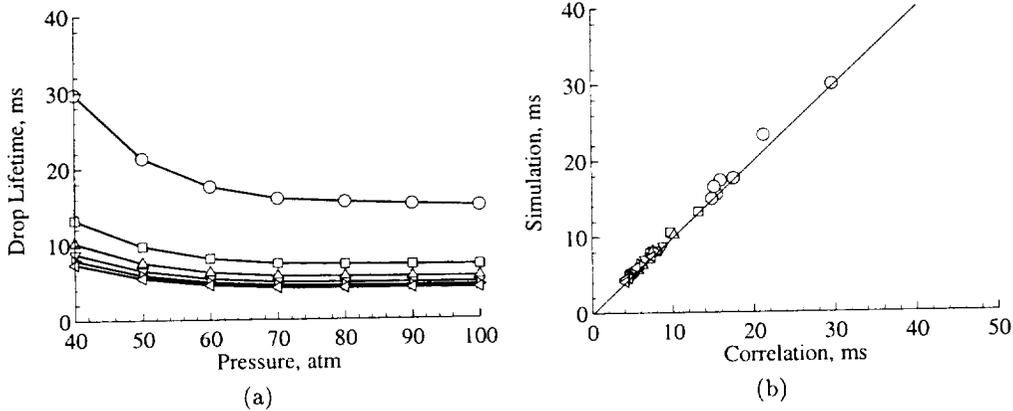
FIGURE 7. Transcritical drop lifetime as a function of pressure and temperature (a) and comparison of the vaporization rate given by DNS versus the correlation given by Eq. (3.6) (b). The initial drop temperature is 300 K. The initial drop diameter is 100 μm. $T_\infty = $ ∘ , 600K; □ , 900K; △, 1200K; ▽, 1500K; ▷, 1800K; ◁, 2100K.
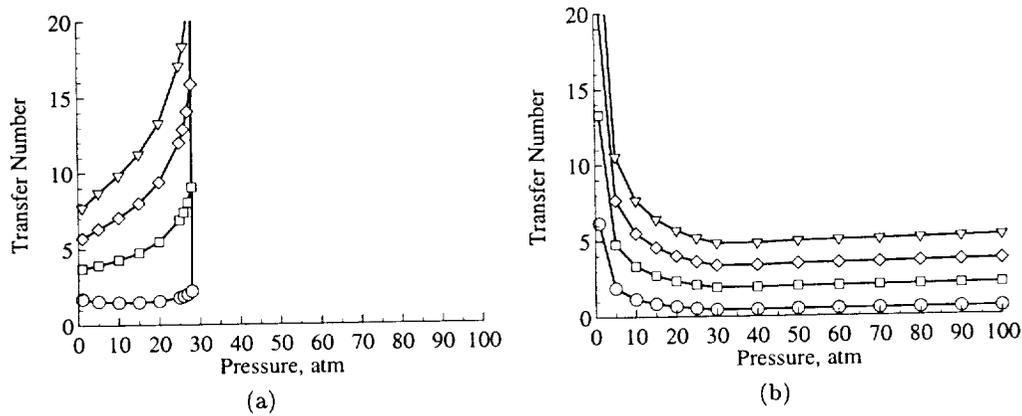
FIGURE 8. Mean variation of transfer number based on the classical low-pressure definition given by Eq. (1.2) (a) and the critical mixing temperature as given by Eq. (3.1) (b) as a function of pressure. $T_\infty = $ ∘ , 600K; □ , 900K; ◇ , 1200K; ▽, 1500K.

of $f(\alpha_s/\alpha_p) = 1.2$. This comparison is plotted in Fig. 7b, which shows respective drop vaporization rates given by the DNS compared with the corresponding rate given by Eq. (3.6). A least-squares fit of these data indicate that the agreement is within a margin of 5 percent.

3.2. Transitional behavior of the transfer number

Figure 8 shows the mean variation of transfer number based on the classical low-pressure definition, as given by Eq. (1.2), and the critical mixing temperature, as given by Eq. (3.1). The results exhibit several interesting trends. Fig. 8a shows that the low-pressure transfer number is strongly dependent on both pressure and ambient temperature. At 1 atm, this quantity is well behaved and varies from approximately 1.75 to 7.75 when the ambient gas temperature is varied from 600 to 1500 K. In the limit as pressure approaches the critical pressure of n-hexane, the low-pressure transfer number goes to infinity since the enthalpy of vaporization goes to zero. In contrast, the high-pressure transfer number
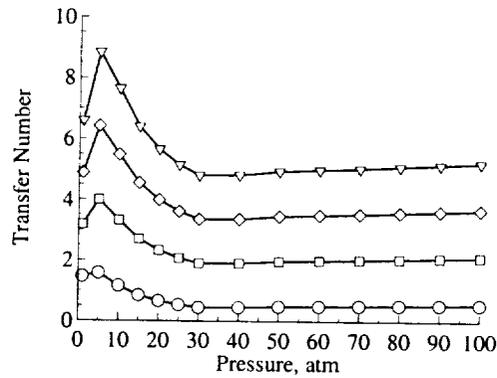
FIGURE 9. Composite transfer number obtained by evaluating Eq. (3.7) using the data given in Fig. 8. $T_\infty = $ ○ , 600K; □ , 900K; ◇ , 1200K; ▽, 1500K.

goes to infinity in the limit as pressure approaches zero, and it is well behaved as the pressure approaches infinity. At pressures above critical, there is a strong sensitivity to the ambient gas temperature but not to pressure. Here a variation from approximately 1 to 6 occurs when the ambient gas temperature is varied from 600 to 1500 K.

A last observation regarding Fig. 8 is that respective curves associated with the low and high transfer numbers intersect at the same pressure (7 atm for the conditions considered here). This implies that the transitional process from the low- to high-pressure transfer numbers is independent of both temperature and pressure and is only a function of the critical mixing pressure. This suggests that the transition process can be handled by using a transfer number defined as the minimum of the low-pressure and high-pressure values:

$$B_T = \min(B_{T,LP}, B_{T,HP}) \tag{3.7}$$

This equation incorporates transitional effects with the correct limiting behavior for pressure approaching 0 and ∞. It also peaks at the correct value of 7 atm; however, this may represent an overprediction. This detail will be addressed in future work. Figure 9 shows the composite transfer number corresponding the the results given in Fig. 8.

3.3. Transitional time-history effects

Equation (3.6) characterizes the transcritical mode of vaporization but not the time-history effects described above. The trends shown in Fig. 4 illustrated this effect quite clearly. For the cases shown, the drop never attains the critical mixing state at pressures below 90 atm. At pressures above 90 atm, the drop undergoes transcritical vaporization sometime during its lifetime. As pressure increases, this transition or the attainment of the critical mixing state occurs progressively earlier in its lifetime. At 220 atm, the drop attains the critical mixing state almost instantaneously.

The total drop lifetime, defined here as τ_v, consists of 1) the time to reach the critical mixing state τ_c, which decreases with pressure, and 2) the time associated with transcritical regression, which also decreases with pressure. To characterize the effects of ambient and drop properties on the attainment of the critical mixing state, we examine the ratio of the time to attain the critical mixing state relative to the total drop lifetime. Figure 10 shows the variation of this ratio as a function of pressure for different ambient temperatures and initial drop diameters. As τ_c/τ_v goes to unity, the drop surface regression is characterized completely by a subcritical vaporization process. As this ratio goes to zero,
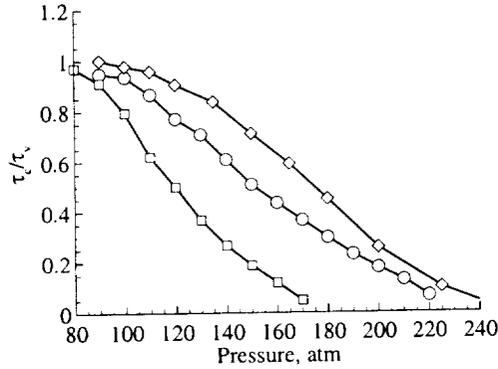
FIGURE 10. Ratio of time for an n-hexane drop to reach the critical mixing state versus total lifetime. Symbols: o , $100\mu m$, 1500K; □ , $100\mu m$, 2000K; ◇ , $200\mu m$, 1500K.
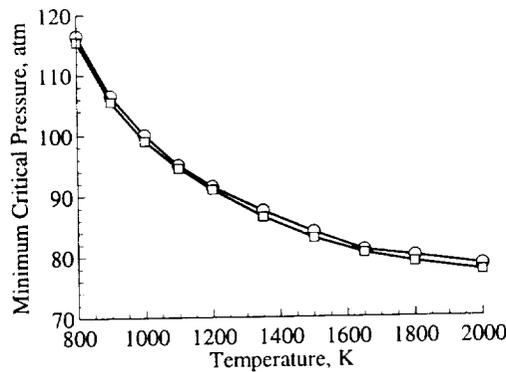
FIGURE 11. Minimum pressure required for an n-hexane drop to attain the critical mixing state. Symbols: o , $d_p = 100\mu m$; □ , $d_p = 100\mu m$.

the surface regression process is characterized completely by transcritical vaporization processes. This ratio decreases with pressure, which implies that τ_c decreases faster than τ_v. The time ratio parameter also decreases as the ambient temperature is increased and as the initial drop diameter is decreased. Both of these effects can be attributed to an inherent decrease in the drop heat-up time.

In Fig. 11, we plot the minimum pressure required for the attainment of critical mixing state as a function of ambient temperature. In order to obtain a minimum pressure value at a fixed ambient temperature, simulations were performed for increasingly higher pressures until a critical mixing state is observed at the drop surface. Thus, the curve in Fig. 11 represents a boundary between the subcritical and transcritical vaporization. Any point above the curve indicates that the critical mixing state will be reached sometime during the drop lifetime. The further a point is from the curve in the supercritical region, the smaller the ratio τ_c/τ_v, which implies the drop attains the critical mixing state earlier in its lifetime. On the other hand, any point below the curve corresponds to a condition of subcritical vaporization where τ_c/τ_v is one and the drop never attains the critical mixing state. This relation is useful in identifying the subcritical and supercritical vaporization regimes in a more quantitative manner. Another important observation from Fig. 11 is

that the minimum pressure required for the attainment of the critical mixing state is independent of the initial drop diameter.

4. Conclusions

This work represents a first step toward the development of a unified high-pressure drop model for spray simulations. The key trends have been quantified and a general correlation has been developed and validated for n-hexane–nitrogen systems. Key trends associated with the transfer number were also established over a relevant range of pressures and were shown to be bounded in the transcritical limit. Issues associated with surface heating and ambient conditions were also identified and analyzed.

To complete the model, this work must be extended to establish the quantitative variation in transfer number for mixing states in the transitional region that occurs at pressures between atmospheric and critical. The time-history associated with surface heating must be incorporated with companion correlations to account for convective effects in the ambient gas and subcritical and transcritical drop deformation processes.

Acknowledgments

REFERENCES

AGGARWAL, S. K., TONG, A., & SIRIGNANO, W. A. 1984 A comparison of vaporization models in spray calculations. *AIAA J.* **22**, 1448-1457.

BIRD, R. B., STEWART, W. E. & LIGHTFOOT, E. N. 1960 *Transport phenomena.* Wiley New York, New York.

ELY, J. F. & HANLEY, H. J. M. 1981a An enskog correction for size and mass difference effects in mixture viscosity predictions. *J. of Research of the National Bureau of Standards.* **86**(6), 597-604.

ELY, J. F. & HANLEY, H. J. M. 1981b Predictions of transport properties. 1. Viscosity of fluids and mixtures. *Industrial and Engineering Chemistry Fundamentals.* **20**(4), 323-332.

ELY, J. F. & HANLEY, H. J. M. 1981c Predictions of transport properties. 2. Thermal conductivity of pure fluids and mixtures. *Industrial and Engineering Chemistry Fundamentals.* **22**(4), 90-97.

FAETH, G. M. 1977 Current Status of Droplet and Liquid Combustion. *Prog. Energy & Combust. Sci.* **3**, 191-224.

FAETH, G. M. 1983 Evaporation and Combustion of Sprays. *Prog. Energy & Combust. Sci.* **9**, 1-76.

FAETH, G. M. 1987 Mixing, Transport, and Combustion in Sprays. *Prog. Energy & Combust. Sci.* **13**, 293-345.

GIVLER, S. D. & ABRAHAM, J. 1996 Supercritical droplet vaporization and combustion studies. *Prog. Energy & Combust. Sci.* **22**, 1-28.

GODSAVE, G. A. E. 1953 Studies of the combustion of drops in a fuel spray - the burning

of single drops of fuel. *Fourth Symposium (International) on Combustion*, Williams and Wilkins, Baltimore, MD, 818-830.

HAYDUK, W. & MINHAS, B. S. 1982 Correlations for prediction of molecular diffusivities in liquid. *Canadian J. of Chem. Eng.* **60**, 295-299.

JIA, H. & GOGOS, G. 1993 High-pressure droplet vaporization; Effects of liquid-phase gas solubility. *Int. J. Heat & Mass Transfer* **36** 4419-4431.

JACOBSEN, R. T. & STEWART, R. B. 1973 Thermodynamic properties of nitrogen including liquid and vapor phases from 63K to 2000K with pressure to 10,000 bar. *J. of Phys. and Chem. Ref. Data.* **2**(4), 757-922.

LAW, C. K. 1982 Recent advances in droplet vaporization and combustion. *Prog. Energy & Comb. Sci.* **8**, 171-201.

MATLOSZ, R. L., LEIPZIGER, S., & TORDA, T. P. 1972 Investigation of liquid drop evaporation in a high temperature and high pressure environment. *Int. J. Heat & Mass Transfer.* **15**, 831-852.

NOMURA, H., UJIIE, Y., RATH, H. J., SATO, J. & KONO, M. 1996 Experimental study of high-pressure droplet evaporation using microgravity conditions. *Twenty-Sixth Symposium (International) on Combustion*, The Combustion Institute, Pittsburgh, 1267-1273.

OEFELEIN, J. C. 1997 *Simulation and analysis of turbulent multiphase combustion processes at high pressures.* Ph.D. Thesis, The Pennsylvania State University, University Park, PA.

REID, R. C., PRAUSNITZ, J. M. & POLING, B. E. 1987 *The properties of gases and liquids.* McGraw-Hill Book Company.

ROWLINSON, J. S. & WATSON, I. D. 1969 The prediction of the thermodynamic properties of fluids and fluid mixtures - I. The principle of corresponding states and its extensions. *Chem. & Eng. Sci.* **24**(8), 1565-1574.

SPALDING, D. B. 1953 The combustion of liquid fuels. *Fourth Symposium (International) on Combustion*, Williams and Wilkins, Baltimore, 847-864.

SHUEN, J. S., YANG, V., & HSIAO, C. C. 1992 Combustion of liquid-fuel droplets in supercritical conditions. *Combust. & Flame.* **89**, 299-319.

SIRIGNANO, W. A. 1983 Fuel droplet vaporization and spray combustion. *Prog. Energy & Comb. Sci.* **9**, 291-322.

TAKAHASHI, S. 1974 Preparation of a generalized chart for the diffusion coefficients of gases at high pressures. *Japanese J. of Chem. Eng.* **7**(6), 417-420.

WILKE, C. R. & LEE, C. Y. 1955 Estimation of diffusion coefficients for gases and vapors. *Industrial Engineering Chemistry.* **47**, 1253-1257.

YANG, V. 2000 Modeling of supercritical vaporization, mixing, and combustion processes in liquid-fueled propulsion systems. *Twenty-Eighth Symposium (International) on Combustion*, The Combustion Institute, Pittsburgh, in print.

ZHU, G. S. & AGGARWAL, S. K. 2000 Transient supercritical droplet evaporation with emphasis on the effects of equation of state. *Int. J. Heat & Mass Transfer.* **43**, 1157-1171.

ZHU, G. S., REITZ, R. D. & AGGARWAL, S. K. 2001 Gas-phase unsteadiness and its influence on droplet vaporization in sub- and super-critical environments. To appear in *Int. J. of Heat & Mass Transfer.*

Simulation and modeling of the behavior of conditional scalar moments in turbulent spray combustion

By N. S. A. Smith†, C. M. Cha, H. Pitsch, AND J. C. Oefelein

A series of direct numerical simulations (DNS) have been conducted to examine the mixing and reaction statistics of spray combustion in forced isotropic turbulence. Particular attention has been given to statistics conditioned on mixture fraction to determine the modifications required for mixture-fraction based gas-phase combustion models. The goal is to apply these models in the presence of evaporating fuel droplets.

1. Introduction

Turbulent combustion in the gas phase is a complex phenomenon which has been the subject of a large body of research. However, even given an appropriate model for the treatment of turbulent gas-phase combustion, there are additional important physical processes which must be addressed if a practical predictive capability is to be derived.

A significant aspect of many combustion systems of practical interest is the presence and behavior of liquid fuel droplets. The strong influence that this condensed-phase species has upon practical combustion modeling is profound. Through the close interaction with the surrounding gas phase, the droplets influence the location, structure, and thermochemical yield of turbulent combustion zones within practical devices.

1.1. *Mixture fraction in a multiphase system*

When modeling turbulent nonpremixed combustion, it is common to employ a chemically conserved scalar, usually referred to as mixture fraction, as a coordinate for the computation of reactive scalar behavior. Examples of mixture fraction based models include the nonpremixed combustion versions of the steady and unsteady laminar flamelet methods of Peters (1984), Peters (1986) and coworkers, and the many variants of the conditional moment closure (CMC) method proposed by Klimenko (1990), Bilger (1993) and coworkers.

For pure gas-phase combustion, mixture fraction can be defined as an appropriate linear combination of reactive (and inert) species mass fractions such that it has no chemical source term. Since mixture fraction is defined as being conserved under chemical reaction, it is solely a measure of the fraction of mass present that originated from one of the two mixing streams. As such, its value is only subject to change due to mixing. This makes it an effective coordinate in which to solve conditionally averaged reactive scalar equations free from large mixing-induced fluctuations.

For liquid fuel combustion, however, mixture fraction is an ambiguous concept, and there are a number of alternatives for the definition. These alternatives result from 1) the

† Aeronautical & Maritime Research Laboratory, DSTO, Australia

question of whether to define it to be invariant under phase reaction or not, and 2) the spatial scale at which the definition is applied. If a mixture fraction ϕ is defined in terms of the gas-phase species alone on a spatial scale that is large compared to the mean free path length of the gas molecules but small compared to the interdroplet spacing, then its conservation equation is

$$\frac{\partial \phi}{\partial t} + u_i \frac{\partial \phi}{\partial x_i} = \frac{\partial}{\partial x_j} \left(\mathcal{D}_\phi \frac{\partial \phi}{\partial x_j} \right) , \tag{1.1}$$

where u_i denotes local velocity and $\mathcal{D}_\phi$ the molecular diffusivity of the scalar. The boundary condition at the irregular gas-liquid interface is given by

$$\left[\rho \mathcal{D}_\phi \frac{\partial \phi}{\partial n} \right]_{surf} = \dot{m} \left(f_{surf} - f_{liq} \right) , \tag{1.2}$$

where $\dot{m}$ is the mass evaporation rate at that surface, n is the surface normal coordinate, and f_{surf} and f_{liq} are the values of mixture fraction at the surface and in the liquid-phase. Klimenko and Bilger (1998) provide plausible probability density functions (PDFs) and scalar dissipation rate profiles for this mixture fraction. These are derived from scaling arguments. Due to the overwhelming computational burden of resolving droplet surfaces in a reacting turbulent simulation, it is not feasible to directly examine the dynamics of ϕ in this study. Here, analysis was limited to examining fields with scales of variation which were commensurate with those of the turbulence simulations.

If a mixture fraction denoted as ξ is defined in terms of the gas-phase species alone on a spatial scale that is large compared to mean free path lengths of gaseous molecules and interdroplet spacing so that it is a spatial average $\xi \equiv \{\phi\}$ of that given above, then its conservation equation is

$$\frac{\partial \xi}{\partial t} + u_i \frac{\partial \xi}{\partial x_i} = \frac{\partial}{\partial x_j} \left(\mathcal{D}_\xi \frac{\partial \xi}{\partial x_j} \right) + \dot{s}_\xi , \tag{1.3}$$

where $\dot{s}_\xi$ is an evaporative source term which represents the average flux of gaseous mass from the droplets, which exist on a spatial scale below the resolution of the equation.

At the spatial scale of the definition of ξ, it is, of course, possible to define a mixture fraction z which includes the mass associated with the droplets and the gas-phase alike,

$$z \equiv (1 - \alpha)\xi + \alpha , \tag{1.4}$$

where α is the mass fraction of the mixture which is associated with the liquid-phase. If α is assumed to be much smaller than unity, then $z \approx \xi + \alpha$ and the following is true,

$$\frac{\partial z}{\partial t} + u_i \frac{\partial z}{\partial x_i} = \frac{\partial}{\partial x_j} \left(\mathcal{D}_z \frac{\partial z}{\partial x_j} \right) + \dot{s}_z , \tag{1.5}$$

where the source term $\dot{s}_z$ is due to the strong differential diffusion between the different components of z. Here an explicit evaporative term is avoided. Note that in the above, slip velocities between the two phases have been assumed to be negligible. This is consistent with small "flow following" droplets.

One can pose the question as to which definition of mixture fraction provides the most convenient set of equations for use in the context of mixture fraction based nonpremixed combustion models. Klimenko and Bilger (1998) advocate the simultaneous use of two mixture fractions ϕ and z in a doubly-conditioned CMC methodology, while Réveillon and Vervisch (1998) employed the ξ mixture fraction in a study of unconditional mean evaporation and mixing statistics.

The level of resolution of the simulations conducted during the Summer Program made it possible to examine the statistics for ξ and z, but not those of ϕ. Due to space constraints, this report is limited to the analysis of ξ mixture fraction and modeling based on this quantity. Note however, that it seems to be possible to treat the differential diffusion associated with $\dot{s}_z$ in the z equation using the methodology of Smith, *et al* (1998) and Smith (1999).

1.2. *Conditionally averaged statistics*

The form of the instantaneous local equation (Eq. 1.3) for the coarse scale gas-phase mixture fraction ξ can be used to derive the corresponding PDF transport equation,

$$\frac{\partial P_\eta}{\partial t} + \frac{\partial}{\partial x_i}\left(\langle u_i \mid \eta \rangle P_\eta\right) = -\frac{\partial^2}{\partial \eta^2}\left(N_\eta P_\eta\right) - \frac{\partial}{\partial \eta}\left(\langle \dot{s}_\xi \mid \eta \rangle P_\eta\right) \tag{1.6}$$

where P_η is the mixture fraction PDF, and N_η denotes the conditional mean scalar dissipation rate which is given by

$$N_\eta \equiv \mathcal{D}_\xi \left\langle (\nabla \xi)^2 \mid \eta \right\rangle . \tag{1.7}$$

The shorthand $\langle \ldots \mid \eta \rangle$ construction denotes the average of the argument taken over all samples where the condition $\xi = \eta$ is met. It can be shown that for the conditional mean mass fraction $(Q_\eta \equiv \langle Y \mid \eta \rangle)$ of any reactive species, the corresponding conditional mean conservation equation can be written as

$$\frac{\partial Q_\eta}{\partial t} + \langle u_i \mid \eta \rangle \frac{\partial Q_\eta}{\partial x_i} = \langle \dot{\omega}_r \mid \eta \rangle + N_\eta \frac{\partial^2 Q_\eta}{\partial \eta^2} - \langle \dot{s}_\xi \mid \eta \rangle \frac{\partial Q_\eta}{\partial \eta} \tag{1.8}$$

where $\dot{\omega}_r$ is the net chemical production rate of mass fraction for the reactive species. It is clear from the equation above that the evaporative source term $\dot{s}_\xi$ plays a role in a pseudo-convective process in mixture fraction space for both the PDF and conditional moment equations.

One of the principal aims of the study was to examine the shape and magnitude of the conditional mean source term $\langle \dot{s}_\xi \mid \eta \rangle$ as a function of mixture fraction for different spray combustion cases. It was hoped that sufficient knowledge of $\langle \dot{s}_\xi \mid \eta \rangle$ could be gained from the simulation to devise an adequate model for the term from known quantities. It was further hoped that this model would allow the above reactive scalar equation to be solved in order to predict the conditional mean evolution of a smoke-like species in the simulations.

2. Simulation conditions

Many different modes of spray combustion exist. Group combustion, where a diffusion flame envelopes large groups of evaporating drops rather than individual droplets, is the most common in gas turbine applications (Kuo (1986)). The DNS were designed to embody the basic physical features of group combustion in the simplest possible flow and mixing configuration.

The DNS involved the Lagrangian tracking of small inertial droplets in forced isotropic incompressible turbulence on a 64^3 grid with a constant Taylor Reynolds number of ~ 50. In each simulation, the droplets were initially of uniform size and organized in a uniformly random distribution within a spherical cloud with a diameter equal to half the edge length of one cube of the periodic cubic domain. During the course of each simulation,

the droplets were redistributed throughout the domain, as a result of turbulent fluid motion, while evaporating to produce gaseous fuel in the turbulent fluid.

The droplets were defined to be sufficiently small so as to be in thermodynamic equilibrium with their surroundings so that their individual evaporation rates could be determined from

$$\frac{dm^k}{dt} = \pi \rho_{gas} \nu_{gas} D^k \frac{\mathcal{S}_h^k}{\mathcal{S}_c} \ln\left(1 + B^k\right) \; , \tag{2.1}$$

where ν_{gas} is the gas kinematic viscosity, D^k is the droplet diameter, $\mathcal{S}_h^k$ is the droplet Sherwood number, $\mathcal{S}_c$ is the Schmidt number of the evaporating species in the gas-phase, and B^k is the local instantaneous Spalding transfer number of the droplet. The Sherwood number of the droplet can be approximated by

$$\mathcal{S}_h^k \approx 2 + 0.6 \left(\left(\mathcal{R}_e^k\right)^{1/2} \mathcal{S}_c^{1/3}\right) \; , \tag{2.2}$$

where $\mathcal{R}_e^k$ is the droplet Reynolds number. The mass contributions from each of the droplets were summed at each step in the simulation to determine the mixture fraction source term $\dot{s}_\xi$ which is required for the solution of Eq. 1.3.

The Spalding transfer number was set to vary linearly with temperature, with values ranging between 3.4 and zero. The peak transfer number value was chosen to correspond with kerosene droplets evaporating within enveloping flames. The corresponding gas-phase stoichiometric mixture fraction ($\xi_s = 0.0625$) of kerosene was employed to specify the location of the peak transfer number in mixture fraction space. To account for individual droplets burning in fuel-lean regions, the transfer number B was set equal to the maximum value for all lean local mixture fractions ξ and was set to vary between zero and the maximum only on the rich side of stoichiometric.

Combustion was simulated using a *fast chemistry* approach so that all properties of the reacting mixture except the concentration of a minor pollutant were functions of the local instantaneous gaseous mixture fraction ξ, which was in turn governed by Eq. 1.3. The instantaneous local equation governing the evolution of the pollutant species mass fraction Y can be written as

$$\frac{\partial Y}{\partial t} + u_i \frac{\partial Y}{\partial x_i} = \frac{\partial}{\partial x_j}\left(\mathcal{D}_Y \frac{\partial Y}{\partial x_j}\right) + \dot{\omega}_r \; , \tag{2.3}$$

where the $\dot{\omega}_r$ denotes the net chemical production rate, and $\mathcal{D}_Y$ denotes the molecular diffusivity, which in practice was set equal to the diffusivity of mixture fraction ($\mathcal{D}_Y = \mathcal{D}_\xi$).

The purpose of including a non-equilibrium minor pollutant in each of the simulations was to provide a reactive scalar against which CMC model predictions could be assessed. The chemical behavior of the pollutant was defined so as to mimic soot in hydrocarbon flames. It was set to be produced under hot fuel-rich conditions and eliminated under hot fuel-lean conditions. The instantaneous local chemical production rate of the pollutant was given by

$$\dot{\omega}_r = k_1(\xi) - k_2(\xi)\frac{Y}{Y_{eq}}, \tag{2.4}$$

where Y_{eq} is a constant that determines the approximate magnitude of the equilibrium pollutant concentration. The terms k_1 and k_2 are rate coefficient functions of mixture

Case	n_d	r_D	f_v	$\langle z \rangle / z_s$	r_τ	G
2	1.e5	0.035	1.e-3	1.0	0.071	52100
4	1.e5	0.027	5.e-4	0.5	0.045	40200
5	1.e4	0.027	5.e-4	0.5	0.045	4020
6	1.e4	0.035	1.e-3	1.0	0.071	5210

TABLE 1. Characteristic parameters for spray combustion simulations. See text for symbol definitions.

fraction defined by

$$k_1(\xi) \equiv \begin{cases} k, & \text{for } \xi_s < \xi < 5\xi_s \\ 0, & \text{otherwise} \end{cases} \tag{2.5}$$

$$k_2(\xi) \equiv \begin{cases} k, & \text{for } 0 < \xi < \xi_s \\ 0, & \text{otherwise} \end{cases} . \tag{2.6}$$

Here, k is an arbitrary rate constant with the value of the stoichiometric mixture fraction set to the same value specified earlier. The value of the non-dimensional rate constant k/Y_{eq} was selected to be small compared to the Kolmogorov timescale to ensure a temporally well resolved chemical evolution of the pollutant in the simulation.

The transfer of conserved properties between Lagrangian droplets and Eulerian quantities of the fluid phase was achieved using tri-linear interpolation in physical space with a consistent summation method over cell volumes.

2.1. Parametric variation between cases

Four different simulations were conducted during the course of the Summer Program to examine the effect of varying droplet size and overall fuel-air ratio on the mixing and reaction behavior. The main features of these simulations are listed in Table 1. The primary differences between the cases result from arbitrary variation in the initial number of droplets n_d and the ratio of initial droplet diameter to the Kolmogorov length scale r_D. Forced turbulent statistics were invariant for all cases.

The packing and interaction between droplets within the computational domain is of increasing concern as the liquid volume fraction f_v increases. The simulations considered here did not allow for droplet-droplet interaction. This limitation restricted the maximum allowable liquid volume fraction to the small values listed in Table 1.

The overall fuel mass fraction in the domain was significant when considering the overall chemical stoichiometry of the computational system. This mass fraction was defined as the fraction of mass in the entire domain (including outside the cluster) which originated in the fuel droplets and is equivalent to the mean combined-phase mixture fraction $\langle z \rangle$ (see Sec. 1.1). It can be seen from Table 1 that two of the simulated cases had an overall fuel-air ratio corresponding to stoichiometric, while the other two cases correspond to half the stoichiometric value.

The ratio of the single droplet evaporative time scale to the Kolmogorov timescale r_τ is indicative of the amount of spatial movement that can occur during the lifetime of a fuel droplet. Large values of r_τ indicate that the droplet can evaporate over a protracted trajectory of motion through the surrounding fluid. The evaporative timescale ratio r_τ was determined using the evaporative rate equation (Eq. 2.1) and the stoichiometric reference condition, from which the well-known D^2-law of single droplet evaporation can be recovered. Under that law, the square of the droplet diameter decreases linearly with
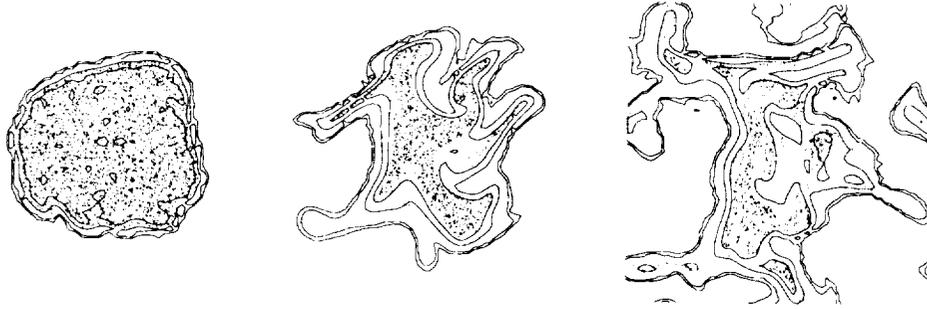
FIGURE 1. Three instances from a typical temporal evolution of a combusting spray cluster on a single slice through the domain over the course of a simulation in the periodic domain. Dots denote droplet location while lines denote isothermal contours.

time. Thus the single drop lifetime is directly proportional to the square of the initial droplet diameter when all other quantities are constant.

It is worth noting that the actual lifetime of the simulated droplet clusters exceeded the tabulated single droplet lifetimes to a degree which depended on the overall fuel-air ratio, and they were at least an order of magnitude greater in each case. This was because during group combustion, the efflux of fuel from other drops causes the conditions surrounding any given drop to be cooler than if it were in isolation.

Chiu and coworkers (see Kuo (1986)) have defined a group combustion number G which describes the ratio of droplet evaporation rate to the rate of mass transport from the droplet cluster. High values of G (e.g., $G > 10^2$) are associated with droplet clusters which are of such fuel type, droplet size, and spacing that allow for the evaporation of droplets within a non-combusting envelope that surrounds a core of non-evaporating droplets and is in turn surrounded at a standoff distance by the flame zone. Chiu calls this regime external sheath combustion. At the other extreme of G (e.g., $G < 10^{-2}$), droplets evaporate at a slower rate so that each individual droplet is enveloped in flame in the so-called single droplet combustion regime.

Following the definition of G, it is possible to simplify and nondimensionalize the definition to give the proportionalities $G \propto n_d r_D \propto f_v r_D^{-2}$. This indicates that for a fixed liquid volume fraction, the propensity for group combustion is proportional to the inverse square of the droplet diameter. From the values of G computed for Table 1, it is clear that all of the simulated cases fall well within the external sheath regime of group combustion.

Figure 1 provides a depiction of the temporal evolution of a typical simulation on a single slice through the domain at three instances over the course of two large-eddy turnover times. It is apparent that the initial spherical form of the cluster is quickly sheared into elongated shapes. Note that in the final (right-hand side) instance in the figure, the periodicity of the simulation is apparent as material is re-advected into the domain.
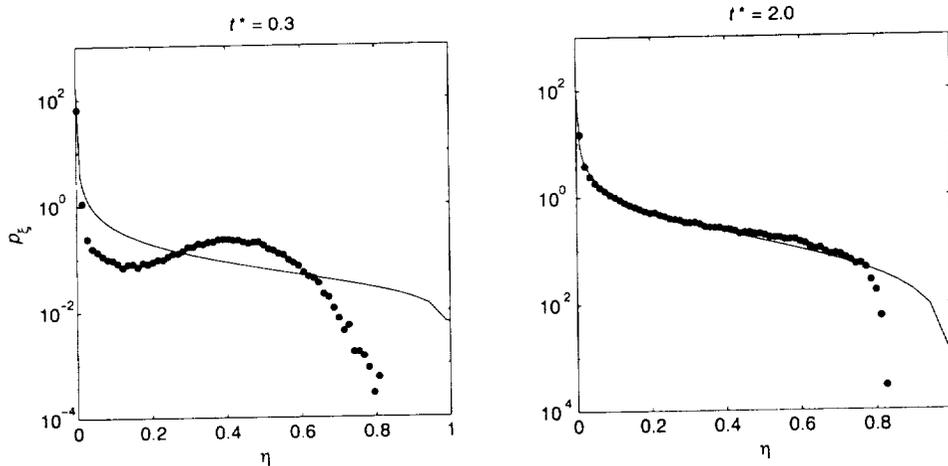
FIGURE 2. Case 6: Solid line $= p_\xi(\eta)$, the two-parameter $(\langle\xi\rangle,\langle\xi'\rangle)$ presumed β-function PDF at times (normalized by the large-eddy turnover time) 0.3 and 2.0; $\bullet$ = DNS data.

3. Simulation results

All of the simulation cases were observed to share the common feature of a monotonic increase in the global mean mixture fraction $\langle\xi\rangle$ from zero to a final steady value dictated by the constant value of $\langle z\rangle$ in each case. The only additional significant difference between the cases was the rate at which this steady value was approached, with the cases with smaller initial droplet diameters having the shorter rise times. The droplets were, in any case, essentially completely evaporated within two eddy turnover times (or about ten Kolmogorov timescales) from the initial condition.

This observed $\langle\xi\rangle$ behavior is consistent with the set of earlier unconditional statistical behavior observed by Réveillon and Vervisch (1998). Other unconditional mean statistical data such as mixture fraction variance $\langle\xi'^2\rangle$, and so on, also followed the findings of this earlier study. The observed behavior of $\langle\xi'^2\rangle$ can be characterized as having an initial brief rise period which results from interactions between fluctuations in the evaporated field and the continuing evaporative process (see Réveillon and Vervisch 1988). This rise is then followed by a monotonic decay in variance towards zero in a manner which is not unlike the decay of scalar variance in a single-phase mixing system.

The remainder of this report will deal with the important conditional statistics of the simulations which were not reported upon before and yet are critical to subsequent modeling. For the sake of brevity, the following results and analysis is limited to simulation Case 6, but the features discussed are evident in all cases.

Figure 2 depicts the evolution of the PDF of ξ over the course of a simulation and provides a β-function presumed form PDF for comparison. Its controlling parameters $\langle\xi\rangle,\langle\xi'^2\rangle$ have been taken directly from the DNS data. Typically, β-function presumed form PDFs are used extensively in mixture fraction based models to relate conditional and unconditional statistical properties in various model operations. Good agreement between actual mixture fraction PDF shapes and the presumed form is an implicit requirement for the application of the majority of these models, one which is usually well satisfied in single-phase systems.

Here, however, the β-function representation of the PDF is a poor approximation in the presence of a large mass of evaporating droplets. Note that in the final plot, the PDF
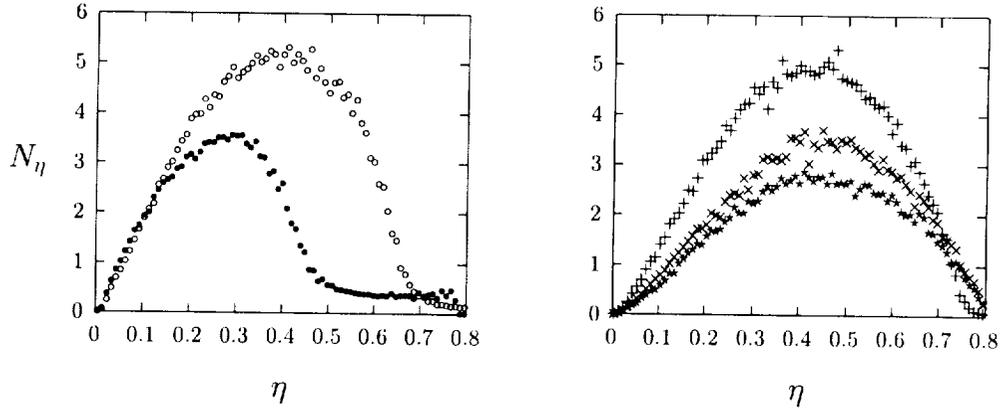
FIGURE 3. Conditional mean scalar dissipation rate (N_η) as a function of mixture fraction derived from DNS data at various times in the evolution of Case 6. Different symbols denote different times (normalized by the large-eddy turnover time): • − 0.1, ○ − 0.2, + − 0.3, × − 0.7, ⋆ − 1.1

agrees closely with the β-function since by that stage there is a total absence of droplets. The incorporation of additional spray-related parameters into a new presumed-form PDF is perhaps possible but was not attempted during the course of this study.

The related behavior of the conditional mean scalar dissipation rate N_η can be seen in Fig. 3. Unlike the case of mixture fraction in a single-phase system, it is evident from the left-hand plot that there is an initial 'pumping up' of the N_η profile before a monotonic decay is manifested in the right-hand plot. Further, the shape of the profile at stages where droplets are present is quite unlike that seen for purely passive scalar dissipation.

In mixture fraction based models for single-phase systems, N_η is required in order to solve Eq. 1.8 and is determined from the evolution of the presumed-form PDF by twice integrating the left-hand side of Eq. 1.6 between bounds (see Klimenko and Bilger 1998). The unusual behavior observed from these simulations renders this methodology doubtful for spray combustion applications. For the moment, however, we will assume that the statistics of ζ can be suitably modeled and focus on feasibility of modeling the combustion when in the presence of droplet evaporation.

4. Model predictions

In this section, we formulate and apply a variant CMC method to model the evolution of the smoke-like pollutant species (see Sec. 2) in the simulated spray combustion.

4.1. Variant model equations

The primary feature of the variant method is a "floating" rich boundary condition, which is treated through an advantageous change in conditioning variable,

$$\zeta \equiv \frac{\eta}{\xi_R}, \tag{4.1}$$

where $\xi_R(t)$ represents the rich boundary which changes in time due to the counteracting effects of droplet evaporation and mixing. Pitsch (1998) has previously applied this type of transformation in relation to flamelet modeling. The change of variables transform

Eq. 1.8 to yield

$$\frac{\partial Q}{\partial t} = \frac{N_\zeta}{\xi_R^2}\frac{\partial^2 Q}{\partial \zeta^2} + \langle \dot\omega_r | \zeta \rangle + \left(\frac{\zeta}{\xi_R}\frac{d\xi_R}{dt} + \frac{\langle \dot s_\xi | \zeta \rangle}{\xi_R} \right)\frac{\partial Q}{\partial \zeta} , \qquad (4.2)$$

where N_ζ corresponds to N_η under the Eq. 4.1 transformation. The initial and lean-boundary conditions for the conditional mean mass fraction of the pollutant are given by

$$Q(\zeta, t = 0) = 0 \quad \text{and} \quad Q(\zeta = 0, t) = 0 ,$$

respectively. To formulate the rich boundary condition, we draw upon results from an analogous simplified problem.

4.2. Laminar single-droplet analogy

A boundary condition for Eq. 4.2 at $\zeta = 1$ ($\eta = \xi_R$) can be found from consideration of a single fuel droplet evaporating in still air. The governing spherically-symmetric, steady, one-dimensional equations in the radial coordinate (r) for this system can be found in Williams (1985). For all species besides fuel, the boundary condition at the drop surface $(r = r_l)$ is,

$$\left(\dot m Y - 4\pi r^2 \rho \mathcal{D}\frac{dY}{dr} \right)_{r=r_l} = 0. \qquad (4.3a)$$

Defining the scalar dissipation rate $\chi \equiv 2\mathcal{D}(d\xi(r)/dr)^2$ for this laminar case and transforming Eq. 4.3a to the scalar ξ space yields

$$\left(\dot m Y(\xi) - \frac{\dot m^2}{4\pi\rho\mathcal{D}}\frac{1}{\ln(1-\xi)^2}\sqrt{\frac{\chi}{2\mathcal{D}}}\frac{dY}{d\xi} \right)_{\xi=\xi_R} = 0, \qquad (4.3b)$$

where $\xi(r_l) \equiv \xi_R$. Equation 4.3b applies to any choice of ξ so long as its value is known at the droplet interface. Both $\dot m(\xi_R)$ and $\chi(\xi_R)$ must also be known in this methodology, but this is not especially difficult given that provisions must already have been made to determine the remainder of these conditional mean profiles.

Equation 4.3b is used to extrapolate the rich boundary condition for Eq. 4.2. Here we simply assume Eq. 4.3a is valid for the turbulent case and conditionally average Eq. 4.3b. A further change of variables given by Eq. 4.1 will yield

$$\left(\langle \dot s_\xi | \zeta \rangle Q - \frac{\langle \dot s_\xi | \zeta \rangle^2}{4\pi\rho\mathcal{D}}\frac{1}{\xi_R \ln(1-\xi_R)^2}\sqrt{\frac{N_\zeta}{\mathcal{D}}}\frac{\partial Q}{\partial \zeta} \right)_{\zeta=1} = 0. \qquad (4.4)$$

This equation is to be enforced at the rich boundary of Eq. 4.2. Equation 4.4 assumes quasi-steadiness since ξ_R is a function of time.

4.3. Results and discussion

The effectiveness of the variant model embodied by Eq. 4.2 can be tested by comparing predictions for conditional mean smoke mass fraction with the evolution observed from the spray combustion simulations.

In this test, *a priori* information is required in the form of the observed N_η and $\langle \dot s_\xi | \eta \rangle$ profiles from the DNS. These observed quantities are mapped to ζ space via linear interpolation. The floating rich bound on mixture fraction (ξ_R) is defined to be that value where $\langle \dot s_\xi | \eta \rangle$ is a maximum. It is noted that, as with the earlier findings of Réveillon and Vervisch (1998), the profile of $\langle \dot s_\xi | \eta \rangle$ was found to exhibit a monotonic increase with mixture fraction at all times and in all cases. The time derivative of the
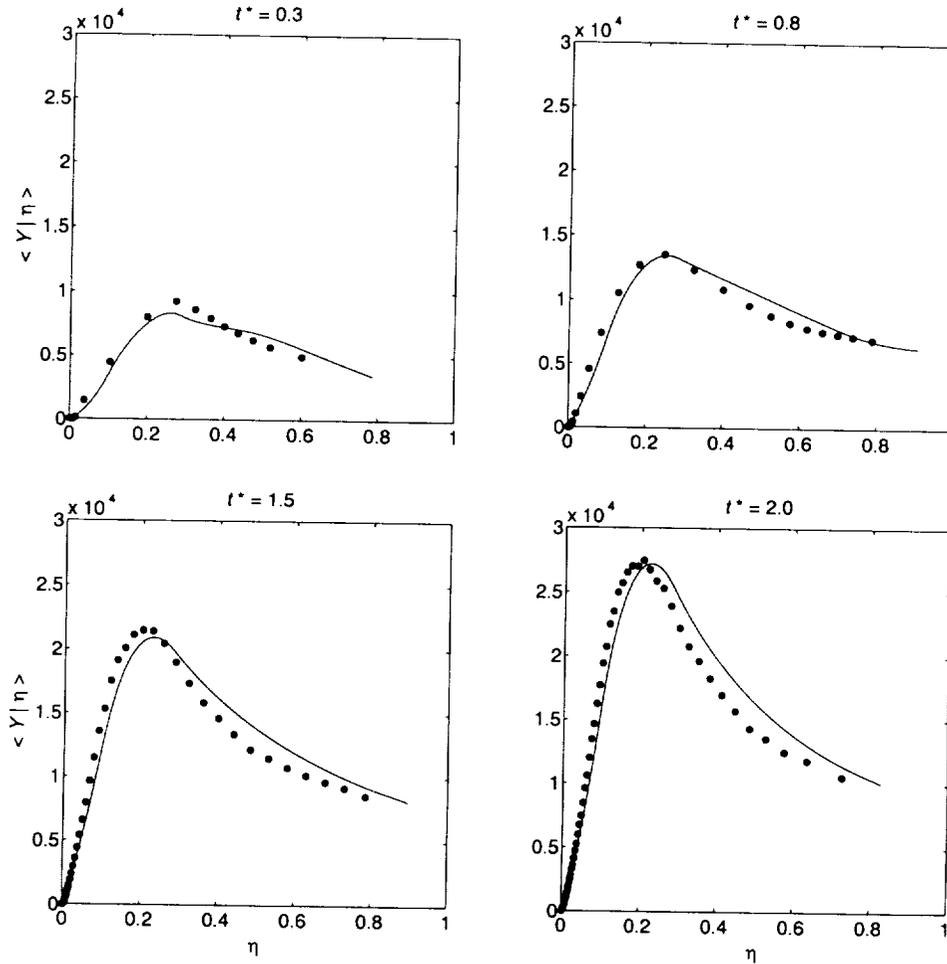
FIGURE 4. Case 6: Solid line $=$ *a priori* modeling solutions of $\langle Y|\eta\rangle$ from Eq. 4.2 at times (normalized by the large-eddy turnover time) 0.3, 0.8, 1.5, and 2.0; $\bullet$ $=$ DNS data.

value of the rich bound $(d\xi_R/dt)$ was calculated from a cubic spline fit to the resultant DNS data for $\xi_R(t)$. Cubic splines were also used to interpolate the *a priori* N_η and $\langle \dot{s}_\xi \mid \eta \rangle$ data in time where temporally-local DNS data was not available in the time record.

Predicted and observed conditional mean results for smoke formation in simulation Case 6 (see Table 1) are shown in Fig. 4. The CMC modeling predictions, which use *a priori* mixing information, are clearly good estimates of the DNS experimental data for all the times of interest. Although not plotted due to space restrictions, the respective model predictions compare equally favorably for all of the other simulation cases. This outcome is encouraging for future model development, which must necessarily focus on finding submodels to obviate the need for the *a priori* information employed in this test.

In order to use Eq. 4.2 in an *a posteriori* role, additional models are required for the interrelated quantities ξ_R, $\langle \dot{s}_\xi \mid \eta \rangle$, and N_η. In theory, it is possible to solve reactive conditional moment equations like Eqs. 1.8 and 4.2 for droplet mass fractions and number densities and in so doing compute $\langle \dot{s}_\xi \mid \eta \rangle$ directly. The differential diffusion inherent in

these equations could be treated in the manner of Smith (1998, 1999). The value of ξ_R and its time derivative would also then be available from the expression,

$$\frac{d\xi_R}{dt} = \left[\frac{1}{P_\eta} \frac{\partial}{\partial \eta} (N_\eta P_\eta) + \langle \dot{s}_\xi \mid \eta \rangle \right]_{\eta=\xi_R} \cdot$$

Further simplification may be possible if it eventuates that the PDF slope term on the right-hand side of the above equation is zero as it is in single-phase mixing cases, so that,

$$\frac{d\xi_R}{dt} = [\langle \dot{s}_\xi \mid \eta \rangle]_{\eta=\xi_R} \cdot \tag{4.5}$$

Alternatively, a simple empirical model for $\langle \dot{s}_\xi \mid \eta \rangle$ could be employed as was done by Réveillon and Vervisch (1998) for a different purpose. For the DNS cases considered here, a least-squares curve-fit of $\langle \dot{s}_\xi \mid \eta \rangle \sim \eta^n$ (for $\eta \in [0, \xi_R]$) reveals that $\langle \dot{s}_\xi \mid \eta \rangle$ is approximately linear ($n \approx 1.1$ averaged over time). Réveillon and Vervisch (1998) found that n varied more widely according to the regime of spray combustion. This empiricism is perhaps best avoided by using the conditional moment modeling approach for $\langle \dot{s}_\xi \mid \eta \rangle$ in tandem with the chemically reactive scalars.

The need to provide accurate N_η data for the solution of the CMC equations is a more difficult problem. This problem is made particularly onerous by the absence of an easily parameterized form for the mixture fraction PDF. Réveillon and Vervisch (1998) make use of the β-function presumed form despite its poor agreement with mixture fraction profiles in spray combustion as observed in this study (see Fig. 2). In fact, the inapplicability of simple presumed form PDFs in spray combustion throws doubt on the validity of their use of their one droplet model (ODM) (Réveillon and Vervisch, 1998).

It may be appropriate as a rough approximation to use the β-function presumed form in conjunction with the unconditional mean and variance equations for mixture fraction (as described by Réveillon and Vervisch) for the single purpose of determining an estimate of N_η. This would be done in the usual manner (Klimenko and Bilger 1998) via the double integration of the left-hand side of Eq. 1.6. While this process would likely give reasonable "bulk" magnitudes for the N_η profile, one should be aware that correct profile shapes would not result and even negative N_η profile sections may emerge from the process.

In the absence of an effective presumed form PDF, the only viable alternative is to employ a stochastic methodology for predicting the evolution of the mixture fraction in the PDF and the CMC equations (Klimenko and Smith 2000). Such a method would involve a significant shift away from traditional CMC and unsteady flamelet methodologies but could prove fruitful even beyond the confines of spray combustion.

5. Final remarks

Direct numerical simulations of the group combustion of spray clusters in isotropic turbulence have revealed some important previously unreported observations. Not unexpectedly, it has been found that when in the presence of evaporative sources, mixture fractions defined in terms of gas-phase mass exhibit statistics which are quite distinct from those of single-phase systems.

Perhaps most importantly, the shape and behavior of the mixture fraction PDF is found to deviate significantly from the forms typically seen in pure gas-phase combustion. This observation poses significant complications for the application of gas-phase mixture fraction based combustion models in a liquid fuel environment. This finding calls into

question models proposed at earlier Summer Programs which do not acknowledge these deviations.

Using *a priori* mixing information from the simulations, a new variant of the conditional moment closure and unsteady flamelet family of models was found to provide very accurate predictions of the conditional mean chemical formation of a smoke-like pollutant in the spray combustion systems studied.

Future work will focus on better understanding and parameterizing the gas-phase based mixture fraction PDF forms in spray combustion through further and a more extensive DNS program. This is the current stumbling block to the immediate application of the widely successful mixture fraction based models to spray combustion.

Acknowledgments

REFERENCES

BILGER, R. W. 1993 Conditional Moment Methods for Turbulent Reacting Flow. *Phys. Fluids.* **5**, 436-444.

KLIMENKO, A. YU. 1990 Multicomponent Diffusion of Various Admixtures in Turbulent Flow. *Fluid Dyn.* **25**, 327-334.

KLIMENKO, A. YU. & BILGER, R. W. 1998 Conditional Moment Closure for Turbulent Combustion, submitted to *Progress in Energy and Combustion Sci.*

KLIMENKO, A. YU. & SMITH, N. S. A. 2000 Private communication.

KUO, K. K. 1986 *Principles of Combustion.* John Wiley and Sons Inc., New York.

PETERS, N. 1984 Laminar diffusion flamelet models in nonpremixed turbulent combustion. *Progress in Energy & Combustion Sci.* **10**, 319-339.

PETERS, N. 1986 Laminar Flamelet Concepts in Turbulent Combustion. *Twenty-First Symposium (International) on Combustion*, the Combustion Institute, Pittsburgh, 1231-1250.

PITSCH, H. 1998 *Modellierung der Zündung und Schadstoffbildung bei der dieselmotorischen Verbrennung mit Hilfe interaktiven Flamelet-Modells. PhD thesis*, RWTH Aachen.

RÉVEILLON, J. & VERVISCH, L. 1998 Accounting for spray vaporization in turbulent combustion modeling. *Proceedings of the Summer Program*, Center for Turbulence Research, NASA Ames/Stanford Univ. 25-38.

SMITH, N. S. A., RUETSCH, G. R., OEFELEIN, J. C., & FERZIGER, J. 1998 Simulation and modeling of reacting particles in turbulent nonpremixed combustion. *Proceedings of the Summer Program*, Center for Turbulence Research, NASA Ames/Stanford Univ. 39-60.

SMITH, N. S. A. 1999 On the differential diffusion of passive scalars in homogeneous turbulence: Implications for combustion modeling. *Proceedings of the 1999 Australian Symposium on Combustion*, University of Newcastle, Australia.

WILLIAMS, F. A. 1985 *Combustion Theory.* Benjamin-Cummings, New York.

The turbulence modeling group

The papers in this section encompass Reynolds averaged modeling (RANS) and large eddy simulation (LES). They are addressed to effects of rotation and stratification on turbulence, to bypass transition to turbulence, and to numerics.

From a practical standpoint, RANS is the only method of turbulent flow prediction that has found widespread use in engineering flows. One of the many roadblocks to use of LES is the need for special purpose codes and intensive user involvement in preparing and performing calculations. The report by Choi addresses the potential for industrial CFD codes to be used for LES applications. In the long run, the objective is to make LES a viable tool for engineering fluid dynamics. The aspect addressed here is the possibility of using codes that have been developed for RANS purposes.

The RANS modeling papers (Ooi, *et al.* and Pettersson-Reif, *et al.*) are outgrowths of earlier work here at Stanford. The mathematical approach grew out of papers of Speziale and co-workers. The observation is that turbulence models respond to sufficiently strong stabilizing forces through a bifurcation between solution branches. A model of rotation effects that evolved out of such analysis is applied to several test cases in the article by Ooi, *et al.* The article by Pettersson-Reif, *et al.* explores the potential to apply the same ideas to stratified turbulence. In that case the bifurcation occurs as a function of the gradient Richardson number.

The report by Ham, *et al.* is on the topic of bypass transition. Direct numerical simulations done here at Stanford revealed a complex process by which this type of transition occurs. The initial stages of transition involve large structures — 'backward jets' — that are well within the large eddy domain. But the key instability process that ultimately cause transition is a highly localized breakdown of these jets, which occurs in the upper part of the boundary layer. It subsequently spawns a turbulent spot that penetrates to the wall. There is some question of whether these later stages of transition can be captured by LES. The spots are quite intermittent; subgrid models that average over span will include laminar and turbulent zones. That could reduce the fidelity of the simulation. This project applied a new time-integration scheme, developed at Waterloo by Ham and Lien, to the problem of transition simulation.

Paul Durbin

Evaluation of an industrial CFD code for LES applications

By Dochul Choi†, Dilip Prasad†, Meng Wang AND Charles Pierce

The feasibility of using an industrial compressible CFD code for large eddy simulations (LES) is evaluated. Dynamic subgrid scale (SGS) models developed at CTR have been implemented into the code and tested in a fully developed turbulent channel flow. In order to evaluate the effects of the SGS model compared with the numerical dissipation inherent in the upwind-biases schemes, computations without any SGS model were also carried out. It is found that the effect of dynamic SGS model decreases with increasing numerical dissipation (low order schemes). The 9th and 11th order schemes have relatively small numerical dissipation, and thus the dynamic SGS model plays useful role. In addition, a wall model was implemented in conjunction with LES. Although the velocity profile obtained with the wall model agrees well with the full LES solution, the magnitude of the pressure fluctuation is found to be overpredicted.

1. Introduction

There is an increasing demand for high fidelity, unsteady CFD capabilities for such applications as turbulence and transition modeling, flow control, aero-acoustics, and combustion system dynamics. Conventional Reynolds Averaged Navier Stokes (RANS) solvers based on various turbulence models often fail to capture unsteady flow physics accurately. This is not surprising in view of the fact that most of these models were developed with the goal of solving steady flow problems. Alternative methods are needed for unsteady CFD analyses in industrial applications.

As computer power becomes more affordable, Large Eddy Simulation (LES) has emerged as a viable and powerful alternative tool in turbulence computations. In recent years, LES has been applied to an increasing number of problems of engineering relevance. This was made possible through the use of parallel computing over under-utilized distributed machines in an industry setting and the availability of relatively cheap processors. The challenge in carrying out LES is that a three-dimensional, unsteady calculation must be carried out on a grid capable of resolving the larger scales of the motion; for flow geometries and Reynolds numbers of engineering interest, this implies that the grid is usually large. Hence, the CPU time required is substantially larger than that for an analogous RANS calculation.

The objective of the present study, carried out as part of the 2000 CTR Summer Program, is to evaluate an industrial CFD code for LES applications. Dynamic subgrid scale (SGS) models developed at CTR were implemented into the code, which was then tested by application to a fully developed channel flow. A significant drawback of contemporary LES methods is the need for a fine grid spacing in the neighborhood of the wall, which leads to prohibitively expensive computations in realistic applications. We attempted to

† United Technologies Research Center, East Hartford, CT 06108

address this issue in this investigation by using a wall model that relieves the grid requirement in the wall region. It is shown that the results obtained by such a treatment show a higher level of wall pressure spectrum.

2. Code description

Over the last few years, LES capability has been added to an existing Euler/RANS code at United Technologies Research Center. This code, called UTNS (Upwind-biased Time-dependent Navier-Stokes Solver), solves the compressible flow equations in conservative form in generalized curvilinear coordinates. The momentum equations are solved together with the continuity and energy equations in a fully coupled, vector form. Spatial differencing is accomplished using finite volumes with upwind biasing. The order of accuracy of the scheme ranges from the first to the 11th order (upwinded) for the convection terms and the second order central differencing for the diffusion terms. Furthermore, there is also an option for second order central differencing for the convection terms which eliminates numerical damping. Temporal advancement is achieved using second order backward differencing with a dual time step, one for physical time step and the other for numerical time step (used as an under relaxation parameter) for sub-iterations. The sub-iteration is carried out using a scalar, implicit, approximate factorization scheme. A third order Runge-Kutta explicit scheme is optional.

The original LES code, developed from the unsteady RANS code, has a simple Smagorinsky subgrid scale (SGS) model with the van Driest wall damping function. The code has been applied to jet-in-cross flows, flows behind flame holders, flows in swirling combustors, and transonic jet mixing. In all of the cases considered thus far, the flows are dominated by large-scale unsteady structures, with relatively small contributions from small scale eddies generated near solid boundaries (Madabhushi *et al.* 1997, Choi *et al.* 1999).

3. Dynamic subgrid scale model

Although the Smargorinsky model is widely used for LES, it has some limitations, the most crucial one being that the model constant needs to be adjusted depending on the flow. Moin *et al.* (1991) have developed a dynamic SGS model for compressible flows by generalizing the model of Germano *et al.* (1991). This procedure uses two filters, a grid filter and test filter (typically twice the grid filter width), to find the optimum model constant as a function of time and position, using a least squares technique (minimizing the difference between the closure assumption and resolved stresses) (Lilly 1992). In LES for compressible flows, density-weighted (Favre) filtering is typically employed. Recently, Boersma & Lele (1999) proposed a standard averaging technique without density weighting. This averaging results in the appearance of extra unknowns which are modeled by a procedure similar to that used for the dynamic SGS model. One of the advantages of this model is the emergence of an SGS mass flux term in the filtered continuity equation, which may help in controlling high wave number numerical instabilities. Following Boersma & Lele (1999), the governing equations of mass, momentum, and energy conservation may be cast into the form

$$\frac{\partial \bar{\rho}}{\partial t} + \frac{\partial \bar{\rho}\,\bar{u}_i}{\partial x_i} = -\frac{\partial}{\partial x_i}\left(\overline{\rho u_i} - \bar{\rho}\,\bar{u}_i\right), \tag{3.1}$$
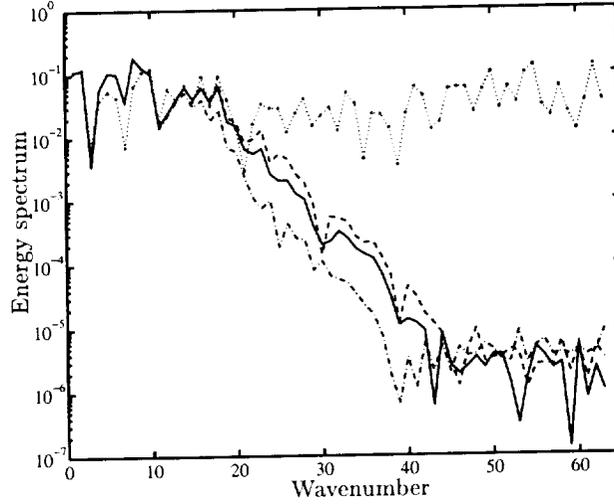
FIGURE 1. Wavenumber spectra of velocity fluctuations based on one dimensional Euler analysis: central differencing ($\cdots\cdots$), 9th order (-- --), 7th order (———), and 5th order (—·—).

$$\frac{\partial \bar{\rho}\,\bar{u}_i}{\partial t} + \frac{\partial \bar{\rho}\,\bar{u}_i\,\bar{u}_j}{\partial x_j} = -\frac{\partial \bar{p}}{\partial x_i} + \frac{\partial \bar{\sigma}_{ij}}{\partial x_j} - \frac{\partial}{\partial x_i}\left(\overline{\rho u_i u_j} - \bar{\rho}\,\bar{u}_i\,\bar{u}_j\right) - \frac{\partial}{\partial t}\left(\overline{\rho u_i} - \bar{\rho}\,\bar{u}_i\right), \quad (3.2)$$

$$\frac{\partial \overline{E}}{\partial t} + \frac{\partial}{\partial x_i}\left(\overline{E}\,\bar{u}_i + \overline{u_i p}\right) = -\frac{\partial q_i}{\partial x_i} + \frac{\partial}{\partial x_i}\left(\overline{u_i \sigma_{ij}}\right) - \frac{\partial}{\partial x_i}\left(\overline{Eu_i} - \overline{E}\,\overline{u_i} + \overline{pu_i} - \overline{p}\,\overline{u_i}\right) \quad (3.3)$$

where $E = \rho T/\gamma + \rho u_i u_i/2$ is the total energy, the stress tensor $\overline{\sigma}_{ij}$ is defined by

$$\overline{\sigma}_{ij} = \overline{\mu}\left[\frac{\partial \bar{u}_i}{\partial x_j} + \frac{\partial \bar{u}_j}{\partial x_i} - \frac{2}{3}\frac{\partial \bar{u}_k}{\partial x_k}\delta_{ij}\right],$$

and the heat flux $q_i = -\bar{k}\frac{\partial \overline{T}}{\partial x_i}$. The last terms on the right-hand side of the mass and momentum conservation equations are the additional terms arising from the standard averaging rather than density weighted averaging. Both models have been implemented into the UTNS-LES code.

4. Implications of upwinding

In order to examine the numerical characteristics of the upwind scheme, a test case was formulated. It is based on the one-dimensional compressible Euler equations solved using 5th and 7th order upwind biased spatial differencing. The 2nd order central differencing scheme is also used to provide a reference behavior. The calculation starts with random fluctuations at every grid point and advances in time. 128 uniformly-spaced grid points and periodic boundary conditions are used. Since there are no diffusion terms present, the level of the fluctuation should remain the same as that of the initial perturbations. Figure 1 shows the kinetic energy spectra as a function of wave number. The results obtained from the central differencing scheme without any artificial damping show that the level remains the same as the initial values. On the other hand, the results obtained from the upwinding scheme show that the energy at high wave numbers is damped. All the curves shown in Fig. 1 are obtained at the 500th time step, which correspond to 16 acoustic time units based on the domain length and the sound speed of the initial state.

Since the resolved stresses of motion between the test scale and grid scale are used to determine the model constant for the dynamic SGS model, the high wave number solution needs to be computed accurately. Note that most of the dynamic SGS applications at CTR are based on the central differencing scheme for incompressible flow. This scheme is energy conserving and hence free of numerical dissipation. For compressible flows, we cannot identify an energy conserving scheme. Therefore, a new method of estimating the model constant, perhaps by using information at lower wavenumber, may be required. Further research on the dynamic SGS model for an upwind type of scheme is needed to generalize the model for application to industrial CFD codes.

5. Fully developed channel flow

As a test case, we considered a fully developed channel flow with a Reynolds number of 180 based on friction velocity and channel half-width. The problem was solved using 32 grid points in the streamwise and spanwise directions and 64 grid points in the wall-normal direction, covering a domain of $4\pi H \times \frac{4}{3}\pi H \times 2H$, where H is the channel half-width. The cell sizes in the flow and spanwise directions are 72 and 24 wall units respectively, while in the shear (wall-normal) direction, they vary from 1 to 13. The physical time step was 50 in wall units. The calculated results are compared with the result obtained using a CTR-developed LES code for incompressible flow using the same grid.

In order to use the periodic boundary conditions in the streamwise direction, two extra source terms are added to the axial momentum equation: (1) the difference between a target flow rate and integrated computed flow rate, and (2) a total drag force. The purpose of this is to fix the Reynolds number and to eliminate any streamwise pressure gradient. Note that once the solutions reach a statistically steady state, the first forcing term vanishes. The LES calculation starts with a fully developed laminar profile with random number fluctuations of up to 10% the initial velocity. Since the basis for comparison is the incompressible solution, the Mach number in the compressible case was set to a value less than 0.2. Favre-averaged version of the dynamic SGS model was used for the test calculation with high-order upwinding schemes (Wake and Choi 1995). Figure 2 shows the mean axial velocity profiles obtained using the 5th, 7th, and 9th order upwinding schemes. Two calculations, one with the dynamic SGS model and the other without any SGS model, were made with each scheme. The aim was to evaluate the effect of the dynamic SGS model in the presence of numerical dissipation. With the 5th order scheme, there is little difference between two calculations. As the order of the scheme is increased and numerical dissipation decreases, the difference between two solutions increases. The dynamic SGS model seems to be overwhelmed by the numerical dissipation of the low-order schemes. When a scheme of 11th order is used, comparison with the CTR-LES code result, shown in Fig. 3, is observed to be very good; the case without any SGS model shows more mixing in the log region as expected. The profiles of Reynolds shear stress are compared in Fig. 4, where the SGS model used in the 11th order scheme is shown to improve the solution.

Attempts were made to use central differencing without artificial damping but were unsuccessful owing to numerical instability caused by odd-even decoupling. For the central difference case, the standard LES filtered equations of Boersma & Lele (1999) were used as well, but they also failed to produce a statistically steady solution. Note that, using the central differencing without damping, we also considered two-dimensional calculations starting from the similar initial condition as used for the LES and found that
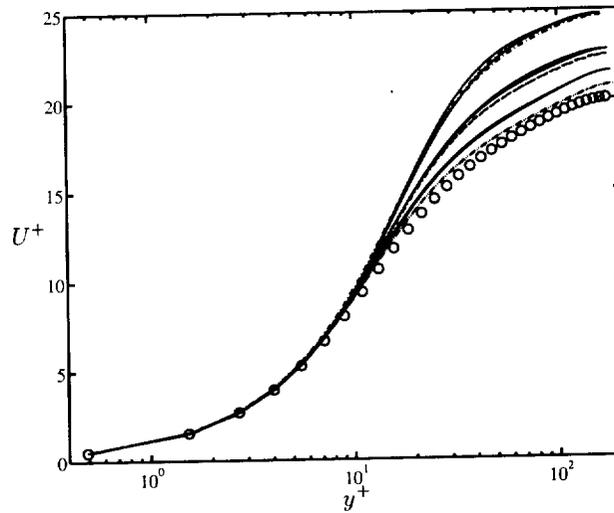
FIGURE 2. Mean velocity profiles obtained using 5th, 7th, and 9th order upwinding schemes (top to bottom) compared with solution from CTR-LES code (o). Solid lines represent computations with SGS model; dashed lines represent those without any SGS model.
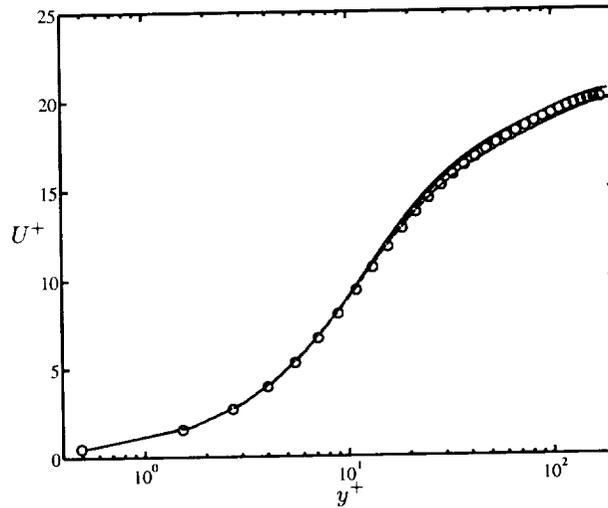
FIGURE 3. Mean velocity profiles obtained using 11th order upwinding scheme compared with solution obtained from CTR-LES code (o). Solid line represents computations with SGS model; dashed line represents those without any SGS model.

the solution reached the steady state and, therefore, became a laminar solution. Thus the presence of three-dimensionality appears to have caused the solution to become unstable.

6. LES with wall model

In order to use LES in practical engineering problems, the stringent grid resolution requirement for high Reynolds number flows in the near wall region needs to be relieved. Wang (1999) reported a factor of 10 reduction in CPU time in an LES for a trailing-
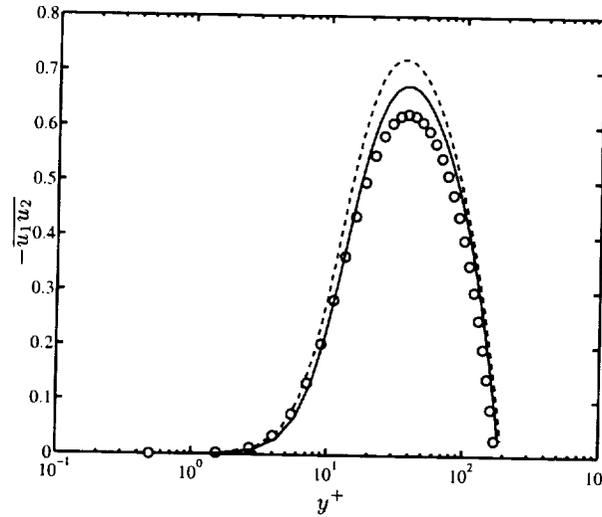
FIGURE 4. Reynolds shear stress profiles obtained using 11th order upwinding scheme compared with solution obtained from CTR-LES code (o). Solid line represents computations with SGS model; dashed line represents those without any SGS model.
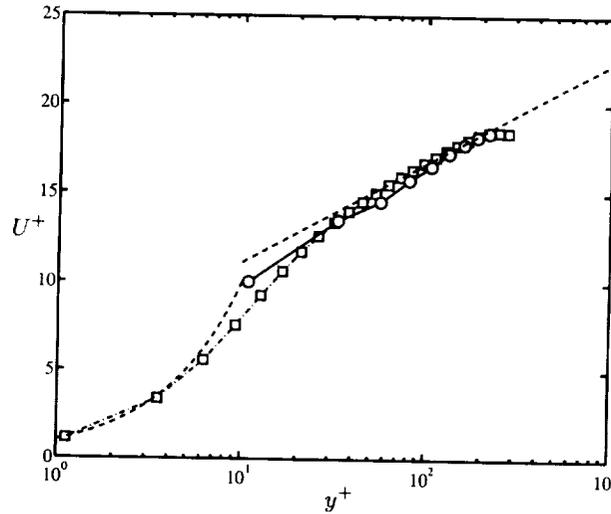
FIGURE 5. Comparison of velocity profiles obtained using LES with wall model (o) and full LES (□).

edge flow using an approximate wall boundary treatment proposed by Cabot and Moin (2000) for incompressible flow. This simple wall model was expanded to the compressible flow equations. The model equations are based on boundary layer approximation of the two tangential direction momentum equations. Modifying the formulation described by Wang (1999) for compressible flow, these equations are integrated from the wall to the first off-wall cell (at a distance δ) according to:

$$\frac{\partial}{\partial x_2}\left(\mu + \mu_t\right)\frac{\partial u_i}{\partial x_2} = F_i, \qquad (6.1)$$
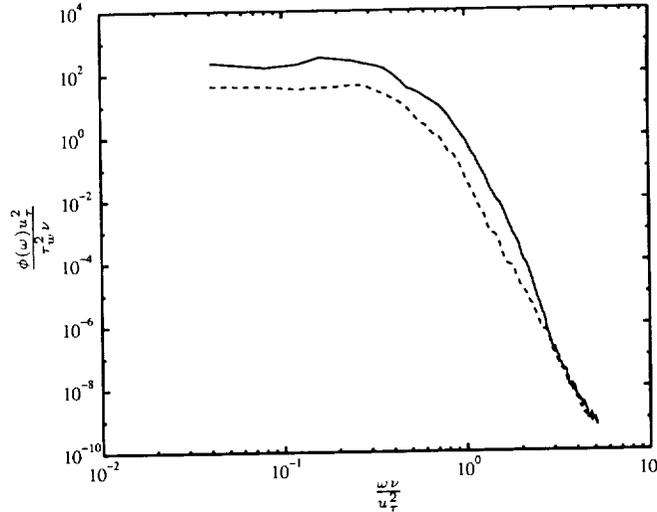
FIGURE 6. Comparison of surface pressure frequency spectra obtained using LES with wall model (———) and full LES (- - - -).

from which the wall shear stress, τ_{wi} is determined to be

$$\tau_{wi} = \mu \left.\frac{\partial u_i}{\partial x_2}\right|_{\text{wall}} = \left[\int_0^\delta \frac{dx_2}{\mu + \mu_t}\right]^{-1} \left\{u_{\delta i} - \int_0^\delta \frac{F_i x_2}{\mu + \mu_t} dx_2\right\}. \tag{6.2}$$

The turbulent eddy viscosity μ_t is modeled by

$$\mu_t = \kappa \rho u_\tau d_n \left[1 - \exp\left(-\frac{\rho u_\tau d_n}{A\mu}\right)\right]^2, \tag{6.3a}$$

where d_n is the distance to the wall, $\kappa = 0.4$ is the von Karman constant, and $A = 19$. The forcing term must, in general, be determined according to

$$F_i = \frac{\partial p}{\partial x_i} + \frac{\partial(\rho u_i)}{\partial t} + \frac{\partial(\rho u_i u_j)}{\partial x_j}; \tag{6.3b}$$

here we use the somewhat crude approximation, $F_i = 0$, the so-called "stress-balance model". The calculated wall shear, τ_{wi}, is then used as a boundary condition for the momentum equations in LES. Figure 5 shows the velocity profile compared to the result obtained from a full LES calculation. With the wall model, the number of grid points in the shear direction is reduced to 32 from 64 while the number of grid points in other directions is kept the same. Note that the actual saving in a real application of LES with wall model will come from reductions in axial and spanwise grid points as well. The profiles agree well with each other. In Fig. 6, the frequency spectra of wall pressure fluctuation from the two calculations are examined. We observe that the simulation employing the wall model overpredicts the magnitude of the pressure fluctuation, and this is similar to the behavior reported by Wang (1999); evidently, further study is needed to improve this approximate formulation.

7. Summary

The feasibility of using an industrial compressible CFD code, UTNS, for LES has been evaluated. This was done using a CTR-developed dynamic SGS model in a simple fully developed turbulent channel flow at a Reynolds number of 180, based on the friction velocity and channel half width. In order to evaluate the effect of the SGS model in the presence of numerical dissipation due to upwinding, a computation without any SGS model was also carried out. Calculations were carried out using upwind-biased schemes of up to the 11th order, and the velocity profiles obtained were compared with those computed using a CTR central differencing LES code. The dynamic SGS model is found to have little effect when there is a large amount of numerical dissipation as in the case of the 5th order scheme. We have found in this study that the 9th and 11th order schemes have relatively small numerical dissipation so that the dynamic SGS model plays a significant role. In order to improve cost effectiveness of LES for practical applications, a RANS type wall model was also implemented. Although the velocity profile obtained using LES in conjunction with the wall model agrees well with the one obtained using the full LES calculation, the magnitude of the pressure fluctuation was found to be higher.

REFERENCES

BOERSMA B. J. & LELE S. K. 1999 Large eddy simulation of compressible turbulent jets. *Annual Research Briefs*, Center for Turbulence Research, NASA Ames/Stanford Univ. 265-377.

CABOT, W. & MOIN P. 2000 Approximate wall boundary conditions in the Large-eddy simulation of high Reynolds number flow. *J. Flow, Turbulence & Combustion.* **63**, 269-291.

CHOI D., BARBER T. J. & CHIAPPETTA, L. M. 1999 Large Eddy Simulation of high Reynolds number jet flows. *AIAA Paper 99-0230.*

GERMANO, M. PIOMELLI, U., MOIN, P. & CABOT, W. H. 1991 A dynamic subgrid-scale eddy viscosity model. *Phys. Fluids A.* **3**, 1760-1765.

LILLY, D. K. 1992 A proposed modification of Germano's subgrid-scale closure method. *Phys. Fluids A.* **4**, 633-635.

MADABHUSHI, R. K. , CHOI D. & BARBER T. J. 1997 Unsteady simulations of turbulent flow behind a triangular bluff body. *AIAA Paper 97-3182.*

MOIN, P., SQUIRES, K., CABOT, W. & LEE, S. 1991 Dynamic subgrid-scale model for compressible turbulence and scalar transport. *Phys. Fluids A.* **3**, 2746-2757.

WAKE, B. E. & CHOI, D. 1996 Investigation of high-order upwinded differencing for vortex convection. *AIAA Paper 95-1719.*

WANG, M. 1999 LES with wall models for trailing-edge aeroacoustics. *Annual Research Briefs*, Center for Turbulence Research, NASA Ames/Stanford Univ. 355-364.

Evaluation of RANS models for rotating flows

By   A. Ooi†, B. A. Petterson Reif‡, G. Iaccarino AND P. A. Durbin

Two- and three-dimensional simulations of the flow in rotating rib-roughened ducts are carried out using several turbulence closures. One and two-equation models have been used together with the four-equation $v^2 - f$ model. In addition, a modification of this model that systematically accounts for system rotation has been used. Results show that the $v^2 - f$ model is superior to the others in predicting wall heat transfer and, for the rotating case, the modified model accurately accounts for the effect of the system frame rotation.

1. Introduction

The two-equation $k - \epsilon$ model (Launder (1974)) with the semi-empirical "wall function" approach for modeling near wall turbulence is the most widely used turbulence closure in the industrial CFD community. There are many situations in which this approach fails, such as turbulent boundary layers at low and transitional Reynolds numbers and flows with massive separation. A variety of alternative models to account for wall effects in such situations have been introduced in the last decade (Chen & Patel (1998), Patel, Rodi & Scheuerer (1985)). Many of these models incorporate *ad-hoc* "damping functions" which have been adjusted to fit experimental or computational data. An alternative approach was taken by Durbin (1991) and Durbin (1993); the standard $k - \epsilon$ formulation was extended using the elliptic relaxation methodology in order to account for nonlocal wall effects. This model $(v^2 - f)$ has been used by Behnia, Parneix, Shabany & Durbin (1999), Ooi, Iaccarino & Behnia (1998), Kalitzin (1998), Parneix & Durbin (1997), and Durbin (1995) to accurately predict heat transfer and velocity profiles for various turbulent flows that are of interest to the engineering community.

Even though it has been proven to be successful in many different situations, the $v^2 - f$ model has also inherited some of the many problems associated with the standard $k - \epsilon$ model. In particular, the $k - \epsilon$ model (as with all single point closures) is unable to properly describe turbulent flows with body force effects arising from system rotation unless *ad hoc* adjustments are made to the turbulence dissipation rate (Gastki & Speziale (1993)). To partly rectify this problem, Pettersson, Durbin & Ooi (1999) proposed an extension to the original linear $v^2 - f$ model that takes into account the turbulence generated by system rotation. This model has been successfully applied to "simple" flows such as the fully developed rotating channel, duct, and the two-dimensional rotating backstep flow by Pettersson, Durbin & Ooi (1999). An improvement to this linear model has since been proposed by Pettersson (2000), who introduced a nonlinear extension that provides a fundamentally more accurate description of the flow physics than the linear formulation of Pettersson, Durbin & Ooi (1999). Even though these models have been developed from rigorous mathematics and understanding of the basic flow mechanisms,

† University of Melbourne, Australia
‡ Norwegian Defence Research Establishment, Norway

they have not yet been tested in a complex three-dimensional rotating flow environment, and the improvements over the original $v^2 - f$ model for practical engineering applications are still to be fully addressed.

2. Turbulence models

The formulation of the two-layer $k - \epsilon$, Spalart-Allmaras (SA), and standard $v^2 - f$ models has been published in many papers (see for example, Chen & Patel (1998) for the two-layer $k - \epsilon$ model, Spalart & Allmaras (1992) for the SA model, and Behnia, Parneix, Shabany & Durbin (1999) for the $v^2 - f$ model) and will not be repeated here. In the modified $v^2 - f$ model proposed by Pettersson, Durbin & Ooi (1999), the C_μ constant in the expression for eddy viscosity is a direct function of the mean strain and rotation rate tensors. The eddy viscosity is given by

$$\mu_T = \rho C_\mu^* v^2 T \qquad (2.1)$$

where T is the turbulence time scale (Durbin (1993)) and C_μ^* is given by

$$C_\mu^* = C_\mu \frac{1 + \alpha_2 |\eta_3| + \alpha_3 \eta_3}{1 + \alpha_4 |\eta_3|} \left(\sqrt{\frac{1 + \alpha_5 \eta_1}{1 + \alpha_5 \eta_2}} + \alpha_1 \sqrt{\eta_2} \sqrt{|\eta_3| - \eta_3} \right)^{-1}. \qquad (2.2)$$

In the original $v^2 - f$ model, $C_\mu^* = C_\mu$ and has a constant value of 0.22. All the α_i's in Eq. (2.2) are model constants given by

$$(\alpha_1, \alpha_2, \alpha_3, \alpha_4, \alpha_5) = \left(0.055, \frac{1}{2}, \frac{1}{4}, \frac{1}{5}, \frac{1}{40} \right). \qquad (2.3)$$

The η_i's are defined from the non-dimensional mean strain and rotation rate tensors

$$\eta_1 = S_{ik}^* S_{ik}^*, \qquad (2.4)$$

$$\eta_2 = W_{ik}^* W_{ik}^* = -W_{ik}^* W_{ki}^*, \qquad (2.5)$$

and

$$\eta_3 = \eta_1 - \eta_2 \qquad (2.6)$$

where

$$S_{ik}^* = \frac{1}{2} T \left(\frac{\partial U_i}{\partial x_k} + \frac{\partial U_k}{\partial x_i} \right) \qquad (2.7)$$

and

$$W_{ik}^* = \frac{1}{2} T \left[\left(\frac{\partial U_i}{\partial x_k} - \frac{\partial U_k}{\partial x_i} \right) + 4.5 \epsilon_{kim} \Omega_m \right]. \qquad (2.8)$$

This modification to the expression for C_μ was obtained so that the $v^2 - f$ model "mimics" the behavior of second moment closure models in the equilibrium limit of rotating homogeneous shear flow. Additional details of this derivation can be found in Pettersson, Durbin & Ooi (1999).
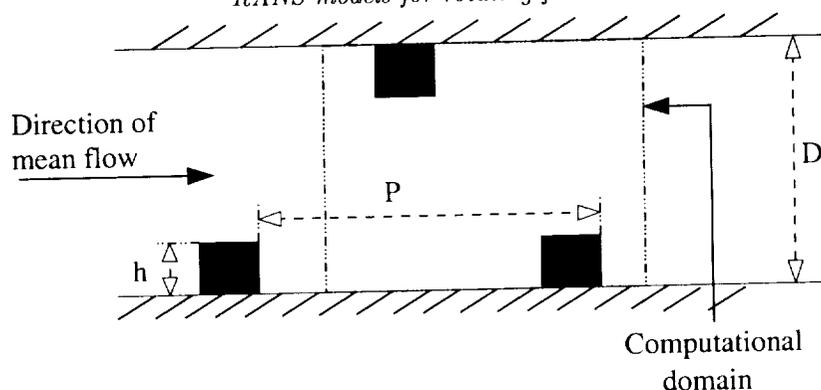
FIGURE 1. Geometry of experimental setup.

3. Test cases, mathematical model, and numerical simulations

Test cases from the 7th ERCOFTAC/IAHR Workshop on Refined Turbulence Modeling were chosen to investigate the performance of various turbulence models. Owing to the simplicity of the geometry, fully developed rotating channel flow was chosen as an ideal initial test case. Data from direct numerical simulation (DNS) of the Navier-Stokes equations are available from Kristoffersen (1993) at $Re_\tau = hu_\tau/\nu = 194$ and $R_0 = 2\Omega h/U_b = 0.1$ to check the accuracy of the simulations. Since the flow is assumed to be fully developed, periodic inflow and outflow boundary conditions were used in the calculations.

The second test case considered here is the turbulent flow in a square duct (width to height ratio of 1:1) with ribs. In the experiment, ribs are placed in a staggered arrangement on the side walls of the duct. This is illustrated in Fig. 1, which shows a side view of the experimental configuration; pitch to rib height (p/h) for the configuration used is 10 while rig height to duct height (h/D) is 0.1. The experimental measurements were taken as part of a study on the flow and heat transfer in rotating square-sectioned U-bends with rib roughened walls. The velocity field six diameters downstream of the bend exit were measured using LDA. The flow is fully developed in this straight section and unaffected by the presence of the bend. Hence, in the numerical simulations, only one portion of the duct is considered with periodic inflow/outflow boundary conditions. In the experimental facility, data from turbulent flow at rotations numbers $Ro = \Omega D/U_m$ of 0 and 0.2 with Reynolds number based on bulk velocity U_b and duct height D of 10^5 were obtained. Both flow and heat transfer data were obtained at $Ro = 0.0$, but only velocity field data were available at $Ro = 0.2$. Measurements were only taken on the symmetry plane of the duct.

The two-dimensional ($2d$) grid used in the calculations is shown in Fig. 2. It has 40,000 quadrilateral cells, and fine grid spacing was used in the vicinity of the walls to ensure the simulations are well resolved. The $2d$ simulations were carried out because the authors initially assumed that the presence of the side walls has a limited effect on the predictions at the symmetry plane where experimental data were available. Three-dimensional ($3d$) simulations carried out later showed that this assumption was incorrect; secondary flow structures have a dramatic effect on the predicted streamwise velocity at the center of the duct. The $3d$ simulations are performed using a grid that is just a spanwise extension of the $2d$ grid; it consist of 800,000 hexahedra cells.

Simulations were carried out using various turbulence models. As there is separation
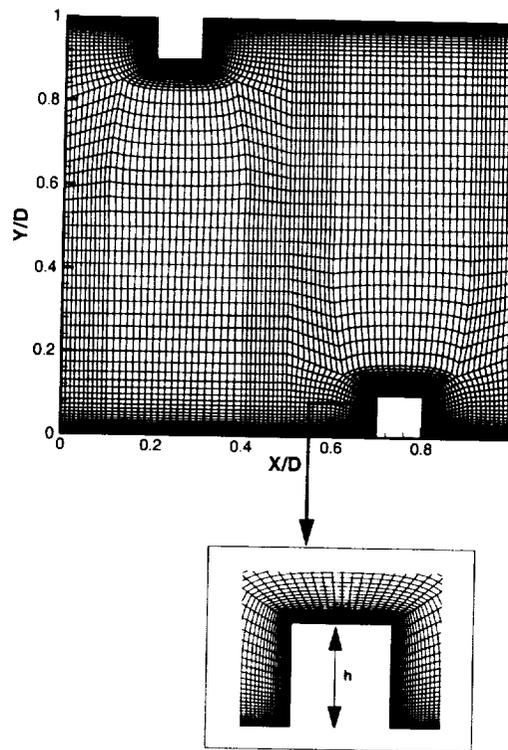
FIGURE 2. Grid used for the simulations.
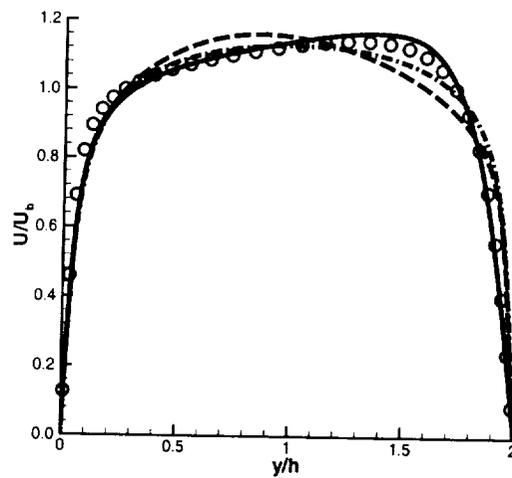
FIGURE 3. Comparison between predicted and experimental data for fully developed channel flow. ● DNS data, ———— $v^2 - f$ model, - - - - SA model, —·— $k - \epsilon$ model.
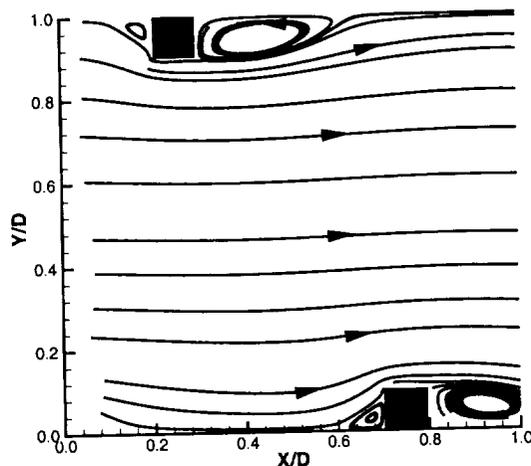
FIGURE 4. Streamlines from 2d calculations.

in the flow, it is expected that all turbulence models based on "wall functions" will not be able to accurately reproduce the experimental data. Hence, only turbulence models that can be integrated all the way to the wall such as two-layer $k - \epsilon$ (proposed by Chen & Patel (1998)), Spalart Allmaras (Spalart & Allmaras (1992)), $v^2 - f$ (Durbin (1991)), and the linear modified $v^2 - f$ (Pettersson, Durbin & Ooi (1999)) were tested.

4. Results

4.1. *1-d rotating channel flow*

Figure 3 shows the results from the rotating channel simulations with $R_0 = 0.1$. System rotation suppresses turbulence on one (stable) side of the channel which leads to asymmetry in the mean velocity profile. This is evident in the DNS data. As is well known, conventional eddy viscosity type closures such as the $k - \epsilon$, SA, and the original $v^2 - f$ models are relatively insensitive to system rotation and will predict a mean velocity profile that is very close to symmetric. The slight asymmetry in the SA prediction is due to the production term of the modified eddy viscosity transport equation. The production term is modeled as $\Omega_{ij}\Omega_{ij}$ whereas the production term in the $k - \epsilon$ model is just $S_{ij}S_{ij}$. Predictions using the modified linear $v^2 - f$ model accurately matche the DNS data.

4.2. *2d rib simulations*

Figure 4 shows the flow pattern obtained with the modified $v^2 - f$ turbulence model for both the non-rotating and rotating cases. The mean flow goes from left to right, and a small separation bubble appears upstream of the rib. Downstream of the rib, another bigger separation bubble is formed. The size of the separation bubble is indicated in Fig. 5, which shows the distribution of friction coefficient C_f at the top of the duct directly downstream from the rib. The data in this figure was obtained using the modified $v^2 - f$ model, and it shows that the predicted size of the separation bubble is smaller for higher values of Ro. This is consistent with the experimental observation of Rothe
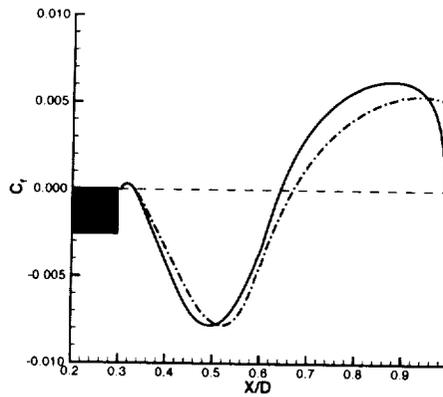
FIGURE 5. Distribution of C_f at the top of the square duct. ——·—— $Ro = 0.0$ and ———— $Ro = 0.2$.
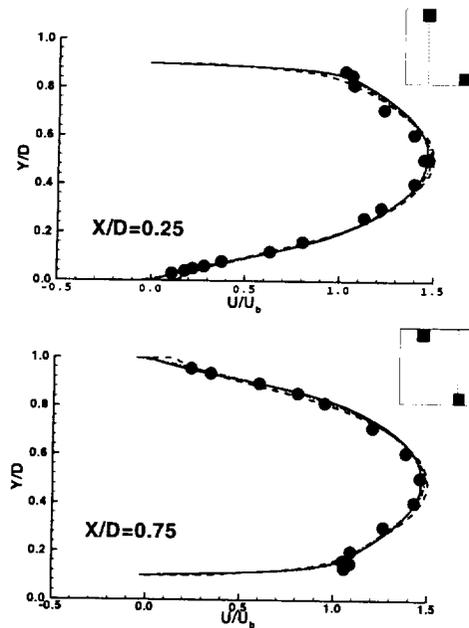
FIGURE 6. Comparison between the predicted streamwise velocity and the experimental values for $Ro = 0.0$. ● Experimental data, — — — $k - \epsilon$ model, ——·—— SA model and ———— $v^2 - f$ model.

(1975). In contrast, all other turbulence models tested predicted a separation length that is independent of Ro.

For the case with $Ro = 0$, a quantitative comparison of the streamwise velocity (U) with experimental data is shown in Fig. 6. This figure shows the predicted streamwise velocity with the corresponding experimental data at two streamwise locations, one station at the center of the upstream rib $(X/D = 0.25)$ and the other one at the center of the downstream rib $(X/D = 0.75)$. For both streamwise stations, all predictions using different turbulence models agree very well with the experimental data close to the center
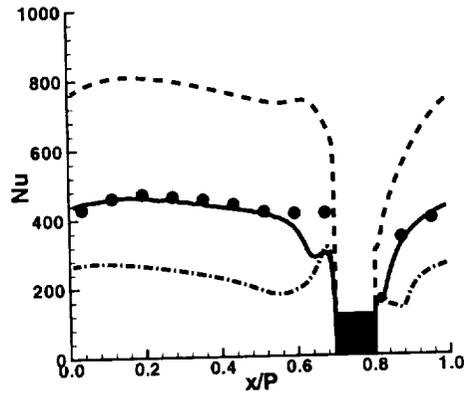
FIGURE 7. Comparison of Nu between predicted and experimental data for $Ro = 0.0$. • Experimental data, $- - - -$ $k - \epsilon$, $- \cdot - \cdot -$ SA and $\underline{\qquad}$ $v^2 - f$.
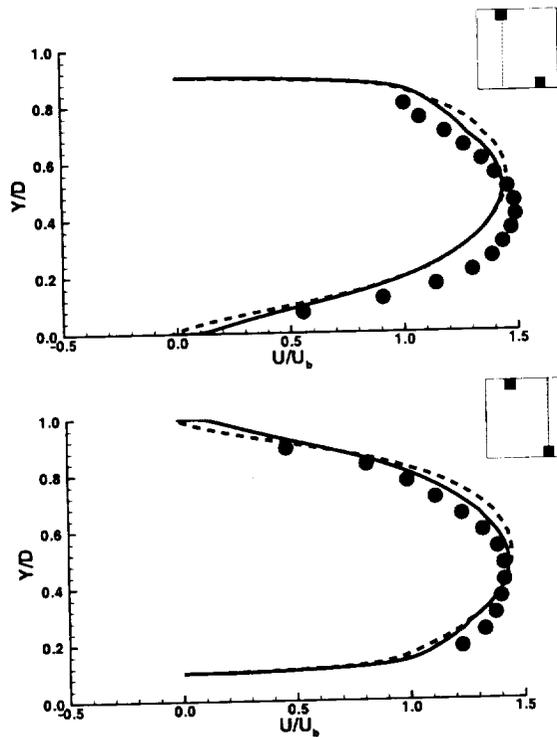
FIGURE 8. Comparison between the original and modified $v^2 - f$ model for $Ro = 0.2$. • Experimental data, $- - - -$ original $v^2 - f$ model, $\underline{\qquad}$ modified $v^2 - f$ model.

of the channel. However, the predicted velocity profiles between the different turbulence models are actually very different close to the walls. This is more clearly illustrated in Fig. 7, which compares the predicted Nusselt, Nu, with the experimental data along the bottom wall of the square duct. The Nu is overpredicted by the $k - \epsilon$ model and is
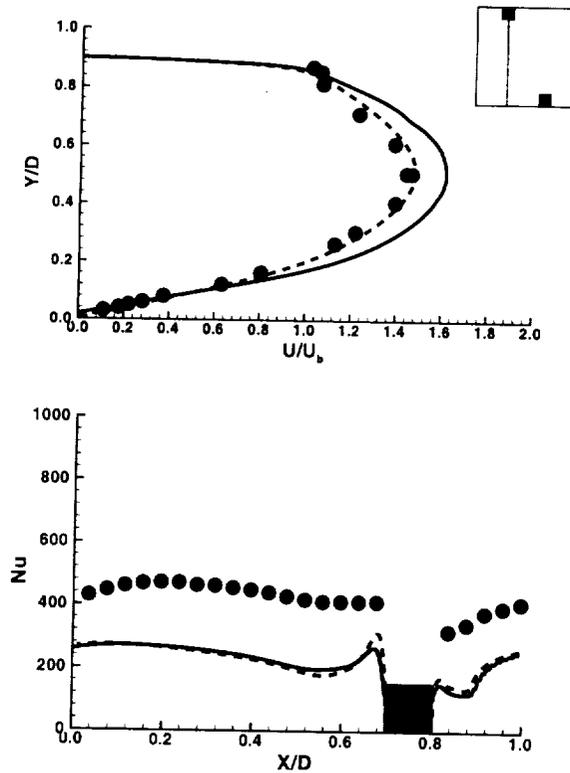
FIGURE 9. Comparison between Spalart Allmaras $2d$ and $3d$ results. ● Experimental data,
———— SA (2d), ——— SA (3d).

underpredicted using the SA model. Predictions using the original $v^2 - f$ model match experimental values very well.

Numerically predicted data for the case with $Ro = 0.2$ is shown in Fig. 8, which compares the data obtained using the modified and the original $v^2 - f$ model at the same streamwise stations. The modified $v^2 - f$ model changes the streamwise velocity profile such that it is a closer match to the experimental data. This indicates that the modified model more accurately models the physics of rotating flows. Unfortunately, no experimental data for Nu is available for this case. Hence, the accuracy of the modified model in predicting Nu for the rotating case is unclear.

4.3. $3d$ rib simulations

Figure 9 shows a comparison between the $2d$ and $3d$ Spalart-Allmaras model results for the case with no rotation. The Nu prediction at the bottom of the duct is similar for both the $2d$ and $3d$ cases. However, the predicted value of the streamwise velocity is remarkably different at the center of the duct. Surprisingly, the $2d$ prediction matches the experimental data better than the $3d$ prediction.

The reason for this could be due to the existence of the secondary flow structures in the $3d$ predictions. This is illustrated in Fig. 10, which shows the streamlines on two streamwise planes in the computational domain. The two planes are chosen to be just after the top rib at $X/D = 0.35$ and at $X/D = 0.50$, which is closer to the center of
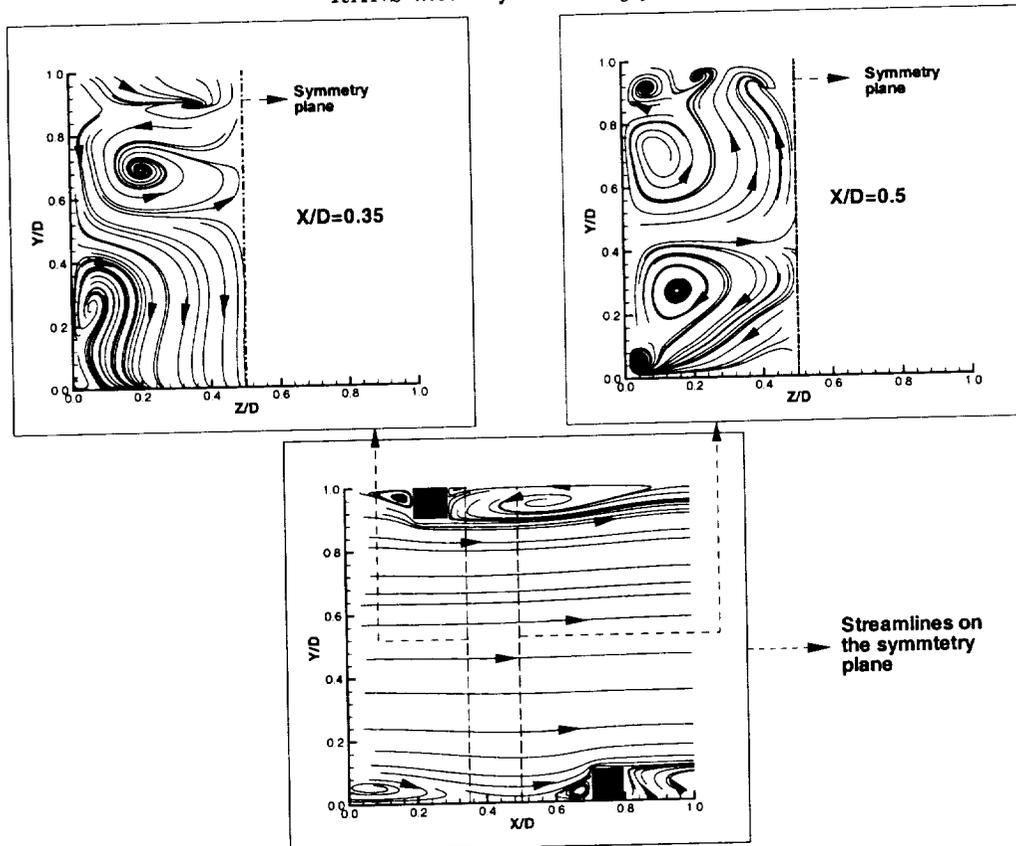
FIGURE 10. Streamlines on various downstream stations for $Ro = 0.0$.
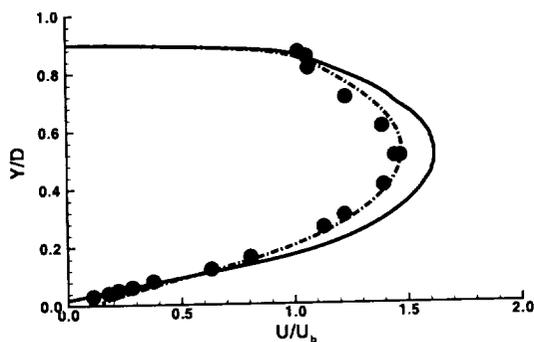
FIGURE 11. Comparison with experimental data for $Ro = 0.0$. • Experimental data, ———— SA (3d), —·— modified $v^2 - f$ (3d).

the separation bubble. It is clear that the secondary flow structures persist downstream, and mean streamwise vortices are formed in the separation bubble at $Y/D > 0.9$. Data obtained from $v^2 - f$ predictions show similar features.

Figure 11 shows how the $3d$ predictions of the velocity on the symmetry plane compares with experimental data. As discussed previously, the SA model overpredicts the velocity

on the centerline. On the other hand, the modified $v^2 - f$ model is able to correctly reproduce the velocity profile on the symmetry plane.

5. Conclusions

This paper presents results from steady-state RANS simulations of rotating and non rotating flow in a square duct. Various different turbulence models were used and, whenever possible, comparisons were made with experimental data. For 2d calculations, it was shown that the velocity field was well predicted with all turbulence models. For the non-rotating case, both the two-layer $k - \epsilon$ and Spalart-Allmaras models give heat transfer predictions that are very different from the experimental data. Both variations of the $v^2 - f$ models tested give very good heat transfer distribution, indicating the superior near-wall modeling using the elliptic relaxation methodology. For the 2d rotating case, the modified $v^2 - f$ model gives a velocity profile that is closer to the experimental values than the original $v^2 - f$ model.

Three-dimensional simulations were also carried out and the differences between the 2d and 3d results were reported. For the non-rotating case, the predicted velocity profile from the 2d calculations using the SA model were actually closer to the velocity profile measured in the experiments. This is especially evident at the center of the square duct. One possible explanation is that the secondary flow structures which exist in the 3d calculations are very complicated and not properly modeled by the SA model. On the other hand, 3d calculations using the modified $v^2 - f$ model produce a velocity profile that matches the experimental values.

REFERENCES

BEHNIA, M., PARNEIX, S., SHABANY, Y. & DURBIN, P. A. 1999 Numerical study of turbulent heat transfer in confined and unconfined impinging jets. *Int. J. Heat and Fluid Flow.* **20**, 1-9.

CHEN, H. C. & PATEL, V. C. 1988 Near-wall turbulence models for complex flows including separation *AIAA J.* **26**(6), 641-648.

DURBIN, P. A. 1991 Near-wall turbulence closure modeling without "damping functions". *Theoret. Comput. Fluid Dyn.* **3**, 1-13.

DURBIN, P. A. 1993 A Reynolds stress model for near-wall turbulence. *J. Fluid Mech.* **249**, 465-498.

DURBIN, P. A. 1995 Separated flow computations with the $k - \epsilon - v^2$ model. *AIAA J.* **33**(4), 659-664.

GATSKI, T. B. AND SPEZIALE, C. G. 1993 On explicit algebraic stress models for complex turbulent flows. *Int. J. Fluid Mech.* **254**, 59-78.

KALITZIN, G. 1998 An implementation of the $v^2 - f$ model with application to transonic flows. *Annual Research Briefs*, Center for Turbulence Research, NASA Ames/Stanford Univ. 171-184.

KRISTOFFERSEN, R. & ANDERSSON, H. I. 1993 Direct simulations of low-Reynolds-number turbulent flow in a rotating channel. *J. Fluid Mech.* **256**, 163-197.

LAUNDER & SPALDING 1974 The numerical computation of turbulent flows. *Comp. Methods Appl. Mech. Engr.* **3**, 269-289.

OOI, A., IACCARINO, G. & BEHNIA, M. 1998 Heat transfer predictions in cavities.

Annual Research Briefs, Center for Turbulence Research, NASA Ames/Stanford Univ. 185-196.

PARNEIX, S. & DURBIN, P. 1997 Numerical simulation of 3D turbulent boundary layers using the V2F model. *Annual Research Briefs*, Center for Turbulence Research, NASA Ames/Stanford Univ. 135-148.

PATEL, V. C., RODI, W. & SCHEUERER, G. 1985 Turbulence models for near-wall and low Reynolds number flows:a review. *AIAA J.* **23**(9), 1308-1319.

PETTERSSON REIF, B. A., DURBIN, P. & OOI, A. 1999 Modeling rotational effects in eddy-viscosity closures. 1999 *Int. J. Heat and Fluid Flow.* **20**, 563-573.

PETTERSSON REIF, B. A. 2000 A nonlinear eddy-viscosity model for near-wall turbulence. *AIAA 2000-135.*

ROTHE, P. H. 1975 The effects of system rotation on separation, reattachment and performance in two-dimensional diffusers.*Stanford University Dissertation, Department of Mechanical Engineering.*

SPALART, P. R. & ALLMARAS, S. R. 1992 A one-equation turbulence model for aerodynamic flows. *AIAA 92-0439.*

On stably stratified homogeneous shear flows subjected to rotation

By B. A. Pettersson Reif†, A. Ooi‡ AND P. A. Durbin

Theoretical aspects of modeling stratified turbulent flows subjected to rotation are considered. The structural equilibrium behavior of second-moment closure (SMC) models is explored, guided by bifurcation analysis. It is shown that the ability of the models to predict a critical gradient Richardson number in the absence of system rotation $Ri_g^{cr} \approx 0.25$ is largely dependent on the model for the pressure-strain correlation tensor. It is also found that the most commonly used linear models are ill-posed when the combined effect of system rotation and stratification is imposed; the models do not exhibit a steady state solution.

1. Introduction

The combined effect of body forces associated with density stratification, system rotation, and streamline curvature is important in a wide variety of turbulent flows. These body forces exert profound effects on the vertical mixing in, for instance, geophysical boundary layers as well as in engineering applications such as turbomachinery flows. The importance is manifested through the direct effects on the turbulence fluctuations; the turbulence can be suppressed (stabilized) or enhanced (destabilized). For instance, the stabilizing effect associated with the flow over a convex surface leads to significantly reduced skin friction.

The most physically appealing approach to account for body force effects within the framework of RANS modeling is full second-moment closures (SMC). The main reason is that body force effects are accounted for in a systematic manner. The more frequently adopted eddy-viscosity type closures such as the standard $k - \varepsilon$ model are not particularly well suited for these situations. It is, therefore, unfortunate that the more elaborate SMC models are not very often employed in practice for complex fluid flow predictions mainly because of numerical stiffness problems.

Analysis of homogeneous shear flow provides theoretical insight on the stabilizing and destabilizing effects of imposed system rotation, flow curvature, or density stratification on the turbulent stresses. This is particularly valuable from a turbulence modeler's perspective since it also provides a mean for systematic approximations of SMC closures.

Equilibrium and bifurcation analysis have emerged as simple and powerful guides to closure model formulations. Analytical solutions of SMCs provide a methodology for a systematic derivation of simpler eddy-viscosity models that retain some of the predictive capabilities of the more elaborate SMC models, in particular, the ability to respond to imposed body forces. Although homogeneous shear flow is superficially simple, it has

† Norwegian Defence Research Establishment, Norway
‡ University of Melbourne, Australia
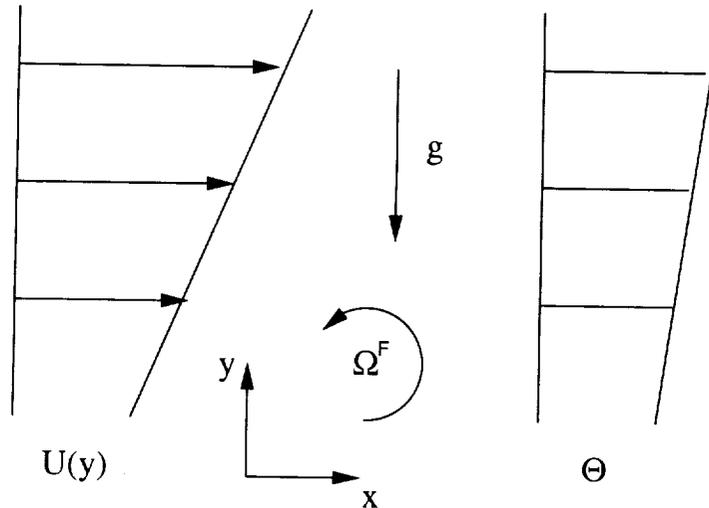
FIGURE 1. Schematic of flow configuration.

proven to be a useful reference point – including for models intended to compute complex flows far from equilibrium.

The present study examines the response of full SMC models in stratified homogeneous shear flow subjected to orthogonal mode rotation, see Fig. 1. The analysis is based on structural equilibrium, and the behavior of these models is elucidated by bifurcation analysis. In contrast to the modeling of passive scalars, density stratification mathematically couples the equations governing the Reynolds stresses and the turbulent heat fluxes; this significantly adds to the complexity of modeling stratified turbulence. The motivation of this study is two-fold: first, to provide some theoretical guidance to closure formulations, in particular for turbulent heat flux modeling, and second, to serve as guidance for improved eddy-viscosity formulations. Equilibrium and bifurcation analyses have successfully been used to incorporate rotational effects in eddy-viscosity models in Pettersson Reif, Durbin & Ooi (1999).

The theoretical analysis is based on the *general* linear models for the Reynolds stresses and turbulent heat fluxes. However, only numerical results obtained with the most widely used model, the IP model, is presented here, but the generality of the approach sets the stage for analyzing all existing linear (or quasi-linear) SMC models. Similar analyses of the Mellor-Yamada SMC have previously been performed, cf. e.g. Hassid & Galperin (1994), Baumert & Peters (2000) and Kantha, Rosati & Galperin (2000). Mellor-Yamada, which also is a subset of the general linear formulation, has received much attention in the geophysical fluid dynamics community, but it has rarely been used in engineering fluid flow predictions; the reason is mainly due to the highly simplified pressure-strain correlation model.

2. Equilibrium and bifurcation analysis

Structural equilibrium of the Reynolds stresses is defined by constant values of the anisotropy tensor $d_t b_{ij} = d_t(\overline{u_i u_j}/k) = 0$ and of the turbulent to mean flow time-scale ratio $d_t(Sk/\varepsilon) = 0$ where S is the mean shear dU/dy. True structural equilibrium requires

also that $d_t(S_{ij}k/\varepsilon) = 0 = d_t(\Omega_{ij}^A k/\varepsilon)$ where

$$S_{ij} = \frac{1}{2}\left(\frac{\partial U_j}{\partial x_i} + \frac{\partial U_i}{\partial x_j}\right) \qquad (2.1)$$

and

$$\Omega_{ij}^A = \frac{1}{2}\left(\frac{\partial U_j}{\partial x_i} - \frac{\partial U_i}{\partial x_j}\right) + \epsilon_{ijk}\Omega_k^F \qquad (2.2)$$

are the mean rate of strain and absolute mean vorticity tensors, respectively. Ω_k^F is the angular velocity of the reference frame about the x_k axis. It should be noted that k and ε themselves are not in general constants at equilibrium. However, the evolution of the kinematic Reynolds stresses $\overline{u_iu_j}$ is the same as k; this is the reason why $d_t b_{ij} = 0$. Similarly, the evolution of the turbulent and mean flow time scales are also identical but not necessarily $d_t(k/\varepsilon) = 0 = d_t\mathcal{S}$.

Equilibrium of the turbulent fluxes is defined by $d_t K_{ij} = 0$ and $d_t(\partial_i\Theta) = -\partial_i U_k \partial_k\Theta$ where $\mathbf{K}$ is the dispersion tensor and Θ is the mean temperature. The dispersion tensor relates the turbulent fluxes to the mean temperature field;

$$\overline{u_i\theta} = -K_{ij}\frac{k^2}{\varepsilon}\frac{\partial\Theta}{\partial x_j}. \qquad (2.3)$$

For equilibrium to be attained, the mean temperature gradient is allowed to evolve as $d_t(\partial_j\Theta) = -\partial_j U_k \partial_k\Theta$.

2.1. *General linear models*

Under the assumption of homogeneity and local isotropy, the transport of the kinematic Reynolds stress tensor in a noninertial frame of reference is governed by

$$d_t\overline{u_iu_j} = \mathcal{P}_{ij} + \mathcal{R}_{ij} + \mathcal{G}_{ij} - \frac{2}{3}\varepsilon\delta_{ij} + \phi_{ij} \qquad (2.4)$$

where

$$\mathcal{P}_{ij} = -\left(\overline{u_iu_k}\partial_k U_j + \overline{u_ju_k}\partial_k U_i\right)$$
$$\mathcal{R}_{ij} = -2\Omega_k^F\left(\epsilon_{jkl}\overline{u_iu_l}\right)$$
$$\mathcal{G}_{ij} = -\beta\left(g_i\overline{u_j\theta} + g_j\overline{u_i\theta}\right).$$

are the rate of production due to mean shear, system rotation, and buoyancy, respectively. The last term, which associated with buoyancy production, is responsible for the intercoupling between the turbulent stress and heat flux fields. The most general linear model for the pressure-strain correlation tensor ϕ_{ij} can be written as

$$\phi_{ij}/k = -C_1 b_{ij}\varepsilon/k + 4/5 S_{ij} + (C_2 + C_3)\left(b_{ik}S_{kj} + b_{jk}S_{ki} - \tfrac{2}{3}\delta_{ij}b_{mn}S_{nm}\right)$$
$$+ (C_2 - C_3)\left(b_{ik}\Omega_{kj}^A + b_{jk}\Omega_{ki}^A\right) + C_4/k\left(\mathcal{G}_{ij} - \tfrac{1}{3}\delta_{ij}\mathcal{G}_{kk}\right).$$

The corresponding equations for the turbulent kinetic energy and the dissipation rate are

$$d_t k = \mathcal{P} - \varepsilon$$
$$d_t\varepsilon = \tfrac{\varepsilon}{k}\left(C_{\varepsilon 1}\mathcal{P} - C_{\varepsilon 2}\varepsilon\right)$$

where $\mathcal{P} = \frac{1}{2}(\mathcal{P}_{kk} + \mathcal{G}_{kk})$. The evolution of the Reynolds stress anisotropy tensor, $b_{ij} = \overline{u_i u_j}/k - 2/3\delta_{ij}$, and the turbulent to mean flow time-scale ratio can then be written as

$$d_t b_{ij} = -\tfrac{8}{15}S_{ij} + b_{ij}\varepsilon/k\,(1 - C_1 - \mathcal{P}/\varepsilon)$$
$$+ (C_2 + C_3 - 1)\left(b_{ik}S_{kj} + b_{jk}S_{ki} - \tfrac{2}{3}\delta_{ij}b_{mn}S_{nm}\right)$$
$$+ (C_2 - C_3 - 1)\left(b_{ik}\Omega^A_{kj} + b_{jk}\Omega^A_{ki}\right)$$
$$+ (1 - C_4)\left(\mathcal{G}_{ij}/k - \tfrac{2}{3}\delta_{ij}\mathcal{G}/k\right) - \Omega^F_k\left(b_{il}\epsilon_{jkl} + b_{jl}\epsilon_{ikl}\right).$$

and

$$d_\tau\left(\frac{\varepsilon}{Sk}\right) = \frac{\varepsilon}{Sk}\left((C_{\varepsilon 1} - 1)\frac{\mathcal{P}}{\varepsilon} - (C_{\varepsilon 2} - 1)\right) \tag{2.5}$$

where $\tau = St$.

Under homogeneous conditions, the transport of turbulent heat flux is governed by

$$d_t\overline{u_i\theta} = \mathcal{P}_{i\theta} + \mathcal{G}_{i\theta} + \phi_{i\theta} \tag{2.6}$$

where

$$\mathcal{P}_{i\theta} = -\overline{u_i u_j}\partial_j\Theta - \overline{u_j\theta}\partial_j U_i$$
$$\mathcal{G}_{i\theta} = -\beta g_i\overline{\theta^2}$$

are the production terms. The corresponding general linear 'pressure-strain' model for turbulent fluxes can be written as

$$\phi_{ic} = -C_{1c}\varepsilon/k\overline{u_i\theta} + (C_{2c} + C_{3c})\overline{u_k\theta}S_{ki} + (C_{2c} - C_{3c})\overline{u_i\theta}\Omega^A_{ki} + C_{4c}\overline{u_i u_j}\partial_j\Theta$$
$$+ C_{5c}\beta g_i\overline{\theta^2}.$$

The last term in (2.7) depends on the *a priori* unknown temperature variance $\overline{\theta^2}$. A simple model equation for the temperature variance is adopted:

$$d_t\overline{\theta^2} = -2\overline{u_k\theta}\partial_k\Theta - C_{\mathcal{R}}\frac{\varepsilon}{k}\overline{\theta^2}. \tag{2.7}$$

The coefficient $C_{\mathcal{R}}$ denotes the ratio between the heat flux time-scale $\overline{\theta^2}/\varepsilon_\theta$ and the mechanical time-scale k/ε. $C_{\mathcal{R}}$ is for simplicity assumed to be constant; the alternative would be to solve a transport equation for the heat flux dissipation rate ε_θ.

The equation governing the evolution of the dispersion tensor **K**, defined in (2.3), can then be written as

$$\partial_j\Theta d_t K_{ij} =$$
$$\partial_j\Theta K_{ij}\varepsilon/k\,[\mathcal{P}/\varepsilon(C_{\varepsilon 1} - 2) + 2 - C_{\varepsilon 2}] + K_{ij}\partial_k\Theta\left(S_{jk} + \Omega^A_{jk}\right)$$
$$+ (1 - C_{4c})\overline{u_i u_k}\varepsilon/k^2\partial_k\Theta$$
$$- (1 - C_{2c} - C_{3c})K_{kj}S_{ki} - (1 - C_{2c} + C_{3c})K_{kj}\Omega^A_{ki}$$
$$+ (1 - C_{5c})\beta g_i\overline{\theta^2}\varepsilon/k^2 - C_{1c}\varepsilon/k K_{ij}\partial_j\Theta.$$

The task is now to solve (2.5) - (2.5) and (2.7) - (2.8) for homogeneous shear flow subjected to orthogonal mode rotation, i.e. $\mathbf{U} = [U(y),0,0]$, $\mathbf{\Omega^F} = [0,0,\Omega^F]$, $\mathbf{g} = [0,-g,0]$ and $\Theta = \Theta(y)$, see Fig. 1. The equilibrium solution of this set of equations depends on two parameters: Ω^F/S and Ri_g. The gradient Richardson number is defined as $Ri_g = \beta g_2\partial_y\Theta/S^2$. Recall that $S = dU/dy$.
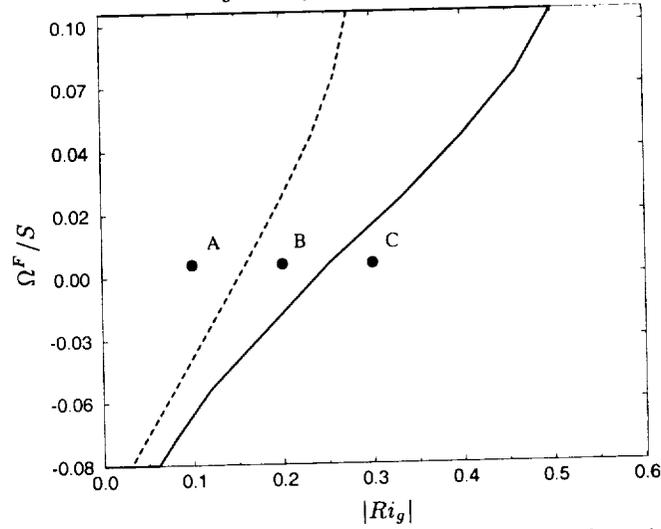
FIGURE 2. Bifurcation diagram for the IP model with $C_4 = 0.1$. Bifurcation line: $----$; Stabilization line: $\underline{\quad\quad}$.

The model coefficients for the IP model are

C_1	C_2	C_3	C_4	$C_{\varepsilon 1}$	$C_{\varepsilon 2}$
1.8	3/5	0.0	0.5	1.5	1.8

whereas the following coefficients in the turbulent flux equation are used

C_{1c}	C_{2c}	C_{3c}	C_{4c}	$C_{\mathcal{R}}$
1.8	2.5	0.0	0.45	1.4

The value $C_4 = 0.5$ is the computationally optimized value suggested by Gibson & Launder (1978).

2.2. Bifurcation of equilibria

Equation (2.5) has two solutions for $d_t(\varepsilon/Sk) = 0$: (i) $\mathcal{P}/\varepsilon = (C_{\varepsilon 2} - 1)/(C_{\varepsilon 1} - 1)$ and (ii) $lim_{t \to \infty}\varepsilon/Sk = 0$. These solution branches, in the three-dimensional phase space $\varepsilon/Sk - Ri_g - \Omega^F/S$, are referred to as the nontrivial and trivial branch, respectively. The solution on the nontrivial branch is thus $\varepsilon/Sk = Fcn(\Omega^F/S, Ri_g)$ and $\mathcal{P}/\varepsilon = const$. It is associated with the exponential solution $k \propto e^{\sigma t}$ where $\sigma \propto \varepsilon/Sk$ depends on the model. On the trivial branch, $\varepsilon/Sk = 0$, and $\mathcal{P}/\varepsilon = Fcn(\Omega^F/S, Ri_g)$ depends on the model. This branch is associated with an algebraic solution $k \propto t^\lambda$ where $\lambda \propto \mathcal{P}/\varepsilon - 1$. So as bifurcation occurs, i.e. when $\varepsilon/Sk = 0$, the exponential evolution of k is replaced by an algebraic. But more importantly, the argument of the algebraic solution becomes *negative* at certain values of Ω^F/S and Ri_g, i.e $\mathcal{P}/\varepsilon < 1$. Hence, the evolution of k changes from an algebraic growth to an algebraic decay beyond the so-called point of stabilization (or neutral point): $\mathcal{P}/\varepsilon = 1$. The turbulence is thus *stabilized* by the imposed body force. It is this particular feature of SMC models that make them superior to traditionally $k - \varepsilon$ models. A more comprehensive description of bifurcation analysis can be found in Durbin & Pettersson Reif (1999).

The response of a particular closure model to an imposed body force can be neatly
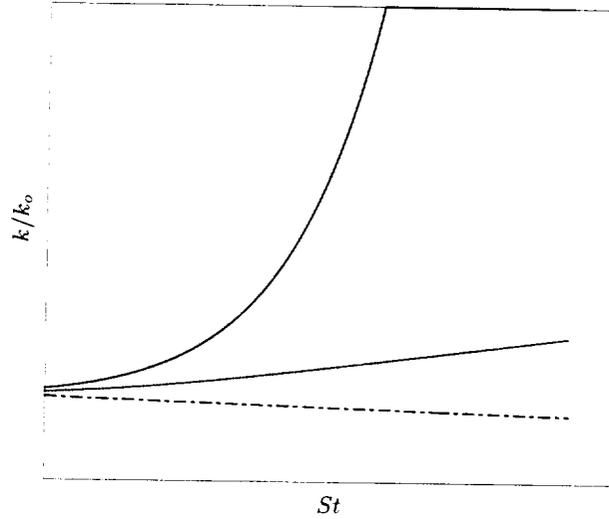
FIGURE 3. Evolution of turbulent kinetic energy in different regimes in the Ω^F/S and Ri_g space, see Fig. 2. A: ———— ; B: ········ ; C: ———— . The turbulent kinetic energy has been normalized with its initial value.
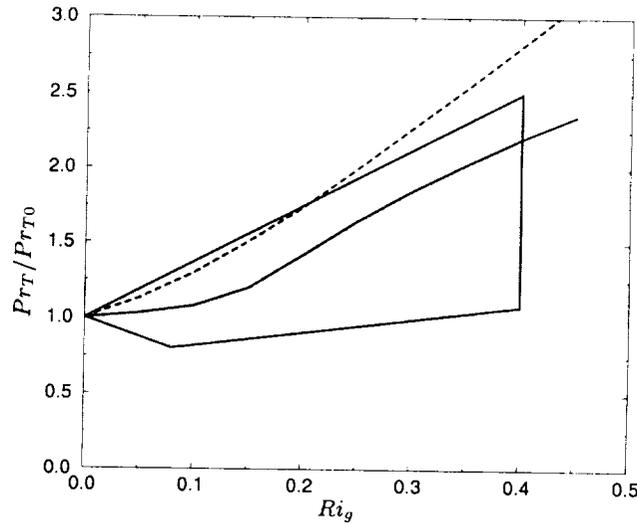
FIGURE 4. Turbulent Prandtl number as a function of gradient Richardson number ($\Omega^F/S = 0$). The shaded region corresponds to the data reported by Rohr, Itsweire, Helland & Van Atta (1988). The lines are IP preditions; ———— : $C_4 = 0.1$; ———— : $C_4 = 0.5$. The turbulent Prandtl number is normalized with its value at $Ri_g = 0$.

summarized in a bifurcation diagram, i.e. a plot that shows ε/Sk versus Ri_g and Ω^F/S. Another issue related to the equilibrium solution of the model equations is whether it is stable or not. Stability in this context should not be confused with stabilization of turbulence; it relates to a characteristic of the solution to the governing model equations. Several solutions ε/Sk might exist for the same pair Ri_g and Ω^F/S, but there should only be one physically realistic stable solution in order for the model formulation to make sense.

3. Results

There is experimental evidence that the critical mean gradient Richardson number $Ri_g^{cr} \approx 0.25$ $(\Omega^F/\mathcal{S} = 0)$; fully turbulent conditions cease to exist as Ri_g is increased beyond Ri_g^{cr}. It has also been well established that homogeneous shear flow relaminarizes due to an imposed system rotation outside the range $-0.1 < \Omega^F/\mathcal{S} < 0.5$. In contrast to pure stratification, there exist *two* critical rotation numbers. SMC models tend to predict, in agreement with linear stability analysis, maximum growth rate of turbulent kinetic energy at $\Omega^F/\mathcal{S} \approx 0.25$ $(Ri_g = 0)$; as the rotation rate is increased from $\Omega^F/\mathcal{S} = 0$ to $\Omega^F/\mathcal{S} = 0.25$, the turbulence is *destabilized*, i.e. the turbulent time scale k/ε decreases. In a stably stratified environment, the magnitude of the critical gradient Richardson number is, therefore, expected to increase for positive $\Omega^F/\mathcal{S}$ up to some point where it again is reduced. On the other hand, for negative and sufficiently high positive rotation rates, $|Ri_g^{cr}|$ is expected to be reduced.

Figure 2 shows the bifurcation and stabilization lines for the IP model. The predictions partly confirm the above conjecture; the magnitude of the critical Richardson number is increased as the rotation is increased. It should be noted that the constant $C_4 = 0.1$ has been used instead of the original value 0.5 suggested by Gibson & Launder (1978) in order to predict $Ri_g^{cr} \approx 0.25$ at $\Omega^F/\mathcal{S} = 0$. The critical gradient Richardson number corresponds to the stabilization line in the figure. If $C_4 = 0.5$ is used, the model predicts $Ri_g^{cr} \approx 0.8$, which is inconsistent with laboratory observations. The accompanying results in Fig. 3 show the evolution of turbulent kinetic energy in the different regions of the bifurcation diagram; it exhibits an algebraic or exponential behavior depending on the values of the imposed parameters.

The turbulent Prandtl number $Pr_T = Ri_g b_{12}/K_{22} = Ri_g/Ri_f$ depends on the predictions at a given Ri_g. Figure 4 displays the turbulent Prandtl number as a function of gradient Richardson number. Two different IP predictions are included in the figure to illustrate the dependence of the model constant C_4. Rohr, Itsweire, Helland & Van Atta (1988) argued that the Pr_T not is strongly dependent on Ri_g as long as $|Ri_g| < |Ri_g^{cr}|$. This behavior is reproduced by the IP model if the value $C_4 = 0.1$ is used.

4. Concluding remarks

It has been demonstrated that the model coefficient C_4 is crucial in terms of the ability to predict $Ri_g^{cr} \approx 0.25$ at zero rotation; the commonly used value $C_4 = 0.4$ should be replaced by $C_4 \approx 0.1$. The experimentally observed variation of the turbulent Prandtl number with the gradient Richardson number can then also be reproduced by the model.

It has only been possible to map the bifurcation diagram in the $\Omega^F/\mathcal{S} - Ri_g$ phase space within a limited range of rotation rates $(Ri_g \neq 0)$, see Fig. 2. This behavior seems closely related to the particular set of model coefficients that is used. However, all commonly known linear and quasi-linear SMCs have been tested, and all of them seem to be 'ill-posed'. It is also interesting to note that under certain conditions the solution of an SMC takes the form of relaxed oscillations; no numerically stable steady state solution could be found for a given set of $\Omega^F/\mathcal{S} - Ri_g$.

It has been demonstrated that the stabilizing effect of stratification can be properly accounted for in a non-rotating frame of reference. The fact that all existing linear models seem ill-posed as system rotation is imposed is a bit worrying. Further work is definitely needed in order to resolve this problem, which probably also is of concern when computing

complex flows relevant in engineering or geophysics. The added complexity of the model equations that results from an imposed density stratification makes this task a challenge.

REFERENCES

BAUMERT, H. & PETERS, H. 2000 Second-moment closures and length scales for weakly stratified turbulent shear flows. *J. Geophys. Res.* **105**, 6453-6468.

DURBIN, P. A. & PETTERSSON REIF, B. A. 2000 On algebraic second moment models. *Flow, Turbulence & Combustion.* **63**, 23-37.

GIBSON, M. M. & LAUNDER, B. E. 1978 Ground effects on pressure fluctuations in the atmospheric boundary layer. *J. Fluid Mech.* **86**, 491-511.

HASSID, S. & GALPERIN, B. 1994 Modeling rotating flows with neutral and unstable stratification. *J. Geophys. Res.* **99**, 12533-12548.

KANTHA, L. H., ROSATI, A. & GALPERIN, B. 2000 Effect of rotation on vertical mixing and associated turbulence in stratified fluids. *J. Geophys. Res.* **105**, 4843-4854.

PETTERSSON REIF, B. A., DURBIN, P. A. & OOI, A. 1999 Modeling rotational effects in eddy-viscosity closures. *Int. J. Heat and Fluid Flow.* **20**, 563-573.

ROHR, J. J., ITSWEIRE, E. C., HELLAND, K. N. & VAN ATTA, C. W. 1988 Growth and decay of turbulence in a stably stratified shear flow. *J. Fluid Mech.* **195**, 77-111.

LES and unsteady RANS of boundary-layer transition induced by periodically passing wakes

By F. E. Ham†, F. S. Lien†, X. Wu, M. Wang, AND P. Durbin

Results from 3-dimensional large-eddy simulation (LES) and 2-dimensional unsteady Reynolds-averaged Navier-Stokes (RANS) simulation of a spatially-evolving flat-plate boundary-layer undergoing transition induced by periodically passing wakes are presented and compared. The LES simulations used a novel kinetic-energy conserving finite-volume discretization of the incompressible Navier-Stokes equations and the standard dynamic Smagorinsky subgrid-scale model. RANS simulations were based on the STREAM code of Lien & Leschziner (1994) with the $v^2 - f$ turbulence model of Lien & Durbin (1996).

When compared to the direct numerical simulation (DNS) of Wu *et al.* (1999), the LES was able to correctly predict the onset of transition. Inspection of the instantaneous flow field in the transition region confirmed that intermittent turbulent spots were being distinctly resolved. A close inspection of the fluctuating velocities near the top of the boundary layer just prior to spot formation confirmed the presence of the "backward jet" inflectional velocity profile proposed by Wu *et al.* (1999) and Jacobs & Durbin (2000) as the precursor to turbulent spot formation, suggesting that the LES is actually capturing the bypass transition mechanism, at least in these initial stages. The transition length predicted by LES, however, was consistently shorter than the DNS result.

The unsteady RANS simulations were also able to correctly predict the onset of transition, in this case by the mechanism of turbulent diffusion from the turbulence kinetic energy of the passing wake into the boundary layer. The transition length predicted by RANS is also in agreement with the DNS; however, the overshoot of average skin friction relative to the flat plate correlation (seen in both the DNS and present LES) was not observed.

1. Introduction

In orderly transition to turbulence, small disturbances in the laminar boundary layer lead to 2-dimensional Tollmien-Schlichting waves that are amplified through various stages leading eventually to a fully turbulent boundary layer. This relatively slow transition process has been extensively studied in relation to flow over aircraft wings, where the free-stream turbulence levels are generally low (Mayle 1991).

In the presence of disturbances external to the boundary layer, however, it is observed experimentally that transition can occur rapidly, "bypassing" the orderly route. Bypass transition is the dominant mode of transition in many turbomachinery applications, where free-stream turbulence intensities are usually well above the threshold level of about 0.5% (Yang *et al.* 1994). Furthermore, when the dominant free-stream disturbances are periodic in time, such as the periodically passing wakes generated by an upstream row of rotors or stators in a turbine cascade, the transition can also become periodic. In

† University of Waterloo, Waterloo, Ontario, Canada
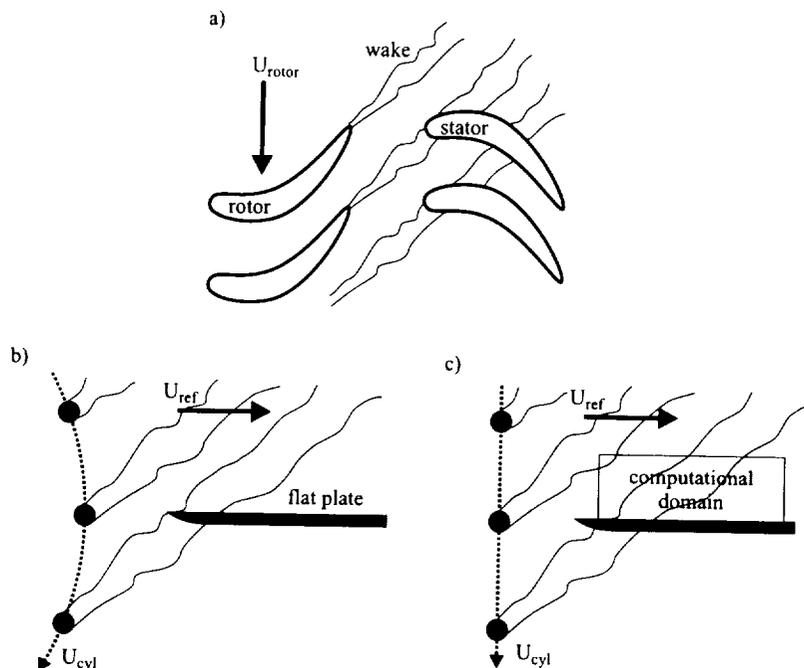
FIGURE 1. a) Schematic of rotor-stator wake interaction; b) layout in the experiments of Liu and Rodi (1991); c) layout in the DNS of Wu et al. (1999), and the present LES and RANS.

this case, the transition is referred to as "wake-induced" (Mayle 1991) but still fits under the broader classification of bypass transition (Fig. 1a).

In an effort to remove some of the geometric and physical complexity associated with the turbine cascade, Liu and Rodi (1991) experimentally investigated the wake-induced transition of a flat-plate boundary layer (Fig. 1b). In their experiments, periodic wakes were generated by a series of cylinders mounted on a rotating squirrel cage upstream of the flat plate. In the absence of the periodic wakes, the relatively low Reynolds number and low free-stream turbulence intensity of 0.3% resulted in a laminar boundary layer over the full length of the test plate. With the wakes, they found that transition first occurred in isolated stripes underneath the disturbed free-stream. The stripes traveled downstream and grew together to eventually form a fully turbulent boundary layer. They also found that the streamwise location of this merger moved upstream with increased wake-passing frequency.

The recent DNS of Wu et al. (1999) was designed following the experiment of Liu and Rodi (1991) and provided new insights into the mechanisms of bypass transition through a detailed analysis of the calculated flow fields (Fig. 1c). Wu et al. found that the transition to turbulence first occurred in isolated spots, which broaden and convect downstream, where they eventually merged with the fully turbulent boundary layer. Analysis of the instantaneous flow field identified long backward jets contained in the fluctuating streamwise velocity field as precursors to turbulent spot formation. They proposed that the backward jets, located near the top of the boundary layer, were associated with a Kelvin-Helmholtz-like inflectional instability that interacts with the free-stream eddies, eventually leading to turbulent spot formation. More recent simulations of bypass tran-

sition under free-stream turbulence (Jacobs and Durbin 2000) also identified backward jets as consistent precursors to turbulent spot formation.

At 52 million and 71 million grid points respectively, the aforementioned transition simulations are some of the largest and most finely resolved ever reported. Interestingly, the bypass transition mechanism they uncovered – the backward jet – is actually a relatively large structure, spanning 100's of wall units in the streamwise direction and about 60 wall units in the spanwise direction. This suggests that a coarser and significantly less expensive LES might be able to capture the bypass transition mechanism.

Yang *et al.* (1994) used LES to study bypass transition of a flat plate boundary layer subject to 5% freestream turbulence intensity. These simulations used the Smagorinsky subgrid scale model modified in an *ad hoc* manner to prevent excessive dissipation in the laminar portion of the boundary layer. They reported good agreement with available experimental data such as the average skin friction coefficient and shape factor, but did not report the resolution of turbulent spots or their precursors. In a more recent LES of natural transition, Huai *et al.* (1997) used the dynamic procedure of Germano *et al.* (1991) to avoid these *ad hoc* modifications. They reported that a localized version (Piomelli and Liu 1995) of the dynamic model gave accurate results both in a statistical sense and in terms of predicting the dynamics of the energy-carrying eddies.

In the present contribution, LES is used to study the wake-induced transition of a flat-plate boundary layer with specific emphasis on the resolution of turbulent spots and their precursors. As a complementary effort, the same problem is simulated using 2-dimensional unsteady RANS. These two results, along with the DNS of Wu *et al.* (1999), represent a truly integrated analysis of this transitional flow and provide a unique opportunity to assess the relative benefits and drawbacks of the various simulation technologies.

2. Governing equations

The tensor equations of motion for the spatially filtered incompressible velocity and pressure fields are given by

$$\frac{\partial \bar{u}_i}{\partial t} + \frac{\partial \bar{u}_j \bar{u}_i}{\partial x_j} = -\frac{\partial \bar{p}}{\partial x_i} + \frac{\partial}{\partial x_j}\left((\nu + \nu_{sgs})\left(\frac{\partial \bar{u}_j}{\partial x_i} + \frac{\partial \bar{u}_i}{\partial x_j} \right) \right) \tag{2.1}$$

$$\frac{\partial \bar{u}_i}{\partial x_i} = 0 \tag{2.2}$$

where the overbar represents spatial filtering on the scale of the grid. Equation (2.1) assumes Boussinesq dynamics to approximate the subgrid stresses, where the subgrid viscosity, ν_{sgs}, is given by the Smagorinsky closure

$$\nu_{sgs} = C\bar{\Delta}^2 \sqrt{2\bar{S}_{ij}\bar{S}_{ij}}. \tag{2.3}$$

In equation (2.3), the resolved strain rate tensor is defined

$$\bar{S}_{ij} = \frac{1}{2}\left(\frac{\partial \bar{u}_j}{\partial x_i} + \frac{\partial \bar{u}_i}{\partial x_j} \right), \tag{2.4}$$

and the grid filter width is defined in terms of the local grid spacing

$$\bar{\Delta} = \left(\bar{\Delta}_x \bar{\Delta}_y \bar{\Delta}_z \right)^{1/3}. \tag{2.5}$$

The Smagorinsky constant, C, is calculated using the dynamic procedure of Germano et al. (1991) and Lilly (1992) with averaging in the homogeneous direction(s) to avoid the numerical instability associated with large negative C values. In addition, the total viscosity $(\nu + \nu_{sgs})$ is not allowed to be negative.

3. Numerical method

The important role of discrete conservation of mass, momentum, and kinetic energy in obtaining accurate solutions to incompressible turbulent flow problems has been argued by several authors (Morinishi et al. 1998, Mittal & Moin 1997). These analyses have considered discrete conservation of the spatial terms as analytical requirements for a proper set of discretized equations. In general, this has meant a staggered arrangement of velocity and pressure and the use of symmetric (central-difference) discretizations for all spatial derivatives. Because of the fractional-step method normally used for time advancement, however, the same conservation requirements cannot be enforced in time. Although the associated errors are generally small and dissipative, the system is not conservative in a discrete sense.

The LES of the present contribution is based on a discretized form of governing Eqs. (2.1) and (2.2) that is 2nd-order accurate and discretely conserves mass, momentum, and kinetic energy (in the inviscid limit) in space and time. The resulting equations closely resemble that given by the 2-level Crank-Nicholson scheme, with a slight modification to the convective term. In the following sections, the conservative discretized equations are introduced, their conservation properties are derived, and the details of their efficient solution is presented.

3.1. *The discretized equations*

Extending the notation of Morinishi et al. (1998) to include time, we introduce the following discrete operators for 2nd-order differencing and averaging on a structured orthogonal grid.

$$\frac{\delta_1 \phi}{\delta_1 x_1}\bigg|_{x_1,x_2,x_3,t} \equiv \frac{\phi\left(x_1 + h_1/2, x_2, x_3, t\right) - \phi\left(x_1 - h_1/2, x_2, x_3, t\right)}{h_1} \tag{3.1}$$

$$\overline{\phi}^{1\,x_1}\bigg|_{x_1,x_2,x_3,t} \equiv \frac{\phi\left(x_1 + h_1/2, x_2, x_3, t\right) + \phi\left(x_1 - h_1/2, x_2, x_3, t\right)}{2} \tag{3.2}$$

$$\widetilde{\phi\psi}^{1\,x_1}\bigg|_{x_1,x_2,x_3,t} \equiv \tfrac{1}{2}\phi\left(x_1 + h_1/2, x_2, x_3, t\right)\psi\left(x_1 - h_1/2, x_2, x_3, t\right) + \\ \tfrac{1}{2}\psi\left(x_1 + h_1/2, x_2, x_3, t\right)\phi\left(x_1 - h_1/2, x_2, x_3, t\right) \tag{3.3}$$

In the above equations, ϕ and ψ represent discrete variables that may be cell-centered or staggered, and h_1 is the grid spacing in the x_1 direction. Discrete operators in the x_2, x_3, and t directions are similarly defined. To avoid confusion in the already cumbersome notation of the following sections, the overbar used in Eqs. (2.1) and (2.2) is dropped, and capital letters are used to represent the discrete velocity and pressure fields.

Using this notation, a 2nd-order accurate discretization of continuity equation (2.2) is

$$\frac{\delta_1 U_i}{\delta_1 x_i} = 0. \tag{3.4}$$

Because Eq. (3.4) is in discrete divergence form, it is *a priori* conservative, and we would

expect the scheme to conserve mass locally and globally. Assuming zero viscous and subgrid stresses, a 2nd-order accurate discretization of the momentum equation is

$$\frac{\delta_1 U_i}{\delta_1 t} + \frac{\delta_1 \overline{\overline{U_j}^{1t}}^{1x_i} \overline{\overline{U_i}^{1t}}^{1x_j}}{\delta_1 x_j} + \frac{\delta_1 P}{\delta_1 x_i} = 0. \tag{3.5}$$

Because all terms in Eq. (3.5) are in discrete divergence form (including the time term, if the concept of discrete divergence is extended to time as well), it is *a priori* conservative. Thus, momentum is conserved locally and globally in space and time.

3.2. *Discrete kinetic energy conservation*

As pointed out by Morinishi *et al.* (1998), local kinetic energy cannot be defined unambiguously on the staggered grid because the velocity components are stored at different locations. The required interpolation of velocity components is consistent if we choose the cell center (the location of P) as the location about which to develop the kinetic energy equation.

The vector dot product of the velocity with the momentum equation (3.5) produces the kinetic energy equation which, including the appropriate discrete 2nd-order interpolations, takes the form

$$\overline{\overline{U_i}^{1t} \left(\frac{\delta_1 U_i}{\delta_1 t} + \frac{\delta_1 \overline{\overline{U_j}^{1t}}^{1x_i} \overline{\overline{U_i}^{1t}}^{1x_j}}{\delta_1 x_j} + \frac{\delta_1 P}{\delta_1 x_i} \right)}^{1x_i} = 0 \tag{3.6}$$

The l.h.s. of (3.6) can be expanded into 3 terms, each of which will be analyzed for conservation separately:

$$(Time) + (Conv.) + (Pres.) = 0. \tag{3.7}$$

Using the identities described by Morinishi *et al.* (1998), the $(Time)$ term can be rearranged as follows

$$(Time) = \overline{\overline{U_i}^{1t} \frac{\delta_1 U_i}{\delta_1 t}}^{1x_i} = \overline{\frac{\delta_1 U_i U_i / 2}{\delta_1 t}}^{1x_i} = \frac{\delta_1 \overline{U_i U_i / 2}^{1x_i}}{\delta_1 t} = \frac{\delta_1 K}{\delta_1 t} \tag{3.8}$$

where the kinetic energy, K, is defined

$$K = \overline{U_i U_i / 2}^{1x_i}. \tag{3.9}$$

Equation (3.8) is in discrete divergence form, and thus the $(Time)$ term of the K equation is conservative. The pressure term can be rearranged as follows

$$(Pres.) = \overline{\overline{U_i}^{1t} \frac{\delta_1 P}{\delta_1 x_i}}^{1x_i} = \frac{\delta_1 \overline{U_i}^{1t} \overline{P}^{1x_i}}{\delta_1 x_i} - P \frac{\overline{\delta_1 U_i}^{1t}}{\delta_1 x_i} \tag{3.10}$$

The first term on the rhs is in divergence form, and the second term involves the discrete continuity equation, which is identically zero. Therefore, the $(Pres.)$ term of the K equation is conservative. Finally, some manipulation of the $(Conv.)$ term yields:

$$(Conv.) = \overline{U}_i^{1t} \frac{\overline{\delta_1 \overline{U_j}^{1t}}^{1x_i} \overline{\overline{U_i}^{1t}}^{1x_j}}{\delta_1 x_j}^{1x_i}$$

$$= \frac{1}{2} \frac{\delta_1 \overline{\overline{U_j}^{1t}}^{1x_i} \overline{\widetilde{U_i^{1t}U_i}^{1t}}^{1x_j}}{\delta_1 x_j}^{1x_i} + \frac{1}{2} \overline{U}_i^{1t} \overline{U}_i^{1t} \frac{\overline{\delta_1 \overline{U_j}^{1t}}}{\delta_1 x_j}^{1x_i} \tag{3.11}$$

The first term on the rhs is in divergence form, and the second term involves the discrete continuity equation, which is identically zero. Therefore the $(Conv.)$ term of the K equation is conservative.

3.3. Solution procedure

The coupled, fully-implicit, non-linear system of equations resulting from this choice of discretization can be quite stiff, particularly on the highly stretched grids typical of LES and DNS of wall-bounded shear flows. In the present work, the system is solved iteratively at each time step using algebraic multigrid with smoothing based on the Symmetric Coupled Gauss-Siedel method of Vanka (1986). The system's stiffness is handled by coarsening preferentially in the direction of greatest coefficient strength, a multigrid technique referred to as semi-coarsening (Wesseling 1992). With the judicious selection of coarse grids, it is possible to reduce the maximum residual by 6 orders of magnitude with about 50 workunits per time step (1 workunit is equivalent to one smoothing sweep through the finest grid). Although relatively expensive per time step when compared to the fractional step approximation, the present fully-implicit system is numerically stable for any choice of computational time step, and the discrete conservation properties ensure the method is not dissipative in space and time.

4. Validation: the transitional channel flow

The temporal transition in a channel has been used in the past to demonstrate the performance of the various dynamic models (Germano et al. 1991, Meneveau et al. 1996). As a validation exercise, the discretely conservative solution method described above was used to solve this flow.

The initial condition consists of a parabolic profile superimposed with a 2-dimensional Tollmien-Schlichting (TS) mode of 2% and a 3-dimensional TS mode of 0.02%. The Reynolds number is 8000 (based on laminar centerline velocity), and the dimensions of the computational domain, normalized by channel half width, are $2\pi \times 2 \times 4\pi/3$ in the streamwise, wall-normal, and spanwise directions respectively. For more details, see Zang et al. (1990). As the solution is integrated ahead in time, the TS modes are amplified and the flow undergoes natural transition, leading eventually to fully developed turbulence.

Figure 2 compares the time history of the calculated wall shear stress with that from the DNS of Zang et al. (1990). The results for two different grid resolutions are reported. When compared to the DNS result, both LES results capture the characteristic shape of the curve, including the drag crisis. In both cases, the peak wall shear is slightly over-predicted although this has been observed before (Meneveau et al. 1996). In the case of the coarse grid simulation, however, the entire transition is significantly delayed. This delay is likely explained by the under-predicted linear amplification rate of the coarse finite differences. Solution of the Orr-Sommerfeld equation using the same wall-normal

FIGURE 2. Time history of average wall shear stress from the transitional channel simulation.
——— fine LES ($32 \times 128 \times 64$); – – – – coarse LES ($32 \times 64 \times 32$); ● DNS of Zang *et al.* (1990)

grid distribution and finite-difference numerics yields an amplification factor (the imaginary part of the eigenvalue) for the imposed 2-dimensional TS mode of $\omega_i = 0.002222$. The "exact" value of $\omega_i = 0.002664$ (Zang & Krist 1989) is higher by a factor of 1.2, corresponding closely to the inverse ratio of the duration of the linear amplification periods of about $220/180 = 1.2$. To show that this should be the case, assume the linear amplification period ends when the amplitude of the imposed 2-dimensional TS mode, ϕ_0, reaches some critical level, ϕ_c. Two different simulations that amplify this mode at different rates will reach the critical amplitude at different times, according to

$$\phi_c = \phi_0 e^{\omega_{i1} \Delta t_1} = \phi_0 e^{\omega_{i2} \Delta t_2}. \tag{4.1}$$

Solving (4.1) for the time ratio yields $\Delta t_1 / \Delta t_2 = \omega_{i2}/\omega_{i1}$.

5. Simulation of wake-induced transition

5.1. *Problem definition*

As in Wu *et al.* (1999), the present LES was designed following the experiment of Liu & Rodi (1991). Dimensions were scaled by the characteristic length scale, L, equal to the minimum distance from the upstream cylinders to the leading edge of the flat plate. Velocities were scaled by characteristic velocity scale U_{ref}, the freestream velocity in the absence of wakes. The problem Reynolds number was $Re = U_{ref}L/\nu = 1.5 \times 10^5$. The downward velocity of cylinders was $U_{cyl}/U_{ref} = 0.7$, and the passing wake period was $T = 1.67L/U_{ref}$, corresponding to case number 4 in the experiments of Liu & Rodi (1991).

5.2. *Boundary conditions*

The application of boundary conditions followed the procedure described in Wu *et al.* (1999) with one exception: the precomputation of the self-similar plane wake used as the inlet condition was appropriately filtered for the coarser grid spacing of the present simulation.

5.3. *Computational domain*

Figure 1c schematically illustrates the computational domain used in the present LES. In an effort to minimize the problem size, the domain selected was only a fraction of the

DNS domain of Wu *et al.* (1999). In the streamwise direction, the domain was shortened to just include the transition, $0.1 < x/L < 1.75$. In the spanwise direction, the domain width was $0 < z/L < 0.1$, and in the wall-normal direction, $0 < y/L < 0.3$.

5.4. *Grid spacing and time step*

The grid spacing requirements for accurate DNS of bypass transition have been well established through grid independence studies performed as a part of recent simulations. For the bypass transition simulations of Jacobs & Durbin (2000), the grid spacing (based on maximum friction velocity) was $\Delta x^+ = 11.7$, $\Delta z^+ = 6.0$. This is in agreement with the earlier recommendations of Rai & Moin (1993). The DNS of Wu *et al.* (1999) used a slightly coarser spacing of $\Delta x^+ = 24$, $\Delta z^+ = 11$ (based on friction velocity at $x = 3$).

The grid spacing requirements for accurate LES of bypass transition, however, are less well established. In the bypass transition LES of Yang *et al.* (1994), the grid spacing was $\Delta x^+ = 80$ and $\Delta z^+ = 14$. Based on the experience gained through the present research, we believe this streamwise spacing to be too coarse to resolve discrete turbulent spots. In the present work, the finest grid size used was $256 \times 64 \times 48$, which corresponded to a grid spacing based on maximum friction velocity of $\Delta x^+ = 45$ and $\Delta z^+ = 17$. In the wall-normal direction, spacing at the wall was $\Delta y^+ = 2$.

The computational time step was set constant at $\Delta t = 0.003L/U_{ref}$, which corresponded to a time step in wall units (based on maximum friction velocity) of $\Delta t^+ = \Delta t u_\tau^2/\nu = 1.3$.

5.5. *Computational details*

The combination of reduced domain size, increased grid spacing, and increased computational time step yielded a reduction in problem size by a factor of about 160 relative to the DNS. Computations were carried out on a parallel PC cluster at the University of Waterloo. Simulations were typically run for 10 wake passing periods (about 5500 time steps), and required about 3 days using 32 nodes of the cluster.

6. Results

6.1. *Instantaneous fields*

The relatively small size of the present LES (about 700,000 grid points) afforded some experimentation with the grid spacing. The first simulations were performed on relatively coarse grids with $\Delta x^+ = 95$ and $\Delta z^+ = 35$. Although transition was observed to occur at approximately the correct location (when compared to the DNS), inspection of the instantaneous velocity fields did not reveal isolated turbulent spots. Further, the spanwise resolution in these coarse simulations was certainly not capable of properly resolving the backward jet structures, which appear to have a width of about 60 wall units.

6.1.1. *Turbulent spots*

In the finest LES, however, distinct turbulent spots were clearly discernible. Figure 3 uses the fluctuating velocities in the wall normal direction at 5 equally spaced times to visualize the transition. The interaction between the passing wake and the laminar boundary layer appears as elongated puffs at $t/T = 0$, but breakdown to a turbulent spot does not occur until some time closer to $t/T = 0.4$. At $t/T = 0.4$, the isolated spot is clearly discernible with its characteristic arrowhead pointing upstream. As the turbulent spot is convected downstream, it grows and eventually merges with the fully turbulent portion of the boundary layer.
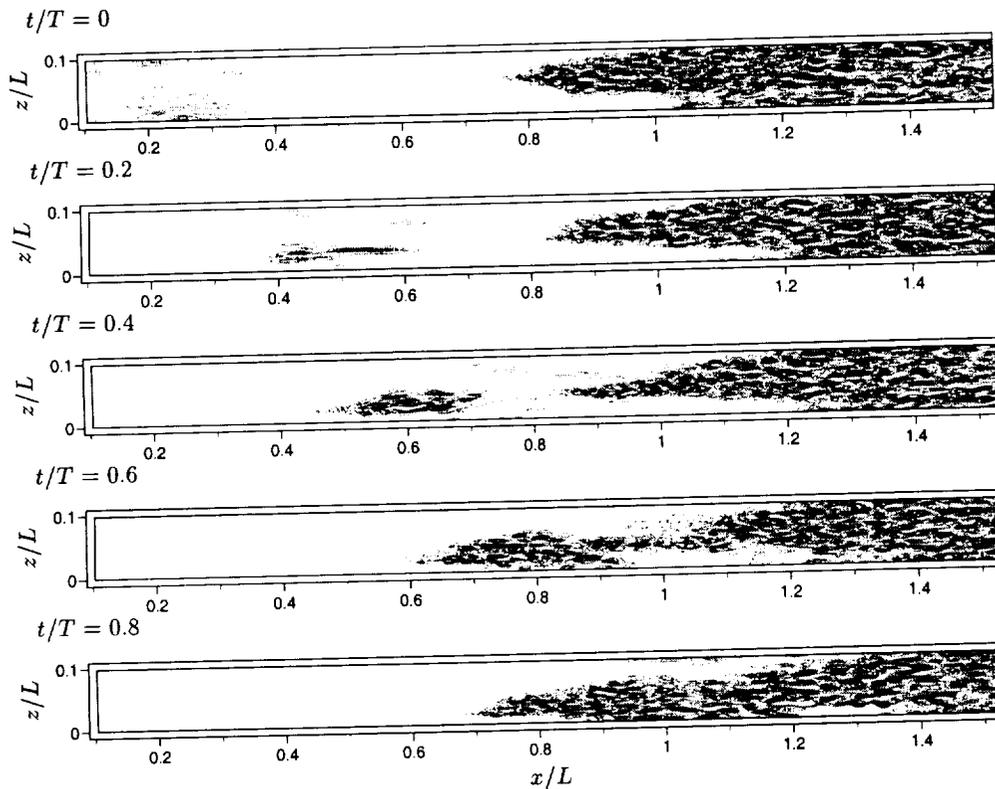
FIGURE 3. Visualization of turbulent spot formation and growth using v-component of fluctuating velocity in the x-z plane near the wall ($y/\delta_{99} = 0.4$ at $x/L = 0.8$). Contours represent $-0.1 < v/U_{ref} < 0.1$ in 0.01 increments.

While qualitatively similar to the DNS result, the following important differences are noted:

(1) The front separating the laminar and fully turbulent portion of the boundary layer is much more irregular in the LES, with long fingers of turbulence reaching significantly upstream. These fingers are thin in the spanwise direction but do not dissipate or convect downstream with the rest of the boundary layer when not being fed by spots.

(2) In the LES, the streamwise location at which the turbulent spots merge with the fully turbulent portion of the boundary layer is in the range of $x = 1$ to 1.2. In the DNS, this location was further downstream at $x = 1.5$ to 1.7.

(3) Close inspection of the turbulent spot reveals the presence of $2 - \Delta$ fluctuations in the velocity field near the upstream edge, indicating under-resolution in the streamwise direction particularly.

6.1.2. *Backward jets*

The backward jet structures observed in the DNS as consistent precursors to turbulent spot formation were also resolved by the LES. By saving restart files regularly, it was possible to stop the simulation when a turbulent spot was identified and restart at an earlier time to look for evidence of spot precursors. Figure 4a) plots the fluctuating velocity vectors in the $x - z$ plane at an elevation near the top of the boundary layer just

a)

b)
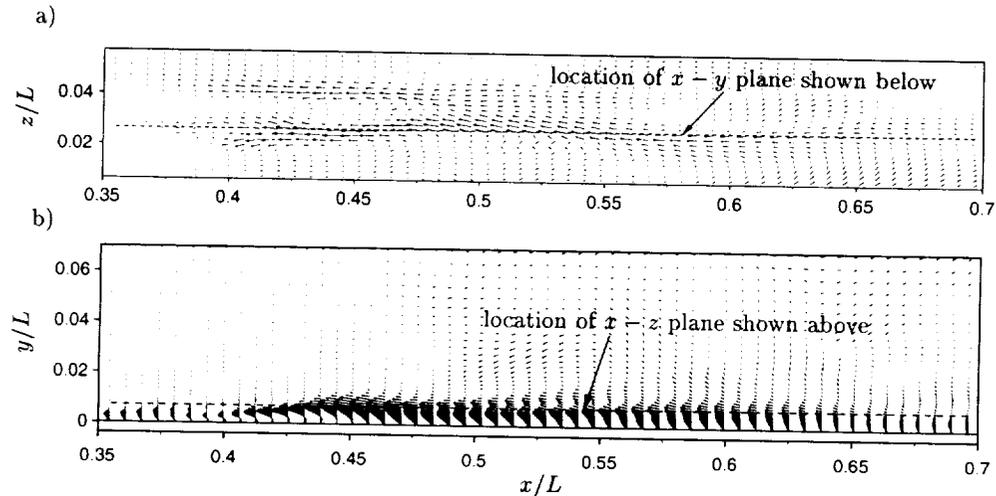
FIGURE 4. Fluctuating velocity vectors upstream of a future turbulent spot showing backward jet structure. a) $x - z$ plane; b) $x - y$ plane.

prior to the appearance of the turbulent spot visualized in Fig. 3. A strong backward jet is evident. The spanwise width of the jet is about 80 wall units, similar to those seen in the bypass transition DNS of Jacobs & Durbin (2000). Figure 4b) shows the fluctuating velocity vectors of the same jet through the $x - y$ plane.

6.2. *Average quantities*

To make our investigation of this transitional flow more comprehensive, unsteady RANS simulations were also performed. These simulations used the STREAM code of Lien & Leschziner (1994), and the $v^2 - f$ turbulence model of Lien & Durbin (1996). Computing time per simulation was approximately 2 hours on a desktop PC. This represents a reduction in computational effort of about 2 orders of magnitude compared to the LES.

Figure 5 compares the average skin friction calculated by the LES and RANS to the DNS of Wu *et al.* (1999). Both the LES and RANS correctly predict the onset of transition. In the case of the LES, however, the transition length is under-predicted. This is consistent with the observation that the turbulent spots merge with the fully turbulent boundary layer further upstream than in the DNS. There are several possible explanations for this although the most compelling is that the dissipation rate given by the standard dynamic model is simply too low in the transition region, where the spanwise averaging used in calculating the model constant includes significant regions of laminar flow. This explanation suggests that another incarnation of the dynamic model might be more appropriate for modeling this type of transitional flow even when a homogeneous direction is present such as the dynamic localization model of Ghosal *et al.* (1995) or the Lagrangian dynamic model of Meneveau *et al.* (1996).

The transition length predicted by RANS agrees with the DNS result although the overshoot of average skin friction relative to the flat plate correlation (seen in both the DNS and present LES) is not observed. No tuning of model constants for this particular flow was done.
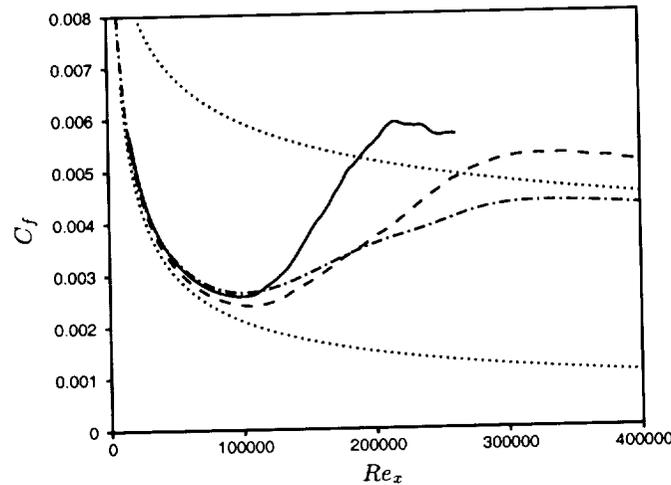
FIGURE 5. Comparison of time averaged skin friction coefficient along flat plate, ——— LES; —·— RANS; – – – – DNS of Wu *et al.* (1999); ········ laminar and turbulent correlations.

7. Conclusions

LES and unsteady RANS simulations have been made of a spatially-evolving flat-plate boundary-layer undergoing transition induced by periodically passing wakes. The LES used a novel kinetic-energy conserving finite-volume discretization of the incompressible Navier-Stokes equations and the standard dynamic Smagorinsky subgrid-scale model. RANS simulations were based on the STREAM code of Lien & Leschziner (1994) with the $v^2 - f$ turbulence model of Lien & Durbin (1996).

Overall, RANS and LES both have benefits when applied to this flow. RANS predicts a slightly superior average skin friction coefficient at enormously reduced computational cost although the performance under more complex conditions (for example, flow in a turbine cascade involving complex geometry, higher freestream turbulence intensity, and pressure gradients) remains to be tested.

The LES was able to resolve both turbulent spots and their backward jet precursors, consistent with the recent DNS results of Wu *et al.* (1999) and Jacobs & Durbin (2000). The location of the onset of transition agreed with the DNS result; however, the transition length was under-predicted. This discrepancy may be related to the spanwise averaging used in the calculation of the subgrid scale model coefficient, and other implementations of the dynamic model might give superior results. The potential improvement from these other models remains to be tested and is the subject of ongoing research.

Acknowledgment

REFERENCES

GERMANO, M., PIOMELLI, U., MOIN, P., & CABOT, W. H. 1991 A dynamic subgrid-scale eddy viscosity model. *Phys. Fluids A.* **3**, no. 7, 1760-1765.

GHOSAL, S., LUND, T. S., MOIN, P. & ASKELVOLL, K. 1995 A dynamic localization model for large-eddy simulation of turbulent flows. *J. Fluid Mech.* **286**, 229-255.

HUAI, X., JOSLIN, R. D. & PIOMELLI, U. 1997 Large-eddy simulation of transition to turbulence in boundary layers. *Theoret. Comput. Fluid Dyn.* **9**, 149-163.

JACOBS, R. G., & DURBIN, P. A. 2000 Simulations of bypass transition. *J. Fluid Mech.*, to appear.

LIEN, F. S. & DURBIN, P. A. 1996 Non-linear $k - \epsilon - v^2$ modeling with application to high lift. *1996 Summer Program Proceedings*, Center for Turbulence Research, NASA Ames/Stanford Univ. 5-22.

LIEN, F. S. & LESCHZINER, M. A. 1994 A general non-orthogonal collocated FV algorithm for turbulent flow at all speeds incorporating second-moment closure. *Comp. Meth. Appl. Mech. Eng.* **114**, 123-167.

LILLY, D. K. 1992 A proposed modification of the Germano subgrid scale closure method. *Phys. Fluids A.* **4**(3), 633-635.

LIU, X. & RODI, W. 1991 Experiments on transitional boundary layers with wake-induced unsteadiness. *J. Fluid Mech.* **231**, 229-256.

MAYLE, R. E. 1991 The role of laminar-turbulent transition in gas turbine engines. *ASME J. of Turbomachinery* **113**, 509-537.

MENEVEAU, C., LUND, T. S. & CABOT, W. H. 1996 A Lagrangian dynamic sungrid-scale model of turbulence. *J. Fluid Mech.* **319**, 353-385.

MITTAL, R. & MOIN, P. 1997 Suitability of upwind-biased finite difference schemes for large-eddy simulation of turbulent flows. *AIAA J.* **35**(8), 1415-1417.

MORINISHI, Y., LUND, T. S., VASILYEV, O. V. & MOIN, P. 1998 Fully conservative higher order finite difference schemes for incompressible flow. *J. Comput. Phys.* **143**, 90-124.

PIOMELLI, U. & LIU, J. 1995 Large eddy simulation of rotating channel flows using a localized dynamic model. *Phys. Fluids A.* **7**, 839.

RAI, M. M. & MOIN, P. 1993 Direct numerical simulation of transition and turbulence in a spatially evolving boundary layer. *J. Comput. Phys.* **109**, 169-192.

VANKA, S. P. 1986 A calculation procedure for three-dimensional steady recirculating flows using multigrid methods. *Comp. Meth. Appl. Mech. Eng.* **55**, 321-338.

WESSLING, P. 1992 An Introduction to Multigrid Methods. John Wiley and Sons.

WU, X., JACOBS, R. G., HUNT, J. C. R. & DURBIN, P. A. 1999 Simulation of boundary layer transition induced by periodically passing wakes. *J. Fluid Mech.* **398**, 109-154.

YANG, Z., VOKE, P. R. & SAVILL, M. A. 1994 Mechanisms and models of boundary layer receptivity deduced from large-eddy simulation of by-pass transition. Direct and large-eddy simulation I, P. R. Voke *et al.* (eds.), Kluwer Academic, Dordrecht, 225-236.

ZANG, T. A., GILBERT, N. & KLEISER, L. 1990 Direct numerical simulation of the transitional zone. Instability and Transition, M. Y. Hussaini & R. G. Voigt (eds.), Springer-Verlag, New York, 283-299.

ZANG, T. A. & KRIST, S. E. 1989 Numerical experiments on stability and transition in plane channel flow. *Theoret. Comput. Fluid Dyn.* **1**, 41-64.

The large eddy simulation group

The eight LES projects in this group were fundamental in nature and aimed at developing improved LES methodology. There were other applied LES projects reported elsewhere in this volume which consisted of evaluating some variants of the LES methodology for industrial use.

Carati and Wray explored the efficacy of the *time* filtered Navier Stokes equations. The equations are closed using a Leonard type expansion and discarding the higher order terms. The equations have a non-linear dependence on the velocity derivative. It was found that lagging this term in time is sufficient for stable numerical solution. The time filtered Navier Stokes calculations with the Leonard closure apparently did not have sufficient dissipation when applied to the problem of decay of isotropic turbulence. Accordingly, additional spatial filtering was performed and two variants of the dynamic eddy viscosity model were included. The space-time filtered equations did produce slightly improved results as compared to the usual spatially filtered equations.

Lagrangian averaging of the flow equations is physically more appealing than the usual spatial or time averaging. This is because averaging is not performed over the turbulent eddies, and thus some of their spatio-temporal features are preserved. Mohseni *et al.* evaluated the so called α equations or the Lagrangian Averaged Navier Stokes equations in the problem of decay of isotropic turbulence. Although there is some ambiguity in the physical interpretation of the variables being solved for, the results from high resolution computations appear to be competitive with those of dynamic LES. However, the results computed with coarse resolution, typical of those expected of robust LES, were not satisfactory. Apparently, the LANS equations are mathematically better understood than the Navier Stokes equations. Hopefully this can be beneficial in analyzing the deficiencies of the model, which in turn could lead to a new predictive tool for turbulent flows.

Recently several investigators have proposed LES methodologies based on advancing two sets of equations, the customary large scale field and the equation for the small scales. For such approaches to be attractive, one should have the benefit of better subgrid scale models and an efficient algorithm for advancing the equations for small scales. Clearly, this approach is more expensive than standard LES with algebraic models, the question is how much more expensive, and whether novel algorithms can be developed that could take advantage of the small scale structures. Hersant, Dubrulle and Wang evaluated the relative importance of several terms in these equations that require closure using turbulent channel data from DNS. They showed that the non-local terms, also known as subgrid scale cross terms, are dominant especially for high Reynolds number data. However, it is not clear that a more accurate modeling of the cross terms is sufficient for actual LES computations, as experience with the mixed models has indicated.

Three papers in this group report on evaluations of wavelet-based turbulence decompositions. The objective is to conduct LES with the least number of degrees of freedom. The wavelet expansions were shown to be particularly efficient in representing turbulent vorticity fields. Moreover, most wavelets tested were able to extract the deterministic or coherent part of the fields, and the remaining subgrid residual fields were nearly Gaussian. Statistics of Gaussian residual fields are, of course, easier to model. The performance of various wavelet decompositions were evaluated using highly resolved DNS fields: Goldstein *et al.* and Farge *et al.* used forced and decaying isotropic turbulence fields at respectable Reynolds numbers, and Schneider *et al.* used forced and unforced

mixing layer fields. In the latter case the flow is dominated by large scale coherent structures, and the wavelet filtering does an impressive job of extracting the coherent part of the fields with about 3% of the wavelet modes. In both flows it is shown that wavelets are more efficient than Fourier modes in capturing the coherent structures embedded in the vorticity fields with the fewest number of modes. It is important to note that all three projects were essentially kinematical studies of the turbulent fields considered, and the efficacy of the wavelet transforms for dynamical LES calculations remains to be determined.

One of the pacing items for LES of high Reynolds number wall-bounded flows is the modeling of turbulence in the vicinity of the wall. In this region turbulence is dominated by small scale vortical structures which require significant computational resources to resolve, and hence for engineering and geophysical applications one resorts to modeling, as opposed to computing, the effect of the inner region on the outer flow LES. At CTR Nicoud had already shown that sub-optimal control theory can be used to deduce wall-boundary conditions that take into account the subgrid scale modeling and numerical errors and produce the correct mean velocity profile. During the Summer Program Baggett *et al.* introduced transpiration velocity boundary conditions as an additional parameter which led to a slight improvement of the results. They also attempted to reduce the streamwise turbulent intensities which were too high in their previous work by including it as a penalty in the cost function. This led to a modest improvement in the turbulent intensity profiles. They also demonstrated that their linear wall model, which was a good fit of their sub-optimal computations, is not very robust when different numerical methods or grid anisotropy are used.

One of the promising applications of LES is in prediction of flow generated noise. Lighthill's acoustic analogy is often used to compute the far-field noise using sources obtained from incompressible computations. Oberai and Wang tested a novel methodology for computation of the far-field noise which uses the surface pressure fluctuations as input to the calculations. They used the data from Wang's LES of a hydrofoil trailing edge. Unfortunately, they discovered that because the formulation is in terms of *apparent* monopoles, it was susceptible to numerical errors. This work is a subject of ongoing investigation at CTR.

Parviz Moin

Time filtering in large eddy simulations

By Daniele Carati† AND Alan A. Wray‡

An explicit time filter is applied to the Navier-Stokes equation prior to a space filter. The time filter is supposed to be smooth, and an exact expansion depending on the time derivatives of the velocity is derived for the associated stress tensor. On the contrary, the effect of the space filter is treated as usual and an eddy viscosity model is introduced in the LES equation. The total stress is thus represented using a new class of mixed models combining time and space derivatives of the LES field.

1. Introduction

Large eddy simulations are usually regarded as numerical experiments in which only the largest structures are computed explicitly while the effects of the small scales are modeled. The separation between large and small scales is traditionally assumed to be obtained by applying a spatial filter to the Navier-Stokes equation. Various types of filters have been introduced, like the Gaussian filter, the top-hat filter, or the Fourier cut-off. However, some of these filters, like the Gaussian and the top-hat filters, do not really reduce the number of degrees of freedom. They simply transform the turbulent field u_i into a new field v_i for which the evolution equation requires as much information to be solved as the Navier-Stokes equation. We will refer to these filters as "smooth filters." In order to reduce the number of degrees of freedom, Fourier cut-off type of filters are required. We will refer to these filters as "projective filters" since they project the turbulent field u_i onto a field $\bar{u}_i$ which can be captured on a coarser grid.

In a recent study, Carati, Winckelmans and Jeanmart (2000) have analyzed the advantages of using a combination of smooth and projective filters for defining the LES field. Their study gives some theoretical support to the use of mixed models (Vreman *et al.*, 1997, Leonard & Winckelmans, 1999, Winckelmans *et al.*, 2000) containing an eddy viscosity term representing the effects of the projective filters and a product of first order derivatives of the velocity characterizing the effects of the smooth filter. In the present study, we will investigate the possibility of replacing the smooth spatial filter by a smooth time filter.

2. Time filtering and the Navier-Stokes τ equation

2.1. *Derivation of the Navier-Stokes τ equation*

Let us consider that the Navier-Stokes equation is filtered using a time averaging:

$$v_i(t) = \int dt'\, G(\frac{t - t'}{\tau})\, u_i(t')\,. \tag{2.1}$$

† Université Libre de Bruxelles, Brussels, Belgium
‡ NASA Ames Research Center, Moffett Field, CA

Here τ is the temporal width of the filter. In this preliminary study, it will be considered as a constant both in space and in time. This guarantees the commutation between the filtering and both the space and time derivatives. For any symmetric filter with a C^∞ Fourier transform (which is true for a very wide class of filters including the top-hat and the Gaussian filters), Carati, Winckelmans and Jeanmart have proved the following equality:

$$\int G(\frac{t - t'}{\tau}) u_i(t')\, u_j(t')\, dt' = \sum_{r,s} c_{rs}\, \tau^{r+s}\, \partial_t^r v_i\, \partial_t^s v_j \, . \tag{2.2}$$

The coefficient c_{rs} is derived from a generating function based on the Fourier transform $\tilde{G}(\omega\tau)$ of $G(\frac{t-t'}{\tau})$. The simplest situation corresponds to the Gaussian filter, in which case the double series reduces to a single one:

$$\int G(\frac{t - t'}{\tau}) u_i(t')\, u_j(t')\, dt' = \sum_{r=0}^{\infty} \frac{\tau^{2r}}{r!}\, \partial_t^r v_i\, \partial_t^r v_j \, . \tag{2.3}$$

The LES equation thus reads:

$$\partial_t v_i + \partial_j \sum_{r=0}^{\infty} \frac{\tau^{2r}}{r!} \frac{\partial^r v_i}{\partial t^r} \frac{\partial^r v_j}{\partial t^r} = -\partial_i p + \nu \nabla^2 v_i \, . \tag{2.4}$$

Keeping all of the terms in the series (2.2) amounts to assuming that the LES is infinitely accurate in time, which is not realistic. Hence, we have to truncate the series. In the case when only the lowest orders in τ are kept, the filtered equation reads:

$$\dot{v}_i = -\partial_i p - \partial_j \left(v_i v_j + \tau^2 \dot{v}_i \dot{v}_j \right) + \nu \nabla^2 v_i \, , \tag{2.5}$$

where we use the same notation p in the equations for both u_i and v_i since it is only used to enforce continuity. Quite remarkably, this lowest order expansion is not restricted to the Gaussian filter and is valid for all symmetric filters with a C^∞ Fourier transform. We will refer to this generic equation as the Navier-Stokes tau (NS-τ) equation. Here $\dot{v}_i$ refers to the Eulerian time derivative: $\dot{v}_i = \partial_t v_i$. The only difference between the NS and the NS-τ equations comes from the term proportional to τ^2 that can be seen as a forcing:

$$f_i \equiv -\partial_j \dot{v}_i \dot{v}_j \, . \tag{2.6}$$

Strictly speaking, f_i has the dimension of a density of force divided by the square of a time since we did not include the factor τ^2 in the definition of f_i. This choice will allow us to keep track explicitly of the power of τ in each term. Of course, this notation hides the fact that the NS-τ equation is implicit in $\dot{v}_i$. Yet, it will be useful in simplifying the discussions on the balance equations.

It is important to remark that the NS-τ equation is not equivalent to the original Navier-Stokes equation since the higher order terms in the series (2.2) have been neglected. However, since the NS-τ is only intended to be used in LES, it is hoped that the higher order terms can be lumped into the subgrid-scale models when projective filters are applied to the NS-τ equation.

2.2. Balance equations

We have not been able to derive a conservation law for the inviscid NS-τ equation. Nevertheless, we have derived two balance equations that can be useful in code checking and in appreciating the effect of the τ term on the dynamics of v_i. First, we consider the

evolution of $\langle v_i v_i / 2 \rangle$:

$$\frac{d}{dt} \frac{1}{2} \langle v_i v_i \rangle = -\tau^2 \langle v_i \partial_j \dot{v}_i \dot{v}_j \rangle = \tau^2 \langle v_i f_i \rangle \,. \tag{2.7}$$

Here, the brackets denote the volume average. Not surprisingly, since the additional τ term acts like a force, its contribution to the "energy" balance takes the usual $\langle v_i f_i \rangle$ form. The equation for the second order time derivative is readily derived from the NS-τ equation,

$$\ddot{v}_i = -\partial_i \dot{p} - \partial_j \left(\dot{v}_i\, v_j + v_i\, \dot{v}_j + \tau^2\, \ddot{v}_i\, \dot{v}_j + \tau^2\, \dot{v}_i\, \ddot{v}_j \right) + \nu \Delta \dot{v}_i \,. \tag{2.8}$$

From this, we can derive another balance equation (always in the limit of zero viscosity):

$$\frac{d}{dt} \frac{1}{2} \langle \dot{v}_i \dot{v}_i \rangle = -\langle \dot{v}_i \partial_j v_i \dot{v}_j \rangle - \tau^2 \langle \dot{v}_i \partial_j \ddot{v}_i \dot{v}_j \rangle \,. \tag{2.9}$$

Using the identity $\langle v_i \partial_j \dot{v}_i \dot{v}_j \rangle + \langle \dot{v}_i \partial_j v_i \dot{v}_j \rangle = \langle \partial_j v_i \dot{v}_i \dot{v}_j \rangle = 0$, we obtain the following balance equation:

$$\frac{d}{dt} \frac{1}{2} \langle v_i v_i + \tau^2 \dot{v}_i \dot{v}_i \rangle = -\tau^4 \langle \dot{v}_i \partial_j \ddot{v}_i \dot{v}_j \rangle \,. \tag{2.10}$$

Finally, we remark that $\langle \dot{v}_i \partial_j \dot{v}_i \dot{v}_j \rangle = 0$. Hence, the time derivative of this quantity also vanishes, which implies, $\langle \dot{v}_i \partial_j \ddot{v}_i \dot{v}_j \rangle = -\langle \ddot{v}_i \partial_j \dot{v}_i \dot{v}_j \rangle = \langle \ddot{v}_i f_i \rangle$ (here we also have used the property $\langle \dot{v}_i \partial_j \dot{v}_i \dot{v}_j \rangle = 0$). The balance equation (2.10) finally reads:

$$\frac{d}{dt} \frac{1}{2} \langle v_i v_i + \tau^2 \dot{v}_i \dot{v}_i \rangle = \tau^4 \langle \ddot{v}_i f_i \rangle \,. \tag{2.11}$$

In the limit of small τ, the right-hand side of this balance will be very small and $\langle v_i v_i + \tau^2 \dot{v}_i \dot{v}_i \rangle$ should be almost conserved. This means that if the "energy" $\langle v_i v_i \rangle$ starts to grow, the average rate of change of v_i, $\langle \dot{v}_i \dot{v}_i \rangle$ should decrease, preventing an exponential growth of the energy. Although these arguments are obviously not fully rigorous, they at least support the idea that the NS-τ equation should not lead to major instabilities in the limit of small τ.

3. Spatial filtering of the NS-τ equation

Since the NS-τ equation implicitly assumes the use of a smooth time filter, its simulation is likely to require the same type of grid as the simulation of the NS equation. It is thus necessary to apply a projective filter on the NS-τ equation. The hope is that the modeling of the subgrid scale tensor will be easier for the NS-τ equation, which should contain less energy in the small scales, than for the original Navier-Stokes equation. The effect of the projective spatial filter, which will be denoted by an overbar, $\overline{v}_i$, should then be taken into account through a model. The total equation for $\overline{v}_i$ would then read:

$$\dot{\overline{v}}_i = -\partial_i \overline{p} - \partial_j \left(\overline{v}_i\, \overline{v}_j + \tau^2\, \dot{\overline{v}}_i\, \dot{\overline{v}}_j \right) + \nu \nabla^2 \overline{v}_i - \partial_j \tau_{ij} \,, \tag{3.1}$$

where $\tau_{ij} = \overline{v_i v_j} - \overline{v}_i \overline{v}_j + \tau^2 \left(\overline{\dot{v}_i \dot{v}_j} - \dot{\overline{v}}_i \dot{\overline{v}}_j \right)$. Let us consider that this projective filter removes all the information related to scales smaller than $\overline{\Delta}$. In this case, τ_{ij} could be modeled through an eddy viscosity term, for which we have used two types of scalings.

3.1. *Kolmogorov scaling for the eddy viscosity*

The Kolmogorov scaling for the eddy viscosity has been introduced in Wong & Lilly, (1994) and Carati *et al.* (1995):

$$\tau_{ij}^M \approx -2\,C_\epsilon\,\overline{\Delta}^{4/3}\,\overline{S}_{ij}\,, \tag{3.2}$$

where $\overline{S}_{ij} = (\partial_i \overline{v}_j + \partial_j \overline{v}_i)/2$. A dynamical approach (Germano, 1992, Germano *et al.*, 1991, Ghosal *et al.*, 1995) has been implemented by considering two levels of discretization. The second level of discretization corresponds to the elimination of scales smaller than $\widehat{\overline{\Delta}}$ and would be obtained either by the application of the operator $\widehat{\cdots}$ to Eq. (3.1):

$$\widehat{\overline{v}}_i = -\partial_i\widehat{\overline{p}} - \partial_j\left(\widehat{\overline{v}_i\,\overline{v}_j} + \tau^2\,\widehat{\dot{\overline{v}}_i\,\dot{\overline{v}}_j}\right) + \nu\nabla^2\widehat{\overline{v}}_i - \partial_j\widehat{\overline{\tau}}_{ij} - \partial_j L_{ij}\,, \tag{3.3}$$

or directly by the application of the operator $\widehat{\overline{\cdots}}$ to Eq. (2.5):

$$\widehat{\overline{v}}_i = -\partial_i\widehat{\overline{p}} - \partial_j\left(\widehat{\overline{v}_i\,\overline{v}_j} + \tau^2\,\widehat{\dot{\overline{v}}_i\,\dot{\overline{v}}_j}\right) + \nu\nabla^2\widehat{\overline{v}}_i - \partial_j T_{ij}\,. \tag{3.4}$$

The comparison of these two versions of the same equation leads to a Germano type identity:

$$\widehat{\overline{\tau}}_{ij} + L_{ij} = T_{ij}\,, \tag{3.5}$$

where

$$T_{ij} = \widehat{\overline{v_i\,v_j}} - \widehat{\overline{v}}_i\,\widehat{\overline{v}}_j + \tau^2\left(\widehat{\overline{\dot{v}_i\,\dot{v}_j}} - \widehat{\dot{\overline{v}}}_i\,\widehat{\dot{\overline{v}}}_j\right)\,, \tag{3.6}$$

$$L_{ij} = \widehat{\overline{v}}_i\,\widehat{\overline{v}}_j - \widehat{\overline{v}_i\,\overline{v}_j} + \tau^2\left(\widehat{\dot{\overline{v}}}_i\,\widehat{\dot{\overline{v}}}_j - \widehat{\dot{\overline{v}}_i\,\dot{\overline{v}}_j}\right)\,. \tag{3.7}$$

Assuming that C_ϵ is independent of the level of discretization, T_{ij} has to be modeled using the same Kolmogorov scaling $T_{ij}^M \approx -2\,C_\epsilon\,\widehat{\overline{\Delta}}^{4/3}\,\widehat{\overline{S}}_{ij}$. If we assume, moreover, that C_ϵ is constant in space, this parameter can be derived by minimizing the volume average of the square of the difference between the right-hand side and the left-hand side of:

$$-2\,C_\epsilon\,\overline{\Delta}^{4/3}\,\widehat{\overline{S}}_{ij} + L_{ij} \approx -2\,C_\epsilon\,\widehat{\overline{\Delta}}^{4/3}\,\widehat{\overline{S}}_{ij}\,, \tag{3.8}$$

which leads to:

$$C_\epsilon \approx \frac{1}{2\left(\widehat{\overline{\Delta}}^{4/3} - \overline{\Delta}^{4/3}\right)}\,\frac{\langle L_{ij}\,\widehat{\overline{S}}_{ij}\rangle}{\langle \widehat{\overline{S}}_{ij}\,\widehat{\overline{S}}_{ij}\rangle}\,. \tag{3.9}$$

3.2. *Smagorinsky scaling for the eddy viscosity*

The Smagorinsky (1963) scaling for the eddy viscosity has also been used

$$\tau_{ij}^M \approx -2\,C\,\overline{\Delta}^2\,\sqrt{2\overline{S}_{kl}\overline{S}_{kl}}\,\overline{S}_{ij}\,. \tag{3.10}$$

In which case, the dynamic prediction for C reads:

$$C \approx \frac{1}{2\left(\widehat{\overline{\Delta}}^2 - \overline{\Delta}^2\right)}\,\frac{\langle L_{ij}\,M_{ij}\rangle}{\langle M_{ij}\,M_{ij}\rangle}\,, \tag{3.11}$$

where

$$M_{ij} = \sqrt{2\widehat{\overline{S}}_{kl}\widehat{\overline{S}}_{kl}}\,\widehat{\overline{S}}_{ij} - \widehat{\sqrt{2\overline{S}_{kl}\overline{S}_{kl}}\,\overline{S}_{ij}}\,. \tag{3.12}$$

4. Solving the spatially filtered NS-τ equation

Solving the NS-τ equation requires solving an implicit quadratic equation for $\dot{v}_i$. Different methods have been considered. First, an iterative scheme has been implemented for solving the unfiltered NS-τ equation:

$$\dot{v}_i^{n+1} = (1 - \lambda)\dot{v}_i^n + \lambda\left(-\partial_i p - \partial_j\left(v_i\,v_j + \tau^2\,\dot{v}_i^n\,\dot{v}_j^n\right) + \nu\nabla^2 v_i\right). \qquad (4.1)$$

Although this method converges, it usually requires many iterations, especially for $\tau/dt \gg 1$. However, when the spatially filtered NS-τ equation is considered, convergence properties appear to be much more favorable. For this reason, we adopted the simplest scheme, namely using the previous time step value of $\dot{v}_i$ in the the right-hand side of the spatially filtered NS-τ equation:

$$\dot{v}_i(t + dt) = -\partial_i p - \partial_j\left(v_i\,v_j + \tau^2\,\dot{v}_i(t)\,\dot{v}_j(t)\right) + \nu\nabla^2 v_i - \partial_j\tau_{ij}. \qquad (4.2)$$

We also report an alternative technique that could be used for solving this implicit equation: by using the equation for the second order time derivative, one still has to solve an implicit relation (for $\ddot{v}_i$), but it is now linear in $\ddot{v}_i$. This motivates the formulation of the NS-τ equation in terms of two variables v_i and $w_i \equiv \dot{v}_i$. The filtered version of these equations is

$$\overline{\dot{v}}_i = \overline{w}_i, \qquad (4.3)$$

$$\overline{\dot{w}}_i = \nu\nabla^2\overline{w}_i - \partial_i\mathcal{P} - \partial_j\left(\overline{w}_i\overline{v}_j + \overline{v}_i\overline{w}_j + \tau^2\overline{\dot{w}}_i\overline{w}_j + \tau^2\overline{w}_i\,\overline{\dot{w}}_j\right) - \partial_j\mathcal{T}_{ij}, \qquad (4.4)$$

where $\mathcal{T}_{ij} = -2\,C_\epsilon\,\overline{\Delta}^{4/3}\mathcal{S}_{ij}$ and $\mathcal{S}_{ij} = (\partial_i\overline{w}_j + \partial_j\overline{w}_i)/2$. The parameter C_ϵ is the same as in (3.9). The only approximation here is that the time derivative of C_ϵ can be neglected. The pressure-type term $\partial_i\mathcal{P}$ is only used for enforcing incompressibility.

This alternative method also has the advantage of carrying all the information required to check the second balance equation derived in Section 2. However, we have not yet implemented this technique.

5. Numerical results

Various tests have been made for different values of τ/dt. It must be noted that this ratio is similar to the ratio between the filter width Δ and the mesh spacing dx in more traditional LES. It is usually considered that $\Delta/dx \geq 1$ is a minimal requirement for numerical accuracy and that much larger values of this ratio will waste computational resources. Hence, values of Δ/dx somewhat larger than 1 are usually considered. The same approach has been adopted here. We have found that $\tau/dt \approx 1$ produces results indistinguishable from $\tau = 0$ and that large values of τ/dt lead to numerical instability when the previous time step value of $\overline{\dot{v}}_i$ is used on the right-hand side of the NS-τ equation. We thus adopted a value, $\tau/dt = 4$, for which the effect of the τ term is observable while the convergence of the NS-τ equation is still ensured.

Tests with both the Kolmogorov and the Smagorinsky scalings for the eddy viscosity have been made. In both cases, the model parameter has been computed dynamically. Tests have been made for decaying turbulence, comparing a 512^3 DNS with a 64^3 LES. The temporal evolution of both the resolved energy and the resolved dissipations are presented in Figs. 1-4. It should be noted that the dynamic Smagorinsky model is known to produce good results for this case though it systematically overpredicts the total en-
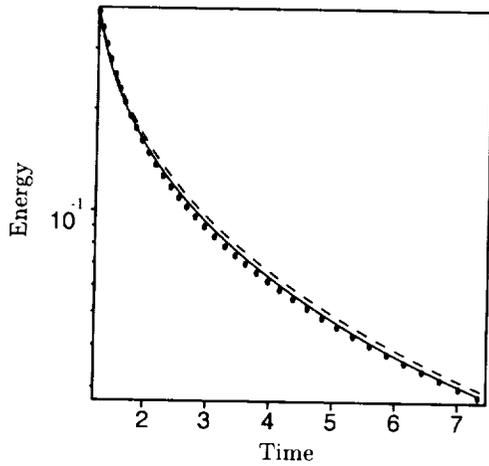
FIGURE 1. Decay of the resolved energy for truncated DNS (•), LES with the dynamic Smagorinsky model (- - - -) and LES with the dynamic Smagorinsky model and the τ term (———).
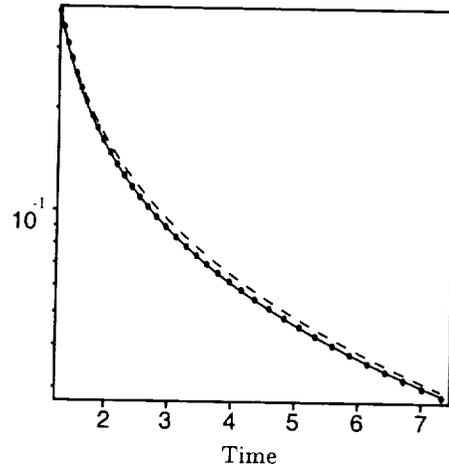
FIGURE 2. Decay of the resolved energy for truncated DNS (•), LES with the dynamic Kolmogorov model (- - - -) and LES with the dynamic Kolmogorov model and the τ term (———).
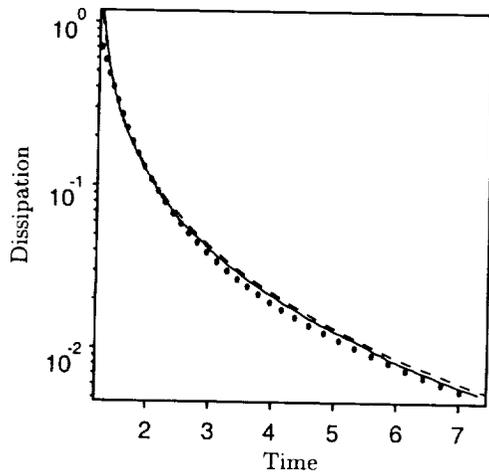
FIGURE 3. Decay of the resolved dissipation for truncated DNS (•), LES with the dynamic Smagorinsky model (- - - -) and LES with the dynamic Smagorinsky model and the τ term (———).
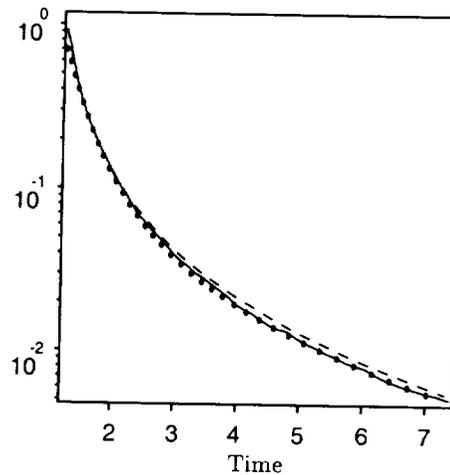
FIGURE 4. Decay of the resolved dissipation for truncated DNS (•), LES with the dynamic Kolmogorov model (- - - -) and LES with the dynamic Kolmogorov model and the τ term (———).

ergy. Also, without the τ term, the Smagorinsky and Kolmogorov scalings are known to produce almost indistinguishable results. The results presented in Figs. 1-4 are interesting in two respects. First, the effect of the time filtering, though quite limited, definitely improves the prediction for both the resolved energy and the resolved dissipation. Remarkably, the improvement is systematically better when the Kolmogorov scaling is used
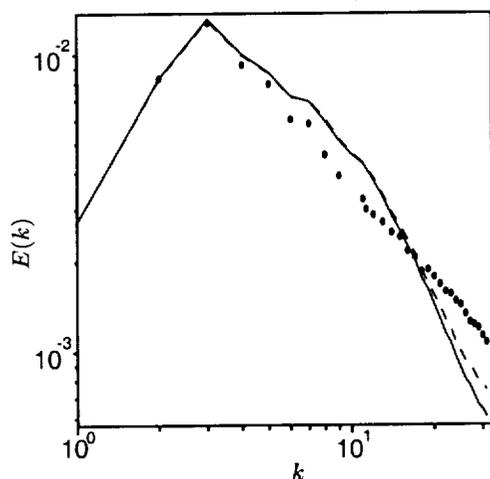
FIGURE 5. Energy spectrum at $t = 2.6$ in the units of Figs. 1-4 for truncated DNS (•), LES with the dynamic Smagorinsky model (− − − −) and LES with the dynamic Smagorinsky model and the τ term (———).
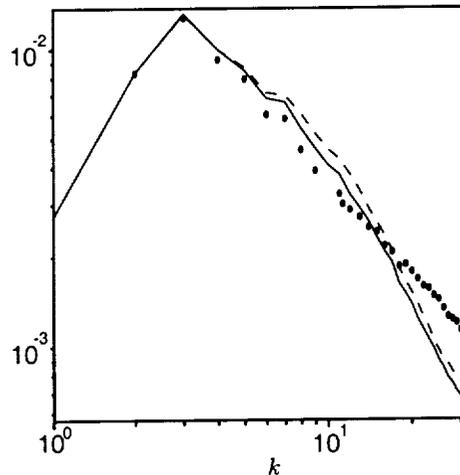
FIGURE 6. Energy spectrum at $t = 2.6$ in the units of Figs. 1-4 for truncated DNS (•), LES with the dynamic Kolmogorov model (− − − −) and LES with the dynamic Kolmogorov model and the τ term (———).

for the eddy viscosity. Actually, when this model is used for the NS-τ equation, the results almost perfectly fit the DNS results.

It should be noted, however, that the energy spectra do not show such a perfect agreement between DNS and LES. In all cases the energy in the low wavenumber range of the LES is overpredicted while the high wavenumber energy is underpredicted. Also, the difference between the Smagorinsky and Kolmogorov scalings is more clearly observed in the spectra. The addition of the τ term does not improve the performance of the dynamic Smagorinsky model in the energy-containing range, but the overprediction of the energy in the low wavenumber range is somewhat improved when the τ term is added to the dynamic Kolmogorov scaling.

6. Conclusion

The combination of a smooth time filter and a projective space filter has been proposed and tested for LES of decaying isotropic turbulence. The effect of the smooth time filtering has been taken into account through an exact expansion which does not require any modeling. Only the first term of this expansion, which is generic for a wide class of smooth filters, has been retained in our approach. The resulting equation, referred to as the Navier-Stokes τ equation, only differs from the original equation by a new forcing term depending on the first order time derivatives of the velocity. As a consequence, the Navier-Stokes τ equation is implicit in this time derivative. Three major points have been learned from this study:

(1) Using the previous time step value of the time derivative in the new term representing the effect of the time filter has been shown to be easily implementable and stable for values of τ/dt of the order of 4.

(2) The effect of the new term is rather limited but does tend to improve the predictions when compared to a pure eddy viscosity model.

(3) The mixed model including the τ term and a dynamic eddy viscosity term is more

sensitive to the type of scaling used for the eddy viscosity than are purely dynamic eddy viscosity models.

REFERENCES

CARATI, D., JANSEN, K. & LUND, T. 1995 On the modeling of the subgrid-scale and filtered-scale stress tensors in LES. Submitted to *J. Fluid Mech.*

CARATI, D., WINCKELMANS, G. S. & JEANMART, H. 2000 On the modelling of the subgrid-scale and filtered-scale stress tensors in large-eddy simulation. Submitted to *J. Fluid Mech.*

GERMANO, M. 1992 Turbulence: the filtering approach. *J. Fluid Mech.* **238**, 325-336.

GERMANO, M., PIOMELLI, U., MOIN, P. & CABOT, W. 1991 A dynamic subgrid-scale eddy-viscosity model. *Phys. Fluids A.* **3**, 1760-1765.

GHOSAL, S., LUND, T., MOIN, P. & AKSELVOLL, K. 1995 A dynamic localization model for large-eddy simulation of turbulent flows. *J. Fluid Mech.* **286**, 229-255.

LEONARD, A. & WINCKELMANS, G. S. 1999 A tensor-diffusivity subgrid model for large-eddy simulation. In *Proceedings of the Isaac Newton Institute Symposium & Third ERCOFTAC Workshop on Direct and Large-Eddy Simulation* (ed. P. Voke, N. Sandham & L. Kleiser), *ERCOFTAC*, **7**. Cambridge, U.K.: Kluwer Academic Pubs. 147-162.

SMAGORINSKY, J. 1963 General circulation experiments with the primitive equations. *Month. Weather Rev.* **91**, 99-164.

VREMAN, B., GEURTS, B. & KUERTEN, H. 1996 Large-eddy simulation of the temporal mixing layer using the mixed Clark model. *Theoret. Comput. Fluid Dyn.* **8**, 309-324.

VREMAN, B., GEURTS, B. & KUERTEN, H. 1997 Large-eddy simulation of the turbulent mixing layer. *J. Fluid Mech.* **339**, 357-390.

WINCKELMANS, G., WRAY, A., VASILYEV, O. & JEANMART, H. 2000 Explicit-filtering large-eddy simulation using the tensor-diffusivity model supplemented by a dynamic Smagorinsky term. Submitted to *Phys. Fluids*.

YEO, W. 1987 A generalized high pass/low pass filtering procedure for deriving and solving turbulent flow equations. *PhD thesis*, Ohio State University.

YEO, W. & BEDFORD, K. 1988 Closure-free turbulence modeling based upon a conjuctive higher order averaging procedure. In *Comp. Meth. in Flow Anal.* (ed. H. Niki & M. Kawahara), Okayama University of Science. 844-851.

WONG, V. & LILLY, D. 1994 A comparison of two subgrid closure methods for turbulent thermal convection. *Phys. Fluids* **6**, 1016-1023.

Numerical simulations of homogeneous turbulence using Lagrangian-averaged Navier-Stokes equations

By Kamran Mohseni†, Steve Shkoller‡, Branko Kosović‡, Jerrold E. Marsden†, Daniele Carati¶, Alan Wray‖ AND Robert Rogallo‖

The Lagrangian-averaged Navier-Stokes (LANS) equations are numerically evaluated as a turbulence closure. They are derived from a novel Lagrangian averaging procedure on the space of all volume-preserving maps and can be viewed as a numerical algorithm which removes the energy content from the small scales (smaller than some *a priori* fixed spatial scale α) using a dispersive rather than dissipative mechanism, thus maintaining the crucial features of the large scale flow. We examine the modeling capabilities of the LANS equations for decaying homogeneous turbulence, ascertain their ability to track the energy spectrum of fully resolved direct numerical simulations (DNS), compare the relative energy decay rates, and compare LANS with well-accepted large eddy simulation (LES) models.

1. Introduction

Over the last thirty years direct numerical simulation of turbulent flows at small to moderate Reynolds numbers has been a valuable asset in understanding turbulence phenomena. In such simulations the motion of eddies ranging in size down to the Kolmogorov dissipation length scale are explicitly accounted for. The main difficulty in the turbulence engineering community is that performing the DNS of typical engineering problems (usually at high Reynolds numbers) is very expensive and, therefore, unlikely to happen in the foreseeable future. This is mainly because the number of degrees of freedom for three-dimensional Navier-Stokes flow grows rapidly with Reynolds number; namely, it is proportional to $Re^{9/4}$. Consequently, increasing the Reynolds number by a factor of 2 will increase the memory size by a factor of 5 and the computational time by a factor of 10.

There are methods for simulating turbulent flows where one does not need to use the brute-force approach in DNS of resolving all scales of motion. A popular alternative is LES, in which only large scales of motion are resolved while the effect of small scales is modeled. The basic idea behind LES is to define a large scale field through a low-pass filtering of the flow variables; therefore, the governing equations for the mean flow quantities (large scales) are obtained by filtering the Navier-Stokes and continuity equations. In inhomogeneous, *e.g.*, wall bounded, flows, the filter width must be a function of position so as to capture the average size of the turbulent eddies that vary in space.

† Division of Engineering and Applied Science, California Institute of Technology
‡ Department of Mathematics, University of California, Davis
¶ Unite de Physique Stat. et des Plasmas, Universite Libre de Bruxelles, Brussels, Belgium
‖ NASA Ames Research Center, Moffett Field, CA

Another method is the Reynolds averaging of the Navier-Stokes equations, or RANS. In this approach the flow field is decomposed into a time- or ensemble- averaged mean flow and a fluctuating perturbation field. Substitution of this field decomposition into the Navier-Stokes equations results in a set of differential equations for the mean flow quantities containing contributions from the time-varying, turbulent motion. This requires the introduction of a turbulence model to describe the effect of these fluctuations on the mean.

The closure problem in LES is a central issue in turbulence modeling. It is believed that turbulence at small scales retains a higher level of homogeneity, which makes it more susceptible to modeling. The rationale is that only the large-scale motions are noticeably affected by the geometry of the domain, while the small scale motions are self-similar or even universal throughout the bulk of the flow. Hence, the main goal of LES modeling is to accurately model the net effect of small scales (subgrid scales) on the dynamics of large scales (grid scales) without solving for the evolution of small scales.

In this study, we consider a new approach introduced in Marsden & Shkoller (2000). Unlike the traditional averaging or filtering approach used for both RANS and LES wherein the Navier-Stokes equations are averaged, the novel Lagrangian approach is based on averaging at the level of the variational principle from which the Navier-Stokes equations are derived. Namely, a new averaged action principle is defined. The least action principle then yields the so-called LAE equations when the flow is deterministic; when the flow is a stochastic process and covariant derivatives are replaced by mean backward-in-time stochastic derivatives, the LANS equations are obtained via the Ito formula of stochastic calculus (just as the Navier-Stokes equations are obtained from the usual non-averaged action principle).

The averaged Euler models were introduced on all of $\mathbb{R}^3$ (the three-dimensional Euclidean space) in Holm, *et al.*(1998), on boundaryless manifolds in Shkoller (1998), on bounded subsets of $\mathbb{R}^3$ with boundary in Marsden, Ratiu, & Shkoller (2000), and on manifolds with boundary in Shkoller (2000a); they were derived to model the mean motion of incompressible flows. A short review of the derivation of the Lagrangian-averaged equations is presented in Section 2.

In this study, we shall concentrate on homogeneous flows, specifically on decaying isotropic turbulence. Such flows are unbounded and thus differ from flow in regions near solid boundaries, but they provide an ideal test case for the adjustment and verification of new turbulence theories and models. An anisotropic version of the LANS equations was recently developed by Marsden & Shkoller (2000). The modeling capabilities of the anisotropic LANS in channel flows will be the topic of a future publication. The anisotropic model provides a natural "dynamic" rescaling that allows the spatial scale for the averaging ($\alpha^2 F$ defined in the next section) to be time dependent as well as orientation dependent.

This report is organized as follows. In the next section a review of the LANS equations is presented. The numerical technique adopted in this study is described in Section 3. Our main numerical results are presented in Section 4 where computations on LAE as well as LANS equations are discussed. Some strategies for calculating the initial Lagrangian-averaged velocity field from the DNS data are discussed. Our findings are summarized in Section 5.

2. Lagrangian-averaged Navier-Stokes equations

In this section, we give a brief summary of the relevant background material on the Lagrangian averaging approach and the resulting LAE and LANS equations. The detailed derivation of the LAE/LANS equations can be found in the article Marsden & Shkoller (2000). Analytic results for classical solutions to these equations can be found in Shkoller (1998), Foias, *et al.*(1999), Shkoller (2000a), Marsden, Ratiu, & Shkoller (2000), Oliver & Shkoller (2000), and Shkoller (2000b).

2.1. *Lagrangian averaging*

The Reynolds decomposition is an Eulerian decomposition of the spatial velocity field of the fluid. The Lagrangian averaging procedure takes an entirely different starting point by decomposing instead the Lagrangian flow of the velocity field. Let $\eta(t,x)$ be the volume-preserving Lagrangian flow of the random variable $u(t,x)$ so that η satisfies the ordinary differential equation $\partial_t \eta(t,x) = u(t,\eta(t,x))$ (or its stochastic counterpart) with initial condition $\eta(0,x) = x$. We choose a stochastic process $\xi^\alpha(t,x)$, parameterized by $\alpha > 0$, such that $\xi^{\alpha=0}(t,x) = x$ for all time t, and for all t and $\alpha > 0$, the map $\xi^\alpha(t,\cdot) : \Omega \to \Omega$ is a volume-preserving near-identity diffeomorphism. We denote the stochastic derivative of ξ^α with respect to α at $\alpha = 0$ by ξ'; if the map $t \mapsto \xi^\alpha(t,\cdot)$ were smooth, the vector ξ' would be given simply by $\xi'(t,x) = (d/d\alpha)|_{\alpha=0}\xi^\alpha(t,x)$. The stochastic process ξ' is an element of a probability space $\mathcal{P}$ with measure dP, and by construction it has expected value zero, $\overline{\xi'} = 0$, i.e., ξ' has mean zero.

We then define a macroscopic flow field $\eta^\alpha(t,x)$ by

$$\eta^\alpha(t,x) = (\xi^\alpha)^{-1}(t,\eta(t,x))), \tag{2.1}$$

or in shorthand notation

$$\eta^\alpha_t = (\xi^\alpha_t)^{-1} \circ \eta_t.$$

η^α is the *fuzzy* particle placement field which is only accurate down to the spatial scale α; namely, a particle labeled x in the fluid container at $t = 0$ is mapped by $\eta^\alpha(t,\cdot)$ to its new position at time t, and this new position $\eta^\alpha(t,x)$ can be determined only to within a distance α of the exact position $\eta(t,x)$. The decomposition (2.1) is a nonlinear Lagrangian decomposition of maps on the group of volume-preserving diffeomorphisms. There is no vector-space structure on this group, so it is not appropriate to suppose an additive decomposition as in the Reynolds decomposition.

We next define the corresponding spatial velocity fields u^α and w^α associated, respectively, with the flows η^α and ξ^α. In particular, we define these velocities by

$$\partial_t \xi^\alpha(t,x) = w^\alpha(t,\xi^\alpha(t,x)), \quad \partial_t \eta^\alpha(t,x) = u^\alpha(t,\eta^\alpha(t,x)).$$

It is now possible, by differentiating (2.1) with respect to time t, to obtain the relationship between u, u^α, and w^α. We find that

$$u^\alpha(t,x) = D(\xi^\alpha)^{-1}(x) \cdot [u(t,\xi^\alpha(t,x) - w^\alpha(t,\xi^\alpha(t,x))]. \tag{2.2}$$

The notation $D(\xi^\alpha)^{-1}(x)$ means the matrix of partial derivatives of the inverse map $(\xi^\alpha)^{-1}$ evaluated at the point x in Ω.

Now, the inviscid portion of the dynamics of the Navier-Stokes equations is governed by a simple variational principle, or action, which is just the time integral of the kinetic

energy of divergence-free vector fields:

$$S = \frac{1}{2} \int_{t_0}^{t_1} \int_{\Omega} |u(t,x)|^2 dxdt.$$

The Euler-Lagrange equations for $S(u)$ are the incompressible Euler equations, and if one allows the flow of the Euler solution to undergo a random walk, then the Navier-Stokes equations immediately arise (see Chorin (1973) and Peskin (1985)).

In order to obtain LANS equations, we shall define an averaged variational principle using our macroscopic or fuzzy Lagrangian description of the fluid. As such, we define the averaged action by

$$S^\alpha = \frac{1}{2} \int_{t_0}^{t_1} \int_{\Omega} \int_{\mathcal{P}} |u^\alpha(t,x)| dP dx dt, \tag{2.3}$$

where we have averaged over all possible perturbations or Lagrangian fluctuations of the exact flow.

At this stage, we asymptotically expand $u^\alpha(t,x)$ about $\alpha = 0$, and make the Taylor hypothesis that the Lagrangian fluctuation is frozen into the mean flow. We obtain (after a convenient rescaling) that

$$u^\alpha(t,x) = u(t,x) + 2\alpha \operatorname{Def} u(t,x) \cdot \xi'(t,x) + O(\alpha^3), \tag{2.4}$$

where

$$\operatorname{Def} \mathbf{u} = \frac{1}{2} \left[\nabla \mathbf{u} + (\nabla \mathbf{u})^T \right].$$

Notice that $u(t,x)$ is the mean of u^α since $\overline{u^\alpha} = u$, and that to $O(\alpha^3)$, $\operatorname{Def} u \cdot \xi'$ is the Eulerian fluctuation. Defining the Lagrangian covariance or fluctuation tensor by

$$F(t,x) = \int_{\mathcal{P}} \xi' \otimes \xi' dP, \tag{2.5}$$

substituting the expansion (2.4) into (2.3), and truncating at $O(\alpha^3)$, we obtain the first-order averaged action principle S_1^α as a function of the divergence-free mean u and the covariance F:

$$S_1^\alpha(u,F) = \frac{1}{2} \int_{t_0}^{t_1} \int_{\Omega} \left[u \cdot u + 2\alpha^2 F : (\operatorname{Def} u \cdot \operatorname{Def} u) \right] dxdt. \tag{2.6}$$

2.2. The LANS and LAE equations

We define the fourth-rank symmetric tensor C by complete symmetrization of $F \otimes \operatorname{Id}$, so that in coordinates

$$C^{ijkl} = \frac{1}{4} \left(F^{lj}\delta^{ik} + F^{kj}\delta^{il} + F^{li}\delta^{jk} + F^{ki}\delta^{jl} \right);$$

we then define the linear operator $\mathcal{C}$, mapping divergence-free vector fields into vector fields, by $\mathcal{C}u = \operatorname{Div}(C : \nabla u)$. By letting the Lagrangian flow of the mean velocity undergo Brownian motions and computing the first variation of $S_1^\alpha(u,F)$, we obtain the anisotropic LANS equations for the mean velocity as

$$\partial_t u + (u \cdot \nabla)u + \mathcal{U}^\alpha(u,F) = -(1 - \alpha^2\mathcal{C})^{-1} \operatorname{grad} p + \nu\triangle u, \tag{2.7}$$

where

$$\mathcal{U}^{\alpha}(u, F) := \alpha^2 (1 - \alpha^2 C)^{-1} \left\{ -\frac{1}{2} \operatorname{Div} [\operatorname{Def} u \cdot (\pounds_u F) + (\pounds_u F) \cdot \operatorname{Def} u] \right.$$
$$- \operatorname{Div} C : (\nabla u \cdot \nabla u) - C : \nabla (\nabla u \cdot \nabla u)$$
$$- C : \operatorname{Div}(\nabla u \otimes \nabla u) + (\operatorname{Div}[\nabla C : \nabla u]) \cdot u$$
$$\left. -(\nabla u)^T \cdot Cu + 2F : \nabla (\operatorname{Def} u^2) - 4 \operatorname{Div}[F \cdot \operatorname{Def} u^2] \right\}. \quad (2.8)$$

The notation $\pounds_u F$ means the Lie derivative of the tensor F in the direction u, and $\cdot$, $:$, etc., means contraction of indices as many times as dots appear. The term $\mathcal{U}^{\alpha}(u, F)$ is analogous to the term $\operatorname{Div} \overline{u' \otimes u'}$ in the RANS equation, which is the divergence of the Reynolds stress. As we noted, the LANS formulation provides a natural turbulent-closure.

In addition to the evolution equation for the mean given by (2.7), the calculus of variations also provides the evolution equation for the covariance tensor as

$$\partial_t F + \pounds_u F = 0. \quad (2.9)$$

These two coupled systems of evolution equations are supplemented by the incompressibility constraint $\operatorname{div} u = 0$, initial conditions $u(0, x) = u_0(x)$, and boundary conditions, for example no slip, $u = 0$ on $\partial \Omega$.

After solving the LANS equations for the mean velocity u, one can then solve for the Eulerian fluctuations $2\alpha \operatorname{Def} u \cdot \xi'$ and "correct" the macroscopic velocity field to $O(\alpha^3)$. This does not require the solution of the Navier-Stokes equations; instead, simple linear advection problems for ξ' need to be solved. Letting the vector ξ' have Cartesian components (ξ_1, ξ_2, ξ_3), these equations are given in component form by

$$\partial_t \xi_i + \xi_{i,j} u^j + u^j{}_{,i} \xi_j = 0. \quad (2.10)$$

Equation (2.10) is obtained from the Taylor hypothesis (Marsden & Shkoller (2000)) and plays the role of the "corrector" in the theory of homogenization.

Equations (2.7) and (2.9) are *anisotropic*, allowing for fluctuation effects to depend on position and direction. There is a corresponding *isotropic* theory in which it is assumed that the covariance tensor F is everywhere equal to the identity Id. In this case, the first-order averaged action principle $S^{\alpha}_{1,\mathrm{iso}}$ is only a function of the mean velocity u and is given by

$$S^{\alpha}_{1,\mathrm{iso}}(u) = \frac{1}{2} \int_{t_0}^{t_1} \int_{\Omega} \left[u \cdot u + 2\alpha^2 \operatorname{Def} u : \operatorname{Def} u \right] dx \, dt. \quad (2.11)$$

Applying the calculus of variations machinery to (2.11) yields the isotropic LANS equation

$$\partial_t u + (u \cdot \nabla)u + \mathcal{U}^{\alpha,\mathrm{iso}}(u) = -(1 - \alpha^2 \Delta)^{-1} \operatorname{grad} p + \nu \Delta u,$$
$$\operatorname{div} u = 0, \quad u(0, x) = u_0(x), \quad (2.12)$$
$$u = 0 \text{ on } \partial \Omega,$$

where

$$\mathcal{U}^{\alpha,\mathrm{iso}}(u) = \alpha^2 (1 - \alpha^2 \Delta)^{-1} \operatorname{Div} \left[\nabla u \cdot \nabla u^T + \nabla u \cdot \nabla u - \nabla u^T \cdot \nabla u \right]. \quad (2.13)$$

The most obvious scenario in which one might assume the covariance is isotropic is in decaying turbulence inside a periodic box. In this case, the isotropic LANS equations are

given by

$$\partial_t u + (u \cdot \nabla)u + \text{Div}\,\mathcal{S}^\alpha(u) = -\operatorname{grad} p + \nu \Delta u,$$
$$\operatorname{div} u = 0, \tag{2.14}$$

with periodic boundary conditions imposed. $\mathcal{S}^\alpha(u)$ is the *Lagrangian subgrid stress tensor* defined by

$$\mathcal{S}^\alpha(u) = \alpha^2 (1 - \alpha^2 \Delta)^{-1} \left[\nabla u \cdot \nabla u^T + \nabla u \cdot \nabla u - \nabla u^T \cdot \nabla u \right].$$

Appropriate interpretation of the Lagrangian averaging process of the DNS data is crucial in any successful comparison of the LANS computations with the DNS results. A few different techniques for initializing LANS equations were considered in this study. Apart from the truncation of the DNS data to the resolution of LANS simulations, we have initialized LANS simulations by Helmholtz filtering or spatial averaging of the DNS data. For the numerical simulations on the experiment by Comte-Bellot & Corrsin (1966) and (1971) we found that using the filter based on the Helmholtz operator or spatial averaging (top hat filter) resulted in a severe reduction of the initial resolved kinetic energy to a fraction of that of a field truncated in Fourier space (i.e., using a Fourier cut-off filter). We point out that such a reduction is independent of the model used and diminishes the value of the tests. Consequently, all of the LANS results reported in this study are initialized by sharply truncating the DNS data to the resolution of the LANS calculation.

3. Numerical method

In this study we focus on the numerical solution of homogeneous turbulence. Our computational domain is a periodic cubic box of side 2π. In a numerical simulation of decaying turbulence, the size of the computational domain puts an upper bound on the growth of the large scales in the flow. This is consistent with the observation in most experiments that the largest scales of motion are of the same order as the size of the experimental apparatus. Given the number of grid points and the size of the computational domain, the smallest resolved length scale or, equivalently, the largest wave number, k_{max}, is prescribed. In a three-dimensional turbulent flow, the kinetic energy cascades in time to smaller, more dissipative scales. The scale at which viscous dissipation becomes dominant and which represents the smallest scales of turbulence is characterized by the Kolmogorov length scale η. In a fully resolved DNS, the condition $k_{max}\eta \gtrsim 1$ is necessary for the small scales to be adequately represented. Consequently, k_{max} limits the highest achievable Reynolds number in a DNS for a given computational box.

The full range of scales in a turbulent flow for even a modest Reynolds number spans many orders of magnitude, and it is not generally feasible to capture them all in a numerical simulation. On the other hand, in turbulence modeling, empirical or theoretical models are used to account for the net effect of small scales on large energy- containing scales. In the next section, the numerical simulations of decaying homogeneous turbulence based on the full DNS, LES modeling, and LANS modeling are presented.

The core of the numerical method used in this study is based on a standard parallel pseudospectral scheme with periodic boundary conditions similar to the one described in Rogallo (1981). The spatial derivatives are calculated in the Fourier domain while the nonlinear convective terms are computed in physical space. The flow fields are advanced
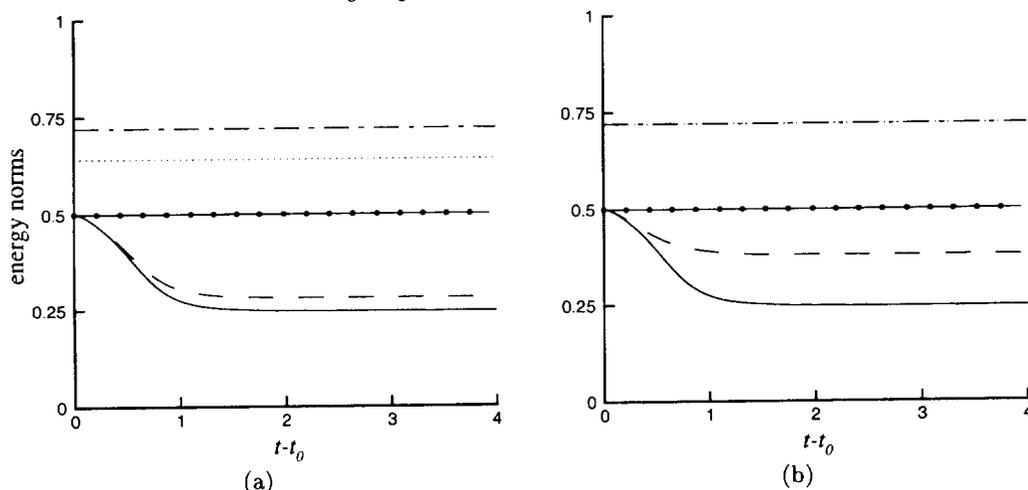
FIGURE 1. LAE simulation $t - t_0 = 1.8$, Euler (——•——). (a) $N_\alpha^3 = 64^3$; for $\alpha = \frac{1}{16}$, $E_{L_2}(\mathbf{u})$ (————), $E_{H^1}(\mathbf{u})$ (——·——); for $\alpha = \frac{1}{20}$, $E_{L_2}(\mathbf{u})$ (— — — —), $E_{H^1}(\mathbf{u})$ (········); (b) $\alpha = \frac{1}{16}$; with $N_\alpha^3 = 48^3$; $E_{L_2}(\mathbf{u})$ (————), $E_{H^1}(\mathbf{u})$ (——·——); and with 64^3, $E_{L_2}(\mathbf{u})$ (— — — —), $E_{H^1}(\mathbf{u})$ (········). Note that in case (b) the curves for $E_{H^1}(\mathbf{u})$ for the different resolutions coincides.

in time in physical space using a fourth order Runge-Kutta scheme. The time step was chosen appropriately to ensure numerical stability. To eliminate the aliasing errors in this procedure, the two thirds rule is used so that the upper one third of wave modes is discarded at each stage of the fourth order Runge-Kutta scheme.

In addition to LANS we also performed simulations using a dynamic SGS model (Germano, *et al.*(1994). Germano, *et al.*(1994) suggested a dynamic procedure in which the model coefficient of an arbitrary functional relationship, selected to represent the subgrid scale stress tensor, can be evaluated as part of the simulation. This procedure, applied to the Smagorinsky eddy-viscosity model, has proven quite versatile and is used here as a representative of a class of LES models. The filter aspect ratio in the dynamic model is a free parameter, and the final result depends on the value of this parameter, particularly in severe test cases such as the one considered here. In order to avoid introducing any further arbitrary parameters, no averaging operation is performed on the model coefficients over the computational domain. However, the LES computations were repeated for various filter aspect ratios, and the parameter that matched the best with the turbulence decay of the DNS data was used in the computations of the next section.

4. Results

In this section, we present results of our numerical simulations of the LANS equations. We first demonstrate the dispersive characteristic of the energy cascade in the LAE equations.

4.1. *Lagrangian-Averaged Euler equations*

In section 2, we argued that the LAE equations redistribute the energy content among the small scales through a nonlinear dispersive mechanism. This is illustrated in Fig. 1 where various energy norms in the LAE simulations (*i.e.*, no viscous dissipation) are contrasted against the energy norm in the Euler equations. The initial condition is the

same as the one described in the next section for the viscous computations. As expected, the H^1(-equivalent) norm of the energy for the LAE equations, given by

$$E_{H^1}(\mathbf{u}) = \frac{1}{2} \int \left[\mathbf{u} \cdot \mathbf{u} + 2\alpha^2 \operatorname{Def} \mathbf{u} \cdot \operatorname{Def} \mathbf{u} \right] d^3x, \qquad (4.1)$$

is a conserved quantity. In the case of periodic boundary conditions, this energy function may also be expressed as $E_{H^1} = \frac{1}{2} \int \mathbf{u} \cdot (1 - \alpha^2 \Delta)\mathbf{u}$. The value of E_{H^1} depends on the initial condition as well as the parameter α. For given initial data and fixed α, on the other hand, the L_2 energy function

$$E_{L_2}(\mathbf{u}) = \frac{1}{2} \int \mathbf{u} \cdot \mathbf{u} \, d^3x \qquad (4.2)$$

drops significantly from its normalized initial value of 0.5. It is precisely the quantity $E_{L_2}(\mathbf{u})$ that we shall compare with the numerical simulation of Navier-Stokes equations. Again, the absolute drop in $E_{L_2}(\mathbf{u})$ depends on the initial velocity as well as the value of α. Since $E_{H^1}(\mathbf{u})$ is constant along solutions of the LAE equations, any decay in $E_{L_2}(\mathbf{u})$ is followed by an increase in $\alpha^2 E_{L_2}(\nabla u)$. After some initial transient all of the energy norms saturate. We remark that, when $\alpha = 0$, the H^1 energy norm (4.1) reduces to the usual L^2 kinetic energy.

In a viscous computation the dispersive decay in $E_{L_2}(\mathbf{u})$ is augmented by the viscous decay in $E_{L_2}(\mathbf{u})$ as the viscous effects remove energy from small scales. Viscous computations are performed in the next section to quantify the nature of the viscous decay.

In Fig. 1(b) the effect of grid resolution on LAE simulations is shown. While the value of $E_{H^1}(\mathbf{u})$ is the same in both 48^3 and 64^3 runs, the L_2 norm of $\mathbf{u}$ and $\nabla \mathbf{u}$ are significantly different after an initial transient. Therefore, the dispersive decay in $E_{L_2}(\mathbf{u})$ strongly depends on the size of the computational domain. However, it is expected that if the smallest resolved scale in the LAE simulations is located in a subinertial range with low energy compared to the peak of the energy spectra, any variation of $E_{L_2}(\mathbf{u})$ with the size of the computational domain would be small. This issue requires further investigation by computations based on an initial field with a large inertial range.

One should note that the conservation of the H^1 norm is slightly sensitive to the accuracy of the implemented numerical scheme. The fourth order Runge-Kutta has proved to be adequate in our case. However, numerical experimentation has shown that lower-order time integration schemes might result in a slight decay in the H^1 norm. All of the reported computations in this study are performed using the same fourth order Runge-Kutta scheme.

4.2. *Decaying turbulence*

The most widely used published data on decaying grid turbulence are due to Comte-Bellot & Corrsin (1966) and (1971), which we will hereafter refer to as CBC. Their data is well documented and has been used widely in the development of DNS, LES, and other turbulence models.

The DNS computations in this study were carried out on the Hewlett-Packard Exemplar V2500 at Caltech. The initial field is taken from Wray (1998). Wray provides a filtered velocity field in physical space, derived from 512^3 data by a sharp truncation in Fourier space to 128^3. All of the computations performed in this study were started with this data. The initial Taylor Reynolds number is $\mathrm{Re}_\lambda = 72$.

The evolution of the energy spectrum as predicted by DNS using 128^3 points is il-
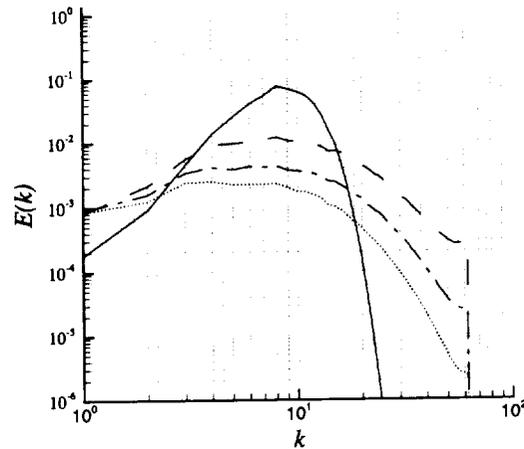
FIGURE 2. Spectrum of the energy, $Re_\lambda = 72$, $N_{DNS}^3 = 128^3$, $t = 0$ (———); $t = 1$ (– – – –);
$t = 2$ (—·—); $t = 3$ (········).

lustrated in Fig. 2. The energy of fully developed isotropic turbulence decays in time while the scales of motion grow; the resulting Re_λ decreases with time. Consequently, a well resolved, fully developed field will remain well resolved as it decays. On the other hand, the integral scales grow in time and will eventually become comparable to the size of the computational box. Since the computational box contains only a small sample of the largest representable eddies, eventually the computation will suffer from a lack of sample in the energy-containing scales. The rather wide initial energy spectrum with a peak around the eighth Fourier mode provides a harsh test case for any turbulence model at such a resolution. As is the case with most subgrid models, the LANS model is expected to perform better when the energy containing range is well resolved. In other words, the model is expected to perform better when the spectral energy peaks at a lower wave number. The simulation of CBC experiments at $Re_\lambda = 72$ used in this study barely satisfies this criterion and provide a severe test case of the LANS turbulence modeling capability. However, this does not imply that the developed inertial range is required for the model to reach optimal performance.

The evolution of total kinetic energy (TKE) of the DNS data is contrasted against various dynamic LES and LANS simulations in Fig. 3, for two resolutions: 48^3 and 64^3. TKE's for DNS data, sharply filtered to the resolution of the LES and LANS computations, are also presented. The best match between the DNS data and the dynamic LES results is achieved for a filter aspect ratio of 2 and 4 in the 48^3 and 64^3 calculations, respectively. In the 64^3 computation both LES and LANS satisfactorily predict the decay rate. However, at the lower resolution of 48^3 both models underestimate the decay rate, with the LANS model being more under-dissipative. It is clear that at such a low resolution the energy-containing part of the spectrum is barely resolved. This is demonstrated in Figs. 4-6 where the evolution of the energy spectrum of various computations are presented. The pile-up of energy at higher wave numbers in the 48^3 runs indicates insufficient dissipation of energy due to inadequate resolution. This is more pronounced in the LANS computations where the model is heavily dependent on the nonlinear dispersive mechanism of the Lagrangian-averaged equations as opposed to the dissipative
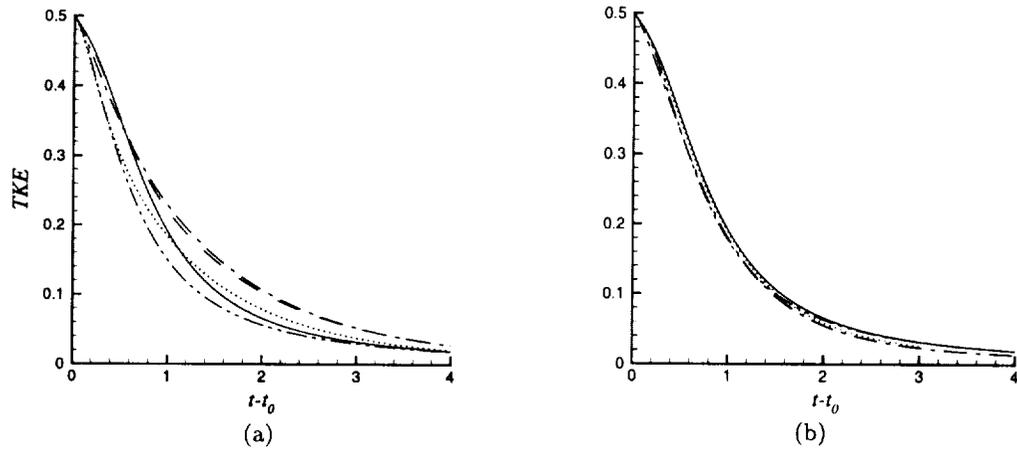
FIGURE 3. Decay of kinetic energy, full DNS 128^3 (———); (a) $N_\alpha^3 = 48^3$, LANS with $\alpha = \frac{1}{16}$ (—·—); LANS with $\alpha = \frac{1}{8}$ (- - - -); dynamic LES with a filter ratio 2 (········); DNS sharply filtered to 48^3 (— —); (b) $N_\alpha^3 = 64^3$, LANS with $\alpha = \frac{1}{16}$ (- - - -); LANS with $\alpha = \frac{1}{20}$ (—·—); dynamic LES with a filter ratio 4 (········); DNS sharply filtered to 64^3 (—·· —).
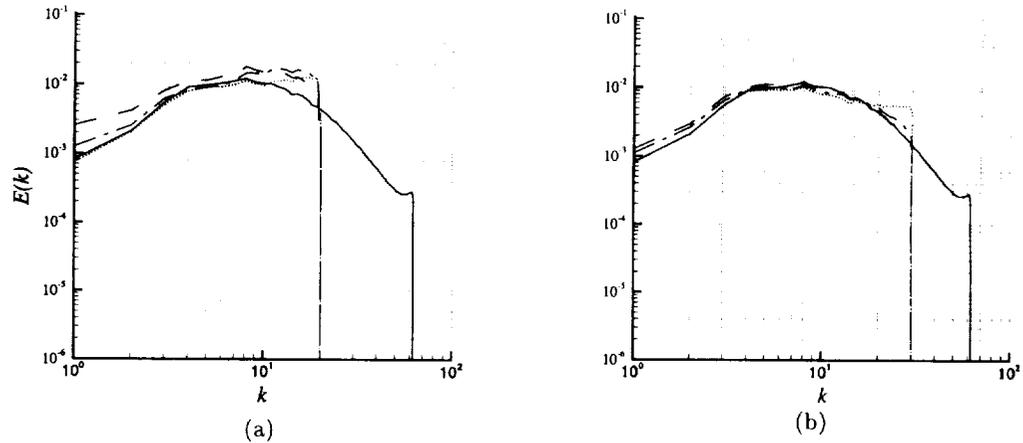
FIGURE 4. The energy spectra at $t = 1$, full DNS 128^3 (———); (a) $N_\alpha^3 = 48^3$, LANS with $\alpha = \frac{1}{16}$ (—·—); LANS with $\alpha = \frac{1}{8}$ (dash); dynamic LES with filter ratio 2 (········); (b) $N_\alpha^3 = 64^3$, LANS with $\alpha = \frac{1}{16}$ (- - - -); LANS with $\alpha = \frac{1}{20}$ (— —); dynamic LES with filter ratio 4 (········).

model in LES. For 64^3 calculations the energy spectrum is predicted reasonably well by both LANS and dynamic LES. LANS computations show better agreement for higher wave numbers. At later times a dip at the peak of the energy spectrum is observed, which is more pronounced in LANS simulations. This might be due to the introduction of the dispersive effects in the LANS equations at scales of the order of α. However, due to the broad-band nature of the energy spectrum with the maximum of the spectrum at a relatively high wavenumber, we could not move α far from the energy-containing range. It is expected that in a higher Reynolds number flow where there is an extended
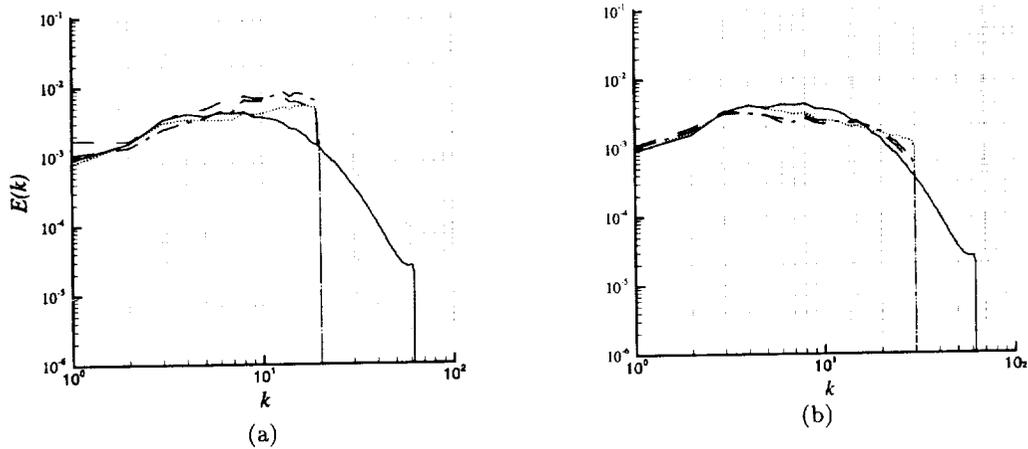
FIGURE 5. The energy spectra at $t = 2$. See Fig. 4 for caption.
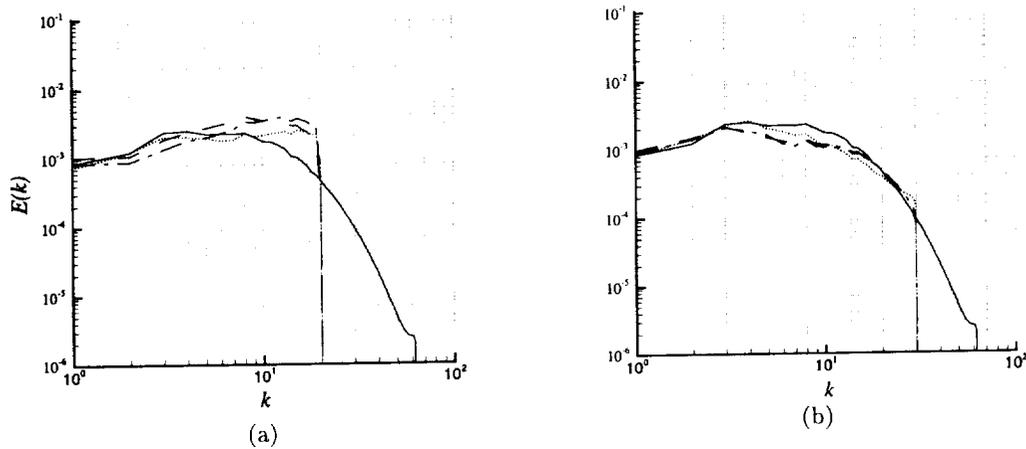
FIGURE 6. The energy spectra at $t = 3$. See Fig. 4 for caption.

inertial range and, therefore, a larger gap between energy-containing scales and α scale, this effect will be diminished. Existence of such a clearance between α scales and the location of the energy peak requires resolving at least a portion of the subinertial range. LES methods will, of course, also work better in such a situation.

5. Conclusions and future directions

We studied the Lagrangian-averaged Navier-Stokes (LANS) equations through numerical simulations of isotropic decaying turbulence. Our conclusions here are made based on the numerical simulations of CBC experiments. The initial energy spectrum at $Re_\lambda = 72$ is broad and the peak of the energy spectrum is around the eighth Fourier mode. Correct prediction of the TKE decay rate and the corresponding spectra for such a broad-band initial spectrum represents a difficult test case for any turbulence model.

We have demonstrated the dispersive (not dissipative) nature of the energy decay in

the Lagrangian-averaged Euler (LAE) equations. This is the essence of the Lagrangian averaging method, where the energy is removed from the small scales while maintaining the crucial features of the large scale flow using dispersive rather than dissipative mechanisms. The final $E_{L_2}(\mathbf{u})$ level depends on the spectrum of the initial field, the size of the computational box, and α.

We found that, if a minimum resolution requirement (for the CBC experiments, half of the DNS resolution) is satisfied, then the LANS equations provide a satisfactory turbulence closure comparable with dynamic LES. The only free parameter in LANS simulations is a length scale α which is representative of the spatial scale of the Lagrangian averaging. However, for lower resolutions both LANS and dynamic LES show a pile-up of energy at higher wave numbers. This indicates insufficient dissipation of energy due to the lack of resolution. We should point out that, in LANS simulations of forced homogeneous turbulence, Chen, *et al.*(1999) observed a milder resolution requirement. The harsher resolution requirement in our case might be due to the broad-band nature of the initial field for the CBC experiment.

Any conclusion on the performance of the LANS equations depends on the way that the DNS data is compared with the results of LANS calculations. First of all, appropriate interpretation of the Lagrangian averaging process of the DNS data is crucial for obtaining the initial velocity field for LANS computations. The same issue arises in comparing LANS results with DNS data at later times. We considered a few different approaches. Apart from truncation of the DNS data to the resolution of LANS simulations, we have initialized LANS simulations by Helmholtz filtering or spatial averaging of the DNS data. For the CBC experiment we found that using the filter based on the Helmholtz operator or spatial averaging (top hat filter) resulted in a severe reduction of the initial resolved kinetic energy to a fraction of that of a field truncated in Fourier space (i.e., using a Fourier cut-off filter). We point out that such a reduction is independent of the model used and diminishes the value of the tests. We therefore use a sharply truncated DNS data as the initial velocity field (u) in LANS simulations.

Recently, Chen, *et al.*(1999) simulated a forced homogeneous turbulent flow and reported favorable results using LANS equations. Here, we demonstrated the modeling capabilities of LANS equations in decaying turbulent flows. Apart from these satisfactory results, LANS equations have many attractive theoretical features that make them a promising candidate for more complicated problems. In this process the next natural step is to test LANS models in anisotropic flows. Numerical simulation of channel flow based on the anisotropic LANS equations is the topic of our future research.

REFERENCES

Chen, S. Y., Foias, C., Holm, D. D., Olson, E., Titi, E. S. & Wynne, S. 1999 The Camassa-Holm equations and turbulence. *Physica D.* **133**, 49-65.

Chorin, A. 1973 Numerical study of slightly viscous flow. *J. Fluid Mech.* **57**, 785-796.

Comte-Bellot, G. & Corrsin, S. 1966 The use of a contraction to improve the isotropy of grid-generated turbulence. *J. Fluid Mech.* **25**, 657-682.

Comte-Bellot, G. & Corrsin, S. 1971 Simple Eulerian time correlation of full and narrow-band velocity signals in grid-generated isotropic turbulence. *J. Fluid Mech.* **48**, 273-337.

Foias, C., Holm, D. D., & Titi, E. S. 1999, manuscript.

Germano, M., Piomelli, U. , Moin, P. & Cabot, W. H. 1994 A dynamic subgrid scale eddy viscosity model. *Phys. Fluids A.* **3**, 1760-1765.

HOLM, D. D., MARSDEN, J. E., & RATIU, T. S. 1998 Euler-Poincaré and semidirect products with applications to continuum theories. *Adv. in Math.* **137**, 1-81.

MARSDEN, J. E., RATIU, T., & SHKOLLER, S. 2000 The geometry and analysis of the averaged Euler equations and a new diffeomorphism group. *Geom. Funct. Anal.* **10**.

MARSDEN, J. E. & SHKOLLER, S. 2000 The anisotropic averaged Euler equations. *Archives for Rational Mechanics and Analysis*, submitted.

OLIVER, M. & SHKOLLER, S. 2000 The vortex blob method as a second-grade non-Newtonian fluid. *Commun. PDE*, to appear.

PESKIN, C. S. 1985 A random-walk interpretation of the incompressible Navier-Stokes equations. *Comm. Pure Appl. Math.* **38**, 845-852.

ROGALLO, R. S. 1981 Numerical experiments in homogeneous turbulence. *NASA Tech. Memo 81315.*

SHKOLLER, S. 1998 Geometry and curvature of diffeomorphism groups with H^1 metric and mean hydrodynamics. *J. Funct. Anal.* **160**, 337-365.

SHKOLLER, S. 2000 On averaged incompressible hydrodynamics. *J. Diff. Geom.*, submitted.

SHKOLLER, S. 2000 Smooth global Lagrangian flow for the 2D Euler and second-grade fluid equations. *Appl. Math. Lett.* **14**.

WRAY, A. A. 1998 In A selection of test cases for the validation of large-eddy simulations of turbulent flows. *AGARD Advisory Report 345.*

Non-locality of scale interactions in turbulent shear flows

By F. Hersant†, B. Dubrulle† AND M. Wang

The scale interactions in turbulent shear flow are evaluated using a channel flow DNS database at $Re_\tau = 590$. The velocity field is filtered using a sharp cut-off filter in the Fourier space, and the relative magnitudes of the advective terms in the small scale equations, derived from Navier-Stokes equations, are computed as a function of wavenumber. We show that the interactions at small scales are non-local in the direction of the mean flow, dominated by the advection of small scales by large scale vortices. This non-locality of interactions suggests that the subgrid-scale model of Dubrulle and Nazarenko (1997) for 2D turbulence is likely to be applicable to turbulent shear flows as well.

1. Introduction

Direct numerical simulation (DNS) based on the Navier-Stokes equations is only possible for relatively low Reynolds numbers. Therefore, filtering is often needed to capture the large-scale structure of the flow, hoping that the effect of small scale fluctuations can be more easily modeled. This is the basis for the classical large eddy simulations (LES) in which the subgrid scale (SGS) stresses are calculated through a statistical prescription. The most frequently used closure in LES is the Smagorinski model in which the SGS stresses are modeled in terms of a turbulent eddy viscosity with a model constant to be calibrated for specific flows.

The presence of the unknown model constant makes this procedure inappropriate for unfamiliar and non-measurable flows such as protoplanetary disks. Hence, it is desirable to develop new models in which arbitrary parameters are eliminated or at least have less impact on the dynamic evolution of the resolved scales. The dynamic SGS model of Germano *et al.* (1991) provides one such example. It employs a *test* filter to calculate the model constant as a function of time and position.

In 1997 Dubrulle and Nazarenko introduced an alternative subgrid scale model for 2D turbulence (hereafter referred to as DN model) based upon a generalization of the Rapid Distortion Theory. This model relies on linearized Navier-Stokes equations forced through the energy cascade mechanism. The assumption underlying this model is that the nonlinear interactions at small scales are mainly non-local and thus have to be treated exactly. This contrasts with the classical Kolmogorov theory of turbulence in which the main interactions are between comparable scales. In the DN model, the less important local interactions are represented by a turbulent viscosity, which plays a secondary role and can be neglected in some special situations (e.g. 2D turbulence).

Laval *et al.* (1999) implemented this model for 2D isotropic turbulence computations. The model gives a much cleaner treatment of the small scales than standard LES

† CNRS, CEA/DAPNIA/SAp, CE Saclay, F-91191 Gif sur Yvette Cedex, France

models and remains cheap in memory and computation time. In 3D homogeneous turbulence, numerical tests have also been performed by Laval *et al.* (2000). They showed that non-local interactions indeed dominate the dynamics, generating coherent structures and intermittency. The local interactions are responsible for energy saturation of the structures and can be modeled by a simple turbulent viscosity.

In many astrophysical and geophysical flows, both 2D and 3D dynamics coexist: when the rotation becomes dynamically important, i.e. for scales larger than the Taylor-Proudman scale, the turbulent eddies have a 2D behavior. On the other hand, these flows are characterized by a strong mean shear flow, which is not the case in the homogeneous turbulence studied by Laval *et al.* Intuitively, we would think that the presence of this mean flow enhances the advection of the small scales and thus renders the non-local approximation even better than in 3D homogeneous turbulence. We present here quantitative support of this idea based on *a priori* tests performed using a DNS database of a turbulent channel flow at $Re_\tau = 590$ (Moser *et al.* (1999)).

2. The Dubrulle and Nazarenko model

The Navier-Stokes equations for an incompressible flow are:

$$\partial_t v_i + v_j \partial_j v_i = -\frac{1}{\rho}\partial_i p + \nu \partial_j \partial_j v_i$$

$$\partial_i v_i = 0 \tag{2.1}$$

where v_i is the velocity component in the ith direction, p the pressure, ρ the (constant) density, and ν the kinematic viscosity. As in standard LES, we define resolved and subgrid scale quantities using a filter function $G(\mathbf{x}, \mathbf{x}')$:

$$v_i(\mathbf{x}, t) = V_i(\mathbf{x}, t) + v_i'(\mathbf{x}, t)$$

$$V_i(\mathbf{x}, t) \equiv \overline{v_i(\mathbf{x}, t)} = \int G(\mathbf{x}, \mathbf{x}')v_i(\mathbf{x}', t)d\mathbf{x}' \tag{2.2}$$

where V_i and v_i' are the resolved and subgrid scale velocity components in the ith direction. The filter function used in the present report is a sharp cut-off in the Fourier space.

Using this filtering operation, one obtains two coupled sets of equations: one for the resolved scales and the other for the unresolved (subgrid) scales. The resolved scale equations are obtained by a mere filtering of Eq. (2.1):

$$\partial_t V_i + \partial_j \overline{V_i V_j} + \partial_j \overline{V_i v_j'} + \partial_j \overline{v_i' V_j} + \partial_j \overline{v_i' v_j'}$$

$$= -\frac{1}{\rho}\partial_i P + \nu \partial_j \partial_j V_i$$

$$\partial_i V_i = 0 \tag{2.3}$$

The subgrid scale equations are obtained by subtracting equations (2.3) from (2.1):

$$\partial_t v_i' + \partial_j V_i V_j + \partial_j V_i v_j' + \partial_j v_i' V_j + \partial_j v_i' v_j'$$

$$- \partial_j \overline{V_i V_j} - \partial_j \overline{V_i v_j'} - \partial_j \overline{v_i' V_j} - \partial_j \overline{v_i' v_j'}$$

$$= -\frac{1}{\rho}\partial_i p' + \nu \partial_j \partial_j v_i'$$

$$\partial_i v_i' = 0 \tag{2.4}$$
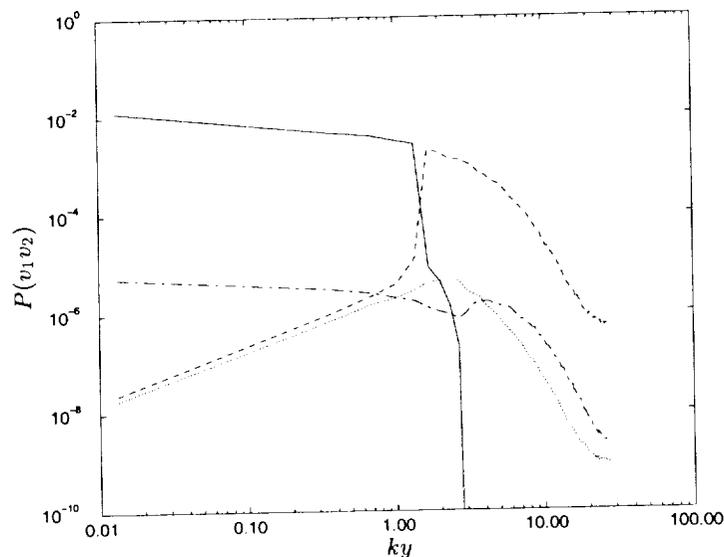
FIGURE 1. Wavenumber spectra of the four Reynolds shear stress components involving the streamwise and the wall-normal velocities, at $y^+ = 100$, for a cut-off wavenumber of $300m^{-1}$ (adapted from Carlier *et al.* (2000)): —— $V_1 V_2$; ———— $V_1 v_2'$; ········ $v_1' V_2$; ——·—— $v_1' v_2'$.

Several terms contribute to the nonlinear interactions: *non-local* terms involving the product of a resolved scale and a subgrid scale component, and a *local* term involving two subgrid scale components. The essence of subgrid scale modeling is to keep only the *non-local* terms and to model the local term by a turbulent viscosity.

The savings in memory achieved with this kind of model are not obvious since all the scales are computed. However the linearity of the subgrid scale equations allows several simplifications. First, they may be decomposed into localized linear modes, which can exploit the intermittency and inhomogeneity of the small scales, thereby decreasing the number of modes needed to reconstruct the subgrid field. Also, the linearity enables the use of semi-Lagrangian schemes of integration, which provides a significant reduction of the computational cost via an increase of the integration time step (see Laval *et al.* (1999) for details of 2D simulations).

3. A priori tests in a channel flow

Carlier *et al.* (2000) have studied the relative importance of local and non-local terms in a high Reynolds number wind tunnel boundary layer at a momentum-thickness based Reynolds number equal to 20600. The results are displayed in Fig. 1, which shows the power spectra of the four instantaneous Reynolds stress components involving v_1 and v_2, defined as $P(v_1 v_2) = |\widehat{v_1 v_2}|^2$ where the caret denotes Fourier transform in the plane parallel to the wall at $y^+ = 100$. The horizontal axis represents the dimensionless wavenumber $k = (k_1^2 + k_3^2)^{1/2}$ (normalized by $1/y$). One sees that for wavenumbers larger than the cut-off, wavenumber ($= 300m^{-1}$), The non-local term $V_1 v_2'$ indeed dominates over the other terms by several orders of magnitudes. However, the hot wire anemometry technique used in the experiment prevents both the measurements of other components of the velocity field and the computation of spatial derivatives, thereby preventing a direct
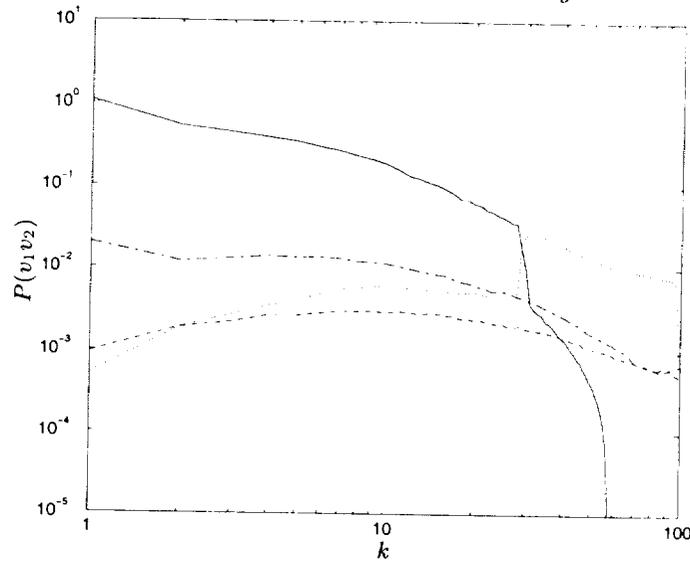
FIGURE 2. Wavenumber spectra of the four Reynolds stress components involving the streamwise and the wall-normal velocities, at $y^+ = 50$, for a cut-off wavenumber of 30: ——— V_1V_2; ········· V_1v_2'; - - - - $v_1'V_2$; — - — $v_1'v_2'$.

check of the non-local hypothesis. It is, therefore, of interest to complement their study via *a priori* tests performed using a DNS database.

The database used in the present study is from the channel flow DNS of Moser *et al.* (1999) at $Re_\tau = 590$ based on the friction velocity and channel half-width. The DNS was conducted on a grid of $384 \times 257 \times 384$, covering a computational box of size $2\pi, 2, \pi$ in the streamwise (x_1), wall-normal (x_2 or y), and spanwise (x_3) directions, respectively. All the variables used are dimensionless, with velocities normalized by the mean friction velocity and spatial coordinates normalized by the channel half-width. The strong inhomogeneity of the mesh in the wall-normal direction prevents the use of Fourier analysis in that direction. Therefore, filtering was performed only in the planes parallel to the wall. A sharp cut-off filter with cut-off wavenumber $k = 30$ was used to separate large and small scales.

Our analysis was performed in two steps: first, we computed the four components of v_1v_2 and their power spectra $P(v_1v_2)$ ($= |\widehat{v_1v_2}|^2$) as a function of wavenumber $k = (k_1^2 + k_3^2)^{1/2}$, analogous to those plotted in Fig. 1, thereby allowing an estimate of the influence of the Reynolds number. The results are presented in Fig. 2. Then, we computed the advective terms in the three subgrid scale equations (2.4), complete with the spatial derivatives and summation over indices. The derivatives were calculated using spectral methods (Fourier in the streamwise and spanwise directions, and Chebychev in the wall-normal direction) consistent with the original DNS. The results, again expressed in terms of their wavenumber spectra $P(v_j\partial_j v_i) = |\widehat{v_j\partial_j v_i}|^2$, are shown in Figs. 3, 4 and 5. Notice that although the examples shown in Figs. 2–5 are for $y^+ = 50$, the same calculations have been repeated for $y^+ = 20$ and $y^+ = 100$ as well, and the results are found to be very similar to those depicted in the figures.

From a comparison of Figs. 1 and 2, one sees that the main influence of the higher Reynolds number (Fig. 1) is to increase the dominance of the non-local term with respect to the others. This is a consequence of the increased scale separation, which has been
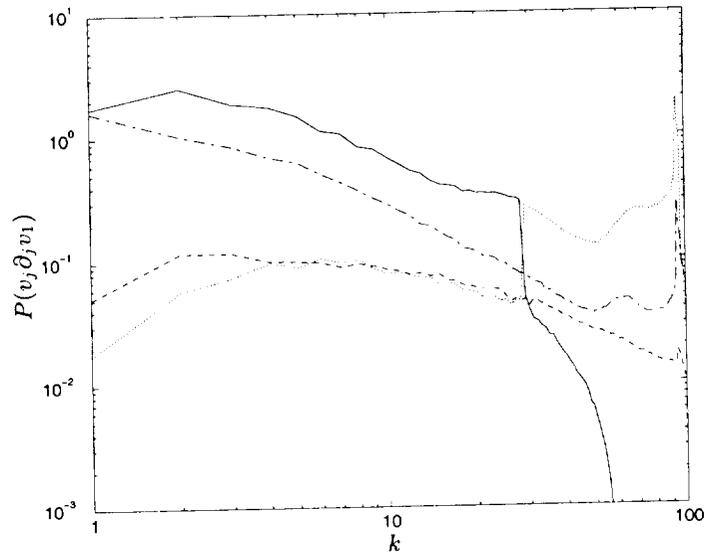
FIGURE 3. Wavenumber spectra of the four components of the divergence of the Reynolds tensor projected in the streamwise direction, at $y^+ = 50$, for a cut-off wavenumber of 30: ——— $V_j \partial_j V_1$; ········ $V_j \partial_j v_1'$; – – – – $v_j' \partial_j V_1$; — ·· — $v_j' \partial_j v_1'$.
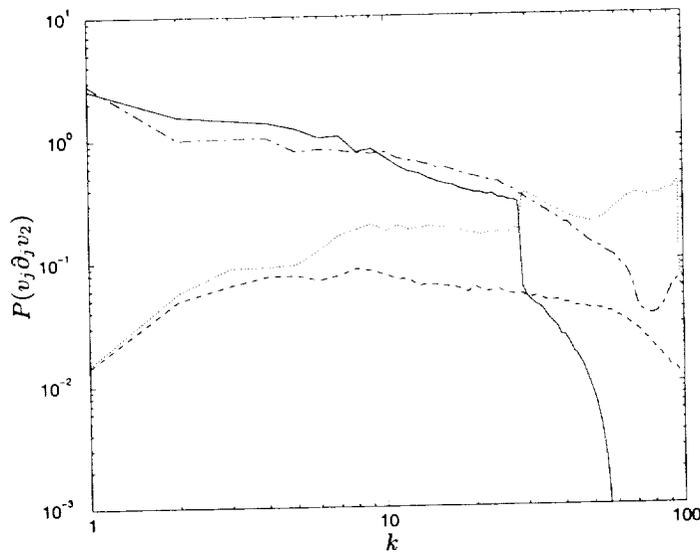
FIGURE 4. Wavenumber spectra of the four components of the divergence of the Reynolds tensor projected in the wall-normal direction, at $y^+ = 50$, for a cut-off wavenumber of 30: ——— $V_j \partial_j V_2$; ········ $V_j \partial_j v_2'$; – – – – $v_j' \partial_j V_2$; — ·· — $v_j' \partial_j v_2'$.

predicted and discussed in Dubrulle & Nazarenko (1997). When the other components of the velocity fields and the derivatives are taken into account, one may note that the non-local hypothesis remains valid for the subgrid scale equations (2.4) in the streamwise (Fig. 3) and spanwise (Fig. 5) directions, while it becomes clearly violated for the equation in the direction normal to the wall (Fig. 4). This is consistent with the belief that the
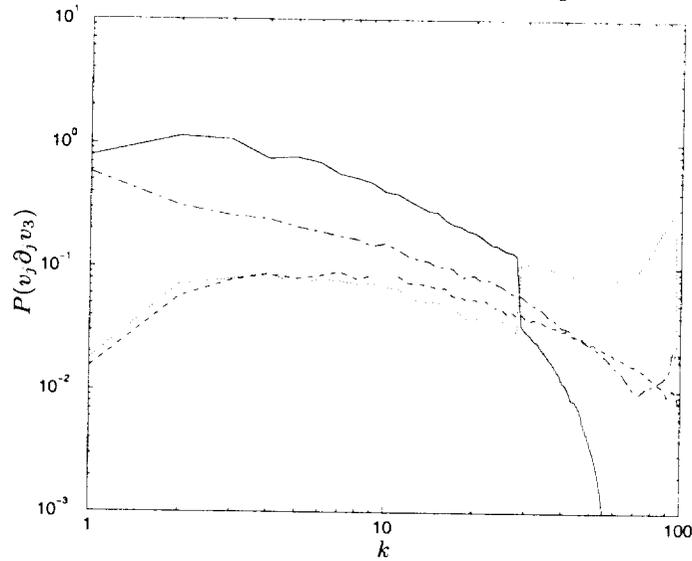
FIGURE 5. Wavenumber spectra of the four components of the divergence of the Reynolds tensor projected in the spanwise direction, at $y^+ = 50$, for a cut-off wavenumber of 30: ——— $V_j \partial_j V_3$; ········ $V_j \partial_j v_3'$; ———— $v_j' \partial_j V_3$; —·—·— $v_j' \partial_j v_3'$.

presence of a mean flow (here in the streamwise direction) favors the development of non-local interactions even at moderate Reynolds numbers. In the absence of a mean flow (like in the direction normal to the wall, or in 3D homogeneous turbulence), the local terms need to be taken into account. On the whole, these results suggest that, in the streamwise and spanwise directions, the local interaction terms could be safely neglected (as in 2D turbulence), while in the direction normal to the wall, they should be modeled by a turbulent viscosity as in 3D homogeneous turbulence.

4. Conclusions

We have shown that, based on *a priori* tests in a channel flow, the model developed by Dubrulle & Nazarenko (1997) should be applicable in turbulent shear flows. As expected, nonlinear interactions in the presence of a mean flow are mainly dominated by the advection of small scales by the large scale motions, including the mean stream. The remaining interactions only involve a small fraction of the flow energy, and their dynamics can be modeled by, for example, a turbulent viscosity.

This is of great interest for protoplanetary disks. In fact accretion disks are believed to have many similarities with Couette-Taylor flows (see e.g. Richard & Zahn (1999)). The presence of rotation may induce some differences. However, the rotation tends to force the large scale motions to have a 2D behavior. Given the success of the Laval *et al.* (1999) model for 2D turbulence, it is hoped that the model will be also valid in 3D rotating shear flows. Obviously, the present *a priori* test results are very encouraging, but further investigations are required to evaluate the influence of rotation more precisely. Dynamical tests are also needed to validate this procedure for 3D turbulence in complex geometries.

Acknowledgments

REFERENCES

CARLIER, J., LAVAL, J. P. & STANISLAS, M. 2000 Some experimental support at large Reynolds number to a new hypothesis for turbulence modeling. Submitted to *C.R.A.S.*

DUBRULLE, B. & NAZARENKO, S. V. 1997 Interactions of turbulence and large scale vortices in 2D incompressible flows. *Physica D.* **110**, 123-138.

GERMANO, M., PIOMELLI, U., MOIN, P. & CABOT, W. H. 1991 A dynamic subgrid-scale eddy viscosity model, *Phys. Fluids A.* **3**, 1760-1765.

LAVAL, J. P., DUBRULLE, B. & NAZARENKO, S. V. 1999 Fast Numerical simulations using a dynamical model for Small Scale Turbulent Motions. Submitted to *Phys. Fluids.*

LAVAL, J. P. & DUBRULLE, B. 2000 Numerical Validation of a Dynamical Turbulent Model of Turbulence. Submitted to *Phys. Rev. Lett.*

LAVAL, J. P., DUBRULLE, B. & NAZARENKO, S.V. 2000 Non-locality and intermittency in 3D Turbulence. Submitted to *Phys. Fluids.*

MOSER, R. D., KIM, J. & MANSOUR, N. N. 1999 Direct numerical simulation of turbulent channel flow up to Re_τ=590. *Phys. Fluids.* **11**, 943-945.

RICHARD, D. & ZAHN, J. P. 1999 Turbulence in differentially rotating flows. What can be learned from the Couette-Taylor experiment. *Astron. Astrophys.* **347**, 734-738.

Evaluation of the use of second generation wavelets in the Coherent Vortex Simulation approach

By D. E. Goldstein†, O. V. Vasilyev†, A. A. Wray‡ AND R. S. Rogallo‡

The objective of this study is to investigate the use of the second generation bi-orthogonal wavelet transform for the field decomposition in the Coherent Vortex Simulation of turbulent flows. The performances of the bi-orthogonal second generation wavelet transform and the orthogonal wavelet transform using Daubechies wavelets with the same number of vanishing moments are compared in *a priori* tests using a spectral direct numerical simulation (DNS) database of isotropic turbulence fields: 256^3 and 512^3 DNS of forced homogeneous turbulence ($Re_\lambda = 168$) and 256^3 and 512^3 DNS of decaying homogeneous turbulence ($Re_\lambda = 55$). It is found that bi-orthogonal second generation wavelets can be used for coherent vortex extraction. The results of *a priori* tests indicate that second generation wavelets have better compression and the residual field is closer to Gaussian. However, it was found that the use of second generation wavelets results in an integral length scale for the incoherent part that is larger than that derived from orthogonal wavelets. A way of dealing with this difficulty is suggested.

1. Introduction

A new adaptive second generation wavelet collocation method for DNS of turbulent flows has recently been developed (Vasilyev & Bowman (2000), Kevlahan *et al.* (2000)). The adaptive wavelet collocation method is appropriate for high Reynolds number turbulence since wavelets (which are localized in both space and scale) adapt the numerical resolution naturally to the intermittent structure of turbulence at small scales. The wavelet method thus allows turbulent flows to be calculated with a greatly reduced number of modes with little loss in accuracy. Furthermore, the computational cost of the algorithm is independent of the dimensionality of the problem and is $O(\mathcal{N})$, where $\mathcal{N}$ is the total number of collocation points actually used in the simulation.

The efficiency of the adaptive wavelet collocation method can be greatly enhanced by combining it with the recently developed Coherent Vortex Simulation (CVS) approach (Farge *et al.* (1999)), which is closely related to the standard large eddy simulation (LES) method. In contrast to LES, in which the velocity field is decomposed into large- and small-scale fields, in CVS the velocity field is decomposed into coherent (filtered) and incoherent (residual) fields. The filtered scales, which represent the coherent non-Gaussian part of the flow, are obtained numerically from the filtered vorticity-transport equation, while the effect of the residual scales, which represent the incoherent Gaussian part of the flow, needs to be modeled. The success of the CVS approach depends on how close the residual field is to Gaussian white noise and how few modes are required for

† University of Missouri-Columbia
‡ NASA Ames Reserach Center, Moffett Field, CA

the filtered field representation. It was shown by Donoho (1993) that wavelet coefficient thresholding is an optimal method for separating Gaussian white noise from a signal. Thus the filtering can be performed in wavelet space using wavelet coefficient thresholding, which can be considered as a non-linear filter that depends on each flow realization. This wavelet filtering is achieved by performing the following three steps:

1. Perform the forward wavelet transform of $\vec{\omega}$.

2. Set to zero those wavelet coefficients, whose magnitude is below the given *a priori* prescribed threshold ϵ, *i.e.* $||\vec{\tilde{\omega}}||_2 \leq \epsilon$, where $\vec{\tilde{\omega}}$ is the wavelet transform of $\vec{\omega}$.

3. Apply the inverse wavelet transform.

As a result of this operation, the filtered vorticity field can be captured by a small fraction of the wavelet coefficients. The anticipated advantages of CVS over current methods are, first, the use of wavelet bases to significantly compress the vorticity field and so require simulation of only a small fraction of the degrees of freedom (those that contain a significant amount of energy and enstrophy), and second, one can presumably model the discarded modes more accurately than in LES since they are closer to Gaussian white noise than those resulting from the linear low pass filters used in LES. Initial work done by Farge *et al.* (1999) on a two-dimensional CVS method shows significant potential. It is anticipated that CVS applied to three-dimensional turbulent flows will provide substantial improvements in computational speed and accuracy over existing methods.

The final goal of our work is to develop a 3D CVS code that is able to simulate realistic scientific and engineering problems in complex domains. An adaptive wavelet collocation solver (Vasilyev & Bowman (2000), Kevlahan *et al.* (2000)) will be used to numerically solve the CVS equations on the adaptive grid. This adaptive wavelet collocation solver uses second generation bi-orthogonal wavelets, enabling it to solve problems in complex domains. It would be logical to use the same second generation wavelets for both the vorticity field filtering and the wavelet collocation solver. However, the use of second generation bi-orthogonal wavelets for coherent field extraction has not been explored up to now. Therefore, the objective of this study is to investigate in *a priori* tests the use of these wavelets only for the filtering of the vorticity field for coherent vortex extraction.

The rest of this paper is organized as follows. Section 2 gives a brief introduction to second generation wavelets. The CVS approach is then introduced in Section 3. Finally, in Section 4 results are presented of a parametric study of two different wavelet transforms applied to both forced and decaying homogeneous turbulence fields.

2. Second generation wavelets

Wavelets are basis functions which are localized in both physical space (due to their finite support) and wavenumber space (*e.g.* Fig. 1). In contrast, the Fourier transform is based on functions (sines and cosines) that are well localized in frequency but do not provide localization in physical space due to their global support. Because of this space/scale localization, the wavelet transform provides both spatial and scale (frequency) information while the Fourier transform only provides frequency information.

Although the wavelet transform with its space/scale localization is an attractive technique to apply to the solution of problems with localized structures such as the simulation of turbulent flows, traditional wavelet transforms have difficulties dealing with boundaries. Traditionally, wavelets ψ_k^j are defined as translates and dilates of one basic wavelet ψ, *i.e.* $\psi_k^j(x) = \psi(2^j x - k)$. These first generation wavelets are defined either in infinite or periodic domains.

Second generation wavelets (Sweldens (1996), Sweldens (1998)) are a generalization of first generation wavelets (Daubechies (1988), Cohen *et al.* (1992)) that supplies the necessary freedom to deal with complex geometries, arbitrary boundary conditions, and irregular sampling intervals. Second generation wavelets form a Reisz basis for some function space, with the wavelets being local in both space and frequency and often having many vanishing polynomial moments, but without the translation and dilation invariance of their first generation cousins. Despite the loss of these two fundamental properties of wavelet bases, second generation wavelets retain many of the useful features of first generation wavelets, including a fast $O(N)$ transform.

The construction of second generation wavelets is based on the lifting scheme that is discussed in detail in Sweldens (1996), Sweldens (1998). Here we just summarize the main advantages of second generation wavelets:

1. Wavelets are constructed in the spatial domain and can be custom designed for complex multi-dimensional domains and irregular sampling intervals.

2. No auxiliary memory is required and the original signal can be replaced with its wavelet transform.

3. The second generation wavelet transform is a factor of two faster than the first.

4. With lifting, the inverse wavelet transform is constructed by simply reversing the order of operations and interchanging addition and subtraction operations.

5. The programming of the second generation wavelet transform is considerably simpler.

6. Second generation wavelets are naturally suitable for wavelet collocation methods, which have been shown to be superior to the wavelet Galerkin approach in handling general boundary conditions and nonlinearities in the equations.

For this study we use a set of second generation wavelets known in the literature as lifted interpolating (LI), or Donoho, wavelets (Sweldens (1996), Vasilyev & Bowman (2000)). In particular, *a priori* tests are done using the lifted interpolating wavelet, hereafter called LI3, that has five vanishing polynomial moments. The LI3 wavelet and its Fourier transform are shown in Fig. 1. For a more in-depth discussion on the construction of these wavelets the reader is referred to the following papers: Sweldens (1996), Sweldens (1998), Vasilyev & Bowman (2000). For a more general discussion of wavelets the following references can be consulted: Daubechies (1992), Mallat (1999).

3. Coherent Vortex Simulation

In a CVS the vorticity field is separated into two parts using a wavelet thresholding filter:

$$\vec{\omega} = \vec{\omega}_> + \vec{\omega}_\le \tag{3.1}$$

where $\vec{\omega}_>$ is the filtered part of the flow defined on an adaptive grid and $\vec{\omega}_\le$ is the Localized Residual Scales (LRS) field that is made as close to Gaussian white noise as possible. We use the term Localized Residual Scales to highlight the fact that there is no particular scale associated with the residual field, *i.e.*, the spectral content of the LRS varies in time and location, unlike in LES of a homogeneous flow.

The formulation for CVS then begins with the vorticity-transport equation:

$$\frac{\partial \vec{\omega}}{\partial t} = -(\vec{V} \cdot \nabla)\vec{\omega} + (\vec{\omega} \cdot \nabla)\vec{V} + \nu\nabla^2\vec{\omega}. \tag{3.2}$$
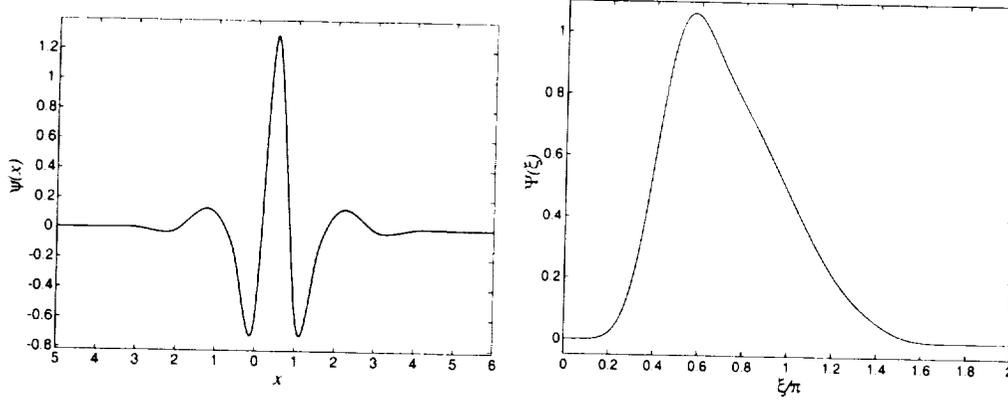
FIGURE 1. Lifted interpolating wavelet ψ and its Fourier transform $\Psi(\xi)$.

As in LES, after application of the wavelet filter we obtain the following CVS equation that describes the evolution of the filtered field:

$$\frac{\partial \vec{\omega}_>}{\partial t} = -(\vec{V}_> \cdot \nabla)\vec{\omega}_> + (\vec{\omega}_> \cdot \nabla)\vec{V}_> + \nu\nabla^2\vec{\omega}_> + \vec{f} \qquad (3.3)$$

where

$$\vec{f} = [(\vec{V} \cdot \nabla)\vec{\omega}]_> - [(\vec{\omega} \cdot \nabla)\vec{V}]_> - (\vec{V}_> \cdot \nabla)\vec{\omega}_> + (\vec{\omega}_> \cdot \nabla)\vec{V}_> \qquad (3.4)$$

is the LRS forcing that needs to be modeled. The localized nature of the LRS will have to be considered in defining residual-scale models for use with CVS. It has been shown that, when a non-linear wavelet thresholding filter is applied to a moderately high Reynolds number isotropic turbulence field, the residual field is closer to being statistically Gaussian than when a Fourier cutoff filter with the same number of modes is used. This has been shown in Farge *et al.* (1999) in 2D and will be shown in Section 4 below in 3D. Thus it is expected that the LRS can be modeled more accurately than for Fourier filtering, but this has not been proven and is a current topic of research.

Solution of the filtered vorticity equation on an adaptive grid can be done using any appropriate solution method. In Farge *et al.* (1999) a 2D CVS method was implemented using an adaptive wavelet-vaguelette algorithm (Fröhlich & Schneider (1997)). In our work we implemented a 3D CVS method using an adaptive wavelet collocation method discussed in Vasilyev & Bowman (2000), Kevlahan *et al.* (2000) that has been shown to work well in 2D flows and can be extended to 3D with little modification. This solver uses the second generation bi-orthogonal LI wavelets discussed in Section 2 and is capable of solving problems in complex domains.

The adaptive wavelet collocation method is ideally suited for the CVS of turbulent flows since every wavelet is uniquely associated with a collocation point. Thus the grid adaptation can be based on the same criterion as in coherent vortex extraction, *i.e.*, at any given time the computational grid consists of points corresponding to wavelets whose coefficients are above an optimal CVS threshold, *i.e.* we do not retain those collocation points whose wavelet coefficients were set to zero in the wavelet filtering operation. With this adaptation strategy a solution is obtained on a grid that "tracks" the coherent vortices.

The CVS method requires at least two major operations per time step:

1. Apply the wavelet thresholding filter to define the adaptive grid.
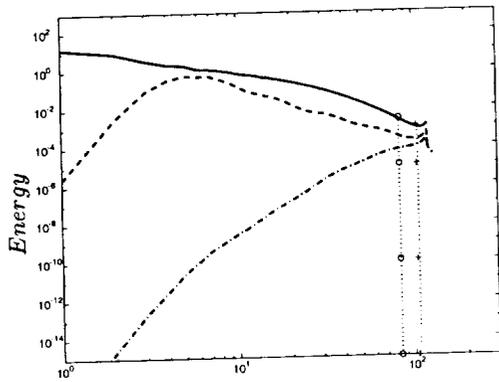
a) Spectra of forced isotropic turbulence, data set F_{256}, $Re_\lambda = 168$.
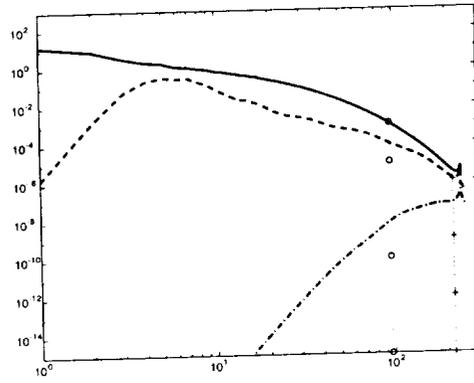
b) Spectra of forced isotropic turbulence, data set F_{512}, $Re_\lambda = 168$.
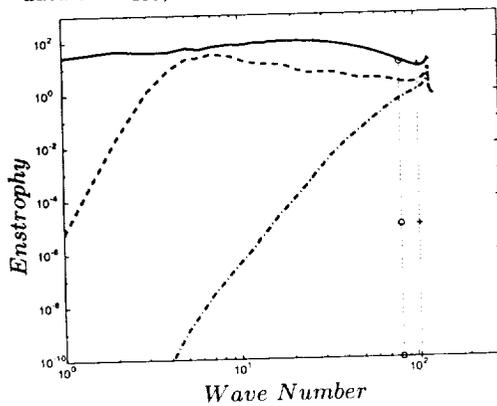
c) Enstrophy of forced isotropic turbulence, data set F_{256}, $Re_\lambda = 168$.
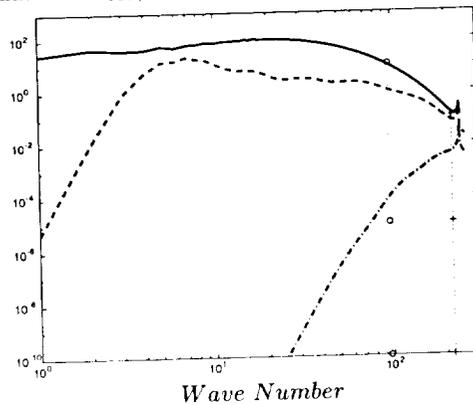
d) Enstrophy of forced isotropic turbulence, data set F_{512}, $Re_\lambda = 168$.

FIGURE 2. Energy and enstrophy spectra of forced isotropic turbulence for data sets F_{256} and F_{512}. Spectra of the full field: (———). Spectra of the LRS field after optimal wavelet compression using DB6 wavelets: (——·——) and LI3 wavelets: (————). The Fourier cutoff filter with compression equivalent to optimal DB6 wavelet filter: (·· + ··) and to optimal LI3 wavelet filter: (·· ○ ··).

2. Numerically solve Eq. 3.3 on the adaptive grid.

Using the same wavelets for these two steps would be most compuptionally efficient. This is why we are interested in investigating the use of second generation bi-orthogonal wavelets for coherent vortex extraction.

Although in this paper we do not discuss the solution of the wavelet filtered vorticity equation (3.3), it is good to point out that since the CVS equations are solved on an adaptive grid, we cannot use spectral methods for the solution of the Poisson equation that relates the vorticity field to the velocity field. The development of an efficient wavelet collocation based method for the solution of the Poisson equation on an adaptive grid is currently a subject of study.
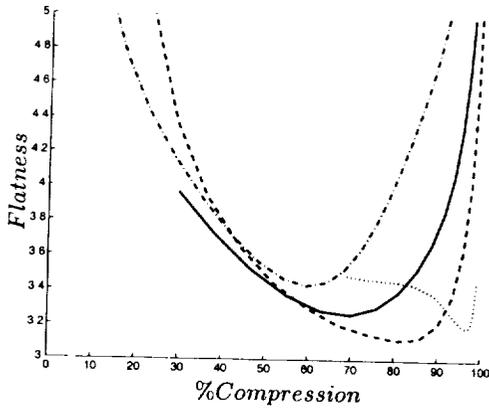
a)   Flatness $(<\omega^4>/<\omega^2>^2)$.   (Note: Flatness of a Gaussian field is 3.0.)
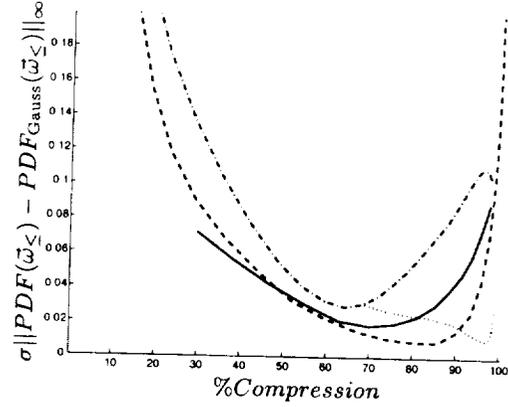
b) L_∞ Error between LRS and Gaussian PDFs with the same mean and variance.
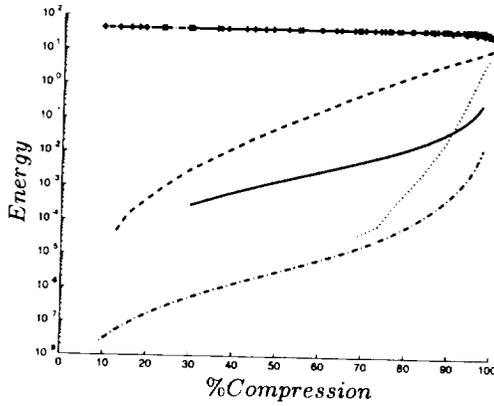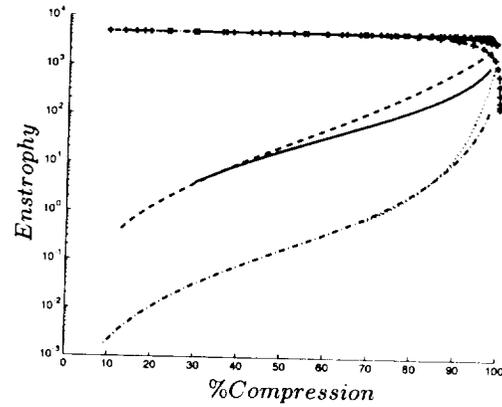
c) Total kinetic energy.

d) Total enstrophy.
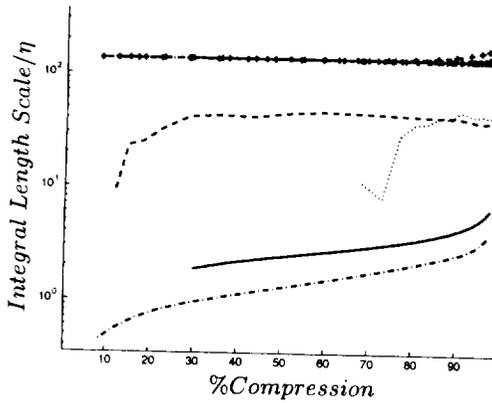
e) Velocity integral length scale.
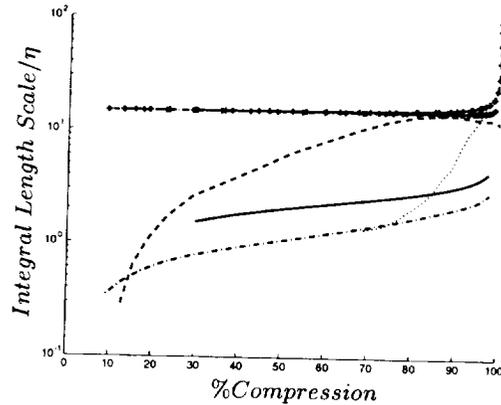
f) Vorticity integral length scale.

FIGURE 3. Filtered and LRS field statistics for isotropic turbulence fields F_{256} and F_{512} after application of wavelet thresholding filter using LI3 and DB6 wavelets. LRS field statistics of F_{256} using DB6 wavelets: (———) and LI3 wavelets: (— — —). LRS field statistics of F_{512} using DB6 wavelets: (— · —) and LI3 wavelets: (········). In plots c) through f) the lines with (+) are the same statistics for the filtered fields. (Note: The filtered statistics are mostly constant until almost 100% compression so these lines are obscured by each other.)
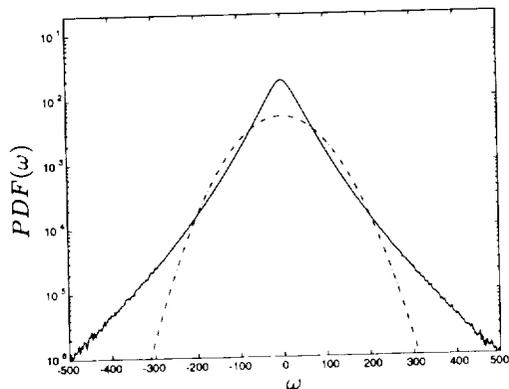
FIGURE 4. PDF of forced isotropic turbulence field F_{256}: (———). Gaussian PDF with same mean and variance: (—·—).
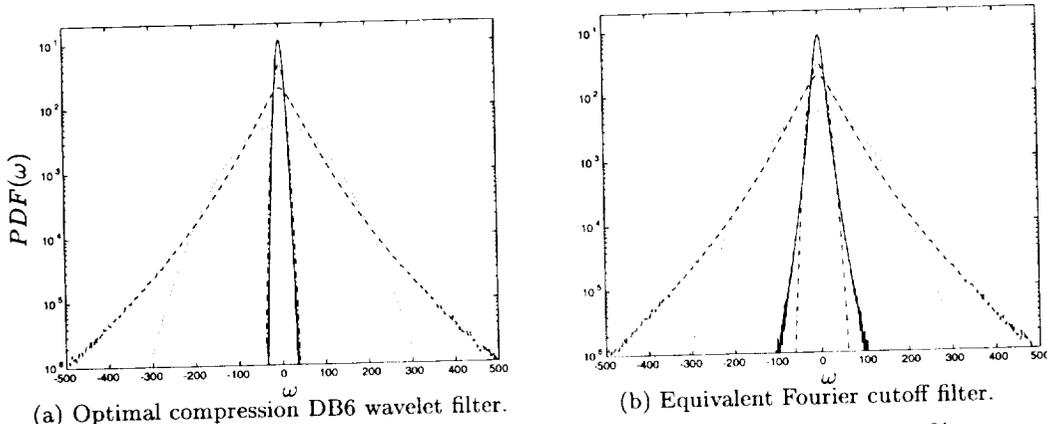
(a) Optimal compression DB6 wavelet filter.

(b) Equivalent Fourier cutoff filter.

FIGURE 5. PDF of forced isotropic turbulence field F_{256} using DB6 wavelet filter at 50% compression (a) and Fourier cutoff filter at the equivalent compression (b). Filtered field: (———), with its associated Gaussian: (········). LRS field: (———), with its associated Gaussian: (—·—).
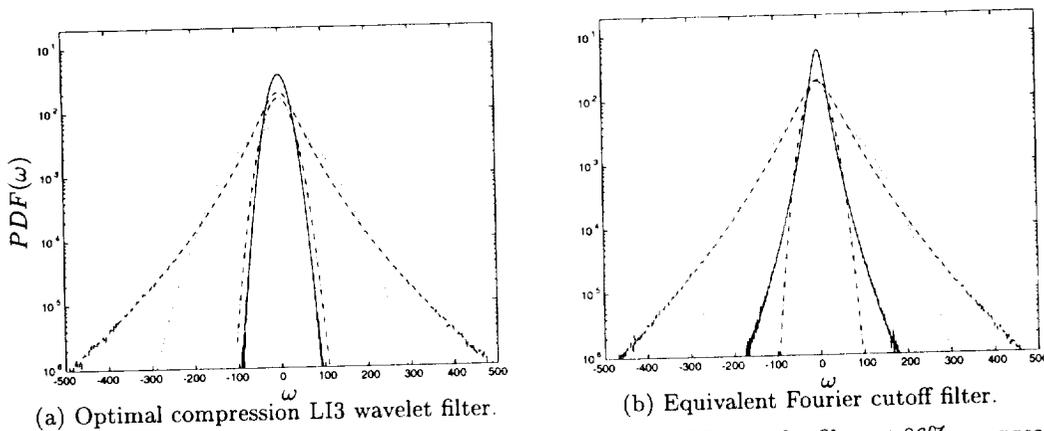
(a) Optimal compression LI3 wavelet filter.

(b) Equivalent Fourier cutoff filter.

FIGURE 6. PDF of forced isotropic turbulence field F_{256} using LI3 wavelet filter at 86% compression (a) and Fourier cutoff filter at the equivalent compression (b). Filtered field: (———), with its associated Gaussian: (········). LRS field: (———), with its associated Gaussian: (—·—).
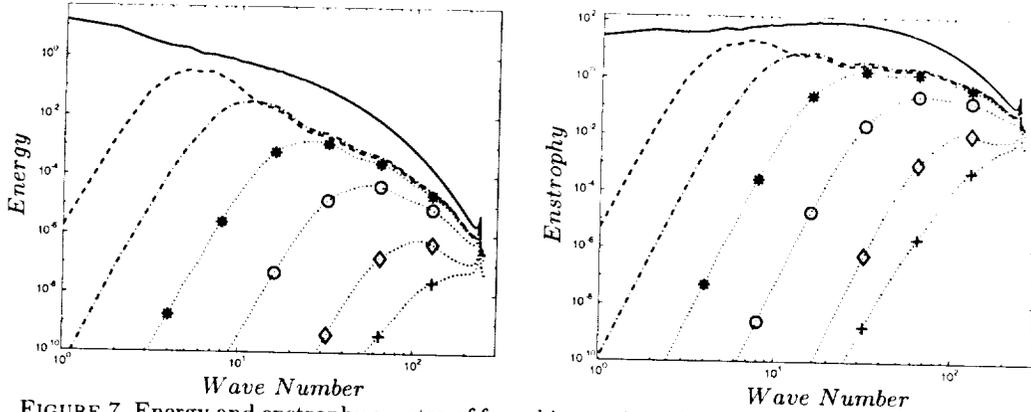
FIGURE 7. Energy and enstrophy spectra of forced isotropic turbulence data set F_{512}, $Re_\lambda = 168$. Spectra of the full field: (———). LRS field spectra after optimal decomposition with DB6 wavelets with 6 levels: (·· + ··). The rest of the lines are the LRS field spectra after optimal wavelet compression with LI3 wavelets with varying number of decomposition levels: 2 levels: (·· ◇ ··), 3 levels: (·· ○ ··), 4 levels: (·· * ··), 5 levels: (—·—), 6 levels: (————).

4. Results and discussion

For the CVS method to work, we want to find the optimal value of ϵ such that the wavelet filter decomposes the vorticity field into a filtered field that contains all the co-herent vortices of significant energy and an LRS field that is as close to Gaussian white noise as possible. One way to find the optimal value of ϵ is to use Donoho's de-noising theorem (Donoho (1993)) that states that if there is a Gaussian white-noise component in the vorticity field and somehow we know its variance, we can extract it using wavelet thresholding with orthogonal wavelets. Donoho's de-noising theorem says that the thresh-old required to extract the Gaussian white-noise component is $\epsilon_{Donoho} = \sqrt{2\sigma^2 \log(N)}$, where σ^2 is the variance of the Gaussian white noise and N is the number of points in the field. However, the variance of the Gaussian white-noise component of the vorticity field is not known. One way to find the LRS field with maximum Gaussianity is to iterate on $\epsilon_{n+1} = \sqrt{2\sigma^2_{LRS_n} \log(N)}$, with σ_{LRS_0} taken as the variance of the full field (Farge et al. (1999)). If there exists an LRS field that is Gaussian white noise, then the iterative process should converge to ϵ_{Donoho}. However, since Donoho's theorem does not directly apply to bi-orthogonal wavelets, another way to find the optimal ϵ needs to be found.

In order to prove the existence of an optimal value for ϵ for second generation wavelets and, possibly, find an efficient way of finding it, a series of parametric studies were performed by varying ϵ to achieve a range of compression from 0% to 100%. The results for the second generation bi-orthogonal (LI) wavelets were compared to the orthogonal Daubechies DB6 wavelets (Daubechies (1992)). Both of these wavelets have five vanishing moments and an effective filter length of 12. We carried out these parametric studies using a number of forced and decaying isotropic turbulence fields from a database of spectral DNS. Due to space restrictions the results from only two representative forced isotropic turbulence fields F_{256} and F_{512} ($Re_\lambda = 168$) will be presented in detail. We also will refer to two decaying isotropic turbulence fields CBC_{256} and CBC_{512} ($Re_\lambda = 55$). More detailed information about these data sets can be found in Jimenez & Wray (1993).

The energy and enstrophy spectra of data sets F_{256} and F_{512} are shown in Fig. 2. Fig-ure 3 shows various statistical quantities (as a function of compression) of the filtered and LRS fields after wavelet thresholding with DB6 and LI3 wavelets. In this paper we define
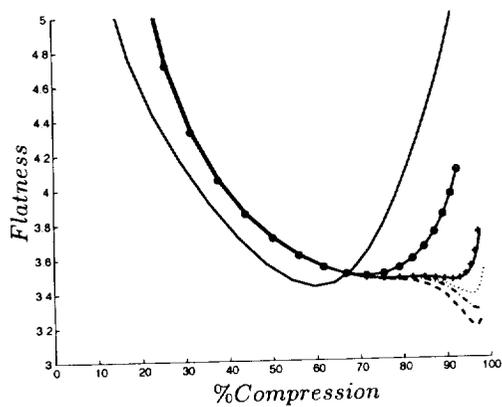
a) Flatness $(< \omega^4 > / < \omega^2 >^2)$. (Note: Flatness of a Gaussian field is 3.0.)
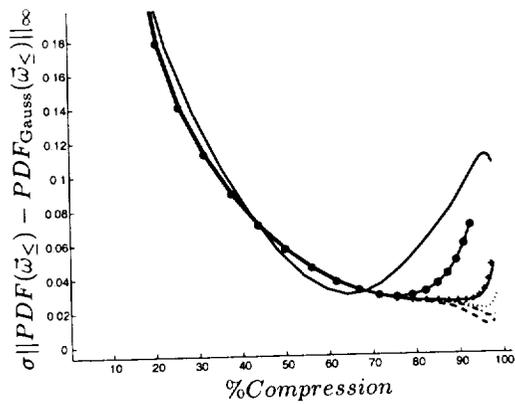
b) L_∞ error between LRS field and a Gaussian PDFs with the same mean and variance.
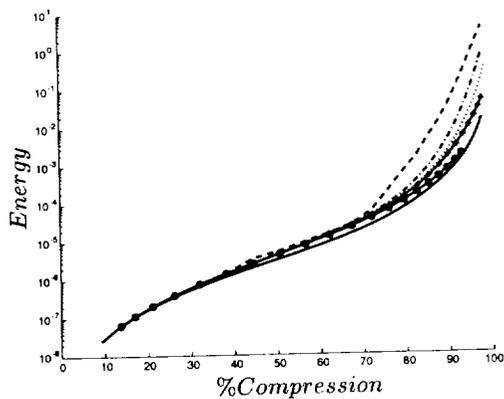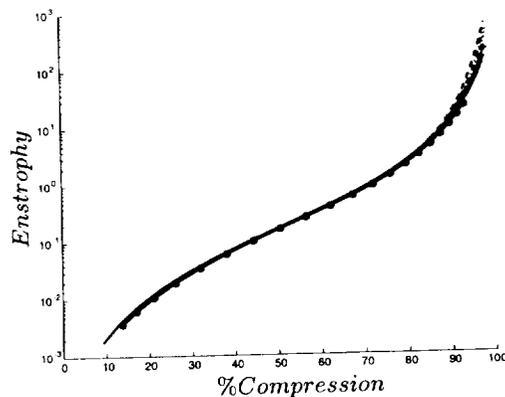
c) Total kinetic energy.

d) Total enstrophy.
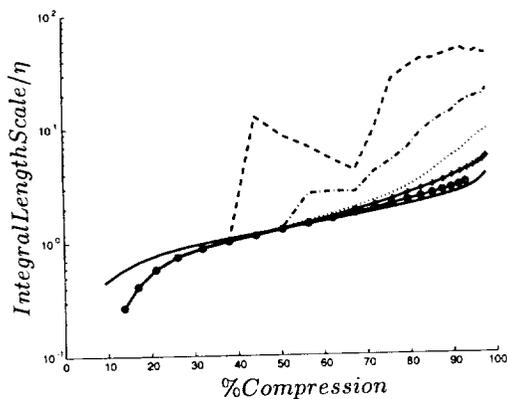
e) Velocity Integral Length Scale.
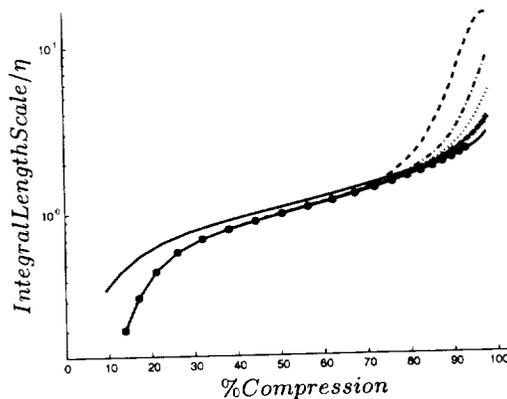
f) Vorticity integral length scale.

FIGURE 8. Comparison of LRS field statistics after wavelet filtering of forced isotropic turbulence data set F_{512}, $Re_\lambda = 168$. LRS field statistics using DB6 wavelets with 6 levels: (————) The rest of the lines are the LRS field statistics after optimal wavelet compression with LI3 wavelets with varying number of decomposition levels: 2 levels: (—●—), 3 levels: (·· + ··), 4 levels: (········), 5 levels: (—·—), 6 levels: (————).

a) Forced isotropic turbulence fields F_{256}:
(— — — —) and F_{512}: (— · —).

b) Decaying isotropic turbulence fields
CBC_{256}: (— — — —) and CBC_{512}: (— · —)
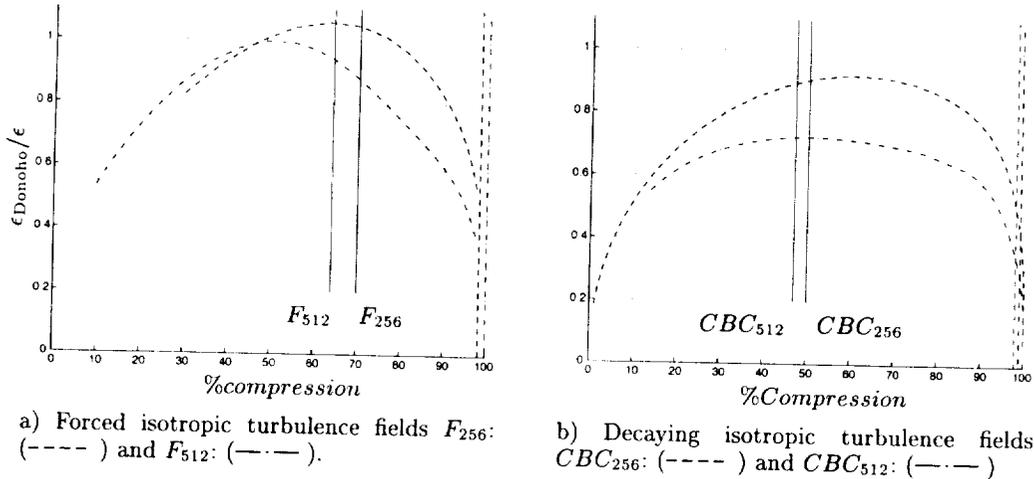
FIGURE 9. Wavelet threshold from Donoho's de-noising theorem scaled by the actual threshold used with DB6 wavelet thresholding. The % compression at minimum flatness is marked for each field by solid vertical lines. The resulting compression when Donoho's theorem is applied to the full vorticity field is shown by vertical lines, 256^3 field: (— — — —), 512^3 field: (— · —).

the compression as $\frac{N_>}{N} \times 100\%$, where $N_>$ is the number of retained wavelet coefficients for a given threshold ϵ. In Fig. 3a we can see that in each case there is a minimum for the flatness. This minimum is interpreted as the optimal wavelet compression of the field in terms of Gaussianity of the LRS field. Figure 3b shows the scaled L_∞ error between the PDF of the LRS field and a Gaussian PDF with the same mean and variance. It can be seen that the minima in Figs. 3a and 3b coincide, showing that the flatness is a good indicator of the Gaussianity of the field. It can also be seen from these plots that the optimal compression of both fields is better for the LI3 wavelets than the DB6 wavelets. However, this does not show the whole story. In Fig. 3c we see that the total kinetic energy in the LRS field is greater for both fields when the LI3 wavelets are used, while the difference is much less if we look at the total enstrophy in Fig. 3d. It is significant that the velocity (Fig. 3e) and vorticity (Fig. 3f) integral length scales of the LRS field are considerably larger for the LI3 wavelets. This indicates that the LI3 wavelets are extracting a more Gaussian LRS field at a higher optimal compression ratio, but this LRS field is more coherent than that from DB6 wavelets. Since the goal of the CVS approach is to extract an incoherent Gaussian white noise, this is considered unfavorable for the LI3 wavelets.

It is also interesting to note that for the LI3 wavelets the optimal compression is considerably greater for the F_{512} data set when compared to the F_{256} case (see Figs. 2a and 2b). In fact, the number of wavelets used to represent the filtered fields is approximately the same for both F_{256} and F_{512} data sets, which means that additional scales are approximated with virtually no extra cost. However, this is not true for the DB6 wavelet filter.

Figure 4 shows the PDF of vorticity for data set F_{256} and the Gaussian PDF with the same mean and variance. In Fig. 5, for data set F_{256}, the PDFs of the filtered and LRS vorticity fields at optimum wavelet compression using DB6 wavelets are compared to those from a Fourier cutoff filter that retains the same number of modes. The difference in the Gaussianity of the LRS field of the two filters can most clearly be seen in the tails.

With both LI3 and DB6 wavelet thresholding the LRS field is clearly more Gaussian in the tails than the residuals from the Fourier cutoff filter. In both cases there is a large difference around zero between the PDF of the LRS field and the corresponding Gaussian PDF; this difference dominates the L_∞ error.

As a possible way to improve the performance of the LI3 wavelets for coherent vortex extraction, we studied the effect of diminishing the number of multiresolution levels used in the wavelet transform. For a resolution of 512^3, the maximum number of levels that can be used with the LI3 and DB6 wavelets before the support of the scaling functions start to overlap at the coarsest level is 6 (see Daubechies (1992) for a more in-depth discussion of the wavelet transform). Figure 7 shows the energy and enstrophy spectra for data set F_{512} and the LRS fields after optimal wavelet compression using DB6 wavelets with 6 levels in the transform, as in Fig. 3. Also shown are the energy and enstrophy spectra of the LRS fields after optimal wavelet compression using LI3 wavelets with 2 through 6 levels of resolution. Note that, as the number of levels of resolution used in the LI3 wavelet transform decreases, the LRS field contains less energy and approaches the energy retained by the DB6 wavelet filter. In Fig. 8 we compare the the same statistics as we did in Fig. 3 for the DB6 wavelet transform to the LI3 wavelet transform with a range of levels of resolution. It can be easily seen in Figs. 8a and 8b that as the number of levels used in the wavelet transform decreases, the LRS field becomes less Gaussian. We also see that the LI3 wavelet transform with four levels results in a LRS field with better Gaussianity (compared to the DB6 wavelet filter) with an optimal compression ratio of 96% vs. 60% for the DB6 wavelet filter. Comparing the total energy and enstrophy (Figs. 8c and 8d) for the LI3 wavelet transform with four levels of resolution to the DB6 wavelet transform, it can be clearly seen that the difference in total kinetic energy is minimal and total enstrophy is almost identical. An interesting trend can be seen in the velocity (Fig. 8e) and vorticity (Fig. 8f) integral length scales: using fewer levels in the LI3 wavelet transform results in less coherence of the LRS field.

Finally, let us discuss the application of Donoho's de-noising theorem to find the optimal wavelet compression using DB6 orthogonal wavelets. Figure 9 shows the normalized threshold coefficient ($\epsilon_{Donoho}/\epsilon$) derived from Donoho's de-noising theorem for the LRS field vs. the % compression of the field. Recall, that a given vorticity field ϵ_{Donoho}, which is a function of the variance of the LRS field, is uniquely defined by the value ϵ used in wavelet filter. The solid vertical lines show the optimal compression as determined by the minimum flatness and L_∞ error. We can see that because the LRS fields are never really Gaussian white noise, the optimal compression and the points where $\epsilon_{Donoho}/\epsilon = 1.0$ do not coincide. In fact, for the decaying isotropic turbulence data sets CBC_{256} and CBC_{512}, which have a lower Re_λ ($Re_\lambda = 55$), $\epsilon_{Donoho}/\epsilon$ never reaches 1.0. We have also superimposed vertical lines that show the optimal compression ratio obtained if Donoho's de-noising theorem is applied using the variance of the full field. We can see that this results in a much higher compression than at the point of maximum Gaussianity (see Fig. 3).

5. Conclusions

The performance of the bi-orthogonal second generation wavelet transform and the orthogonal wavelet transform using Daubechies wavelets with the same number of vanishing moments is compared in *a priori* tests using a spectral DNS database of isotropic turbulence fields: 256^3 and 512^3 DNS of forced homogeneous turbulence ($Re_\lambda = 168$) and 256^3 and 512^3 DNS of decaying homogeneous turbulence ($Re_\lambda = 55$). The results of

these *a priori* tests indicate that lifted interpolating bi-orthogonal wavelets are able to extract a more Gaussian LRS field at a higher optimal compression ratio than orthogonal DB wavelets. However the extracted LRS field is more coherent than when using orthogonal DB wavelets. This problem can be overcome by reducing the number of levels of resolution in the wavelet transform. In addition, it was found that the optimal wavelet compression did not coincide with the theoretical compression predicted by Donoho's de-noising theorem. The most probable explanation for this is that the LRS field never actually becomes Gaussian white noise.

Future work in this area will include comparing the second generation wavelets wavelets to other orthogonal wavelets and implementing the CVS approach in the adaptive second generation wavelet collocation method.

Acknowledgments

REFERENCES

COHEN, A., DAUBECHIES, I., & FEAUVEAU, J. 1992 Bi-orthogonal bases of compactly supported wavelets. *Comm. Pures and Appl. Math.* **45**, 485-560.

DAUBECHIES, I. 1988 Orthonormal bases of compactly supported wavelets. *Comm. Pure and Appl. Math.* **41**, 909-996.

DAUBECHIES, I. 1992 *Ten Lectures on Wavelets.* no. 61 in CBMS-NSF Series in Applied Mathematics, SIAM, Philadelphia.

DONOHO, D. 1993 Unconditional bases are optimal bases for data compression and for statistical estimation. *Appl. Comput. Harmon. Anal.* **1**, 100-115.

FARGE, M., SCHNEIDER, K., & KEVLAHAN, N. 1999 Non-Gaussianity and coherent vortex simulation for two-dimensional turbulence using an adaptive orthogonal wavelet basis. *Phys. Fluids.* **11**(8), 2187-2201.

FRÖHLICH, J. & SCHNEIDER, K. 1997 An adaptive wavelet-vaguelette algorithm for the solution of pdes. *J. Comput. Phys..* **130**, 174-190.

JIMÉNEZ, J. & WRAY, A. A. 1993 The structure of intense vorticity in isotropic turbulence. *J. Fluid Mech.* **255**, 65-90.

KEVLAHAN, N. K. R., VASILYEV, O. V., & CHERHABILI, A. 2000 An adaptive wavelet method for turbulence in complex geometries. In *Proceedings of the 16th IMACS World Congress 2000*, 411-39.pdf, IMACS.

MALLAT, S. G. 1999 *A Wavelet Tour of Signal Processing.* Academic Press, Paris.

SWELDENS, W. 1996 The lifting scheme: A custom-design construction of biorthogonal wavelets. *Appl. Comput. Harmon. Anal.* **3**(2), 186-200.

SWELDENS, W. 1998 The lifting scheme: A construction of second generation wavelets. *SIAM J. Math. Anal.* **29**(2), 511-546.

VASILYEV, O. V. & BOWMAN, C. 2000 Second generation wavelet collocation method for the solution of partial differential equations. To appear in *J. Comp. Phys.*

CVS decomposition of 3D homogeneous turbulence using orthogonal wavelets

By Marie Farge†, Kai Schneider‡, Giulio Pellegrino¶,
A. A. Wray‖ AND R. S. Rogallo‖

This paper compares the filtering used in Coherent Vortex Simulation (CVS) decomposition with an orthogonal wavelet basis, with the Proper Orthogonal Decomposition (POD) or Fourier filtering. Both methods are applied to a field of DNS data of 3D forced homogeneous isotropic turbulence at microscale Reynolds number $R_\lambda = 168$. We show that, with only $3\%N$ retained modes, CVS filtering separates the coherent vortex tubes from the incoherent background flow. The latter is structureless, has an equipartition energy spectrum, and has a Gaussian velocity probability distribution function (PDF) and an exponential vorticity PDF. On the other hand, the Fourier basis does not extract the coherent vortex tubes cleanly and leaves organized structures in the residual high-wavenumber modes whose PDFs are stretched exponentials for both the velocity and the vorticity.

1. Introduction

Since the work presented in this paper has been performed at NASA-Ames, we recall the comments on turbulence research made by Hugh L. Dryden, the first director of NACA (later NASA) (Dryden (1948)).

Dryden begins his paper by saying:

There have been no notable advances in the theory of fully-developed turbulent motion during the last decade. [...] In the period 1934-1938 Taylor developed his statistical theory of turbulence, which was so fruitful in treating the problem of isotropic turbulence. Von Kármán extended the theory, clothed it in more elegant mathematical form, and attempted, with incomplete success, to treat the problem of shear flow. [...] At the Fifth International Congress of Applied Mechanics in 1938 [...] Tollmien and Prandtl suggested that the turbulent fluctuations might consist of two components, one derivable from a harmonic function and the other satisfying an equation of the heat conduction type, i.e. a nondiffusive and a diffusive component or viscosity independent and viscosity dependent type.

Tollmien and Prandtl's suggestion to split the turbulent fluctuations into non-diffusive and diffusive components is very similar to the concept behind CVS which we introduced in Farge, Schneider & Kevlahan (1999). CVS tracks the nonlinear dynamics using an adaptive wavelet basis which captures the regions of strong vorticity gradients at all scales (Schneider Kevlahan & Farge (1997), Schneider & Farge (1998)) and discards the diffusive components which have reached a statistical equilibrium as characterized by

† Laboratoire de Météorologie Dynamique, Ecole Normale Supérieure, Paris, France
‡ Centre de Mathématiques et d'Informatique, Université de Provence, Marseille, France
¶ Institüt für Chemische Technik, Universität Karlsruhe (TH), Germany
‖ NASA Ames Research Center, Moffett Field, CA

a Gaussian velocity probability distribution and energy equipartition spectrum (Farge, Schneider & Kevlahan (1999), Farge & Schneider (2000)). This will be shown in this paper.

Later, Dryden affirms that:

The mixing length concept seems wholly inadequate [...], the "mean free path", mixing length, or scale of the turbulent processes is large compared with the thickness of the boundary layer. Considerable masses of fluid move as more or less coherent units. The process cannot be smoothed by averaging over a small volume because it is not possible to choose dimensions small compared with a single fluid element. The mixing length idea, that the turbulent fluctuations and the turbulent shear stress are directly related to the mean speed at a point and its derivatives at that point, must be abandoned. Shall the flow then be regarded as a mean flow that merely transports and distorts large eddies superposed on the flow, these eddies being of varying size and intensity?

This comment of Dryden, stating that the turbulent flows are composed of coherent units of varying size and intensity which cannot be smoothed by averaging, supports our proposal for using the wavelet representation to study turbulent flows (Farge & Rabreau (1988), Farge (1992)). We showed, using the continuous wavelet transform, that coherent vortices in two-dimensional turbulent flows are multiscale eddies with activity covering the entire inertial range. Later on, during the CTR Summer Program 1990, we confirmed that the same is true for three-dimensional turbulent flows and that coherent vortices are responsible for the for flow intermittency (Farge, Guezennec, Ho & Meneveau (1990)).

Finally Dryden concludes by saying that:

The rapidly developing theory of random functions (Bass (1945)) may possibly form the mathematical framework of an improved theory of turbulence. However it is necessary to separate the random processes from the non-random processes. It is not yet fully clear what the random elements are in turbulent flows. The experimental results described suggest that the ideas of Tollmien and Prandtl, that the measured fluctuations include both random and non-random elements, are correct, but as yet there is no known procedure either experimental or theoretical for separating them.

Over the last ten years (Farge (1992), Farge, Goirand, Meyer, Pascal & Wickerhaüser (1992), Farge, Schneider & Kevlahan (1999)), we have developed the filtering process that forms the basis of the CVS method to separate the turbulent fluctuations into organized and random components. It is based on a nonlinear filtering of the vorticity projected on an orthogonal wavelet basis. We derived this procedure using theorems of Donoho and Johnstone, proving optimality of the wavelet representation for denoising signals in the presence of Gaussian white noise, in the sense that wavelet-based estimators minimize the maximum L^2-error for functions with inhomogeneous regularity(Donoho (1993), Donoho & Johnstone (1994)).

In this paper we use CVS filtering to decompose a 3D forced homogeneous isotropic turbulent flow into organized and random components. The microscale Reynolds number is $R_\lambda = 168$ and the simulation has resolution $N = 256^3$.

2. CVS decomposition

We consider the vorticity field $\vec{\omega}(\vec{x}) = \nabla \times \vec{V}$, computed at resolution $N = 2^{3J}$, N being the number of grid points and J the number of octaves in each of the three spatial directions. Each component is developed into an orthogonal wavelet series with largest scale $l_{max} = 2^0$ and smallest scale $l_{min} = 2^{J-1}$ using a 3D multi-resolution analysis
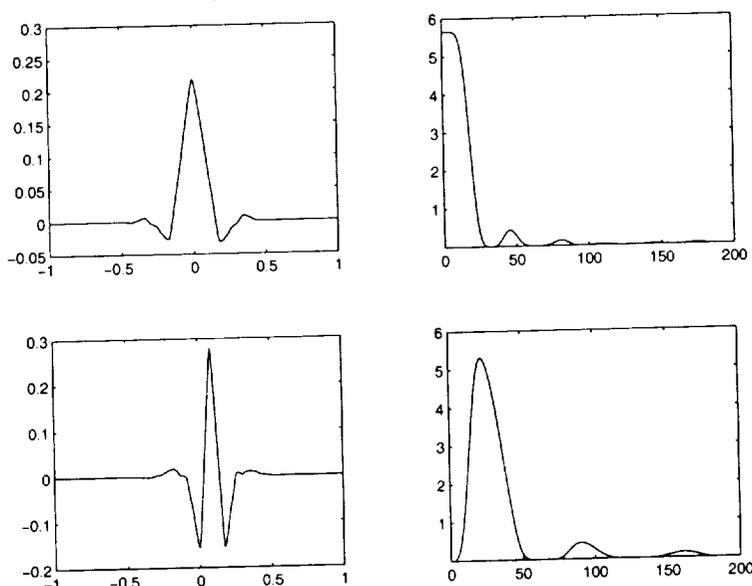
FIGURE 1. Coiflet 12. Top: Scaling function ϕ. Bottom: Corresponding wavelet ψ. (Left: in physical space, right: in Fourier space.)

(MRA) (Daubechies (1992), Farge (1992)):

$$\omega(\vec{x}) = \bar{\omega}_{0,0,0}\,\phi_{0,0,0}(\vec{x}) + \sum_{j=0}^{J-1}\sum_{i_x=0}^{2^j-1}\sum_{i_y=0}^{2^j-1}\sum_{i_z=0}^{2^j-1}\sum_{\mu=1}^{2^n-1} \tilde{\omega}^{\mu}_{j,i_x,i_y,i_z}\,\psi^{\mu}_{j,i_x,i_y,i_z}(\vec{x}) \quad , \quad (2.1)$$

with $\phi_{j,i_x,i_y i,i_z}(\vec{x}) = \phi_{j,i_x}(x)\,\phi_{j,i_y}(y)\,\phi_{j,i_z}(z)$, and

$$\psi^{\mu}_{j,i_x,i_y,i_z}(\vec{x}) = \begin{cases} \psi_{j,i_x}(x)\,\phi_{j,i_y}(y)\,\phi_{j,i_z}(z) & ;\ \mu = 1 \quad, \\ \phi_{j,i_x}(x)\,\psi_{j,i_y}(y)\,\phi_{j,i_z}(z) & ;\ \mu = 2 \quad, \\ \phi_{j,i_x}(x)\,\phi_{j,i_y}(y)\,\psi_{j,i_z}(z) & ;\ \mu = 3 \quad, \\ \psi_{j,i_x}(x)\,\phi_{j,i_y}(y)\,\psi_{j,i_z}(z) & ;\ \mu = 4 \quad, \\ \psi_{j,i_x}(x)\,\psi_{j,i_y}(y)\,\phi_{j,i_z}(z) & ;\ \mu = 5 \quad, \\ \phi_{j,i_x}(x)\,\psi_{j,i_y}(y)\,\psi_{j,i_z}(z) & ;\ \mu = 6 \quad, \\ \psi_{j,i_x}(x)\,\psi_{j,i_y}(y)\,\psi_{j,i_z}(z) & ;\ \mu = 7 \quad, \end{cases} \qquad (2.2)$$

where $\phi_{j,i}$ and $\psi_{j,i}$ are the one-dimensional scaling function (see Fig. 1 top) and the corresponding wavelet (see Fig. 1 bottom), respectively. Due to the orthogonality, the scaling coefficients are given by $\bar{\omega}_{0,0,0} = \langle \omega\,,\ \phi_{0,0,0}\rangle$ and the wavelet coefficients are given by $\tilde{\omega}^{\mu}_{j,i_x,i_y,i_z} = \langle \omega\,,\ \psi^{\mu}_{j,i_x,i_y,i_z}\rangle$, where $\langle\cdot,\cdot\rangle$ denotes the L^2-inner product.

For the orthogonal wavelet basis we use Coiflets 12 (Daubechies (1992)), *i.e.* wavelets with $M = 4$ vanishing moments and a filter length of $3M = 12$ (see Fig. 1 bottom). The advantage of the Coiflets is that they are almost symmetric and that the corresponding scaling functions (see Fig. 1 top) have also M vanishing moments.

We then split the vorticity field into coherent vorticity $\vec{\omega}_C(\vec{x})$ and incoherent vorticity $\vec{\omega}_I(\vec{x})$ by applying nonlinear thresholding to the wavelet coefficients. The choice of the threshold value ϵ is based on theorems derived by Donoho and Johnstone (Donoho (1993), Donoho & Johnstone (1994)) and is $\epsilon = (4/3Z\log_{10} N)^{1/2}$. Note that ϵ only depends on the total enstrophy Z and the number of grid points N, and there are no adjustable
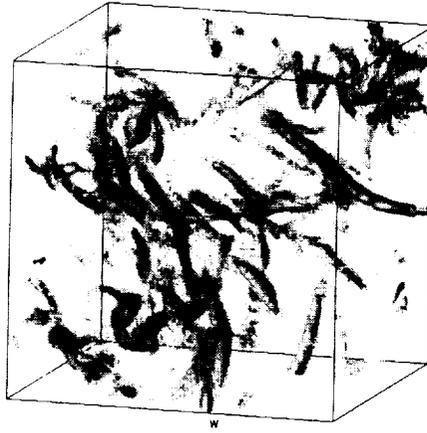
FIGURE 2. Total field: vorticity modulus (isosurfaces $|\vec{\omega}| = 3\sigma, 4\sigma, 5\sigma$, σ being the variance).

parameters. The coherent vorticity field $\vec{\omega}_C$ is reconstructed from the wavelet coefficients whose modulus is larger than ϵ and the incoherent vorticity field $\vec{\omega}_I$ from the wavelet coefficients whose modulus is smaller than or equal to ϵ. The two fields thus obtained, $\vec{\omega}_C$ and $\vec{\omega}_I$, are orthogonal, which ensures separation of the total enstrophy into $Z = Z_C + Z_I$ because the interaction term $\langle \vec{\omega}_C, \vec{\omega}_I \rangle$ vanishes.

Finally we use the Biot-Savart law $\vec{V} = \nabla \times (\nabla^{-2}\vec{\omega})$ to reconstruct the coherent $(\vec{V}_C)$ and incoherent $\vec{V}_I$ velocity fields from the corresponding vortices. Since wavelets are almost eigenfunctions of the Biot-Savart kernel (Daubechies (1992)), *i.e.* their localization in both physical and spectral space is well preserved (see Fig. 1), the total energy may be written $E = E_C + E_I - \varepsilon$, with $E = \langle \vec{V}, \vec{V} \rangle$ and $\varepsilon < 0.6\%E$ (see Table I).

The implementation of the CVS decomposition is based on the fast wavelet transform of each vorticity component, thresholding of the coefficients, and the inverse fast wavelet transform for the reconstruction of the coherent and incoherent vortices. The computational cost of the fast wavelet transform is $O(N)$, where N is the number of grid points. The constant of the leading order term corresponds to the filter length $3M$ and depends on the wavelet we use.

3. Application to 3D homogeneous turbulence

We now apply the CVS decomposition to 3D forced homogeneous isotropic turbulence, computed by direct numerical simulation (DNS) at microscale Reynolds number $R_\lambda = 150$ with resolution $N = 256^3$ (for details see Jimenez & Wray (1993)).

In Fig. 2 we plot the modulus of the vorticity fluctuations in the total flow field on a 64^3 subcube. We observe that the field contains well defined vortex tubes, as has been previously observed in laboratory and numerical experiments (Douady, Couder & Brachet (1991), Vincent Meneguzzi (1991)), which are responsible for much of the intermittency of this flow. After decomposing the vorticity field into an orthogonal wavelet series, we calculate the square of each wavelet amplitude, which corresponds to the enstrophy retained in that mode. Subsequently, we sort them by decreasing order of magnitude and compute their partial sum to obtain the compression curve of the wavelet basis. In Fig. 3
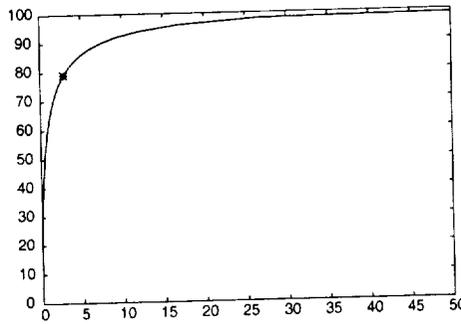
FIGURE 3. Compression curve: % retained enstrophy versus % number of retained wavelets. The star corresponds to the Donoho-Johnstone threshold.

we plot the percentage of retained enstrophy versus the fraction of retained wavelet modes. This curve shows that very few wavelet modes contain most of the enstrophy and that, above 10% of the modes, it saturates rapidly. This saturation corresponds to a quasi-equipartition of the enstrophy, which is characteristic of random fields. In Fig. 3 we indicate by a star the Donoho-Johnstone threshold. This cutoff retains 3% of the wavelet coefficients and 79% of the enstrophy. The coherent vorticity $\vec{\omega}_C$ is then reconstructed from the retained wavelet coefficients, and the incoherent vorticity $\vec{\omega}_I$ is the remainder.

In Table 1 we find that only 3% wavelet modes correspond to the coherent flow, which retains 98.9% of the energy and 79.1% of the enstrophy, while the remaining 97.1% incoherent modes have only 0.5% of the energy and 21% of the enstrophy. The ratio of statistical moments show that the velocity and vorticity skewness is negligible and that this property is preserved by the CVS decomposition. The coherent velocity has the same flatness ($F = 2.9$) as the total velocity, but the incoherent velocity presents a much smaller flatness ($F = 3.4$). The coherent vorticity has a strong flatness ($F = 9.6$) while the incoherent vorticity, likewise, has a reduced flatness ($F = 4.8$).

In Fig. 4 we display the modulus of the coherent (left) and incoherent (right) vorticity fields. Note that the values of the vorticity isosurfaces are the same for the total and the coherent fields while they have been reduced by a factor 2 for the incoherent field since its amplitude is much smaller. In the coherent vorticity (Fig. 4, left) we recognize the same vortex tubes as those present in the total field. In contrast, the incoherent vorticity (Fig. 4, right) is structureless and does not exhibit any organized structures. Hence, the CVS decomposition disentangles the intermittent from the non intermittent contributions, with all the vortex tubes retained in the coherent modes whatever the scale where they are active.

The energy spectra for the total, coherent and incoherent velocity fields, computed using the Biot-Savart law from the corresponding vorticity fields, are plotted in Fig. 5 (left). The spectrum of the coherent contribution is nearly identical to the spectrum of the total flow in the inertial range, i.e. it has $k^{-5/3}$ behavior. Only in the dissipative range does the coherent spectrum decay more rapidly than the incoherent one, since we conjecture that some of the coherent energy is transferred into incoherent energy which is then dissipated. The incoherent contribution exhibits a k^2 scaling which corresponds to energy equipartition. The incoherent velocity field is decorrelated, which makes sense since the incoherent vorticity is structureless (see Fig. 4, right).

To check the dynamical behavior of the coherent and incoherent contributions, we computed their energy transfer in wavenumber space. For practical reasons this has been

quantity	total	coherent	incoherent	large scales	small scales
% of coefficients	100 %	2.9 %	97.1 %	2.9 %	97.1 %

	$\vec{\omega}$	$\vec{\omega}_C$	$\vec{\omega}_I$	$\vec{\omega}_L$	$\vec{\omega}_S$
Enstrophy Z	4895	3872	1024	3455	1440
Enstrophy (percentage)	100 %	79.1 %	20.9 %	70.6 %	29.4 %
Skewness S	-.048	-.056	0.000	-.041	-.002
Flatness F	8.7	9.6	4.8	6.1	9.6

	$\vec{V}$	$\vec{V}_C$	$\vec{V}_I$	$\vec{V}_L$	$\vec{V}_S$
Energy E	43.01	42.56	0.23	42.69	0.33
Energy (percentage)	100.0 %	98.9 %	0.5 %	99.2 %	0.8 %
Skewness S	0.051	0.052	0.000	0.053	0.003
Flatness F	2.9	2.9	3.4	2.8	6.8

TABLE 1. Statistical properties of the vorticity and velocity fields for CVS (left) and POD (right) decompositions.

done at reduced resolution $N = 128^2$. Figure 5 (right) shows that the coherent flow is responsible for most of the energy transfer, giving an energy cascade from large to small scales, and almost vanishes in the viscous range. In contrast, the incoherent flow does not contribute to the energy transfer in the inertial range, but dominates in the dissipative range. From these observations, we put forward the following scenario for the turbulent cascade: the energy injected into the large scales is nonlinearly transferred towards the small scales by nonlinear interactions between the vortex tubes. At the smallest scales, this becomes transfer of coherent energy into incoherent energy which is then dissipated at small scale. We conjecture that, on the contrary, the incoherent background flow does not transfer energy into the coherent flow as it is structureless and well decorrelated. To confirm this we are planning to analyze the nonlinear and the linear terms of 3D Navier-
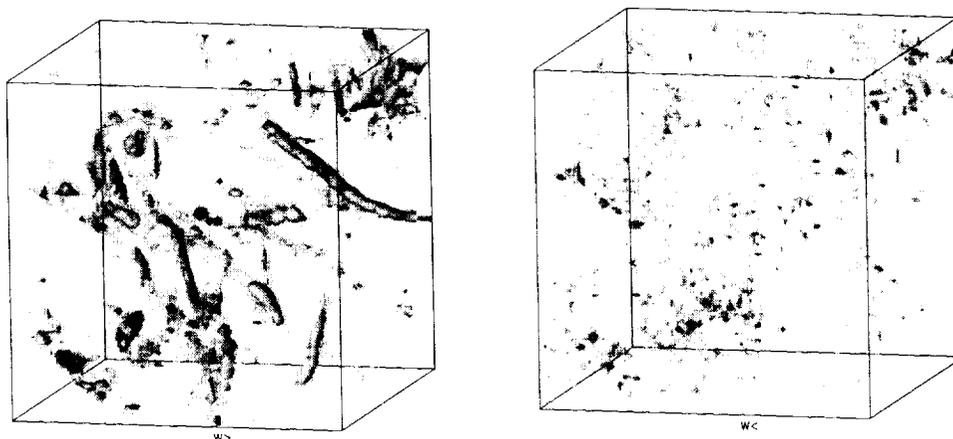
FIGURE 4. CVS decomposition: coherent (left) and incoherent (right) contributions (isosurfaces $|\vec{\omega}| = 3\sigma, 4\sigma, 5\sigma$ and $3/2\sigma, 2\sigma, 5/2\sigma$, respectively).
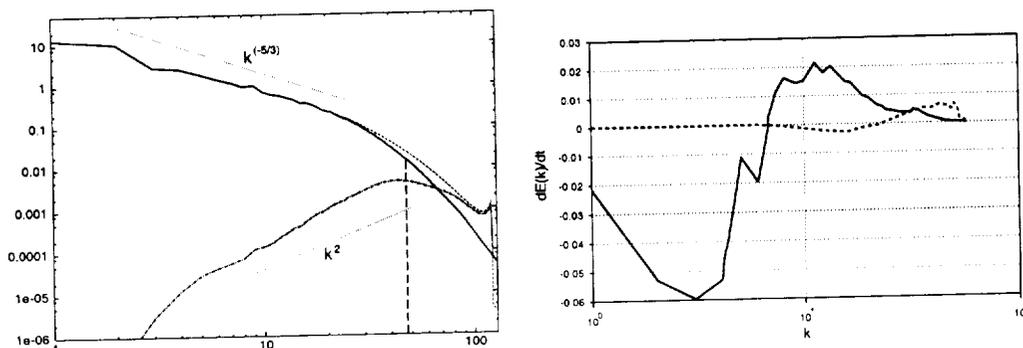
FIGURE 5. Energy spectra $E(k)$,left (Total: - - - - ; coherent: ———— ; incoherent: —·—— ; Fourier cut: ———) and energy transfers $d_t E(k)$, right (coherent: ———— ; incoherent: - - - -).

Stokes equations in wavelet space, as we have done for 2D Navier-Stokes equations in the turbulent regime (Schneider & Farge (1998)).

Figure 6 (left) shows the PDF of the velocity in semilogarithmic coordinates. The coherent velocity has the same Gaussian distribution as the total velocity. The PDF of the incoherent velocity is also Gaussian, but its variance is reduced by a factor 13. In contrast to the velocity, the PDF of vorticity (Fig. 7, left) is a stretched exponential with significant tails. The coherent vorticity has the same PDF as the total vorticity including the tails, while the incoherent vorticity has an exponential PDF with much weaker tails.

Since the CVS filtering is based on wavelet denoising and decorrelating without any dynamical assumption or pattern recognition procedure, we now check *a posteriori* that we have actually separated the vortex tubes from the background flow. The coherent vortex tubes can be described as local steady solutions of Euler equations which correspond to regions where there is a depletion of nonlinearity, which happens when the vorticity and velocity vectors are aligned. This situation maximizes the flow helicity $H = \vec{V} \cdot \vec{\omega}$ and corresponds to flow Beltramization (Moffatt H. K. (1985)). To study this tendency towards alignment of the vorticity $\vec{\omega}$ and the velocity $\vec{V}$, we plot in Fig. 8 the PDF of
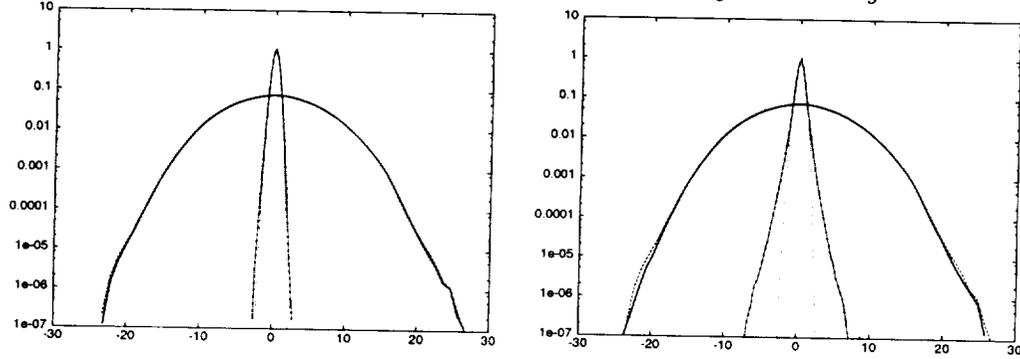
FIGURE 6. PDF of velocity: CVS (left) and POD (right) decompositions. Total: ---- ;
coherent: ——— ; incoherent: ——·— ; Gaussian fit: ········ .
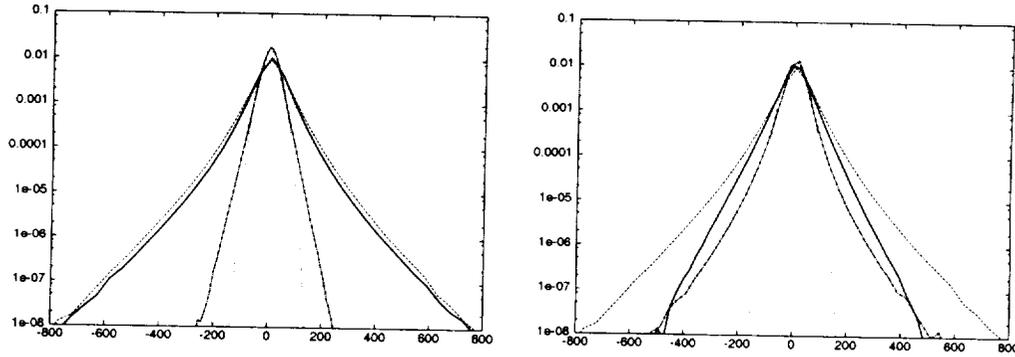
FIGURE 7. PDF of vorticity: CVS (left) and POD (right) decompositions. Total: ---- ;
coherent: ——— ; incoherent: ——·— ; Gaussian fit: ········ .
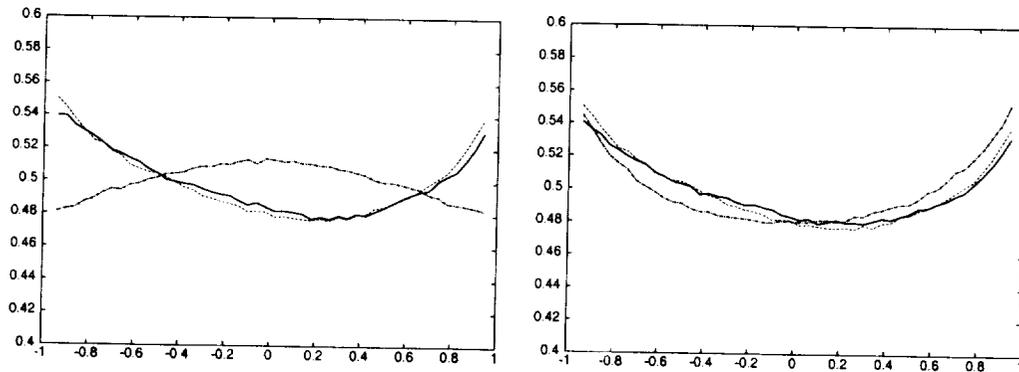
FIGURE 8. PDF of cosine of the angle between velocity and vorticity vectors: CVS (left) and
POD (right) decompositions. Total: ---- ; coherent: ——— ; incoherent: ——·— .

$\cos\alpha = \frac{\vec{\omega}\cdot\vec{V}}{|\vec{\omega}||\vec{V}|}$. We observe that the coherent contribution has the same tendency towards Beltramization as the total flow, which is characterized by the two maxima encountered in both PDFs for $\alpha = 0°$ (alignment) and $180°$ (anti-alignment). In contrast, the incoherent contribution is more evenly distributed with a maximum at $\alpha = 90°$, which indicates a tendency towards a local two-dimensionalization since the probability that the vortex stretching term $\vec{\omega} \cdot \nabla\vec{V}$ vanishes is large. This observation, together with the evidence for strong dissipation in the incoherent contribution (see transfers in Fig. 5),

agrees with a remark of Moffatt: *Euler flows contain blobs of maximal helicity (positive or negative) which may be interpreted as 'coherent structures', separated by regular surfaces on which vortex sheets, the site of strong viscous dissipation, may be located* (Moffatt H. K. (1985)). Following this picture the coherent vorticity corresponds to the coherent structures, which tend to maximize helicity where vorticity and velocity vectors tend to align with each other, while the incoherent vorticity corresponds to foliated regions which tend to maximize dissipation.

The results discussed here confirm those we obtained for the CVS decomposition of 3D forced homogeneous isotropic turbulent flow computed by DNS at microscale Reynolds number $R_\lambda = 150$ (Vincent Meneguzzi (1991)) with resolution $N = 240^3$ (Farge, Schneider & Pellegrino (2000), Farge & Schneider (2000), Farge, Pellegrino & Schneider (2000)).

4. Divergence problem

Due to the fact that the CVS filtering is nonlinear and the vector valued wavelet basis we have used here (the Coifman 12 wavelet, see Fig. 1) is not divergence-free, *i.e.* $\nabla \cdot \vec{\psi} \neq 0$, the CVS filtering does not yield coherent and incoherent vortices that are divergence-free. We found that, for the case studied here, the divergent contribution of the vorticity field remains below 3% of the total enstrophy. The same problem is also encountered for vortex methods applied to 3D turbulent flows (Winckelmans (1995)). However, the corresponding coherent and incoherent velocity fields are divergence-free since they were reconstructed using the Biot-Savart kernel.

There are several ways to insure that the coherent vorticity remains divergence-free:

- use divergence-free orthogonal wavelets (Lemarié (1992)),
- decompose ω into $\omega = \omega_{div=0} + \nabla\phi$. Then ϕ can be calculated by taking the divergence which leads to a Poisson equation $\nabla^2\phi = \nabla \cdot \omega$,
- apply the previous decomposition, not to the solution, but to the wavelet basis itself, which can be done as a precalculation since the wavelet decomposition is a linear transformation.

We are planning to explore these solutions in future work. It may also be that the divergent contribution of the coherent vorticity field does not significantly affect the flow evolution. To check this we will compare two CVS decompositions for the same flow, one using divergence-free wavelets and the other one using the Coifman 12 wavelet as here, and compute the contribution of the divergent coherent vorticity to the nonlinear terms to see if it remains small.

5. Comparison between CVS and POD decompositions

The procedure CVS decomposition uses to separate turbulent flows into organized and random fluctuations differs from the POD (for details see Berkooz, Holmes & Lumley (1993)). POD, also called Principal Component Analysis (PCA) or Karhunnen-Loève decomposition, computes the auto-correlation tensor of an ensemble of realizations, then diagonalizes it and retains only those eigenmodes corresponding to the $N_>$ largest eigenvalues. This yields the best basis for the ensemble of realizations with respect to the L^2-norm.

In the POD procedure the retained modes are defined *a priori* for all realizations. In contrast, CVS performs the separation *a priori* and selects from a given set of basis functions, the orthogonal wavelets, those having the strongest coefficients. Hence the selection
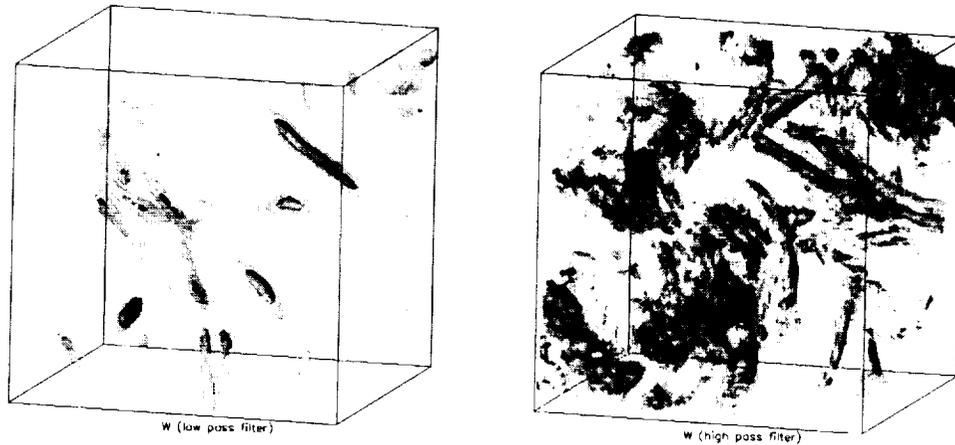
FIGURE 9. POD decomposition: low wavenumber (left) and high wavenumber (right) contributions (isosurfaces $|\vec{\omega}| = 3\sigma, 4\sigma, 5\sigma$ and $3/2\sigma, 2\sigma, 5/2\sigma$, respectively).

procedure is nonlinear, as the retained basis functions depend on the flow realization. From a statistical point of view, the CVS method is based on a Bayesian approach while POD is based on a non-Bayesian (also called frequentist) approach. For the time integration the CVS *a priori* retains the wavelets whose coefficients are larger than the threshold ϵ and some of their neighbors. This selection of the active wavelets is nonlinear because it depends on the direction of the energy and enstrophy transfers in wavelet space which evaluated at the previous time step. Note that the computational cost of POD decomposition scales as N^3, while it scales as N for the CVS decomposition.

For a homogeneous isotropic turbulent flow such as the one studied here, the POD yields the Fourier basis since the correlation tensor is translationally invariant. So we now project the vorticity field on a Fourier basis and split the flow into low and high wavenumber contributions. Note that for this linear separation it doesn't matter whether we decompose the vorticity or the velocity fields, as the Fourier basis diagonalizes the curl operator. To get the same compression ratio as CVS, *i.e.* 3% of the modes retained, the cut-off wavenumber is $k_c = 48$ (see Fig. 5, left). This is a particular case of LES filtering, and the 97% high wavenumber modes are the LES subgrid scale modes.

In Fig. 9 we plot the modulus of vorticity for the POD decomposition. In the low wavenumber modes (left) we observe some vortex tubes. If we compare them with those retained in the CVS coherent vorticity (Fig. 4, left) we find that only a subset of the vortex tubes is extracted and that their structure is smoothed due to the low pass filtering produced by POD in this case. Consequently, the small scale contributions of the vortex tubes are contained in the high wavenumber modes (Fig. 9, right), which exhibit organized structures similar to those found in the total vorticity field (Fig. 2).

Table 1 shows that POD retains 99.2% of the energy, while CVS retains only 98.9%. On the other hand, CVS retains 79.1% of the enstrophy, while POD retains only 70.6%Z. The skewness of velocity and vorticity is negligible, a property preserved by both the CVS and POD decompositions.

In Fig. 7 the vorticity PDFs show that both the large and small scale contributions have strong variance, with the peak of the small scale PDF being slightly larger than that of the large scale PDF. It is important to note that the vorticity PDFs are interchanged

compared to the CVS decomposition. The vorticity PDF of the large scales retained by POD is exponential (with flatness 6.1), while it is stretched exponential (with flatness 9.6) for the discarded small scales. The vorticity PDF of the coherent modes retained by CVS is stretched exponential (with flatness 9.6), while it is exponential (with flatness 4.8) for the discarded incoherent vorticity.

Moreover, the velocity PDFs for POD (Fig. 6, right) show that, although the large scale contribution is Gaussian (with flatness 2.9), this is not the case for the small scale contribution which maintains a stretched exponential behavior as for the vorticity PDF (with flatness 6.8). In contrast, the velocity PDFs for CVS (6, left) are Gaussian for both the coherent and the incoherent modes. This non-Gaussian behavior of both the vorticity and velocity PDFs of the POD/LES small scales may make modeling of its effect on the resolved large scales difficult. This difficulty is much less acute with the CVS decomposition since the PDFs of the incoherent contribution is Gaussian for the velocity (6, left) and exponential for the vorticity (7, left).

Concerning the alignment properties between vorticity and velocity, we found that both the large and small scale contributions have the same PDF of $\cos \alpha$ as the total flow (8, right). This is further evidence that coherent vortex tubes are present in both components since, in contrast to CVS, the POD decomposition does not separate different topological behaviors.

6. Conclusion

We have demonstrated that CVS decomposes a 3D forced homogeneous isotropic turbulent flow into organized vortex tubes and a random incoherent background flow. For the same 3D flow, POD, which in this case uses the Fourier basis and is essentially a LES decomposition, does not extract all of the vortex tubes since a lot of organized structures remain in the small scales. Furthermore, the small scales have a stretched exponential probability distribution for both the velocity and the vorticity. In contrast, the incoherent modes of the CVS decomposition have an exponential PDF for the vorticity and a Gaussian distribution for the velocity. Moreover, they are structureless and their energy spectrum shows an energy equipartition, which is not the case for the POD small scales.

In conclusion, we conjecture that modeling of the effect of the discarded modes on the resolved modes may be better justified for CVS than for POD. One should keep in mind that LES of turbulent flows is performed by integrating only one flow realization at a time. The statistics are obtained afterwards by space, time, or ensemble averaging several realizations over time if the flow is statistically steady. Therefore, POD, which is by construction the best basis to represent with a reduced number of modes an ensemble of flow realizations, is not necessarily the best decomposition for computing the flow evolution realization by realization.

We think that the classical strategy of projecting the flow onto a basis and truncating the series to a fixed number of resolved modes can be improved. CVS adopts a nonlinear strategy, which adapts the number of resolved modes to each flow realization, by projecting the flow at each time step onto a wavelet basis, retaining only the strongest wavelet coefficients. In this case all degrees of freedom which contribute to the flow nonlinearity, *i.e.* the coherent modes, are computed whatever their scale, while the remaining degrees of freedom, *i.e.* the incoherent modes, are discarded and modeled, perhaps by a linear dissipation.

The CVS procedure that we have applied to 2D turbulent flows (Farge, Schneider &

Kevlahan (1999)) can be generalized to 3D turbulent flows since we have shown that the incoherent modes are structureless, decorrelated, have an energy equipartition spectrum, and have a Gaussian PDF of the velocity.

A crucial step in the demonstration of the potential of the CVS method is to design an adaptive wavelet solver for the 3D Navier-Stokes equations written in vorticity-velocity formulation, which combines an Eulerian projection of the solution with a Lagrangian procedure for the basis adaption. We have done this for 2D turbulent flows, and we are presently developing it for 3D turbulent flows.

Acknowledgments

REFERENCES

BASS, J. 1945 Les fonctions aléatoires et leur interprétation mécanique. *Revue Sci.* **83**, 3-20.

BERKOOZ, G., HOLMES, P. & LUMLEY, J. L. 1993, The proper orthogonal decomposition in the analysis of turbulent flows. *Ann. Rev. Fluid Mech.* **25**, 539-575.

DAUBECHIES, I. 1992 *Ten Lectures on wavelets.* SIAM, Philadelphia.

DOUADY, S., COUDER, Y. & BRACHET, M. E. 1991 Direct observation of the intermittency of intense vorticity filaments in turbulence. *Phys. Rev. Lett.* **67**, 983-990.

DONOHO, D. 1993 Unconditional bases are optimal bases for data compression and statistical estimation. *Appl. Comput. Harmon. Anal.* **1**, 100-115.

DONOHO, D. & JOHNSTONE, I. 1994 Ideal spatial adaption via wavelet shrinkage. *Biometrica.* **81**, 425-455.

DRYDEN, H. L. 1948 Recent advances in the mechanics of boundary layer flow. *Adv. in Applied Mech.* **1**, 1-40.

FARGE, M. & RABREAU, G. 1988 Transformée en ondelettes pour détecter et analyser les structures cohérentes dans les écoulements turbulents bidimensionnels. *C. R. Acad. Sci. Paris Série II b.* **307**, 433-440.

FARGE, M., GUEZENNEC, Y., HO, C. M., & MENEVEAU, C. 1990 Continuous wavelet analysis of coherent structures. *Summer Program Proceedings*, Center for Turbulence Research, NASA Ames/Stanford Univ. 331-343.

FARGE, M. 1992 Wavelet Transforms and their Applications to Turbulence. *Ann. Rev. of Fluid Mech.* **24**, 395-457.

FARGE, M., GOIRAND, E., MEYER, Y., PASCAL, F. & WICKERHAÜSER, V. M. 1992 Improved predictability of two-dimensional turbulent flows using wavelet packet compression. *Fluid Dyn. Res.* **10**, 229-345.

FARGE, M., SCHNEIDER, K., & KEVLAHAN, N. 1999 Non-Gaussianity and Coherent Vortex Simulation for two-dimensional turbulence using an adaptive orthonormal wavelet basis. *Phys. Fluids.* **11**(8), 2187-2201.

FARGE, M. & SCHNEIDER, K. 2000 Coherent Vortex Simulation (CVS), a semi-deterministic turbulence model using wavelets. *Flow, Turb. Combust.*, submitted.

FARGE, M., SCHNEIDER, K. & PELLEGRINO, G. 2000 Vortex tube extraction in three-

dimensional turbulence using orthogonal wavelets. *Advances in Turbulence VIII*, eds. C. Dopazo *et al.*, CIMNE, Barcelona. 797-800.

FARGE, M., PELLEGRINO, G. & SCHNEIDER, K. 2000 Coherent vortex extraction in 3D turbulent flows using orthogonal wavelets. *Phys. Rev. Lett.*, submitted.

JIMENEZ, J. & WRAY, A. A. 1993 The structure of intense vorticity in isotropic turbulence. *J. Fluid Mech.* **255**, 65-90.

LEMARIÉ, P. G. 1992 Analyses multirésolutions non orthogonales, commutation entre projecteurs de dérivation et ondelettes à divergence nulle. *Revista Mat. Iberoamericana.* **8**, 221-236.

MOFFATT, H. K. 1985 Magnetostatic equilibria and analogous Euler flows of arbitrary complex topology. *J. Fluid Mech.* **150**, 359-378.

SCHNEIDER, K., KEVLAHAN, N. & FARGE, M. 1997 Comparison of an adaptive wavelet method and nonlinearly filtered pseudo-spectral methods for two-dimensional turbulence. *Theoret. Comput. Fluid Dyn.* **9**, 191-206.

SCHNEIDER, K. & FARGE, M. 1997 Wavelet forcing for numerical simulation of two-dimensional turbulence. *C. R. Acad. Sci. Paris, Série II b.* **325**, 263-270.

SCHNEIDER, K. & FARGE, M. 1998 Wavelet approach for modelling and computing turbulence. *Lecture Series 1998-05 Advances in turbulence modelling*, von Karman Institute for Fluid Dynamics, Bruxelles. 1-132.

SCHNEIDER, K. & FARGE, M. 2000 Numerical simulation of temporally growing mixing layer in an adaptive wavelet basis. *C. R. Acad. Sci. Paris Série II b.* **328**, 263-269.

VINCENT, A. & MENEGUZZI, M. 1991 The spatial structure and statistical properties of homogeneous turbulence. *J. Fluid Mech.* **225**, 1-25.

WINCKELMANS, G. S. 1995 Some progress in large-eddy simulation using the 3D vortex particle method. *Annual Research Briefs*, Center for Turbulence Research, NASA Ames/Stanford Univ. 391-415.

CVS filtering of 3D turbulent mixing layers using orthogonal wavelets

By Kai Schneider†, Marie Farge‡, Giulio Pellegrino¶ AND Michael Rogers‖

Coherent Vortex Simulation (CVS) filtering has been applied to DNS data of forced and unforced time-developing turbulent mixing layers. CVS filtering splits the turbulent flow into two orthogonal parts, one corresponding to coherent vortices and the other to incoherent background flow. We have shown that the coherent vortices can be represented by few wavelet modes and that these modes are sufficient to reproduce the vorticity probability distribution function (PDF) and the energy spectrum over the entire inertial range. The remaining incoherent background flow is homogeneous, has small amplitude, and is uncorrelated. These results are compared with those obtained for the same compression rate using large eddy simulation (LES) filtering. In contrast to the incoherent background flow of CVS filtering, the LES subgrid scales have a much larger amplitude and are correlated, which makes their statistical modeling more difficult.

1. Introduction

In the turbulent regime the solutions of Navier-Stokes equations exhibit coherent vortices whose nonlinear interactions are responsible for the flow evolution. Since these coherent vortices are well localized and excited on a wide range of scales, we have proposed to use the wavelet representation of the vorticity field to extract them (Farge, Schneider & Kevlahan (1999)). Orthogonal wavelet bases are well suited for this because they are made of self-similar functions well localized in both physical and spectral spaces (Farge (1992), Daubechies (1992)). In (Farge, Schneider & Kevlahan (1999)) we have introduced a new method, called Coherent Vortex Simulation (CVS), to compute turbulent flows. It is based on the wavelet filtered Navier-Stokes equations and their solution in an adaptive wavelet basis which is dynamically adapted during the flow evolution (Schneider & Farge (2000)). Here we first present the vector valued wavelet algorithm used to extract coherent vortices out of turbulent flows. Then we employ this algorithm to analyze DNS computations of two time-developing three-dimensional turbulent mixing layers (Rogers & Moser (1994)). The results are compared with those obtained for the same compression using an ideal low-pass filter, as used for LES computation. Finally, we draw some conclusions for developing CVS computations for three-dimensional turbulent flows.

2. Wavelet method for coherent vortex extraction

In (Farge, Schneider & Kevlahan (1999), Farge, Pellegrino & Schneider (2000)) we have proposed a wavelet-based method to extract coherent vortices out of 2D and 3D turbulent

† CMI, Université de Provence, Marseille, France
‡ LMD-CNRS, Ecole Normale Supérieure, Paris, France
¶ ICT, Universität Karlsruhe (TH), Germany
‖ NASA Ames Research Center, Moffett Field, CA

flows. The algorithm for the 3D case is described below. We consider the vorticity field $\vec{\omega}(\vec{x}) = \nabla \times \vec{V}$, computed at resolution $N = 2^{3J}$, N being the number of grid points and J the number of octaves. Each component is developed into an orthogonal wavelet series from the largest scale $l_{max} = 2^0$ to the smallest scale $l_{min} = 2^{J-1}$ using a 3D multi-resolution analysis (MRA) (Daubechies (1992), Farge (1992)):

$$\omega(\vec{x}) = \bar{\omega}_{0,0,0}\ \phi_{0,0,0}(\vec{x})\ +\ \sum_{j=0}^{J-1}\sum_{i_x=0}^{2^j-1}\sum_{i_y=0}^{2^j-1}\sum_{i_z=0}^{2^j-1}\sum_{\mu=1}^{2^n-1} \tilde{\omega}^\mu_{j,i_x,i_y,i_z}\ \psi^\mu_{j,i_x,i_y,i_z}(\vec{x})\ ,\quad (2.1)$$

with $\phi_{j,i_x,i_y,i_z}(\vec{x}) = \phi_{j,i_x}(x)\ \phi_{j,i_y}(y)\ \phi_{j,i_z}(z)$, and

$$\psi^\mu_{j,i_x,i_y,i_z}(\vec{x}) = \begin{cases} \psi_{j,i_x}(x)\ \phi_{j,i_y}(y)\ \phi_{j,i_z}(z) & ; \mu = 1 \ , \\ \phi_{j,i_x}(x)\ \psi_{j,i_y}(y)\ \phi_{j,i_z}(z) & ; \mu = 2 \ , \\ \phi_{j,i_x}(x)\ \phi_{j,i_y}(y)\ \psi_{j,i_z}(z) & ; \mu = 3 \ , \\ \psi_{j,i_x}(x)\ \phi_{j,i_y}(y)\ \psi_{j,i_z}(z) & ; \mu = 4 \ , \\ \psi_{j,i_x}(x)\ \psi_{j,i_y}(y)\ \phi_{j,i_z}(z) & ; \mu = 5 \ , \\ \phi_{j,i_x}(x)\ \psi_{j,i_y}(y)\ \psi_{j,i_z}(z) & ; \mu = 6 \ , \\ \psi_{j,i_x}(x)\ \psi_{j,i_y}(y)\ \psi_{j,i_z}(z) & ; \mu = 7 \ , \end{cases} \qquad (2.2)$$

where $\phi_{j,i}$ and $\psi_{j,i}$ are the one-dimensional scaling function and the corresponding wavelet, respectively. Due to orthogonality, the scaling coefficients are given by $\bar{\omega}_{0,0,0} = \langle \omega\,,\ \phi_{0,0,0}\rangle$ and the wavelet coefficients are given by $\tilde{\omega}^\mu_{j,i_x,i_y,i_z} = \langle \omega\,,\ \psi^\mu_{j,i_x,i_y,i_z}\rangle$, where $\langle \cdot,\cdot\rangle$ denotes the L^2-inner product.

We then split the vorticity field into $\vec{\omega}_C(\vec{x})$ and $\vec{\omega}_I(\vec{x})$ by applying a nonlinear thresholding to the wavelet coefficients. The threshold is defined as $\epsilon = (4/3Z \log N)^{1/2}$, and it only depends on the total enstrophy Z and on the number of grid points N without any adjustable parameters. The choice of this threshold is based on theorems (Donoho (1993), Donoho & Johnstone (1994)) proving optimality of the wavelet representation to denoise signals in the presence of Gaussian white noise since this wavelet-based estimator minimizes the maximal L^2-error for functions with inhomogeneous regularity. The coherent vorticity field $\vec{\omega}_C$ is reconstructed from the wavelet coefficients whose modulus is larger than ϵ and the incoherent vorticity field $\vec{\omega}_I$ from the wavelet coefficients whose modulus is smaller or equal to ϵ. The two fields thus obtained, $\vec{\omega}_C$ and $\vec{\omega}_I$, are orthogonal, which ensures a separation of the total enstrophy into $Z = Z_C + Z_I$ because the interaction term $\langle \vec{\omega}_C\,,\vec{\omega}_I\rangle$ vanishes. We then use Biot-Savart's relation $\vec{V} = \nabla \times (\nabla^{-2}\vec{\omega})$ to reconstruct the coherent velocity $\vec{V}_C$ and the incoherent velocity $\vec{V}_I$ for the coherent and incoherent vortices, respectively.

In the present paper we apply the above algorithm to two high resolution direct numerical simulations (DNS) of 3D turbulent flows with a Taylor microscale Reynolds number of about $R_\lambda = 150$. The first computation is a forced mixing layer computed at resolution $384 \times 120 \times 128$ and evolved for 40 eddy turnover times (Rogers & Moser (1994)). The vorticity field is interpolated onto a physical space grid that is either coarsened to $N = 64^3$ for flow visualization (Fig. 1, Fig. 2), or refined to $N = 512 \times 256 \times 128$ in order to compute the energy spectra and vorticity PDFs using the full resolution compatible with the dyadic wavelet representation (Fig. 3). The second computation is an unforced mixing layer computed at resolution $512 \times 180 \times 192$ and evolved for 60 eddy turnover times (Rogers & Moser (1994)). Again the vorticity has been interpolated onto different physical space grids for flow visualization ($N = 64^3$ for Fig. 5, Fig. 6, and Fig. 8), and statistical analysis ($N = 512 \times 256 \times 128$ for Fig. 7).
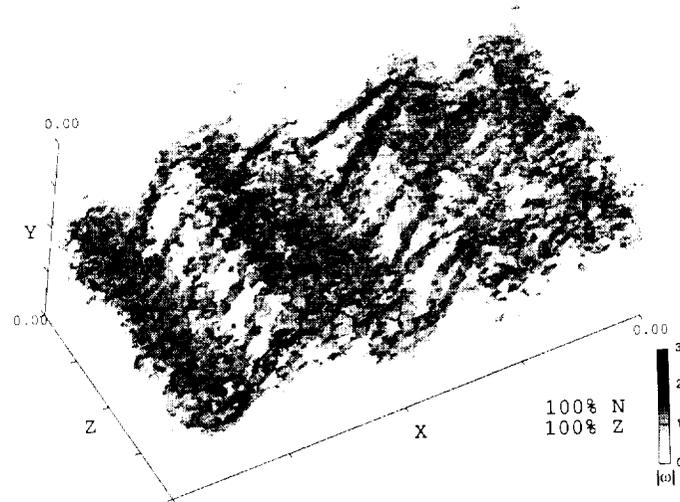
FIGURE 1. Total vorticity of the forced 3D mixing layer at resolution $N = 64^3$.

3. Application to the forced mixing layer

Figure 1 shows the modulus of vorticity for the total flow in the forced case (at low resolution $N = 64^3$). We observe well pronounced longitudinal vortex tubes, called ribs, which result from a 3D instability and are wrapped onto four transverse rollers that are produced by the 2D Kelvin-Helmholtz instability. The coherent vorticity (see Fig. 2 top), which is contained in 5.7% (at low resolution $N = 64^3$) or 3% (at high resolution $N = 512 \times 256 \times 128$) of the total number N of wavelet coefficients, captures most of the turbulent kinetic energy and enstrophy, even at high wavenumbers.

Moreover, the PDF of the coherent vorticity is similar to that of the total flow (see Fig. 3 bottom left). The incoherent vorticity (see Fig. 2 bottom), which is represented by 94.3% (at low resolution $N = 64^3$) or 97% (at high resolution $N = 512 \times 256 \times 128$) of the total number N of wavelet coefficients, contains little of the turbulent kinetic energy and enstrophy. It is nearly homogeneous with a very low amplitude and contains no structure. The PDF of the incoherent vorticity (Fig. 3 bottom left) follows an exponential law with a much reduced variance compared to the PDF of the total flow.

The similarity between the 1D energy spectra (Fig. 3 top left) in the streamwise direction for the coherent part of the flow and for the total flow indicates that the energetic turbulent motions are well captured by the filtering. In contrast, the incoherent part contains very little energy and is well uncorrelated with flat energy spectrum.

In Fig. 4 we display vertical profiles of the three vorticity components $\omega_x, \omega_y, \omega_z$ averaged in the streamwise and spanwise directions. Examination of the the spanwise component ω_z (Fig. 4, bottom) shows that the coherent vorticity exactly follows the total vorticity, while the incoherent vorticity oscillates weakly around zero with amplitudes less than 4% of the minimal value $\bar{\omega}_{z,min}$. The vertical component ω_y (Fig. 4, middle) of the total flow vanishes since the flow is homogeneous in the streamwise and spanwise directions. The coherent and incoherent components oscillate around zero with amplitudes of about 1% of $\bar{\omega}_{z,min}$. The streamwise component ω_x profiles (Fig. 4, top) are similar to the spanwise ones in that the coherent component follows the total one, while
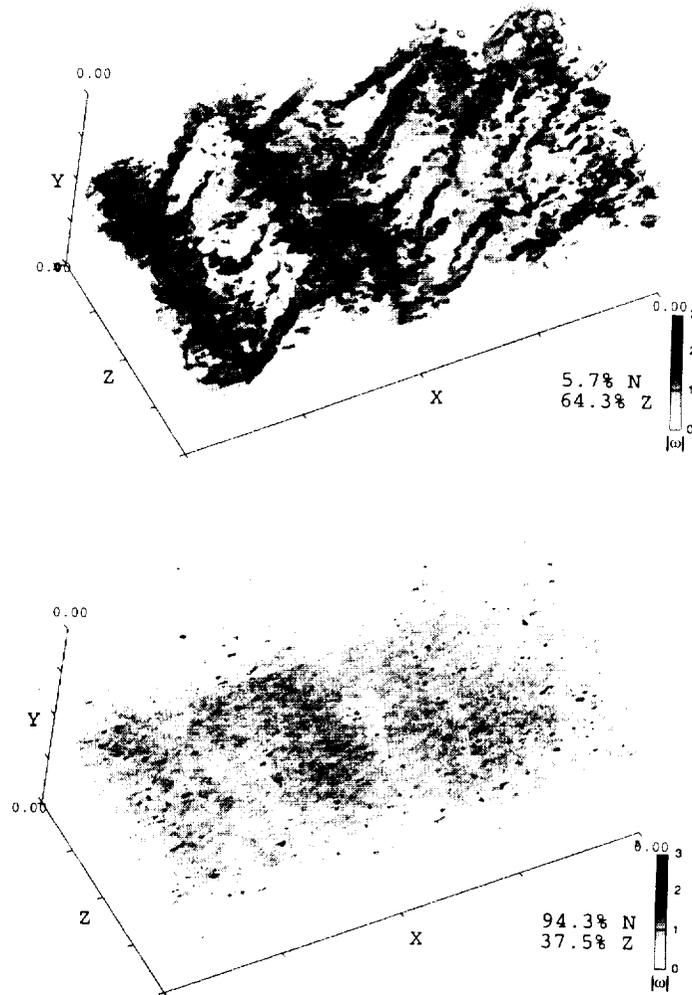
FIGURE 2. Forced mixing layer. Top: Coherent vorticity. Bottom: Incoherent vorticity.

the incoherent vorticity oscillates weakly around zero with amplitudes less than 4% of the minimal value $\bar{\omega}_{z,min}$.

4. Application to the unforced mixing layer

Figure 5 shows the modulus of vorticity for the total flow for the unforced mixing layer at resolution $N = 64^3$. In contrast to the forced mixing layer (Fig. 1), we observe much less pronounced longitudinal vortex tubes and transverse rollers, with little, if any, large-scale structures.

The coherent vorticity (Fig. 6 top), which is contained in 8% (at low resolution $N = 64^3$) or 3% (at high resolution $N = 512 \times 256 \times 128$) of the total number N of wavelet

1D energy spectra E(k_x)
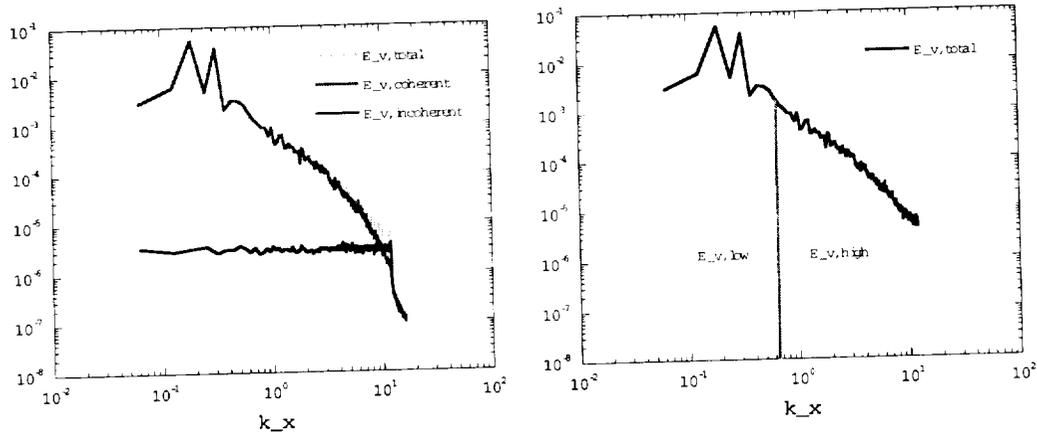
Vorticity PDF p(ω)
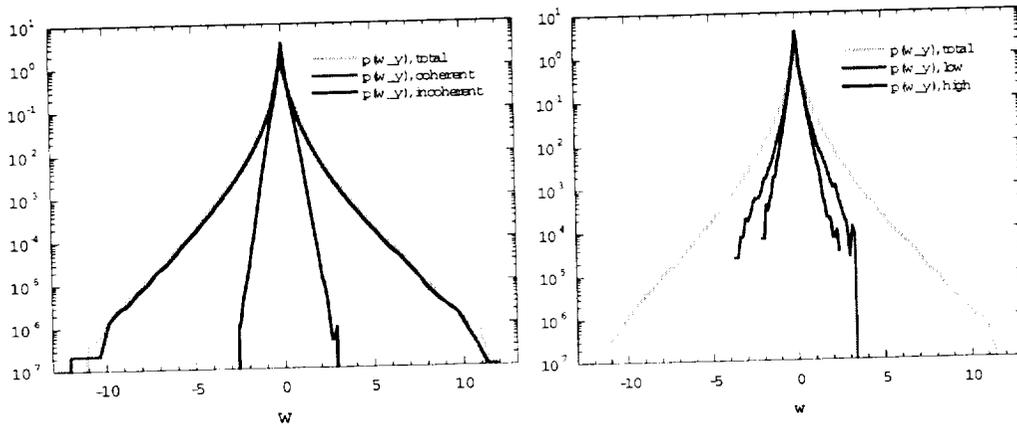
FIGURE 3. Comparison of CVS (left) with LES (right) filtering for the forced mixing layer at resolution $N = 512 \times 256 \times 128$. Energy spectra (top) and PDF of vorticity (bottom) of total, coherent (3% N) and incoherent (97% N) flow using CVS filtering and of low wavenumber and high wavenumber components using LES filtering.

coefficients, shows small-scale organized structures, while the incoherent vorticity (Fig. 6 bottom), which represents 92% (at low resolution $N = 64^3$) or 97% (at high resolution $N = 512 \times 256 \times 128$) of the total number N of wavelet coefficients, is homogeneous, structureless, and has a much weaker amplitude.

This is also confirmed by the vorticity PDF (Fig. 7 bottom left), where the coherent vorticity presents the same non-Gaussian distribution as the total vorticity. In contrast, the incoherent vorticity follows an exponential law with a much reduced variance compared to the total vorticity. Moreover, we have verified, as for the forced case, that the coherent flow has the same spectral distribution as the total flow for all but the highest dissipative wavenumbers (Fig. 7 top left), while the incoherent flow is uncorrelated and exhibits a flat energy spectrum.
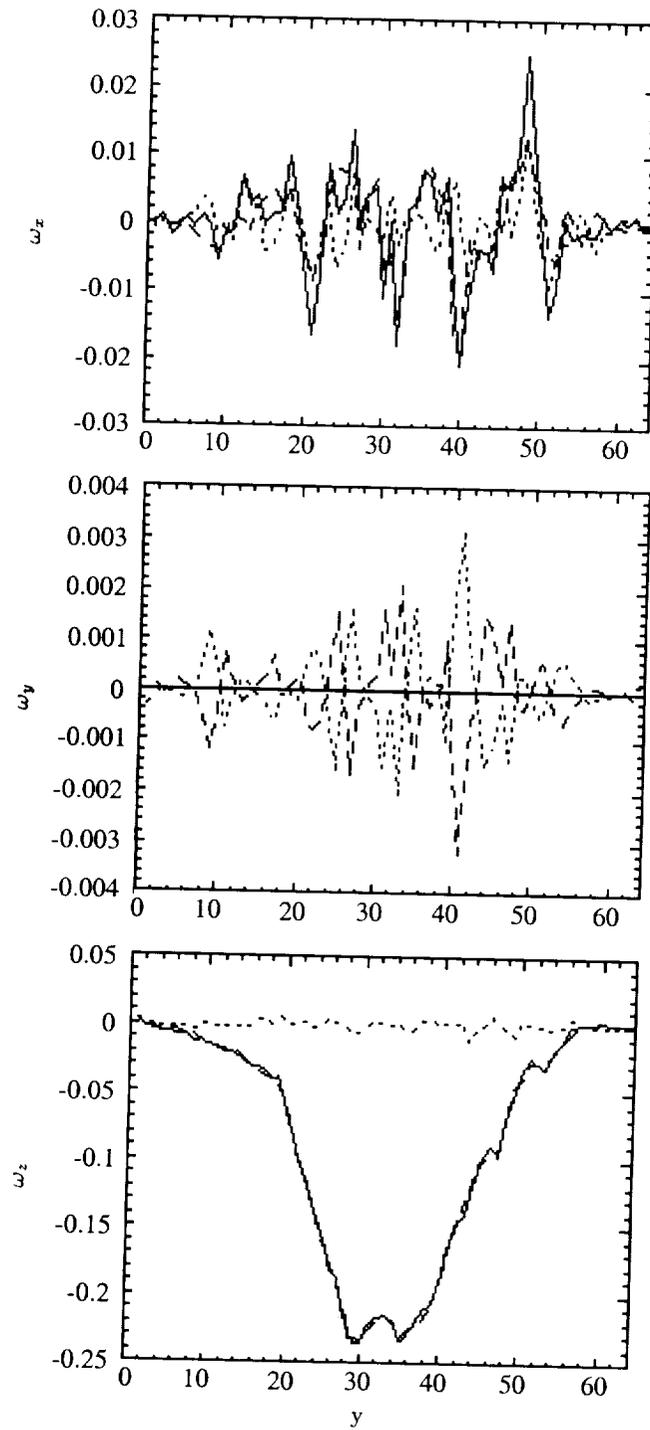
FIGURE 4. Averaged cuts of $\omega_x, \omega_y, \omega_z$ for total, coherent and incoherent vorticity for the forced mixing layer. Symbols: ———— , total; — — — , coherent; — - — - , incoherent.
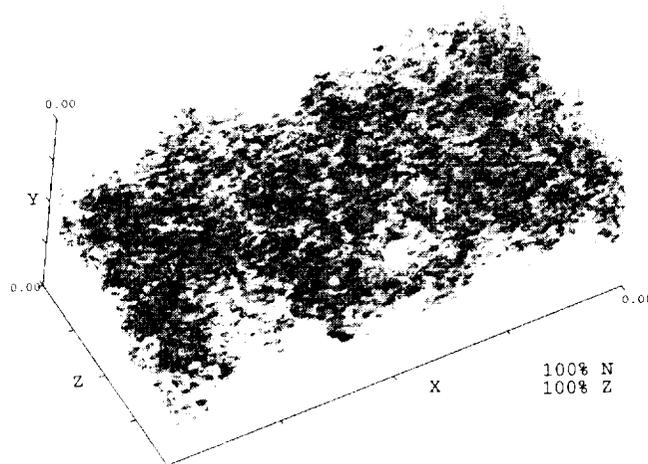
FIGURE 5. Total vorticity of the unforced 3D mixing layer at resolution $N = 64^3$.

5. Comparison between CVS and LES filtering

We now consider the results obtained with the LES filtering applied to the two time developing mixing layers we have studied. We choose the simplest LES filter and use a low-pass Fourier filter with a cut-off at the wavenumber $k = 25$, which therefore retains 9% of the $N = 512 \times 256 \times 128$ Fourier modes. The discarded Fourier modes correspond to the subgrid scales. This comparison is actually quite unfair for the CVS filtering since it retains even less, namely 3% of the N wavelet modes.

The LES filtering keeps only the scales larger than the cutoff wavenumber (Fig. 3 and 7 top, right), and hence the coherent vortices are smoothed. As a result, the extrema of vorticity are strongly reduced (see PDF on Fig. 3 and 7 bottom, right). In contrast, the CVS filtering retains the organized features, whatever their scales, and in this case the shape of the vorticity PDF is fully preserved even for large values of vorticity (Fig. 3 and 7 bottom, left).

If we now consider the results obtained with the LES filtering applied to the unforced mixing layer for the same compression rate, we observe that both low and high wavenumber components (Fig. 8) present localized structures and that the vorticity PDF for both components (Fig. 7 right) has about the same variation. In fact the high wavenumber modes, which ought to be modeled in LES to avoid numerical divergence, have a more non-Gaussian distribution than the low wavenumber modes which are resolved by LES; therefore, the turbulence modeling cannot be based on the assumption of a Gaussian behavior for the discarded high wavenumber modes.

Concerning turbulence parameterization, *i.e.* the statistical modeling of the effect of the discarded modes on the retained modes, we can draw the following conclusions:

• The CVS filtering disentangle the organized from random components of turbulent flows.

• The LES filtering does not produce subgrid-scale modes that are uncorrelated, and there are, therefore, many organized structures present in the subgrid-scale flow that can interact nonlinearly and transfer energy back to larger scales (backscatter).

• The incoherent modes discarded by CVS have very weak amplitude, are almost ho-
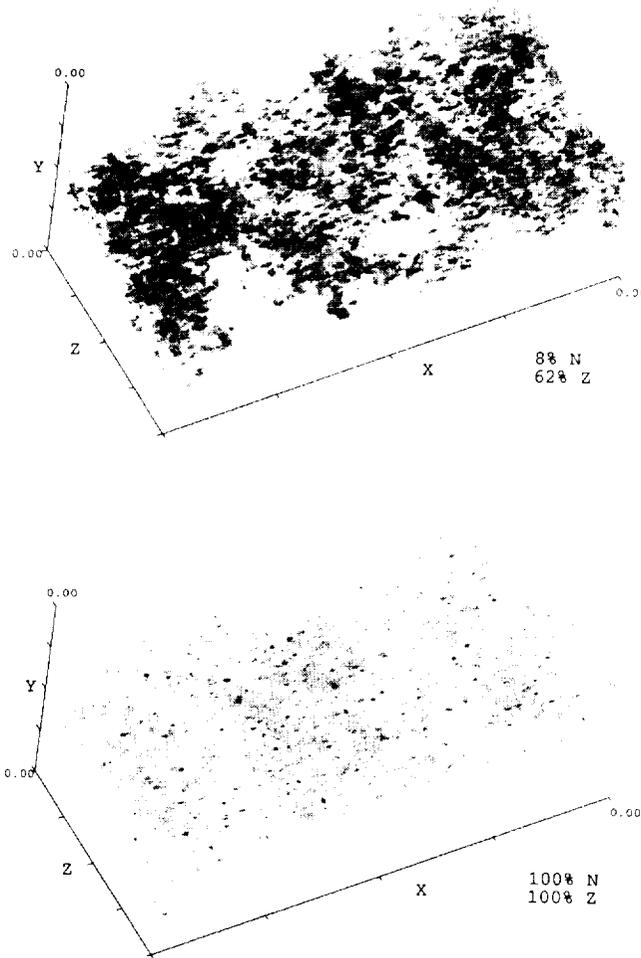
FIGURE 6. Unforced mixing layer. Top: Coherent vorticity. Bottom: Incoherent vorticity.

mogeneous in space, and are well decorrelated, which should avoid the transfer of energy from the incoherent modes to the coherent modes and, therefore, controls backscattering.

• The variability of the total field is not retained by the LES filtering and, as a consequence, the discarded high-wavenumber modes contain much more vorticity than the incoherent modes discarded by the CVS filtering.

• For LES, if we do not model the effect of the subgrid scale modes on the resolved modes, the energy accumulates at the cutoff and the computation diverges.

• For CVS, if we do not model the effect of the discarded incoherent modes on the resolved coherent modes, there is no risk of divergence since energy can be transferred in both directions all along the fully resolved inertial range – the only consequence of no turbulence model may be some extra dissipation.

We conjecture that the derivation of a turbulence model is easier with CVS filter-

1D energy spectra E(k_x)

Vorticity PDF p(ω)
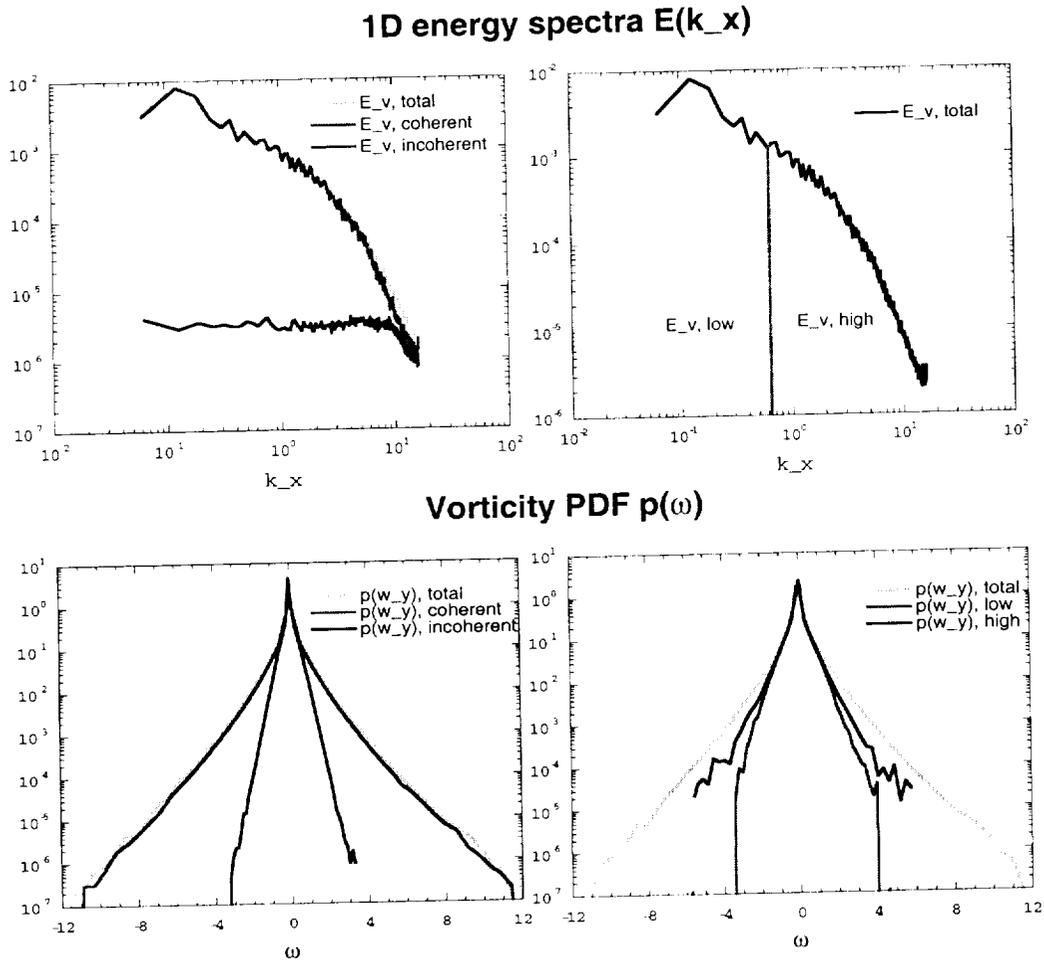
FIGURE 7. Comparison of CVS (left) with LES (right) filtering for the unforced 3D mixing layer, at resolution $N = 512 \times 256 \times 128$. Energy spectra (top) and PDF of vorticity (bottom) of total, coherent (3% N) and incoherent (97% N) flow using CVS filtering and of low wavenumber and high wavenumber components using LES filtering.

ing than with LES filtering because the discarded modes in this case are statistically well behaved, homogeneous, uncorrelated, and have an exponential PDF with a small variability.

6. Divergence problem

Due to the fact that the CVS filtering is nonlinear and the vector valued wavelet basis is not divergence-free, *i.e.* $\nabla \cdot \vec{\psi}_\lambda \neq 0$, the CVS filtering does not yield coherent and incoherent vorticity that is completely divergence-free. For the flow examined here, however, the divergent contribution of the vorticity field was less than 3% of the total enstrophy. The same problem is also encountered for vortex methods applied to 3D turbulent flows (Winckelmans (1995)). However, the corresponding velocity fields are
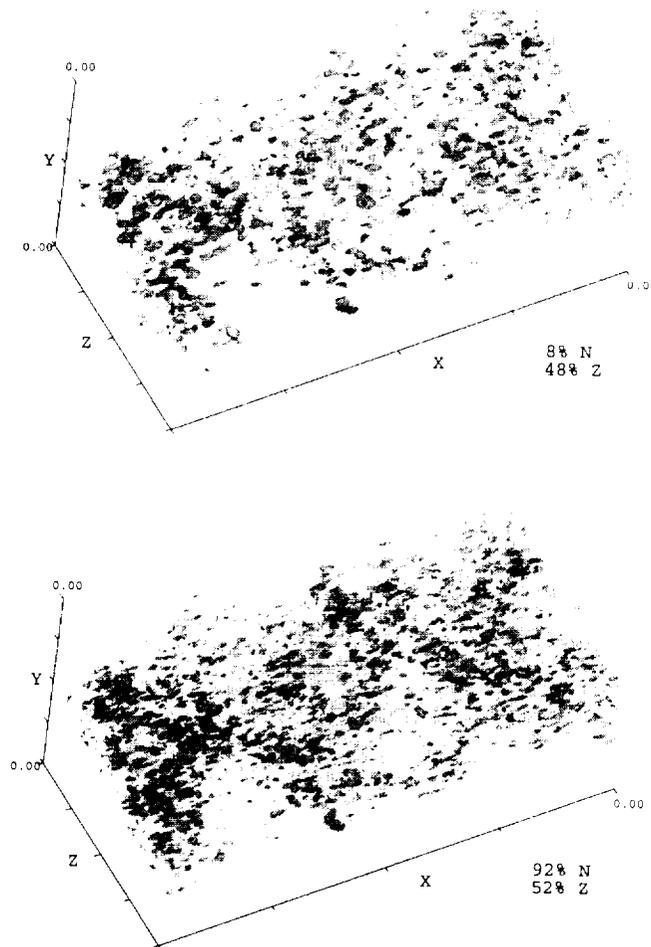
FIGURE 8. Unforced case. Top: Low wavenumber vorticity of the turbulent mixing layer reconstructed from 8% of the wavelet coefficients and containing 48% of the total enstrophy. Bottom: High wavenumber vorticity reconstructed from 92% of the Fourier coefficients and containing 52% of the total enstrophy.

divergence-free since they have been reconstructed using the Biot-Savart kernel. There are several possible ways to insure that the coherent vorticity remains divergence-free:

• use divergence-free orthogonal wavelets (Lemarié (1992)),

• decompose ω into $\omega = \omega_{div=0} + \nabla\phi$. Then ϕ can be calculated by taking the divergence which leads to a Poisson equation $\nabla^2\phi = \nabla \cdot \omega$.

• apply the previous decomposition, not to the solution, but to the wavelet basis itself, which can be done as a precalculation since the wavelet decomposition is a linear transformation.

7. Conclusion and perspectives

The CVS method is based on the projection of the vorticity field on an orthogonal wavelet basis and the decomposition of the vorticity field into two orthogonal components, using a nonlinear thresholding of the wavelet coefficients. The coherent vorticity field is reconstructed from the few wavelet coefficients larger than a given threshold, which depends only on the resolution and on the total enstrophy, while the incoherent vorticity is reconstructed from the many remaining weak wavelet coefficients. The coherent and incoherent velocity fields are then derived from the coherent and incoherent vorticity fields using Biot-Savart's equation.

In this paper we have applied this method to two 3D time developing mixing layers, forced and unforced, at resolution $N = 512 \times 256 \times 128$. We have shown that the coherent flow corresponds to only $3\%N$ wavelet modes, presents the same non-Gaussian PDF of vorticity, and retains most of the energy and enstrophy, with the same spectral distribution, as the total flow. Moreover, the remaining incoherent flow is structureless, exhibits a much narrower PDF of vorticity with an exponential distribution, and presents an energy equipartition spectrum. This suggests the possibility of parameterizing the effect of the incoherent flow on the coherent flow using a low-order statistical model. The advantage of the CVS filtering in comparison to the LES filtering was also demonstrated. The small scale flow, which is discarded in LES and replaced by a subgrid scale model, exhibits many coherent structures, has a much wider PDF of vorticity, and does not present an energy equipartition spectrum.

The success of the CVS filtering procedure suggests the possibility of extending the CVS method to solve the 3D Navier-Stokes equations directly in an adaptive wavelet basis. In (Schneider & Farge (2000)) we have shown that the CVS computation of a 2D mixing layer gives the same results as those from a standard DNS. The dynamical adaption of the grid in physical space allows the important coherent part of the flow to be evolved with a reduced number of active degrees of freedom. Thus the CVS computation combines a Eulerian representation of the flow with a Lagrangian adaption strategy for the active degrees of freedom, which are remapped at each time step using the CVS filtering.

REFERENCES

DAUBECHIES, I. 1992 it Ten Lectures on wavelets. SIAM, Philadelphia.

DONOHO, D. 1993 Unconditional bases are optimal bases for data compression and statistical estimation. *Appl. Comput. Harmon. Anal.* **1**, 100.

DONOHO, D. & JOHNSTONE, I. 1994 Ideal spatial adaption via wavelet shrinkage. *Biometrica.* **81**, 425-455.

FARGE, M. 1992 Wavelet Transforms and their Applications to Turbulence. *Ann. Rev. of Fluid Mech.* **24**, 395-457.

FARGE, M., SCHNEIDER, K., & KEVLAHAN, N. 1999 Non-Gaussianity and Coherent Vortex Simulation for two-dimensional turbulence using an adaptive orthonormal wavelet basis. *Phys. Fluids* **11**(8), 2187-2201.

FARGE, M. & SCHNEIDER, K. 2000 Coherent Vortex Simulation (CVS), a semi-deterministic turbulence model using wavelets. *Flow, Turb. Combust.*, submitted.

FARGE, M., PELLEGRINO, G. & SCHNEIDER, K. 2000 Coherent vortex extraction in 3D turbulent flows using orthogonal wavelets. *Phys. Rev. Lett.*, submitted.

LEMARIÉ P. G. 1992, Analyses multirésolutions non orthogonales, commutation entre projecteurs de dérivation et ondelettes à divergence nulle. *Revista Mat. Iberoamericana.* **8**, 221-236.

ROGERS, M. & MOSER, R. 1994 Direct simulation of a self-similar turbulent mixing layer. *Phys. Fluids.* **6**(2), 903-923.

SCHNEIDER, K. & FARGE, M. 1997 Wavelet forcing for numerical simulation of two-dimensional turbulence. *C. R. Acad. Sci. Paris, Série II b.* **325**, 263-270.

SCHNEIDER, K. & FARGE, M. 1998 Wavelet approach for modelling and computing turbulence. *Lecture Series 1998-05 Advances in turbulence modelling.* Von Karman Institute for Fluid Dynamics, Bruxelles, 132 pages.

SCHNEIDER, K. & FARGE, M. 2000 Numerical simulation of temporally growing mixing layer in an adaptive wavelet basis. *C. R. Acad. Sci. Paris Série II b.* **328**, 263-269.

WINCKELMANS, G. S. 1995 Some progress in large-eddy simulation using the 3D vortex particle method. *Annual Research Briefs*, Center for Turbulence Research, NASA Ames/Stanford Univ. 391-415.

Sub-optimal control based wall models for LES — including transpiration velocity

By J. S. Baggett†, F. Nicoud‡, B. Mohammadi¶, T. Bewley‖, J. Gullbrand
AND O. Botella

Most current wall models for the large eddy simulation (LES) of high Reynolds number turbulent boundary layers are *ad hoc* parameterizations of the wall stresses needed to close the finite-difference approximation to the viscous operator in terms of the tangential flow velocities at the first off-wall grid point. These models cannot compensate for the numerical and subgrid-scale modeling errors that are intrinsic to the severely under-resolved LES in the near-wall region. By using the wall stress boundary conditions as control to force the solution towards the desired mean velocity profile, it is possible to find better wall stress models (Nicoud *et al.* (2000)). We consider the use of transpiration velocity in addition to the wall stresses as part of the approximate boundary conditions. In this work, optimal control theory is used to find a combination of wall stresses and transpiration velocity that improves the prediction of the mean velocity profile and the turbulence intensities in a coarse grid LES of high Reynolds number turbulent channel flow.

1. Introduction

1.1. *Background*

One of the primary reasons that large eddy simulation (LES) is not yet practical for many flows of engineering interest is the high resolution required in turbulent boundary layers. The only way to simulate many flows is to completely bypass the simulation of the near-wall turbulence and to model its effects on the flow away from the wall. If the near-wall flow is not computed, then the no-slip boundary condition does not apply and the wall stresses are required to close the usual finite difference approximations to the viscous terms.

The simplest wall stress models correlate the wall stresses to the tangential velocities at the first off-wall grid points. More complex models for the wall stresses rely on the integration of boundary layer equations on an auxiliary mesh embedded near the wall. See Cabot & Moin (2000) for a recent review of wall stress models. These models perform adequately at low to moderate Reynolds numbers in simple flows, but they fail to produce good results at higher Reynolds numbers even in simple channel flow (Nicoud *et al.* (2000)). The current generation of wall stress models attempts to reproduce the physics of the wall stresses averaged over the filter width of the outer LES computation. However, none of these models can compensate for the numerical and subgrid-scale (SGS) modeling errors that are intrinsic to an LES computation which necessarily relies on a low-order numerical scheme and an exceedingly coarse near-wall mesh.

† University of Wisconsin – La Crosse, WI, USA
‡ CERFACS, France
¶ University of Montpellier and INRIA, France
‖ Univ. Calif. San Diego, CA, USA

To find wall models in the form of approximate boundary conditions that can compensate for the errors intrinsic to under-resolved LES, we use techniques from optimal control theory. In our approach, a sub-optimal control strategy is used in which the objective is to force the outer LES towards a desired solution by using the approximate boundary conditions as control. In previous work (Nicoud *et al.* (2000)), this approach was tested by using wall stress boundary conditions as a control to force the mean velocity of a coarse-grid LES of channel flow at high Reynolds number towards a logarithmic velocity profile. It was found that the resulting wall stress boundary conditions yielded much better results in terms of the mean velocity profile than existing wall stress models at high Reynolds numbers. Furthermore, it was found that the resulting wall stresses were well correlated with the local velocity field and that the dynamically relevant portion of the wall stresses could be predicted by a relatively simple linear model.

Furthermore, it was found that the wall stresses generated by the sub-optimal control strategy, while improving the prediction of the mean velocity profile considerably, did not improve the prediction of the velocity fluctuations. This may have been due to the inadequacy of the dynamic Smagorinsky subgrid-scale model in the anisotropic logarithmic region of the channel flow, but it could also have been that wall stress boundary conditions alone cannot fully compensate for the errors in the vicinity of the computational boundary. Generally, any improvements in the prediction of the outer flow were limited primarily to a region extending only a few grid cells from the wall.

When wall stress boundary conditions are used to model the influence of the near-wall region on the outer flow, it is usually assumed that the wall-normal velocity is identically zero at the boundary. However, since the no-slip boundary condition cannot be applied without adequate near-wall resolution, perhaps it does not make sense to insist that the velocity normal to the boundary is zero. After all, a wall model should capture the effects of the near-wall turbulence on the outer flow, including such hallmarks of near-wall turbulence as ejections and sweeps. In any case, the combination of non-zero boundary-normal velocity with wall stresses should allow the approximate boundary condition wall model to influence more of the computational domain than wall stress boundary conditions alone since the boundary-normal velocity effects the entire flow directly via the continuity equation.

It is the objective of the current work to test the effect of including a transpiration velocity approximate boundary condition (net transpiration will be zero) in addition to the wall stress boundary conditions in the sub-optimal control framework first explored in Nicoud *et al.* (2000). The sub-optimal control framework, including transpiration velocity, was first presented in Nicoud & Baggett (1999), but it is presented again here in a slightly more general form. We also discuss whether or not simple, algebraic models derived from the sub-optimally controlled simulations are likely to be successful.

2. Sub-optimal control framework

2.1. *Channel flow*

We consider the LES of incompressible, turbulent channel flow on a uniform mesh with 32 volumes in the streamwise and spanwise directions and 33 volumes in the wall-normal direction. A staggered grid system is used with second order finite differences for the spatial derivatives and a third-order Runge-Kutta discretization for the time advancement. Periodic boundary conditions are imposed in the two directions x_1 and x_3 (or x and z) parallel to the walls. The SGS model is the Smagorinsky model with the coefficient determined by the plane-averaged dynamic procedure of Germano *et al.* (1991). Unless

otherwise stated, all quantities are nondimensionalized by the friction velocity, u_τ, and channel half-height, h. The channel walls are at $y = \pm 1$. The skin friction Reynolds number is defined as $\mathrm{Re}_\tau = u_\tau h/\nu$. When the mean flow is statistically converged, the mean streamwise pressure gradient is equal to the wall stress, that is, $-\partial P/\partial x = \langle \tau_w \rangle = 1$. All of the simulations in this work were performed at $\mathrm{Re}_\tau = 4000$ in a computational domain with dimensions $2\pi h \times 2h \times 2\pi h/3$ in the streamwise (x_1 or x), wall-normal (x_2 or y), and spanwise (x_3 or z) directions, respectively.

The governing equations are:

$$\frac{\partial u_i}{\partial t} + \frac{\partial u_i u_j}{\partial x_j} = -\frac{\partial P}{\partial x_i} + \frac{\partial}{\partial x_j}\left((\nu + \nu_t)\left(\frac{\partial u_i}{\partial x_j} + \frac{\partial u_j}{\partial x_i}\right)\right)$$

(2.1)

$$\frac{\partial u_j}{\partial x_j} = 0$$

The pressure, P, contains a mean forcing component such that $\langle -\partial P/\partial x \rangle = 1$. Note that no specific notation is used to describe spatial filtering associated with the LES formulation; rather, each variable herein should be understood as the filtered counterpart of the actual variable (e.g. $u_i \equiv \bar{u}_i$).

Since the no-slip boundary condition does not apply on the coarse mesh used here, the boundary conditions that are supplied are the wall stresses τ_{12}^w and τ_{32}^w as well as the normal velocity at the wall, v_w. The boundary conditions, specified in terms of the control parameter, ϕ, which is defined below, on (2.1) are:

$$\frac{\partial u}{\partial y_n} + \frac{\partial v_n}{\partial x} = \frac{1}{\nu_w}\phi_u$$

$$v_n = \phi_v$$

(2.2)

$$\frac{\partial w}{\partial y_n} + \frac{\partial v_n}{\partial z} = \frac{1}{\nu_w}\phi_w$$

where the subscript n stands for the outward normal to the wall and ν_w is the wall value of the total dynamic viscosity $\nu + \nu_t$ (in this work $\nu_w \equiv \nu$). The control parameter ϕ is defined as $\phi = (\phi_u, \phi_v, \phi_w) = (\tau_{12}^w, v_w, \tau_{32}^w)$ at $y = +1$ and $\phi = (\phi_u, \phi_v, \phi_w) = -(\tau_{12}^w, v_w, \tau_{32}^w)$ at $y = -1$.

2.2. Objective function

In the sub-optimal control approach, the boundary conditions (specified by the control parameter ϕ) are used as control to minimize an objective function at each time step. The goal is to provide numerical boundary conditions to the flow solver so that the overall solution is consistent with what is expected in a channel flow. The objective function is specified as follows:

$$\mathcal{J}(u;\phi) = \sum_{i=1,3} \mathcal{J}_{\mathrm{mean},i}(u;\phi) + \sum_{i=1}^{3} \mathcal{J}_{\mathrm{rms},i}(u;\phi) + \sum_{i=1}^{3} \mathcal{J}_{\mathrm{penalty},i}(\phi).$$

(2.3)

The objective function consists of the three components. $\mathcal{J}_{\mathrm{mean}}$ measures the distance from the plane-averaged LES solution to a desired reference velocity profile. The second component, $\mathcal{J}_{\mathrm{rms}}$ measures the distance from the plane-averaged velocity fluctuation intensities to desired target profiles. Finally, the third component, $\mathcal{J}_{\mathrm{penalty}}$ penalizes the use of large controls ϕ. The component objective functions are defined below.

For the mean streamwise velocity the target or reference profile is taken as a logarithmic velocity profile throughout the channel: $u^+_{1,\text{ref}} = \kappa^{-1} \ln y^+ + C$. The spanwise velocity reference profile is simply $u_{3,\text{ref}} \equiv 0$. The difference between the reference velocity profile and the plane-averaged LES solution is a function of the wall-normal coordinate, y, and can be expressed as

$$\delta_{u_i}(y) = \frac{1}{A} \int \int (u_i - u_{i,\text{ref}}) \, dx \, dz \qquad (i = 1, 3) \tag{2.4}$$

where A is the channel area in the homogeneous plane. Note that any reference profile suitable for a parallel flow could have been used. Notably, a more realistic shape could have been used near the channel center. However, the logarithmic profile is well suited for the near-wall region since we are using a coarse mesh and the Reynolds number, $\text{Re}_\tau = 4000$, is sufficiently high so that the first grid point lies in the logarithmic region ($y^+ \approx 121$). The mean component of the objective function is then:

$$\mathcal{J}_{\text{mean},i}(u; \phi) = \alpha_i \int_{-1}^{+1} \delta_{u_i}(y)^2 \, dy, \qquad (i = 1, 3) \tag{2.5}$$

Note that there is no need to specify a target profile for the plane-averaged wall-normal velocity since that will be identically zero at each time step provided there is no net transpiration velocity through the boundaries.

The velocity fluctuation intensities are targeted through the $\mathcal{J}_{\text{rms}}$ component of the objective function. The plane-averaged, mean square velocity fluctuations are compared at each time step to the mean square velocity fluctuations, $(u'_{i,\text{ref}})^2$, from the LES of Kravchenko, Moin & Moser (1996) which was performed at the same Reynolds number, $\text{Re}_\tau = 4000$, using a zonally defined mesh to resolve the near-wall region. The distance between the plane-averaged mean square velocity fluctuations and their reference profiles can be measured as

$$\delta_{u'_i}(y) = \frac{1}{A} \int \int \left((u_i - \langle u_i \rangle)^2 - u'^2_{i,\text{ref}} \right) \, dx \, dz, \qquad (i = 1, 2, 3), \tag{2.6}$$

where $\langle u_i \rangle$ denotes the average over the homogeneous directions of the velocity component u_i. The velocity fluctuation intensity component of the objective function is then

$$\mathcal{J}_{\text{rms},i}(u; \phi) = \beta_i \int_{-1}^{+1} \delta_{u'_i}(y)^2 \, dy \qquad (i = 1, 2, 3) \tag{2.7}$$

Finally, to prevent numerical instabilities it is necessary to regularize the control, that is, the approximate boundary conditions, by including a penalty component in the overall objective function:

$$\mathcal{J}_{\text{penalty},i}(\phi) = \frac{\gamma_i}{A} \int_{y=\pm 1} \phi^2_{u_i} \, dx \, dz + \frac{\lambda}{A} \int_{y=\pm 1} \delta_{i2} \phi^4_{u_2} \, dx \, dz \qquad (i = 1, 2, 3). \tag{2.8}$$

The first term in the penalty component attempts to prevent the mean square norm of the control parameter from becoming too large. In the case of transpiration velocity control, however, it was found that it is necessary to prevent the transpiration velocity from becoming too large at any single point, hence the second term in the penalty component (2.8) was added.

Note that each component of the objective function includes a scalar parameter: α_i, β_i, γ_i, or λ. These scalars allow the relative importance of the various objectives to be changed in the overall objective.

2.3. Adjoint problem

The gradient of the objective function $\mathcal{J}$ with respect to the control parameter ϕ is estimated by using the Fréchet differential (Vainberg (1964)) defined for any functional F as:

$$\frac{DF}{D\phi}\tilde{\phi} = \lim_{\epsilon \to 0} \frac{F(\phi + \epsilon\tilde{\phi}) - F(\phi)}{\epsilon}, \tag{2.9}$$

where $\tilde{\phi}$ is an arbitrary direction. From (2.3) the gradient $\mathcal{J}$ is:

$$\frac{D\mathcal{J}}{D\phi}\tilde{\phi} = \sum_{i=1,3} \alpha_i \int\int\int_\Omega 2\frac{\delta_{u_i}}{A}\mathcal{U}_i \, dx \, dy \, dz$$

$$+ \sum_{i=1}^3 \beta_i \int\int\int_\Omega 2\frac{\delta_{u'_i}(u_i - \langle u_i \rangle)}{A}\mathcal{U}_i \, dx \, dy \, dz \tag{2.10}$$

$$+ \lambda\frac{4}{A}\int\int_{y=\pm 1} \phi_{u_2}^3\tilde{\phi}_{u_2} \, dx \, dz + \sum_{i=1}^3 \gamma_i\frac{2}{A}\int\int_{y=\pm 1} \phi_{u_i}\tilde{\phi}_{u_i} \, dx \, dz$$

where $\mathcal{U}_i$ denotes the Fréchet derivative of u_i[†]. The gradient of $\mathcal{J}$ cannot be calculated directly from (2.10) since the derivatives $\mathcal{U}_i$ are unknown.

To calculate an approximation to the gradient of $\mathcal{J}$, we start by assuming that the equation of state, (2.1), is discretized in time by a semi-implicit discretization:

$$u_i^{n+1} + \Delta t\left[\frac{\partial P}{\partial x_i} + \frac{\partial u_i u_j}{\partial x_j} - \frac{\partial}{\partial x_j}\left((\nu + \nu_t)\left(\frac{\partial u_i}{\partial x_j} + \frac{\partial u_j}{\partial x_i}\right)\right)\right]^{n+1} = \text{RHS}^n \tag{2.11}$$

$$-\Delta t\frac{\partial u_j^{n+1}}{\partial x_j} = 0$$

with the boundary conditions (2.2). The terms which depend only on the variables at the previous time step n are gathered in the generic notation RHS^n and disappear in the analytical development.

We now formulate an adjoint problem to find the gradient (2.10). The first step is to take the derivative of (2.11) with respect to the control ϕ:

$$\mathcal{U}_i + \Delta t\left[\frac{\partial \mathcal{P}}{\partial x_i} + \mathcal{U}_j\frac{\partial u_i}{\partial x_j} + u_j\frac{\partial \mathcal{U}_i}{\partial x_j} - \frac{\partial}{\partial x_j}\left((\nu + \nu_t)\left(\frac{\partial \mathcal{U}_i}{\partial x_j} + \frac{\partial \mathcal{U}_j}{\partial x_i}\right)\right)\right] = 0 \tag{2.12}$$

$$-\Delta t\frac{\partial \mathcal{U}_j}{\partial x_j} = 0$$

with boundary conditions:

$$\frac{\partial \mathcal{U}}{\partial y_n} + \frac{\partial \mathcal{V}_n}{\partial x} = \frac{1}{\nu_w}\tilde{\phi}_u$$

$$\mathcal{V}_n = \tilde{\phi}_v \tag{2.13}$$

$$\frac{\partial \mathcal{W}}{\partial y_n} + \frac{\partial \mathcal{V}_n}{\partial z} = \frac{1}{\nu_w}\tilde{\phi}_w.$$

[†] Technically, the second term in (2.10) should include the integral $\int\int\int_\Omega 2\frac{\delta_{u'_i}(u_i - \langle u_i \rangle)}{A}(\mathcal{U}_i - \langle \mathcal{U}_i \rangle) \, dx \, dy \, dz$, but we make the approximation that $\langle \mathcal{U}_i \rangle \equiv 0$ since $|\langle \mathcal{U}_i \rangle| \ll |\mathcal{U}_i|$ in general.

The right-hand side term in (2.12) is now zero since the flow field at time step n does not depend on the control ϕ for the current time step. Therefore, the superscript '$n + 1$' has been dropped for clarity. Note also in (2.12) that the Fréchet derivative of the eddy viscosity was assumed to be zero, that is, $D\nu_t/D\phi = 0$. The latter approximation can be justified for short time intervals; see Collis & Chang (1999). Moreover, this system of equations is linear in the variables $\mathcal{U}_i$ and $\mathcal{P}$, where $\mathcal{P}$ is the Fréchet derivative of the pressure. Therefore it can be written in the form:

$$\mathcal{A}\Theta = 0, \tag{2.14}$$

where $\mathcal{A}$ is the linear operator acting on the vector $\Theta = (\mathcal{U}_i, \mathcal{P})^T$. The linear system (2.14) with unknown boundary conditions (2.13) cannot be solved directly; instead, an adjoint operator, $\mathcal{A}^*$, is formulated by considering the equation

$$\langle \mathcal{A}\Theta, \Psi \rangle = \langle \Theta, \mathcal{A}^*\Psi \rangle + \text{BT}, \tag{2.15}$$

where $\langle \cdot, \cdot \rangle$ stands for the inner product defined as the integral over the flow domain of the dot product of the two vectors and Ψ is the adjoint state vector $\Psi = (\eta_i, \pi)^T$. Finding the adjoint operator, $\mathcal{A}^*$, and the boundary terms, BT, is a straightforward exercise in integrating by parts. The adjoint operator acting on the adjoint state vector, that is, $\mathcal{A}^*\Psi$ is defined by the equations:

$$\mathcal{A}^*\Psi = \begin{cases} \eta_i + \Delta t \left[\frac{\partial \pi}{\partial x_i} + \eta_j \frac{\partial u_j}{\partial x_i} - u_j \frac{\partial \eta_i}{\partial x_j} - \frac{\partial}{\partial x_j} \left[(\nu + \nu_t) \left(\frac{\partial \eta_i}{\partial x_j} + \frac{\partial \eta_j}{\partial x_i} \right) \right] \right] \\ -\Delta t \frac{\partial \eta_j}{\partial x_j} \end{cases} \tag{2.16}$$

and the boundary terms are:

$$\text{BT} = \Delta t \int \int_{y=\pm 1} (\text{Press} + \text{Conv} + \text{Visc}) \, dx \, dz \tag{2.17}$$

with

$$\begin{aligned} \text{Press} &= \mathcal{P}\eta_{2n} - \mathcal{V}_n \pi \\ \text{Conv} &= \eta_i \mathcal{U}_i v_n \\ \text{Visc} &= -\nu_w \left[\eta_i \left(\frac{\partial \mathcal{U}_i}{\partial y_n} + \frac{\partial \mathcal{V}_n}{\partial x_i} \right) - \mathcal{U}_i \left(\frac{\partial \eta_i}{\partial y_n} + \frac{\partial \eta_{2n}}{\partial x_i} \right) \right]. \end{aligned} \tag{2.18}$$

From (2.14), the relation (2.15) defining the adjoint operator reduces to

$$\langle \mathcal{A}^*\Psi, \Theta \rangle = -\text{BT}. \tag{2.19}$$

2.4. *Gradient estimate*

We now have the liberty to choose boundary conditions and right-hand side terms for the adjoint problem such that the relation (2.19) can be utilized to calculate the gradient of $\mathcal{J}$. By comparing Eqs. (2.10), (2.17), (2.18) and (2.19), it appears that a judicious choice for the definition of the adjoint problem is:

$$\mathcal{A}^*\Psi = \frac{2}{A} \begin{pmatrix} \alpha_1 \delta_u + \beta_1 \delta_{u'}(u - \langle u \rangle) \\ \beta_2 \delta_{v'}(v - \langle v \rangle) \\ \alpha_3 \delta_w + \beta_3 \delta_{w'}(w - \langle w \rangle) \\ 0 \end{pmatrix} \tag{2.20}$$

with boundary conditions at the wall:

$$\eta_1 v_n + \nu_w \frac{\partial \eta_1}{\partial y_n} = 0$$

$$\eta_{2n} = 0 \tag{2.21}$$

$$\eta_3 v_n + \nu_w \frac{\partial \eta_3}{\partial y_n} = 0.$$

In doing so, (2.19) can be re-written as:

$$\frac{DJ}{D\phi}\tilde{\phi} = -\Delta t \int \int_{y=\pm 1} \left[\eta_1 \tilde{\phi}_u + \left(\pi - 2\nu_w \frac{\partial \eta_{2n}}{\partial y_n} \right) \tilde{\phi}_v + \eta_3 \tilde{\phi}_w \right] dx\,dz$$

$$+ \lambda \frac{4}{A} \int \int_{y=\pm 1} \phi_{u_2}^3 \tilde{\phi}_{u_2}\, dx\,dz + \sum_{i=1}^{3} \gamma_i \frac{2}{A} \int \int_{y=\pm 1} \phi_{u_i} \tilde{\phi}_{u_i}\, dx\,dz$$

Since (2.22) is valid for all directions $\tilde{\phi}$, the gradient of J may be extracted:

$$\frac{DJ}{D\phi_1} = \Delta t \eta_{1,w} + \frac{2\gamma_1}{A}\phi_1$$

$$\frac{DJ}{D\phi_2} = \Delta t \left(\pi_w - 2\nu_w \frac{\partial \eta_{2n}}{\partial y_n} \right) + \frac{2\gamma_2}{A}\phi_2 + \frac{4\lambda}{A}\phi_2^3 \tag{2.22}$$

$$\frac{DJ}{D\phi_3} = \Delta t \eta_{3,w} + \frac{2\gamma_3}{A}\phi_3,$$

where the subscript w stands for the values at the wall. A control procedure using a simple steepest descent algorithm at each time step may now be proposed such that:

$$\phi^{n+1,k+1} = \phi^{n+1,k} - \mu \frac{DJ(\phi^{n+1,k})}{D\phi} \tag{2.23}$$

where the parameter μ can be varied to change the rate of convergence and the extra superscript k refers to the subiterations in the descent algorithm. Note that the adjoint operator depends on the state vector $(u_i, P)^T$ at time $n + 1$ so that the state equation and the adjoint problem must be solved simultaneously to obtain the sub-optimal approximate boundary conditions. The adjoint problem (2.20) with boundary conditions (2.21) is discretized and solved using the same numerics as the flow solver. Note that the resulting gradient of the objective function is an approximation since the spatial terms in (2.11) are assumed to be continuous, the gradient of the eddy viscosity, $D\nu_t/D\phi$, is assumed to be zero, and we have omitted a term in (2.10). An exact adjoint problem could be formulated from the fully discretized equations of state, but this is considerably more difficult than the current approach. More details about the algorithm used to solve the adjoint problem may be found in Nicoud *et al.* (2000).

3. Results

3.1. *Objective function for mean flow only*

The first test is to see if the addition of the transpiration velocity control to the wall stress controls results in an improvement of the prediction of the mean velocity profile. In the following, the reference mean velocity profile is taken as $u_{ref}^+ = 2.41 \ln y^+ + 5.2$. This version of the logarithmic law was suggested by P. Bradshaw (private communication) for high Reynolds number flows. To test the influence of transpiration velocity only on
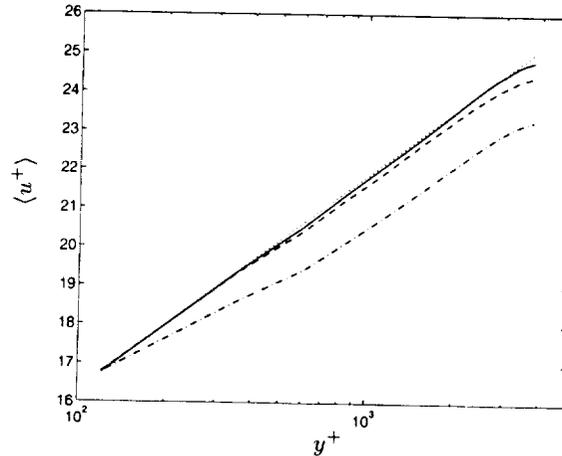
FIGURE 1. Mean velocity profiles with objective to control mean flow only. (———): control includes wall stresses and transpiration; (— — — —): control includes wall stresses only; (—·—): no control, uses wall stress model of Piomelli *et al.* (1989); (········): logarithmic reference profile, $u^+_{ref} = 2.41 \ln y^+ + 5.2$.

the mean velocity profile, the constants β_i in the objective function, (2.3), are set to zero so that only the desired mean velocity profile is targeted. For this simulation the parameters in the objective function (2.3) were: $\alpha_1 = \alpha_3 = 1, \beta_1 = \beta_2 = \beta_3 = 0, \gamma_1 = \gamma_3 = 10^{-4}, \gamma_2 = 0.02$, and $\lambda = 0$. The relaxation parameter in the steepest descent algorithm was $\mu = 10^3$.

Figure 1 shows that, indeed, the addition of the transpiration control improves the mean velocity profile slightly over the case when only wall stress controls are considered. Also shown in Fig. 1 is the mean velocity profile obtained by using the simple wall stress model of Piomelli *et al.* (1989) that correlates the streamwise wall stress to the streamwise velocity at a point away from the wall and slightly downstream. The latter model yields results that are typical of most current wall stress models for this flow configuration.

The improvement in the mean velocity profile is encouraging. However, Fig. 2 shows the root mean square (rms) velocity fluctuations for the sub-optimal wall stress boundary conditions with and without the addition of transpiration velocity control. The rms velocity fluctuations actually increase with the addition of transpiration, which is certainly in the wrong direction since the fluctuation intensities are already over-predicted.

3.2. Objective function including mean flow and rms velocities

In Nicoud *et al.* (2000) it was shown that sub-optimal wall stress boundary conditions alone had little effect on the velocity fluctuation intensities even when the objective function included a component that targeted the fluctuations. The addition of a transpiration velocity control improves matters to some extent. For this simulation the parameters in the objective function (2.3) were: $\alpha_1 = \alpha_3 = 1, \beta_1 = \beta_2 = \beta_3 = 3 \times 10^{-4}, \gamma_1 = 5 \times 10^{-5}, \gamma_2 = 10^{-3}, \gamma_3 = 4 \times 10^{-6}$ and $\lambda = 5 \times 10^{-3}$. The relaxation parameter in the steepest descent algorithm was $\mu = 500$ for ϕ_{u_2} and 10^5 for ϕ_{u_1} and ϕ_{u_3}.

Figure 3 shows the rms velocities when the rms component is included in the objective function. As illustrated in Fig. 3, the prediction of the rms velocities improves when the transpiration velocity control is added; however, the streamwise rms velocity is still over-predicted near the wall. Not shown for this simulation is the mean velocity profile, which
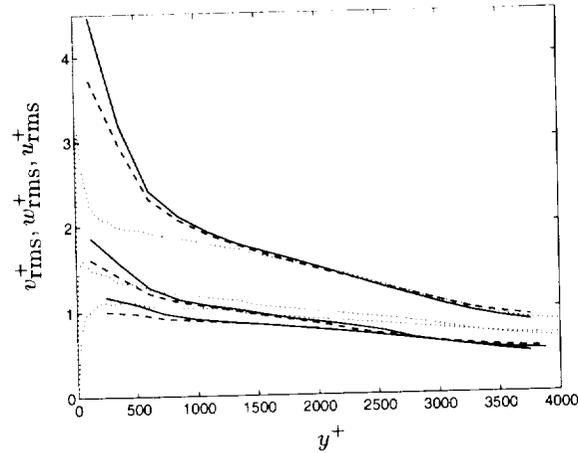
FIGURE 2. Velocity fluctuation intensities with objective to control mean flow only. (———): control includes wall stresses and transpiration; (— — —): control includes wall stresses only; (········): reference profiles of Kravchenko, Moin & Moser (1996).
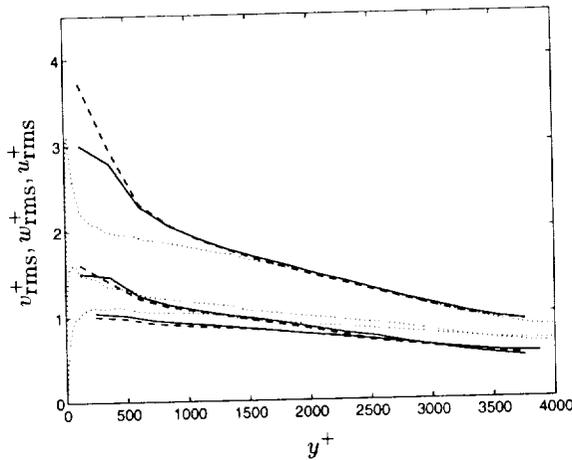
FIGURE 3. Velocity fluctuation intensities with objective to control mean flow and rms velocities. (———): control includes wall stresses and transpiration; (— — —): control includes wall stresses only; (········): reference profiles of Kravchenko, Moin & Moser (1996).

in this case is not as good as the mean velocity profile that is achieved in the previous section when only the mean velocity profile is targeted by the controls. If shown, it would lie between the two mean velocity profiles in Fig. 1 corresponding to control by wall stress only and control by wall stress plus transpiration velocity. Furthermore, the region in which the improved predictions occur is limited to approximately the first three grid cells adjacent to the wall.

The results of this simulation show that the prediction of velocity fluctuation intensities can be improved by the addition of a wall-normal velocity approximate boundary condition. But, the fact that the mean velocity profile is not as well predicted when the velocity fluctuations are targeted through the objective function suggests that the objectives of getting the correct mean velocity profile *and* the correct rms velocities may be competing objectives.

3.3. *Validating the gradient of the objective function*

The fact that there was not more improvement in the prediction of the objective profiles with the addition of the transpiration velocity control might suggest that the approximate gradient of the objective function is inaccurate. To validate the gradient computation, finite difference approximations to the gradient were calculated. This is relatively simple to do. Given a control vector ϕ and a velocity field u, choose a small value of ϵ and perturb the control vector at one point by the amount ϵ (e.g. add ϵ to τ_{12}^w at one point on the lower wall) to obtain a new control vector $\phi + \epsilon\tilde{\phi}$. Now advance the velocity field one time step and explicitly calculate the value of the objective function (2.3), that is, calculate $\mathcal{J}(\phi + \epsilon\tilde{\phi})$. The approximate gradient in the direction $\tilde{\phi}$ is then:

$$\frac{D\mathcal{J}}{D\phi}\tilde{\phi} \approx \frac{\mathcal{J}(\phi + \epsilon\tilde{\phi}) - \mathcal{J}(\phi)}{\epsilon} \qquad (3.1)$$

By comparing the approximation (3.1) to a centered difference approximation, it was found that $\epsilon = 10^{-3}$ produces good approximations to the gradient. By successively perturbing the control vector ϕ at every point, it is possible to approximate the entire gradient $D\mathcal{J}/D\phi$. This finite difference gradient approximation can then be compared to the gradient approximated by the adjoint problem described above.

In the case when only wall stress boundary condition controls are used (as in Nicoud *et al.* (2000)), it was found that the correlation between the two gradient approximations was generally in excess of 90%. When the transpiration velocity control is considered in addition to the wall stress controls as in the present work, it was found that the correlation between the two gradient approximations was generally in excess of 80%, but in some cases it was lower. Thus we are led to believe that the adjoint problem defined above may be yielding satisfactory approximations to the gradient of the objective function, but further work is necessary to determine if the gradient approximation can be improved.

3.4. *Is there a simple, linear, general model?*

In Nicoud *et al.* (2000) the data from the sub-optimally controlled simulation at $\mathrm{Re}_\tau = 4000$ in which the wall stresses were used as control was used to derive a simple, linear model to predict the wall stresses from the local velocity field. In short, linear regression was used to find the localized convolution coefficients for the velocity field that best predicted the wall stresses in a least squares sense. This procedure yielded a wall stress model that was inexpensive to compute and accurately reproduced the results of the sub-optimally controlled simulation. Furthermore, this same linear model was able to yield similarly good predictions of the mean velocity profile for Reynolds numbers ranging from $\mathrm{Re}_\tau = 180$ to $\mathrm{Re}_\tau = 20000$ when the same grid was used as for the sub-optimally controlled simulation. Even when the grid was refined by the same amount in each direction so that the aspect ratio of the grid remained unchanged, the same linear model continued to produce good results. Further details about the derivation of this wall model can be found in Nicoud *et al.* (2000).

Unfortunately, as we show here, this simple linear model is not going to be a panacea. Figure 4 shows the mean velocity profiles for several channel flow LES's at $\mathrm{Re}_\tau = 4000$ all using the same number of grid points as the simulations discussed above and using the simple linear wall stress model derived in Nicoud *et al.* (2000). In each case some reasonable modification has been made. For instance, a fully conservative fourth order finite difference scheme was used, and, as shown in the figure, the mean-velocity is under-predicted. To test the effects of the numerics on the efficacy of the wall model, two
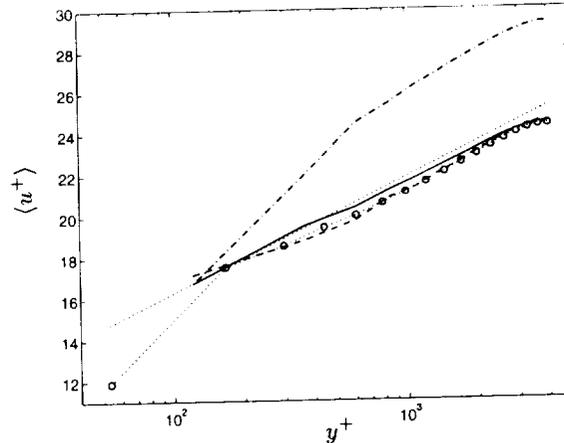
FIGURE 4. Mean velocity profiles using fixed, simple linear model for the wall stresses derived in Nicoud *et al.* (2000). (⋯⋯⋯): logarithmic reference profile, $u^+_{ref} = 2.41 \ln y^+ + 5.2$; (———): model reproduces mean profile when used in same setting that it was derived; (– – – –): same model with fourth-order finite differences; (—·—): same model with modified dynamic procedure as in Cabot & Moin (2000); (·· o ··): same model with stretched wall-normal grid.

different things were tried: stretching the grid in the wall-normal direction and modifying the dynamic procedure as suggested by Cabot & Moin (2000). As Figure 4 shows, the simple linear wall stress model performs worse in every one of these cases than in the original simulation for which it was designed.

4. Discussion

It was expected that the addition of the transpiration velocity control would allow the wall model to influence a larger fraction of the flow domain than when using wall stress controls alone. This expectation is is due to two suppositions: 1) a transpiration velocity boundary condition directly effects the entire flow domain through the continuity equation, and 2) the transpiration velocity control should enhance the level resolved turbulence in the near-wall cells leading to less reliance on the inaccurate Smagorinsky SGS model. However, the addition of the transpiration velocity control, while improving matters, does not completely fix everything.

It seems unlikely that approximate boundary condition wall models can do much better than those produced by these sub-optimally controlled simulations (of course, there is still some room to improve the simulations in this work by finding better gradient approximations and exploring other combinations of parameters). There are other culprits at work here, however; for instance, the Smagorinsky SGS model is known to be unable to correctly predict the subgrid-scale stresses in the logarithmic region at this coarse resolution (Baggett, Jiménez & Kravchenko (1997)). Further efforts to solve the problem of approximate boundary conditions for LES need to be made in tandem with improving the subgrid-scale model in the anisotropic logarithmic region. The only alternative is to start the LES computation at some plane parallel to the wall beyond which the LES can be trusted. In that case, the boundary conditions for all the velocity components need to be supplied in the interior of the turbulent flow, and that problem has been shown to be extremely difficult; see Cabot & Moin (2000) for a review of some of these attempts at finding "off-wall" boundary conditions.

The simple, linear, wall stress model derived in Nicoud *et al.* (2000) was shown not to be robust to changes in the numerical scheme and/or the SGS model. It therefore seems unlikely that any single, explicitly defined simple model is unlikely to work in the variety of flows necessary to make it useful as a predictive tool for LES. Perhaps a more promising direction is to employ some kind of online optimization or control to force the LES solution near the computational boundaries to match an adaptively computed RANS solution. To this end, B. Mohammadi has proposed a new generalized objective function that would allow the use of more general non-parallel reference velocity profiles by targeting the tangential velocities:

$$\mathcal{J}_{\text{mean},i}(u;\phi) = \int_{-1}^{+1} \left(\delta_{u_t}(y)^2 + \delta_t(y) \right) dy, \qquad (4.1)$$

with

$$\delta_{u_t}(y) = \frac{1}{A} \int \int (u_t - u_{t,\text{ref}}) \, dx \, dz \qquad (4.2)$$

and

$$\delta_t(y) = \frac{1}{A} \int \int \|\vec{t} - \vec{t}_{\text{ref}}\| \, dx \, dz \qquad (4.3)$$

where $u_t = \vec{u} \cdot \vec{t}$ is the tangential (to the wall) velocity component. Preliminary computations of the gradient of this objective function by finite difference approximations show that the gradients of this new objective function are very different than those of (2.3).

REFERENCES

BAGGETT, J. S., JIMÉNEZ, J. & KRAVCHENKO, A. G. 1997 Resolution requirements in large-eddy simulations of shear flows. *Annual Research Briefs*, Center for Turbulence Research, NASA Ames/Stanford Univ. 51-66.

CABOT, W. & MOIN, P. 2000 Approximate wall boundary conditions in the large-eddy simulation of high Reynolds number flow. *Flow Turb. Combust.* **63**, 269-291.

COLLIS, S. S. & CHANG, Y. 1999 On the use of LES with a dynamic subgrid-scale model for the optimal control of wall bounded turbulence. In D. Knight and L. Sakell, eds., *Recent Advances in DNS and LES*. Kluwer.

GERMANO, M., PIOMELLI, U., MOIN, P. & CABOT, W. 1991 A dynamic subgrid-scale eddy viscosity model. *Phys. Fluids.* **3**, 1760-1765.

KRAVCHENKO, A. G., MOIN, P. & MOSER, R. 1996 Zonal embedded grids for numerical simulations of wall-bounded turbulent flows. *J. Comp. Phys.* **127**, 412-423.

NICOUD, F., BAGGETT, J. S., MOIN, P. & CABOT, W. 2000 LES wall modeling based on suboptimal control theory. To appear *in Phys. Fluids.*

NICOUD, F. & BAGGETT, J. S. 1999 On the use of optimal control theory for deriving wall models for LES. *CTR Annual Research Briefs*, Center for Turbulence Research, NASA Ames/Stanford Univ. 329-341.

PIOMELLI, U., FERZIGER, J., MOIN, P., & KIM, J. 1989 New approximate boundary conditions for large eddy simulations of wall-bounded flows.*Phys. Fluids.* **1**, 1061-1068.

VAINBERG, M. 1964 *Variational methods for the study of nonlinear operators.* Holden Day.

Computation of trailing edge noise from an incompressible flow calculation

By Assad A. Oberai† AND M. Wang

A new methodology for calculating low Mach number trailing edge noise is developed and tested. The input to this methodology is the fluctuating surface pressure obtained from an incompressible, turbulent flow calculation. The surface pressure is used to calculate an intermediate incident pressure. This pressure in conjunction with the sound-hard boundary condition yields the scattered pressure which accounts for the effect of the rigid airfoil. Through numerical experiments it is found that the proposed methodology is sensitive to noise in the data. Modifications that circumvent this sensitivity are under consideration.

1. Introduction

The purpose of this study is to compute noise generated by turbulent flow over a lifting surface. It is well known that if the Mach number is small then such problems can be solved using Lighthill's acoustic analogy (see Lighthill (1954)) as a starting point. In the frequency domain, Lighthill's analogy requires the solution of the Helmholtz equation to obtain a correction to the pressure. In the near field, this "correction" contains both hydrodynamic and acoustic components of pressure, whereas in the far field, it reduces to the acoustic pressure.

In particular, we wish to extend and apply the formulation developed in Oberai & Hughes (2000). In that study, the authors split pressure into an incident part and a scattered part. The incident field contains noise generated by fluid flow in the absence of the airfoil. The scattered field accounts for the effect of the rigid airfoil and is determined by applying the sound hard condition on the surface of the airfoil. This approach is akin to the works of Crighton & Leppington (1971), Chandiramani (1973), Chase (1971) and Howe (1998), among others. The distinguishing feature of the approach used in Oberai & Hughes (2000) and incorporated in our formulation is the numerical computation of the scattered field. This allows us to account for the effect of the geometry of the airfoil accurately, in particular, to model the effect of the finite chord on pressure directivity and scaling.

The work done in Oberai & Hughes (2000) was based on the vortex sound theory and was applied to the case where noise sources in the fluid were idealized as frozen vortices that are convected past the airfoil. In this study we consider the development of this methodology in the context of Lighthill's acoustic analogy and apply it to the case where the sources are determined from an incompressible, turbulent calculation. The calculation we have used for this purpose is the large-eddy simulation of turbulent flow over a wedge. The details of this calculation are provided in Wang & Moin (2000).

The layout of this manuscript is as follows: In Section 2, we develop the methodology

† Division of Mechanics and Computation, Stanford University

to compute noise in a general setting. In Section 3, we describe the specific steps involved in applying this methodology to our problem. In Section 4, we present numerical results, and we end with conclusions in Section 5.

2. Derivation of the methodology

We begin with time-harmonic version of Lighthill's analogy for a given non-dimensional frequency ω. This equation is valid in the fluid domain Ω_f, exterior to a rigid structure denoted by Ω_s, with a wet boundary denoted by Γ_s.

$$-\nabla^2 \tilde{p} - k^2 \tilde{p} = \nabla \cdot (\nabla \cdot \tilde{\mathbf{T}}) \quad \text{in } \Omega_f \tag{2.1}$$

$$\nabla \tilde{p} \cdot \mathbf{n} = 0 \quad \text{on } \Gamma_s \tag{2.2}$$

$$\lim_{r \to \infty} r(\tilde{p}_{,r} - ik\tilde{p}) = 0 \tag{2.3}$$

In the above equations, p denotes pressure-like variable that reduces to the acoustic pressure in the far-field, $k = \omega M$ is the wavenumber, $M = U/C_0$ is the Mach number, where U is the free-stream velocity, and C_0 is the speed of sound in the undisturbed ambient medium. The sign $\tilde{\ }$ over a quantity indicates its Fourier transform in time. In solving (2.1) through (2.3), it is assumed that Lighthill's turbulence tensor $\mathbf{T}$ is known. For our case, $\mathbf{T}$ is determined by solving the incompressible, Navier-Stokes equations and is given by:

$$T_{ij} = u_i u_j \tag{2.4}$$

where u_i is the fluid velocity in the ith direction. Equation (2.2) is the sound hard condition applied on the surface of the airfoil denoted by Γ_s. Equation (2.3) is the Sommerfeld condition that requires all waves to be outgoing at infinity. Throughout this paper all variables are assumed to be non-dimensional. Spatial coordinates $\mathbf{x}$ are non-dimensionalized by L, a suitably chosen length parameter. Time t is non-dimensionalized by U/L. Density ρ is non-dimensionalized by ρ_∞, its reference value in the undisturbed ambient fluid. Pressure is non-dimensionalized by the quantity $\rho_\infty U^2$.

Following the development in Oberai & Hughes (2000), we split the pressure p in the above equation into an "incident" part denoted by p_I and a "scattered" part denoted by p_S. The incident part is determined by replacing the rigid airfoil by the undisturbed ambient fluid. The equations that determine p_I are:

$$-\nabla^2 \tilde{p}_I - k^2 \tilde{p}_I = \nabla \cdot (\nabla \cdot \tilde{\mathbf{T}}) \quad \text{in } \Omega_f \bigcup \Omega_s \tag{2.5}$$

$$\lim_{r \to \infty} r(\tilde{p}_{I,r} - ik\tilde{p}_I) = 0 \tag{2.6}$$

The equations for the scattered part of the pressure may be determined by subtracting the equations for the incident pressure from the equations for the total pressure. These are given by

$$-\nabla^2 \tilde{p}_S - k^2 \tilde{p}_S = 0 \quad \text{in } \Omega_f \tag{2.7}$$

$$\nabla \tilde{p}_S \cdot \mathbf{n} = -\nabla \tilde{p}_I \cdot \mathbf{n} \quad \text{on } \Gamma_s \tag{2.8}$$

$$\lim_{r \to \infty} r(\tilde{p}_{S,r} - ik\tilde{p}_S) = 0 \tag{2.9}$$

Note that the equations for the scattered pressure are driven only by the normal derivative of the incident pressure on Γ_s and do not involve any variables from the fluid calculation.

It is well known that for the trailing-edge problem the incident pressure which represents the noise generated by quadrupoles in free space contributes very little to the far-field noise. In fact, it has been established that (see Crighton & Leppington (1971) for example),

$$|\tilde{p}_I| = \begin{cases} |\tilde{p}_S| \times O(M) & \lambda \gg l \\ |\tilde{p}_S| \times O(M^{1/2}) & \lambda \ll l \end{cases} \tag{2.10}$$

where λ is the acoustic wavelength and l is the chord length of the airfoil. Thus for small M, the contribution from the incident pressure may be neglected. In that case, we require the incident pressure only on the surface of the airfoil to calculate the scattered pressure. For the case when the acoustic sources are less than a fraction of a wavelength away from the trailing-edge, we may treat the calculation of the incident pressure to be incompressible. This amounts to setting $k = 0$ in (2.5) and (2.6). This approximation allows us to express the incident pressure in terms of the the surface pressure p_f obtained from the incompressible flow calculation. This derivation is described in the following paragraph.

Let $G(\mathbf{x}, \mathbf{y})$ be the free space Green's function for the Laplacian in three dimensions. Then for $k = 0$ in (2.5) we have,

$$p_I(\mathbf{x}) = -\int_{\Omega_f \bigcup \Omega_s} G(\mathbf{x}, \mathbf{y}) \, \nabla \cdot (\nabla \cdot \mathbf{T}(\mathbf{y})) \, d\Omega \tag{2.11}$$

$$= -\int_{\Omega_f} G(\mathbf{x}, \mathbf{y}) \, \nabla \cdot (\nabla \cdot \mathbf{T}(\mathbf{y})) \, d\Omega \tag{2.12}$$

$$= \int_{\Omega_f} G(\mathbf{x}, \mathbf{y}) \, \nabla_{\mathbf{y}}^2 \, p_f(\mathbf{y}) \, d\Omega \tag{2.13}$$

$$= \int_{\Omega_f} \nabla_{\mathbf{y}}^2 \, G(\mathbf{x}, \mathbf{y}) \, p_f(\mathbf{y}) \, d\Omega$$

$$+ \int_{\Gamma_s} \left(- G(\mathbf{x}, \mathbf{y})_{,n_y} \, p_f(\mathbf{y}) + G(\mathbf{x}, \mathbf{y}) \, p_{f,n}(\mathbf{y}) \right) d\Gamma \tag{2.14}$$

$$= p_f(\mathbf{x}) + \int_{\Gamma_s} \left(- G(\mathbf{x}, \mathbf{y})_{,n_y} \, p_f(\mathbf{y}) + Re^{-1} G(\mathbf{x}, \mathbf{y}) u_{n,nn} \right) d\Gamma \tag{2.15}$$

$$\approx p_f(\mathbf{x}) - \int_{\Gamma_s} G(\mathbf{x}, \mathbf{y})_{,n_y} \, p_f(\mathbf{y}) \, d\Gamma \tag{2.16}$$

To arrive at (2.13) from (2.12) In the above derivation, we have made use of the pressure-Poisson equation satisfied by the fluid pressure p_f in an incompressible calculation. To arrive at (2.14) from (2.13), we have used Green's formula (see Courant & Hilbert(1989) page 252.) To arrive at (2.15) from (2.14), we have made use of the fact that $p_{f,n} = Re^{-1} u_{n,nn}$, on the surface of the airfoil. This expression can be derived from momentum equation in the wall normal direction and the continuity equation. Finally, to arrive at (2.16), we have assumed that Re is sufficiently large such that the second term in the surface integral in (2.15) may be neglected.

Taking the normal derivative of the incident pressure in (2.16),taking the limit when $\mathbf{x}$ approaches the surface of the airfoil, and making use of the fact that $\tilde{p}_{f,n}$ may be neglected once again, we arrive at the following convenient expression for the normal

FIGURE 1. Cross-sectional view of the model airfoil.

derivative of the incident pressure:

$$\nabla p_I(\mathbf{x}) \cdot \mathbf{n} = -\int_{\Gamma_s} G(\mathbf{x}, \mathbf{y})_{,n_x \ n_y} \ p_f(\mathbf{y}) \ d\Gamma \qquad (2.17)$$

Equation (2.17) in conjunction with Eqs. (2.7)-(2.9) defines a complete set of equations that need to be solved to determine the far-field acoustic pressure. It is noteworthy that the only input to these equations from the fluid calculation is the knowledge of the surface pressure.

3. Implementation of the proposed methodology

The methodology derived in the previous section involves two steps. The first is the calculation of the normal derivative of the incident pressure using (2.17), and the second is the calculation of the scattered field, obtained by solving (2.7) through (2.9). In this section we describe how these calculations are performed.

3.1. *Calculation of the incident pressure*

The cross-sectional view of the model airfoil is shown in Fig. 1. In the figure and the following development, subscript 1 denotes the stream-wise direction, subscript 3 denotes the span-wise direction, and subscript 2 denotes the direction normal to the flat portion of the upper surface of the wedge. The surface of the wedge is denoted by Γ_s. Since the airfoil is assumed to be infinite in the span-wise extent in the flow calculation, we have $\Gamma_s = \bar{\Gamma}_s \times (-\infty, \infty)$, where $\bar{\Gamma}_s$ is a curve in the $y_3 = 0$ plane. The free-space Green's function for the Laplacian in three dimensions denoted by G is given by:

$$G(\mathbf{x}, \mathbf{y}) = \frac{1}{4\pi} \frac{1}{|\mathbf{x} - \mathbf{y}|} \qquad (3.1)$$

The calculation of the normal derivative of the incident pressure on Γ_s involves using (3.1) in (2.17) and evaluating the surface integral for each point $\mathbf{x}$. This calculation can be simplified if we take into account the fact that all variables in the fluid calculation, including the surface pressure, can be expressed as:

$$\bar{p}_f(y_1, y_2, y_3) = \sum_{j=-N/2+1}^{N/2} \hat{p}_f(y_1, y_2) e^{i(2\pi j/L_z)y_3}$$

$$= \sum_{k_3} \hat{p}_f e^{ik_3 y_3} \qquad (3.2)$$

where L_z is the size of the computational domain in the span-wise direction.

Using (3.1) and (3.2) in (2.17) we arrive at

$$\tilde{p}_{I,n} = \sum_{k_3} \frac{1}{4\pi} \int_{\bar{\Gamma}} \int_{-\infty}^{\infty} (\frac{3}{r^5} f_1 - \frac{1}{r^3} f_2) \ \hat{p}_f \ e^{ik_3 y_3} \ dy_3 \ dy_1 dy_2$$

$$= \sum_{k_3} \frac{1}{4\pi} \int_{\bar{\Gamma}} \hat{p}_f \left(f_1 \int_{-\infty}^{\infty} \frac{3c^{ik_3 y_3}}{r^5} dy_3 - f_2 \int_{-\infty}^{\infty} \frac{e^{ik_3 y_3}}{r^3} dy_3 \right) dy_1 dy_2 \qquad (3.3)$$

where

$$r^2 = (x_1 - y_1)^2 + (x_2 - y_2)^2 + (x_3 - y_3)^2 \qquad (3.4)$$

$$f_1 = (x_1 - y_1)(x_1 - y_1)n_{x_1}n_{y_1} + (x_1 - y_1)(x_2 - y_2)n_{x_1}n_{y_2}$$
$$+ (x_2 - y_2)(x_1 - y_1)n_{x_2}n_{y_1} + (x_2 - y_2)(x_2 - y_2)n_{x_2}n_{y_2} \qquad (3.5)$$

$$f_2 = n_{x_1}n_{y_1} + n_{x_2}n_{y_2} \qquad (3.6)$$

Now letting

$$\bar{r}^2 = (x_1 - y_1)^2 + (x_2 - y_2)^2 \ , \ \bar{y}_3 = y_3 - x_3 \qquad (3.7)$$

in (3.3) we have

$$\tilde{p}_{I,n} = \sum_{k_3} \hat{p}_{I,n} e^{ik_3 y_3} \qquad (3.8)$$

$$\hat{p}_{I,n} = \frac{1}{2\pi} \int_{\bar{\Gamma}} \hat{p}_f \left(\frac{3f_1}{2} \int_{-\infty}^{\infty} \frac{e^{ik_3 \bar{y}_3}}{(\bar{r}^2 + \bar{y}_3^2)^{5/2}} d\bar{y}_3 \right.$$
$$\left. - \frac{f_2}{2} \int_{-\infty}^{\infty} \frac{e^{ik_3 \bar{y}_3}}{(\bar{r}^2 + \bar{y}_3^2)^{3/2}} d\bar{y}_3 \right) dy_1 dy_2 \qquad (3.9)$$

Evaluating the integral in the $\bar{y}_3$ direction (see Gradshteyn & Ryzhik(1994)) we get

$$\hat{p}_{I,n} = \frac{1}{2\pi} \begin{cases} \int_{\bar{\Gamma}} \hat{p}_f \left(f_1 |k_3|^2 K_2(|k_3|\bar{r}) - \frac{f_2}{r} |k_3| K_1(|k_3|\bar{r}) \right) dy_1 dy_2 & k_3 \neq 0 \\[4mm] \int_{\bar{\Gamma}} \frac{\hat{p}_f}{\bar{r}^2} \left(2f_1 - f_2 \right) dy_1 dy_2, & k_3 = 0 \end{cases} \qquad (3.10)$$

where $K_n(z)$ is the modified Bessel function of order n (see Abramowitz & Stegun (1970), pg. 374). Equations (3.10) and (3.8) are the expressions used to evaluate the normal derivative of the pressure field. Through the use of a Fourier transform in the y_3 direction, we have transformed the surface integral in (2.17) to a line integral for each k_3 in (3.10).

3.2. *Evaluation of the scattered field*

Once the incident field is known, it remains to solve Eqs. (2.7) through (2.9) to determine the scattered field. To solve these equations we write an equivalent weak formulation for the problem, given by: Find $\tilde{p}_S \in \mathcal{S} = H^1(\Omega_a)$, such that

$$(\nabla w, \nabla \tilde{p}_S) - k^2(w, \tilde{p}_S) - (w, M(\tilde{p}_S))_{\Gamma_a} = -(w, \nabla \tilde{p}_I \cdot \mathbf{n})_{\Gamma_s}, \forall w \in \mathcal{S} \qquad (3.11)$$

In the above equation the inner product $(\cdot, \cdot)$ is defined as

$$(w, u) \equiv \int_{\Omega_a} w^* u \, d\omega \qquad (3.12)$$

where Ω_a is the bounded domain obtained by truncating the unbounded fluid domain Ω_f at the surface Γ_a. The Euler-Lagrange equations associated with (3.11) are the Helmholtz equation (2.7), the boundary condition on Γ_s (2.8), and the following boundary condition on Γ_a

$$\nabla \tilde{p}_S \cdot \mathbf{n} = M(\tilde{p}_S) \qquad (3.13)$$
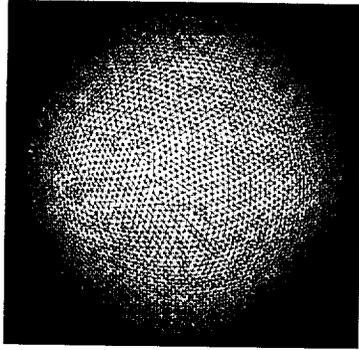
FIGURE 2. Finite element mesh on the truncating surface.
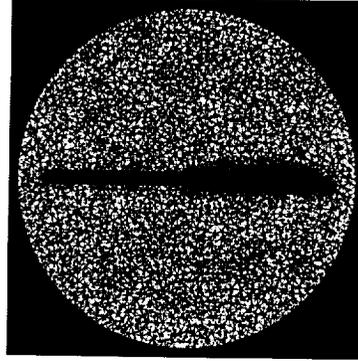
FIGURE 3. Finite element mesh through the mid-span.

In this example we choose Γ_a to be a sphere and M to be the exact Dirichlet to Neumann (DtN) map (see Grote & Keller (1995)) that renders (3.11) equivalent to (2.7) through (2.9). We solve (3.11) using a Galerkin approximation and the finite element discretization.

4. Numerical results and discussion

The time-history of surface pressure obtained from the fluid calculation was split into 8 windows of equal length (see Wang & Moin (2000) for details on the fluid calculation). Data for each of these windows was then Fourier transformed in time to obtain the surface pressure distribution for each frequency ω. Each of these sets were further Fourier transformed in the y_3 direction, and (3.10) was used to evaluate the contribution of each mode (k_3) to the incident pressure. The contribution from all of the modes was then summed using using an inverse Fourier transform (3.8) to obtain $\tilde{p}_{I,n}$.

To calculate the scattered pressure field, (3.11) was solved using a Galerkin approximation and finite element discretization. The truncating boundary for the acoustic calculation denoted by Γ_a was chosen to be a sphere of radius 12.5 units. On this surface the truncated modified DtN map (Grote & Keller (1995)) was applied. The acoustic domain completely encloses the wedge whose chord length is 21.5 units. The details of the geometry of the wedge are described in Wang & Moin (2000). For the acoustic calculation the span-wise length of the wedge was chosen to be 4 units. The incident surface pressure was applied on a strip of width $L_z = 0.5$ units in the span-wise direction, centered along the mid-span of the wedge. In the LES calculation only the part of the wedge 8 units upstream from the trailing edge was modeled. Thus surface pressure data was available for only this portion. To account for this in the acoustic calculation, starting from a location 4.5 units upstream of the trailing edge, $\tilde{p}_{I,n}$ was linearly scaled down to zero at 8 units from the trailing edge.

The resulting linear system of equations was solved using the QMR algorithm in conjunction with the SSOR preconditioner, with the special matrix-vector product algorithms described in Oberai, Malhotra, & Pinsky (1998). We employed 761,017 tetrahedral finite elements to model the acoustic domain. This corresponds to 147,036 unknowns. The surface mesh on the truncating surface is shown in Fig. 2, and the finite element mesh though the mid-plane of the wedge is shown in 3. In this figure we observe the clustering of the mesh near the surface of the airfoil to resolve the incident pressure field.
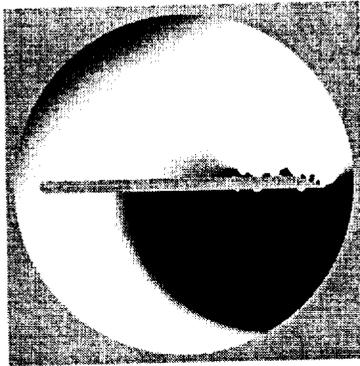
FIGURE 4. Real part of the solution for $\omega = 3.376$.
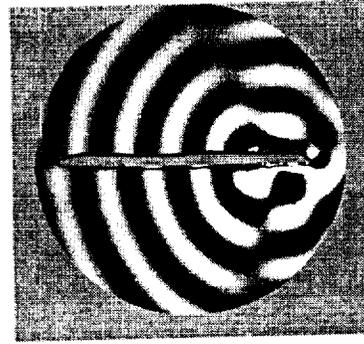
FIGURE 5. Real part of the solution for $\omega = 20.28$.

The problem of trailing edge noise shows an interesting behavior with the variation of the ratio of the acoustic wavelength to the chord length $(\lambda/l.)$ In the low frequency regime $\lambda/l \gg 1$, the far-field pressure directivity is like that of a dipole, and the scaling of *non-dimensional* pressure (non-dimensionalized by $\rho_\infty U^2$) intensity with the Mach number is of order M^2. In the high frequency regime, $\lambda/l \ll 1$, the far-field pressure directivity is like that of a cardioid, and the scaling of pressure intensity is of order M^1. In Oberai & Hughes (2000), using an approach analogous to the one developed herein, the authors were able to recover these two theoretical extremes and also shed light on the intermediate range of frequencies. However, in that study the authors modeled the noise sources as idealized line vortices and derived an analytical expression for the incident pressure field for the acoustic calculation. It is one of the goals of this study to validate the applicability of this approach for the case when the flow field and hence the noise sources are obtained from a LES of turbulent flow. Through extensive numerical tests we have found the numerical noise in the data from the turbulent calculation is sufficient to corrupt the behavior of the solution substantially, and the approach described above may lead to erroneous results. We base our conclusion on the unphysical far-field directivity pattern obtained for some test cases and, more quantitatively, on the incorrect scaling of pressure intensity with Mach number obtained for most test cases.

First, we present results for a fixed Mach number $(M = 0.088)$ at two frequencies $(\omega = 3.376 \& 20.28.)$ The real part of the solution for these cases is shown in Figs. 4 and 5, and the imaginary parts of the solution are shown in Figs. 6 and 7. The corresponding far-field directivity patterns are shown in Figs. 8 and 9. While these pictures appear reasonable, at least qualitatively, it is difficult to draw any definitive conclusions from them.

To assess whether the proposed approach captures the characteristics of the trailing edge problem, we examine the variation of total far-field acoustic intensity $\tilde{\phi}$ with the Mach number. We define the total acoustic intensity as

$$\tilde{\phi} = \lim_{R \to \infty} \int_{\Gamma_R} |\tilde{p}_S|^2 \, d\Gamma \qquad (4.1)$$

It can be easily verified that this quantity tends to a constant value in the limit $R \to \infty$ and that in the low frequency regime $\lambda \gg l$ it varies with Mach number as $\tilde{\phi} = O(M^2)$, while in the high frequency regime $\lambda \ll l$ it varies as $\tilde{\phi} = O(M^1)$. In Fig. 10, for a given frequency $\omega = 10.14$, we have plotted $\tilde{\phi}$ as a function of Mach number. In this
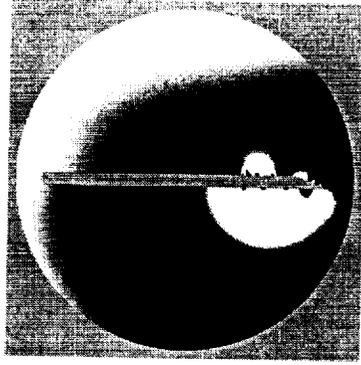
FIGURE 6. Imaginary part of the solution for
$\omega = 3.376$.
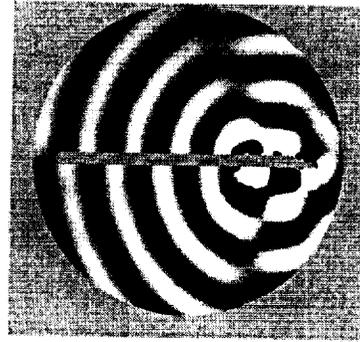
FIGURE 7. Imaginary part of the solution for
$\omega = 20.28$.
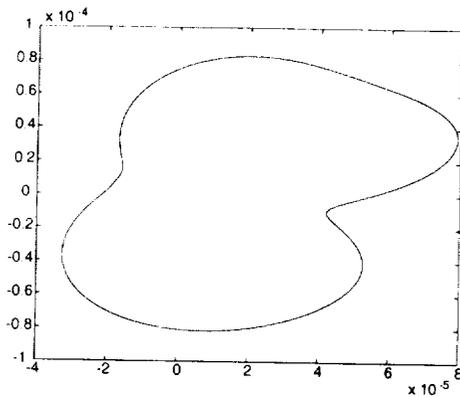
FIGURE 8. Far-field pressure directivity for
$\omega = 3.376$.
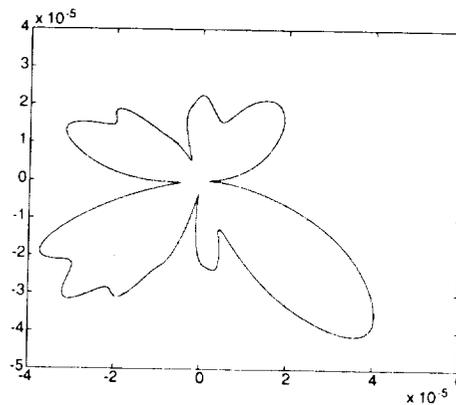
FIGURE 9. Far-field pressure directivity for
$\omega = 20.28$.

plot $M \in (0.026, 0.158)$, which corresponds to $l/\lambda \in (0.89, 5.3)$. In this regime we would expect $\tilde{\phi} = O(M^1)$, associated with a cardioid-like directivity. However, from the plot we observe that $\tilde{\phi} = O(M^0)$, which is the scaling for a monopole source. This indicates the inability of the proposed approach to solve the problem accurately.

This shortcoming can be understood analytically by applying the proposed approach to a simplified problem. Consider the noise produced by a distribution of quadrupole sources above a rigid infinite plate. Let the position of the plate be given by $y_2 = 0$. The solution to this problem is the sum of the noise produced in free space by the quadrupoles above the plate and the noise produced by a fictitious distribution obtained by mirroring the original sources about $y_2 = 0$. It can be easily shown (see Goldstein (1976)) that for compact acoustic sources $L \ll \lambda$, the intensity of noise scales as $O(M^4)$. To solve this problem using the approach developed in this paper, we would first calculate the incident pressure $\tilde{p}_{I,n}$ associated with the given distribution of quadrupoles. Thereafter, we would calculate the scattered field given by:

$$\tilde{p}_S(\mathbf{x}) = \int_{\Gamma_s} G_S(\mathbf{x}, \mathbf{y}) \, \tilde{p}_{I,n}(\mathbf{y}) d\Gamma \tag{4.2}$$

In the above integral G_S is the sound-hard Green's function. For the infinite plate, using
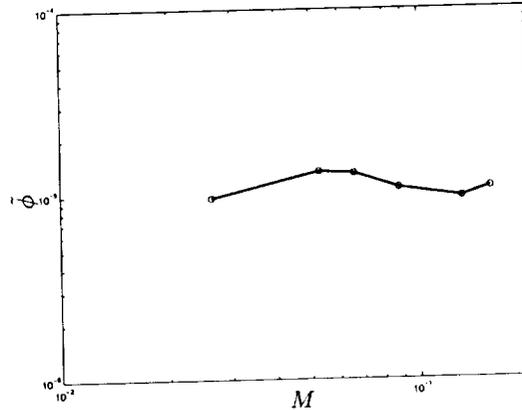
FIGURE 10. Total far-field acoustic intensity $\tilde{\phi}$ as a function of Mach number M, for $\omega = 10.14$.

the method of images, this is given by

$$G_S(\mathbf{x}, \mathbf{y}) = \frac{1}{4\pi}\left(\frac{e^{ik|\mathbf{x}-\mathbf{y}|}}{|\mathbf{x}-\mathbf{y}|} + \frac{e^{ik|\mathbf{x}-\mathbf{y}'|}}{|\mathbf{x}-\mathbf{y}'|}\right) \tag{4.3}$$

where $\mathbf{y}' \equiv [y_1, -y_2, y_3]^T$. Using this expression in (4.2) and evaluating the integral for an observation point in the far-field and a compact acoustic source around the origin, we get:

$$\tilde{p}_S(\mathbf{x}) \approx \frac{1}{2\pi}\frac{e^{ik|\mathbf{x}|}}{|\mathbf{x}|} \times \int_{\Gamma_s} \tilde{p}_{I,n}(\mathbf{y})d\Gamma$$

$$\approx O(M^0) \times \int_{\Gamma_s} \tilde{p}_{I,n}(\mathbf{y})d\Gamma \tag{4.4}$$

For this result to have the correct behavior with Mach number (i.e. $O(M^4)$), the integral in (4.4) must behave as $O(M^4)$. For acoustic sources obtained from an incompressible flow calculation, $\tilde{p}_{I,n}$ has no Mach number dependence, and the best case scenario is given by the case when the integral in the above equation vanishes. For turbulent flow calculations it is unreasonable to expect that $\tilde{p}_{I,n}$ can be determined with sufficient accuracy for this to happen. Therefore, we can expect the proposed formulation to yield results consistent with the presence of spurious monopoles while the true solution precludes their possibility. This is precisely what is observed in Fig. 9.

5. Conclusions

We have developed and implemented a formulation to calculate noise generated by low-Mach number flows. The advantages of this approach are that in the acoustic problem it accounts for the geometry of the structure accurately and requires only the surface pressure from an incompressible fluid calculation. We have applied this methodology to compute the noise generated by a turbulent flow over a trailing edge. We have found that this approach is not robust enough to provide accurate results with pressure data obtained from turbulent calculations. This is attributed to the fact that in calculating the scattered field, all sources are treated as monopole sources. Therefore, to accurately predict noise that has higher-order multipole components, the incident pressure needs to

be evaluated extremely accurately so that cancellations may lead to the right acoustic component. For the problem solved in this study, we have found that this is not the case.

To overcome this drawback it seems natural to work with an approach that takes as input sources of the highest multipole order in the solution (quadrupoles for our case.) One such approach is to solve the weak form of Lighthill's equations (2.1) through (2.3). This has been done in Oberai, Roknaldin & Hughes (2000), where the authors were able to reproduce the dipole character of the acoustic solution for the low frequency case. As a continuation of this study, we will explore the applicability of this approach to our problem.

REFERENCES

ABRAMOWITZ, M. & STEGUN, I. A. 1970 Handbook of Mathematical Functions. Dover Publications Inc.

CHANDIRAMNI, K. L. 1973 Diffraction of evanescent waves, with applications to aerodynamically scattered sound and radiation from unbaffled plates. *J. Acoust. Soc. Am.* **55(1)**, 18-29.

CHASE, D. M. 1986 Sound Radiated by Turbulent Flow off a Rigid Half-Plane Obtained from a Wavevector Spectrum of Hydrodynamic Pressure. *J. Acoust. Soc. Am.* **52(3)**, 1011-1023.

COURANT R. & HILBERT D. 1989 *Methods of Mathematical Physics*. John Wiley & Sons.

CRIGHTON, D. G. & LEPPINGTON, F. G. 1970. On the scattering of aerodynamic noise. *J. Fluid Mech.* **46(3)**, 577-597.

GOLDSTEIN M. E. 1976 *Aeroacoustics*. McGraw-Hill, Inc.

GRADSHTEYN, I. S. & RYZHIK, I. M. 1994 *Table of integrals, series, and products*. Academic Press.

GROTE, M. J. & KELLER, J. B. 1995 On non-reflecting boundary conditions. *J. Comput. Phys.* **122(2)**, 231-243.

HOWE, M. S. 1998 Trailing Edge Noise at Low Mach Numbers. *J. Sound Vib.* **225(2)**, 211-238.

LIGHTHILL, M. J. 1954 On Sound Generated Aerodynamically I. General Theory. *Proc. Roy. Soc. (London).* **211A, 1107**, 1-32.

OBERAI, A. A. & HUGHES, T. J. R. 2000 Computation of trailing-edge noise for a finite chord airfoil. *In preparation.*

OBERAI A. A., MALHOTRA, M. AND PINSKY, P. M. 1995 Implementation of the Dirichlet-to-Neumann radiation condition for iterative solution of the Helmholtz equation. *App. Num. Math.* **27(4)**, 443-464.

OBERAI, A. A., ROKNALDIN, F. & HUGHES, T. J. R. 2000 Computational Procedures for Determining Structural Acoustic Response due to Hydrodynamic Sources. To appear in *Comp. Meth. Appl. Mech. & Engr.*

WANG, M., & MOIN, P. 2000 Computation of trailing-edge flow and noise using large-eddy simulation. To appear in *AIAA J.*

Participants' Countries/Institutions

Country	Institution
Australia	Defence Science Technology Organisation University of Melbourne
Belgium	Universite Libre de Bruxelles
Canada	University of Waterloo
France	Service d'astrophysique, CE Saclay CERFACS CNRS Domaine Universitaire Ecole Centrale Paris University of Montpellier II
Germany	Univ. Karlsruhe (TH)
Italy	University of Rome
Netherlands	Delft University of Technology
Norway	Kongsberg Defence & Aerospace
Switzerland	ABB Alstom Power Technology Swiss Federal Institute of Technology Zurich
USA	California Institute of Technology DOW Chemical Northwestern University Pennsylvania State University Stanford University United Technologies Research Center University of California at Berkeley University of California at Los Angeles University of California at Davis University of California at San Diego University of Illinois at Chicago University of Missouri-Columbia University of San Diego University of Wisconsin-La Crosse